

SOLID MECHANICS AND ITS APPLICATIONS

Martin Philip Bendsøe, Niels Olhoff
and Ole Sigmund (Eds.)

IUTAM Symposium on
**Topological Design
Optimization of
Structures, Machines
and Materials**

IUTAM

 Springer

IUTAM Symposium on Topological Design Optimization of Structures,
Machines and Materials

SOLID MECHANICS AND ITS APPLICATIONS

Volume 137

Series Editor: G.M.L. GLADWELL
Department of Civil Engineering
University of Waterloo
Waterloo, Ontario, Canada N2L 3G1

Aims and Scope of the Series

The fundamental questions arising in mechanics are: *Why?*, *How?*, and *How much?*
The aim of this series is to provide lucid accounts written by authoritative researchers giving vision and insight in answering these questions on the subject of mechanics as it relates to solids.

The scope of the series covers the entire spectrum of solid mechanics. Thus it includes the foundation of mechanics; variational formulations; computational mechanics; statics, kinematics and dynamics of rigid and elastic bodies; vibrations of solids and structures; dynamical systems and chaos; the theories of elasticity, plasticity and viscoelasticity; composite materials; rods, beams, shells and membranes; structural control and stability; soils, rocks and geomechanics; fracture; tribology; experimental mechanics; biomechanics and machine design.

The median level of presentation is the first year graduate student. Some texts are monographs defining the current state of the field; others are accessible to final year undergraduates; but essentially the emphasis is on readability and clarity.

For a list of related mechanics titles, see final pages.

IUTAM Symposium on Topological Design Optimization of Structures, Machines and Materials

Status and Perspectives

Edited by

MARTIN PHILIP BENDSØE

*Technical University of Denmark,
Kgs. Lyngby, Denmark*

NIELS OLHOFF

*Aalborg University, Aalborg East,
Denmark*

and

OLE SIGMUND

*Technical University of Denmark,
Kgs. Lyngby, Denmark*



Springer

A C.I.P. Catalogue record for this book is available from the Library of Congress.

ISBN-10 1-4020-4729-0 (HB)
ISBN-13 978-1-4020-4729-9 (HB)
ISBN-10 1-4020-4752-5 (e-book)
ISBN-13 978-1-4020-4752-7 (e-book)

Published by Springer,
P.O. Box 17, 3300 AA Dordrecht, The Netherlands.

www.springer.com

Printed on acid-free paper

All Rights Reserved

© 2006 Springer

No part of this work may be reproduced, stored in a retrieval system, or transmitted in any form or by any means, electronic, mechanical, photocopying, microfilming, recording or otherwise, without written permission from the Publisher, with the exception of any material supplied specifically for the purpose of being entered and executed on a computer system, for exclusive use by the purchaser of the work.

Printed in the Netherlands.

TABLE OF CONTENTS

Preface	xi
In Memoriam – John E. Taylor (1931–2005)	xiii
Level Sets, FEM, and Sound	
Coupling the Level Set Method and the Topological Gradient in Structural Optimization <i>Grégoire Allaire and François Jouve</i>	3
Parametric Shape and Topology Optimization with Radial Basis Functions <i>Michael Yu Wang and Shengyin Wang</i>	13
Generalized Shape Optimization Using X-FEM and Level Set Methods <i>Pierre Duysinx, Laurent Van Miegroet, Thibault Jacobs and Claude Fleury</i>	23
Topology Design of Three-Dimensional Structures Using Hybrid Finite Elements <i>C.S. Jog</i>	33
Topology Optimization of Vibrating Bi-Material Structures with Respect to Sound Radiation <i>Niels Olhoff and Jianbin Du</i>	43
Classics Revisited	
Force Fields within Michell-Like Cantilevers Transmitting a Point Load to a Straight Support <i>Cezary Graczykowski and Tomasz Lewiński</i>	55
Reflections on Truss and Continuum Topology Optimal Designs <i>Pauli Pedersen and Niels L. Pedersen</i>	67

Some Basic Issues of Topology Optimization	77
<i>George I.N. Rozvany, Vanda Pomezanski, Osvaldo M. Querin, Zsolt Gaspar and Janos Logo</i>	

Composites and Cellular Structures

On Discrete Material Optimization of Laminated Composites Using Global and Local Criteria	89
<i>Jan Stegmann and Erik Lund</i>	

Analysis and Continuum Topology Optimization of Periodic Solids with Linearized Elastic Buckling Criterion	99
<i>Miguel Matos Neves</i>	

Design of Cellular Structure for Optimum Efficiency of Heat Dissipation – A Three-Dimensional Formulation	107
<i>Bo Wang and Gengdong Cheng</i>	

Layout of Tileable Multistable Structures Using Topology Optimization	117
<i>Jitendra Prasad and Alejandro R. Diaz</i>	

Topology Optimization of Dispersion Properties in Optical Fibres	127
<i>Jesper Riishede and Kristian Hougaard</i>	

Optimal Design with Small Contrast	137
<i>Grégoire Allaire and Sergio Gutiérrez</i>	

Eigenfrequency and Buckling Optimization of Laminated Composite Shell Structures Using Discrete Material Optimization	147
<i>Erik Lund and Jan Stegmann</i>	

Effect of Internal Length Scale on Optimal Topologies for Cosserat Continua	157
<i>Massimiliano Gei, Marco Rovati and Daniele Veber</i>	

Mathematical Programming and Modelling

Cellular Automata Paradigm for Topology Optimisation	169
<i>Mostafa M. Abdalla, Shahriar Setoodeh and Zafer Gürdal</i>	

<i>Table of Contents</i>	vii
A One Shot Approach to Topology Optimization with Local Stress Constraints <i>Roman Stainko and Martin Burger</i>	181
A Concept for Global Optimization of Topology Design Problems <i>Mathias Stolpe, Wolfgang Achtziger and Atsushi Kawamoto</i>	185
Image Processing Ideas and Level Sets	
Impedance Imaging for Inhomogeneities of Low Volume Fraction <i>Yves Capdeboscq</i>	197
The Phase-Field Method in Optimal Design <i>Blaise Bourdin and Antonin Chambolle</i>	207
Level Set based Shape Optimization of Geometrically Nonlinear Structures <i>Seonho Cho, Seung-Hyun Ha and Min-Geun Kim</i>	217
Industry and Software	
Industrial Implementation and Applications of Topology Optimization and Future Needs <i>Claus B.W. Pedersen and Peter Allinger</i>	229
Recent Developments in the Commercial Implementation of Topology Optimization <i>Uwe Schramm and Ming Zhou</i>	239
Mechanisms and Multiphysics	
Configuration Design of Rigid Link Mechanisms by an Optimization Method: A First Step <i>Yoon Young Kim, Gang Won Jang, Jung Hun Park, Jin Seup Hyun and Sang Jun Nam</i>	251
The Pressure Load Problem Re-Visited <i>Peter Michael Clausen and Ole Sigmund</i>	261
Topology Optimization in Magnetic Fields <i>Jeonghoon Yoo</i>	269

Electro-Mechanical Topology Optimization Considering Non-Matching Meshes <i>Michael Raulli</i>	277
--	-----

Waves

Structural Topology Optimization of Mechanical Resonators, Actuators and Sensors <i>Shinji Nishiwaki, Emilio C.N. Silva, Kazumi Matsui, Kenjiro Terada, Kazuhiro Izui and Masataka Yoshimura</i>	291
Topology Optimization of Wave Transducers <i>Eddie Wadbro and Martin Berggren</i>	301
Optimal Mode Coupling in Simple Planar Waveguides <i>David C. Dobson</i>	311

Geometry Modelling

Topology Optimization by Penalty (TOP) Method <i>T.E. Bruns</i>	323
Topology Optimization with CAMD for Structures Undergoing Finite Deformation <i>K. Matsui, K. Terada and S. Nishiwaki</i>	333
Spectral Level Set Methodology in the Design of a Morphing Airfoil <i>Alexandra A. Gomes and Afzal Suleman</i>	343

Acoustics and Fluids and Actuators

Topology Optimization for Acoustic-Structure Interaction Problems <i>Gil Ho Yoon, Jakob Søndergaard Jensen and Ole Sigmund</i>	355
Topology Optimization of Mass Distribution Problems in Stokes Flow <i>Allan Gersborg-Hansen, Martin Berggren and Bernd Dammann</i>	365
Topology Optimization for Acoustic Problems <i>Maria Bayard Dühning</i>	375

<i>Table of Contents</i>	ix
Topology Optimization of Wave-Propagation Problems <i>Jakob S. Jensen and Ole Sigmund</i>	387
Topology Optimization of Piezoelectric Actuators Considering Geometric Nonlinearities <i>Eduardo Lenz Cardoso and Jun Sérgio Ono Fonseca</i>	391
Mathematical Programming Issues	
The Worst-Case Multiple Load FMO Problem Revisited <i>Michal Kočvara and Michael Stingl</i>	403
Simultaneous Optimization of Truss Topology and Geometry, Revisited <i>Wolfgang Achtziger</i>	413
Topology Optimization by Sequential Integer Linear Programming <i>Krister Svanberg and Mats Werme</i>	425
Bio	
Bio-Inspired Material Design and Optimization <i>Xu Guo and Huajian Gao</i>	439
Protein Sequence Design on the Basis of Topology Optimization Techniques – Using Continuous Modeling of Discrete Amino Acid Types <i>G.K. Ananthasuresh</i>	455
Topological Derivatives, Reliability, and Other Features	
Topological-Shape Sensitivity Method: Theory and Applications <i>A.A. Novotny, R.A. Feijóo, E. Taroco and C. Padra</i>	469
Topological Derivatives for Contact Problems – Conical Differentiability and Asymptotic Analysis <i>Jan Sokółowski and Antoni Żochowski</i>	479
Reliability-Based Topology Optimization (RBTO) <i>Semyung Wang, Heegon Moon, Chwail Kim, Jenam Kang and Kyung K. Choi</i>	493

A Feature-Based Structural Topology Optimization Method <i>Gengdong Cheng, Yulin Mei and Xiaoming Wang</i>	505
---	-----

Composites and Graded Materials

Design of Fiber Reinforced Shafts Subject to Local Stress Constraints through Inverse Homogenization – A Preliminary Study on Fiber Size Effect <i>Robert Lipton and Michael Stuebner</i>	517
--	-----

Hierarchical Optimization of Material and Structure for Thermal Transient Problems <i>J.M. Guedes, E. Lubrano, H.C. Rodrigues and S. Turteltaub</i>	527
--	-----

Optimization of Foam Filled Structures Using Gradient Algorithms <i>A. Lipka and E. Ramm</i>	537
---	-----

Fluids and Materials

The Darcy–Stokes Topology Optimization Problem <i>Niclas Wiker, Anders Klarbring and Thomas Borrvall</i>	551
---	-----

Topology Optimization of Fluid Problems by the Lattice Boltzmann Method <i>Anton Evgrafov, Georg Pingen and Kurt Maute</i>	559
---	-----

A Class of Optimal Two-Dimensional Multimaterial Conducting Laminates <i>Nathan Albin, Andrej Cherkaev and Vincenzo Nesi</i>	569
---	-----

New Approaches

Multidisciplinary Topology Design and Partial Differential Games <i>Abderrahmane Habbal</i>	585
--	-----

Coupling Topological Gradient and Gauss–Newton Method <i>Jérôme Fehrenbach and Mohamed Masmoudi</i>	595
--	-----

Author Index	605
--------------	-----

Subject Index	607
---------------	-----

PREFACE

This book contains the refereed and edited versions of papers presented at the IUTAM Symposium on *Topological Design Optimization of Structures, Machines and Materials: Status and Perspectives*, held at Rungstedgaard, near Copenhagen, Denmark, October 26–29, 2005. The symposium was attended by 74 scientists from 19 countries, and the programme was intensive and included also two evenings for presentations and discussions.

It is now more than 15 years ago that the so-called homogenization method was proposed as a basis for computational means to optimize the topology and shape of continuum structures. From initially being capable mainly of treating minimum compliance design we now see the basic material distribution idea of the methodology applied to a wide range of structural and mechanical problems as well as to problems that couple structural response to other physical responses. Also, the method has provided insight for micro-mechanical studies, meaning that the method has given feedback to the area which provided impetus to the field of topological design optimization in its creation. Finally, topological design is now an integral part of most FEM software systems and it has become a standard industrial tool in some fields.

The IUTAM Symposium provided a forum for the exchange of ideas for future developments in the area of topological design optimization. This encompassed the application to fluid-solid interaction problems, acoustics problems, and to problems in biomechanics, as well as to other multiphysics problems. New basic modelling paradigms, covering new geometry modelling such as level-set methods and topological derivatives, as well as developments in computational approaches were also focus areas.

Without the sponsorship from the International Union of Theoretical and Applied Mechanics (IUTAM) and the International Society for Structural and Multidisciplinary Optimization (ISSMO), and the financial support from the Danish Center for Applied Mathematics and Mechanics (DCAMM), the Villum Kann Rasmussen Foundation, and the Poul Due Jensen Foundation, the symposium and this book would not have been possible. The financial support from the Department of Mechanical Engineering, Aalborg University, and from the Department of Mathematics and the Department of Mechanical Engineering, Technical University of Denmark, is also gratefully acknowledged.

The editors are indebted to the members of the Scientific Committee, Professors Gregoire Allaire, Gengdong Cheng, Alejandro R. Diaz, Noboru Kikuchi, Yoon Young Kim, Kurt Maute, and Helder C. Rodrigues, for their advice and help in organizing the symposium. The organization of the symposium was a shared effort between the Technical University of Denmark and University of Aalborg, Denmark, and the smooth running of the production of this volume is greatly attributed to the competent work of Jan Stegmann, University of Aalborg, and of Jolanda Karada, Karada Publishing Services. We are also grateful to Ciro Soto who provided the picture of John E. Taylor.

Lyngby and Aalborg, December 2005

Martin P. Bendsøe
Niels Olhoff
Ole Sigmund



In memory of
John E. Taylor
April 17, 1931–October 24, 2005

Level Sets, FEM and Sound

COUPLING THE LEVEL SET METHOD AND THE TOPOLOGICAL GRADIENT IN STRUCTURAL OPTIMIZATION

Grégoire Allaire and François Jouve

*Centre de Mathématiques Appliquées (UMR 7641), Ecole Polytechnique,
91128 Palaiseau, France*

gregoire.allaire@polytechnique.fr, francois.jouve@polytechnique.fr

Abstract: A numerical coupling of two recent methods in shape and topology optimization of structures is proposed. On the one hand, the level set method, based on the shape derivative, is known to easily handle boundary propagation with topological changes. However, in practice it does not allow for the nucleation of new holes. On the other hand, the bubble or topological gradient method is precisely designed for introducing new holes in the optimization process. Therefore, the coupling of these two methods yields an efficient algorithm which can escape from local minima. It has a low CPU cost since it captures a shape on a fixed Eulerian mesh. The main advantage of our coupled algorithm is to make the resulting optimal design more independent of the initial guess.

Keywords: Shape and topology optimization, level set method, topological gradient.

1. INTRODUCTION

Numerical methods of shape and topology optimization based on the level set representation and on shape differentiation make possible topology changes during the optimization process. But they do not solve the inherent problem of ill-posedness of shape optimization which manifests itself in the existence of many local minima, usually having different topologies. The reason is that the level set method can easily remove holes but can not create new holes in the middle of a shape. In practice, this effect can be checked by varying the initialization which yields different optimal shapes with different topologies. This absence of a nucleation mechanism is an inconvenience mostly in 2-d: in 3-d, it is less important since holes can appear by pinching two boundaries.

In [2] we have proposed, as a remedy, to couple our previous method with the topological gradient method (cf. [9–11, 20, 21]). Roughly speaking it amounts to decide whether or not it is favorable to nucleate a small hole in

a given shape. Creating a hole changes the topology and is thus one way of escaping local minima. Our coupled method of topological and shape gradients in the level set framework is therefore much less prone to finding local, nonglobal, optimal shapes. For most of our 2-d numerical examples of compliance minimization, the expected global minimum is attained from the trivial full domain initialization.

We provide a new 2-d numerical example showing that the level set method coupled to the topological gradient can reach an optimum of the objective function, very close to the one obtained by the homogenization method, starting from a trivial initial state. Then a new 3-d example is proposed. Although its solution has a rather complicated topology, it is obtained by the regular level set method, with different initializations, as well as by the coupled method. Thus the introduction of the topological gradient is not useful to reach such a complex 3-d solution.

2. SETTING OF THE PROBLEM

We restrict ourselves to linear elasticity. A shape is a bounded open set $\Omega \subset \mathbb{R}^d$ ($d = 2$ or 3) with a boundary made of two disjoint parts Γ_N and Γ_D , submitted to respectively Neumann and Dirichlet boundary conditions. All admissible shapes Ω are required to be a subset of a working domain $D \subset \mathbb{R}^d$. The shape Ω is occupied by a linear isotropic elastic material with Hooke's law A defined, for any symmetric matrix ξ , by $A\xi = 2\mu\xi + \lambda(\text{Tr}\xi)\text{Id}$, where μ and λ are the Lamé moduli. The displacement field u is the solution of the linearized elasticity system

$$\begin{cases} -\text{div}(A e(u)) = f & \text{in } \Omega \\ u = 0 & \text{on } \Gamma_D \\ (A e(u))n = g & \text{on } \Gamma_N, \end{cases} \quad (1)$$

where $f \in L^2(D)^d$ and $g \in H^1(D)^d$ are the volume forces and the surface loads. If $\Gamma_D \neq \emptyset$, (1) admits a unique solution in $u \in H^1(\Omega)^d$. The objective function is denoted by $J(\Omega)$. In this paper, only the compliance will be considered:

$$J(\Omega) = \int_{\Omega} f \cdot u \, dx + \int_{\Gamma_N} g \cdot u \, ds = \int_{\Omega} A e(u) \cdot e(u) \, dx. \quad (2)$$

To avoid working on a problem with a volume constraint, we introduce a Lagrange multiplier ℓ and consider the minimization

$$\inf_{\Omega \subset D} \mathcal{L}(\Omega) = J(\Omega) + \ell|\Omega|. \quad (3)$$

3. SHAPE DERIVATIVE

To apply a gradient method to the minimization of (3) we recall the classical notion of shape derivative (see e.g. [15, 17, 19, 22]). Starting from a smooth open set Ω , we consider domains of the type $\Omega_\theta = (\text{Id} + \theta)(\Omega)$, with Id the identity mapping of \mathbb{R}^d and θ a vector field in $W^{1,\infty}(\mathbb{R}^d, \mathbb{R}^d)$. For small θ , $(\text{Id} + \theta)$ is a diffeomorphism in \mathbb{R}^d .

Definition: The shape derivative of J at Ω is defined as the Fréchet derivative at 0 of the application $\theta \rightarrow J((\text{Id} + \theta)(\Omega))$, i.e.

$$J((\text{Id} + \theta)(\Omega)) = J(\Omega) + J'(\Omega)(\theta) + o(\theta) \quad \text{with} \quad \lim_{\theta \rightarrow 0} \frac{|o(\theta)|}{\|\theta\|} = 0,$$

where $J'(\Omega)$ is a continuous linear form on $W^{1,\infty}(\mathbb{R}^d, \mathbb{R}^d)$.

We recall the following classical result (see [4] and references therein).

Theorem 1 (shape derivative for the compliance): *Let Ω be a smooth bounded open set and $\theta \in W^{1,\infty}(\mathbb{R}^d, \mathbb{R}^d)$. If $f \in H^1(\Omega)^d$, $g \in H^2(\Omega)^d$, $u \in H^2(\Omega)^d$, then the shape derivative of (2) is*

$$\begin{aligned} J'(\Omega)(\theta) &= \int_{\Gamma_N} \left(2 \left[\frac{\partial(g \cdot u)}{\partial n} + Hg \cdot u + f \cdot u \right] - Ae(u) \cdot e(u) \right) \theta \cdot n \, ds \\ &\quad + \int_{\Gamma_D} Ae(u) \cdot e(u) \theta \cdot n \, ds, \end{aligned}$$

where H is the mean curvature defined by $H = \text{div } n$.

4. TOPOLOGICAL DERIVATIVE

One drawback of the method of shape derivative is that no nucleation of holes inside the domain are allowed. Numerical methods based on the shape derivative may therefore fall into a local minimum. A remedy to this inconvenience has been proposed as the bubble method, or topological asymptotic method [10, 11, 21]. The main idea is to test the optimality of a domain to topology variations by removing a small hole with appropriate boundary conditions.

We give a brief review of this method that we shall call in the sequel topological gradient method. Consider an open set $\Omega \subset \mathbb{R}^d$ and a point $x_0 \in \Omega$. Introduce a fixed model hole $\omega \subset \mathbb{R}^d$, a smooth open bounded subset containing the origin. For $\rho > 0$ we define the translated and rescaled hole $\omega_\rho = x_0 + \rho\omega$ and the perforated domain $\Omega_\rho = \Omega \setminus \bar{\omega}_\rho$. The goal is to study the variations of the objective function $J(\Omega_\rho)$ as $\rho \rightarrow 0$.

Definition: If the objective function admits the following so-called topological asymptotic expansion for small $\rho > 0$

$$J(\Omega_\rho) = J(\Omega) + \rho^d D_T J(x_0) + o(\rho^d),$$

then $D_T J(x_0)$ is called the topological derivative at point x_0 .

If the model hole ω is the unit ball, the following result gives the expression of the topological derivative for the compliance $J(\Omega)$ with Neumann boundary conditions on the hole (see [11, 21]).

Theorem 2: Let ω be the unit ball of \mathbb{R}^d . If $f = 0$, $g \in H^2(\Omega)^d$ and $u \in H^2(\Omega)^d$, then $\forall x \in \Omega \subset \mathbb{R}^2$, if $C_2 = \pi(\lambda + 2\mu)/(2\mu(\lambda + \mu))$,

$$D_T J(x) = C_2 \{4\mu Ae(u) \cdot e(u) + (\lambda - \mu)tr(Ae(u))tr(e(u))\}(x),$$

and $\forall x \in \Omega \subset \mathbb{R}^3$, if $C_3 = \pi(\lambda + 2\mu)/(\mu(9\lambda + 14\mu))$,

$$D_T J(x) = C_3 \{20\mu Ae(u) \cdot e(u) + (3\lambda - 2\mu)tr(Ae(u))tr(e(u))\}(x).$$

The above expressions are nonnegative. This means that, for compliance minimization, there is no interest in nucleating holes if there is no volume constraint. However, if a volume constraint is imposed, the topological derivative may have negative values due to the addition of the term $-\ell|\omega|$. For the minimization problem (3), the corresponding topological gradient is $D_T \mathcal{L}(x) = D_T J(x) - \ell|\omega|$. At the points x where $D_T \mathcal{L}(x) < 0$, holes are introduced into the current domain.

5. LEVEL SET METHOD FOR SHAPE OPTIMIZATION

Consider $D \subset \mathbb{R}^d$ a bounded domain in which all admissible shapes Ω are included, i.e. $\Omega \subset D$. Following the idea of Osher and Sethian [16], the boundary of Ω is represented by means of a level set function ψ such that $\psi(x) < 0 \Leftrightarrow x \in \Omega$. The normal n to the shape Ω is recovered as $\nabla\psi/|\nabla\psi|$ and the mean curvature H is given by $\text{div}(\nabla\psi/|\nabla\psi|)$.

During the optimization process, the shape $\Omega(t)$ is going to evolve according to a fictitious time parameter $t > 0$ which corresponds to descent stepping. The evolution of the level set function is governed by the following Hamilton–Jacobi transport equation [16]

$$\frac{\partial\psi}{\partial t} + V|\nabla\psi| = 0 \quad \text{in } D, \quad (4)$$

where $V(t, x)$ is the normal velocity of the shape's boundary. The choice V is based on the shape derivative computed in Theorem 1

$$\mathcal{L}'(\Omega)(\theta) = \int_{\partial\Omega} v \theta \cdot n \, ds, \quad (5)$$

where the integrand $v(u, n, H)$ depends on the state u , the normal n and the mean curvature H . The simplest choice is to take the steepest descent $\theta = -vn$. This yields a normal velocity for the shape's boundary $V = -v$. Another choice consists in smoothing the velocity field vn by applying the Neumann-to-Dirichlet map to $-vn$ (see e.g. [4, 7, 14]). The method described in detail in [12] is used in all the numerical computations below.

The main point is that the Lagrangian evolution of the boundary $\partial\Omega$ is replaced by the Eulerian solution of a transport equation in the whole fixed domain D . Likewise the elasticity equations for the state u are extended to the whole domain D by using the so-called ‘‘ersatz material’’ approach. The Hamilton–Jacobi equation (4) is solved by an explicit upwind scheme (see e.g. [18]) on a Cartesian grid with a time stepping satisfying a CFL condition. To regularize the level set function (which may become too flat or too steep), it is periodically reinitialized by solving another Hamilton–Jacobi equation which admits, as a stationary solution, the signed distance to the initial interface [18].

6. OPTIMIZATION ALGORITHM

For the minimization problem (3) we propose an iterative coupling of the level set method and of the topological gradient method. Both methods are gradient-type algorithms, so our coupled method can be thought of as an alternate directions descent algorithm.

The level set method relies on the shape derivative $\mathcal{L}'(\Omega)(\theta)$ of Section 3, while the topological gradient method is based on the topological derivative $D_T \mathcal{L}(x)$ of Section 4. These two types of derivative define independent descent directions that we simply alternate as follows.

In a first step, the level set function ψ is advected according to the velocity $-v$. Then, holes are introduced into the current domain Ω where the topological derivative $D_T \mathcal{L}(x)$ is minimum and negative.

In practice, it is better to perform more level set steps than topological gradient steps. Therefore, the main parameter of our coupled algorithm is an integer n_{opt} which is the number of gradient steps between two successive applications of the topological gradient. Our proposed algorithm is structured as follows:

1. Initialization of the level set function ψ_0 corresponding to an initial guess Ω_0 (usually the full working domain D).
2. Iteration until convergence, for $k \geq 0$:

- (a) **Elasticity analysis.** Computation of the state u_k solving a problem of linear elasticity on Ω_k . This yields the shape derivative, the velocity v_k and the topological gradient.
- (b) **Shape gradient.** If $\text{mod}(k, n_{\text{top}}) < n_{\text{top}}$, the current shape Ω_k , characterized by the level set function ψ_k , is deformed into a new shape Ω_{k+1} , characterized by ψ_{k+1} which is the solution of the Hamilton–Jacobi equation (4) after a time interval Δt_k with the initial condition ψ_k and a velocity $-v_k$. Δt_k is chosen such that $\mathcal{L}(\Omega_{k+1}) \leq \mathcal{L}(\Omega_k)$.
- (c) **Topological gradient.** If $\text{mod}(k, n_{\text{top}}) = 0$, nucleation step: Ω_{k+1} is obtained by inserting new holes into Ω_k according to the topological gradient.

For details about the shape gradient step and the topological gradient step, we refer to our previous works [2–4].

7. A NUMERICAL EXAMPLE IN 2-D

It is a variation of the classical cantilever, but its optimal solution seems to have a more complex topology. It consists in a rectangular domain of dimensions 10×8 with a square hole whose boundaries are submitted to an homogeneous Dirichlet boundary condition. The domain is meshed with a regular 150×120 grid. Figure 1 shows the composite and penalized solutions obtained by the homogenization method (see [1, 5, 6]). Since the composite solution is a global optimum of the problem, it will be used as a reference. Figure 2 shows the solution obtained by the algorithm coupling shape and topological sensitivity, starting from the full domain, with 1 step of topological gradient every 10 iterations. Figure 4 shows different solutions obtained by the level set algorithm (without topological gradient) for different numbers of initial holes, ranging from 0 to 160.

The convergence history of Figure 6 gives some hints on the efficiency of the level set method without topological gradient: first, it confirms that a “to-

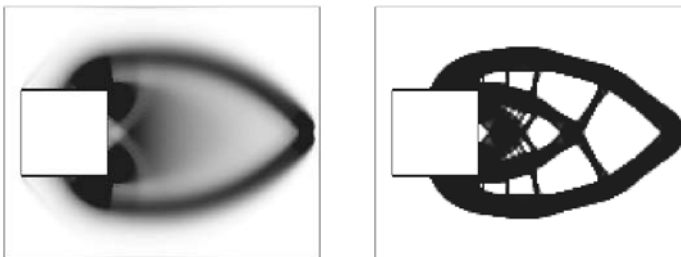


Figure 1. Homogenization method: composite (left) and penalized (right) solutions.



Figure 2. The initial configuration (full domain) and the solution obtained by the level set method with topological gradient.

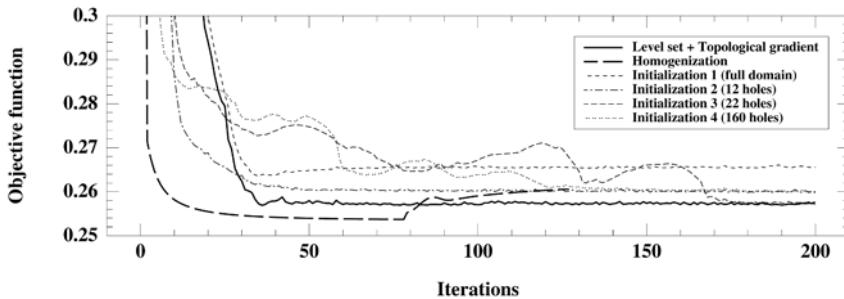


Figure 3. Convergence history of the homogenization method, the level set method with topological gradient (full domain initialization), and the plain level set method with 4 different initial states.

topologically poor” initialization cannot convergence to a good solution; second, it shows that initializing with “many holes” is not a good idea too. The good strategy lies in between, but it is generally not easy to find. The topological gradient allows the convergence to a good solution, starting from the full domain, without the need of adjusting any tricky numerical parameters. Remark that the solution computed from initialization 3 (22 holes) is also good, but it has been reached after an history where it had to escape from many local minima, using the tolerance of the algorithm to small increases of the objective function.

8. A NUMERICAL EXAMPLE IN 3-D

We propose and test-case that have a very topologically complex solution. It is defined by Figure 5 (left). The bottom face is submitted to a uniform Dirichlet boundary condition.

The domain is meshed with 10976 hexaedral elements. The coupled method, level set plus topological gradient every 5 iterations, has been compared to the nominal level set method starting from two initial states (full do-

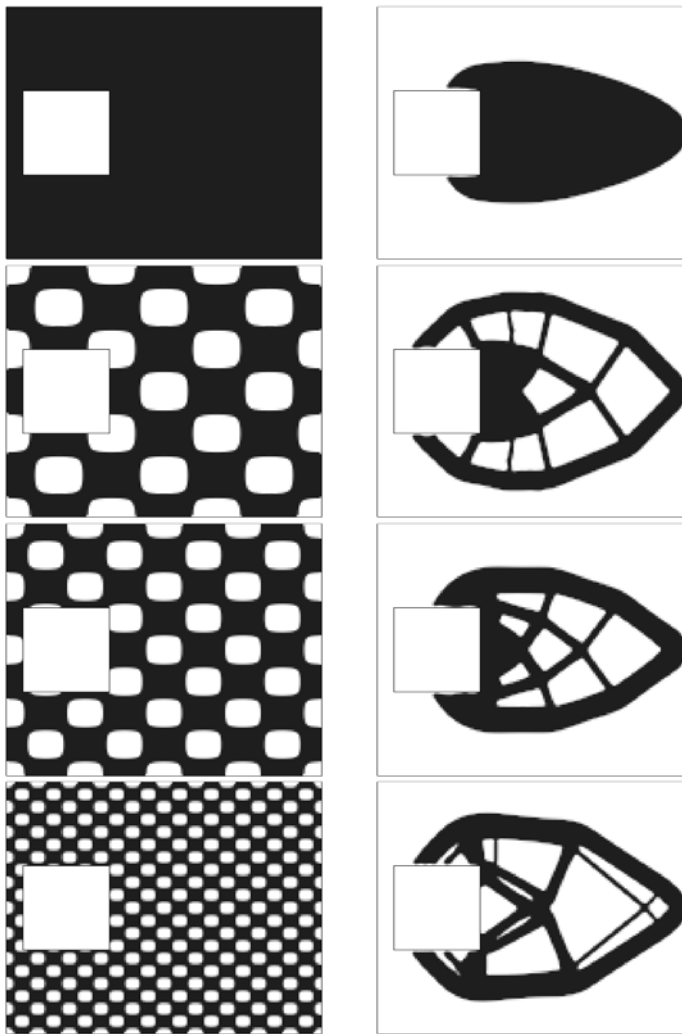


Figure 4. Four solutions obtained by the plain level set method (right) with four different initializations (left): full domain, 12 holes, 22 holes and 160 holes.

main and 8 holes uniformly distributed). The 3 solutions obtained cannot be distinguished on a picture. Figure 5 shows 3 views of the solution and Figure 6 confirms that the objective functions of the converged solutions are very close.

As suspected in [2], the topological gradient seems not to be as efficient and useful in 3-d as it is in 2-d.

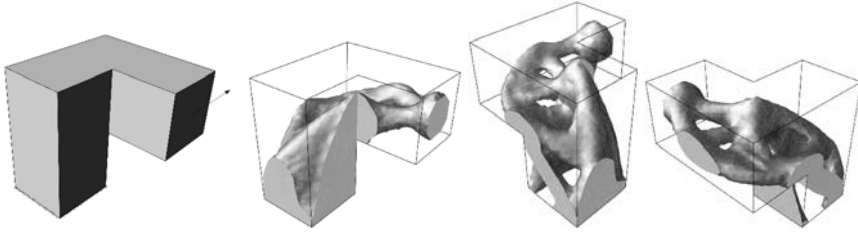


Figure 5. Three different views of the optimal shape obtained for the problem defined on the left.

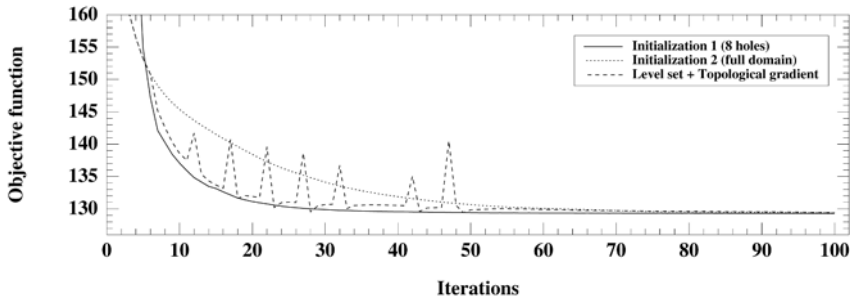


Figure 6. Convergence history of the 3d problem for the plain level set method with two different initializations, and the level set method with topological gradient.

REFERENCES

- [1] Allaire, G., *Shape Optimization by the Homogenization Method*, Springer Verlag, New York (2001).
- [2] Allaire, G., De Gournay, F., Jouve, F. and Toader, A.-M., Structural optimization using topological and shape sensitivity via a level set method, *Control and Cybernetics*, 34, 59–80 (2005).
- [3] Allaire, G., Jouve, F. and Toader, A.-M., A level set method for shape optimization, *C. R. Acad. Sci. Paris, Série I*, 334, 1125–1130 (2002).
- [4] Allaire, G., Jouve, F. and Toader, A.-M., Structural optimization using sensitivity analysis and a level set method, *J. Comp. Phys.*, 194(1), 363–393 (2004).
- [5] Bendsøe, M., *Methods for Optimization of Structural Topology, Shape and Material*, Springer Verlag, New York (1995).
- [6] Bendsøe, M. and Sigmund, O., *Topology Optimization. Theory, Methods, and Applications*, Springer Verlag, New York (2003).
- [7] Burger, M., A framework for the construction of level set methods for shape optimization and reconstruction, *Interfaces and Free Boundaries*, 5, 301–329 (2003).
- [8] Burger, M., Hackl, B. and Ring, W., Incorporating topological derivatives into level set methods, *J. Comp. Phys.*, 194(1), 344–362 (2004).
- [9] Cea, J., Garreau, S., Guillaume, P. and Masmoudi, M., The shape and topological optimizations connection, IV WCCM, Part II (Buenos Aires, 1998), *Comput. Methods Appl. Mech. Engrg.*, 188, 713–726 (2000).

- [10] Eschenauer, H. and Schumacher, A., Bubble method for topology and shape optimization of structures, *Structural Optimization*, 8, 42–51 (1994).
- [11] Garreau, S., Guillaume, P. and Masmoudi, M., The topological asymptotic for PDE systems: The elasticity case, *SIAM J. Control Optim.*, 39(6), 1756–1778 (2001).
- [12] De Gournay, F., PhD Thesis, Ecole Polytechnique (2005).
- [13] Liu, Z., Korvink, J.G. and Huang, R., Structure topology optimization: Fully coupled level set method via FEMLAB, *Struct. Multidisc. Optim.*, 29(6), 407–417 (2005).
- [14] Mohammadi, B. and Pironneau, O., *Applied Shape Optimization for Fluids*, Clarendon Press, Oxford (2001).
- [15] Murat, F. and Simon, S., Etudes de problèmes d’optimal design, in *Lecture Notes in Computer Science, Vol. 41*, pp. 54–62, Springer Verlag, Berlin (1976).
- [16] Osher, S. and Sethian, J.A., Front propagating with curvature dependent speed: Algorithms based on Hamilton–Jacobi formulations, *J. Comp. Phys.*, 78, 12–49 (1988).
- [17] Pironneau, O., *Optimal Shape Design for Elliptic Systems*, Springer-Verlag, New York (1984).
- [18] Sethian, J.A., *Level Set Methods and Fast Marching Methods: Evolving Interfaces in Computational Geometry, Fluid Mechanics, Computer Vision and Materials Science*, Cambridge University Press (1999).
- [19] Simon, J., Differentiation with respect to the domain in boundary value problems, *Num. Funct. Anal. Optim.*, 2, 649–687 (1980).
- [20] Sokołowski, J. and Żochowski, A., On the topological derivative in shape optimization, *SIAM J. Control Optim.*, 37, 1251–1272 (1999).
- [21] Sokołowski, J. and Żochowski, A., Topological derivatives of shape functionals for elasticity systems, *Mech. Structures Mach.*, 29(3), 331–349 (2001).
- [22] Sokołowski, J. and Zolesio, J.P., *Introduction to Shape Optimization: Shape Sensitivity Analysis*, Springer Ser. in Comp. Math., Vol. 10, Springer, Berlin (1992).
- [23] Wang, M.Y., Wang, X. and Guo, D., A level set method for structural topology optimization, *Comput. Methods Appl. Mech. Engrg.*, 192, 227–246 (2003).
- [24] Wang, X., Yulin, M. and Wang, M.Y., Incorporating topological derivatives into level set methods for structural topology optimization, in *Optimal Shape Design and Modeling*, T. Lewinski et al. (eds), Polish Acad. of Sc., Warsaw, pp. 145–157 (2004).

PARAMETRIC SHAPE AND TOPOLOGY OPTIMIZATION WITH RADIAL BASIS FUNCTIONS

Michael Yu Wang and Shengyin Wang

*Department of Automation and Computer-Aided Engineering, The Chinese University
of Hong Kong, Shatin, NT, Hong Kong*

yuwang@acae.cuhk.edu.hk (M.Y. Wang)

Abstract: This paper describes a parametric optimization technique for shape and topology optimization. The proposed method is a generalization of the classical method of level sets which are represented with discrete grids. In using radial basis functions (RBFs), the proposed formulation projects the geometric motion of the level sets of an implicit function onto its parametric representation. The resulting method provides a set of new capabilities for general shape and topology optimization, particularly treating it as a parameter problem with the RBF implicit models. Numerical examples are presented in the paper, suggesting the potential of the method.

Keywords: Shape and topology optimization, radial basis functions, level set method, parameter design.

1. INTRODUCTION

The finite element (FE) based strategy for structural topology optimization has received wide attention and experienced considerable progress recently since the seminal work of Bendsøe and Kikuchi [4]. A wide range of approaches and techniques have been developed as reviewed in detail in [1, 5].

The method of implicit moving interface using the level set technique has been an emerging scheme for shape and topology optimization [2, 11, 12]. The level set method introduced by Osher and Sethian [8] is a simple and versatile method for computing and analyzing the motion of an interface in two or three dimensions. Since interfaces may easily develop sharp corners, break apart, and merge together, the level set method has a wide range of applications, including problems in fluid mechanics, combustion, solids modelling, computer animation and image processing [9].

Along with its benefits, the discrete representation also limits the utility of the classical level set method. The level set function has no analytical form, and the entire design domain must be discretized into a rectilinear grid for level set processing, often through a distance transform. In applying the classical level set method for structural topology optimization, the implementation requires an appropriate choice of the upwind scheme, extension velocity and reinitialization algorithm [9, 12]. Furthermore, there is no nucleation mechanism in the conventional level set method, if the Hamilton–Jacobi equation is solved under a strict condition for numerical stability [7, 10]. Indeed, new holes cannot be created in the interior of a material region because the Hamilton–Jacobi equation satisfies a maximum principle and reinitialization must be applied to the level set function to ensure its regularity [7]. Although some attempts have been made to incorporate the topological derivatives into the level set schemes [7], it is shown to be difficult to combine the intrinsically discontinuous topological derivatives with the continuous shape derivatives [13]. Hence, the numerical considerations of discrete computation have severely limited the primary advantages of the level set methods in solid optimization. Other attempts have also been made to use an implicit function as a regularization method without invoking the discrete level set system [3].

In this paper, we describe an extension of the level set methodology with a parameterized implicit representation. The proposed scheme retains topological benefits of the implicit representation of evolving surfaces while avoiding the drawbacks of a grided spatial discretization. In other words, we can treat shape and topology optimization as a parameter optimization problem. A parameterized implicit surface can be propagated under an arbitrary speed function. The propagation occurs by changing the implicit’s parameters with the use of a common search algorithm in conventional parameter optimization.

We employ the popular radial basis functions (RBFs) to provide a parameterized implicit representation of shapes. The proposed RBF-level set method is implemented in the framework of minimum compliance design that has been extensively studied in the topology optimization field. Numerical examples are given to illustrate the success of the method for 2D structures.

2. TOPOLOGY OPTIMIZATION WITH LEVEL SET MODEL

In the level set framework, a surface is represented implicitly through a level set function $\Phi(\mathbf{x})$, which is Lipschitz-continuous, and the surface itself is the zero isosurface or zero level set $\{\mathbf{x} \in \mathbb{R}^d \mid \Phi(\mathbf{x}) = 0\}$ ($d = 2$ or 3) [9]. In shape and topology optimization of a solid, the solid structure is defined as

$$\begin{aligned}
 \Phi(\mathbf{x}) &= 0 & \forall \mathbf{x} \in \partial \Omega \cap D \\
 \Phi(\mathbf{x}) &< 0 & \forall \mathbf{x} \in \Omega \setminus \partial \Omega \\
 \Phi(\mathbf{x}) &> 0 & \forall \mathbf{x} \in (D \setminus \Omega)
 \end{aligned} \tag{1}$$

where $D \subset \mathbb{R}^d$ is a fixed design domain in which all admissible shapes Ω (a smooth bounded open set) are included, i.e., $\Omega \subset D$.

With this implicit representation, the structural topology optimization process operates on the implicit scalar function $\Phi(\mathbf{x})$ defined in Equation (1) [2, 12], often using a gradient method for the minimization of an objective function $J(\Phi)$. In the present study, only a relatively simple unconstrained minimum compliance design problem presented in [2] with a design-independent load is considered, which can be expressed as

$$\min_{\Phi(\mathbf{x})} J(\Phi) = \int_D (\boldsymbol{\varepsilon}(\mathbf{u}))^T \mathbf{C} \boldsymbol{\varepsilon}(\mathbf{u}) H(-\Phi) \, d\Omega + \ell \int_D H(-\Phi) \, d\Omega, \tag{2}$$

where \mathbf{u} is the displacement field, $\boldsymbol{\varepsilon}(\mathbf{u})$ the strain field, $H(\Phi)$ the Heaviside step function of the implicit function $\Phi(\mathbf{x})$, ℓ a positive Lagrange multiplier, and the volume V of the admissible design can be written as

$$V = \int_D H(-\Phi) \, d\Omega. \tag{3}$$

Given a local perturbation of the boundary, $\dot{\mathbf{x}}$ for $x \in \partial \Omega$, of the admissible domain Ω , the resulting change in the objective function $J(\Phi)$ gives rise to the so-called shape derivative [2, 12], written as

$$\frac{dJ}{dt} = - \int_{\partial \Omega} ((\boldsymbol{\varepsilon}(\mathbf{u}))^T \mathbf{C} \boldsymbol{\varepsilon}(\mathbf{u}) - \ell) v_n \, ds, \tag{4}$$

where t is the artificial time, and v_n the normal velocity representing the perturbation $v_n(\mathbf{x}) = (\nabla \Phi) \cdot \dot{\mathbf{x}}$ for $x \in \partial \Omega$.

Following the development in [8], the change in the surface of the solid as a result of the normal velocity v_n is captured by changing its underlying level set function via:

$$\frac{\partial \Phi}{\partial t} + v_n |\nabla \Phi| = 0. \tag{5}$$

This is known as the Hamilton–Jacobi equation. Hence, moving the boundary of the shape ($\Phi(\mathbf{x}) = 0$) along the normal direction is equivalent to transporting Φ by solving the Hamilton–Jacobi equation (5).

With the above shape derivative of Equation (4) and the time derivative of (Equation 5), it is natural to define the normal velocity v_n as a descent change for the minimization of the objective function [2, 12], as

$$v_n = -G = (\boldsymbol{\varepsilon}(\mathbf{u}))^T \mathbf{C} \boldsymbol{\varepsilon}(\mathbf{u}) - \ell. \tag{6}$$

Thus, by substituting the normal velocity v_n of Equation (6) into Equation (5), one obtains the level set propagation equation that, when integrated, defines a moving boundary of the solid that evolves under the minimization of the objective function [2, 12].

3. RBF-PARAMETERIZED IMPLICIT

In the conventional level set-based topology optimization, a general analytical function for $\Phi(t, \mathbf{x})$ is not known. Thus, it must be discretized for level set processing, often through a distance transform. In an Eulerian approach, a numerical procedure for solving the Hamilton–Jacobi PDE is indispensable. This procedure requires appropriate choice of the upwind schemes, extension velocities and reinitialization algorithms, which may limit the utility of the level set method. Some of the limitations are discussed earlier. For example, reinitialization prevents a level set function from nucleation of holes in the interior of material regions [7, 10]. Another major limitation lies in the discrete representation.

Therefore, a better method is to retain topological benefits of the implicit representation of a level set model while avoiding the drawbacks of using its discrete samples on a fixed grid or mesh. In the present study, we propose to generalize the level set function $\Phi(t, \mathbf{x})$ to include alternative implicit surface representations which provide a free-form representation with parameterization. To this end, a level set method using radial basis functions (RBFs) is developed for structural topology optimization.

Radial basis functions are radially-symmetric functions centered at a particular point [6], or knot, which can be expressed as follows:

$$\varphi_i(\mathbf{x}) = \varphi(\|\mathbf{x} - \mathbf{x}_i\|), \quad \mathbf{x}_i \in D, \quad (7)$$

where $\|\cdot\|$ denotes the Euclidean norm on \mathbb{R}^d [6], and \mathbf{x}_i the position of the knot. Only a single fixed function form $\varphi: \mathbb{R}^+ \rightarrow \mathbb{R}$ with $\varphi(0) \geq 0$ is used as the basis to form a family of independent functions.

There is a large class of possible radial basis functions. Commonly used RBFs include thin-plate splines, polyharmonic splines, Sobolev splines, Gaussians, multiquadrics, compactly supported RBFs [6], and others. Among these common functions, the multiquadric (MQ) spline appears to be the overall best performing RBF, which can be written as

$$\varphi_i(\mathbf{x}) = \sqrt{\|\mathbf{x} - \mathbf{x}_i\|^2 + c_i^2}, \quad (8)$$

where c_i is the free shape parameter which is commonly assumed to be a constant for all i in most applications [6].

In the present RBF implicit modelling, MQ is used to define the scalar implicit function $\Phi(\mathbf{x})$ with N MQs centered at N knot positions:

$$\Phi(\mathbf{x}) = \sum_{i=1}^N \alpha_i \varphi_i(\mathbf{x}) + p(\mathbf{x}), \quad (9)$$

where α_i is the weight, or expansion coefficient, of the radial basis function positioned at the i -th knot \mathbf{x}_i , and $p(\mathbf{x})$ a first-degree polynomial to account for the linear and constant portions of $\Phi(\mathbf{x})$ and to ensure polynomial precision [6]. For three dimensional (3D) problems, $p(\mathbf{x})$ is given by

$$p(\mathbf{x}) = p_0 + p_1x + p_2y + p_3z \quad (10)$$

in which p_0 , p_1 , p_2 and p_3 are the coefficients of the polynomial $p(\mathbf{x})$. Because of the introduction of this polynomial, to ensure a unique solution, the coefficients in Equation (9) must be subject to a set of orthogonality or side constraints [6]:

$$\sum_{i=1}^N \alpha_i = 0; \quad \sum_{i=1}^N \alpha_i x_i = 0; \quad \sum_{i=1}^N \alpha_i y_i = 0; \quad \sum_{i=1}^N \alpha_i z_i = 0. \quad (11)$$

Thus, Equation (9) can be re-written in a vector form as

$$\Phi(\mathbf{x}) = \mathbf{g}^T(\mathbf{x}) \boldsymbol{\alpha}, \quad (12)$$

where

$$\mathbf{g}(\mathbf{x}) = [\varphi_1(\mathbf{x}) \quad \cdots \quad \varphi_N(\mathbf{x}) \quad 1 \quad x \quad y \quad z]^T \in \mathbb{R}^{(N+4) \times 1}, \quad (13)$$

$$\boldsymbol{\alpha} = [\alpha_1 \quad \cdots \quad \alpha_N \quad p_0 \quad p_1 \quad p_2 \quad p_3]^T \in \mathbb{R}^{N+4}. \quad (14)$$

4. RADIAL BASIS FUNCTION PROPAGATION

As aforementioned, in the level set-based topology optimization methods, moving the boundary of the shape along a descent gradient direction to find an optimal shape and topology is equivalent to transporting the scalar implicit function $\Phi(\mathbf{x})$ by solving the Hamilton–Jacobi equation (5) and thus the optimal propagation of the front is performed by solving the Hamilton–Jacobi PDE [2, 12]. In the present study with RBF implicit representation, it is assumed that the space and time are separable and the time dependence of the implicit function Φ is due to the generalized expansion coefficients $\boldsymbol{\alpha}$ of the RBFs in Equation (14). Then, the implicit function Equation (12) becomes time dependent as follows:

$$\Phi = \Phi(\mathbf{x}, t) = \mathbf{g}^T(\mathbf{x}) \boldsymbol{\alpha}(t). \quad (15)$$

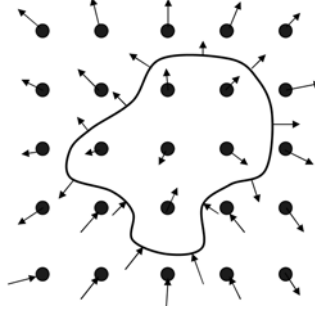


Figure 1. An extension velocity field for the level set method.

Substituting Equation (15) into the Hamilton–Jacobi equation (5) yields

$$\mathbf{g}^T \frac{d\boldsymbol{\alpha}}{dt} + v_n |(\nabla \Phi)^T \boldsymbol{\alpha}| = 0. \quad (16)$$

To time advance the initial values $\boldsymbol{\alpha}$, a collocation method is introduced. In the present Eulerian type approach, all the nodes of the fixed mesh are taken as the fixed knots of the RBF interpolation for the implicit function $\Phi(\mathbf{x})$. As an extension, Equation (16) is then applied to each of these knots of the RBF interpolation, rather than only the points at the front. The normal velocity v_n in Equation (16) is thus extended as v_n^e to all these knots in the design domain D . This is illustrated in Figure 1, where each of the grid point is considered as a knot of the RBF.

According to Equation (6), a natural extension of the normal velocity can be obtained if the strain field is defined over the entire design domain D by assuming $\boldsymbol{\varepsilon}(\mathbf{u}) = 0$, $\mathbf{u} \in (D \setminus \Omega)$. Since both the strain energy density inside the design domain and the constraint-related Lagrange multiplier are included, this extension velocity is physically meaningful.

Using Euler’s method, an approximate solution to Equation (16) can be found. It should be noted that the ODE may be rather stiff, since its counterpart of the Hamilton–Jacobi PDE has a numerical stability condition known as the Courant–Friedrichs–Lewy (CFL) condition [9]. A small time step is advised. After obtaining the approximate solution at each time step, the time-dependent shape and topology can be updated by using Equation (15). The reader is referred to [14] for details.

5. PARAMETRIC SHAPE AND TOPOLOGY OPTIMIZATION

We are further interested in the shape evolution of implicit surface representation by a parametric method. To this end, we consider the RBF level set

function

$$\Phi(\mathbf{x}(t), \boldsymbol{\alpha}(t)) = 0; \quad (17)$$

as the solution \mathbf{x} with a set of shape parameters $\boldsymbol{\alpha}$.

Assuming the shape changes through a velocity field $v_n(t)$, we can find the shape evolution in the form of a parameter change directly from Equation (16) as

$$v_n = -\frac{1}{\|\nabla\Phi\|} \left(\sum_{i=1}^N \varphi_i \dot{\alpha}_i + \dot{\alpha}_0 \right). \quad (18)$$

The resulting equation couples the changes in parameters $\dot{\boldsymbol{\alpha}}(t)$ with the speed function $v_n(t)$ on the surface of the solid. Now, we can substitute Equation (18) into Equation (4). The resulting equation couples the change in parameters $\dot{\boldsymbol{\alpha}}$ with the resulting change in the objective function of the optimization J . Essentially, we have derived the parametric sensitivity of the objective function with respect to the coefficients $\boldsymbol{\alpha}$ of the RBF implicit surface representation:

$$\frac{\partial J}{\partial \boldsymbol{\alpha}} = \left[\frac{\partial J}{\partial \alpha_1}, \frac{\partial J}{\partial \alpha_2}, \dots \right]^T, \quad (19)$$

$$\frac{\partial J}{\partial \alpha_i} = \int_{\partial\Omega} G \frac{1}{\|\nabla\Phi\|} \varphi_i \, ds, \quad i = 1, 2, \dots, N, \quad (20)$$

$$\frac{\partial J}{\partial \alpha_0} = \int_{\partial\Omega} G \frac{1}{\|\nabla\Phi\|} \, ds, \quad (21)$$

where G is given in Equation (6).

Therefore, we have transformed the general shape and topology optimization problem into a parameter optimization problem. This would enable us to use algorithms that are based on sensitivity analysis to derive a search strategy in the parameter space. The costly grid discretization in the classical level set method is thus avoided. Therefore, we may call the method presented here *parametric shape and topology optimization*.

A standard search method is to use the parameter sensitivity to define a search direction and a move step, such as the steepest descent method in mathematical programming. More elaborate techniques such as the method of moving asymptote (MMA) are also feasible.

6. NUMERICAL EXAMPLES OF A MICHELL TYPE STRUCTURE

In this section, numerical examples in two dimensions are presented to illustrate the present RBF-level set method for structural topology optimization. First, we show a Michell type example with the RBF propagation scheme discussed in Section 4. The Michell type structure, as shown in Figure 2, is loaded

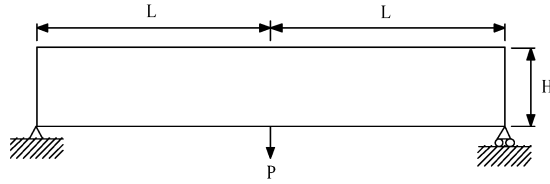
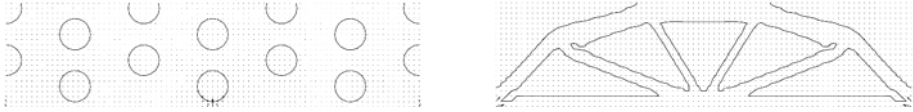


Figure 2. Definition of the minimum compliance design problem.



(a) Initial front and extension velocity

(b) Final front and extension velocity

Figure 3. Front and extension velocity for the Michell type structure.

with a concentrated vertical force of P at the center of the bottom edge. The basic parameters are assumed to be $L = 4$, $H = 1$, thickness $t = 1.0$, load $P = 1$, $E = 1$ for solid material, $E = 1 \times 10^{-5}$ for void material, $\nu = 0.3$, and the fixed Lagrange multiplier $\ell = 10$. It is also assumed that the time step size $\tau = 10^{-4}$ and the mesh size 80×20 .

Figure 3 shows extension velocities at each knot and the front for the initial and final designs. The final design is quite similar to a truss structure with pin-like connection at some joints.

Next, we illustrate the parametric scheme discussed in Section 5. For this scheme, we employ the inverse multi-quadric (IMQ) spline as the basis function, defined as

$$\varphi_i(\mathbf{x}) = 1/\sqrt{\|\mathbf{x} - \mathbf{x}_i\|^2 + c_i^2}, \quad (22)$$

where $c_i = 0.05$. The volume ratio is fixed at 0.4. The rest parameters remain the same. For the parametric scheme, we use the method of moving asymptote (MMA) that is popular for the topology optimization problem solutions.

The initial design and the corresponding level set function are shown Figure 4, while the final optimal solution and its corresponding level set function are shown in Figure 5.

7. CONCLUSIONS

In this study, we focus on level set based methods for structural shape and topology optimization. Radial basis functions are used to define a general implicit representation with weight coefficients as parameters. This enables level set algorithms to avoid a costly discrete computational scheme and use a mathem-

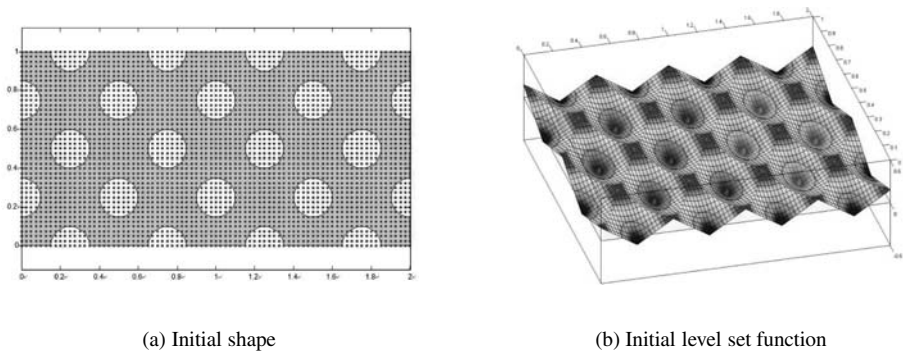


Figure 4. The initial design and level set function.

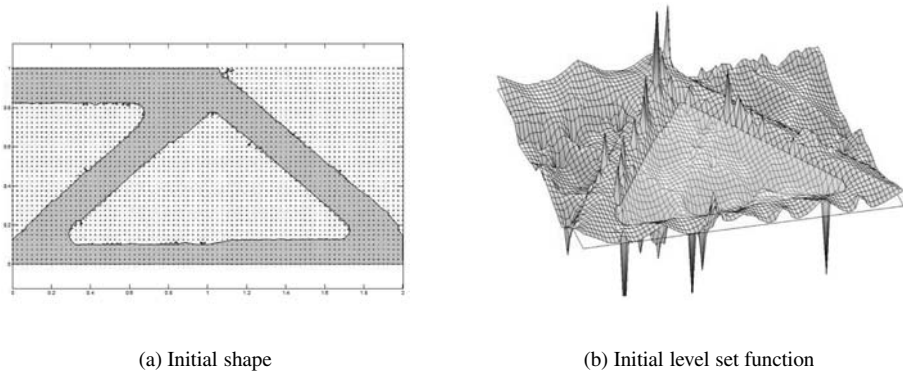


Figure 5. The final design and level set function.

atically more convenient parameter search technique instead. The formulation applies to the general problem of shape and topology optimization with the surface of the solid object evolving under a speed function. Numerical examples of 2D structures are given to show the success of the present method. It is suggested that the introduction of the radial basis functions to the conventional level set methods possesses promising potentials in parametric shape and topology optimization.

Any serious application of the parametric optimization techniques with RBF implicit surface representation described here requires careful numerical analysis for stability and convergence, and should be demonstrated on a wide variety of situations. In particular, the capability of hole nucleation needs thorough analysis and verification. We plan to develop the depth of analysis required and investigate general 3D applications.

ACKNOWLEDGEMENTS

This research work is supported in parts by the Research Grants Council of Hong Kong SAR (Project Nos. CUHK4164/03E and CUHK416205), a Post-doctoral Fellowship from the Chinese University of Hong Kong (No. 04/ENG/1), and the Natural Science Foundation of China (NSFC) (Grants No. 50128503 and No. 50390063), which the authors gratefully acknowledge.

REFERENCES

- [1] G. Allaire, *Shape Optimization by the Homogenization Method*, Springer, New York (2001).
- [2] G. Allaire, F. Jouve and A.-M. Toader, Structural optimization using sensitivity analysis and a level-set method, *Journal of Computational Physics*, 194, 363–393 (2004).
- [3] T. Belytschko, S.P. Xiao and C. Parimi, Topology optimization with implicit functions and regularization, *International Journal for Numerical Methods in Engineering*, 57(8), 1177–1196 (2003).
- [4] M.P. Bendsøe and N. Kikuchi, Generating optimal topologies in structural design using a homogenization method, *Computer Methods in Applied Mechanics and Engineering*, 71, 197–224 (1988).
- [5] M.P. Bendsøe and O. Sigmund, *Topology Optimization: Theory, Methods and Applications*, Springer-Verlag, Berlin (2003).
- [6] M.D. Buhmann, *Radial Basis Functions: Theory and Implementations*, Cambridge Monographs on Applied and Computational Mathematics, Vol. 12, Cambridge University Press, New York (2004).
- [7] M. Burger, B. Hackl and W. Ring, Incorporating topological derivatives into level set methods, *Journal of Computational Physics*, 194, 344–362 (2004).
- [8] S. Osher and J.A. Sethian, Front propagating with curvature dependent speed: Algorithms based on hamilton-jacobi formulations, *Journal of Computational Physics*, 78, 12–49 (1988).
- [9] S.J. Osher and R.P. Fedkiw, *Level Set Methods and Dynamic Implicit Surfaces*, Springer-Verlag, New York (2002).
- [10] J.A. Sethian, *Level Set Methods and Fast Marching Methods*, 2nd edition, Cambridge Monographs on Applied and Computational Mathematics, Cambridge University Press, Cambridge, UK (1999).
- [11] M.Y. Wang and X. Wang, PDE-driven level sets, shape sensitivity and curvature flow for structural topology optimization, *Computer Modeling in Engineering & Sciences*, 6(4), 373–395 (2004).
- [12] M.Y. Wang, X. Wang and D. Guo, A level set method for structural topology optimization, *Computer Methods in Applied Mechanics and Engineering*, 192, 227–246 (2003).
- [13] M.Y. Wang and P. Wei, Topology optimization with level set method incorporating topological derivative, in *6th World Congress on Structural and Multidisciplinary Optimization*, Rio de Janeiro, Brazil (2005).
- [14] S.Y. Wang and M.Y. Wang, Radial basis functions and level set method for structural topology optimization, *International Journal for Numerical Methods in Engineering*, in press, doi:10.1002/nme.1536 (2005).

GENERALIZED SHAPE OPTIMIZATION USING X-FEM AND LEVEL SET METHODS

Pierre Duysinx, Laurent Van Miegroet, Thibault Jacobs and Claude Fleury
*Automotive Engineering/Multidisciplinary Optimization, Aerospace and Mechanics
Department, University of Liège, Chemin des Chevreuils, 1, building B52, 4000 Liège, Belgium*
P.Duysinx@ulg.ac.be, L.Vanmiegroet@ulg.ac.be, Th.Jacobs@ulg.ac.be, C.Fleury@ulg.ac.be

Abstract: This paper presents an intermediate approach between parametric shape optimization and topology optimization. It is based on using the recent Level Set description of the geometry and the novel eXtended Finite Element Method (X-FEM). The method takes benefit of the fixed mesh work using X-FEM and of the curves smoothness of the Level Set description. Design variables are shape parameters of basic geometric features. The number of design variables of this formulation is small whereas various global and local constraints can be considered. The Level Set description allows to modify the connectivity of the structure as geometric features can merge or separate from each other. However no new entity can be introduced. A central problem that is investigated here is the sensitivity analysis and the way it can be carried out efficiently. Numerical applications revisit the classical elliptical hole benchmark from shape optimization.

Keywords: Shape optimization, topology optimization, X-FEM, level set.

1. INTRODUCTION

Topology optimization has experienced an incredible soar since the seminal work of Bendsøe and Kikuchi [2] and is now available within several commercial packages and finite element codes. It is used with great success in industrial applications. Practically, one major advantage of the optimal material distribution formulation is to be able to work on a fixed regular mesh. The drawback is that this formulation comes to very large scale optimization problems, so that one generally considers very simple design problems as the minimum compliance problem with a single volume constraint. Introducing local constraints can lead to very huge problems difficult to handle, whereas controlling geometrical constraints, which are mainly related to manufacturing

considerations, requires some sophistications. Finally the optimal structure picture needs to be interpreted to construct a parametric CAD model.

Meanwhile, shape optimization, which had received attention since the beginning of the eighties, has been quite unsuccessful in industrial applications. However, shape optimization of internal and external boundaries is of great interest to improve the detailed design of structures against many criteria as restricted displacements, various kinds of stress criteria, buckling, etc. The shape optimization introduces a few design variables since the design problem is formulated on the parameterized CAD model level. The major difficulty is related to the mesh management problems coming from the large shape modifications. Mesh distortions and Finite Element errors can be reduced using remeshing between two iterations and mesh adaptation tools. However a major technical problem stems also from the sensitivity analysis that requires the calculation of the so-called velocity field. It turns out that shape optimization remains generally quite fragile and delicate to use in industrial context.

In order to circumvent the technical difficulties of the moving mesh problems, a couple of researches have tried to formulate shape optimization with fixed mesh analyses using fictitious domains as in [5], based on fixed grid finite elements in [7] or more recently using projection methods as in [9]. The present work relies on the novel *eXtended Finite Element Method* (X-FEM) that has been proposed as an alternative to remeshing methods (see [8] or [3] for instance). The X-FEM method is naturally associated with the *Level Set* [11] description of the geometry to provide a very efficient treatment of difficult problems involving discontinuities and propagations. Up to now the X-FEM method has been mostly developed for crack propagation problems [8], but the potential interest of the X-FEM and the level set description for other problems like topology optimization was identified very early in Belytschko et al. [4], Wang et al. [14] or Allaire et al. [1].

The authors see the X-FEM and the Level Set description as an elegant way to fill the gap between topology and shape optimization. The method can be qualified as *generalized shape optimization* as it has smooth boundary descriptions while allowing topology modifications as holes can merge and disappear. X-FEM enables working on a fixed mesh, as in topology optimization, circumventing the technical difficulties of shape optimization. The structural shape description uses basic level set features (circles, rectangles, etc.) that can be freely combined to generate any shapes. The design variables are parameters of the Level Set features, while constraints can, in principle, be either global (compliance, volume) or local (stress) responses as in shape optimization. A key issue of the problem is the sensitivity analysis. A semi analytical approach has been developed. The work presents clearly validated solutions and still open questions and difficulties. For the numerical applications a complete solution of shape optimization using Level Set description and X-FEM

has been implemented in the object oriented software, OOFELIE (Open Object Finite Element Lead by Interactive User) [10].

The layout of the paper is thus the following. The Extended Finite Element Method and the Level Set representation are reminded in Sections 2 and 3. Section 4 states the generalized shape optimization problem with X-FEM and the Level Set description. Sensitivity analysis is addressed in Section 5. Finally, in Section 6 an academic applications of shape optimization is reinvestigated to illustrate the proposed extended finite elements and their application to generalized shape optimization.

2. THE EXTENDED FINITE ELEMENT METHOD

The eXtended Finite Element Method [3, 8] is a recent method that has been firstly developed for the simulation and the analysis of structures presenting moving boundaries. The main strength of this method is its ability to include discontinuities inside the finite elements. Hence, this method enables to include geometric boundaries, material or phase changes that are not coincident with the mesh.

2.1 The Basis of the Method

In order to allow any types of discontinuities inside the elements and therefore to be able to represent discontinuities in the physics fields, it is necessary to add special shape functions to the finite element approximation. For example, in the case of cracked structures, the displacement field is discontinuous and to model the discontinuity, one has to add discontinuous shape functions. The classical finite element approximation used is then extended to embed the discontinuous shape function as in the following equation:

$$\mathbf{u}(\mathbf{x}) = \sum_i u_i N_i(\mathbf{x}) + \sum_j a_j N_j(\mathbf{x}) H(\mathbf{x}), \quad (1)$$

where $N_i(\mathbf{x})$ are the classical shape functions associated to degrees of freedom u_i . The $N_j(\mathbf{x})H(\mathbf{x})$ are the discontinuous shape functions constructed by multiplying a classical $N_j(\mathbf{x})$ shape function with a Heaviside function $H(\mathbf{x})$ (presenting a switch value where the discontinuity lies). These extended shape functions are supported only by the enriched (extended) degrees of freedom a_j . Note that, usually, only the elements near the discontinuity support extended shape functions whereas the other elements remain unchanged. The modification of the displacement field approximation does not introduce a new form of the discretised finite element equilibrium equation but leads to an enlarged problem to solve (see [3] for details):

$$\mathbf{K} \cdot \mathbf{q} = \mathbf{g} \Leftrightarrow \begin{bmatrix} K_{uu} & K_{ua} \\ K_{au} & K_{aa} \end{bmatrix} \begin{bmatrix} u \\ a \end{bmatrix} = \begin{bmatrix} f_u^{\text{ext}} \\ f_a^{\text{ext}} \end{bmatrix}. \quad (2)$$

As the elements can now present discontinuous shape functions, the numerical integration scheme has to be modified in order to take care of the discontinuity. In our implementation, the elements embedding a singularity are divided into sub-triangular elements aligned with this discontinuity over which an integration is processed.

2.2 Representing Holes

The modeling of material-void interfaces with X-FEM [12] is slightly different from the cracked structure case. For void inclusions and holes, the displacement field is approximated by:

$$\mathbf{u}(\mathbf{x}) = \sum_i u_i N_i(\mathbf{x}) V(\mathbf{x}), \quad (3)$$

where $V(\mathbf{x})$ takes value ‘1’ if the node lies inside the material and ‘0’ otherwise. The elements lying outside the material are removed from the system of equations, whereas the partially filled elements are integrated using the X-FEM integration procedure over solid sub-domain. Modeling holes with the X-FEM is a very appealing method for the shape optimization but also for the topology optimization as no remeshing is needed and no approximation is done on the nature of the voids in opposition to the power penalization of intermediate densities (SIMP) method used in topology optimization.

3. THE LEVEL SET DESCRIPTION

The explicit representation of the structural shape of parametric CAD representation forbids deep boundary or topological changes such as creation or fusion of holes. This limitation is one of the main reasons of the low performance generally associated to the shape optimization. Conversely, the Level Set method developed by Sethian [11] which consists of representing the boundary of the structure with an implicit method allows this kind of deep changes.

The Level Set method is a numerical technique first developed to track moving interfaces. It is based upon the idea of representing implicitly the interfaces as a Level Set curve of a higher dimension function $\psi(\mathbf{x}, t)$. The boundaries of the structure is then conventionally represented by the zero level, i.e. $\psi(\mathbf{x}, t)=0$ of this function ψ , whereas the filled region is attached to the positive part of the ψ function. In practice, this function is approximated on a fixed mesh by a discrete function which is usually the signed distance function to the curve Γ :

$$\psi(\mathbf{x}, t) = \pm \min_{\mathbf{x}_\Gamma \in \Gamma(t)} \|\mathbf{x} - \mathbf{x}_\Gamma\|. \quad (4)$$

The sign is positive (negative) if \mathbf{x} is inside (outside) the boundary defined by $\Gamma(t)$. Applied to the X-FEM framework, the Level Set is defined on the

structural mesh and a geometrical degree of freedom representing its Level Set function value is associated at each finite element node. The Level Set is then interpolated on the whole design domain with the classical shape function of the finite element approximation:

$$\psi(\mathbf{x}, t) = \sum_i \psi_i N_i(\mathbf{x}). \quad (5)$$

The combination of different level sets is also one of the appealing characteristic of this method. This property allows easy treatment of merging interfaces and connectivity modifications.

4. PROBLEM FORMULATION

The formulation of the optimization problem is similar to a shape optimization problem, but its solution is greatly simplified thanks to the use of the X-FEM and Level Set description.

The geometry and the material layout are specified using Level Sets representations. The user has a library of basic geometric features (in Level Sets) that can be combined to create almost any structural geometry. The available features are circles, ellipsis, squares, triangles, etc. The design variables are chosen among the geometric parameters of these features.

The optimization problem aims at finding the best shape to minimize a given objective function while satisfying mechanical and geometrical design restrictions. The mechanical constraints can either be global responses (e.g. compliance) or local ones as displacements or stress constraints. However, in this preliminary study only static criteria are available.

The number of design variables is generally small as in shape optimization. However the number of constraints may be large if a lot of local stress restrictions, e.g. stress constraints are considered. Nonetheless, large scale problems as in topology optimization are avoided.

The design problem is stated as a general constrained optimization problem:

$$\begin{aligned} \min_{\mathbf{x}} \quad & g_0(\mathbf{x}) \\ \text{s.t.} \quad & g_j(\mathbf{x}) \leq g_j^{\max} \quad j = 1 \dots m \\ & \underline{x}_i \leq x_i \leq \bar{x}_i \quad i = 1 \dots n. \end{aligned} \quad (6)$$

The solution to this problem is carried out using the so-called *sequential convex programming*. At each iteration, the X-FEM analysis problem is solved and a sensitivity analysis is performed. The solution of the optimization problem is then found by using a CONVex LINearization, CONLIN [6]. The new design point is evaluated and if necessary the procedure is repeated until convergence.

Because of the X-FEM, the geometry has not to coincide with the mesh and the generalized shape optimization problem is carried out on a *fixed mesh*. This

circumvents the mesh perturbation problems of classical shape optimization. Sensitivity analysis does not require anymore the velocity field. The present formulation is then, up to a certain point, simpler. However, some technical difficulties can be encountered if a finite difference or a semi-analytical scheme is used for sensitivity analysis as explained in the next section. Basically, the problem is that the perturbation must not change the number of degrees of freedom of the X-FEM approximation.

The Level Set approach is very convenient to modify the geometry because the level sets (and so the holes) can penetrate each other or disappear. Creation of new holes is more problematic since it leads to a non smooth problem. Topological derivatives have then to be used to treat rigorously the problem. This capability is not yet implemented in the present work.

5. THE SENSITIVITY ANALYSIS METHOD

As in classical shape optimization, the sensitivity analysis of mechanical responses (such as compliance, displacement, stress ...) is carried out using a semi-analytic approach. In this approach the derivatives of stiffness matrix and load vectors are calculated by finite differences after perturbation of the level set parameter by δx :

$$\frac{\partial \mathbf{K}}{\partial x} \simeq \frac{\mathbf{K}(x + \delta x) - \mathbf{K}(x)}{\delta x} \quad \text{and} \quad \frac{\partial \mathbf{f}}{\partial x} \simeq \frac{\mathbf{f}(x + \delta x) - \mathbf{f}(x)}{\delta x}. \quad (7)$$

In the classical shape optimization, the computing complexity of the stiffness matrix sensitivity is due to the modifications of the mesh associated to the perturbation δx and to the velocity field calculation. In the present X-FEM based approach, one has not to bother with the mesh perturbations as one works on a fixed grid. However, this method exhibits a different drawback with respect to the general shape optimization as the number of elements may vary. The critical situation happens (see Figure 1) when a boundary is very close to a node. Thus, during the perturbation δx of the level set, new elements, previously empty, could become partly filled with material and then appear into the formulation. Thus the number of degrees of freedom would change and the dimension of the stiffness matrix would be modified between the level set perturbation.

The strategy that is implemented presently to circumvent the difficulty is the following. As one has only the displacement (u_i) for the elements that are present in the reference configuration, only these elements are taken into account while the contributions coming from the new partly filled elements are ignored. Hence, no new elements are introduced and the size of the stiffness matrix remains unchanged.

This strategy obviously involves an error because it ignores the contributions related to new elements. However, practically the contribution of these

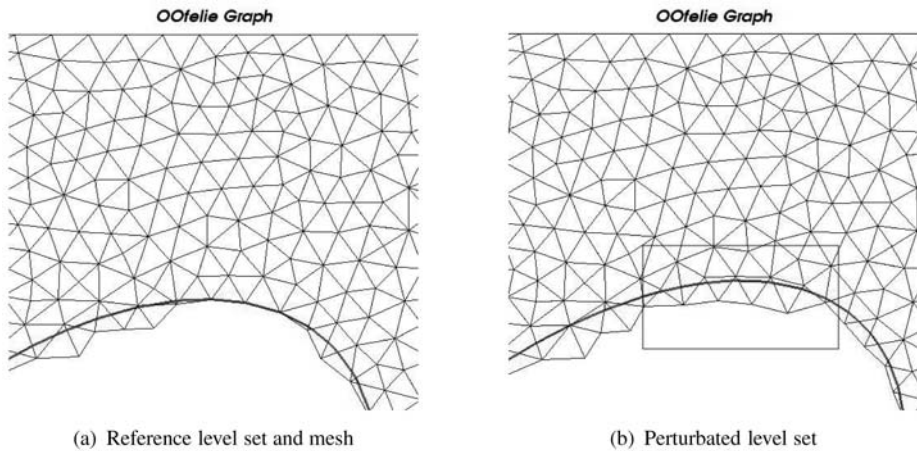


Figure 1. Sensitivity difficulty with semi-analytic approach.

elements is so small that the neglected contribution does not alter the precision of the sensitivity. The quality of the approximation is illustrated in the application section with the elliptical hole problem.

Of course the ultimate solution to the problem should resort to a fully analytical sensitivity of the stiffness matrix, but this would be rather restrictive for industrial applications. On-going work is devoted to investigate two kinds of other strategies to reduce the error of the semi-analytic approach:

(1) One can keep a narrow band (boundary layer) of elements with very soft mechanical properties around the level set $\psi = 0$ in order to prevent the variation of the total number of degrees of freedom.

(2) One could define a tolerance zone around the Level Set. If the discontinuity in an element lies inside this zone, add the connected elements to the set of cut ones.

These two alternative methods have the advantage of keeping the number of degrees of freedom constant and then they do not create or remove elements during the perturbation step. Hence, the computation of the sensitivity would lead to a more accurate result as all elements are taken into account in the perturbed stiffness matrix. However, the presence of these elements will probably introduce a dependency upon the mechanical properties associated to the narrow softening elements band like in topology optimization with the power p coefficient in the *SIMP* law. Moreover, the use of this two methods does not take fully advantage of the X-FEM as we re-introduce an approximation of the void as a weak material.

6. APPLICATIONS

6.1 Implementation

The X-FEM method and its Level Set description have been implemented in an object oriented (C++) multiphysics finite element code, OOFELIE that is commercialized by *Open Engineering* [10].

In OOFELIE, any mechanical result can be chosen as objective functions and constraints that is: compliance and potential energy, all stress components, displacements and geometric results. However in this study, solely compliance minimization is used. Implementation of the X-FEM method is available in 2-D problems with a library of both quadrangle and triangle elements. The CONLIN optimizer by Fleury [6] has also been coupled in the OOFELIE environment and an optimization framework has been created.

6.2 Plate with an Elliptical Hole

The plate with a hole is a classical benchmark from shape optimization. To remind the reader, a large plate with a hole in the middle is subjected to a biaxial stress field. The goal of the optimization problem is to find the optimal shape to minimize the compliance of the structure with a constraint on the total volume of the hole. From the analytical solution, we know that the solution is an elliptical hole aligned with the principal stresses. Figure 2 left shows the quarter of the initial design domain, an elliptic hole with a 45° orientation.

Here the particular values are considered. The dimensions of the plate are $2 \times 2 \times 1$ m. The domain is covered with a transfinite mesh with 30 nodes on each side. The applied biaxial stress field is $\sigma_x=2\sigma_0$ and $\sigma_y=\sigma_0$ and the material properties associated are: Young modulus $E = 1 \text{ N/m}^2$, Poisson's

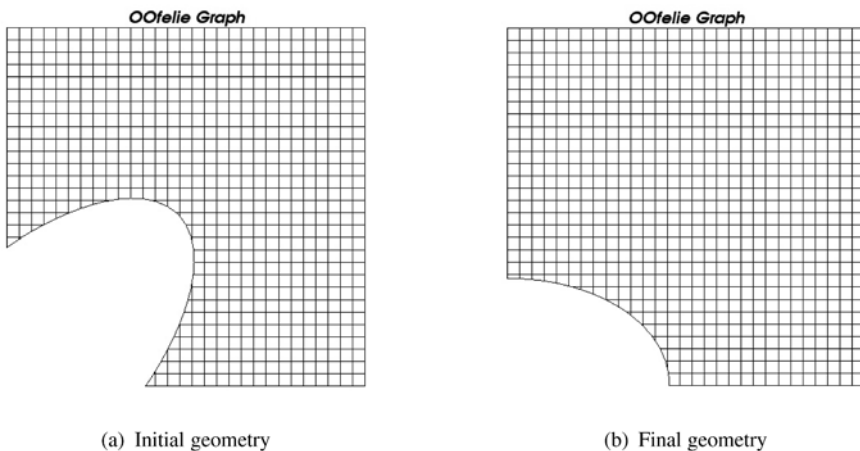


Figure 2. Plate with a hole.

Table 1. Validation of semi-analytical sensitivity analysis approximation.

<i>Design variables</i>	<i>Finite differences</i>	<i>Semi-analytical approach</i>	<i>Relative error (%)</i>
$a = 0.6$	3698.0000	3691.3344	0, 1802
$\theta = \pi/4$	478.0000	477.0641	0.1957
$a = 0.6$	783.8000	781.3920	0.3072
$\theta = 0$	11.6239	11.6235	0.0029

ration $\nu = 0.3$. The plane stress state is assumed. The variables are the angle θ and the long axis a .

Three iterations with CONLIN optimizer are necessary to come to the solution, an ellipsis aligned with the principle stresses (see Figure 2(b)).

Let us remark the discretization of the geometry using the level set. The boundaries are represented using the linear finite element shape functions, so that the boundary is approximated using piecewise linear segments. This can lead to discretization errors of the geometry as noted in [13].

The elliptical hole serves also to validate the approximated semi-analytical sensitivity analysis that has been proposed in Section 5. Table 1 gives the sensitivities of compliance calculated by finite differences and semi-analytical approach for different combination of the design variables a and θ . The results were obtained with a relative perturbation of the design variables of $\delta = 10^{-4}$. The results show the quality of the proposed semi-analytical approximation.

7. CONCLUSION

An intermediate approach between shape and topology optimization has been developed using extended finite elements and Level Set description. The method combines the advantage of the fixed mesh approach of topology optimization and the smooth curve description of shape optimization. Obtained results show that this new approach is promising and deserve further efforts.

The investigation of a semi-analytic sensitivity analysis with X-FEM and Level Set is an original contribution of the paper. The problem of elements becoming partially filled has been identified and a first strategy to circumvent the problem has been validated. On-going work explores other alternative approaches.

The solution of 2-D problems is presently available. Future work is devoted to attack 3-D problems, dynamic problems, and multiphysic (electro-mechanical) problems.

ACKNOWLEDGMENTS

Part of this work has been realized in the framework of project ARC MEMS, Action de recherche concertée 03/08-298 funded by the Communauté Française de Belgique and by project RW 02/1/5183, MOMIOP funded by the Walloon Region of Belgium.

REFERENCES

- [1] Allaire, G., Jouve, F. and Toader, A.M., Structural optimization using sensitivity analysis and a level-set method, *Journal of Computational Physics*, 194(1), 363–393 (2004).
- [2] Bendsøe, M.P. and Kikuchi, N., Generating optimal topologies in structural design using a homogenization method, *Computer Methods in Applied Mechanics and Engineering*, 71, 197–224 (1988).
- [3] Belytschko, T., Parimi, C., Moes, N., Sukumar, N. and Usui, S., Structured extended finite element methods for solids defined by implicit surfaces, *International Journal for Numerical Methods in Engineering*, 56, 609–635 (2003).
- [4] Belytschko, T., Xiao, S. and Parimi, C., Topology optimization with implicit functions and regularization, *International Journal for Numerical Methods in Engineering*, 57, 1177–1196 (2003).
- [5] Dankova and Haslinger, J., Numerical realization of a fictitious domain approach used in shape optimization. Part I. Distributed controls, *Applications of Mathematics*, 41(2), 123–147 (1996).
- [6] Fleury, C., CONLIN: An efficient dual optimizer based on convex approximation concepts, *Structural Optimization*, 1, 81–89 (1989).
- [7] Garcia-Ruiz, M.J. and Steven, G.P., Fixed grid finite element in elasticity optimization *Engineering Computations*, 16(2), 145–164 (1999).
- [8] Moes, N., Dolbow, J., Sukumar, N. and Belytschko, T., A Finite Element Method for Crack Growth without Remeshing, *International Journal for Numerical Methods in Engineering*, 46, 131–150 (1999).
- [9] Norato, J., Haber, R., Tortorelli, D. and Bendsøe, M.P., A geometry projection method for shape optimization, *International Journal for Numerical Methods in Engineering*, 60(14), 2289–2312 (2004).
- [10] OOFELIE, An Object Oriented Finite Element Code Led by Interactive Execution, Internet resources: www.open-engineering.com.
- [11] Sethian, J., *Level Set Methods and Fast Marching Methods: Evolving Interfaces in Computational Geometry, Fluid Mechanics, Computer Vision and Materials Science*, Cambridge University Press (1999).
- [12] Sukumar, N., Chopp, D.L., Noës, N. and Belytschko, T., Modelling holes and inclusions by Level Set in the extended finite element method, *Computer Methods in Applied Mechanics and Engineering*, 190, 6183–6200 (2001).
- [13] Van Miegroet, L., Moes, N., Fleury, C. and Duysinx, P., Generalized shape optimization based on the level set method, in *Proceedings of the 6th World Congress of Structural and Multidisciplinary Optimization*, J. Herskowitz (ed.), Rio de Janeiro, Brazil, May 30–June 3 (2005).
- [14] Wang, M., Wang, X. and Guo, D., A level set method structural topology optimization, *Computer Methods in Applied Mechanics and Engineering*, 191, 227–246 (2003).

TOPOLOGY DESIGN OF THREE-DIMENSIONAL STRUCTURES USING HYBRID FINITE ELEMENTS

C.S. Jog

Department of Mechanical Engineering, Indian Institute of Science, Bangalore 560012, India
jogc@mecheng.iisc.ernet.in

Abstract: Conventional three-dimensional isoparametric elements are susceptible to problems of locking when used to model plate/shell geometries or when the meshes are distorted etc. Hybrid elements that are based on a two-field variational formulation are immune to most of these problems, and hence can be used to efficiently model both “chunky” three-dimensional and plate/shell type structures. Thus, only one type of element can be used to model “all” types of structures, and also allows us to use a standard dual algorithm for carrying out the topology optimization of the structure. We also address the issue of manufacturability of the designs.

Keywords: Dual algorithm, three-dimensional structures, hybrid elements.

1. INTRODUCTION

Topology optimization, which involves distributing a given amount of material in a pattern of solids and voids so as to optimize a given performance functional, has been extensively used to find optimal designs of two-dimensional structures, and in recent times, also of three-dimensional structures (see, e.g., [1] and [2]). Fernandes et al. [3] extend the work of Haber et al. [4] to the three-dimensional case, by introducing microstructure to the material model, and then penalizing the microstructure to generate solid-void designs. Similar to the approach introduced in [4], they introduce a constraint on the perimeter both to avoid “checkerboard” instabilities, and to make the problem well-posed. Borrvall et al. [5] use a regularized penalty in place of the perimeter constraint to generate solid-void designs that are free of checkerboard instabilities.

Beckers [6, 7] introduced the use of dual algorithms for carrying out discrete variable topology optimization. Dual algorithms are ideally suited for this pur-

pose since they work in the space of Lagrange multipliers associated with the constraints, and typically the number of constraints is far lesser compared to the number of design variables. In addition, they work with discrete design variables, so that solid-void topologies can be generated directly with no need for penalization of “intermediate” densities. One of the main disadvantages of the methodology followed in [3, 4] (as noted by the Fernandes et al. [3] in their “Conclusions” section) is the high sensitivity of their algorithm to penalization parameters associated with the intermediate density penalization and perimeter functions. In fact, a lot of trial and error can be involved before the “right” parameters are identified. In contrast, the use of a dual algorithm completely bypasses the use of such parameters.

In many practical topology optimization problems, one has thin shell-type structures that are connected to “chunky” three-dimensional objects. If one uses isoparametric brick elements to model the entire structure, then, to avoid locking, one would need to use an extremely refined mesh, which can be prohibitively expensive. On the other hand, if one uses shell elements to model the thin part and brick elements to model the chunky part, then one needs transition elements to connect the brick and shell elements that are used to model the structure. This makes the topology design algorithm also complicated since brick elements have only translational, while shell elements have both translational and rotational degrees of freedom. An alternative is to use hybrid elements, where the stresses are interpolated independently of the displacements, thus resulting in high accuracy, and in addition, also use the same data input structure as conventional isoparametric elements.

One other issue that we address in this work is that of manufacturability. The optimal topologies in the three-dimensional case that arise from, say, a straight-forward extension of the strategy proposed in [8, 9] for the compliance optimization problem, will, in general, have cavities that are enclosed, making them difficult to manufacture. We propose a modified version that links design variables along a user-specified direction, so that only through holes are allowed in the resulting structure; we shall refer to such a design as a “2.5D” structure since the geometry and loading are as in a three-dimensional problem, but the resulting topologies are two-dimensional, and can be manufactured using a process such as extrusion. Other strategies to make the designs manufacturable are discussed, in, e.g., [10].

2. HYBRID ELEMENT FORMULATION AND SENSITIVITY ANALYSIS

We shall use the 27-node hybrid brick element that has been formulated and discussed in detail in [11]. Let \mathbf{u} , $\boldsymbol{\epsilon}_c$, $\boldsymbol{\tau}_c$, \mathbf{C} , \mathbf{b} and $\bar{\mathbf{t}}$ denote the displacement, engineering strain, stress and constitutive matrix, and the prescribed body

force and traction field acting over part of the surface Γ_f . The two-field variational formulation is obtained by enforcing the equilibrium equations, traction boundary condition and the strain-displacement relation in a weak sense.

Let the displacement and stress fields be interpolated as $\mathbf{u} = \mathbf{N}\hat{\mathbf{u}}$ and $\boldsymbol{\tau}_c = \mathbf{P}\hat{\boldsymbol{\beta}}$. It can be shown that the finite element system of equations is given by

$$\mathbf{K}\hat{\mathbf{u}} = \hat{\mathbf{f}}, \quad (1)$$

where, with $\mathbf{H} = \int_{\Omega} \mathbf{P}^t \mathbf{C}^{-1} \mathbf{P} d\Omega$, $\mathbf{G} = \int_{\Omega} \mathbf{P}^t \mathbf{B} d\Omega$,

$$\mathbf{K} = \mathbf{G}^t \mathbf{H}^{-1} \mathbf{G}. \quad (2)$$

Once the displacement field is found using Equation (1), the stress and strain fields in an element are recovered using the relations

$$\boldsymbol{\tau}_c^{(e)} = \mathbf{P}_{(e)} \hat{\boldsymbol{\beta}}_{(e)} = \mathbf{P}_{(e)} \mathbf{H}_{(e)}^{-1} \mathbf{G}_{(e)} \hat{\mathbf{u}}_{(e)}, \quad \boldsymbol{\epsilon}_c^{(e)} = \mathbf{C}^{-1} \boldsymbol{\tau}_c^{(e)}. \quad (3)$$

As mentioned in the Introduction, the key point in the hybrid formulation is the choice of the stress interpolation matrix $\mathbf{P}_{(e)}$, and this has been discussed in detail in [11]. We note in the following section that the sensitivity expressions also remain unaffected.

3. FORMULATION OF THE 3D TOPOLOGY OPTIMIZATION PROBLEM

Following [8, 9], the dual formulation corresponding to the optimization problem of minimizing the compliance subject to the volume and perimeter constraints can be stated as:

Find the optimum values of the dual variables associated with the volume and perimeter constraints, $\boldsymbol{\lambda}^* \equiv (\lambda_1^*, \lambda_2^*)$, that solve

$$\min_{\boldsymbol{\lambda}} L(\boldsymbol{\lambda}), \quad \lambda_1, \lambda_2 \geq 0$$

where

$$L(\boldsymbol{\lambda}) = \max_{\rho} \min_{\mathbf{u}} \Pi(\mathbf{u}, \rho) - \lambda_1 \left(\int_{\Omega} \rho d\Omega - \bar{V} \right) - \lambda_2 (P - \bar{P}).$$

In the above equation, Π denotes the potential energy given by

$$\Pi = \frac{1}{2} \int_{\Omega} \boldsymbol{\epsilon}_c^t \boldsymbol{\tau}_c d\Omega - \hat{\mathbf{u}}^t \hat{\mathbf{f}} = \frac{1}{2} \hat{\mathbf{u}}^t \mathbf{K} \hat{\mathbf{u}} - \hat{\mathbf{u}}^t \hat{\mathbf{f}}, \quad (4)$$

which is identical to the expression in an isoparametric formulation.

The densities are updated using the condition

$$\begin{aligned} \rho_i &= \rho_{\max} \text{ if } \frac{(\rho_i^0)^2}{\rho_{\max}\rho_{\min}} \int_{\Omega_i} \left. \frac{\partial W}{\partial \rho_i} \right|_{\rho_i^0} d\Omega > \lambda_1 V_i + \lambda_2 \left. \frac{\partial P}{\partial \rho_i} \right|_{\rho_i^0}, \\ \rho_i &= \rho_{\min} \text{ if } \frac{(\rho_i^0)^2}{\rho_{\max}\rho_{\min}} \int_{\Omega_i} \left. \frac{\partial W}{\partial \rho_i} \right|_{\rho_i^0} d\Omega < \lambda V_i + \lambda_2 \left. \frac{\partial P}{\partial \rho_i} \right|_{\rho_i^0}, \end{aligned} \quad (5)$$

where ρ^0 is the density field at the current iteration, and $W = \epsilon^t \tau_c / 2$ is the strain energy density function.

Using the fact that the density variables ρ_i are discontinuous across element boundaries, the strain energy sensitivity expression required in the above formulae can be shown to be

$$\int_{\Omega_i} \frac{\partial W}{\partial \rho_i} d\Omega = \int_{\Omega_i} \epsilon^t \frac{\partial C}{\partial \rho_i} \epsilon d\Omega, \quad (6)$$

which is the same expression as in the standard displacement-based formulation! To avoid checkerboarding and other instabilities, a smoothing strategy similar to that described in [8] is used.

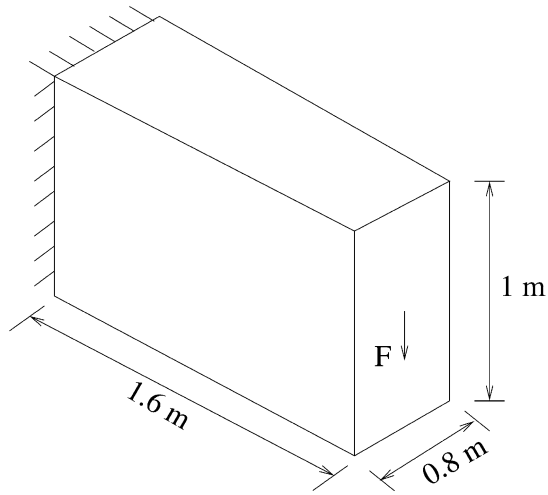
To generate “2.5D” topologies, instead of using Equation (5) for each element, we use it for each *group of elements*, so that in Equation (6), i now varies over the number of groups of elements, Ω_i is taken to be the domain occupied by the i -th group, and V_i denotes the total volume occupied by the i -th group of elements. Smoothing is carried out in the plane perpendicular to the linking direction.

4. NUMERICAL EXAMPLES

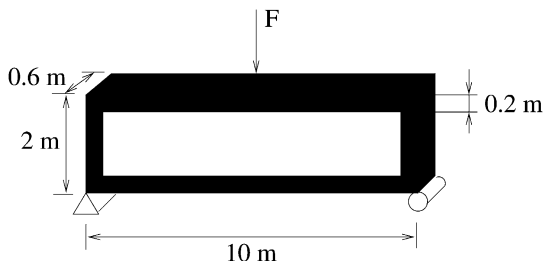
Numerical examples are presented in this section to demonstrate the 3D and 2.5D topologies, and to also demonstrate the effect of the perimeter constraint. The first two examples are the same as those in [3]; the PT75 β element is used to generate all the designs except in one case, where the PT18 β element [12] is used. We use the starting strategy that was labeled as Start-II in [9] in all the examples.

Example 1: Cantilever beam example

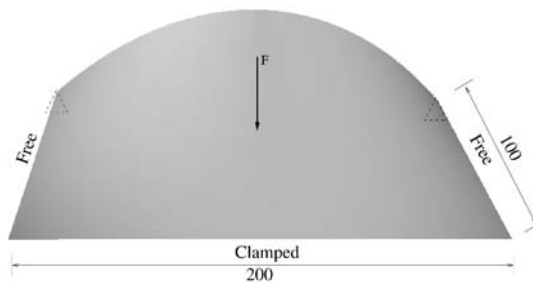
The candidate region and loading conditions are shown in Figure 1a. The applied load is $F = 10$ kN, and the Young modulus and Poisson ratio are 200 GPa and 0.3. The specified volume fraction is 40%. A mesh of $16 \times 10 \times 4$ cubical elements is used to model half the structure (due to symmetry). A move limit of 0.002 is used to gradually reduce the volume to the desired target volume. The number of iterations are approximately 200 and 50 for obtaining the 3D



(a)



(b)



(c)

Figure 1. Candidate domain and loading for the (a) cantilever beam (b) MBB beam (c) conoid shell examples.

and 2.5D topologies, respectively, which are shown in Figure 2. As expected, the compliance of the 2.5D design is higher than that of the 3D design.

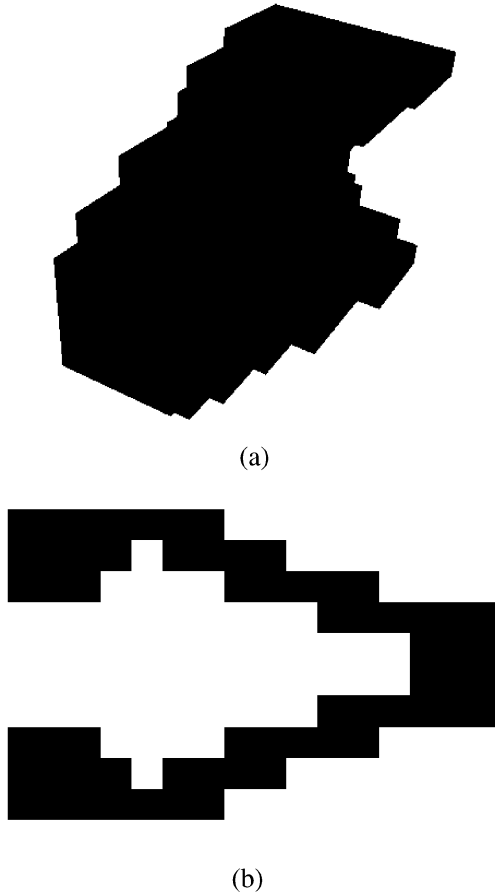
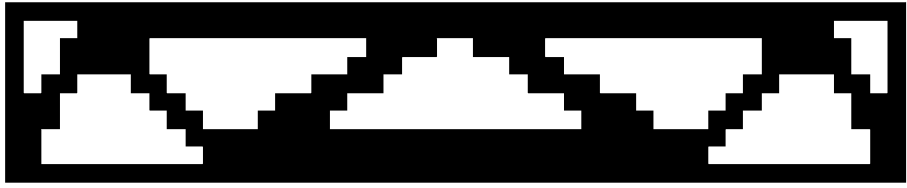


Figure 2. Optimal 3D and 2.5D topologies for the cantilever example (move limit=0.002), $\bar{V} = 40\%$: (a) $J = 0.051$ N-m; (b) $J = 0.0724$ N-m.

Example 2: MBB example

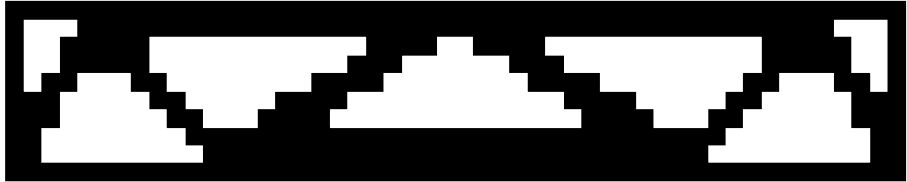
The purpose of this example is to show how 2.5D designs are a natural choice from a manufacturability viewpoint when the thickness of the candidate domain is small compared to the other two dimensions, and also to show the control over the 2.5D topologies that can be obtained by varying the perimeter. The candidate region and loading conditions are shown in Figure 1b. The point load is applied at the center of the top surface, and has a magnitude of $F = 180$ kN, and the Young modulus and Poisson ratio are 210 GPa and 0.3. The specified volume fraction with respect to the total initial volume of the entire structure is 60%. The elements on the outer periphery are constrained to be solid. Meshes of $25 \times 10 \times 3$ (coarse mesh, PT75 β elements) and $50 \times 20 \times 6$ (fine mesh, PT18 β elements) cubical elements are used to model half the structure. The



(a)



(b)



(c)



(d)



(e)

Figure 3. Optimal 2.5D topologies for the MBB example (move limit=0.024), $\bar{V} = 60\%$: (a) $\bar{P} = 44$, $P = 45.36$, $J = 22.2$ N-m (b) $\bar{P} = 47$, $P = 46.64$, $J = 22.8$ N-m (c) $\bar{P} = 49$, $P = 49.3$, $J = 18.35$ N-m (d) $\bar{P} = 49$, $P = 49.3$, $J = 17.6$ N-m (PT18 β) (e) $\bar{P} = \infty$, $P = 54.9$, $J = 18.7$ N-m.

move limit used is 0.024. The fine mesh has been used to get the design in Figure 3d, while the coarse mesh has been used to get the remaining designs

in that figure. The number of iterations are (approximately) 100, 100, 90, 120 and 100, respectively. The specified perimeter for cases (c) and (d) are the same, and in accordance with the theory, we obtain almost identical topologies (although, as is well known, such agreement may not always be obtained, due to the presence of lots of local optima in the topology design problem). Note

- the absence of instabilities, and the very good agreement between \bar{P} and P in all the cases.
- that there is no trial and error involved in adjusting any of the parameters in the formulation in order to satisfy the volume and perimeter constraints.
- the reduction in the compliances of the optimal designs as the perimeter is increased on a *given* mesh.
- that, as a result of carrying out linking of the design variables along the thickness direction, all the designs can be easily manufactured by a process such as extrusion.

Example 3: Conoid shell

This example was attempted in [13] using shell elements and an optimality criterion method, and will be solved here using the PT75 β elements and a dual algorithm. A shell of thickness $t = 0.1$ defined by the surface $z(x, y) = y(1 - x^2/10^4)/2$ is subjected to a central point load $F = 10^{-4}$ as shown in Figure 1c. The straight edge is clamped, while both ends of the curved edge are supported by a hinge. The problem data is $E = 2.1 \times 10^5$, $\nu = 0.3$, and the specified volume fraction is 60%. A move limit of 2.785 was used and convergence was achieved in 160 iterations. The optimal designs obtained using (a) shell elements and an optimality criterion method, and (b) PT75 β elements and a dual algorithm (without smoothing), are shown in Figure 4. As can be seen, in spite of using completely different types of elements and optimization strategies, the topologies obtained are almost identical.

5. CONCLUSIONS

The use of hybrid elements allows us to analyze both “chunky” three-dimensional and shell type structures accurately, and hence allows us to use a unified dual algorithm. Quite fortuitously, it turns out that to switch from a dual optimization strategy based on standard displacement-based elements to one based on hybrid elements, one needs only to

1. Compute the stiffness matrix using Equation (2), and
2. Recover the stresses and strains using Equations (3),

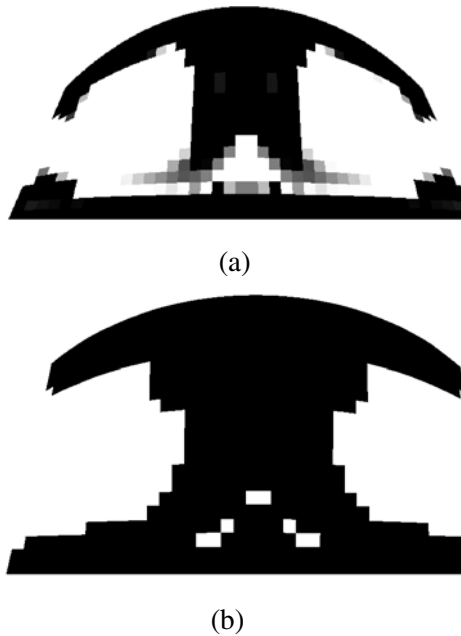


Figure 4. Conoid shell example $\bar{V} = 60\%$: Topologies obtained using (a) shell elements and an optimality criterion method [13]; (b) PT75 β hybrid elements and a dual algorithm.

since all other aspects of the optimization algorithm such as compliance or strain energy computation, sensitivity analysis etc. are identical.

Since enclosed holes in optimal three-dimensional topologies can be difficult to manufacture, we have also suggested a method to obtain two-dimensional topologies even though the domain and loading are three-dimensional. This method links design variables along a user-defined linking direction generating a uniform topology along this direction, thus making it easy to manufacture the resultant topologies using a process such as stamping or extrusion. In case, one wishes to obtain a fully three-dimensional optimal topology, the linking is deactivated.

REFERENCES

- [1] Altair Engineering Inc., Altair OptiStruct: User's manual.
- [2] Bendsøe, M.P. and Sigmund, O., *Topology Optimization—Theory, Methods and Applications*, Springer Verlag, Berlin (2003).
- [3] Fernandes, P., Guedes, J.M. and Rodrigues, H., Topology optimization of three-dimensional linear elastic structures with a constraint on “perimeter”, *Computers and Structures*, 73, 583–594 (1999).

- [4] Haber, R.B., Jog, C.S. and Bendsøe, M.P., A new approach to variable-topology shape design using a constraint on the perimeter, *Structural Optimization*, 11, 1–12 (1996).
- [5] Borrvall, T. and Petersson, J., Large-scale topology optimization in 3D using parallel computing, *Computer Methods in Applied Mechanics and Engineering*, 190, 6201–6229 (2001).
- [6] Beckers, M., Topology optimization using a dual method with discrete variables, *Structural Optimization*, 17, 14–24 (1999).
- [7] Beckers, M., Dual methods for discrete structural optimization problems, *International Journal for Numerical Methods in Engineering*, 48, 1761–1784 (2000).
- [8] Jog, C.S., A robust dual algorithm for topology design of structures in discrete variables, *International Journal for Numerical Methods in Engineering*, 50(7), 1607–1618 (2001).
- [9] Jog, C.S., Topology design of structures using a dual algorithm and a constraint on the perimeter, *International Journal for Numerical Methods in Engineering*, 54(7), 1007–1019 (2002).
- [10] Zhou, M., Shyy, Y.K. and Thomas, Y.L., Checkerboard and minimum member size control in topology optimization, *Structural and Multidisciplinary Optimization*, 21, 152–158 (2001).
- [11] Jog, C.S., A 27-node hybrid brick and a 21-node hybrid wedge element for structural analysis, *Finite Elements in Analysis and Design*, 41, 1209–1232 (2005).
- [12] Pian, T.H. and Tong, P., Relations between incompatible displacement model and hybrid stress model, *International Journal for Numerical Methods in Engineering*, 22, 173–181 (1986).
- [13] Jog, C.S., Higher-order shell elements based on a Cosserat model, and their use in the topology design of structures, *Computer Methods in Applied Mechanics and Engineering*, 193, 2191–2220 (2004).

TOPOLOGY OPTIMIZATION OF VIBRATING BI-MATERIAL STRUCTURES WITH RESPECT TO SOUND RADIATION

Niels Olhoff and Jianbin Du

Institute of Mechanical Engineering, Aalborg University, DK-9220 Aalborg East, Denmark

Abstract: This paper deals with topological design optimization of vibrating bi-material elastic structures of given volume, domain and boundary conditions, with the objective of minimizing the sound power radiated from the structural surfaces into a surrounding acoustic medium. The structural vibrations are excited by a time-harmonic mechanical loading with prescribed forcing frequency and amplitude, and structural damping is not considered. It is assumed that air is the acoustic medium and that a feedback coupling between the acoustic medium and the structure can be neglected. Certain conditions are assumed, where the sound power radiated from the structural surface can be estimated by using a simplified approach instead of solving the Helmholtz integral equation. This implies that the computational cost of the structural-acoustical analysis can be considerably reduced. Numerical results are presented for plate and pipe-like structures with different sets of boundary conditions.

Keywords: Topology design, bi-material structures, sound power radiation, time-harmonic loading, structural-acoustical analysis.

1. INTRODUCTION

Although problems of passive design against vibration and noise were already undertaken many years ago, only during the last decade such problems have benefited from the novel methodology of topology optimization [1–4]. Up to now, works on topological design optimization of vibrating elastic structures have been mainly focused on (i) maximization of intrinsic properties of the structures, like fundamental and higher order eigenfrequencies, eigenfrequency gaps, and phononic band gaps [5–9], (ii) minimization of dynamic compliance [9–12], and (iii) optimization of structural response including wave guidance [7, 13].

Unlike the aforementioned works, the present paper takes into account the interaction between the structure and its surrounding acoustic medium, and re-

duces the sound radiation level (noise) of the structure by directly minimizing the total sound power flow from the structural surface. A bi-material model is employed in the topology optimization. This implies that the boundary shape of the structure is not changed during the design, which leads to a great simplification of the sensitivity analysis since the calculation associated with the shape gradients of the acoustic pressure loading is avoided.

2. MINIMIZATION OF SOUND POWER RADIATION USING TOPOLOGY OPTIMIZATION

In this section, we consider topological design optimization of a vibrating bi-material elastic structure with the objective of minimizing the total sound power (energy flux) Π radiated from the structural surface S into a surrounding acoustic medium. The structural vibrations are assumed to be excited by a time-harmonic mechanical surface loading vector $\mathbf{p}(t) = \mathbf{P}e^{-i\omega_p t}$ with prescribed forcing frequency ω_p and amplitude vector \mathbf{P} on S or part thereof. Assuming that damping can be neglected, the corresponding structural displacement response vector can be stated as $\mathbf{U}e^{-i\omega_p t}$, and the problem of minimizing Π can be formulated as follows:

$$\begin{aligned} \min_{\rho_e} \quad & \left\{ \Pi = \int_S I_n dS = \int_S \frac{1}{2} \text{Re}(p_f v_n^*) dS \right\} \\ \text{subject to} \quad & (\mathbf{K} - \omega_p^2 \mathbf{M})\mathbf{U} = \mathbf{P} + \mathbf{L}\mathbf{P}_f, \\ & \mathbf{C}_\alpha \mathbf{P}_f = \mathbf{G}\mathbf{U} - \mathbf{H}\mathbf{P}_f, \\ & \sum_{e=1}^{N_E} \rho_e V_e - V^{*1} \leq 0, \quad V^{*1} = \alpha V_0, \\ & 0 < \underline{\rho} \leq \rho_e \leq 1, \quad e = 1, \dots, N_E. \end{aligned} \quad (1)$$

Here, the symbols p_f and v_n^* in the expression for Π represent the acoustic pressure and the complex conjugate of the normal velocity of the structural surface, and \mathbf{P}_f denotes the corresponding vector of amplitudes of the acoustic pressure on the structural surface S . The symbol \mathbf{L} represents the fluid-structural coupling matrix and the symbols \mathbf{K} and \mathbf{M} denote the N -dimensional structural stiffness and mass matrices, where N is the number of DOFs. The expression $\mathbf{K} - \omega_p^2 \mathbf{M}$ in (1) represents the dynamic stiffness matrix which we may denote by \mathbf{K}_D . The matrices \mathbf{G} , \mathbf{H} and \mathbf{C}_α can be generated by the discretized Helmholtz integral and calculation of the spatial angle along the structural surface [14]. We consider a bi-material design problem where N_E is the total number of finite elements and the symbol ρ_e denotes the volumetric density of the stiffer material in element e and plays the role of the design variable in the problem [9]. The symbol α denotes the fraction of the given volume V^{*1} of the

stiffer material (material *1) and is given by V^{*1}/V_0 , where V_0 is the volume of the admissible design domain. The remaining part of the total volume V_0 is occupied by a softer material (material *2) as explained in Section 2.3.

2.1 Calculation of Sound Power Flow from the Surface of a Vibrating Structure

The first two constraint equations in (1) denote the structural-acoustic coupling equations (without incoming acoustic waves) and imply quite complicated computations since these equations must be solved in each iterative step of the solution procedure. For simplification, one may consider a special case where the vibration frequency of the structure has a sufficiently high value. In this case, the radiation impedance at the boundary of the structure is approximately the same as the characteristic impedance of the acoustic medium [15, 16]. This implies that the acoustic pressure p_f and normal velocity v_n of the structural surface approximately satisfy the following linear relationship:

$$p_f = \gamma_f c v_n, \quad (2)$$

where c is the sound speed and γ_f is the specific mass (mass density) of the acoustic medium. Tests performed by Sorokin in [17] for simple beam and sphere examples show that the accuracy of (2) depends on not only the frequency level but also the size of the structure and the shape of the vibration mode of the structure. Generally speaking, the accuracy of the approximation increases with increasing values of the frequency, but may decrease with a change of the vibration mode. Nevertheless, the tests also show that even for lower frequencies, (2) may still yield a good approximation of the distribution (up to a multiplying factor) of the sound pressure along the structural surface. This is actually useful for our problem of optimizing the global sound radiation, because even a scaled distribution of the sound pressure along the structural surface can yield a topology design which is close to the optimum one.

If we further assume weak coupling, i.e., ignore the acoustic pressure in the structural equation, the first constraint in (1) will be simplified to the equation of a vibrating structure subjected only to the external mechanical loading \mathbf{P} ,

$$(\mathbf{K} - \omega_p^2 \mathbf{M})\mathbf{U} = \mathbf{P}. \quad (3)$$

With the above simplification, the first two constraint equations in problem (1) may be replaced by Equations (2) and (3), and the sound power flow from the structural surface can be calculated as follows:

$$\Pi = \frac{1}{2} \gamma_f c \omega_p^2 \mathbf{U}^T \mathbf{S}_n \mathbf{U}, \quad (4)$$

where

$$\mathbf{S}_n = \sum_{e=1}^{N_E} \mathbf{S}_{ne} = \sum_{e=1}^{N_E} \left(\int_{S_e} \mathbf{N}^T \mathbf{n} \mathbf{n}^T \mathbf{N} dS \right)$$

may be termed the surface normal matrix. The symbols \mathbf{n} and \mathbf{N} denote the unit normal and the shape function.

2.2 Sensitivity Analysis

Using Equation (3) and applying the adjoint method, the sensitivity of the objective function (i.e. the total sound power flow) in problem (1) with respect to the design variables ρ_e is given by

$$\Pi' = \gamma_f c \omega^2 [\mathbf{U}_s^T \mathbf{P}' - \mathbf{U}_s^T (\mathbf{K}' - \omega_p^2 \mathbf{M}') \mathbf{U}], \quad (5)$$

where prime denotes partial derivative with respect to ρ_e . The symbol \mathbf{U}_s is the solution to the equation $(\mathbf{K} - \omega_p^2 \mathbf{M}) \mathbf{U}_s = \mathbf{S}_n \mathbf{U} \equiv \mathbf{f}_s$, where \mathbf{f}_s may be regarded as a pseudo surface load vector. Specifically, we only consider the case of design-independent mechanical load in the present paper, so the sensitivity \mathbf{P}' of the mechanical load in (5) will be zero. The sensitivities of the stiffness and mass matrices, i.e. \mathbf{K}' and \mathbf{M}' , can be derived by introducing the material models (see Section 2.3).

Based on the above sensitivity results, the optimization problem (1) may be solved by using the well-known MMA method [18] or an optimality criterion method, e.g. the fixed point method.

2.3 SIMP Model for Topology Optimization of Bi-Material Structures

Following [19], the SIMP model for single-material design [2, 20] can be easily extended to bi-material design by using the rule of mixtures. Like in eigenfrequency design, penalization of the ratio between stiffness and mass is the important aspect [8, 21], so in the present paper, the penalization is applied simultaneously to the stiffness and mass (i.e. to the dynamic stiffness \mathbf{K}_D), especially in the case of high loading frequencies. Thus, the following interpolation is used:

$$\mathbf{K}_{De}(\rho_e) = \rho_e^r \mathbf{K}_{De}^{*1} + (1 - \rho_e^r) \mathbf{K}_{De}^{*2}, \quad (6)$$

where \mathbf{K}_{De}^{*1} and \mathbf{K}_{De}^{*2} are the element dynamic stiffness matrices corresponding to the two different, given solid elastic materials *1 and *2, and the penalization power r is taken to be 3 for both stiffness and mass. Note that it follows from (6) that for a given element, $\rho_e = 1$ implies that the element fully consists of the solid material *1, while $\rho_e = 0$ means that the element fully consists of the solid material *2.

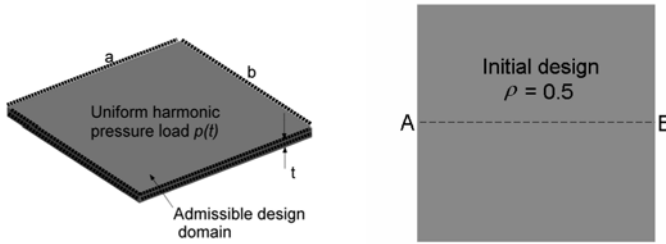


Figure 1. Plate-like structure ($a = 20$, $b = 20$, $t = 1$) subjected to uniformly distributed harmonic pressure loading on its upper surface. All edges of the plate are clamped.

3. NUMERICAL EXAMPLES

3.1 Minimization of Sound Power Radiated from a Bi-Material Plate-Like Structure Excited by Time-Harmonic, Uniformly Distributed Pressure Loading

The first example concerns optimum topology design of a bi-material plate-like structure with clamped edges (see Figure 1). A time-harmonic, uniformly distributed transverse external load $p(t) = P \cos \omega t$ is applied to the upper surface of the plate. The design objective is to minimize the total sound power radiated from the surface of the plate to its surrounding acoustic medium, i.e. air, for a prescribed loading frequency $\omega = \omega_p$ and a volume fraction of up to 50% for the given stiffer material *1, which has the Young's modulus $E^{*1} = 10^{11}$, Poisson's ratio $\nu = 0.3$ and the specific mass $\gamma_m^{*1} = 7800$ (SI units are used throughout). The soft material *2 has the properties $E^{*2} = 0.1E^{*1}$, $\gamma_m^{*2} = 0.1\gamma_m^{*1}$, and $\nu = 0.3$. The specific mass of the fluid (i.e. air) is $\gamma_f = 1.2$ and the sound speed $c = 343.4$.

The plate is modeled by 3D 8-node isoparametric elements ($40 \times 40 \times 1$ mesh). Five different loading frequencies, $\omega_p = 10, 100, 500, 1000$ and 100000 are considered, and the corresponding optimum topologies of the plate are presented in Figures 2(a)–2(e), where the stiffer material *1 is represented by black and the soft material *2 by grey. It can be seen that, as the loading frequency increases, the optimum topology of the structure shows a more and more complicated periodicity.

Figures 3 and 4 show the distribution of the power flow from the structural surface of the initial design ($\rho = 0.5$) and the final optimum design. The total sound power flow to the acoustic medium is reduced from 3.50×10^{-4} to 4.01×10^{-7} for $\omega_p = 100$, from 3.68×10^{-7} to 1.84×10^{-8} for $\omega_p = 500$, and from 1.03×10^{-7} to 5.61×10^{-9} for $\omega_p = 1000$, respectively. Moreover, if we study the variation of the sound pressure (amplitude) along the reference

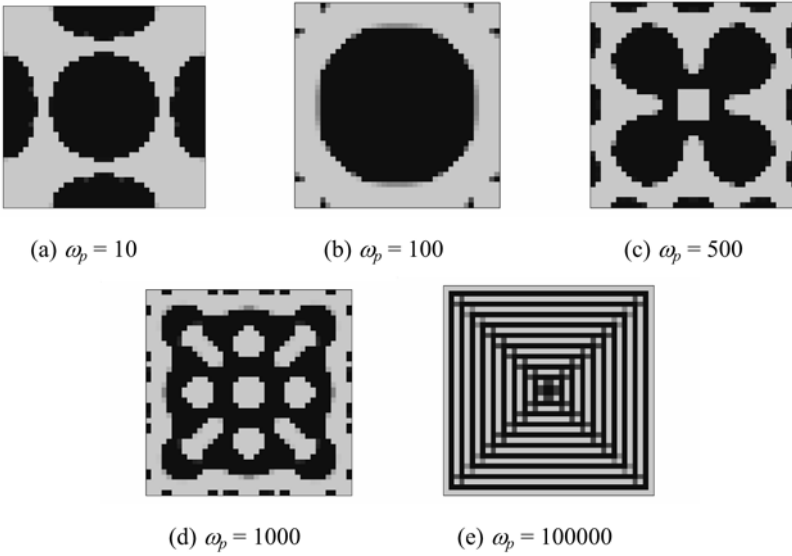


Figure 2. Optimum topologies of clamped bi-material plate-like structures for different loading frequencies. (a) $\omega_p = 10$, (b) $\omega_p = 100$, (c) $\omega_p = 500$, (d) $\omega_p = 1000$, (e) $\omega_p = 100000$.

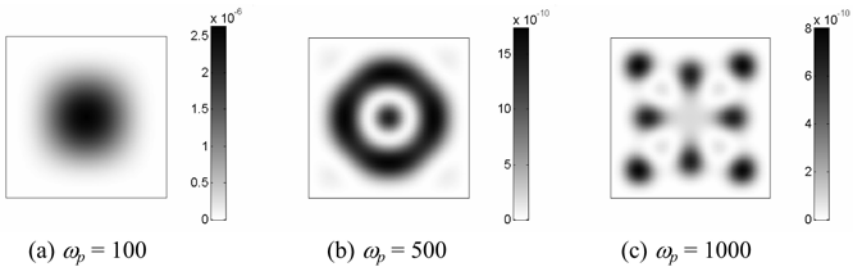


Figure 3. Distribution of the power flow from the structural surface of the initial design. (a) $\omega_p = 100$, (b) $\omega_p = 500$, (c) $\omega_p = 1000$.

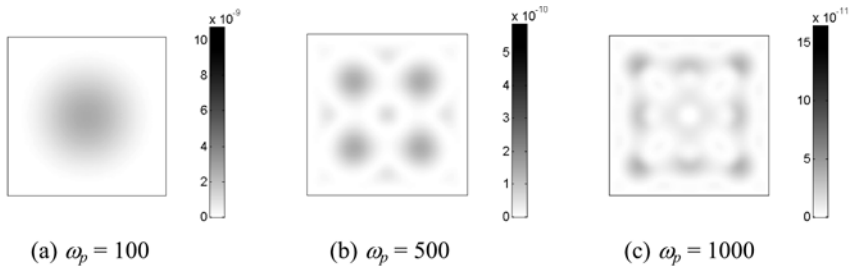


Figure 4. Distribution of the power flow from the structural surface of the optimum design. (a) $\omega_p = 100$, (b) $\omega_p = 500$, (c) $\omega_p = 1000$.

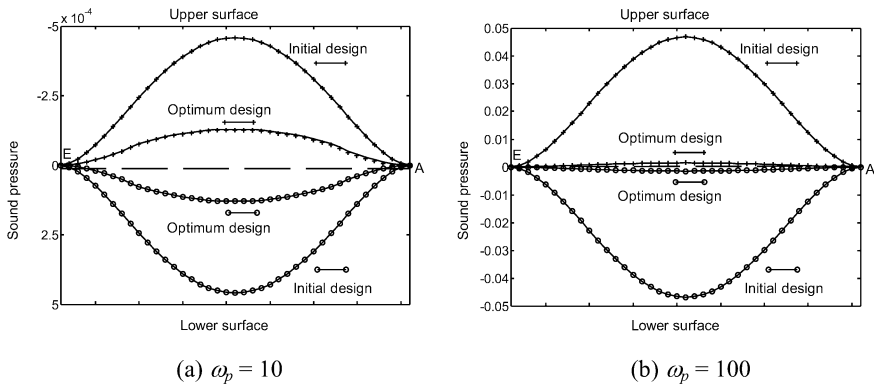


Figure 5. Sound pressure along the reference line EA on the lower and upper surfaces of the plate for the initial and the optimum design (see Figures 1 and 2). (a) $\omega_p = 10$, (b) $\omega_p = 100$.

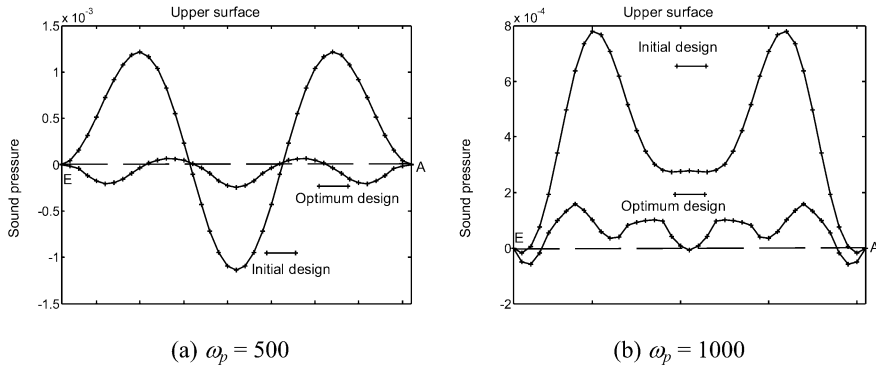


Figure 6. Sound pressure along the reference line EA on the upper surface of the plate for the initial design and the optimum design (see Figures 1 and 2). (a) $\omega_p = 500$, (b) $\omega_p = 1000$.

line EA of the plate (see Figures 1, 5 and 6), we find that the optimum design does not change the wave number of the sound pressure for low values of the loading frequency (see Figure 5). However, for higher values of the loading frequency, Figure 6 shows that both the wave shape and wave numbers of the sound pressure are changed by the optimum design. Specifically, Figure 5 also shows that the phase of the sound pressure is inverted when the loading frequency is increased from 10 to 100.

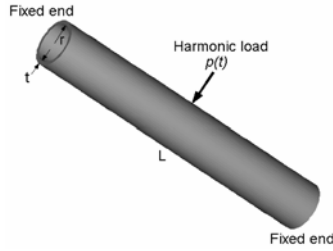


Figure 7. Clamped-clamped pipe-like structure ($L = 0.4$, $r = 0.025$, $t = 0.005$) subjected to a concentrated harmonic load $p(t) = P \cos \omega_p t$ at the middle of its external surface.

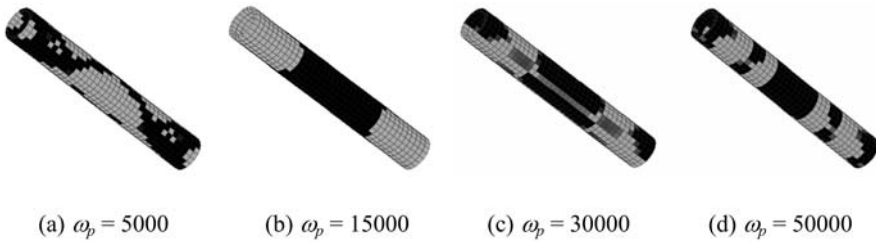


Figure 8. Optimum topologies of bi-material pipe-like structures for different loading frequencies. (a) $\omega_p = 5000$, (b) $\omega_p = 15000$, (c) $\omega_p = 30000$, (d) $\omega_p = 50000$.

3.2 Minimization of Sound Power Radiated from a Bi-Material Pipe-Like Structure Excited by a Concentrated Time-Harmonic Load

As a second example, we consider optimum topology design of a bi-material pipe-like structure with clamped ends and loading conditions as shown in Figure 7. The design objective, the material volume fraction and the material properties (structure and fluid) are the same as in Section 3.1.

The pipe is modeled by 3D 8-node isoparametric elements ($40 \times 20 \times 1$ mesh). The optimum topologies of the pipe for four different loading frequencies, $\omega_p = 5000$, 15000, 30000, and 50000, are given in Figures 8(a)–8(d), where the stiffer material *1 is represented by black and the soft material *2 by grey. The corresponding vibration modes of the pipe in the optimum designs are shown in Figures 9(a)–9(d). In comparison with the initial design ($\rho = 0.5$), the total sound power radiated to the acoustic medium from the final design is reduced from 8.14×10^{-7} to 4.11×10^{-8} for $\omega_p = 5000$, from 2.28×10^{-6} to 4.56×10^{-8} for $\omega_p = 15000$, from 1.25×10^{-4} to 2.32×10^{-7} for $\omega_p = 30000$, and from 2.39×10^{-6} to 7.87×10^{-8} for $\omega_p = 50000$.

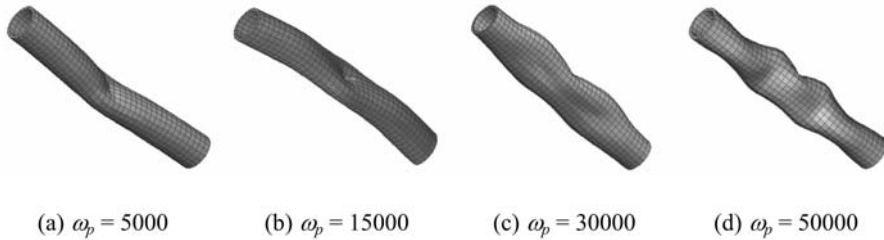


Figure 9. Vibration modes of the pipe in the final optimum designs. (a) $\omega_p = 5000$, (b) $\omega_p = 15000$, (c) $\omega_p = 30000$, (d) $\omega_p = 50000$.

ACKNOWLEDGEMENT

Useful discussions with Professor S.V. Sorokin are gratefully acknowledged.

REFERENCES

- [1] Bendsøe, M.P. and Kikuchi, N., Generating optimal topologies in structural design using a homogenization method, *Comput. Methods Appl. Mech. Engrg.*, 71(2), 197–224 (1988).
- [2] Bendsøe, M.P., Optimal shape design as a material distribution problem, *Struct. Optim.*, 1, 193–202 (1989).
- [3] Bendsøe, M.P. and Sigmund, O., *Topology Optimization: Theory, Methods and Applications*, Springer, Berlin (2003).
- [4] Eschenauer, H. and Olhoff, N., Topology optimization of continuum structures: A review, *Appl. Mech. Rev.*, 54(4), 331–389 (2001).
- [5] Diaz, A.R. and Kikuchi, N., Solutions to shape and topology eigenvalue of optimization problems using a homogenization method, *Int. J. Num. Mech. Engrg.*, 25, 1487–1502 (1992).
- [6] Krog, L.A. and Olhoff, N., Optimum topology and reinforcement design of disk and plate structures with multiple stiffness and eigenfrequency objectives, *Computers & Structures*, 72, 535–563 (1999).
- [7] Sigmund, O. and Jensen, J.S., Systematic design of phononic band-gap materials and structures by topology optimization, *Philosophical Transactions of the Royal Society London, Series A (Mathematical, Physical and Engineering Sciences)*, 361, 1001–1019 (2003).
- [8] Jensen, J.S. and Pedersen, N.L., On maximal eigenfrequency separation in two-material structures: The 1D and 2D scalar cases, *J. Sound and Vibration*, 289, 967–986 (2006).
- [9] Olhoff, N. and Du, J., Topology optimization of structures against vibration and noise, in *Proceedings of the 12th International Congress on Sound and Vibration ICSV12*, Lisbon, Portugal 20 pp. (2005).
- [10] Ma, Z.D., Kikuchi, N. and Cheng, H.C., Topological design for vibrating structures, *Comput. Methods Appl. Mech. Engrg.*, 121, 259–280 (1995).
- [11] Min, S., Kikuchi, N., Park, Y.C., Kim, S. and Chang, S., Optimal topology design of structures under dynamic loads, *Struct. Optim.*, 17, 208–218 (1999).

- [12] Jog, C.S., Topology design of structures subjected to periodic loading, *J. Sound and Vibration*, 253(3), 687–709 (2002).
- [13] Jensen, J.S., Phononic band gaps and vibrations in one- and two-dimensional mass-spring structures, *J. Sound and Vibration*, 266, 1053–1078 (2003).
- [14] Christensen, S.T., Sorokin, S.V. and Olhoff, N., On analysis and optimization in structural acoustics – Part I: Problem formulation and solution techniques, *Struct. Optim.*, 16, 83–95 (1998).
- [15] Herrin, D.W., Martinus, F., Wu, T.W. and Seybert, A.F., A new look at the high frequency boundary element and Rayleigh integral approximations, Society of Automotive Engineers, Inc. (2003).
- [16] Lax, M. and Feshbach, H., On the radiation problem at high frequencies, *Journal of the Acoustical Society of America*, 19, 682–690 (1947).
- [17] Sorokin, S.V., Private communication (2005).
- [18] Svanberg, K., The method of moving asymptotes – A new method for structural optimization, *Int. J. Numer. Meth. Engrg.*, 24, 359–373 (1987).
- [19] Bendsoe, M.P. and Sigmund, O., Material interpolation schemes in topology optimization, *Arch. Appl. Mech.*, 69, 635–654 (1999).
- [20] Rozvany, G., Zhou, M. and Birker, T., Generalized shape optimization without homogenization, *Struct. Optim.*, 4, 250–252 (1992).
- [21] Pedersen, N.L., Maximization of eigenvalues using topology optimization, *Struct. Multidisc Optim.*, 20, 2–11 (2000).

Classics Revisited

FORCE FIELDS WITHIN MICHELL-LIKE CANTILEVERS TRANSMITTING A POINT LOAD TO A STRAIGHT SUPPORT

Cezary Graczykowski¹ and Tomasz Lewiński²

¹*Institute of Fundamental Technological Research, Polish Academy of Sciences, Świętokrzyska 21, 00-049 Warszawa, Poland*

²*Institute of Structural Mechanics, Faculty of Civil Engineering, Warsaw University of Technology, al. Armii Ludowej 16, 00-637 Warsaw, Poland*

Abstract: The paper concerns distribution of the force fields within Michell cantilevers supported on a segment of a straight line. The allowable yield stresses for tension and compression are not necessarily equal. The paper puts emphasis on checking the final results for the optimal weight by computing the weight in two manners: as a virtual work or, alternatively, by finding the force fields, the density of fibres and then by summing up the weights of all the parts of the optimal cantilever, i.e. the weights of the reinforcing bars and the weights of all the fibrous domains. If this duality gap vanishes, the solution is correct.

Keywords: Michell-like cantilevers, minimum weight problem, topology optimization.

1. INTRODUCTION

The Michell problem can be expressed in terms of average stress fields as a minimum weight problem or in terms of displacements as a maximization problem, see Strang and Kohn (1983). The latter problem can be interpreted as an equilibrium problem of a body with locking, see Golay and Seppacher (2001), Lewiński and Telega (2001). The known analytical solutions were found just within the framework of this formulation. In particular, the Michell (1904) cantilever supported on a circle (see Hemp, 1973) was found by guessing the kinematically admissible virtual displacements realizing the optimality conditions $\varepsilon_I = 1$, $\varepsilon_{II} = -1$ concerning the principal values of the tensor of virtual strains in the problem in which the allowable yield local stresses for tension (σ_T) and compression (σ_C) are equal: $\sigma_T = \sigma_C$. The weight of the optimal cantilever is equal up to a factor to the value of the work of the point load applied to a joint on the displacement of this joint. Let us emphasize here

that this displacement is finite since the reinforcing bars connected at this joint transmit the point load thus eliminating possible stress singularities. We see that having the virtual displacements the computation of the weight becomes straightforward. On the other hand, computation of this weight within the average stress-based formulation is more complex. Note that none of the available exact solutions to the Michell problem was solved with using the stress-based formulation. This would require finding the minimizer of the weight (expressed in terms of average stresses) among all candidates which are statically admissible. This is not an easy task, since this set is affine and hard to parameterize. It is easier to recover the average stress fields upon finding the Hencky net, the latter being featured by the displacement-based optimality criteria (see Hemp, 1973, sec. 4.3). The average stresses found this manner should be correlated with longitudinal forces in the reinforcing bars. For instance, the weight of the cantilever supported on a circle is equal to the sum of weights of the reinforcing bars and the fibrous interior. The weight computed this manner is exactly equal to the virtual work of the applied point load. The relevant analytical proof has been only recently published, see Graczykowski and Lewiński (2005a). This problem has been solved under the condition of $\sigma_T = \sigma_C$, its generalization to the case of unequal permissible stresses being unsolved till now, see Rozvany's (1997) criticism on a part of Michell's (1904) work.

Note here that the most advanced numerical results have been recently obtained by Gilbert et al. (2005) by the truss approximation method.

The main feature of Michell trusses is their discrete-continuous structure: the mass is concentrated along the edge lines connecting the point load with the support. The lines where the mass is concentrated are interpreted as bars, i.e. usual bars of finite cross sections. They are subjected to tension or compression. Optimization removes bending and transverse shearing. The volume of the optimum structure is a sum of the volume occupied by the material forming the bars and the volume of fibres in the interior part. In the present paper we consider Michell cantilevers supported along a straight segment, lying inside a domain bounded by half-lines starting from the ends of the segment. The results of the papers by Lewiński et al. (1994) can be generalized to the case of unequal permissible local stresses, cf. Graczykowski and Lewiński (2005b). Our aim here is to consider average stresses within such optimal cantilevers, perform the local and global analyses of equilibrium. Other cases of position of the point load are discussed in Graczykowski and Lewiński (2006).

2. STRESS FIELDS WITHIN PRAGER–HILL CANTILEVERS

We tackle the problem of transmitting the force P applied at point P to the support RN by a plane structure lying within the infinite domain bounded by the half-lines RR_1 and NN_1 and by RN , cf. Figure 1. The axial stress σ should be bounded: $-\sigma_C \leq \sigma \leq \sigma_T$. The aim is to find the lightest structure satisfying the above conditions. A graphical solutions to this problem were sketched by Prager (1959) and Rozvany (1997). The analytical construction of the net of fibres within $ABDC$ and the relevant virtual displacement fields satisfying the desired optimality conditions:

$$\bar{\varepsilon}_I = 1, \quad \bar{\varepsilon}_{II} = -\kappa \tag{1}$$

with $\kappa = \sigma_T/\sigma_C$, were published recently, see Graczykowski and Lewiński (2005b). Let us recall that if $\angle NRA = \gamma_2$, $\angle RNA = \gamma_1$, we have $\tan\gamma_1 = \kappa^{1/2}$ and $\tan\gamma_2 = \kappa^{-1/2}$. Thus $r_2 = \kappa^{1/2}r_1$, where $r_1 = |NA|$, $r_2 = |RA|$. see Rozvany (1997). We introduce notation: $\theta_1 = \angle ANC$, $\theta_2 = \angle BRA$. The circular domains BRA , ANC are called fans; they are filled up with infinitely thin radial bars, called fibres. The boundary bars RB and NC have finite cross sections – they are typical truss members. The domain $ABDC$ is parameterized with a special curvilinear system (α, β) . The units of α and β are radians. The vertices of $ABDC$ have the coordinates: $A(0, 0)$, $B(0, \theta_2)$, $C(\theta_1, 0)$, $D(\theta_1, \theta_2)$. This system is orthogonal; its Lamé coefficients $A(\alpha, \beta)$, $B(\alpha, \beta)$ are also radii of curvatures of the parametric lines. The parametric lines (α, β) are determined by Cartesian coordinates $x(\alpha, \beta)$, $y(\alpha, \beta)$ measured along the (x, y) axes, as in Figure 1.

The formulae for $x(\alpha, \beta)$, $y(\alpha, \beta)$, $A(\alpha, \beta)$, $B(\alpha, \beta)$ were published in Graczykowski and Lewiński (2005b). Let us mention only that the Hencky net in $ABDC$ is characterized by $\phi(\alpha, \beta) = \beta - \alpha$; here ϕ represents an angle between a tangent to the α -line at point (α, β) and the x axis, see Hemp (1973), where this notation is explained in detail.

The conditions (1) determine the virtual displacement field $\bar{u} = (u, v)$; u and v represent displacements along α and β lines. The integration technique explained in Hemp (1973) makes it possible to find the integral formula for $u(\alpha, \beta)$ and $v(\alpha, \beta)$. However, to make these formulae useful for further analysis of longer cantilevers one should put them in terms of known special functions. It turns out that the functions introduced by Chan (1975, Appendix) and named $G_n(\alpha, \beta)$, $F_n(\alpha, \beta)$ in Lewiński et al. (1994) suffice to express all the unknowns explicitly, not only A , B , u , v within $ABDC$ but also their extensions as well as stress fields.

These functions satisfy the hyperbolic equation $LH_n = 0$, where $H = G$ or F and $L = \frac{\partial^2}{\partial\alpha\partial\beta} - 1$. Just this equation governs the behavior of Lamé coeffi-

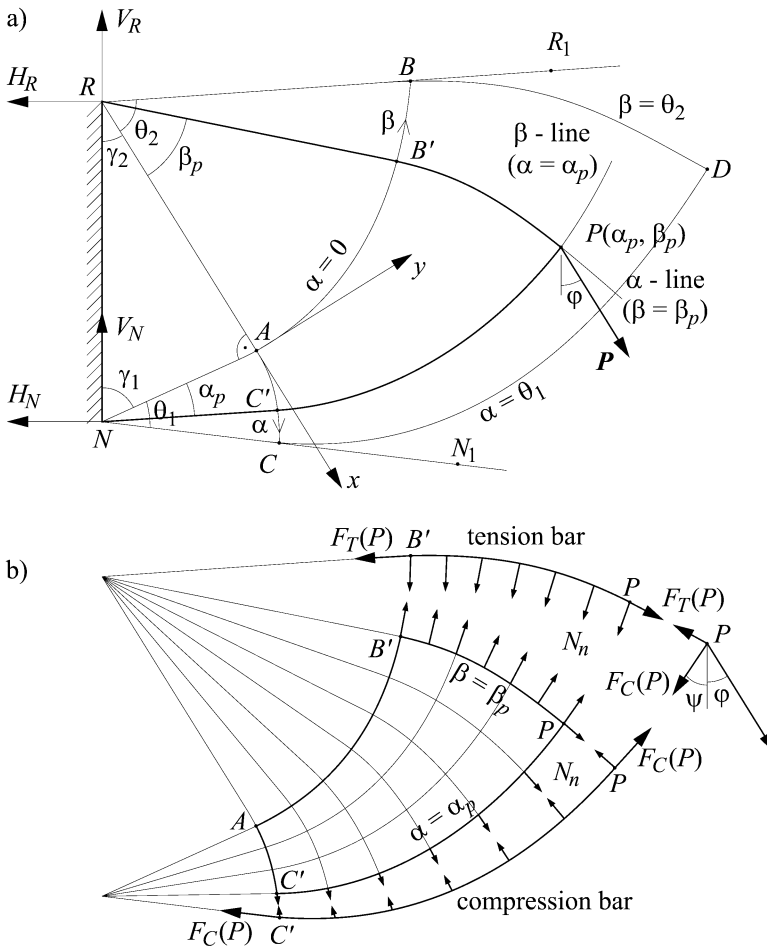


Figure 1. Prager-Hill cantilever. The feasible domain is determined by \$RN\$ and the angles \$\angle R_1RN\$, \$\angle N_1NR\$.

icients, rotated coordinate functions \$\bar{x}\$, \$\bar{y}\$ defined by \$\bar{x} + i\bar{y} = \exp(-i\phi)(x + iy)\$ as well as the auxiliary displacement fields

$$\begin{aligned} u^0(\alpha, \beta) &= u(\alpha, \beta) - (\kappa + 1)\alpha A(\alpha, \beta), \\ v^0(\alpha, \beta) &= v(\alpha, \beta) + (\kappa + 1)\beta B(\alpha, \beta). \end{aligned} \tag{2}$$

In the present paper we show that the force fields associated with the Hencky net of the \$ABDC\$ domain, caused by a point load \$\mathbf{P}\$ at point \$P = P(\alpha_p, \beta_p)\$, lying within \$ABDC\$, can also be expressed in terms of Chan's functions \$G_n\$. The optimal cantilever occupies the domain \$RB'PC'N\$, see Figure 1. Having found the force fields we can compute the volume by direct integration over the

fibrous domains $RB'A$, NAC' and $AB'PC'$ and along the lines of reinforcing bars $RB'P$ and $NC'P$. It turns out that the volume computed this manner confirms the correctness of the whole solution. The problem of finding force fields in the cantilever of Figure 1 has never been discussed till now.

We shall use notation of a classical plate theory. The average stress resultants referred to the (α, β) system will be denoted by N_I , N_{II} since α and β lines are lines of principal directions of tensor \mathbf{N} . We do not use notation: σ_I , σ_{II} to distinguish between average and local stresses. Let us recall that the differential equations of equilibrium referred to the (α, β) system have here the form

$$-\frac{\partial(BN_I)}{\partial\alpha} + \frac{\partial B}{\partial\alpha}N_{II} = 0, \quad -\frac{\partial(AN_{II})}{\partial\beta} + \frac{\partial A}{\partial\beta}N_I = 0. \quad (3)$$

These equations are identical with the first two differential equations of membranes parameterized by an orthogonal curvilinear system. It is Hemp (1973) who discovered that equations (3) can be simplified by changing the unknowns $T_1 = BN_I$, $T_2 = AN_{II}$. By using the differential constraints linking A and B we reduce (3) to the form

$$T_2 = \frac{\partial T_1}{\partial\alpha}, \quad T_1 = \frac{\partial T_2}{\partial\beta} \quad (4)$$

not involving Lamé coefficients. Thus we see that $LT_1 = 0$, $LT_2 = 0$, which makes it possible to apply the Riemann method, already used for finding the Hencky net (α, β) . Note that T_1, T_2 are of force dimension. They measure the forces per unit angles and not per unit lengths. From mechanics point of view these fields have similar meaning to axial forces in truss members. If we put (4) in the variational form

$$\iint \left[T_1 \left(\frac{\partial \bar{u}}{\partial \alpha} + \bar{v} \right) + T_2 \left(\frac{\partial \bar{v}}{\partial \beta} + \bar{u} \right) \right] d\alpha d\beta = \int_{\alpha=\text{const}} \hat{T}_1 \bar{u} d\beta + \int_{\beta=\text{const}} \hat{T}_2 \bar{v} d\alpha \quad (5)$$

for all kinematically admissible \bar{u}, \bar{v} we note that (5) can be discretized to the variational equilibrium equation of a truss. Here \hat{T}_1 (\hat{T}_2) are given loadings normal to the edges $\alpha = \text{const}$ ($\beta = \text{const}$). We write (5) symbolically as

$$\iint T_1 d\beta (d\bar{u} + \bar{v}d\alpha) + \iint T_2 d\alpha (d\bar{v} + \bar{u}d\beta) = \bar{L}_{\text{ext}}, \quad (6)$$

where \bar{L}_{ext} represents the virtual work of given loading. Note that

$$d\bar{u} + \bar{v}d\alpha = (A d\alpha)\bar{e}_I, \quad d\bar{v} + \bar{u}d\beta = (B d\beta)\bar{e}_{II} \quad (7)$$

represent elongations of α and β fibres of lengths $A d\alpha$ and $B d\beta$, respectively. We remember that $T_1 d\beta$ is a longitudinal force in the strip of width $B d\beta$ along

the α -line and $T_2 d\alpha$ is such a force in the strip of width $A d\alpha$ along the β -line. The associated elongations of these strips are $\bar{\Delta}_\alpha = A d\alpha \bar{\varepsilon}_I$, $\bar{\Delta}_\beta = B d\beta \bar{\varepsilon}_{II}$. Let us imagine that the Hencky net (α, β) is replaced by a net of finite number of α and β lines constructed from straight segments, treated further as members of a certain truss. We imagine that the forces $T_1 d\beta$ and $T_2 d\alpha$ are now concentrated along the members. These forces are now treated as axial forces Z_K^α, Z_L^β in the truss; here K, L index the members. They do a virtual work on elongations $\bar{\Delta}_\alpha^K$ and $\bar{\Delta}_\beta^L$. Thus Equation (6) is replaced with

$$\sum_K Z_K^\alpha \bar{\Delta}_\alpha^K + \sum_L Z_L^\beta \bar{\Delta}_\beta^L = \bar{L}_{\text{ext}} \quad (8)$$

and if the independent virtual displacements of nodes are denoted by $\bar{q}_1, \dots, \bar{q}_s$, then \bar{L}_{ext} is replaced by $\bar{\mathbf{q}}^T \mathbf{Q}$ with \mathbf{Q} being the vector of effective nodal forces. To note that (8) represents equations of nodes of the approximating truss we should put Z_K^α, Z_L^β into one column \mathbf{Z} , put elongations $\bar{\Delta}_\alpha^K, \bar{\Delta}_\beta^L$ into one column $\bar{\mathbf{\Delta}}$ and correlate them with nodal virtual displacements by linear equations: $\bar{\mathbf{\Delta}} = \mathbf{B}\bar{\mathbf{q}}$, \mathbf{B} being a geometry matrix. Thus Equation (8) implies $\bar{\mathbf{\Delta}}^T \mathbf{Z} = \bar{\mathbf{q}}^T \mathbf{Q}$ hence $\mathbf{B}^T \mathbf{Z} = \mathbf{Q}$, because $\bar{\mathbf{q}}$ is arbitrary. We conclude that Equation (6) can be approximated by truss equilibrium equations, with arbitrary accuracy.

Let us come back to the problem of equilibrium of the cantilever of Figure 1. We should decompose it into two reinforcing bars $B'P$ (in tension, $F_T > 0$) and $C'P$ (in compression, $F_C < 0$), the node P subjected to three forces of magnitudes: $F_T(P), F_C(P), P$, the fibrous domain $B'PC'A$, the fans $RB'A, NAC'$ with edge bars RB', NC' and the rectangle RAN is empty. Kinematic consideration starts from RAN domain and moves to the right. On the contrary, static analysis starts from equilibrium of node P and moves left. The net is already found (see Graczykowski and Lewiński (2005b)) so we know the angle ψ between tangent to $C'P$ at P and the vertical line RN : $\psi = \gamma_1 + \alpha_p - \beta_p$. Angle φ is directed counterclockwise, see Figure 1a.

Note first that the longitudinal forces F_T and F_C do not vary along $B'P$ and $C'P$, since no tangent loading is applied. Thus $F_T = F_T(P)$ and $F_C = F_C(P)$. The magnitudes of forces $F_T(P), F_C(P)$ found from equilibrium equations of node P

$$F_C(P) = -P \cos(\psi + \varphi), \quad F_T(P) = P \sin(\psi + \varphi) \quad (9)$$

determine the longitudinal forces in the bars $B'P$ and $C'P$. Since $B'R$ ($C'N$) is a smooth extension of $B'P$ ($C'P$) at B' (C') the axial forces in RB' (and NC') are still equal to $F_T(P)$ (and $F_C(P)$). Note that the bar $RB'P$ works like a cord, since it slides along $B'P$. The bar PC' is compressed with no buckling allowed. The equilibrium equations of both the bars determine the magnitude

of the normal loading N_n . Since Lamé coefficients are equal here to the radii of curvatures we obtain

$$N_n = -F_C(P) \quad \text{for } \alpha = \alpha_p, \quad N_n = -F_T(P) \quad \text{for } \beta = \beta_p, \quad (10)$$

see Figure 1b. These formulae provide the boundary conditions

$$T_1(\alpha_p, \beta) = -F_C(P), \quad T_2(\alpha, \beta_p) = -F_T(P) \quad (11)$$

We can apply now Riemann's method, as explained in Lewiński et al. (1994, equation (17)) and find

$$\begin{aligned} T_1(\alpha, \beta) &= -F_C G_0(\alpha_p - \alpha, \beta_p - \beta) + F_T G_1(\alpha_p - \alpha, \beta_p - \beta), \\ T_2(\alpha, \beta) &= -F_T G_0(\alpha_p - \alpha, \beta_p - \beta) + F_C G_1(\beta_p - \beta, \alpha_p - \alpha). \end{aligned} \quad (12)$$

Having found T_1 , T_2 we can compute their boundary values along AB' and AC' , which determines force fields within the circular fans $RB'A$, NAC' . It occurs that the circumferential stresses vanish and the radial stresses are constant along the radii. Now we know the force fields T_1 , T_2 within the whole structure and we know the axial forces in the ribs. The last step is to compute the reactions: H_R , V_R , H_N , V_N by considering equilibrium conditions of nodes R and N . The concentrated forces at R , N and P should give zero total vector and zero total moment around an arbitrary point (say, P). These three algebraic equations should confirm that the whole static analysis has been done correctly.

3. EQUIVALENCE OF TWO FORMULAE FOR THE WEIGHT OF THE OPTIMAL PRAGER-HILL CANTILEVER

Virtual work of the force P determines the volume of the optimal cantilever:

$$\mathcal{V} = \frac{P}{\sigma_T} [u(P) \sin(\varphi + \psi) - v(P) \cos(\varphi + \psi)], \quad (13)$$

where $P = P(\alpha_p, \beta_p)$; the functions u , v being given in section 9 of Graczykowski and Lewiński (2005b). Both the fields u and v are expressed in terms of Chan functions. To be sure that this result is correct we shall compute this volume directly by summing up the volumes of all the parts of the structure. Density of fibres within $AB'PC'$ is given by

$$h(\alpha, \beta) = \frac{T_1(\alpha, \beta)}{\sigma_T B(\alpha, \beta)} - \frac{T_2(\alpha, \beta)}{\sigma_C A(\alpha, \beta)}. \quad (14)$$

We know that $T_2 < 0$. For the NAC' fan the formula for density h does not contain the first term. For the $RB'A$ fan the function h is expressed by the first

term. To compute the integral

$$\mathcal{V}_{AB'PC'} = \int_0^{\alpha_p} \int_0^{\beta_p} h(\alpha, \beta) A(\alpha, \beta) B(\alpha, \beta) d\alpha d\beta, \quad (15)$$

with h being given by (14), T_1 , T_2 given by (12) and A , B given by (4) in Graczykowski and Lewiński (2005b) one should apply the integration rules (31)–(36) of Lewiński et al. (1994).

The expressions for $\mathcal{V}_{NAC'}$ and $\mathcal{V}_{RB'A}$ can be found by similar integration. Now we compute the volume of the tension (T) bar

$$\mathcal{V}_T = \frac{F_T(P)}{\sigma_T} \left(\int_0^{\alpha_p} A(\alpha, \beta_p) d\alpha + r_2 \right). \quad (16)$$

The formula for the volume \mathcal{V}_c of the compression bar is similar.

This integration can be performed by using properties of Chan's functions. By summing up the volumes of material used for construction of fibrous domains $AB'PC'$, NAC' , $RB'A$ and of the ribs $RB'P$, $NC'P$ we arrive at \mathcal{V} coinciding exactly with formula (13). We say that the duality gap between the dual and primal formulations vanishes.

4. FAMILY OF CANTILEVERS DESIGNED WITHIN A STRIP. BENCHMARK RESULTS

Let us consider the case of $\kappa = 3$, $\theta_1 = \pi/6$, $\theta_2 = \pi/3$. Then the feasible domain is a strip, see Figure 2. The force P is assumed to act parallel to the RN supporting line, or $\varphi = 0$, its application point P being on the midperpendicular to RN at a distance d from RN . Let $\xi = d/a$, with $a = |RN|$. Thus the family of problems is indexed by ξ . If $\xi = \sqrt{2}/2$ the optimal structure is composed of two bars and one circular fan. If $\xi > \sqrt{2}/2$, point P lies at the right side of P_0 , where $|RP_0| = |RA| = a\sqrt{3}/2$, $|RO| = a/2$. Let the volume of the optimal cantilever be denoted by \mathcal{V} and its non-dimensional counterpart by $\bar{\mathcal{V}} = \mathcal{V}/(Pa/\sigma_T)$. The values of $\bar{\mathcal{V}}$ are set up in Table 1 for subsequent values of the distance $d = \xi a$ of the force P to the RN line. The same table gives also the curvilinear coordinates (α_p, β_p) of subsequent position of point P .

The midperpendicular of RN crosses subsequent domains of kinematic division, as introduced in Graczykowski and Lewiński (2005b, 2006). Thus the graph of the volume of Figure 3 refers not to one but to several types of the cantilevers: for $0 \leq \xi \leq \sqrt{3}/6$ the optimal structure is composed of two bars; for $\sqrt{3}/6 \leq \xi \leq \sqrt{2}/2$ the optimal structure is composed of one circular fan and two bars; for $\sqrt{2}/2 \leq \xi \leq 1.522008$ the solution is called Prager–Hill cantilever; for $1.522008 \leq \xi \leq 2.036580$ the solution includes additionally one Chan-like domain; for $2.036580 \leq \xi \leq 3.028582$ the solution includes two Chan-like domains and one Hill-like domain more.

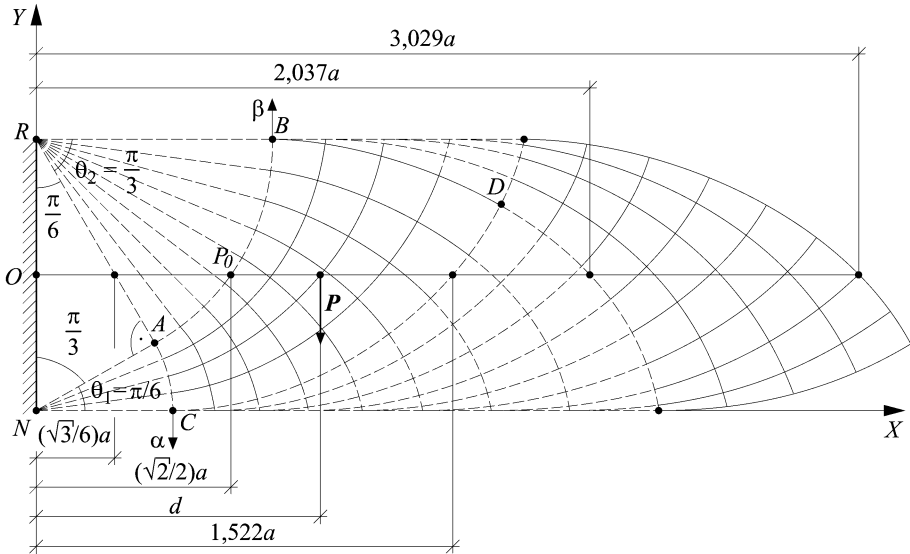


Figure 2. Case of: $\kappa = 3$, $\theta_1 = \pi/6$, $\theta_2 = \pi/3$, $\varphi = 0$. Chan's domains are indicated by dashed lines.

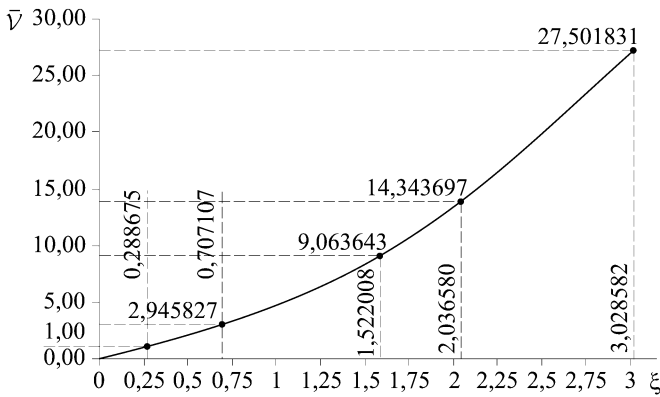


Figure 3. Non-dimensional volume \bar{V} of the optimal cantilevers.

Nonetheless, the graph of the volume versus ξ is smooth, even at points $\xi = \sqrt{3}/6$, $\sqrt{2}/2$, 1.522008, 2.036580, 3.028582, where the structure of the solution switches to a more complicated form.

The results set up in Table 1 are benchmark results for possible numerical checks based on a ground structure method or other numerical-oriented basis.

Table 1. Non-dimensional volume \bar{V} of the optimal cantilevers.

ξ	α_p	β_p	\bar{V}
0	–	–	0
0.25	–	–	0.86602540
0.5	–	0.26179939	1.88962418
0.75	0.03909955	0.45996378	3.18119647
1	0.23418873	0.61048885	4.77413280
1.25	0.38788355	0.73867388	6.68710224
1.5	0.51357763	0.84847879	8.86123302
1.75	0.66391239	0.94562854	11.27758404
2	0.80344224	1.03477767	13.93605154
2.25	0.93237717	1.16472612	16.83306684
2.5	1.05679215	1.29767843	19.99191059
2.75	1.17798254	1.42731919	23.40492241
3	1.29752093	1.55600661	27.06729757

5. FINAL REMARKS

Construction of Hencky nets within the trapezoidal domains, as outlined in Graczykowski and Lewiński (2005b), is complemented here by the analysis of force fields within the fibrous domains and in the reinforcing ribs. The force fields and Lamé fields determine the density of fibers as well as the cross sections of the ribs. Integration of the mass density confirms the values of the volumes of the optimal cantilevers found previously by the Michell-like kinematic formulae.

REFERENCES

- Chan, H.S.Y. (1967) Half-plane slip-line fields and Michell structures, *Q. J. Mech. Appl. Math.*, 20, 453–469.
- Chan, H.S.Y. (1975) Symmetric plane frameworks of least weight, in *Optimization in Structural Design*, A. Sawczuk and Z. Mróz, (eds), Springer-Verlag, Berlin, pp. 313–326.
- Gilbert, M., Darwich, W., Tyas, A. and Shepherd, P. (2005) Application of large-scale layout optimization techniques in structural engineering practice, in *6th World Congress of Structural and Multidisciplinary Optimization*, Rio de Janeiro, 30 May–3 June 2005, Brasil, CD ROM, in press.
- Golay, F. and Seppecher, P. (2001) Locking materials and the topology of optimal shapes, *Eur. J. Mech. A/Solids*, 20, 631–644.
- Graczykowski, C. and Lewiński, T. (2005a) The lightest plane structures of a bounded stress level, transmitting a point load to a circular support, *Control and Cybernetics*, 34, 227–253.
- Graczykowski, C. and Lewiński, T. (2005b) New designs of Michell-like cantilevers corresponding to different allowable tensile and compressive stresses, in *6th World Congress of Structural and Multidisciplinary Optimization*, Rio de Janeiro, 30 May–3 June 2005, Brazil, CD ROM, in press.

- Graczykowski, C. and Lewiński, T. (2006) Michell cantilevers constructed within trapezoidal domains – Part I: Geometry of Hencky nets, Part II: Virtual displacement fields, Part III: Force fields, Part IV: Complete exact solutions of selected optimal designs and their approximations by trusses of finite number of joints, *Struct. Multidisc. Optimiz.*, in press.
- Hemp, W.S. (1973) *Optimum Structures*, Clarendon Press, Oxford.
- Lewiński, T. and Telega, J.J. (2001) Michell-like grillages and structures with locking, *Arch. Mech.*, 53, 303–331.
- Lewiński, T., Zhou, M. and Rozvany, G.I.N. (1994) Extended exact solutions for least-weight truss layouts – Part I: Cantilever with a horizontal axis of symmetry, Part II: Unsymmetric cantilevers, *Int. J. Mech. Sci.*, 36, 375–398, 399–419.
- Michell, A.G.M. (1904) The limits of economy of material in frame-structures, *Phil. Mag.*, 8, 589–597.
- Prager, W. (1959) On a problem of optimal design, in *Proc. IUTAM Symp. on Non-Homogeneity in Elasticity and Plasticity*, W. Olszak (ed.), Pergamon Press, London, pp. 125–132.
- Rozvany, G.I.N. (1997) Some shortcomings in Michell's truss theory, *Struct. Optimiz.*, 12, 244–250.
- Strang, G. and Kohn, R.V. (1983) Hencky–Prandtl nets and constrained Michell trusses, *Comp. Meth. Appl. Mech. Eng.*, 36, 207–222.

REFLECTIONS ON TRUSS AND CONTINUUM TOPOLOGY OPTIMAL DESIGNS

Pauli Pedersen and Niels L. Pedersen

Department of Mechanical Engineering, Solid Mechanics, Technical University of Denmark, Nils Koppels Allè, Building 404, DK-2800 Kgs. Lyngby, Denmark

pauli@mek.dtu.dk

Abstract: In continuum topology optimization the resulting optimal designs are highly depending on the amount of material available, relative to the size of the possible design space. To obtain black and white solutions (material or no material), penalization's are applied, and for the problems of low density we see a clear tendency toward solutions which more or less are truss or frame structures. Often the accuracy of the finite element models for the continuum is then at the limits with respect to accuracy.

The purpose of the presented project is to make a comparison between optimal designs found by known methods for topology optimization of continuum structures and optimal designs of structures modeled as trusses. For a statically determined truss each bar can be designed independently and therefore must be fully stressed in an optimal design. We want to put focus on the basic knowledge which gives optimality criteria for single load cases with only a single constraint.

Truss and continuum examples are analyzed, optimized, and evaluated to get further insight into the influence from the basic modeling, being truss or continuum. Stiffness as well as strength are important aspects of optimal design, and elastic energy density is a general measure of these constraints.

Keywords: Optimal design, trusses, 2D continuum, penalization, free material.

1. INTRODUCTION

In structural optimization as well as in structural analysis, the choice of a proper model is important. The choice of necessary dimensions, 1D, 2D or 3D; for non-continua, truss or frame; for 2D problems plane stress, plane strain or alternatives; for finite element models the choice of elements and mesh. For structural optimization we have the further complication that what might be a proper model for the initial design, might not be a proper model for the optimal design. This is well known in relation to re-meshing in shape optimization.

In optimal design of an initial continuum design that tends towards a truss or frame, a shift of model might also be appropriate. With this in mind we analyze and optimize trusses and continua to get a better understanding of the modeling issue.

Available basic knowledge related to truss design is described in Section 2 including a specific example of a bridge design. The importance of including stability constraints is clearly demonstrated.

Available basic knowledge related to 2D and 3D continuum design is described in Section 3. With the truss bridge problem in a continuum setting we show the influence from penalization to 0–1 design (white and black).

Finally in Section 4 we want to focus on the free material design. Solutions to these non-isotropic problems are obtained by isotropic, zero Poisson's ratio analysis. Results with Poisson's ratio as an additional parameter are presented and discussed.

2. BASIC KNOWLEDGE ON TRUSS DESIGN

Trusses are structures that are simple to analyze, because each point of the structure is only subjected to a unidirectional state of stress/strain. The basic element of a truss is a bar and the bars are connected through joints that only transfer a normal force (tensile or compression) to each bar. In addition to being simple structures, trusses are also very efficient structures with the possibility of designing fully stressed structures, where each point in the structure is used to its limit. For a statically determined truss, each bar can be designed independently and therefore in an optimal design must be fully stressed.

If we assume that allowable stresses and joint positions are given, then the problem of finding a truss of minimum mass is a linear programming problem. Such optimal design problems can be solved using the simplex optimization procedure, and this was done already by Dorn et al. (1964) and by Fleron (1964). With only a single load case, local stability is taken into account, and we can prove that a statically determined truss is a solution. Stated more generally we have:

If each bar n of the truss is designed with a minimum cost ϕ_n (fully stressed), which as a function of the actual non-negative bar force P_n , satisfies

$$\frac{d\phi_n}{dP_n} \geq 0 \text{ and } \frac{d\phi_n}{dP_n} \text{ non-increasing with } P_n, \text{ i.e. } \frac{d^2\phi_n}{dP_n^2} \leq 0, \quad (1)$$

then there exists at least one statically determinate truss that minimizes the cost of the total truss.

A proof of this theorem is available in chapter 16 of the book by Pedersen (2003). The proof follows from equilibrium, change in equilibrium by intro-

ducing an additional bar and the corresponding change in the total cost. We directly deal with three-dimensional trusses, and supports are treated as unknown bar forces. In the literature on mathematical programming, as in Gass (1964) and in Hadley (1964) we can find geometrical interpretations showing directly that the optimal solution is at a vertex of the convex feasible space described by the linear constraints. When the objective is a concave function and not just a linear function the solution is still at a vertex, but local optima may exist if the concave functions are too curved relative to the curvature of the feasible space. In the actually solved problems of topology design of trusses such local optima have not been seen.

In addition to some specified joint positions and the actual loads to be transferred, only few parameters are needed for the optimization. In most of the examples we use the same values for these data and therefore list them here: Modulus of elasticity $E = 2.0 \cdot 10^{11}$ Pa, stress limit of proportionality $\sigma_P = 1.6 \cdot 10^8$ Pa, allowable tensile stress $\sigma_T = 2.0 \cdot 10^8$ Pa, maximum allowable compressive stress $\sigma_C = 1.6 \cdot 10^8$ Pa, factor of safety for slender columns $\xi = 2.5$, mass density $\rho = 7500$ kg/m³, and the cross-sectional parameter $\alpha = \sqrt{I}/A$ where A is the cross-sectional area and I is the cross-sectional moment of inertia. We shall study the influence of local stability on the optimal topology by changing the cross-sectional parameter α . Also for visualization of the results, we need cross-sectional outer dimensions. Therefore we specialize to truss members with circular cross-section (pipes) with outer diameter d_o and inner diameter d_i , specified by the ratio μ , i.e., $d_i = \mu d_o$ with $0 \leq \mu < 1$. With well known formulas for the cross-sectional area A and for the cross-sectional moment of inertia I we get $\alpha = \alpha(\mu)$ and $d_o = d_o(A, \alpha)$

$$\alpha = \frac{1}{2} \sqrt{\frac{1 + \mu^2}{\pi(1 - \mu^2)}} ; \quad \mu = \sqrt{\frac{4\pi\alpha^2 - 1}{4\pi\alpha^2 + 1}} ; \quad d_o = \sqrt{2A(4\pi\alpha^2 + 1)/\pi}. \quad (2)$$

In the graphical illustrations of the trusses, the width of a bar is shown proportional to the diameter d_o in order to see more directly the obtained designs. At number of examples are available in chapter 3 of the book by Pedersen (2003). Here we only discuss the “bridge” example, illustrated in Figure 1.

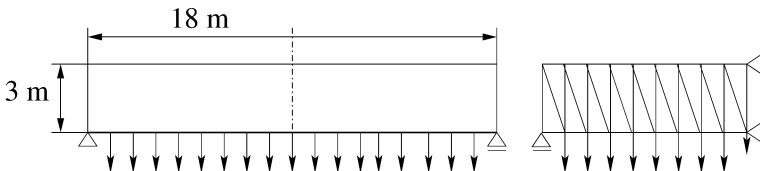


Figure 1. Truss with assumed symmetry and uniformly distributed loads. Initial topology shown on half the model for analysis and optimization.

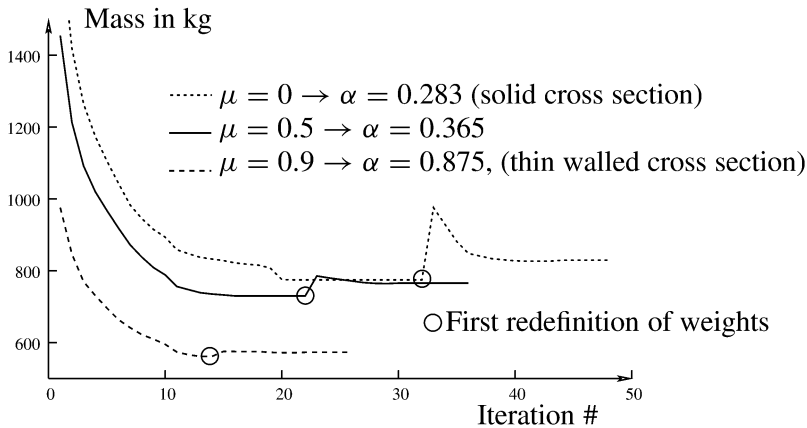


Figure 2. Total mass as a function of simplex iterations, including 5 redefinitions of weight loads. Only the first of these redefinitions are visible in the figure.

Figure 2 shows the convergence results for three cross sectional cases. Figure 3 shows the final topology and size designs when self weights are included in the optimization. The following points should be noted

- The topology designs are to a large extent influenced by the buckling constraints. Even with thin walled cross sections (design c)) we see that the less allowable compressive stress (80% of tensile stress) controls the optimal design.
- With solid cross sections (design a)) as much load as possible is carried by tensile members. The design is therefore much depending on the actual boundary conditions for the model.
- Both design b) and design c) show the characteristic of the combined cantilever and hanging simply supported part.
- No optimization of the joint positions are performed in the present examples, although the procedure for this is well known.

3. BASIC KNOWLEDGE ON CONTINUUM DESIGN

We start with some basis knowledge from size (thickness or density) optimization, as it can be found in Pedersen (1998) for non-linear elasticity or in Wasitynski (1960) for linear elasticity. If the objective is to minimize compliance (minimize elastic energy) for given total mass then we have (for optimal stiffness design with homogeneous assumptions and design independent loads):

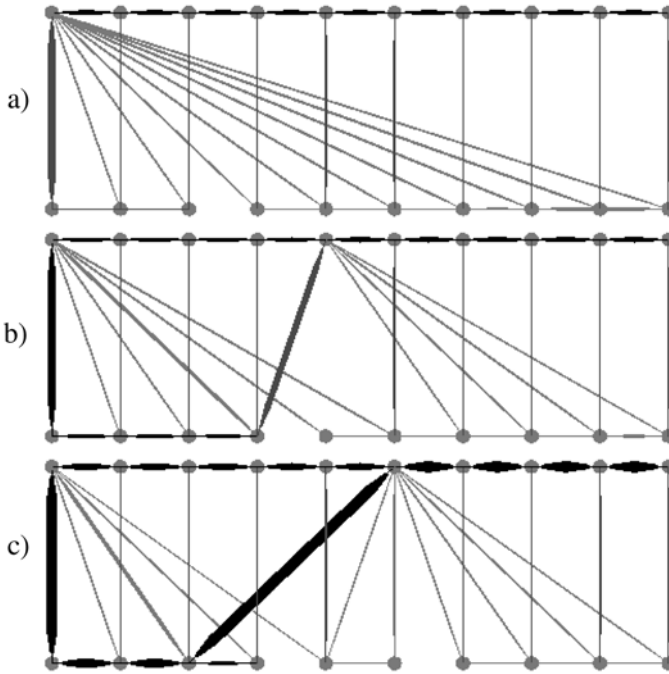


Figure 3. Half of the optimal bridge models, assuming symmetry as shown in Figure 1. Optimal truss topology with a) solid cross sections, b) thickness equal to half radius, c) thin walled cross section. All topologies with self weight. The width of the lines corresponding to the outer diameter of the pipes with thin tensile bars compared to the more dominating compressive bars. The gray lines are tensile bars, while the black bars are in compression.

The ratio between sub-domain energy and sub-domain mass should be the same in all the design sub-domains.

Let the design parameters be h_e , then homogeneous mass relations are obtained with $M = \sum_e M_e = \sum_e h_e^m \bar{M}_e$, where M is the total mass, M_e is the mass in domain e , m is a given positive value, and \bar{M}_e is independent of the design parameters. The homogeneous energy relations are obtained with $U = \sum_e U_e = \sum_e h_e^n \bar{U}_e$, where U is the total elastic energy, U_e is the elastic energy in domain e , n is a given positive value, and \bar{U}_e is *explicitly (for fixed strains)* independent of the design parameters.

Restricted to problems with constant mass density we get, in all design domains, the same mean elastic energy density. Furthermore, if the model has constant elastic energy density within a design domain, then the result for the optimal design is *uniform elastic energy density* u^* , i.e.

$$u_e^* = \bar{u} \text{ for all free design domains,} \quad (3)$$

where lower and upper size constraints are not reached. The symbolism here is a super-index $*$ related to the optimal design, and a overhead bar $\bar{}$ indicating a constant value for each domain e (mean value).

Assume now that the necessary condition (3) give a global minimum solution, then for any other design the total elastic energy U is larger (or equal to)

$$U = \sum_e u_e V_e \geq U^* = \sum_e u^* V_e^* = \bar{u} \sum_e V_e^* = \bar{u} \sum_e V_e = \sum_e u_e^* V_e, \quad (4)$$

where V_e^* is the optimal volume of the design domain e . For an alternative design with design volumes V_e we have the same total volume $V = \sum_e V_e = \sum_e V_e^*$. From (4) we get

$$\sum_e (u_e - u_e^*) V_e \geq 0. \quad (5)$$

With positive volumes V_e we read from (5), that at least one u_e is not less than u_e^* . Thus if the strongest design is defined by minimum of maximum u_e , then:

The stiffest design characterized by the optimality condition (3) is also the strongest design.

We note that the strength may also be defined in relation to the von Mises stress or an alternative effective stress, and these measures are not always proportional to the energy density. For a detailed discussion of these aspects, see Pedersen (1998).

As an example of actual design optimization we choose a continuum bridge model with dimensions and loads equal to the truss example in Section 2. From the results in Figures 4, 5, and 6 we can draw some conclusions which are general for many other examples.

- Traditional recursive iterations lead to solutions with uniform distribution of energy density (or as used here to uniform distribution of the von Mises' stress), within the limits of parametrization and finite element modeling. The number of iterations is 5–10.
- More design freedom is possible with less volume percentage and therefore the design advantages are bigger. For the 25% example in Figure 6 without penalization the compliance decreases from 781 Nm to 414 Nm, and the maximum von Mises' stress decreases from $5.9 \cdot 10^8$ Pa to $2.2 \cdot 10^8$ Pa.
- Less design freedom as with 75% gives less differens between the non-penalized and the penalized (black and white) designs. Compliance only

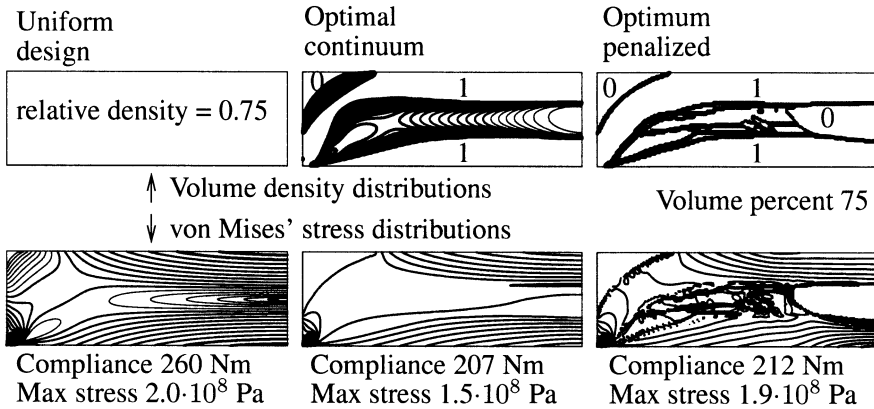


Figure 4. Optimal design for a 2D linear elastic “bridge” model with total relative volume density is 75%. Upper row shows the isolines of the designs and the lower row shows the isolines of the resulting von Mises’ stresses. In the domains without isolines we have constant volume density or constant von Mises’ stress, respectively. The numbers 1 and 0 indicate where there is full density and void, respectively.

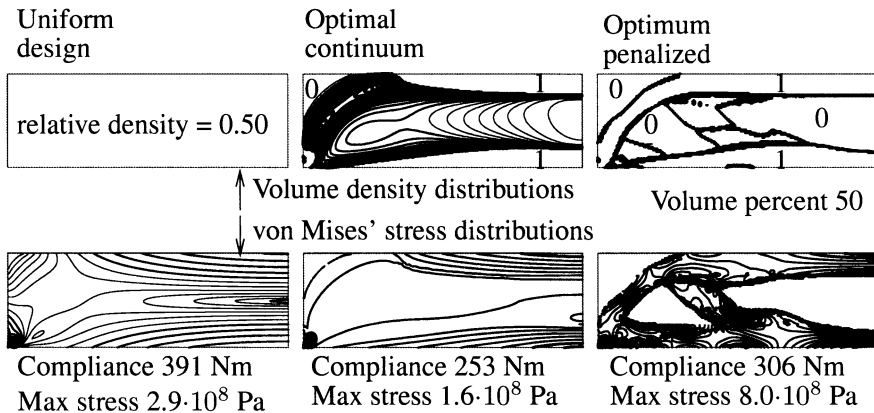


Figure 5. Optimal design for a 2D linear elastic “bridge” model with total relative volume density is 50%. Upper row shows the isolines of the designs and the lower row shows the isolines of the resulting von Mises’ stresses. In the domains without isolines we have constant volume density or constant von Mises’ stress, respectively. The numbers 1 and 0 indicate where there is full density and void, respectively.

increased from 207 Nm to 212 Nm, and maximum von Mises’ stress from $1.5 \cdot 10^8$ Pa to $1.9 \cdot 10^8$ Pa.

- When the volume percent is low, as with 25%, the optimized and penalized design needs a further processing with shape optimization. The present finite element models have 43200 triangular elements and von

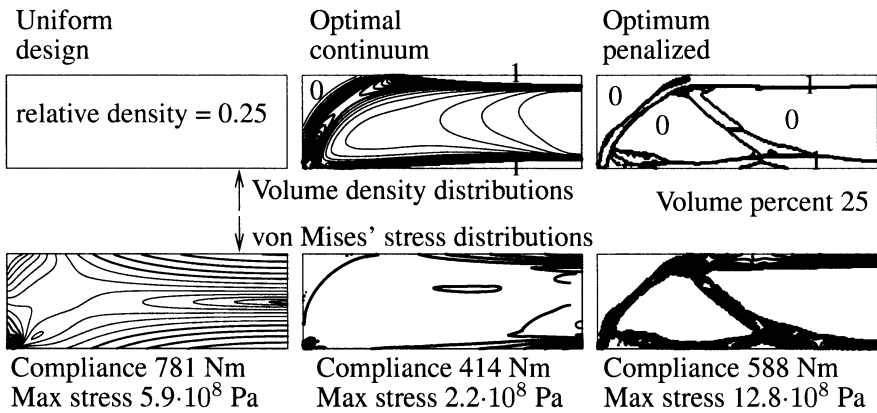


Figure 6. Optimal design for a 2D linear elastic “bridge” model with total relative volume density is 25%. Upper row shows the isolines of the designs and the lower row shows the isolines of the resulting von Mises’ stresses. In the domains without isolines we have constant volume density or constant von Mises’ stress, respectively. The numbers 1 and 0 indicate where there is full density and void, respectively.

Mises’ stresses as high as $12.8 \cdot 10^8$ Pa are found in the penalized model, to be compared with the value of $2.2 \cdot 10^8$ Pa for the non-penalized optimal design.

4. FREE MATERIAL DESIGN AND INFLUENCE FROM POISSON’S RATIO

In Bendsøe et al. (1994) we have obtained analytical results for the individual design of material constitutive components with the objective of minimizing the compliance. The single constraint for the optimization problem is a given total size of the constitutive matrix, measured by the Frobenius norm or by the trace norm.

For 2D-problems the resulting optimal constitutive matrix is

$$[C]_{\text{optimal}} = \frac{C}{(\epsilon_1 + \epsilon_2)^2} \begin{bmatrix} \epsilon_1^2 & \epsilon_1 \epsilon_2 & 0 \\ \epsilon_1 \epsilon_2 & \epsilon_2^2 & 0 \\ 0 & 0 & 0 \end{bmatrix}, \quad (6)$$

where C is a reference modulus and the actual principal strains are ϵ_1, ϵ_2 . The theory is also valid for 3D-problems and the results also hold for non-linear elasticity modeled by power law non-linearity, see Pedersen (1998).

The matrix $[C]$ presented in (6) have only one non-zero eigenvalue, and thus only stiffness in relation to the specific strain condition for which it is designed. We can obtain the same effective strain and strain energy density with an isotropic, zero Poisson’s ratio material, but then the corresponding

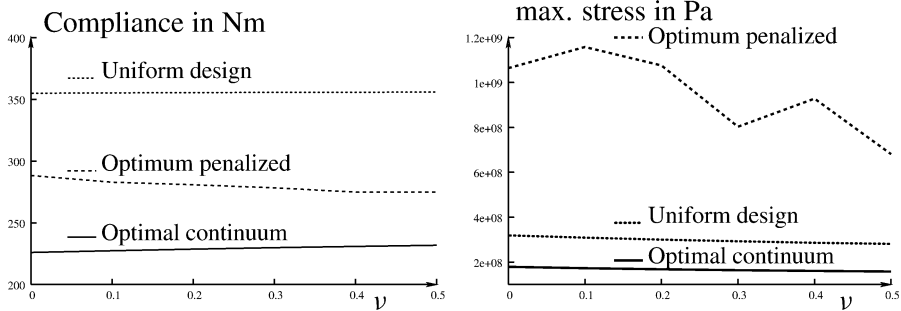


Figure 7. Optimization results as a function of Poisson's ratio ν for a total relative volume density of 50%, and plane stress. Left: compliance Right: maximum von Mises' stress.

material cost is three times greater for the 2D-problem with $[C] = C[I]$ (six times greater for the 3D-problem). As shown in Bendsøe et al. (1994), the zero Poisson's ratio material is valuable in numerical calculation, because of the degeneracy of the ultimate optimal material (6).

With this in mind we analyze and optimize the problem in Figure 5 taking Poisson's ratio ν as a further parameter in the range of $\nu = 0-0.5$ (the results in Figures 4, 5, and 6 are based on $\nu = 0.3$). Figure 7 to the left shows the compliance as a function of Poisson's ratio, and to the right shows the maximum von Mises' stress as a function of Poisson's ratio. To the results in Figure 7 we add the following comments:

- For the uniform design as well as for the optimal continuum, the compliance is weakly increasing with increasing Poisson's ratio for this plane stress model. (A plane strain model will give opposite results.) To physically understand this relation we note that the shear modulus G (multiple eigenvalue of the constitutive matrix) is decreasing with increasing ratio ν . Note that the influence from penalization is clearly visible.
- The maximum von Mises' stress is decreasing with increasing Poisson's ratio. A physical explanation may be that a more flexible model levels out the stress concentrations. Even for the moderate volume fraction of 50%, the influence of penalization amounts to an increase with a relatively large factor, as compared to the non-penalized optimal design. For the penalized design a clear monotone decrease of the maximum von Mises' stress is not seen, which may be related to the sensitive finite element modeling (43200 elements).

5. CONCLUSIONS

Attention is put on basic knowledge related to truss and continuum optimal design. Although this knowledge is related to single load cases it should be kept in mind, especially in relation to benchmark tests.

In truss optimal design stability constraints must be incorporated. This implies a primary focus on compressive members, and from this follows a major importance of boundary conditions and selected cross sectional shapes. For benchmark tests the statically determined optimal solutions are most valuable.

In continuum optimal design, solutions with a uniform distribution of elastic energy play the role of reference. Under certain assumptions the stiffest design will also be the strongest design. When penalization to 0–1 design is needed, it implies a more compliant design and often with drastic stress concentrations.

The examples in this note are modeled as two dimensional linear elasticity. However, the conclusions are valid in 3D and for non-linear power law elasticity. Even these extended problems can be solved without practical problems, such as CPU time.

When several load cases and/or several constraints (such as displacements and eigen frequency constraints) are involved, then mathematical programming must be applied, as shown e.g. in Pedersen and Nielsen (2003). However the basic knowledge presented in this note should not be forgotten and attempts as by da Silva Smith (1997) need further investigations.

REFERENCES

- Bendsøe, M.P., Guedes, J.M., Haber, R.B., Pedersen, P. and Taylor, J.E. (1994) An analytical model to predict optimal material properties in the context of optimal structural design, *J. Applied Mechanics*, 61, 930–937.
- da Silva Smith, O. (1997) Topology optimization of trusses with local stability constraints and multiple loading conditions – A heuristic approach, *Structural Optimization*, 13, 155–166.
- Dorn, W.S., Gomory, R.E. and Greenberg, H.J. (1964) Automatic design of optimal structures, *J. de Mechanique*, 3, 25–52.
- Fleron, P. (1964) The minimum weight of trusses, *Bygningsstatistiske Meddelelser*, 35, 81–96.
- Gass, S.I. (1964) *Linear Programming*, McGraw-Hill, Tokyo, 280 pp.
- Hadley, G. (1964) *Nonlinear and Dynamic Programming*, Addison-Wesley, 484 pp.
- Pedersen, N.L. and Nielsen, A.K. (2003) Optimization of practical trusses with constraints on eigenfrequencies, displacements, stresses and buckling, *Struct. Multidisc. Optim.*, 25(5–6), 436–445.
- Pedersen, P. (1998) Some general optimal design results using anisotropic power law non-linear elasticity, *Structural Optimization*, 15, 73–80.
- Pedersen, P. (2003) *Optimal Designs – Structures and Materials – Problems and Tools*, <http://www.fam.mek.dtu.dk/pp.html>. 314 pages.
- Wasiutynski, Z. (1960) On the congruency of the forming according to the minimum potential energy with that according to equal strength, *Bull. de l'Academie Polonaise des Sciences, Serie des Sciences Techniques*, 8(6), 259–268.

SOME BASIC ISSUES OF TOPOLOGY OPTIMIZATION

George I.N. Rozvany¹, Vanda Pomezanski¹, Osvaldo M. Querin²,
Zsolt Gaspar¹ and Janos Logo¹

¹*Research Group: Computational Structural Mechanics, Hungarian Academy of Sciences and Budapest University of Technology and Economics, Műegyetem rkpt 3, Km. 35, H-1521 Budapest, Hungary*

²*School of Mechanical Engineering, The University of Leeds, Leeds LS2 9JT, U.K.*

Abstract: The aim of this paper is to discuss some issues of pivotal importance in topology optimization, which receive inadequate attention in the literature.

Keywords: Topology optimization, topology benchmarks, checkerboard control, analytical solutions, hyper-optimality, SIMP, non-gradient methods.

1. INTRODUCTION

Topology optimization has become one of the most popular research topics in structural mechanics, because (a) it requires unusual mathematical and numerical concepts and (b) it results in much greater savings than shape or size optimization. Whilst the number of papers dealing with (i) new methods, (ii) new mechanical problems, and (iii) new industrial applications of topology optimization is rather staggering, some fundamental issues of this field have not been sufficiently researched and therefore the correctness and accuracy of methods and applications in a large number of papers is somewhat questionable. The paper dealt with the following issues:

- (a) New classes of exact analytical solutions for structural topologies with a view to providing benchmarks for numerical topology optimization methods and applications.

Such solutions include those for

- (i) Pre-existing members,
- (ii) Unequal permissible stresses in tension and compression, and
- (iii) Simultaneous optimization of structural topology and supports of non-zero cost.

- (b) New corner contact (or “checkerboard”) suppression methods.
- (c) Quantitative methods for checking on the “goodness” or quality of numerical topology optimization methods and numerically obtained solutions.
- (d) Topology design based on so-called “extended optimality” or “hyper-optimality”.
- (e) Gradient-type methods (e.g. SIMP) vs. non-gradient methods (such as ESO).
- (f) The dependence of gradient-type methods on certain heuristic features.

2. NEW CLASSES OF EXACT ANALYTICAL SOLUTIONS IN TOPOLOGY OPTIMIZATION

The first author and his research associates have derived exact analytical solutions for the exact optimal topology of trusses, grillages, shell grids and perforated plates. They are working on a number of extensions of these theories, out of which we consider three in this paper.

2.1 Optimal Topologies with Pre-Existing Members or Elements

Numerical results for optimal topologies of perforated plates in plane stress are often checked by comparing them with exact analytical solutions for least-weight (Michell) trusses.

For the former problem class, it is usual to prescribe a “non-design” region, in which all elements must remain of full thickness or density (called also “black” elements). An example of such a problem is given in Figure 1.

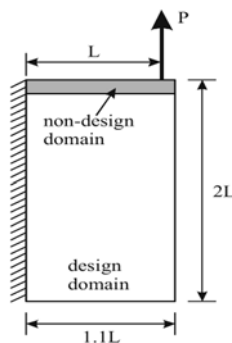


Figure 1. Example of a discretized topology design problem with a non-design domain.

2.1.1 Optimality Conditions. The optimality conditions for topologies with pre-existing members are presented in the context of “grid-like continua”, consisting of members that may have infinitesimal spacing. Some of these were termed by Prager (e.g. Prager and Rozvany, 1977) “truss-like continua”, “grillage-like continua” and “shell-grid-like continua”. The layout (topology and geometry) and cross-sections of the members are to be optimized. Using the so-called “optimal layout theory” of Prager and Rozvany (1977), we start off with a “structural universe” (called by others “ground structure”), containing all potential members or elements, out of which the optimal ones are to be selected. For grid-like continua, the structural universe may consist of an infinite number of (infinitesimal) elements, (i) at all points contained in the design domain and (ii) in all directions. An optimal solution is obtained by finding

- (a) a statically admissible stress field \mathbf{Q}^s satisfying equilibrium for the given loads and static boundary conditions,
- (b) a kinematically admissible (“adjoint”) strain field \mathbf{q}^k satisfying kinematic continuity and boundary conditions, such that
- (c) the optimal stress-strain relations $\mathbf{q}(\mathbf{Q})$ are given by the subgradients of the so-called “specific cost functions” $w = \psi(\mathbf{Q})$, which express the relationship between the (usually “generalized”) stresses \mathbf{Q} and the material weight (w) per unit area or unit volume of the design domain. Examples of generalized stresses are axial forces F in truss elements or bending moments M in beam elements.

The adjoint strain field is a fictitious one, but for so-called “self-adjoint” problems it is proportional to the real strain field. The sub-gradients are the usual derivatives in differentiable regions, but consist of the convex combinations of adjacent derivatives at slope-discontinuities. Detailed presentations of the optimal layout theory (which is a generalization of a classical truss optimization method by Michell, 1904) can be found in the first author’s books (Rozvany, 1976, 1989). Considering a truss element subject to a stress constraint, for example, the specific cost function for so-called “plastic design” (based on only statical admissibility, Prager and Shield, 1967) is

$$A = k|F|, \quad (1)$$

where A is the cross-sectional area, k is a constant and F is the member force. Then the adjoint strain is the longitudinal strain ε and the optimal strain-stress relation are given graphically in Figure 2a. Note that for vanishing members in the structural universe we have $F = 0$, but by Figure 2a the strains must still satisfy an inequality constraint.

For a pre-existing truss element with a cross-sectional area of B , we show the optimality conditions graphically in Figures 2b and c (for details, see Rozvany et al., 2006).

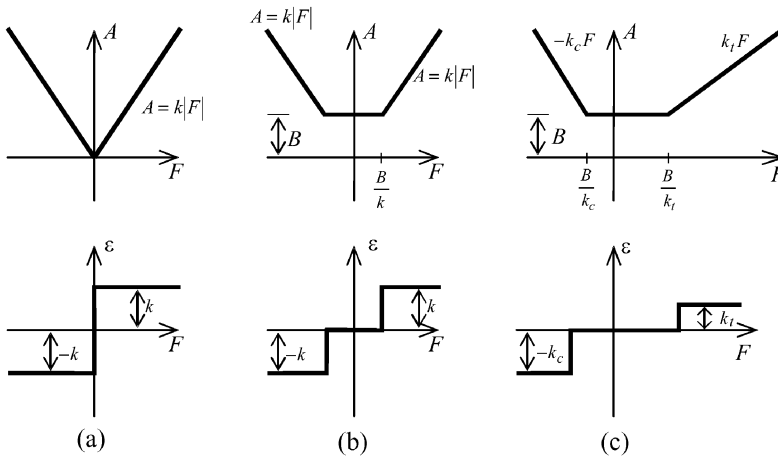


Figure 2. Examples of specific cost functions and adjoint strains: (a) traditional Michell truss element, (b) pre-existing member with equal permissible stresses in tension and compression, and (c) the same, but with different permissible stresses.

Notes:

- (i) Although the above theory is illustrated in the context of least-weight trusses, it can be readily extended to other structures.
- (ii) The problems considered in Figure 2 are convex and therefore (a)–(c) above constitute necessary and sufficient conditions for global optimality.
- (iii) The Michell problem in Figure 2a is self-adjoint, but its extensions in Figures 2b and 2c are not.
- (iv) The Prager–Rozvany (e.g., 1977) layout theory was originally developed for so-called “plastic design”, in which only static admissibility of the stresses is required. However, it is also valid for elastic structures, if the optimal layout is statically determinate (as for Michell trusses, see Sved, 1954).

2.1.2 Illustrative Examples. Consider the problem in Figure 1 but in the context of least-weight (Michell) trusses.

If we do not have any pre-existing member, then the known optimal solution (Lewinski et al., 1994) is shown in Figure 3a, in which the number of radial members in the “fan” is infinite. Note that there is no “concentrated member” along the line segment QR .

Next we investigate the problem, in which a pre-existing member is along the line segment QR . The optimal solutions are shown in Figures 3b and 3c (for details and proofs, see Rozvany et al., 2006).

The results in Figure 3a and 3b were confirmed numerically using the SIMP method (Rozvany and Zhou, 1991); for details, see Rozvany et al. (2006).

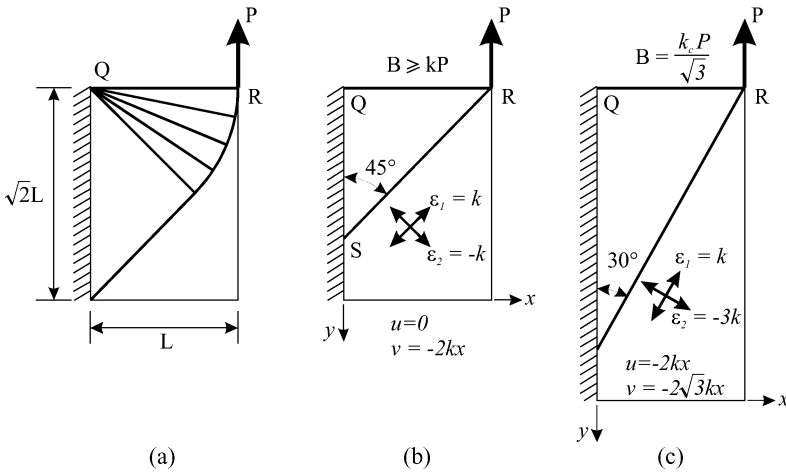


Figure 3. Examples of exact optimal truss topologies: (a) without pre-existing members, (b) with a not fully stressed pre-existing member, equal permissible stresses, and (c) with a fully stressed pre-existing member, unequal permissible stresses.

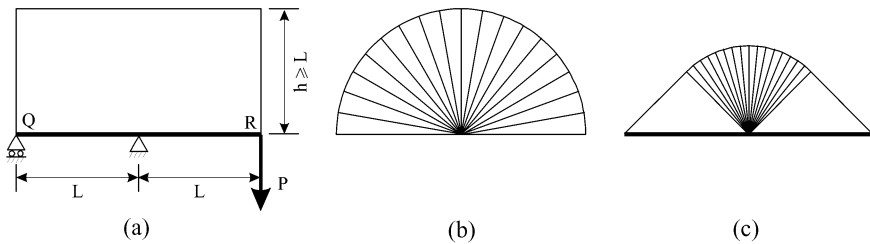


Figure 4. Example based on Michell's (1904) solutions: (a) supports and loading, (b) optimal topology without pre-existing member, (c) optimal topology with pre-existing member along QR .

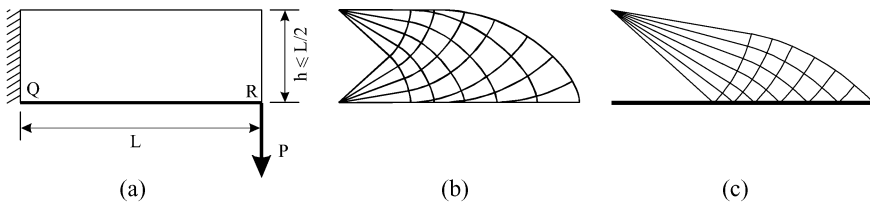


Figure 5. Example based on the cantilever problem (e.g. Lewinski et al., 1994): (a) to (c) as for Figure 4.

Further examples are shown in Figures 4 and 5, in which we show (a) the support conditions and loading, (b) the known optimal solution without pre-existing members (Michell, 1904; Lewinski et al., 1994) and (c) the solution for a not fully stressed pre-existing member along QR (with zero adjoint strain along QR).

2.2 Trusses with Unequal Permissible Stresses in Tension and Compression

In an earlier paper (Rozvany, 1996), the first author (a) pointed out an error in Michell's (1904) optimality criteria, (b) located the source of this error in Michell's proof, (c) proved that Michell's original optimality criteria are valid for a restricted class of support conditions and (d) presented an example showing that significant savings can be achieved by using the correct optimality conditions instead of Michell's conditions.

Based on the correct optimality criteria for unequal permissible stresses in tension and compression, Graczykowski and Lewinski (2005) developed mathematical methods for deriving systematically exact extended Michell trusses for a variety of support conditions (one of these topologies was selected by Springer for the cover design of SMO). The above work is an extension of two papers by Lewinski et al. (1994).

2.3 Simultaneous Optimization of Structural Topology and Supports of Non-Zero Cost

Optimality criteria for exact analytical solutions and examples were presented at a DCAMM symposium (Rozvany, 2003). Earlier numerical solutions by Buhl (2002) were verified by reference to older classical solutions by the first author (Rozvany and Gollub, 1990). The extended theory is based on any support cost function depending on the reaction forces. Buhl assumed a constant support cost, which is less realistic.

2.4 New Corner Contact (or “Checkerboard”) Suppression Methods

One of the most severe computational difficulties in FE-based topology optimization is caused by solid (or “black”) ground elements connected only through a corner node. This configuration may appear in checkerboard patterns, diagonal element chains or as isolated hinges. Corner contacts in nominally optimal topologies are caused by discretization errors associated with simple (e.g. four-node) elements (e.g. Sigmund and Petersson, 1998), which grossly overestimate the stiffness of corner regions with stress concentrations. In fact, it was shown by Gaspar (Rozvany et al., 2003) that both checkerboard patterns and diagonal element chains may give an infinite compliance, if the latter is calculated by an exact analytical method. This makes them the worst possible solution, if an exact analysis is used in compliance minimization. Corner contacts may be suppressed by:

- (a) a more accurate FE analysis of the ground elements,
- (b) modification of the original problem by using geometrical constraints or “diffused” sensitivities (filters),
- (c) employing a constraint preventing corner contacts directly, or
- (d) correcting selectively the discretization errors by appropriately penalizing corner contacts.

Method (a) may use several simple FEs per ground element (e.g. Rozvany and Zhou, 1991), or higher order elements (Sigmund and Petersson, 1998). Disadvantages of this approach are (i) greatly increased DOF for a given number of ground elements and (ii) some diagonal chains remaining in the solution (Gaspar et al., 2002).

Method (b), for example perimeter control (Haber and Bendsøe, 1996) or filtering (e.g. Sigmund, 1994), changes the original topology optimization problem and usually results in a lower resolution, which may – in some cases – be highly non-optimal (Rozvany et al., 2003) in terms of the original problem.

Methods (c) and (d) are similar, in so far as they both employ a “Corner Contact Function” (CCF) that has a high value for corner contacts and a low value for any other configuration around a corner node. This function is used in (c) above in an additional constraint preventing corner contacts (e.g. Poulsen, 2002) or in (d) as additional term in the objective function representing penalty for corner contacts. The latter approach seems the most rational, because it rectifies the discretization errors, which lower incorrectly the value of the objective function (e.g. compliance). Various new CCFs were investigated recently; for details, see Pomezanski et al. (2005). An early corner contact function was suggested by Bendsøe et al. (1993).

3. QUANTITATIVE METHODS FOR CHECKING ON THE “GOODNESS” OF NUMERICAL TOPOLOGY OPTIMIZATION METHODS

In spite of the abundance of new computational techniques and applications in structural topology optimization, methods used for proving the validity, quality and convergence of topology optimization procedures are often highly questionable. For the above “proof”, the majority of papers consider compliance design for plane-stress perforated plate problems with support and loading conditions, for which the optimal (Michell) truss solutions are known. Most authors are quite satisfied if their discrete plate solution vaguely reminds them of the corresponding exact truss solution, without even showing the details of the latter.

If we impose only behavioural constraints on our topology problem, the theoretical exact solution usually contains an infinite number of perforations or cavities. This means that with mesh refinement, the number of cavities in FE-based solutions will keep on increasing. However, if we know the exact analytical solution (with an infinite number of cavities), then we can show numerically that the discretized solutions indeed tends to the exact solution (both in volume and configuration), as we increase the number of ground elements and decrease the volume fraction. Various computational difficulties in this procedure and methods for overcoming them were discussed at the WCSMO-6 meeting (Rozvany et al., 2005).

4. TOPOLOGY DESIGN BASED ON SO-CALLED “EXTENDED OPTIMALITY” OR “HYPER-OPTIMALITY”

In a typical 2D topology optimization problem, we have a perforated plate of given thickness in plane stress, and we either minimize the compliance for a given volume (volume fraction) or minimize the volume (volume fraction) for a given compliance. In “extended” or “hyper-optimization” of the topology, the plate thickness and volume fraction are variable, and we minimize the product of total volume and total compliance. Obviously, hyper-optimization chooses an optimal solution from an infinitely larger feasible set than conventional topology optimization. Solutions of hyper-optimization were given in a paper by Rozvany et al. (2002). It was found that hyper-optimal topologies may even have a volume fraction of 100% or tending to 0%.

5. GRADIENT-TYPE METHODS (E.G. SIMP) VS. NON-GRADIENT METHODS (SUCH AS ESO)

This topic was discussed in detail at the meeting.

6. THE DEPENDENCE OF GRADIENT-TYPE METHODS ON CERTAIN HEURISTIC FEATURES

Even gradient-type topology optimization methods have some heuristic features. The solution strongly depends, for example, on the corner contact control (checkerboard suppression) method used. The widely used “filtering method” is almost entirely heuristic at present. Even within a given corner contact control method, the solution strongly depends on the choice of so-called “tuning parameters”. The effect of the above parameters on the solution is being studied.

ACKNOWLEDGMENTS

The authors are indebted to OTKA (National Basic Scientific Research Program, Hungary), Grant No. KO-1940/2002 and to the School of Mechanical Engineering, The University of Leeds, for financial support.

REFERENCES

- Bendsøe, M.P. and Sigmund, O. (2003) *Topology Optimization*, Springer, Berlin.
- Bendsøe, M.P., Diaz, A. and Kikuchi, N. (1993) Topology and generalized layout optimization of elastic structures, in *Topology Design of Structures*, Proc. NATO ARW held in Sesimbra, 1992, M.P. Bendsøe and C.A. Mota Soares (eds), Kluwer Academic Publishers, Dordrecht.
- Buhl, T. (2000) Simultaneous topology optimization of structure and supports, *Struct. Multidisc. Optim.*, 23, 257–261.
- Gaspar, G., Logo, J. and Rozvany, G.I.N. (2002) Addenda and corrigenda to a paper (Rozvany, G.I.N. (2001) Aims, scope, methods, history and unified terminology of computer-aided topology optimization in structural mechanics, *Struct. Multidisc. Optim.*, 21, 90–108), *Struct. Multidisc. Optim.*, 24, 338–342.
- Haber, R.B. and Bendsøe, M.P. (1996) A new approach to variable-topology shape design using constraint on the perimeter, *Struct. Optim.*, 11, 1–12.
- Lewinski, T. (2006) Variational proof of optimality criteria for Michell structures with pre-existing members, *Struct. Multidisc. Optim.*, accepted.
- Lewinski, T., Zhou, M. and Rozvany, G.I.N. (1994) Extended exact solutions for least-weight truss layouts. Part I. Cantilever with a horizontal axis of symmetry. Part II. Unsymmetric cantilevers, *Int. J. Mech. Sci.*, 36, 375–419.
- Michell, A.G.M. (1904) The limits of economy of material in frame structures, *Phil. Mag.*, 8, 589–597.
- Pomezanski, V., Querin, O.M. and Rozvany, G.I.N. (2005) CO-SIMP: Extended SIMP algorithm with direct CORner CONTACT CONTROL, *Struct. Multidisc. Optim.*, 30, 164–168.
- Poulsen, T.A. (2002) A simple scheme to prevent checkerboard patterns and one node connected hinges in topology optimization, *Struct. Multidisc. Optim.*, 24, 396–399.
- Prager, W. and Rozvany, G.I.N. (1977) Optimization of structural geometry (invited lecture), in *Dynamical Systems*, Proc. Univ. Florida Int. Symposium, Gainesville, March 1976, A.R. Bednarek and L. Cesari (eds), Academic Press, New York, pp. 265–294.
- Prager, W. and Shield, R.T. (1967) A general theory of optimal plastic design, *J. Appl. Mech.*, 34, 184–186.
- Rozvany, G.I.N. (1976) *Optimal Design of Flexural Systems*, Pergamon, Oxford.
- Rozvany, G.I.N. (1989) *Structural Design via Optimality Criteria*, Kluwer Academic Publishers, Dordrecht.
- Rozvany, G.I.N. (1996) Some shortcomings of Michell's truss theory, *Struct. Optim.*, 12, 244–250.
- Rozvany, G.I.N. (1998) Exact analytical solutions for some popular benchmark problems in topology optimization, *Struct. Optim.*, 15, 42–48.
- Rozvany, G.I.N. and Gollub, W. (1990) Michell layouts for various combinations of line supports. Part I, *Int. J. Mech. Sci.*, 32, 1021–1043.
- Rozvany, G.I.N. and Zhou, M. (1991) Applications of COC method in layout optimization, in *Proc. Conf. on Eng. Optim. in Design Processes*, Karlsruhe, 1990, H. Eschenauer, C. Mattheck and N. Olhoff (eds), Springer, Berlin, pp. 59–70.

- Rozvany, G.I.N., Querin, O.M., Gaspar, Z. and Pomezanski, V. (2002) Extended optimality in topology design, *Struct. Multidisc. Optim.*, 24, 257–261.
- Rozvany, G.I.N., Querin, O.M., Gaspar, Z. and Pomezanski, V. (2003) Weight increasing effect of topology simplification, *Struct. Multidisc. Optim.*, 25, 459–465.
- Rozvany, G.I.N., Pomezanski V., Gaspar Z. and Querin, O.M. (2005) Some pivotal issues in structural optimization, in *6th World Congress on Structural and Multidisciplinary Optimization*, Book of Abstracts and CD-ROM Proceedings, Rio de Janeiro, 30 May–3 June 2005, p. 147. Short paper: http://www.wcsmo6.org/Papers/5951_Rozvany.pdf (2 pp.)
- Rozvany, G.I.N., Querin, O.M., Logo, J. and Pomezanski, V. (2006) Exact analytical theory of topology optimization with some pre-existing members or elements, *Struct. Multidisc. Optim.*, in press.
- Sigmund, O. (1994) Design of material structures using topology optimization, Ph.D. Thesis, Dept. Solid Mech., TU Denmark.
- Sigmund, O. and Petersson, J. (1998) Numerical instabilities in topology optimization: A survey on procedures dealing with checkerboards, mesh-dependencies and local minima, *Struct. Optim.*, 16, 68–75.
- Sved, G. (1954) The minimum weight of certain redundant structures, *Aust. J. Appl. Sci.*, 5, 1–3.

Composites and Cellular Structures

ON DISCRETE MATERIAL OPTIMIZATION OF LAMINATED COMPOSITES USING GLOBAL AND LOCAL CRITERIA

Jan Stegmann and Erik Lund

Department of Mechanical Engineering, Aalborg University, Pontoppidanstraede 101, DK-9220 Aalborg East, Denmark

js@ime.aau.dk, el@ime.aau.dk

Abstract: Discrete Material Optimization is introduced as a method for doing material optimization on general laminated composite shell structures where the objective is to minimize maximum strain values. The method relies on ideas from multiphase topology optimization and uses gradient information in combination with mathematical programming to solve a discrete optimization problem. The method can be used to solve the orientation problem of orthotropic materials and the material selection problem as well as problems involving both. The method has previously been applied to compliance minimization and its applicability to min-max problems is demonstrated for two simple examples and the results compared to designs obtained using compliance minimization.

Keywords: Optimization, shell, penalization, stress, laminate.

1. INTRODUCTION

The strive for lighter and stronger structures has in recent years resulted in an increasing use of advanced materials such as composite materials. In particular fiber reinforced polymers (FRPs) have become very popular due to their very high strength to weight ratio. For structural applications FRPs are stacked in a number of layers, each consisting of strong fibers bonded together by a resin, to form a laminate. The design problem is then to determine the stacking sequence by proper choice of material and fiber orientation of each FRP layer in order to obtain the desired structural performance. For complicated geometries this is a very challenging design problem that calls for use of sophisticated structural optimization tools. In such cases it is convenient to introduce methods that can solve the discrete material selection problem together with the continuous fiber orientation and thickness distribution problem, and one such approach is the Discrete Material Optimization (DMO) method introduced by

the authors (Stegmann, 2004; Stegmann and Lund, 2005; Lund and Stegmann, 2005). The shape and thickness of the composite structure are assumed to be fixed, and the problem deals entirely with design of the lay-up of the laminated composite.

The goal of this work is to solve the material optimization problem efficiently for general laminated composite shell structures where the objective is to minimize the maximum strain in some or all parts of the structure. This objective is of great importance for practical design applications since failure of laminated composites is often evaluated based on maximum principal strain. The platform for implementation is the finite element based analysis and optimization code MUST (MULTidisciplinary Synthesis Tool), developed at the Institute of Mechanical Engineering, Aalborg University (MUST, 2005).

In the following we provide a brief review of the parametrization and the optimization problem statement and subsequently present two numerical examples which focus on comparing the local strain criteria solutions to solutions obtained using compliance minimization. First, the analysis aspects of the optimization are revised and the basic notation introduced.

2. ANALYSIS OF LAMINATED COMPOSITES

Each layer, k , in the laminate is characterized by the constitutive matrix, \mathbf{C}_k^l , which is a function of the spatial orientation, θ_k , of the orthotropic material in that layer such that $\mathbf{C}_k^l = \mathbf{C}_k^l(\theta_k)$. It is assumed that all layers are perfectly bonded together, which constitutes an equivalent single layer (ESL) description, and thus displacements and strains will be continuous across the thickness. This type of model provides a good approximation of the structural stiffness while interlaminar effects such as delamination are not predicted.

2.1 Finite Element Formulation

The structural response of a laminate subjected to a given set of boundary conditions is obtained using the finite element method. The finite elements used are 4-node shell elements with full integration and assumed natural strains to circumvent problems with shear locking, see e.g. Dvorkin and Bathe (1984) for details. The linear element stiffness matrix, \mathbf{K}^e , is obtained as the sum over all layers, N^l :

$$\mathbf{K}^e = \sum_{k=1}^{N^l} \int_V (\mathbf{B}_k^l)^T \mathbf{C}_k^l \mathbf{B}_k^l dV, \quad (1)$$

where \mathbf{B}_k^l is the linear strain-displacement matrix of the k -th layer. In the usual way the global stiffness matrix is obtained by summation over the total number of elements, N^e , whereby we may write the linear static equilibrium equations as $[\sum_{m=1}^{N^e} \mathbf{K}_m^e] \mathbf{u} = \mathbf{p}$, in which the vectors \mathbf{u} and \mathbf{p} contain the global

nodal displacements and consistent nodal loads, respectively. For local criteria we need the strain vector, $\boldsymbol{\varepsilon} = (\varepsilon_{11}, \varepsilon_{22}, \varepsilon_{33}, 2\varepsilon_{12}, 2\varepsilon_{23}, 2\varepsilon_{13})^T$, which can be expressed for any given layer from the strain-displacement relation as $\boldsymbol{\varepsilon}^l = \mathbf{B}^l \bar{\mathbf{u}}$. By application of Hooke's law we obtain the linear stresses, $\boldsymbol{\sigma} = (\sigma_{11}, \sigma_{22}, \sigma_{33}, \tau_{12}, \tau_{23}, \tau_{13})^T$, directly in a layer as $\boldsymbol{\sigma}^l = \mathbf{C}^l \mathbf{B}^l \bar{\mathbf{u}}$ where $\bar{\mathbf{u}}$ indicates the element nodal displacements.

3. OPTIMIZATION OF LAMINATED COMPOSITES

A major aspect of optimization with laminated composites is finding the optimal orientation of the orthotropic materials. The classical gradient-based approach to this problem is to use the fiber angle, θ_k , of each layer as a continuous design variable but this poses a major difficulty as the problem becomes non-convex. This is, off course, not a new realization and several methods have already been proposed to circumvent the problem of local optimum solutions.

The most widely used methods in practical engineering are the mathematical programming techniques, which have been integrated in several commercially available codes. The DMO method can be characterized as a gradient based technique that introduces a new parametrization of the problem.

4. THE DMO PARAMETRIZATION

Discrete Material Optimization is essentially an extension of the ideas used in structural topology optimization but in stead of choosing between solid and void we want to choose between multiple distinct materials. This can be stated as: *for all elements and layers in the structure find one distinct material from a set of pre-defined candidate materials such that the design performance is improved.* To achieve this we employ the multi-phase topology optimization strategy introduced by Sigmund and co-workers (Sigmund and Torquato, 1997; Gibiansky and Sigmund, 2000) in which the total material stiffness is computed as a weighted sum of candidate material stiffnesses.

In the present context this means that the constitutive matrix is computed as a weighted sum of a finite number of constitutive matrices, each representing a given candidate material that may be used in the lay-up. The orientation of orthotropic materials is encompassed by treating different orientations (represented by the fibre angles, θ_i) as different candidate materials and thus computing the constitutive matrix at a number of discrete angles, i.e. $\mathbf{C}_i = \mathbf{C}(\theta_i)$. Consequently, the design variables are no longer the fiber angles but the scaling factors (or weight functions) on each constitutive matrix in the weighted sum. Other materials such as polymeric foam, balsa wood, aluminum, CFRP, etc. may also be included in the weighted sum to allow selection of both best material and best orientation. The objective of the optimization is then to drive the influence of all but one of these constitutive matrices to zero for each layer by

driving all but one weight function to zero. As such, the methodology is very similar to that used in topology optimization, which is further emphasized by the fact that the method is still limited to operate on a fixed design domain, i.e. thicknesses and shape are not changed.

4.1 The Methodology

The DMO parametrization is, as in topology optimization, invoked at the finite element level. The layer constitutive matrix, \mathbf{C}^l , is expressed as a weighted sum of candidate materials, each characterized by a constitutive matrix, \mathbf{C}_i . In general, this may be expressed as a sum over the number of candidate materials for the layer, n^l :

$$\mathbf{C}^l = \sum_{i=1}^{n^l} w_i \mathbf{C}_i = w_1 \mathbf{C}_1 + w_2 \mathbf{C}_2 + \cdots + w_{n^e} \mathbf{C}_{n^e}, \quad 0 \leq w_i \leq 1. \quad (2)$$

It follows that the number of candidate materials is also the number of layer design variables and if N^l is the number of layers in a given element, the total number of design variables for a multi-layered element, n^e , is the sum over all layers $n^e = \sum_{k=1}^{N^l} n_k^l$.

The weights, w_i , in Equation (2) must have values between 0 and 1 as no matrix can contribute more than the physical material properties and a negative contribution is physically meaningless. In this way the weights on the constitutive matrices become “switches” that turn on and off stiffness contributions such that the objective is minimized and a distinct choice of candidate material is made. The task of the optimization is therefore to eliminate the influence of all but one of these materials by driving all but a single weight factor, w_i , to zero.

5. ELEMENT LEVEL PARAMETRIZATION

The simplest choice of weight functions would be to extend the classical topology optimization parametrization to multiple design variables, x_i , as:

$$\mathbf{C}^l = \sum_{i=1}^{n^l} \underbrace{(x_i)^p}_{w_i} \mathbf{C}_i = (x_1)^p \mathbf{C}_1 + (x_2)^p \mathbf{C}_2 + \cdots + (x_{n^l})^p \mathbf{C}_{n^l}, \quad 0 \leq x_i \leq 1. \quad (3)$$

Here, each design variable scales only one constitutive matrix and thus has no effect on any of the other candidate materials. To push the design variables towards 0 and 1 the SIMP method has been adopted by introducing the power, p , as a penalization of intermediate values of x_i , see e.g. Bendsøe and Sigmund (2003) for details. The method in Equation (3) is not very efficient as it fails to push the design to its limit values. Consequently, an alternative interpolation has been proposed, which is a simple extension of Equation (3):

$$\mathbf{C}^l = \sum_{i=1}^{n^l} (x_i)^p \underbrace{\prod_{j=1; j \neq i}^{n^l} [1 - (x_j)^p]}_{w_i} \mathbf{C}_i. \quad (4)$$

The difference from Equation (3) is the term $[1 - x_j]^p$, which is included so that an increase in x_i automatically involves a decrease in all other weights. This helps drive the design towards 0/1 and the method has proven quite effective for particularly compliance minimization problems. However, the sum of the weight functions in Equation (4) is not 1 and consequently, the stiffness computed from Equation (1) will be unrealistically low, which leads to non-physical displacements and strains. For pure fiber angle optimization with compliance objective this does not pose a problem, but for problem of min max strain we must require that $\sum_{i=1}^{n^l} w_i = 1.0$. Thus a normalization of the weights is introduced as:

$$w_i = \frac{\hat{w}_i}{\sum_{k=1}^{n^e} \hat{w}_k}, \quad i = 1, \dots, n^l, \quad (5)$$

where the weight functions \hat{w}_i are computed as w_i in Equation (4). The weights in Equation (5) have been used for the examples presented in this work to ensure that stiffness, strains and stresses are realistic. However, using these weights alters the effect of the penalization and renders the parametrization less effective than Equation (4) used directly with respect to driving the weights to 0/1. Consequently, the normalized weighting scheme, Equation (5), converges slower to a design where all layers in all elements have been assigned a distinct material – the degree of “distinctiveness” is called the DMO convergence measure, which is just the ratio of converged elements/layers to total number of element/layers, see details in Stegmann and Lund (2005).

6. THE OPTIMIZATION PROBLEM

The DMO problem is stated as a mathematical programming problem, which is solved using the Method of Moving Asymptotes (Svanberg, 1987). Minimization of maximum local quantities is formulated as a min-max problem, subject to an optional constraint on total mass, m_c . The problem is stated using a bound formulation as described in Bendsøe et al. (1983) and Olhoff (1989):

$$\begin{aligned} \text{Objective : } & \min_{\mathbf{x}, \beta} \beta \\ \text{Subject to : } & \epsilon_k(\mathbf{x}) \leq \beta, \quad k = 1 \dots n^a \\ & (m \leq m_c) \\ & \mathbf{0} \leq \mathbf{x}_{\min} \leq \mathbf{x} \leq \mathbf{1} \end{aligned} \quad (6)$$

The number of strain values in Equation (6) becomes very large for models involving many elements and layers and consequently, an active set strategy is used in which only a user-specified fraction of strain values is used. The number of values in the active set is designated n^a as indicated in Equation (6).

In solving the optimization problem Equation (6) we need the sensitivities of the k -th strain, which is obtained using the chain rule for the i -th design variable since the objective is implicitly a function of the displacements and directly a function of the design variables (in the case of strains), i.e. we may write $\epsilon_k = \epsilon_k(\mathbf{u}(\mathbf{x}), \mathbf{x})$ and obtain the approximated derivative as:

$$\frac{d\epsilon_k}{dx_i} \simeq \frac{\epsilon_k(\mathbf{u}(\mathbf{x}) + \frac{d\mathbf{u}}{dx_i} \Delta x_i) - \epsilon_k(\mathbf{u}(\mathbf{x}))}{\Delta x_i}. \quad (7)$$

When evaluating Equation (7) we need the displacement sensitivities, which are obtained in the standard way using direct differentiation:

$$\mathbf{K} \frac{d\mathbf{u}}{dx_i} = -\frac{\partial \mathbf{K}}{\partial x_i} \mathbf{u} + \frac{\partial \mathbf{p}}{\partial x_i}. \quad (8)$$

This equation is easy to solve since the sensitivity of the stiffness can be evaluated analytically and the factored stiffness matrix is already available from the static solution.

7. NUMERICAL EXAMPLES

The DMO method has been implemented in the finite element based system MUST, which is aimed at analysis and design of structural problems as well as multidisciplinary problems such as fluid-structure interaction problems (MUST, 2005). The system is capable of reading input from an external pre-processor such as ANSYS. To run the optimization it is only necessary to add some specific information about the optimization run.

In the following two simple examples are presented in order to illustrate the results obtained using local strain criteria and compare to minimum compliance results.

7.1 Example 1 – Single-Layer Plate

First a single layer clamped plate subjected to uniform pressure is solved for both maximum integral stiffness and subsequently for minimization of the maximum strain. The strain value used is the first principal strain, which is the largest strain occurring in the structure. The plate has dimension 100×100 [mm] and thickness of 0.05 mm. The material is an orthotropic glass/epoxy with $E_x = 54$ GPa, $E_y = 18$ GPa, $G_{xy} = G_{xz} = G_{yz} = 9$ GPa and $\nu_{xy} = 0.25$ and it may be oriented at the fiber angles $[90^\circ, \pm 45^\circ, 0^\circ]$,

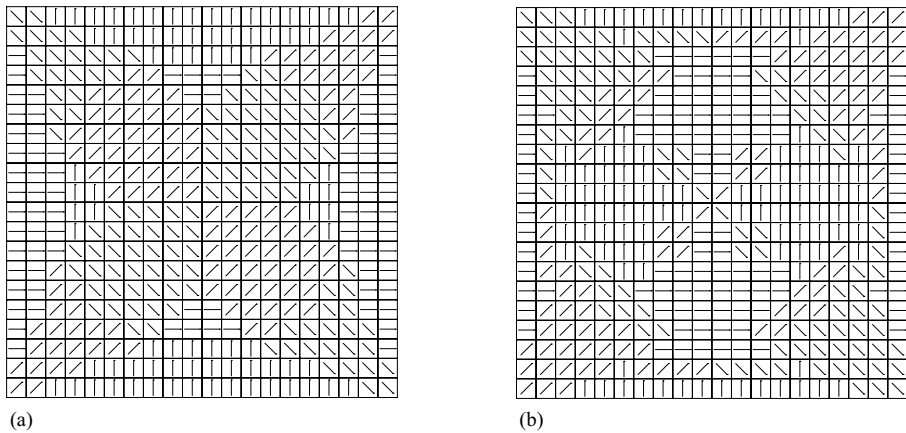


Figure 1. Fiber angle distribution in clamped plate subject to distributed load – design optimized for maximum stiffness (a) and min-max first principal strain (b).

which brings the number of candidate materials to 4 per element. The plate is modeled using a mesh of 20×20 4-node MITC stabilized shell elements whereby the total number of design variables is 1600. The active set tolerance is set to 90% so that only elements that are strained to more than 90% of the maximum strain are included in the optimization. The SIMP power is increased from 2.0 to 6.0 in steps of 1.0 every 10 iterations.

The results of the two optimizations are shown in Figure 1 where a clear difference in fiber angle distribution can be noted. The fiber angle distribution obtained using the min-max optimization is more localized than the fiber angles obtained using minimum compliance optimization, which is in good agreement with the nature of the two objectives used.

The center point displacement in the minimum compliance design is 15% lower than in the min-max strain design, but the strain levels are significantly lower in the min-max strain solution, see Figure 2. As can be seen, the maximum strain is around 14% lower than in the minimum compliance design and in general, the large strains occur over a larger area.

7.2 Example 2 – Single-Layer Spherical Cap

Now a spherical cap is investigated to evaluate the capabilities of the proposed method for a doubly-curved shell. The base of the shell structure is spanned by a 1000×1000 [mm] square and the center point rises 100 mm above the base. The four sides are prescribed by parabolas and the surface is generated by dragging one parabola along an identical parabola. In mathematical terms the surface may be described as $z(x, y) = h - \frac{2h}{l^2}(x^2 + y^2)$ where h is the height of the center point and l is the side-length, here 100 and 1000 [mm],

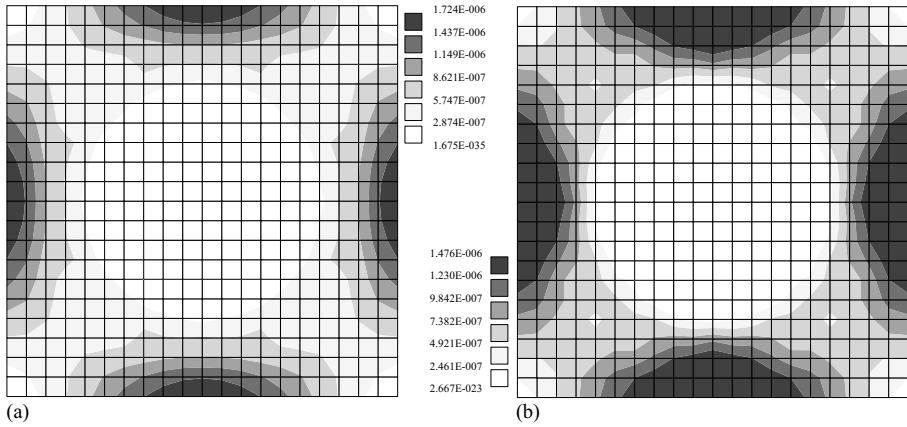


Figure 2. Principal strain distribution in clamped plate subject to distributed load – design optimized for maximum stiffness (a) and min-max first principal strain (b).

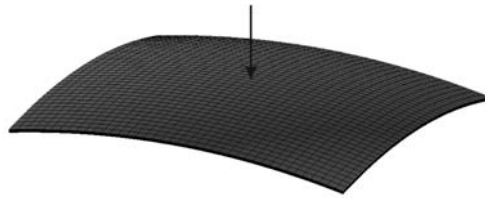


Figure 3. Geometry of hinged spherical cap example shown with actual thickness; all edges are hinged, i.e. all translational displacements are fixed.

respectively. The thickness of the shell is 8 mm and the structure is loaded by a single load in the center point and the model is hinged on the four edge curves. The entire shell geometry is modelled using a 30×30 mesh of 4-node MITC-stabilized shell elements. The geometry and mesh are shown in Figure 3. As candidate materials we again use a glass/epoxy composite with $E_x = 54$ GPa, $E_y = 18$ GPa, $G_{xy} = G_{xz} = G_{yz} = 9$ GPa and $\nu_{xy} = 0.25$ and the permissible fiber angles $[90^\circ, \pm 45^\circ, 0^\circ]$, which results in 4 design variables per element and thus 3600 design variables in total. As before, the active set tolerance is 90% and the SIMP power is increased from 2.0 to 6.0 in steps of 1.0 every 10 iterations.

The optimal design is found for both compliance and min-max strain and again, there are notable differences in the resulting fiber angles as shown in Figure 4. As in the previous example, the fiber angles obtained using min-max optimization are more localized than those obtained using a global criteria.

As in Example 1 the minimum compliance design is stiffer but this time only by approximately 4%. The maximum strain in the design by min-max optimization is approximately 3% lower compared to the minimum compliance design as shown in Figure 5.

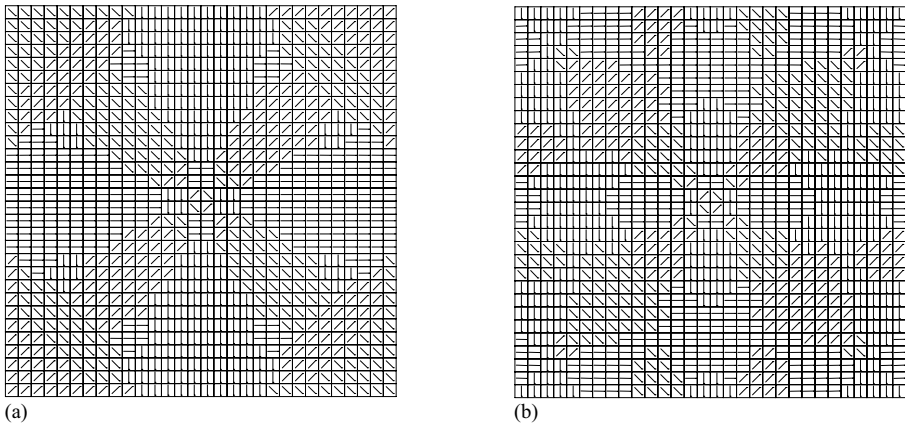


Figure 4. Fiber angle distribution in spherical cap subjected to concentrated center point load – design optimized for maximum stiffness (a) and min-max first principal strain (b).

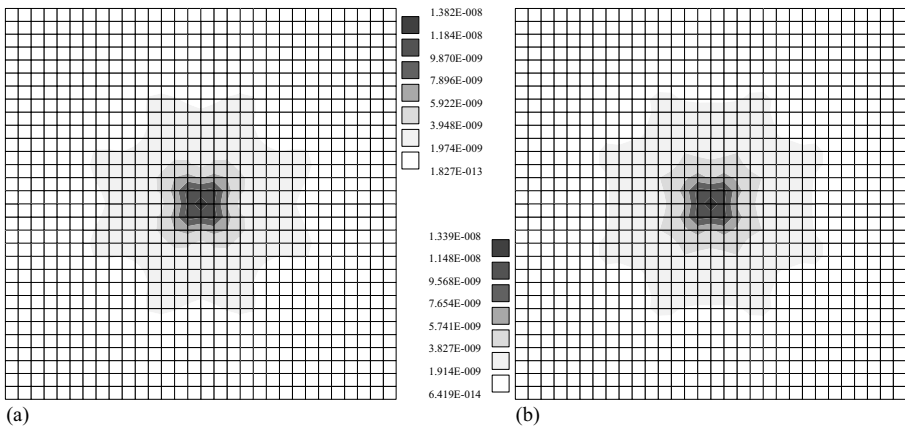


Figure 5. Principal strain distribution in spherical cap subjected to concentrated center point load – design optimized for maximum stiffness (a) and min-max first principal strain (b).

8. CONCLUDING REMARKS

In the present paper Discrete Material Optimization (DMO) is introduced as a new gradient based technique for minimizing the maximum strain by optimizing material choice and material orientation. The method operates on a fixed domain, i.e. shape and thicknesses are defined *a priori* and remain fixed, and as such we deal entirely with solving a laminate lay-up problem.

In the two numerical examples presented the DMO method is able to successfully reduce the strain level in the structure. Comparison with minimum compliance optimization results indicate that the min-max formulation performs as expected. So far the major drawback of the DMO methodology is the

large number of design variables and, with the introduction of local criteria, a large number of criteria functions. This renders the optimization problem computationally expensive to solve and thus it presently constitutes a practical limit on the problems that can be considered. For compliance minimization the authors have successfully solved problems involving up to around 750, 000 design variables on a standard PC (Lund and Stegmann, 2005). For both min-max and minimum compliance problems the vast majority of time is spent on computing the design sensitivities for all design variables. However, patch design variables may be used to reduce the number of design variables and the active set strategy can be used to reduce the number of criteria functions, thus reducing computational cost.

REFERENCES

- Bendsøe, M., Olhoff, N. and Taylor, J. (1983) A variational formulation for multicriteria structural optimization, *Journal of Structural Mechanics*, 11, 523–544.
- Bendsøe, M. and Sigmund, O. (2003) *Topology Optimization – Theory, Methods and Applications*, second edition, Springer, Berlin.
- Dvorkin, E. and Bathe, K. (1984) A continuum mechanics based four-node shell element for general nonlinear analysis, *Engineering Computations*, 1, 77–88.
- Gibiansky, L. and Sigmund, O. (2000) Multiphase composites with extremal bulk modulus, *Journal of the Mechanics and Physics of Solids*, 48, 461–498.
- Lund, E. and Stegmann, J. (2005) On structural optimization of composite shell structures using a discrete constitutive parameterization, *Wind Energy*, 8(1), 109–124.
- MUST (2005) Institute of Mechanical Engineering, Aalborg University, Denmark, www.ime.aau.dk/must.
- Olhoff, N. (1989) Multicriterion structural optimization via bound formulation and mathematical programming, *Structural Optimization*, 1, 11–17.
- Sigmund, O. and Torquato, S. (1997) Design of materials with extreme thermal expansion using a three-phase topology optimization method, *Journal of the Mechanics and Physics of Solids*, 45, 1037–1067.
- Stegmann, J. (2004) Analysis and optimization of laminated composite shell structures, Ph.D. Thesis, Institute of Mechanical Engineering, Aalborg University, Denmark. Special Report No. 54, available at www.ime.aau.dk/~js.
- Stegmann, J. and Lund, E. (2005) Discrete material optimization of general composite shell structures, *International Journal for Numerical Methods in Engineering*, 62(14), 2009–2027.
- Svanberg, K. (1987) The method of moving asymptotes – A new method for structural optimization, *Numerical Methods in Engineering*, 24, 359–373.

ANALYSIS AND CONTINUUM TOPOLOGY OPTIMIZATION OF PERIODIC SOLIDS WITH LINEARIZED ELASTIC BUCKLING CRITERION

Miguel Matos Neves

IDMEC-IST Technical University of Lisbon, Av. Rovisco Pais, 1049-001 Lisboa, Portugal

maneves@dem.ist.utl.pt

Abstract: A methodology for a linearized elastic buckling analysis based on a two-scale asymptotic method for periodic materials is generalized to three-dimensional case and implemented at microscale level. The present two-scale method provides a set of uncoupled problems for the linearized elastic stability analysis at the macroscale and the microscale material levels respectively. For the microscale level problem, it is considered an infinite and periodic structured medium for a given average (at the macroscale level) strain. Using the Floquet–Bloch wave theory within the finite element method and a continuum topology optimization problem, implicitly assuming repetitive cells, the minimum critical buckling strain is obtained and maximized while the cell volume fraction is kept constant. The performance of the implemented methodology is tested for different cases. Results obtained with finite repetitive medium for periodic open cells versus closed cells keeping the same cell volume fraction are discussed.

Keywords: Two-scale periodic materials, linearized elastic stability, Floquet–Bloch wave theory, topology optimization.

1. INTRODUCTION

The spatially periodic microstructures studied here are modeled as a perfectly periodic repetition of a unit or base cell. For these, the respective homogenized or effective elastic properties are found by the mathematical theory of homogenization which is a classical averaging technique [1].

When tailoring these materials for extremal elastic properties with a given volume fraction (material density) slender members are often present as a consequence of using a linearized elasticity model. So, a limiting rule for the microstructural design of periodic materials is the elastic buckling phenomena, since there is a limit to the reduction in the slenderness of the cell elements.

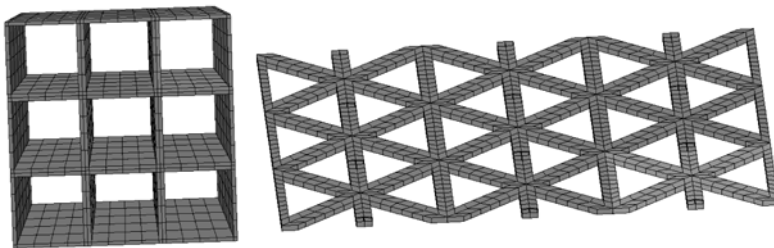


Figure 1. Three-dimensional representations of 3 by 3 cells of 2D periodic microstructures.

The characterization of the elastic stability of periodic materials and its optimization are still a challenging problem that continues receiving some interest from researchers in the area.

A first work in microstructural design against buckling of microstructured medium was due to Bendsøe and Triantafyllidis [2]. They presented a tractable size optimization model for an infinite rectangular frame. The case of axially deformed layered composites under plane-strain conditions was investigated by Triantafyllidis and Maker [3]. In 1993, Geymonant et al. [4] illustrated the completeness of the Bloch wave representation for capturing the first instability in finite strained periodic composites. Schraad and Triantafyllidis [5] used the nonlinearly elastic lattice model to study the influence of scale on the onset of failure.

The present work uses a linearized elastic buckling model [6] combining the same kind of topology optimization techniques described for the “inverse homogenization” problems (see, for example, [7–11]) and an eigenvalue buckling analysis combined with a Bloch wave technique [12].

This article is organized as follows. Section 2 contains a brief description of the mechanical model for the linearized elastic buckling of a periodic material. In Section 3, the topology optimization problem is stated. In Section 4, results from finite repetitive medium obtained through a classical buckling finite element analysis for periodic open cells versus closed are presented.

2. THE LINEARIZED ELASTIC BUCKLING PROBLEM WITH BLOCH WAVE RELATIONS

A mathematical model for linearized elastic buckling analysis of structures with periodic materials was presented by Neves et al. [6]. This model states a linearized elastic stability condition for an infinite medium that has stress stiffening as the only non-linear effect.

The problem of finding the first critical macroscale strain factor P_r^Y reduces to the following equation at microscale:

$$(\mathbf{K}_Y(k) - P_r^Y * \mathbf{K}G_Y(k))\phi^r = 0, \quad (1)$$

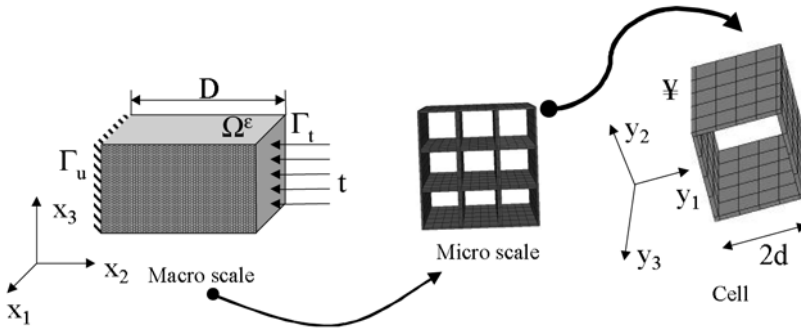


Figure 2. Schematic representation of the two scales x and y and the repetitive base cell.

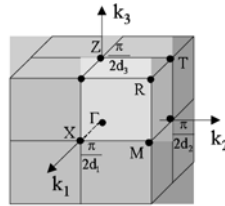


Figure 3. Brillouin zone for wave numbers k .

where \mathbf{K}_Y and $\mathbf{K}G_Y$ are stiffness and geometric matrices, respectively; \mathbf{k} is the wave vector that runs over the Brillouin zone (see Figure 3) allowing to cover possible wavelengths; P_r^Y is the critical strain factor at macroscale \mathbf{x} and ϕ^r are the associated eigenmodes at microscale \mathbf{y} .

The boundary displacements of the cell are imposed by the Bloch wave relations:

$$\phi(y_1 + 2d_1, y_2 + 2d_2, y_3 + 2d_3) = e^{i(k_1 y_1 + k_2 y_2 + k_3 y_3)} \phi(y_1, y_2, y_3). \quad (2)$$

Note that Equation (2) requires evaluation of the stress field at cell level (microscale \mathbf{y}). For a model description, see [12].

Figure 4 illustrates the obtained critical strain factors as function of wave numbers $k = (k_1, k_2, 0)$ for a macroscale strain of $\varepsilon = C\{-1, -1, 0, 0, 0, 0\}$ (where C is a given constant) assuming a unitary Young’s modulus and unitary cell dimensions $2 * d_1$ and $2 * d_2$.

For the square honeycomb structure with volume fraction of $\rho = 0.19$ (discretized with solid finite elements of 8 nodes), the plot of the critical strain factor as a function of wave numbers makes it evident that shear mode (long wave length) is associated with the lowest critical strain factor ($P_{cr}^Y = P_1^Y = 0.024$) and not with the periodic mode at the origin point $k_1 = k_2 = 0.0$.

Different behaviour has the hexagonal honeycomb with volume fraction of $\rho = 0.19$ presenting a periodic mode very near to that of a shear mode ($P_{cr}^Y =$

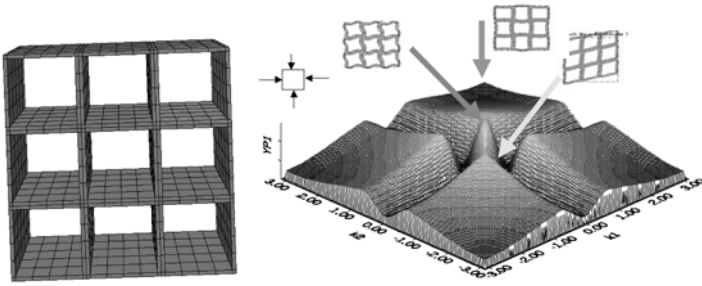


Figure 4. 3 by 3 cells of a square honeycomb and a plot of its critical strain factors versus wave numbers k for biaxial compression.

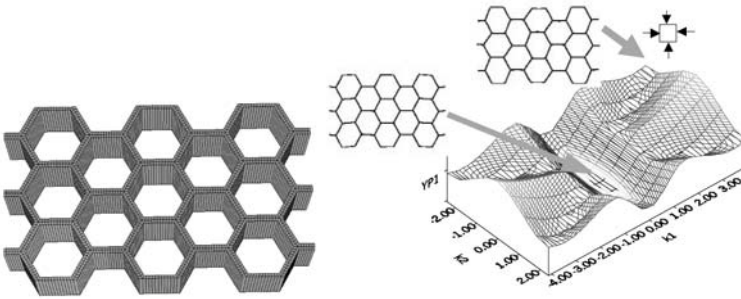


Figure 5. Critical strain factors versus wave numbers k for biaxial compression.

0.008). Figure 5 has no discontinuity near the origin. Both global and local buckling behaviour present near critical values at origin which gives safety for a mechanical of materials approach to get critical strain factors.

3. THE OPTIMIZATION PROBLEM

To explore the potentialities of Bloch wave technique mentioned in Section 2 the following optimization problem is formulated. This maximizes the lowest critical strain factor P_1^Y for a given load at macroscale and a fixed amount of volume of material.

$$\begin{aligned} & \max_{\mu} \min_{i=1, \dots, n} P_i^Y(\mathbf{k}) \\ & \text{subject to: } \int_Y \mu(\mathbf{y}) dY = V_0. \end{aligned} \tag{3}$$

Figure 6 presents an obtained optimal reinforcement for square honeycomb under uniaxial compression (for details, see [12]).

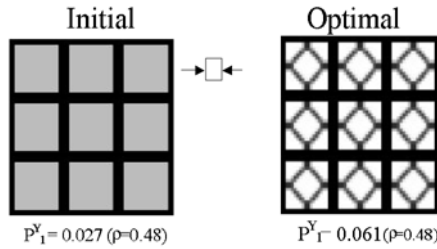


Figure 6. Optimal reinforcement.

4. OPEN CELLS VERSUS CLOSED CELLS: ON THE OPTIMALITY OF THE BONE MICROSTRUCTURE

Studies on the optimality of periodic structures concluded with the observation that cancellous bone structure does present a non-optimal stiffness [13]. The reason is that cancellous bone is comprised of open wall cells that present non-optimal stiffness.

A question arises from it: what other criteria can make cancellous bone optimal? This question is still a open problem. One possible criterion often mentioned is a buckling constraint preventing very thin plates to develop.

The present stage of this study does not allow a definitive answer to this question but several considerations are presented.

Several finite repetitions of aluminum-made open wall cells and closed wall cells, as shown in Figures 7 and 8 respectively, were tested for the same volume fraction and subject to same uniaxial compressive load.

A comparison of the linearized elastic buckling performance between several open wall cells and closed wall cells was done using a standard finite ele-

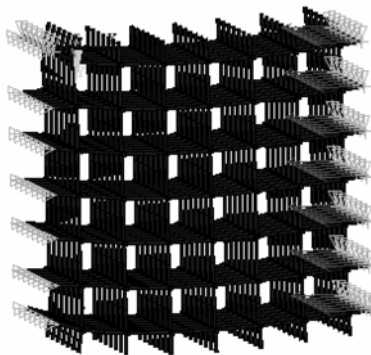


Figure 7. Obtained critical eigenmode and representation of finite element boundary conditions for the finite repetition test with uniaxial compression.

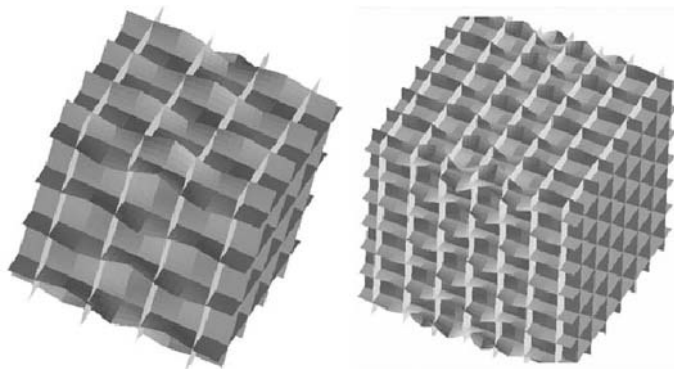


Figure 8. Critical eigenmodes obtained with closed wall cells.

ment eigenvalue buckling analysis. The main results are presented in Figure 9, for the same boundary conditions and uniaxial compressive load.

From the obtained results for volume fractions of 0.1 we observed that closed wall cells present critical load factors near to that obtained with the open wall cells.

For volume fractions less than 0.1 the open cells built with beams presented better buckling performance than the closed cells built with plates. For volume fractions great than 0.1 the closed cells have better buckling performance than the open cells. We observed that independently of the volume fraction value the critical eigenmodes were global for open cells and local for closed cells.

Notwithstanding the particular test conditions used, this result is up to certain extent unexpected for the high volume fractions. It shows that in general we can not simply assume a repetitive structure built of open cells as being optimal with respect to elastic buckling behavior. Results obtained show that open wall cells with low volume fractions that present non-optimal stiffness have associated a best elastic buckling performance.

The results obtained in this section are a small but new contribution for the understanding of the structural influence on bone-remodeling mechanism. This is an important motivation for future numerical studies.

ACKNOWLEDGMENTS

This work is partially supported by Fundação para a Ciência e Tecnologia, Project POCTI/EME/44728/2002 (MMN), FEDER and IDMEC-IST. The author is grateful to Professor Krister Svanberg, from the Royal Institute of Technology, Stockholm, for having supplied his MMA code.

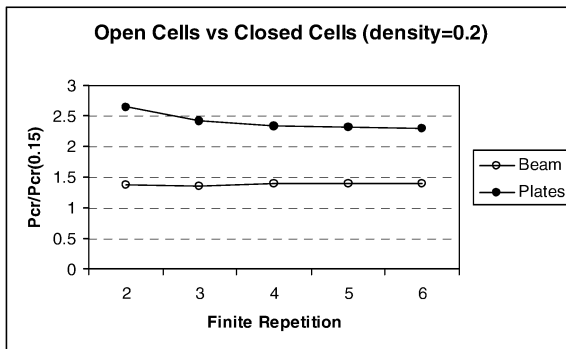
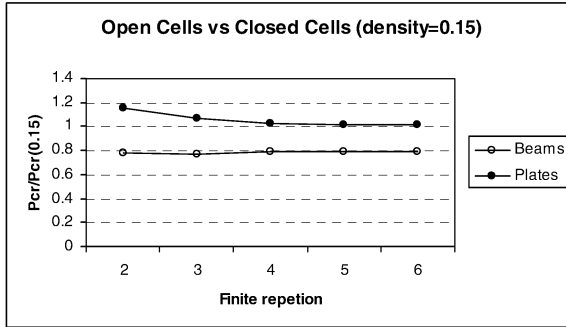
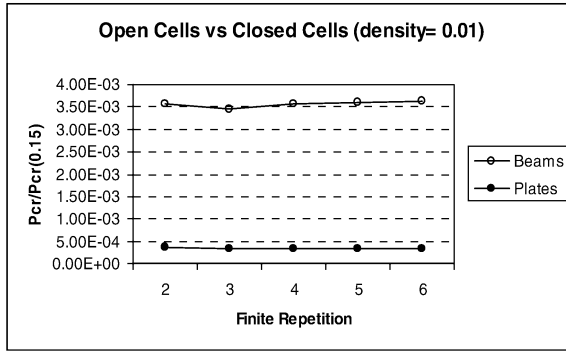


Figure 9. Comparison of buckling response between open and closed cells with a finite repetition of cells for different volume fractions: 0.01, 0.15 and 0.20. Critical factors were divided by the lowest load factor obtained with the closed cells for a volume fraction of 0.15.

REFERENCES

- [1] Sanchez-Palencia, E., *Non-Homogeneous Media and Vibration Theory*, Lecture Notes in Physics, Vol. 127, Springer, Berlin (1980).
- [2] Bendsøe, M.P. and Triantafyllidis, N., Scale effects in the optimal design of a microstructured medium against buckling, *Int. J. Solids Struct.*, 26, 725–741 (1990).
- [3] Triantafyllidis, N. and Maker, B.N., On the comparison between microscopic and macroscopic instability mechanism in a class of fiber reinforced composites, *J. Appl. Mech.*, 52, 794–800 (1985).
- [4] Geymonat, G., Müller, S. and Triantafyllidis, N., Homogenization of non-linear elastic materials, Microscopic bifurcation and macroscopic loss of rank-one convexity, *Arch. Rat. Mech. Anal.*, 122, 231–290 (1993).
- [5] Schraad, M.W. and Triantafyllidis, N., Scale effects in media with periodic and nearly periodic microstructures, Part II: Failures mechanisms, *J. Appl. Mech.*, 64, 763–771 (1997).
- [6] Neves, M.M., Sigmund, O. and Bendsøe, M.P., Topology optimization of periodic microstructures with a penalization of highly localized buckling modes, *Int. J. Numer. Meth. Engng.*, 54, 809–834 (2002).
- [7] Bendsøe, M.P. and Sigmund, O., *Topology Optimization: Theory, Methods and Applications*, Springer (2003).
- [8] Sigmund, O., Tailoring materials with prescribed elastic properties, *Mech. of Mat.*, 20(4), 351–368 (1995).
- [9] Sigmund, O., A new class of extremal composites, *J. Mech. Phys. Solids*, 48, 397–428 (2000).
- [10] Neves, M.M., Rodrigues, H.C. and Miranda Guedes, J., Optimal design of periodic linear elastic microstructures, *Computers & Structures*, 76, 421–429 (2000).
- [11] Neves, M.M., Rodrigues, H.C. and Guedes, J.M.: Generalized topology design of structures with a buckling load criterion, *Struct. Opt.*, 10, 71–78 (1995).
- [12] Neves, M.M., Bendsøe, M.P. and Sigmund, O., Topology optimization of periodic microstructures with a buckling constraint, in *Proceedings of the Fifth World Congress on Computational Mechanics (WCCM V)*, July 7–12, 2002, Vienna, Austria, H.A. Mang, F.G. Rammerstorfer and J. Eberhardsteiner, J. (eds), Vienna University of Technology, Austria, ISBN 3-9501554-0-6, <http://wccm.tuwien.ac.at> (2002).
- [13] Sigmund, O., On the optimality of the bone microstructure, in *Synthesis in Bio Solid Mechanics*, P. Pedersen and M.P. Bendsøe (eds), Kluwer Academic Publishers, Dordrecht, pp. 221–234 (1999).

DESIGN OF CELLULAR STRUCTURE FOR OPTIMUM EFFICIENCY OF HEAT DISSIPATION

A Three-Dimensional Formulation

Bo Wang and Gengdong Cheng

State Key Laboratory of Structural Analysis for Industrial Equipments, Department of Engineering Mechanics, Dalian University of Technology, Dalian 116023, P.R. China

wangbooo@hotmail.com, chenggd@dlut.edu.cn

Abstract: A general model of cylindrical structure filled with linear metal cellular material is constructed to simulate a multi-tubular heat exchanger in this paper. Optimum design of cellular material distribution aims at maximization of heat dissipation rate while minimizing the prescribed flow pressure. Three-dimensional variation of temperature is considered. Five types of inner cell topology and various fluid nominal velocities are compared. We discuss in general the guideline for multi-tubular heat exchanger design to maximize heat dissipation efficiency based on insights from these optimization results. In the final part, a CPU cooler design is studied by our presented approach.

Keywords: Topology optimization, cellular materials, multi-tubular heat exchanger, heat dissipation, concurrent design of materials and structures.

1. BACKGROUND AND MODEL DESCRIPTION

In the modern industrial production, multi-tubular heat exchanger is a very important thermal component. Heat sink in the electronic equipment [1, 2] and monolithic catalyst support in the chemical reaction engineering [3, 4] are the examples of multi-tubular heat exchanger. The primary consideration for multi-tubular heat exchanger design is the efficiency of heat dissipation through solid conduction and forced convection. Obviously, a good heat exchanger should have an optimum material distribution within the cross section in order to dissipate as much heat as possible. For decades numerical techniques, based on discrete model [5, 6] or continuous model [4, 7], are largely employed in heat exchanger design. Groppi and Tronconi studied the deviations between the two types of models by numerical experiment. A major merit of the continuous model is to allow for remarkable saving in computa-

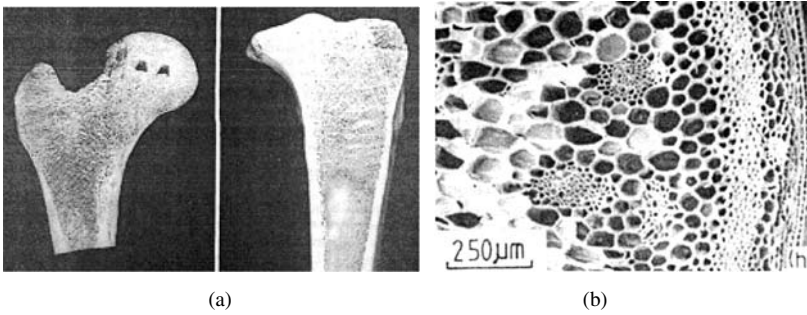


Figure 1. Structural morphology of nature: (a) Cross-sectional views of the head of a femur and the tibia; (b) Cross-sectional views of stalk of a plant.

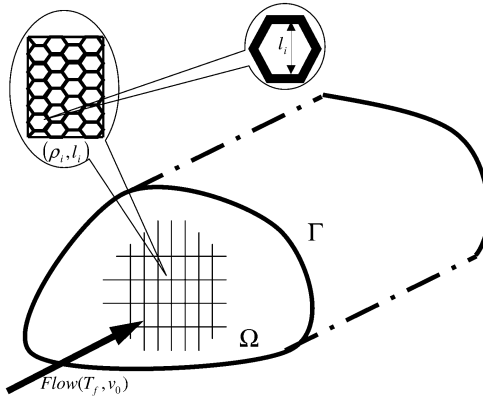


Figure 2. Cylinder structure filled with linear metal cellular material.

tional efforts and a better accuracy [8]. In previous work, people have generally focused on materials with certain pre-defined, uniformly distributed periodic microstructures. In comparison, when we examine bio-structures in nature (such as the head of a femur and the tibia, stalk of a plant, see Figure 1 [9]) we discovered that their morphology is very complicated and their microstructure is much more diverse. In addition, their material distribution on macro-level is far away from uniform. This inspires our study on concurrent material and structural optimum design in order to achieve a non-uniform design within the cross section of the heat exchanger.

A multi-tubular heat exchanger is shown in Figure 2. It is a cylindrical structure made of linear metal cellular material. The outer surface Γ of the cylindrical structure is subject to thermal boundary condition. Cooling or heating fluid is forced to pass through the cylinder in order to transfer heat with the cell structure walls. Flow temperature varies along the length of the cylinder. Three-dimensional variation of the temperature, i.e., variation within cross

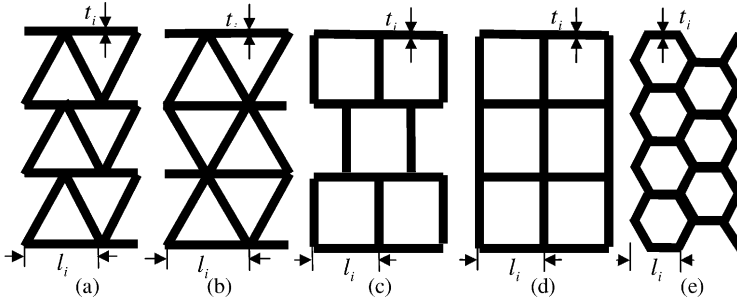


Figure 3. Micro morphology of the five types of cellular cell: (a) Triangle-4; (b) Triangle-6; (c) Square-3; (d) Square-4; (e) Hexagon.

section area and along the generating line of the cylinder is considered in the problem formulation. For purpose of illustration a hexagonal cell is shown in Figure 2. The idea of our work is to find optimum design of material distribution within the cross section for maximization of heat dissipation efficiency under prescribed flow pressure based on the continuous model and topology optimization technique [10, 11]. Both relative density and local cell size distribution of cellular material are to be optimized under the total material volume constraints. Thermal performances of five types of cellular cells are investigated.

To describe material distribution of the total cross section, we divide the cross section into a number of sub-domains, which could be one element or a group of elements in the finite element setting. In each sub-domain, the material distribution or the arrangements of cells are uniform and are characterized by the cell size l_i , cell wall thickness t_i , relative density ρ_i (array density ρ^* divided by solid cell wall density ρ_s); Figure 3 illustrates the cell shapes and arrangements. For simplicity, all cellular arrays are assumed to be perfect, free of process-induced geometrical imperfections. The surface area density α_A and corresponding hydraulic diameter D_h are functions of ρ_i and l_i as

$$\alpha_A = c_a \frac{\sqrt{1 - \rho_i}}{l_i}; \quad D_h \equiv 4 \frac{1 - \rho_i}{\alpha_A} = 4 \frac{l_i \sqrt{1 - \rho_i}}{c_a}. \quad (1)$$

The coefficient c_a and the other five coefficients for the five types of inner cell are listed in Table 1.

2. GOVERNING EQUATIONS OF THREE-DIMENSIONAL HEAT TRANSFER

In order to study the three-dimensional heat transfer of the cellular structure, the cylindrical structure is cut into a number of slices along its axial direc-

Table 1. Six coefficients for five types of cell shape and cell arrangement.

Inner Cell type	c_l	c_a	ζ_x	ζ_y	Nu	c_f
Triangle-4	$1/\sqrt{3}$	$4\sqrt{3}$	0.5	1/3	2.35	13.3
Triangle-6	$1/\sqrt{3}$	$4\sqrt{3}$	0.5	0.5	2.35	13.3
Square-3	1	4.0	0.5	0.4	2.980	14.17
Square-4	1	4.0	0.5	0.5	2.980	14.17
Hexagon	$\sqrt{3}$	$4\sqrt{3}/3$	0.5	0.5	3.353	15.07

tion. The coordinates of the two end cross sections of a typical slice are z and $z + \Delta z$. We assume that at each cross section z fluid temperature is uniform and denoted by $T_f(z)$. The governing equation is developed in the following. We assume steady-state heat transfer, fully developed laminar flow, constant physical properties of the fluid phase and negligible axial heat transfer in the solid phase by conduction. To describe fluid phase temperature change over the length of the slice we apply the steady state enthalpy balances for fluid phase. So the average fluid temperatures of the two neighboring cross sections satisfy the following equation

$$T_f(z + \Delta z) = T_f(z) + \frac{Q_i}{c_p \rho_f \nu_0 S}, \quad (2)$$

where $T_f(z + \Delta z)$ is the average fluid temperature of the cross section $z + \Delta z$, and Q_i is the heat dissipation rate of the fluid over the i -th slice; c_p is the mass specific heat; and S is the area of the structural cross section. Enthalpy balance for solid phase on the cross section of the slice gives

$$\frac{\partial}{\partial x} \left(k_x \frac{\partial T}{\partial x} \right) + \frac{\partial}{\partial y} \left(k_y \frac{\partial T}{\partial y} \right) - h \alpha_A (T - T_f(z)) = 0, \quad (x, y) \in \Omega. \quad (3)$$

Associated thermal boundary conditions are considered in our formulation. It should be emphasized that the Enthalpy balance governing differential equation (3) is developed based on the concept of meso-structural model and homogenization. For low-density foam the apparent thermal conductivity is related linearly to its local relative density ρ_i [9]. The local heat transfer coefficient h and the apparent thermal conductivities in two orthogonal directions k_x and k_y are given as

$$h = \text{Nu } k_f / D_h; \quad \begin{cases} k_x = \zeta_x \rho_i k_s + (1 - \rho_i) k_f, \\ k_y = \zeta_y \rho_i k_s + (1 - \rho_i) k_f. \end{cases} \quad (4)$$

Here Nusselt number Nu and coefficients ζ_x and ζ_y (see [12]) have been listed in Table 1. k_s and k_f and are thermal conductivity of the cell wall and fluid respectively.

Equation (3) and the associated thermal boundary conditions can be solved by FEM. Detailed derivations of FEM formulation can be found in [7, 13].

In the following numerical treatment, the design domain is meshed into quadrilateral elements. The total number of elements is n and the number of slice is ns . By applying the standard FEM procedure we obtain the total heat dissipation rate from the structure.

$$Q = \sum_{i=1}^{ns} \sum_{i=1}^n \int_{\Omega^e} ((h\alpha_A)^2 N^T N T^e - (h\alpha_A)^e N T_f(z)) \, d\Omega. \quad (5)$$

The pressure drop ΔP needed to force the fluid through the cylinder is

$$\Delta P = (2 \times c_f \times L \times \rho_f \times v_0 \times \mu_f) \sum_{j=1}^n s_j (1 - \rho_j) \left(\sum_{i=1}^n c_t^2 l_i^2 s_i (1 - \rho_i)^3 \right)^{-1}, \quad (6)$$

where v_0 is the nominal velocity of fluid flow, s_i is the area of the i -th element, the parameters ρ_f and μ_f denote the density and kinematic viscosity of fluid flow, respectively, and the frictional coefficients c_f and coefficients c_t have been listed in Table 1.

3. MATHEMATICAL FORMULATION OF OPTIMUM TOPOLOGY DESIGN (OTD)

The heat dissipation performance of the structure is commonly gauged by the ratio of total heat dissipation rate Q from the structure to the pressure drop ΔP needed to force the fluid through. In this work the ratio is referred to as Ψ ; the higher this ratio, the better the structure performance. The optimum design problem for maximizing the efficiency of heat dissipation is written as

$$\begin{aligned} \text{Find} \quad & \boldsymbol{\rho} = \{\rho_1, \rho_2, \dots, \rho_n\}; \quad \mathbf{l} = \{l_1, l_2, \dots, l_n\} \\ \text{Max} \quad & \Psi = \frac{Q}{\Delta P} \\ \text{S.t.} \quad & \mathbf{K}_T(\boldsymbol{\rho}, \mathbf{l}) \mathbf{T} = \mathbf{R}(\boldsymbol{\rho}, \mathbf{l}) \\ & \sum_{i=1}^n \rho_i s_i \leq V \\ & c_t l_i (1 - \sqrt{1 - \rho_i}) \geq \underline{t} \quad i = 1, 2, \dots, n \\ & l_i \geq 2 \sqrt{\frac{s_i}{nc_t H}} \\ & \frac{4}{c_a \mu_f} \frac{v_0 l_i}{\sqrt{1 - \rho_i}} \leq 2300 \end{aligned} \quad (7)$$

$$0 < \underline{\rho} \leq \rho_i \leq \bar{\rho}; \quad \underline{l} \leq l_i \leq \bar{l},$$

In Equation (7) the set of constraints include the governing equation, material volume limitation, manufacture technique limitation, the constraint on minimum number H of cells in one element (meso-structural model), the condition to ensure fully developed laminar flow and the upper and lower bounds of design variables respectively. The above optimization formulation is solved by the well-known Sequential Quadratic Programming approach. In all of the following examples, numerical iteration starts from initial uniform design, i.e., uniform aperture and local density for all elements.

4. NUMERICAL EXAMPLES

Numerical results of double examples are presented here. In the first example we study optimum design of a cylindrical structure of square cross section, filled with the square-4 type cellular metal cell. The thermal performance of optimum topology design (OTD) is compared with optimum uniform design (OUD) under various fluid nominal velocities. The results confirm the optimum of OTD. In the end, we discuss the effect of other types of inner cell for the thermal performance. In the second example, we construct an optimization design for CPU cooler.

4.1 Example 1

Here we consider a cylinder structure of $64 \text{ mm} \times 64 \text{ mm}$ square cross section and 25 cm length. Cooling water of temperature 283 K surrounds the structure. The fluid temperature is 700 K at inlet. The data of parameters are $v_0 = 11 \text{ m/s}$, $c_p = 1030 \text{ J/kg}\cdot\text{K}$, $\rho_f = 0.7048 \text{ kg/m}^3$ and $\mu_f = 26.71 \times 10^{-6} \text{ m}^2/\text{s}$. The thermal conductivity of metal and fluid are $k_s = 200 \text{ W/m}\cdot\text{K}$ is $k_f = 0.02 \text{ W/m}\cdot\text{K}$, respectively. The number of elements and design variables are 144 and 288, respectively. The upper bound for material volume is 0.3. Only the square-4 type cell is considered. The initial design is the optimum uniform design (OUD), which has uniform local volume density ρ and cell size l for all elements and meets the set of constraints in (7). To obtain the optimum uniform design, we calculate the thermal performances of a set of uniform designs, and pick the optimum uniform design among them. Maximum heat dissipation performance 31.81 is attained at the uniform design $\rho = 0.1$ and $l = 3 \text{ mm}$. By allowing non-uniform distribution of local relative density and cell size the optimum heat dissipation performance is 41.36, which increases by 30% as compared with the performance of OUD. And the optimum material volume is 0.18154. The final material distribution is schematically shown in Figure 4(a). In Figure 4(b), the structural temperature fields in the longitudinal section for OUD (top) and OTD (bottom) are presented. There is a very long hot-core of

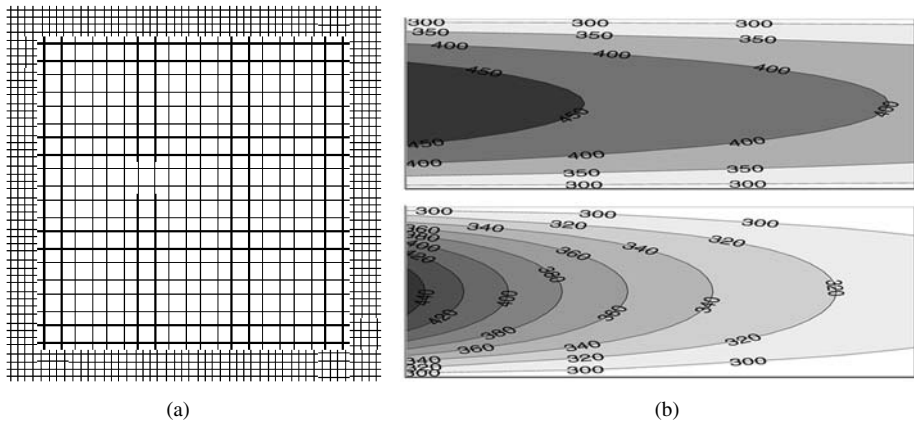


Figure 4. (a) Material distribution by OTD; (b) Structural temperature fields in the longitudinal section (the top is OUD and the bottom is OTD).

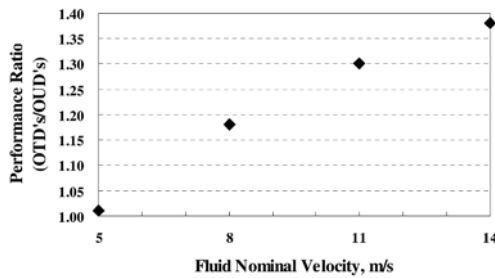


Figure 5. Ratio of performance of heat dissipation (OTD's/OUD's).

higher temperature from 400 K to 450 K through the structure of OUD. But, in the OTD, the hot-core is very short only at inlet and the gradient of temperature is much smaller than in the OUD. In addition, the OTD significantly reduces the temperature difference between the fluid and cell wall based on insights from the optimization results.

To study the effect of fluid nominal velocity, Figure 5 presents the ratio of the performance of OTD to performance of OUD. As the nominal velocity of fluid flow increases, the ratio increases. It means that OTD becomes more and more valuable with increasing the fluid nominal velocity.

Now let us study the effect of various types of inner cell for the performance of heat dissipation. Figure 6(a) presents unitary performance of heat dissipation for three types of inner cell versus fluid nominal velocities. At a same nominal velocity $v_0 = 11$ m/s, optimum performances are 12.37, 41.36 and 98.30 for triangle-6, square-4 and hexagon cell respectively, and the optimum material volumes are 0.26508, 0.18154 and 0.13471 respectively. Figure 6(b)

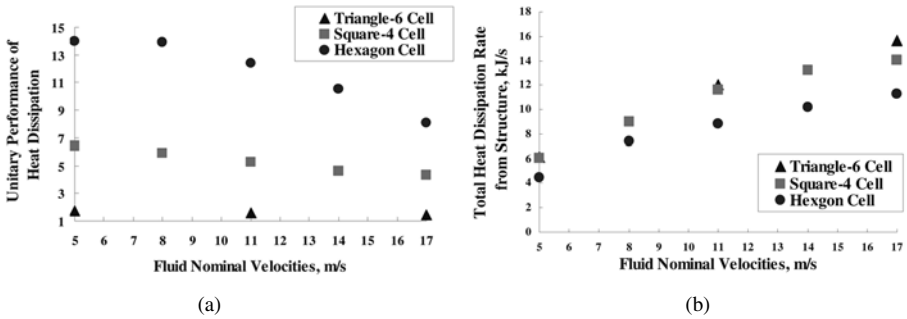


Figure 6. Comparison for various inner cell types: (a) Unitary performance of heat dissipation; (b) Total heat dissipation from structure.

shows another important comparison of the total heat dissipation rate from structure. It can be seen from the two figures that as the nominal velocity of fluid flow increases, the total heat dissipation rate increases and the performance of heat dissipation decreases. The performances of cylindrical structure with hexagon and square cell are much better than the structure with triangle-6 cell, and the total heat dissipation rate from the structure with square and triangle-6 cell are better than the structure with hexagon cell.

4.2 Example 2

In this section, we construct a cylindrical structure of square cross section of $10\text{ cm} \times 10\text{ cm}$ and 10 cm length to simulate a CPU cooler. The performance of heat dissipation is the most important thermal index for the CPU cooler design. The number of elements and design variables is 100 and 200, respectively. The fluid temperature is 293 K at inlet. The bottom side is maintained at a uniform constant temperature of 373 K . At the other three sides, the ambient temperature is 293 K and convection heat transfer coefficient $\beta = 20\text{ W/m}\cdot\text{K}$. The data of parameters are $c_p = 1005\text{ J/kg}\cdot\text{K}$, $\rho_f = 1.060\text{ kg/m}^3$, $v_0 = 10\text{ m/s}$ and $\mu_f = 20.1 \times 10^{-6}\text{ m}^2/\text{s}$, respectively. The thermal conductivity of metal and fluid are $k_s = 200\text{ W/m}\cdot\text{K}$ and $k_f = 0.02\text{ W/m}\cdot\text{K}$. Only the square-4 type cell is considered. The optimum design is schematically shown in Figure 7(a). The performance of our presented OTD is 43.32, which increases by 80% as compared with the performance of OUD. The optimum material volume is 0.151. Figure 7(b) shows the temperature profiles along its axial direction. Compared with the OUD, the temperatures of gas and cooler of OTD are all increased, which indicates the material distribution of present OTD is more beneficial for heat exchange. We can conclude that the material distribution is too novel to be predefined.

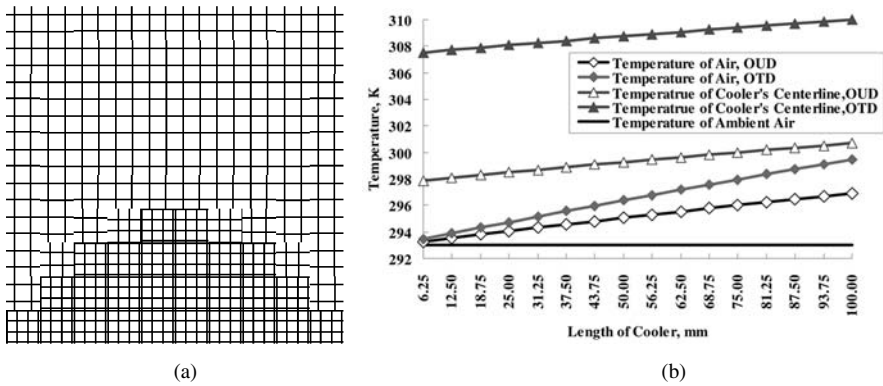


Figure 7. CPU cooler design: (a) Optimum material distribution; (b) Temperature profiles.

5. CONCLUSIONS

A general mathematical model for optimum design of a multi-tubular heat exchanger for optimum efficiency of heat dissipation is studied in this paper. Structural topology optimization methodology is applied to formulate the problem. Thermal analysis is based on a continuous model, and a three-dimensional temperature distribution is considered. The effectiveness of our approach is demonstrated by numerical examples. By optimizing the distribution of the local volume density and cell size, the efficiency of the heat dissipation could be greatly improved. Based on insights from the numerical results, square and hexagon cells show their superiority for the performance of heat dissipation, and the OTD would become more and more valuable as the fluid nominal velocity increases. Although optimal design obtained with the above formulation remains a challenge to the present manufacture techniques, it provides a guideline for the material design.

ACKNOWLEDGMENTS

This project is supported by the Major Program (10332010), Major Research Plan (90205029) and Program for Innovative Research Team (10421002) of the Natural Science Foundation of China. Their financial contributions are gratefully acknowledged.

REFERENCES

- [1] Dong Liu and S.V. Garimella, Analysis and optimization of the thermal performance of microchannel heat sinks, *Inter. J. for Numerical Methods in Heat & Fluid Flow*, 15(1), 7–26 (2005).

- [2] Shial Lin Beh, C.K. Ooi, G.A. Quadir and K.N. Seetharamu, Steady and unsteady thermal analysis of a triple stack cold plate with heat losses, *Inter. J. for Numerical Methods in Heat & Fluid Flow*, 15(1), 96–112 (2005).
- [3] T. Boger and A.K. Heibel, Heat transfer in conductive monolith structures, *Chemical Engineering Science*, 60, 1823–1835 (2005).
- [4] G. Groppi and E. Tronconi, Design of novel monolith catalyst supports for gas/solid reactions with heat exchange, *Chemical Engineering Science*, 55, 2161–2171 (2000).
- [5] T.J. Lu, H.A. Stone and M.F. Ashby, Heat transfer in open-cell metal foams, *Acta Mater.*, 46(10), 3619–3635 (1998).
- [6] S. Gu, T.J. Lu and A.G. Evans, On the design of two-dimensional cellular metals for combined heat dissipation and structural load capacity, *Inter. J. of Heat and Mass Transfer*, 44, 2163–2175 (2001).
- [7] Bo Wang and GengDong Cheng, Design of cellular structures for optimum efficiency of heat dissipation, *Structural and Multidisciplinary Optimization*, in press (2005).
- [8] G. Groppi and E. Tronconi, Continuous vs. discrete models of nonadiabatic monolith catalysts, *AIChE Journal*, 42(8), 2382–2387 (1996).
- [9] L.J. Gibson and M.F. Ashby, *Cellular Solids: Structure and Properties*, 2nd edn., Cambridge University Press, Cambridge (1997).
- [10] M.P. Bendsøe and N. Kikuchi, Generating optimal topologies in structural design using homogenization method. *Comp. Meth. Appl. Mech. Engrg.*, 71, 197–224 (1988).
- [11] M.P. Bendsøe, Optimal shape design as a material distribution problem, *Struct. Optim.*, 1, 193–202 (1989).
- [12] T.J. Lu and C. Chen, Thermal transport and fire retardance properties of cellular aluminium alloys, *Acta Mater.*, 47, 1469–1485 (1999).
- [13] Bo Wang and GengDong Cheng, Design of multi-tubular heat exchanger for optimum efficiency of heat dissipation, in preparation (2005).

LAYOUT OF TILEABLE MULTISTABLE STRUCTURES USING TOPOLOGY OPTIMIZATION

Jitendra Prasad and Alejandro R. Diaz
*Mechanical Engineering Department, Michigan State University,
East Lansing, MI 48824, U.S.A.*

Abstract: This work presents a formulation for the design of *tileable* bistable structures using a topology optimization method. Modeling is based on a ground structure approach, where each member is represented using a non-linear beam. A member is either hinged or fixed at either end and a rubber-like material is used to model the hinges. The optimization is implemented using a genetic algorithm. The methodology developed is illustrated with an example.

Keywords: Bistable structures, bistable mechanisms, compliant mechanisms, tileable structures, periodic structures.

1. INTRODUCTION

A bistable structure has two different stable configurations when not loaded. A two-bar truss with fixed ends loaded at the middle joint is a simple example of a bistable structure (Figures 1(a, b)). Figure 1(c) shows a typical plot of the force applied on this bistable structure *versus* the displacement of the loaded joint. The origin of the plot (state C) corresponds to the first stable configuration (Figure 1(a)). Under a monotonically increasing force, the loaded joint gradually deflects downward until it reaches state D, where the structure becomes unstable and snaps through to state H. When the structure is unloaded from H, the structure settles at state G with zero load. The state G corresponds to the second stable configuration (Figure 1(b)).

Bistable structures are used in, e.g., mechanical switches, snap-shut lids, valves, spectacle frames. Such structures also find applications as switching devices in micro-electro-mechanical systems (MEMS), actuators and sensors.

Prasad and Diaz (2005) used a ground structure of nonlinear beam elements to design bistable structures. Hinges were modeled using a small cross-sectional area at either end of the member. In the present work, the hinges

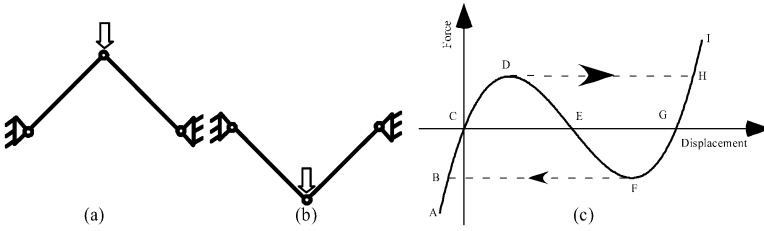


Figure 1. An example of bistable structure; (a) first stable configuration, (b) second stable configuration.

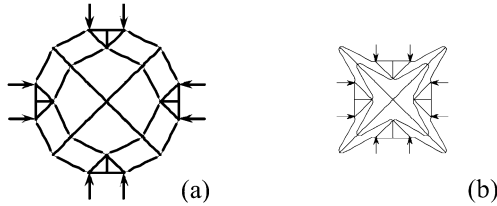


Figure 2. A 2D bistable structure; (a) 1st stable configuration, (b) 2nd stable configuration.

are modeled using a rubber-like material, which would be useful to keep the stresses within limits. An arc-length-method is used to analyze the new model.

2. AN EXAMPLE OF TILEABLE STRUCTURES

Figure 2(a) shows an example of a *two-dimensional bistable* structure, i.e., a structure that can be loaded in both horizontal and vertical directions. The thin regions shown in the figure represent the rubber-like material used to model hinges. Figure 2(b) shows the second stable configuration of this structure. Two-dimensional bistable structures may be joined in series to achieve large displacements with small forces. Similarly, they can be joined in parallel when a high critical force for the snap through is desired.

We use the term *tileable* structure to refer to a basic or fundamental cell which can be repeated periodically to fill a plane. For example, the bistable structure shown in Figure 2 can be repeated periodically to tile a plane, joining each unit end-to-end via rigid connectors (shown as solid rectangles). Two stable equilibrium configurations of such structure are shown in Figure 3. The dotted box shows a basic or fundamental cell of the periodic structure. Such tileable structures may have potential to be used as smart materials, e.g., as a substitute for a shape memory alloy.

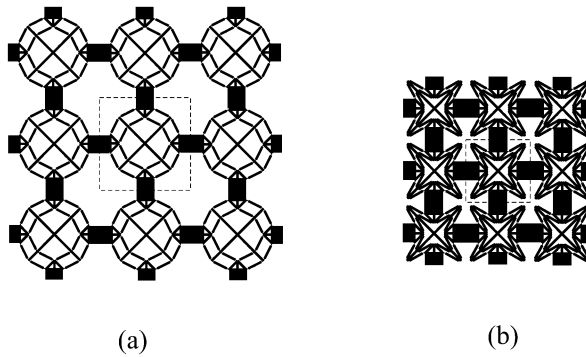


Figure 3. A 3×3 periodic arrangement of bistable structures; (a) first equilibrium configuration, (b) second equilibrium configuration.



Figure 4. A member (bar) of the ground structure.

3. THE FINITE ELEMENT MODEL

A corotational element based on Timoshenko beam theory (Crisfield, 1991, p. 219) is used for non-linear finite element analysis of the structure. The analysis is quasi static and all inertia forces are ignored. A scaled arc-length method (Al-Rasby, 1991; Bruns et al., 2002), suitable for analyzing structures undergoing instability (snap through or buckling), has been used for the solution of the non-linear equations. While such instability is typically avoided (e.g. to prevent buckling, as in Neves, 1995), here such instability is a desirable feature.

3.1 The Ground Structure and Design Variables

A version of the classical ground structure approach in truss topology optimization (e.g., Dorn et al., 1964) was used in the present work. Every bar in the ground structure is divided into two regions – shown as dark and light gray regions in Figure 4. Material properties for the region shown in light gray are variable, taking three possible values, namely, values corresponding to ‘no material’, a ‘compliant’ material and a ‘stiff’ material. The region shown dark is made from either ‘no material’ or the ‘stiff’ material.

In this work the compliant material is a rubber-like material, e.g. natural rubber, silicone rubber or a polyurethane elastomer. The stiff material is rel-

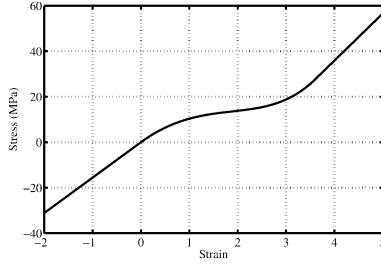


Figure 5. Prescribed normal stress as a function of normal strain in the compliant material.

actively stiff and approximately linear material, e.g. polypropylene. Material properties are characterized by – (a) the normal stress (σ) vs. normal strain (ε) relationship and (b) the shear stress (τ) vs. shear strain (γ) relationship for the material. Figure 5 shows a representative plot of σ vs. ε in a compliant material, viz. polyurethane elastomer. The τ vs. γ relationship for both stiff and compliant material is assumed to be linear.

The material and layout of the structure are controlled by two binary design variables for each bar α , labeled ρ_α and μ_α . Variable ρ_α controls the layout of the structure: $\rho_\alpha = 1$ means bar α is present, $\rho_\alpha = 0$ means bar α is removed. When a bar is present, its material is controlled by variable μ_α . $\mu_\alpha = 1$ indicates that the light gray regions of bar α are made of the compliant material, i.e. α bar is hinged at both ends. $\mu_\alpha = 0$ means that bar α is made of the stiff material. Thus, the normal stress in the light gray region of bar α may be written as

$$\sigma_\alpha^{\text{gray}}(\rho_\alpha, \mu_\alpha, \varepsilon) = \rho_\alpha(\mu_\alpha\sigma^1(\varepsilon) + (1 - \mu_\alpha)\sigma^2(\varepsilon)),$$

where the superscripts (1) and (2) refer to properties of the compliant and stiff material, respectively. Similarly, the shear stress in the light gray region of bar α may be written as

$$\tau_\alpha^{\text{gray}}(\rho_\alpha, \mu_\alpha, \gamma) = \rho_\alpha(\mu_\alpha\tau^1(\gamma) + (1 - \mu_\alpha)\tau^2(\gamma)).$$

The normal stress in the dark region of bar α may be expressed as

$$\sigma_\alpha^{\text{dark}}(\rho_\alpha, \varepsilon) = \rho_\alpha\sigma^2(\varepsilon),$$

while the shear stress in the dark region of bar α is

$$\tau_\alpha^{\text{dark}}(\rho_\alpha, \gamma) = \rho_\alpha\tau^2(\gamma).$$

3.2 The Objective Function

The measure of performance of a bistable structure considered here is the spatial difference between the two stable configurations of the structure. The ob-

jective function (to be maximized) is

$$\phi = (\mathbf{x}^C - \mathbf{x}^G)\mathbf{W}(\mathbf{x}^C - \mathbf{x}^G). \quad (1)$$

\mathbf{x}^C and \mathbf{x}^G are vectors of nodal degrees of freedom at the two stable configurations, corresponding to states C and G in Figure 1(c). Matrix \mathbf{W} is a diagonal matrix with diagonal entries $W_{ii} = d_i^2$, where $\mathbf{d} \in \mathcal{R}^n$ is a unit vector used to control the desired direction of snap-through and ns is the total number of degrees of freedom in the structure.

If a structure has two stable configurations, ϕ is a measure of the ‘distance’ between the two configurations. Naturally, many substructures of a ground structure will not be bistable and thus they will *not* have two stable configurations. For such structures ϕ is zero. Thus the objective function of the problem is set simply to find *any* bistable structure within the set of all substructures of the ground structure.

3.3 The Optimization Problem

The optimization problem is formally written as

Find $\boldsymbol{\rho} = \{\rho_1, \rho_2, \dots, \rho_{n_b}\} \in \{0, 1\}^{n_b}$, $\boldsymbol{\mu} = \{\mu_1, \mu_2, \dots, \mu_{n_b}\} \in \{0, 1\}^{n_b}$ that maximize $\phi(\boldsymbol{\rho}, \boldsymbol{\mu}) = (\mathbf{x}^C - \mathbf{x}^G)^T \mathbf{W}(\mathbf{x}^C - \mathbf{x}^G)$

$$\text{subject to } \sum_{a=1}^{n_b} \rho_a \leq n_{\max}, \quad (2)$$

where n_{\max} is the maximum number of bars allowed in the bistable structure. n_b is the total number of bars in the ground structure.

3.4 The Solution Scheme

The optimization problem is solved using a genetic algorithm (GA). The constraint on the total number of bars in the solution is implemented by adding a penalty function to the objective function. Three additional penalty functions are devised to rank candidate solutions which cannot be analyzed because they are not well-formed structures (e.g. insufficiently supported or disconnected structures). Such candidates may be retained in the population as they may have the potential to evolve into the optimal solution. With the addition of the penalty functions, the original objective function (ϕ) is modified into the following new objective function to be *minimized*:

$$\hat{\phi} = -w\phi + \psi, \quad (3)$$

where

$$\psi = \psi_1 + \psi_2 + \psi_3 + \psi_4, \quad (4)$$

and w is a constant scaling factor, which can be selected such that $w\phi \approx 1$. Functions ψ_1 , ψ_2 , ψ_3 and ψ_4 are described below.

3.4.1 Penalty Function ψ_1 . A structure with no member at the loading port is penalized by ψ_1 , which is defined as

$$\psi_1 = \frac{1}{\delta_{\max}} \sum_{j=1}^{n_f}, \quad (5)$$

where δ_j is the shortest distance between the structure and the j -th loading port. δ_{\max} is the maximum distance between any two nodes in the structure and n_f is the number of loading ports.

3.4.2 Penalty Function ψ_2 . A structure with a number of members that exceeds a prescribed maximum is penalized by ψ_2 , given by

$$\psi_2 = \begin{cases} \frac{(n_a - n_{\max})}{(n_t - n_{\max})} & \text{if } n_a > n_{\max} \\ 0 & \text{if } n_a \leq n_{\max} \end{cases}, \quad (6)$$

where n_a is the actual number of members present in the structure. $n_t > n_{\max}$ is a prescribed constant used to control the slope of this penalty (e.g., $n_t = 2 * n_{\max}$). n_t is chosen to keep $\psi_2 \approx 1$.

3.4.3 Penalty Function ψ_3 . A disjoint structure is penalized by ψ_3 , given by

$$\psi_3 = \frac{N_s}{N_t}, \quad (7)$$

where N_s is the total number of disjoint substructures present in the structure and N_t is a prescribed scaling factor (e.g., $N_t = 2$). In order to measure N_s , the structure is represented as an undirected graph. N_s is the number of components of the graph.

3.4.4 Penalty Function ψ_4 . A structure which is not sufficiently supported and may allow a rigid-body motion is penalized by ψ_4 , given by

$$\psi_4 = N_x + N_y + N_\theta, \quad (8)$$

where $N_x = 0$ if the structure is supported in x -direction, i.e., the structure does not allow a rigid body translation in x -direction, otherwise $N_x = 1$ and similarly for N_y . If the structure does not allow a rigid body rotation, then $N_\theta = 0$, otherwise $N_\theta = 1$.

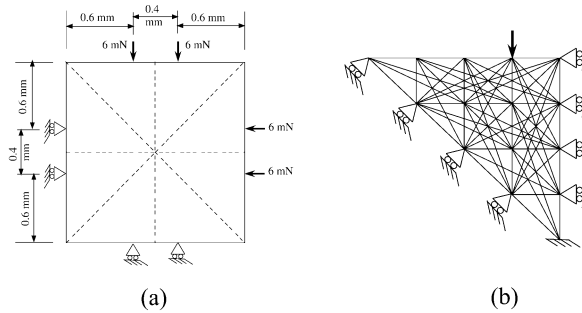


Figure 6. Design space and boundary conditions; (a) full design space, (b) ground structure.

4. EXAMPLE

In this example the goal is to design a two-dimensional bistable structure that will operate loaded as shown in Figure 6(a), and will fit within a $1.6 \text{ mm} \times 1.6 \text{ mm}$ package space, as shown. This package space is partitioned into 8 triangles, whose boundaries are marked by dashed lines in the figure. The structure will be assumed to be symmetric about these lines. The ground structure is laid on one of these triangles and the appropriate boundary conditions are applied to enforce symmetry (Figure 6(b)). The total number of bars in the triangular ground structure (n_b) is 62 and the maximum allowable number of bars in a solution is 8. In accordance with Section 4.1, every bar in the ground structure is discretized into 2 regions, where the length of each light gray region is one-eighth of the total length of the corresponding member (bar). A load $F = 6 \text{ mN}$ is applied.

The cross-sectional area of the bars is $2 \times 10^{-3} \text{ mm}^2$. All entries in the weight matrix \mathbf{W} are zero except $W_{mm} = 1$, where m is the degree-of-freedom associated with load F . This means that we want to maximize snap-through in the direction of the external load. The stiff material is polypropylene with Young's modulus 1380 MPa and Poisson's ratio 0.3. The compliant material is assumed to be linear in shear with shear modulus 5.2 MPa. The σ - ε plot for the compliant material is given in Figure 5.

The scaling factor w (Equation (4)) used here is $w = 7.7125 \text{ mm}^{-2}$, which corresponds to $w\phi = 1$ for the bistable structure shown in Figure 2. The solution obtained by the GA is shown along with its second stable configuration in Figure 7. The objective function value for this structure is $0.1317 \text{ (mm}^2\text{)}$, or $\hat{\phi}$ is -1.0159 with penalty function $\psi = 0$, i.e., only slightly better than the structure in Figure 2. The corresponding force displacement diagram is shown in Figure 7(c). The critical force required for the snap through is approximately 5.5 mN in one direction (forward) and 3.0 mN in the other (backward).

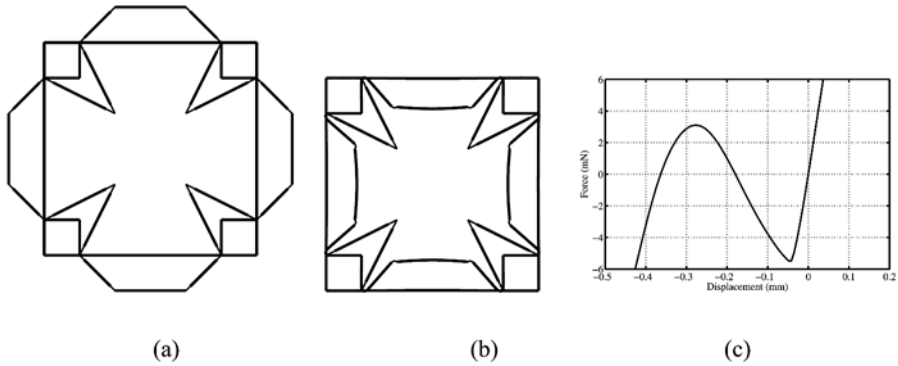


Figure 7. Bistable structure obtained by the GA; (a) first stable configuration, (b) second stable configuration; (c) load-displacement curve.

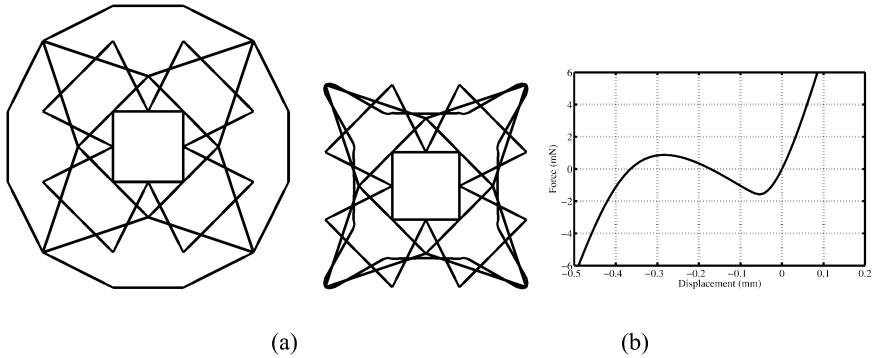


Figure 8. Another bistable structure; (a) first stable configuration, (b) second stable configuration, (c) load-displacement curve.

Another solution to this problem is shown in Figure 8. As shown in Figures 7 and 8, a few members overlap in the second stable configuration. One way to handle the overlapping problem is to allow one of these two substructures to have a small curvature out of the plane.

5. A DIFFERENT APPROACH

From the solutions in the previous section it is clear that in all cases bistability is achieved by distributing several two-bar structures around the domain and creating a supporting structure around them, as illustrated in Figure 9 below. This suggests that a different strategy may be more computationally attractive and may avoid several of the other drawbacks associated with the GA approach (e.g., the possibility of interference as the structure deforms).

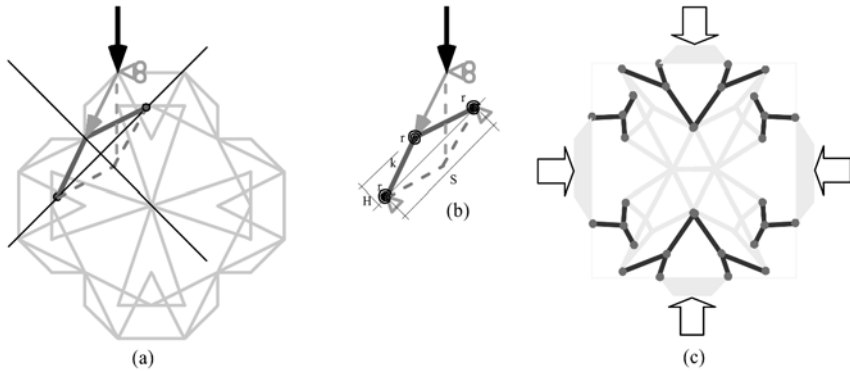


Figure 9. Operation of typical bistable solution (a) is based on simple two-bar structures (b) repeated and supported by an underlying structure (c).

In this approach, simple two-bar structures such as the one in Figure 9(b) are randomly distributed over the two-dimensional tile and connected to loading ports. Interference can be avoided using simple set intersection algorithms. The load-displacement characteristics of the resulting structure can be easily estimated as a function of position and geometry (e.g., using H , S in Figure 9(b) as parameters). In this way many such structures can be explored with minimal computational effort. From this set, instances with load-displacement curves that exhibit desirable properties can be extracted for further investigation (e.g., the structure in Figure 9(c)). For these structures an underlying supporting structure is built and further analysis can take place using the finite element model discussed in the previous section.

6. CONCLUSION

The present work provides the concepts and numerical methodology to automatically design tileable multistable structures. The methodology used here does not account for the interfering or overlapping structures. However, overlapping can be avoided by providing a few members with small curvature out of the plane. A more efficient optimization method such as a gradient-based algorithm should be used in future work, replacing the (GA), in order to get consistent and faster results. An improvement in the objective function is being undertaken which would facilitate the design of *specific* features of the load-displacement curve.

REFERENCES

- Al-Rasby, S.N. (1991) Solution techniques in nonlinear structural analysis, *Computers and Structures*, 40(4), 985–993.

- Bruns, T.E., Sigmund, O. and Tortorelli, D.A. (2002) Numerical methods for the topology optimization of structures that exhibit snap-through, *Int. J. Num. Meth. Engrg.*, 55, 1215–1237.
- Crisfield, M.A. (1991) *Non-Linear Finite Element Analysis of Solids and Structures*, Vol. 1, Wiley, Chichester.
- Dorn, W.C., Gomory, R.E. and Greenberg, H.J. (1964) Automatic design of optimal structures, *J. Mec.*, 3.
- Neves, M.M., Rodrigues, H. and Guedes, J.M. (1995) Generalized topology design of structures with a buckling load criterion, *Structural and Multidisciplinary Optimization*, 10(2), 71–78.
- Prasad, J. and Diaz, A.R. (2005), Synthesis of bistable periodic structures using topology optimization and a genetic algorithm, in *Proc. of ASME 2005 Design Engineering Conferences (DETC'05)*, Long Beach, California, Paper DETC2005-84904.

TOPOLOGY OPTIMIZATION OF DISPERSION PROPERTIES IN OPTICAL FIBRES

Jesper Riishede and Kristian Hougaard

Department of Mechanical Engineering, DTU, Building 404, 2800 Kgs. Lyngby, Denmark

jri@mek.dtu.dk, kh@mek.dtu.dk

Abstract: In this paper, the possibility of using topology optimization for tailoring the dispersion properties in optical fibres is discussed. A method for finding the sensitivities of the dispersion coefficient is introduced, along with different constraints for confining the light to the centre of the fibre geometry. The modal analysis of the fibre geometries is carried out with a finite-difference approximation to the scalar Helmholtz wave equation. The results, obtained by optimizing the refractive index distribution over the cross section of the fibre, show that it is possible to match the value of the dispersion coefficient at both a single and at multiple wavelengths.

Keywords: Topology optimization, optical fibres, dispersion properties.

1. INTRODUCTION TO OPTICAL FIBRES

Optical fibres are used as transmission media for electromagnetic waves in the visible and near infrared spectrum. An optical fibre typically consists of a cylindrical silica (SiO_2) core with a radius of about 3–10 μm , surrounded by a circular silica cladding region, with a radius of about 60 μm . The refractive index is lower in the cladding region compared to the core region. Such a fibre structure is known as a *step-index fibre* [1]. The index step allows for confinement of light to the core region, due to a process known as *total internal reflection* (TIR). Due to TIR light incident on the core/cladding interface is reflected back into the core region, and the light can then propagate along the fibre with very low losses (down to 0.2 dB/km, corresponding to losing half the energy after 15 km).

The guidance of light in optical fibres is governed by Maxwell's equations, which generally needs to be solved using full vectorial methods. However, if fibres with relatively low index contrasts between the core and the cladding are considered, Maxwell's equations may be reduced to the scalar Helmholtz wave

equation [2]:

$$\nabla^2 \tilde{\psi}(x, y, z) + n(x, y)^2 k^2 \tilde{\psi}(x, y, z) = 0. \quad (1)$$

Here ∇ is the Laplacian operator, $\tilde{\psi}$ is the electric or magnetic field distribution, which we will denote the optical field. n is the refractive index distribution, which is invariant in the z -direction, along the axis of the fibre. k is the wavenumber, defined as $k = 2\pi/\lambda$, where λ is the free space wavelength of the light.

Since the fibre is invariant in the z -direction, it can be shown that solutions to (1) may be written as a transversal solution multiplied by a harmonically oscillating function:

$$\tilde{\psi}(x, y, z) = \psi(x, y) \exp(i\beta z). \quad (2)$$

Inserting (2) into (1) we obtain:

$$\nabla_{\perp}^2 \psi(x, y) + n(x, y)^2 k^2 \psi(x, y) = \beta^2 \psi(x, y) \quad (3)$$

where ∇_{\perp} is the transverse Laplacian operator $[\frac{\partial}{\partial x}, \frac{\partial}{\partial y}]$, and β is referred to as the propagation constant. (3) is now an eigenvalue equation, with the eigenvalue β^2 and the optical field distribution as eigenvector. From now on, the x - and y -dependency of ψ and n is assumed.

In general, (3) needs to be solved using numerical tools. Our approach is to make a finite-difference discretization of the term $\nabla_{\perp}^2 + n^2 k^2$ in (3), which then results in a matrix, Φ . We then solve the resulting matrix eigenvalue problem using MATLAB:

$$\Phi \psi = \beta^2 \psi. \quad (4)$$

The solutions to (3) and (4) are referred to as *modes* in the optical fibre. These modes are either guided modes or cladding modes. Figure 1 shows the index distribution of a step-index fibre, and three of the optical modes. The guided modes (b and c) have the majority of the optical field confined to the core area, which results in low propagation losses, and these are the modes used for transmission of light. The cladding modes (d) has the optical field spread out in the whole cross section of the fibre, and they are extremely lossy. Most often so-called single mode fibres are used. Here, the fibre parameter and the wavelength are chosen, so only a single guided mode exist. This means that all the guided light is located in the fundamental mode (Figure 1b).

2. DISPERSION IN OPTICAL FIBRES

An important parameter, to describe the optical modes is the *effective index*, defined as:

$$n_{\text{eff}} = \frac{\beta}{k}. \quad (5)$$

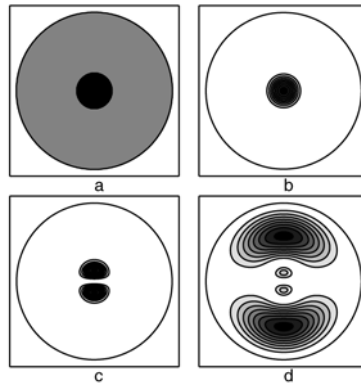


Figure 1. Index profile of a step index fibre (a), and three of the optical modes for the fibre. Fundamental mode (b), second order mode (c) and cladding mode (d).

The effective index can be seen as the average index of the mode, and depends on how the light is distributed in the fibre. When the wavelength of the light changes, the effective index also changes. This affects the propagation speed of the light, and means that two different wavelengths travel with different velocities in the fibre. This is known as fibre dispersion, and is an important limiting factor in communication systems today. The problem arises because an optical pulse has a finite spectral width, which means that it consists of light with wavelengths in a small region around the center wavelength. Due to dispersion, each of these pulse components travel with different velocities, and as a consequence a sharp pulse is quickly broadened, as it travels down along an optical fibre. The effect of dispersion is illustrated in Figure 2, where a bit sequence is transmitted using an optical pulse train. Four bit slots (time periods for each bit) is indicated by the vertical dashed lines. A 1-bit is sent as a light pulse, and a 0-bit is sent as no light in the bit slot. In the beginning, the bit sequence is easily recognised, but after travelling some distance, the bit sequence is distorted. Eventually, it is not possible to detect the original bit sequence. If the bit slots are made wider, the detection becomes easier, but the bit rate is reduced.

The degree of pulse broadening depends on the value of the dispersion coefficient [3]:

$$D = -\frac{\lambda}{c} \frac{\partial^2 n_{eff}}{\partial \lambda^2}, \quad (6)$$

where c is the speed of light in vacuum. The dispersion is calculated in the unit $ps/(km \cdot nm)$, and denotes the number of picoseconds between two wavelengths separated by 1 nm, after propagating 1 km in a fibre.

To overcome the dispersion limitations, so-called *dispersion compensating fibres* (DCF) have been developed [4]. In these fibres, a more complex fibre

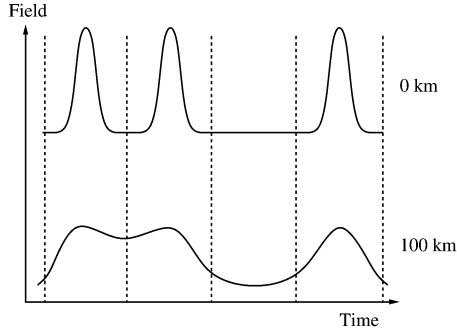


Figure 2. Effects of dispersion on a bit sequence transmitted as optical pulses. The top curve shows the launched optical signal, and the bottom curve shows the signal after it has travelled 100 km in the optical fibre.

geometry is used, which results in different dispersion properties. The idea is to reverse the dispersion caused by the single mode fibres, by adding an extra length of DCF. In such a fibre, the dispersion, at some desired wavelength, should have the opposite sign as in a step-index fibre. This way the speed of the different wavelengths are changed, to allow the slow components to catch up again.

3. FORMULATION OF THE DESIGN PROBLEM

In the present optimisation problem, we are interested in optimising the refractive index distribution over the cross section of the fibre in order to obtain a specific value of the dispersion at a given wavelength. For this purpose, we formulate the design problem as a task of minimizing an objective function of the form:

$$f = (D - D^*)^2. \quad (7)$$

Here, D is the dispersion of the fibre design found during each iteration of the optimisation process and D^* represents the target value of the dispersion.

From (6) it is seen that the dispersion in an optical fibre is proportional to the second derivate of the effective index, n_{eff} , which is again related to the eigenvalue, β^2 , of the Helmholtz wave equation as shown in Equation (3). In a straight forward approach, the calculation of the sensitivity of f with respect to the design variable will give rise to a problem involving a third order derivative of an eigenvalue. To circumvent this problem, we instead choose a simplified approach, where the dispersion is expressed by a three point finite-difference scheme:

$$D \approx -\frac{\lambda}{c} \frac{n_{\text{eff},1} - 2n_{\text{eff},2} + n_{\text{eff},3}}{(\Delta\lambda)^2}. \quad (8)$$

Here, we find the second derivate at the wavelength λ by calculating the effective index, n_{eff} , at three different wavelengths separated by $\Delta\lambda$. The advantage of this approach is that the problem of finding sensitivities is reduced to finding a first order derivative of the eigenvalue. However, this advantage comes at the cost of having to solve three eigenvalue problems for each dispersion calculation, so the calculation time rises by approximately a factor of three.

In order to represent the topology of the fibre structure, we introduce a design variable, γ_i , having a value between 0 and 1 in each grid point of the design domain. The relation between the design variable and the refractive index is given by the expression:

$$n_i = n_{\min} + \gamma_i(n_{\max} - n_{\min}), \tag{9}$$

where n_{\max} and n_{\min} represent the maximum and minimum value of the refractive index, respectively. By choosing γ as the design variable, the sensitivity of the objective function may be written as an expression of the form:

$$\begin{aligned} \frac{\partial f}{\partial \gamma_i} &= \frac{\partial f}{\partial D} \frac{\partial D}{\partial n_i} \frac{\partial n_i}{\partial \gamma_i} \\ &= 2(D - D^*)(n_{\max} - n_{\min})\gamma_i \frac{\partial D}{\partial n_i}. \end{aligned} \tag{10}$$

This illustrates that the main objective in the present formulation of the design problem consists in determining the derivative of the dispersion with respect to the refractive index in the i -th grid point. By differentiating the three point dispersion formula in Equation (8) we are faced with the task of finding the first derivative of the effective index with respect to n_i . From the definition of n_{eff} in (5), the first order derivative of the effective index may be written as:

$$\frac{\partial n_{\text{eff}}}{\partial n_i} = \frac{\partial(\sqrt{\beta^2}/k_0)}{\partial n_i} = \frac{1}{k_0^2} \frac{1}{2n_{\text{eff}}} \frac{\partial(\beta^2)}{\partial n_i}, \tag{11}$$

where the last term corresponds to the derivative of the eigenvalue, β^2 , of the Helmholtz wave equation (3). In the specific case where this equation is solved with a finite-difference approximation, the derivative of the eigenvalue with respect to the refractive index in a single grid point is given as:

$$\frac{\partial(\beta^2)}{\partial n_i} = \psi^T \frac{\partial \Phi}{\partial n_i} \psi = 2n_i k_0^2 \psi_i^2. \tag{12}$$

Here, it is utilized that the Φ -matrix only contains information of n_i in the diagonal element of the i -th row [5], so the sensitivity in (12) does therefore only depends on n_i and the corresponding value of the eigenvector, ψ_i , in that particular grid point. If this result is combined with the three point formula in

Equation (8), the following expression for the derivative of the dispersion is obtained:

$$\frac{\partial D}{\partial n_i} = -\frac{\lambda}{c} \frac{n_i}{(\Delta\lambda)^2} \left(\frac{\psi_{1,i}^2}{n_{\text{eff},1}} - 2 \frac{\psi_{2,i}^2}{n_{\text{eff},2}} + \frac{\psi_{3,i}^2}{n_{\text{eff},3}} \right), \quad (13)$$

where it is emphasised that the effective indices and eigenvectors are calculated at three different wavelengths. Inserting (13) into (10) yields the final expression for the sensitivity of the dispersion with respect to the design variable, γ .

4. DISPERSION OPTIMIZATION AT A SINGLE WAVELENGTH

As a first example of applying the theory introduced in the previous section, we will try to optimize the dispersion at a single wavelength. For this purpose, we choose a design domain of size $20 \times 20 \mu\text{m}$, discretized in 200×200 grid points, resulting in a total number of design variables of 40000. Also, we impose a volume constraint on the design variable, demanding that the sum of γ , over the entire design domain should be larger than a certain fraction of the total area.

The modelling of the fibre geometry is carried out with a finite-difference mode solver [5] where fibre geometry and the Helmholtz wave equation is approximated on a finite calculation domain using a homogeneous discretization grid. The truncation of the calculation domain is done by imposing a Dirichlet boundary condition that forces the field to be zero on the edge of the calculation domain. This is equivalent to having a perfectly reflecting boundary. Obviously, this choice of boundary condition may affect the solution, but as the mode field of the fibre decays exponentially away from the core, the boundary condition will provide a valid representation of the actual physical problem, as long as the mode is well confined to the core region. This is the reason for imposing the volume constraint discussed above, since the requirement of using a certain amount of high-index material will ensure a well confined mode.

The aim of the first optimization example, is to obtain a dispersion of 1 ps/(km nm) at a wavelength of $1 \mu\text{m}$. In this case, the maximum and minimum value of the refractive index is set to 1.44 and 1.458 respectively, which corresponds to typical values of the refractive index contrast in silica fibres. To ensure that light will be confined to the centre of the calculation domain, the initial value of the design variables, γ_i , are chosen so that that the index distribution has a circular high index region, with a diameter of $2 \mu\text{m}$ in the centre of the design domain. Furthermore, the limit of the volume constraint is chosen to be 20% of the calculation domain.

The optimization step is carried out using the *method of moving asymptotes* (MMA) [6]. Figure 3 shows the dispersion curve obtained by minimizing the objective function, and it is seen that the aim of the optimization, i.e. to obtain a

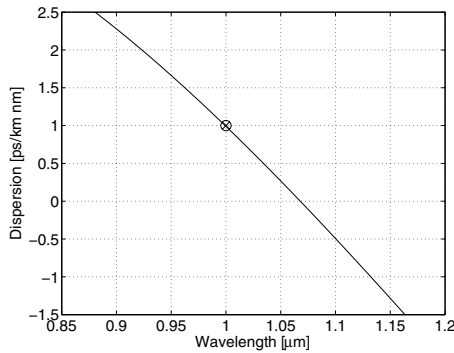


Figure 3. The dispersion curve obtained after optimizing the waveguide structure. The optimization goal of having a dispersion of 1 ps/(km nm) at $\lambda = 1 \mu\text{m}$ has been achieved.

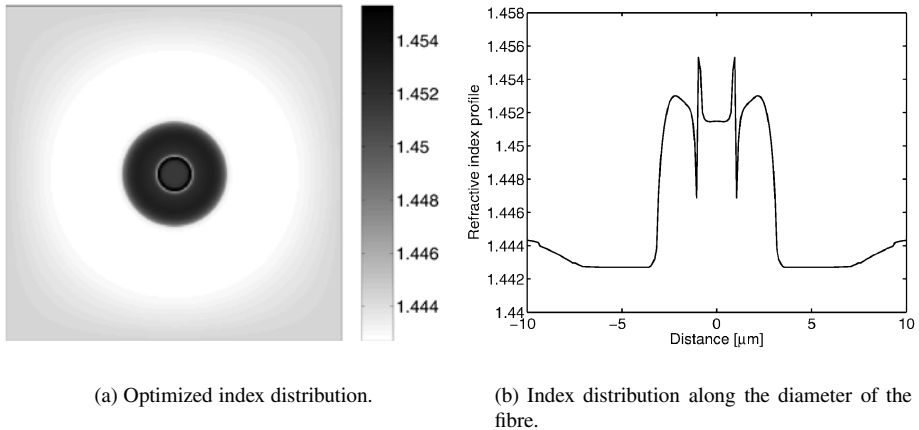


Figure 4. Index distribution of the optimized fibre geometry.

dispersion of 1 ps/(km nm) at $\lambda = 1 \mu\text{m}$, has been achieved. This result therefore illustrates that the basic idea of using topology optimization for tailoring the dispersion properties of optical fibres is indeed feasible.

The index distribution of the optimized waveguide geometry is shown in Figure 4a, along with a cross section along the diameter of the fibre, shown in Figure 4b. Both figures show that additional material has been added to the core region of the fibre during the optimisation. In this way, the desired value of the dispersion has been obtained. From an optimization point of view, the task of tailoring the dispersion in a single point is relatively easy, since there exists a large amount of waveguide structures that meet this requirement. However, many of these structures will not be practically usable, because they are no longer single moded. For instance, this is the case for the fibre design

shown in Figure 4b, where the core region has become too wide compared to the wavelength. This means that a second order mode is allowed to exist in the core region of the fibre. The presence of higher order modes at the wavelength of operation is a highly undesired property, since the different modes travel along the fibre with different velocity. This gives rise to a significant increase in the dispersion (pulse broadening), and therefore modern optical telecommunication systems are all based on single mode fibres to avoid this detrimental property. As a consequence, special care should be taken to keep the fibre design single-mode during the optimization procedure.

5. DISPERSION OPTIMIZATION AT MULTIPLE WAVELENGTHS

In order to address some of the issues introduced in the previous section, we will here discuss some modifications to the formulation of the optimization problem. As a first modification, we will modify the method to consider dispersion design at multiple wavelengths simultaneously. In practice, this means that we will be able to control the value of the dispersion coefficient as well as the slope of the dispersion curve. Thereby, the optimization problem becomes more complicated and the amount of possible solutions decreases significantly.

The objective function of the multi-wavelength optimization problem is simply defined as a sum of the form:

$$S = \sum_i S_i, \quad (14)$$

where S_i is the value of objective function for the individual wavelength calculations. To avoid some of the problems with multi-mode fibre structures, we replace the previously used volume constraint with a constraint on the effective area of the guided mode. Basically, the effective area represents a measure of the degree of confinement and it is defined as [7]:

$$A_{\text{eff}} = \frac{\left(\int \psi^2 dA \right)^2}{\int (\psi^2)^2 dA}. \quad (15)$$

By ensuring that A_{eff} stays below a certain value, the diameter of the core region is not allowed to increase during the optimization, as it was the case in the previous example. As a consequence, the existence of higher order modes may be avoided. One of the challenges of imposing the effective area constraint is that we need to calculate the sensitivities of A_{eff} with respect to the design variables. In this process we need to find the derivate of the eigenvector, ψ ,

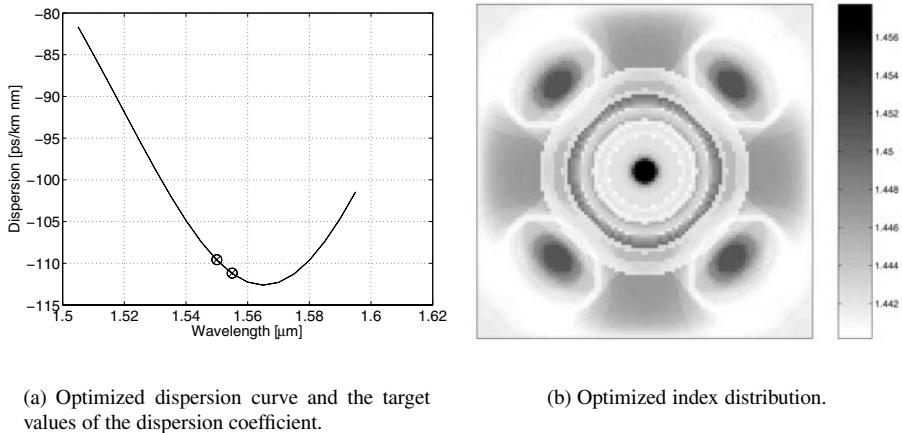


Figure 5. Optimization of a dispersion compensating fibre at two wavelengths.

which is a quite cumbersome task, because it involves solving a singular matrix problem. The solution consist in reformulating the effective area as:

$$\tilde{A}_{\text{eff}} = A_{\text{eff}} + l^T (\Phi \psi - \beta^2 \psi) + c (\psi^T \psi - 1), \quad (16)$$

where l and c are a vector and a scalar Lagrangian multiplier, respectively. The problem is then solved by combining the adjoint method [8] with Nelson's method [9] for solving singular matrix problems. An in-depth discussion of this approach is given in the work by Tcherniak [10].

Figure 5(a) shows the result from optimizing the dispersion at multiple wavelengths. As the dispersion curve in Figure 5(a) illustrates, the dispersion is optimized at two wavelengths, $\lambda = 1.55 \mu\text{m}$ and $\lambda = 1.555 \mu\text{m}$, which are typical wavelengths used for optical communication. The value of the dispersion coefficient is optimized to match a value of -5 times the dispersion in a conventional single mode fibre. This means that 200 meters of such a fibre may be used to compensate for the dispersion in 1 km of conventional transmission fibre. As seen from Figure 5(a), the optimized dispersion curve has an excellent agreement with the target values of the dispersion coefficient. This result demonstrates that topology optimization also provides an efficient tool for optimizing dispersion at several wavelengths simultaneously.

The index distribution of the fibre design obtained from the multi-wavelength optimization step is shown in Figure 5(b). Just as in the single wavelength case, the fibre geometry is circular symmetric around the core area, but has some high index lobes further away from the core region. The resulting mode field distribution (not shown) is very localized to the core region. This fact demonstrates that the effective area constraint used in the multiple wavelength case provides an efficient way of eliminating the presence

of higher-order modes, while keeping the mode field confined to the central region of the design domain.

6. CONCLUSION

We have presented a numerical model based on topology optimization for designing the dispersion properties in optical fibres. It has been successfully demonstrated that the proposed method is capable of finding fibre designs, where the dispersion matches predefined values at both one and two wavelengths. One of the main challenges in this work has been the task of confining the guided modes to the centre of the design domain, while keeping the fibre singlemoded. An efficient solution to this problem was found by imposing a constraint on the effective area of the guided modes. It is believed that the presented method holds some interesting prospects, in particular due to the possibility of tailoring the dispersion at several wavelengths, which may be used to predict novel fibre designs that provide dispersion compensation over a very large spectral interval.

ACKNOWLEDGEMENT

The authors are financially supported by the EURYI-project, Synthesis and Topology Optimization of Optomechanical Systems, European Science Foundation.

REFERENCES

- [1] B. Saleh and M. Teich, *Fundamentals of Photonics*, John Wiley & Sons (1991).
- [2] A. Snyder and J. Love, *Optical Waveguide Theory*, Chapman and Hall (1983).
- [3] G. Agrawal, *Fiber-Optic Communications Systems*, John Wiley & Sons (1997).
- [4] L. Grüner-Nielsen et al., Dispersion compensating fibres, *Optical Fibre Technology*, 6 (2000).
- [5] Jesper Riishede et al., A 'poor man's approach' to modelling micro-structured optical fibres, *Journal of Optics A, Pure and Applied Optics*, 5 (2003).
- [6] K. Svanberg, Method of moving asymptotes – A new method for structural optimization, *International Journal for Numerical Methods in Engineering*, 24 (1987).
- [7] G. Agrawal, *Nonlinear Fibre Optics*, Academic Press (1989).
- [8] M.P. Bendsøe and O. Sigmund, *Topology Optimization, Theory, Methods and Applications*, Springer-Verlag (2002).
- [9] Nelson R.B., Simplified calculation of eigenvector derivatives, *AIAA Journal*, 14(9), 1201–1205 (1976).
- [10] D. Tcherniak, Topology optimization of resonating structures using SIMP method, *International Journal for Numerical Methods in Engineering*, 54, 1605–1622 (2002).

OPTIMAL DESIGN WITH SMALL CONTRAST

Grégoire Allaire and Sergio Gutiérrez

CMAP, Ecole Polytechnique, 91128 Palaiseau, France

gregoire.allaire@polytechnique.fr, sergio@cmap.polytechnique.fr

Abstract: This paper is concerned with optimal design problems where we assume that the coefficients in the state equation have small contrast. Making an asymptotic expansion up to second order with respect to the contrast greatly simplifies the optimization problem. By using the notion of H -measures we are able to prove general existence theorems for small amplitude optimal design and to provide simple and efficient numerical algorithms for their computation. A key feature of this type of problems is that optimal microstructures are always simple laminates.

Keywords: Optimal design, homogenization, H -measures.

1. INTRODUCTION

The homogenization method has been very successful for relaxing ill-posed problems of shape optimization [1, 5, 6, 15, 18]. Unfortunately, in full mathematical rigor, the homogenization approach is complete only for a few, albeit important, choices of the objective function (mostly self-adjoint problems like compliances or eigenvalues optimization). This restriction is not just a mathematical problem: for general objective functions numerical practice shows that all generalizations of the homogenization method do not work as well in some cases (e.g., partial relaxations as in [1, 3, 7], or SIMP method [5]). The extension of the homogenization method to cost functions depending on the gradient of the state (or strain or stress) is a very difficult problem, although some progress was made in [4, 9, 12, 13, 17]. The goal of the present paper is to extend the homogenization method to new objective functions by making a strong simplifying assumption, namely that the two component phases involved in the optimal design have close coefficients or material properties. More precisely we consider two-phase optimal design problems in the context of conductivity or linearized elasticity and we make an asymptotic expansion of the coefficients in terms of the small amplitude parameter that characterizes the variations between the two phases. Restricting ourselves to terms up

to second order greatly simplifies the situation. However, the small amplitude optimal design problem is still ill-posed and requires relaxation. The nice feature of our approach is that this relaxation is quite simple because the necessary and delicate tools of homogenization are replaced by more basic results on so-called H -measures. These H -measures are quadratic default measures, introduced by Gérard [8] and Tartar [16]. They can be interpreted as two-point correlation functions of the underlying microstructure.

We give the relaxed formulation of very general objective functions, including ones depending on the gradient of the state. A key feature is that optimal microstructures in small amplitude optimization can always be found in the class of simple or rank-one laminates. In other words, there are only two relevant design parameters in our method: the local volume fraction and the angle of lamination (which governs the anisotropy of the optimal microstructure). Another feature of our small amplitude method is that the coefficient of the state or adjoint equations are uniform and independent of the design. Indeed, all the geometric parameters appear as right hand sides in the equations. This implies a drastic reduction of the CPU cost of the method because, once the rigidity finite element matrix has been factorized by a Cholesky method, it is stored and used throughout the optimization process for different right hand sides at each iteration. For the optimization process we use a simple gradient steepest descent algorithm. We implemented our method only in two space dimensions using the FreeFem++ package for finite elements [10]. There is no conceptual difficulty in extending the method to three space dimensions where the gain in CPU time is even higher. A final word of caution: our small amplitude approximation is not meaningful in the context of “standard” structural optimization which amounts to optimize the distribution of a given material with a very weak one mimicking holes (the so-called ersatz material approach). However, it makes sense, for example, in the context of reinforced plane structures: a typical problem is to find the region where to reinforce the thickness of a plate by pasting some tape on top of it. Our method can be useful for this plane reinforcement problem and our numerical examples can be interpreted in this sense. Further details on our method can be found in [2].

2. A MODEL PROBLEM IN CONDUCTIVITY

2.1 Small Amplitude Asymptotic

We consider mixtures of two conducting phases characterized by two symmetric positive definite tensors A^0 and A^1 . We denote by η the amplitude or contrast or aspect ratio between the two materials, $A^1 = A^0(1 + \eta)$. We assume that the contrast is small, $|\eta| \ll 1$. Denoting by χ the characteristic function of the region occupied by phase A^1 , we define a conductivity tensor

$$A(x) = (1 - \chi(x))A^0 + \chi(x)A^1 = A^0(1 + \eta\chi(x)).$$

For a smooth bounded open set $\Omega \subset \mathbf{R}^N$, with boundary $\partial\Omega = \Gamma_D \cup \Gamma_N$, and for given source terms $f \in H^{-1}(\Omega)$ and $g \in L^2(\partial\Omega)$, we consider the following boundary value problem

$$\left. \begin{aligned} -\operatorname{div}(A \nabla u) &= f \quad \text{in } \Omega, \\ u &= 0 \quad \text{on } \Gamma_D, \quad A \nabla u \cdot n = g \quad \text{on } \Gamma_N, \end{aligned} \right\} \quad (1)$$

which admits a unique solution in $H^1(\Omega)$. Typically we want to minimize an objective function of the type

$$J(\chi) = \int_{\Omega} j(u) \, dx,$$

where j is a smooth integrand with adequate growth conditions. We define a set of admissible designs \mathcal{U}_{ad} made of characteristic functions $\chi \in L^\infty(\Omega; \{0, 1\})$ which satisfy the volume constraint $\int_{\Omega} \chi(x) \, dx = \Theta|\Omega|$. We consider the following optimal design problem

$$\inf_{\chi \in \mathcal{U}_{ad}} J(\chi). \quad (2)$$

Assuming that the amplitude or contrast η is small, we perform a second-order expansion in the state equation and in the objective function

$$u = u^0 + \eta u^1 + \eta^2 u^2 + O(\eta^3). \quad (3)$$

Plugging this ansatz in (1) yields three equations for (u^0, u^1, u^2)

$$\left. \begin{aligned} -\operatorname{div}(A^0 \nabla u^0) &= f \quad \text{in } \Omega, \\ u^0 &= 0 \quad \text{on } \Gamma_D, \quad A^0 \nabla u^0 \cdot n = g \quad \text{on } \Gamma_N, \end{aligned} \right\} \quad (4)$$

$$\left. \begin{aligned} -\operatorname{div}(A^0 \nabla u^1) &= \operatorname{div}(\chi A^0 \nabla u^0) \quad \text{in } \Omega, \\ u^1 &= 0 \quad \text{on } \Gamma_D, \quad A^0 \nabla u^1 \cdot n = -\chi A^0 \nabla u^0 \cdot n \quad \text{on } \Gamma_N, \end{aligned} \right\} \quad (5)$$

$$\left. \begin{aligned} -\operatorname{div}(A^0 \nabla u^2) &= \operatorname{div}(\chi A^0 \nabla u^1) \quad \text{in } \Omega, \\ u^2 &= 0 \quad \text{on } \Gamma_D, \quad A^0 \nabla u^2 \cdot n = -\chi A^0 \nabla u^1 \cdot n \quad \text{on } \Gamma_N. \end{aligned} \right\} \quad (6)$$

Remark that u^0 does not depend on χ and thus only u^1, u^2 depends on χ . Similarly, we make a Taylor expansion in the objective function, and, neglecting the remainder term, we introduce a function \mathcal{J}_{sa} which only depends on u^0, u^1, u^2

$$\begin{aligned} \mathcal{J}_{sa}(u^0, u^1, u^2) &= \int_{\Omega} j(u^0) \, dx + \eta \int_{\Omega} j'(u^0) u^1 \, dx \\ &\quad + \eta^2 \int_{\Omega} \left(j'(u^0) u^2 + \frac{1}{2} j''(u^0) (u^1)^2 \right) \, dx. \end{aligned} \quad (7)$$

DEFINITION 1 We call “small amplitude” optimal design problem the second-order asymptotic of problem (2), namely

$$\inf_{\chi \in \mathcal{U}_{ad}} \left\{ J_{sa}(\chi) = \mathcal{J}_{sa}(u^0, u^1, u^2) \right\} \quad (8)$$

where \mathcal{J}_{sa} is defined by (7) and u^0, u^1, u^2 are solutions of the state equations (4), (5), (6) respectively.

2.2 Relaxation by H -Measures

As most optimal design problems, the small amplitude problem (8) is ill-posed in the sense that it does not admit a minimizer in general. Therefore we relax it by using H -measure, a tool which was introduced by Gérard [8] and Tartar [16]. It is a default measure which allows to pass to the limit in quadratic functions of weakly converging sequences in $L^2(\mathbf{R}^N)$.

The general procedure for computing the relaxation of (8) is to consider a sequence (minimizing or not) of characteristic functions χ_n and to pass to the limit in (8) and its associated state equations. Up to a subsequence there exists a limit density θ such that χ_n converges weakly-* to θ in $L^\infty(\Omega; [0, 1])$. We denote by u^0, u_n^1, u_n^2 the solutions of (4), (5), and (6) respectively, associated to χ_n (recall that (4) does not depend on χ_n). In a first step, it is easy to pass to the limit in the variational formulation of (5) to obtain that u_n^1 converges weakly to u^1 in $H^1(\Omega)$ which is the solution of

$$\left. \begin{aligned} -\operatorname{div}(A^0 \nabla u^1) &= \operatorname{div}(\theta A^0 \nabla u^0) \quad \text{in } \Omega, \\ u^1 &= 0 \quad \text{on } \Gamma_D, \quad A^0 \nabla u^1 \cdot n = -\theta A^0 \nabla u^0 \cdot n \quad \text{on } \Gamma_N. \end{aligned} \right\} \quad (9)$$

The main difficulty comes from (6) which admits the variational formulation

$$\int_{\Omega} A^0 \nabla u_n^2 \cdot \nabla \phi \, dx = - \int_{\Omega} \chi_n A^0 \nabla u_n^1 \cdot \nabla \phi \, dx \quad (10)$$

for any test function $\phi \in H^1(\Omega)$ which vanishes on Γ_D . The sequence u_n^2 is obviously bounded in $H^1(\Omega)$ and, up to a subsequence, it converges weakly to a limit u^2 in $H^1(\Omega)$. As usual with weak convergence the limit of the product $\chi_n \nabla u_n^1$ is not the product of the limit $\theta \nabla u^1$! However since it is a quadratic expression, we can use the theory of H -measures [16] to describe its limit. We can prove that the limit of (10) is

$$\int_{\Omega} A^0 \nabla u^2 \cdot \nabla \phi \, dx = - \int_{\Omega} \theta A^0 \nabla u^1 \cdot \nabla \phi \, dx + \int_{\Omega} \theta(1-\theta) A^0 M A^0 \nabla u^0 \cdot \nabla \phi \, dx \quad (11)$$

where the H -measure matrix moment $M(x)$ is defined by

$$M = \int_{\mathbb{S}^{N-1}} \frac{\xi \otimes \xi}{A^0 \xi \cdot \xi} \nu(x, d\xi) \quad (12)$$

with ν , a probability measure with respect to ξ (see [2] for details). In other words u^2 is the solution of an equation similar to (6) except that χ is replaced by θ and there is an additional geometric term in the right hand side of (11), depending on the H -measure matrix moment M . We now can pass to the limit in the objective function $J_{sa}(\chi_n)$ to obtain

$$\lim_{n \rightarrow +\infty} J_{sa}(\chi_n) = J_{sa}^*(\theta, \nu) = \mathcal{J}_{sa}(u^0, u^1, u^2)$$

where u^0, u^1, u^2 are now solutions of the relaxed state equations (4), (9), (11), respectively. It is then a standard matter to prove the following result.

PROPOSITION 2 *The relaxation of (8) is thus*

$$\min_{(\theta, \nu) \in \mathcal{U}_{ad}^*} \left\{ J_{sa}^*(\theta, \nu) = \mathcal{J}_{sa}(u^0, u^1, u^2) \right\} \quad (13)$$

where $\mathcal{J}_{sa}(u^0, u^1, u^2)$ is defined by (7), u^0, u^1, u^2 are solutions of (4), (9), (11), respectively, and \mathcal{U}_{ad}^* is defined by

$$\mathcal{U}_{ad}^* = \left\{ (\theta, \nu) \in L^\infty(\Omega; [0, 1]) \times \mathcal{P}(\Omega, \mathbf{S}_{N-1}) \text{ s.t. } \int_{\Omega} \theta \, dx = \Theta |\Omega| \right\}, \quad (14)$$

where $\mathcal{P}(\Omega, \mathbf{S}_{N-1})$ is the set of probability measures on $\Omega \times \mathbf{S}_{N-1}$. More precisely, there exists at least one minimizer (θ, ν) of (13), any minimizer (θ, ν) of (13) is attained by a minimizing sequence χ_n of (8) in the sense that χ_n converges weakly-* to θ in $L^\infty(\Omega)$, ν is the H -measure of $(\chi_n - \theta)$, and $\lim_{n \rightarrow +\infty} J_{sa}(\chi_n) = J_{sa}^*(\theta, \nu)$, any minimizing sequence χ_n of (8) converges in the previous sense to a minimizer (θ, ν) of (13).

REMARK 3 *A simpler, albeit formal, method for computing the limits of u_n^1 and u_n^2 is to assume that the sequence χ_n of characteristic functions is periodically oscillating, i.e. $\chi_n(x) = \chi(x, nx)$ where $y \rightarrow \chi(x, y)$ is Y -periodic. Then, using formal two-scale asymptotic expansions it is possible to compute the limits of u_n^1 and u_n^2 , as well as the first-order corrector term for u_n^1 , i.e.*

$$u_n^1(x) = u^1(x) + \frac{1}{n} u^{11}(x, nx) + O\left(\frac{1}{n^2}\right).$$

Making a Fourier expansion of $\chi(x, y) = \sum_{k \in \mathbf{Z}^N} \hat{\chi}(x, k) e^{2i\pi k \cdot y}$, we can compute explicitly u^{11} and u^2 , and the H -measure is given by

$$\nu(x, \xi) = \frac{1}{\theta(1-\theta)} \sum_{k \neq 0 \in \mathbf{Z}^N} |\hat{\chi}(x, k)|^2 \delta\left(\xi - \frac{k}{|k|}\right).$$

2.3 Optimality Conditions

PROPOSITION 4 *The relaxed small amplitude problem (13) can be solved by restricting the set of probability measures $\mathcal{P}(\Omega, \mathbf{S}_{N-1})$ to its subset of Dirac masses. In other words, there exists an optimal design solution of (13) which is a simple laminate. Furthermore, the corresponding optimal H -measure, which is a Dirac mass, does not depend on the density θ .*

REMARK 5 *The main consequence of Proposition 4 is that not all possible composite materials have to be considered in the relaxed small amplitude problem (13) but just the simple laminates of rank one. It turns out that this property holds true for all generalizations of (13) [2]. Another interesting consequence of Proposition 4 is that the optimization with respect to ν can be done once and for all at the beginning of the optimization process since it is independent of the exact values of θ .*

The fact that simple laminates are always optimal may seem paradoxical in view of the well-known results about rank- N laminates being optimal for compliance optimization in elasticity [1, 6, 18]. However, one needs to understand that we do not optimize the original objective function but its second-order small-amplitude asymptotic expansion. Therefore, simple laminates are merely optimal, up to second-order, for the original objective function.

Proof. To simplify the formula for $J_{sa}^*(\theta, \nu)$ by eliminating u^2 , we introduce an adjoint state p^0 (which does not depend on (θ, ν)), solution in $H^1(\Omega)$ of

$$\left. \begin{aligned} -\operatorname{div}(A^0 \nabla p^0) &= j'(u^0) \quad \text{in } \Omega, \\ p^0 &= 0 \quad \text{on } \Gamma_D, \quad A^0 \nabla p^0 \cdot n = 0 \quad \text{on } \Gamma_N. \end{aligned} \right\} \quad (15)$$

By doing some integration by parts in (15) and (11), we obtain

$$\begin{aligned} J_{sa}^*(\theta, \nu) &= \int_{\Omega} j(u^0) dx + \eta \int_{\Omega} j'(u^0) u^1 dx + \eta^2 \int_{\Omega} \frac{1}{2} j''(u^0) (u^1)^2 dx \\ &\quad - \eta^2 \int_{\Omega} \theta A^0 \nabla u^1 \cdot \nabla p^0 dx + \eta^2 \int_{\Omega} \theta(1 - \theta) A^0 M A^0 \nabla u^0 \cdot \nabla p^0 dx \end{aligned} \quad (16)$$

which is now explicitly affine in M , defined by (12), and thus in ν . Minimizing $J_{sa}^*(\theta, \nu)$ with respect to ν amounts to minimize a scalar affine function on the convex set of probability measures $\mathcal{P}(\Omega, \mathbf{S}_{N-1})$. Therefore any minimizer ν^* can be replaced by another minimizer which is a Dirac mass concentrated at a direction ξ^* which minimizes the integrand of the last term in (16). Remark that ξ^* does not depend on θ . Furthermore, replacing a minimizer ν^* by the Dirac mass concentrated at ξ^* does not change θ , u^0 , u^1 and p^0 . Thus one can restrict the minimization in ν to the subset of $\mathcal{P}(\Omega, \mathbf{S}_{N-1})$ made of Dirac masses of the type $\nu(x, \xi) = \delta(\xi - \xi^0(x))$. •

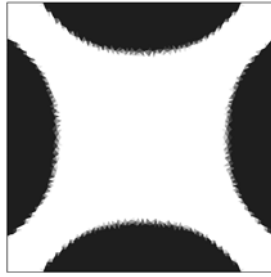


Figure 1. Gradient minimization. $\eta = -0.5$, Volume=40%.

After the optimal H -measure ν , a Dirac mass concentrated on $\xi^*(x)$, has been found, we can easily compute the derivative of J_{sa}^* with respect to θ by introducing another adjoint state p^1 (this is standard and we refer to [2] for details).

2.4 Generalizations

The same method and the same results can be obtained for various other problems. For example, it is possible to derive the same results for an objective function that depends on the gradient of the state. We can also generalize our approach to the system of linearized elasticity by considering mixtures of two linear isotropic phases [2]. Furthermore, we can consider so-called multiple loads problems, i.e. several state equations associated to a single objective function. It is even possible to consider the case of a multi-physics problem, i.e. the coefficients of the different state equations can be different although they share the same geometry or microstructure (a typical example would be thermo-elasticity where a conductivity problem is coupled to an elasticity system). In all such cases, once again, simple laminates are optimal microstructures.

3. ALGORITHM AND NUMERICAL EXAMPLES

3.1 Optimization Algorithm

Recall that there are two design parameters for our relaxed small-amplitude optimization problem: the lamination angle and the local proportion θ . We proved that the lamination direction of the optimal microstructure does not depend on θ , and that it is explicitly given in terms of u^0 and p^0 which do not vary during the optimization process. Therefore, the optimal lamination angle is computed once and for all before we start a gradient-based steepest descend method for the local proportion θ .

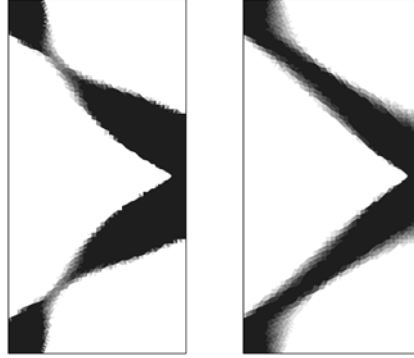


Figure 2. Compliance minimization for the short cantilever: $\eta = -0.1$ (left), $\eta = -0.99$ (right), volume=25%.

The boundary value problems are solved using FreeFem++ [10] and we take advantage of the fact that all the problems we need to solve have the same elliptic differential operator, namely $\text{div}(A^0 \nabla \cdot)$. Therefore the factorization of the stiffness matrix is performed only once during the initialization and is saved for all subsequent finite elements resolutions during the iterations. This of course speeds up considerably the code. For all states u^i and adjoint states p^i we use P_2 Finite Elements, while the local proportion θ is discretized with P_0 Finite Elements (as well as the lamination direction ξ^*). As is well known (see [1, 5] and references therein) we prefer the $P_2 - P_0$ combination to the simpler $P_1 - P_0$ in order to avoid the so-called checkerboard numerical instability.

The subsequent figures show the local proportion of the material with higher conductivity or with higher stiffness, meaning higher values of both Lamé parameters. In other words, if η is negative (which is always the case below), we display $(1 - \theta)$. The volume, when mentioned in the caption, always refers to the percentage of volume occupied by the better conductor or the stiffer material.

3.2 Diffusion Problem

Since the inception of the homogenization method a classical test case is the so-called torsion problem (see [1] for further references). It amounts to solve (1) in the unit square $\Omega = (0, 1) \times (0, 1)$ with Dirichlet boundary conditions and a source term $f \equiv 1$. We minimize $J_2(\chi) = \int_{\Omega} |\nabla u|^2 dx$. In Figure 1 we plot the resulting optimal shape for the relaxed small amplitude problem. The phase conductivities are 0.5 and 1, and the proportion of the best conductor is 40%. This result is slightly different than that obtained by Lipton and Velo (see

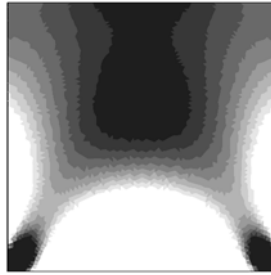


Figure 3. Strain minimization of a square clamped at the bottom and vertically loaded at the top: $\eta = -0.1$, volume=50%.

Figure 1:a in [11]) using a partial relaxation of the problem. Different values of η and different refinement of the mesh yield similar results.

3.3 Elasticity Problem

In all the following examples we take the reference material A^0 with Lamé coefficients $\lambda = 0.73$ and $\mu = 0.376$. As we said in the introduction, one should interpret the following results in the context of reinforcing a plane structure by adding to it a layer at a location that is optimal.

Let us first consider the so-called short cantilever problem subject to compliance minimization. We choose $\Omega = (0, 1) \times (0, 2)$ (discretized by 8765 triangles) clamped on its left side and with a unit vertical load at the middle of the right side. After 50 iterations the resulting optimal designs for $\eta = -0.1$ and $\eta = -0.99$ are shown on Figure 2 (recall that dark colors correspond to the stiffer material). The latter design is quite similar to the usual short cantilever with two bars making a 90 degree angle at the position where the load is applied, giving then the impression that the approach developed here for the small amplitude case, might very well be used at least in some cases when the amplitude is not necessarily so small.

Next we minimize the norm of the strain tensor, i.e. $J(\chi) = \int_{\Omega} |e(u)|^2 dx$. The domain is the unit square $\Omega = (0, 1)^2$, which is discretized with 8654 triangles, clamped at the bottom and vertically loaded at the top. The resulting optimal design, shown in Figure 3, looks like a bridge with two pillars.

ACKNOWLEDGMENTS

This work has partially been supported by the ECOS project C04E07 of cooperation between Chile and France, and by the ACI project GUIDOPT of the French Ministry of Research.

REFERENCES

- [1] G. Allaire, *Shape Optimization by the Homogenization Method*, Springer-Verlag (2002).
- [2] G. Allaire and S. Gutierrez, *Optimal Design in Small Amplitude Homogenization*, CMAP preprint 576, submitted (2005).
- [3] G. Allaire, F. Jouve and H. Maillot, Topology optimization for minimum stress design with the homogenization method, *Struct. Multidiscip. Optim.*, 28(2–3), 87–98 (2004).
- [4] J.C. Bellido and P. Pedregal, Explicit quasiconvexification for some cost functionals depending on derivatives of the state in optimal designing, *Discr. Contin. Dyn. Syst.*, 8(4), 967–982 (2002).
- [5] M. Bendsoe and O. Sigmund, *Topology Optimization. Theory, Methods, and Applications*, Springer Verlag, New York (2003).
- [6] A. Cherkhaev, *Variational Methods for Structural Optimization*, Springer Verlag, New York (2000).
- [7] P. Duysinx and M. Bendsoe, Topology optimization of continuum structures with local stress constraints, *Int. J. Num. Meth. Engng.*, 43, 1453–1478 (1998).
- [8] P. Gerard, Microlocal defect measures, *Comm. Partial Diff. Equations*, 16, 1761–1794 (1991).
- [9] Y. Grabovsky, Optimal design problems for two-phase conducting composites with weakly discontinuous objective functionals, *Adv. in Appl. Math.*, 27, 683–704 (2001).
- [10] F. Hecht, O. Pironneau and K. Ohtsuka, *FreeFem++ Manual*, downloadable at <http://www.freefem.org>
- [11] R. Lipton and A. Velo, Optimal design of gradient fields with applications to electrostatics, in *Nonlinear Partial Differential Equations and Their Applications*, D. Cioranescu and J.-L. Lions (eds), College de France Seminar, Vol. XIV, Elsevier, pp. 509–532 (2002). *Stud. Math. Appl.*, 31 (2002).
- [12] R. Lipton, Relaxation through homogenization for optimal design problems with gradient constraints, *J. Optim. Theory Appl.*, 114(1), 27–53 (2002).
- [13] R. Lipton, Stress constrained G closure and relaxation of structural design problems, *Quart. Appl. Math.*, 62(2), 295–321 (2004).
- [14] G. Milton, *The Theory of Composites*, Cambridge University Press (2001).
- [15] F. Murat and L. Tartar, Calcul des variations et homogénéisation, Les Méthodes de l’Homogénéisation Théorie et Applications en Physique, Coll. Dir. Etudes et Recherches EDF, 57, Eyrolles, Paris, pp. 319–369 (1985). English translation in *Topics in the Mathematical Modelling of Composite Materials*, A. Cherkhaev and R. Kohn (eds), Progress in Nonlinear Differential Equations and Their Applications, Vol. 31, Birkhäuser, Boston (1997).
- [16] L. Tartar, H -measures, a new approach for studying homogenization, oscillations and concentration effects in partial differential equations, *Proc. of Royal Soc. Edinburgh*, 115A, 193–230 (1990).
- [17] L. Tartar, *Remarks on optimal design problems*, in *Calculus of Variations, Homogenization and Continuum Mechanics* (Marseille, 1993), Ser. Adv. Math. Appl. Sci., Vol. 18, World Sci. Publishing, River Edge, NJ, pp. 279–296 (1994).
- [18] L. Tartar, An introduction to the homogenization method in optimal design, in *Optimal Shape Design* (Tróia, 1998), A. Cellina and A. Ornelas (eds), Lecture Notes in Mathematics, Vol. 1740, Springer, Berlin, pp. 47–156 (2000).

EIGENFREQUENCY AND BUCKLING OPTIMIZATION OF LAMINATED COMPOSITE SHELL STRUCTURES USING DISCRETE MATERIAL OPTIMIZATION

Erik Lund and Jan Stegmann

*Institute of Mechanical Engineering, Aalborg University, Pontoppidanstraede 101,
DK-9220 Aalborg East, Denmark*

el@ime.aau.dk, js@ime.aau.dk

Abstract: The design problem of maximizing the lowest eigenfrequency or the buckling load factor of laminated composite shell structures is investigated using the so-called Discrete Material Optimization (DMO) approach. The design optimization method is based on ideas from multi-phase topology optimization where the material stiffness is computed as a weighted sum of candidate materials, thus making it possible to solve discrete optimization problems using gradient based techniques and mathematical programming. The potential of the DMO method to solve the combinatorial problem of proper choice of material, stacking sequence and fiber orientation simultaneously is illustrated for two multi-layered multi-material plate examples.

Keywords: Laminate design optimization, composite structures, discrete material optimization, topology optimization, eigenvalue problems.

1. INTRODUCTION

Composite shell structures are today used in many engineering applications and may be composed as a combination of many different materials such as Fiber Reinforced Polymers (GFRP/CFRP) together with foam, wood and isotropic materials, which are then bonded together by a resin to form a laminate. Thus, the well-known design problem of determining the best thickness and fiber orientation of each FRP layer must be expanded by including the material selection problem in order to obtain a desired structural performance. In such cases it is convenient to introduce methods that can solve the discrete material selection problem together with the continuous fiber orientation and thickness distribution problem, and one such approach is the Discrete Material Optimiz-

ation (DMO) method introduced by the authors, see [1, 2]. In this work focus is put on linear eigenvalue problems using eigenfrequencies or buckling behavior as criteria function.

The DMO method is based on ideas from multi-phase topology optimization (see Sigmund and co-workers [3, 4]) where the material stiffness (or density) is computed as a weighted sum of candidate materials. In this way the discrete problem of choosing the best material (with the right orientation) is converted to a continuous formulation where the design variables are the scaling factors (or weight functions) on each candidate material.

2. ANALYSIS OF LAMINATED COMPOSITE SHELL STRUCTURES

The finite element method is used for determining the structural response of the laminated composite. The structure is typically composed of multiple materials and multiple layers, and the laminated shell structure may, in general, be curved or doubly-curved. The materials used in this work may be fiber reinforced polymers oriented at a given angle θ_k for layer k or it may be softer isotropic core materials. All materials are assumed to behave linearly elastic and the structural behavior of the laminate is described using an equivalent single layer theory where the layers are assumed to be perfectly bonded together and thus, displacements and strains will be continuous across the thickness. Such theories are known to be sufficiently accurate for modelling of the structural stiffness. For computational efficiency the element used for the design optimization in this work is a four node isoparametric shell element with full integration where the problem of shear locking is avoided by using the method of assumed natural strains for the transverse shear interpolation (MITC).

2.1 Eigenfrequency Analysis

In this work the objective of designing the structure w.r.t. eigenfrequencies is formulated as maximizing the lowest eigenfrequency. Other eigenfrequency objectives can easily be formulated but are omitted here for brevity. The free vibration frequency analysis can be written as

$$\mathbf{K}\Phi_j = \lambda_j\mathbf{M}\Phi_j, \quad \lambda_j = \omega_j^2, \quad j = 1, 2, \dots, \quad (1)$$

where \mathbf{K} is the global stiffness matrix, \mathbf{M} the global mass matrix, λ_j the eigenvalue, ω_j the eigenfrequency, and Φ_j the corresponding eigenvector. The eigenvalues are assumed ordered by magnitude, such that λ_1 is the lowest eigenvalue.

2.2 Linear Buckling Analysis

In case of using the buckling behavior as objective function the analysis is restricted to linear buckling predictions, i.e., the structure is assumed to be perfect with no geometrical imperfections and the buckling load found will be an upper limit for the real value. First the static equilibrium equation for the structure is solved using

$$\mathbf{K}\mathbf{D} = \mathbf{F}. \quad (2)$$

Here \mathbf{D} is the global displacement vector and \mathbf{F} the global load vector. Based on the displacement field the element layer stresses can be computed, whereby the stress stiffening effects due to the mechanical loading can be evaluated by computing the element initial stress stiffness matrix \mathbf{K}_σ^e (also termed the element geometric stiffness matrix). By summation over all elements the global stress stiffness matrix \mathbf{K}_σ is obtained, and the linearized buckling problem can be established as

$$(\mathbf{K} + \lambda_j \mathbf{K}_\sigma) \Phi_j = \mathbf{0}, \quad j = 1, 2, \dots, \quad (3)$$

where the eigenvalues again are assumed ordered by magnitude, such that λ_1 is the lowest buckling load factor and Φ_1 is the corresponding eigenvector.

3. DESIGN SENSITIVITY ANALYSIS AND OPTIMIZATION OF LINEAR EIGENVALUE PROBLEMS

The objective of the design problem considered is to maximize the lowest eigenfrequency or buckling load factor of the laminated composite structure using gradient based techniques, and thus the sensitivities should be computed in an efficient way.

3.1 Design Sensitivity Analysis of Simple Eigenvalues

The design variables are termed x_i , $i = 1, \dots, I$, and the direct approach to obtain the eigenvalue sensitivity in case of a distinct, i.e. simple eigenvalue λ_j , is to differentiate (1) with respect to a design variable x_i , premultiply by Φ_j^T and make use of (3), then the following expression is obtained for the eigenvalue sensitivity of simple eigenvalue λ_j , see, e.g., [5, 6]

$$\frac{d\lambda_j}{dx_i} = \Phi_j^T \left(\frac{d\mathbf{K}}{dx_i} - \lambda_j \frac{d\mathbf{M}}{dx_i} \right) \Phi_j, \quad (4)$$

where it has been assumed that the eigenvectors have been \mathbf{M} -orthonormalized, such that $\Phi_j^T \mathbf{M} \Phi_j = 1$. In case of buckling analysis, the mass matrix \mathbf{M} in (4) is replaced by $-\mathbf{K}_\sigma$.

For the DMO parametrization proposed in this work where the geometry is fixed and only the material is changed, the stiffness matrix derivative $d\mathbf{K}/dx_i$ only involves the derivative of the element layer constitute matrix \mathbf{C}_k^l with respect to x_i . In the next section the DMO interpolation scheme used for determining the constitute matrix is described, and the derivative of this interpolation is computed analytically.

In case of buckling analysis the stress stiffness matrix is an implicit function of the displacement field, i.e. $\mathbf{K}_\sigma = \mathbf{K}_\sigma(\mathbf{D}(\mathbf{x}), \mathbf{x})$, which must be taken into account as

$$\frac{d\mathbf{K}_\sigma}{dx_i} = \frac{\partial\mathbf{K}_\sigma}{\partial x_i} + \frac{\partial\mathbf{K}_\sigma}{\partial\mathbf{D}} \frac{d\mathbf{D}}{dx_i}. \quad (5)$$

Thus, the displacement sensitivities $d\mathbf{D}/dx_i$ must be computed which is done efficiently using the direct differentiation approach, i.e., the static equilibrium equation, (2), is differentiated with respect to a design variable x_i

$$\mathbf{K} \frac{d\mathbf{D}}{dx_i} = \frac{\partial\mathbf{F}}{\partial x_i} - \frac{\partial\mathbf{K}}{\partial x_i} \mathbf{D}, \quad (6)$$

where the load sensitivity $\partial\mathbf{F}/\partial x_i$ is zero for the DMO design variables used, unless volume forces are considered. The displacement sensitivities are computed analytically by solving (6) for each design variable x_i , reusing the stiffness matrix \mathbf{K} from the analysis, but the stress stiffness matrix sensitivities $d\mathbf{K}_\sigma/dx_i$ in (5) are computed by central difference approximations at the element level. This approach is mainly used in order to facility easy implementation of sensitivity analysis for all different types of laminate design variables and no inaccuracy problems have been observed for the central difference approximation of element stress stiffness matrix sensitivities.

3.2 Design Sensitivity Analysis of Multiple Eigenvalues

So far multiple eigenvalues and corresponding eigenvectors have not been mentioned. In this case the eigenvectors are not unique, which complicates the sensitivity analysis and optimization due to the non-differentiability of the eigenvalues. In such situations the sensitivity analysis described in [7] is used together with the optimization algorithm developed in [8]. The details are omitted here for brevity.

3.3 The Mathematical Programming Problem

In case of only simple, distinct eigenvalues, the optimization problem of maximizing the lowest eigenfrequency or buckling load factor λ_1 is reformulated

using a bound formulation, see [9], as

$$\begin{aligned}
 \text{Objective : } & \max_{\mathbf{x}, \beta} \beta \\
 \text{Subject to : } & \lambda_j \geq \beta, \quad j = 1, \dots, N_\lambda \\
 & M \leq \overline{M} \\
 & \underline{x}_i \leq x_i \leq \overline{x}_i, \quad i = 1, \dots, I
 \end{aligned} \tag{7}$$

where \overline{M} is the upper limit on the mass M of the structure. By introducing the bound parameter β the lowest N_λ eigenvalues are considered when solving the minimax problem, such that the case of crossing eigenvalues (mode switching) during the optimization is taken into account.

The derivative of the mass constraint in (7) is also computed analytically, and having obtained all the necessary design sensitivities, the mathematical programming problem is solved using the Method of Moving Asymptotes by Svanberg [10]. The closed loop of analysis, design sensitivity analysis and optimization is repeated until convergence in terms of no change of the design variables is reached or until the maximum number of design iterations have been performed.

4. THE DISCRETE MATERIAL OPTIMIZATION APPROACH

The design parametrization method applied in this work is denoted Discrete Material Optimization (DMO), that can be used for efficient design of general laminated composite shell structures, see [1, 2, 11]. The approach developed is to formulate the optimization problem using a parametrization that allows us to do efficient gradient based optimization on real-life problems while reducing the risk of obtaining a local optimum solution. To this end we will use the mixed materials strategy suggested by Sigmund and co-workers [3, 4] for multi-phase topology optimization, where the total material stiffness is computed as a weighted sum of candidate materials.

In the present context this means that the stiffness of each layer of the laminated composite will be computed from a weighted sum of a finite number of candidate constitutive matrices, each representing a given lay-up of the layer. Consequently, the design variables are no longer the fiber angles or layer thicknesses but the scaling factors (or weight functions) on each constitutive matrix in the weighted sum. For example, we could choose a stiff orthotropic material oriented at three angles $\theta_1 = 0^\circ$, $\theta_2 = 45^\circ$ and $\theta_3 = 90^\circ$ and a soft isotropic material, thereby obtaining a problem having four design variables per layer. The objective of the optimization is then to drive the influence of all but one of these constitutive matrices to zero for each ply by driving all but one weight

function to zero. As such, the methodology is very similar to that used in topology optimization. This is further emphasized by the fact that penalization is used on the design variables to make intermediate values un-economical. At the beginning of the optimization, the constitutive matrices used in the analysis thus consist of contributions from several candidate materials, but at the end of the design optimization, the parametrization for the weight functions has to fulfill the demand, that one distinct candidate material has been chosen.

4.1 Parametrization for Single Layered Laminate Structures

As in topology optimization the parametrization of the DMO formulation is invoked at the finite element level. The element constitutive matrix, \mathbf{C}^e , for a single layered laminate structure may in general be expressed as a sum over the element number of candidate material configurations, n^e :

$$\mathbf{C}^e = \sum_{i=1}^{n^e} w_i \mathbf{C}_i = w_1 \mathbf{C}_1 + w_2 \mathbf{C}_2 + \dots + w_{n^e} \mathbf{C}_{n^e}, \quad 0 \leq w_i \leq 1, \quad (8)$$

where each candidate material is characterized by a constitutive matrix \mathbf{C}_i . The weight functions w_i must all have values between 0 and 1 in order to be physically allowable. Furthermore, in case of solving buckling problems or having a mass constraint as in the optimization problems studied here, it is necessary that the sum of the weight functions is 1.0, i.e., $\sum_{i=1}^{n^e} w_i = 1.0$. If this demand is not fulfilled, physically meaningless results will be obtained. Several new parametrization schemes have been developed, see details in [1, 2], and we give here a short outline of the most effective implementation.

We apply for each element a number of design variables x_i^e , $i = 1, \dots, n^e$, and write

$$w_i = \frac{\hat{w}_i}{\sum_{k=1}^{n^e} \hat{w}_k}, \quad i = 1, \dots, n^e, \quad (9)$$

$$\hat{w}_i = (x_i^e)^p \prod_{j=1; j \neq i}^{n^e} (1 - (x_j^e)^p).$$

To push the design variables x_i^e towards 0 and 1 the SIMP method known from topology optimization has been adopted by introducing the power, p , as a penalization of intermediate values of x_i^e . The power p is typically set to 2 in the beginning of the optimization process and then increased by 1 for every 10 design iterations until p is 6. Moreover, the term $(1 - (x_j^e)^p)_{j \neq i}$ is introduced such that an increase in x_i^e results in a decrease of all other weight functions. Finally, the weights have been normalized in order to satisfy the constraint that

the sum of the weight functions is 1.0. Note that the expression in (9) means that complicated additional constraints on the design variables x_i^e are avoided and only simple box constraints have to be dealt with.

It should be noted that the normalization introduced in (9) makes the interpolation less effective in driving the weights to 0/1 since the normalization alters the effect of the penalization. Consequently, the normalized weighting scheme converges slower to a design where a distinct material have been selected than if the weight functions \hat{w}_i are used.

4.2 Parametrization for Multi Layered Laminate Structures and Patch Variables

The only difference between single and multi layered laminate structures is that the interpolation given above has to be used for all layers, i.e., the layer constitutive matrix \mathbf{C}_k^l for layer k is computed as

$$\mathbf{C}_k^l = \sum_{i=1}^{n^l} w_i \mathbf{C}_i, \quad (10)$$

where n^l is the number of candidate materials for the layer.

The design variables x_i may be associated with each finite element of the model or the number of design variables may be reduced by introducing patches, covering larger areas of the structure. This is a valid approach for practical design problems since laminates are typically made using fiber mats covering larger areas.

5. MAXIMUM LOWEST EIGENFREQUENCY DESIGN OF 16-LAYER CLAMPED PLATE

Several examples have been studied in order to investigate the performance of the DMO method, and examples involving pure fiber angle optimization of plate structures made of unidirectional composites yield results similar to those obtained using optimality criteria based methods as described in [12].

The example included here illustrates the potential of the DMO method for solving the combinatorial problem of proper choice of material, stacking sequence and fiber orientation simultaneously for maximum lowest eigenfrequency design of a clamped plate. The plate has dimension 0.1×0.1 m and consists of 16 layers of equal thickness 0.0003 m, yielding a total thickness of 0.0048 m. One candidate material is unidirectional glass/epoxy, i.e. an orthotropic material with $E_x = 5.4 \cdot 10^{10}$ Pa, $E_y = E_z = 1.8 \cdot 10^{10}$ Pa, $\nu = 0.25$, $G_{xy} = G_{xz} = 9.0 \cdot 10^9$ Pa, $G_{yz} = 3.4 \cdot 10^9$ Pa, and $\rho = 1900$ kg/m³. The other candidate material is an isotropic polymer foam material and has $E_x = 1.25 \cdot 10^8$ Pa, $\nu = 0.3$, and $\rho = 100$ kg/m³.

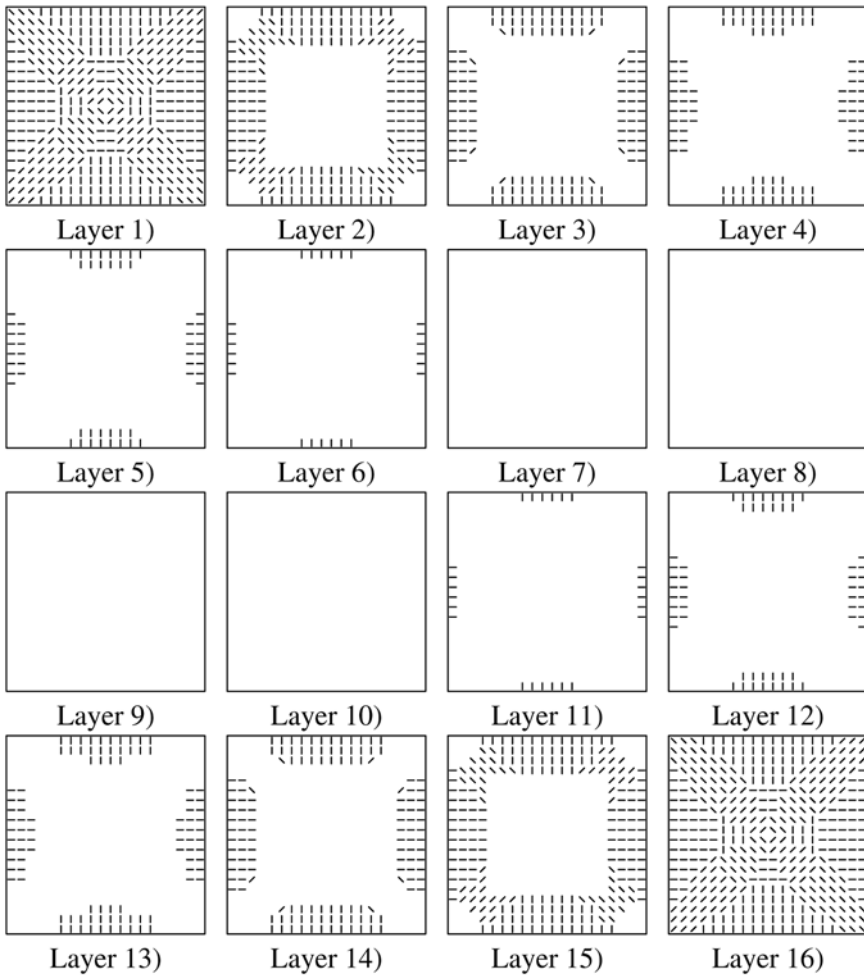


Figure 1. Optimized material directions (fiber angles) for maximum lowest eigenfrequency design of 16-layer clamped plate when 5 DMO variables per element are used (soft material together with orthotropic material oriented at 0° , $\pm 45^\circ$, and 90°). White means that the isotropic soft material has been selected. The lowest eigenfrequency is distinct for the optimized design.

The upper and lower layers have 4 DMO design variables per element associated with the orthotropic material oriented at 0° , $\pm 45^\circ$, and 90° , respectively, and the remaining 14 interior layers have 5 DMO variables, allowing the optimizer also to choose the soft isotropic material. The mass constraint is set such that $2/3$ of the total volume should be filled with soft material. A 20 by 20 mesh of 4-node shell elements is used, and the result of the optimization can be seen in Figure 1.

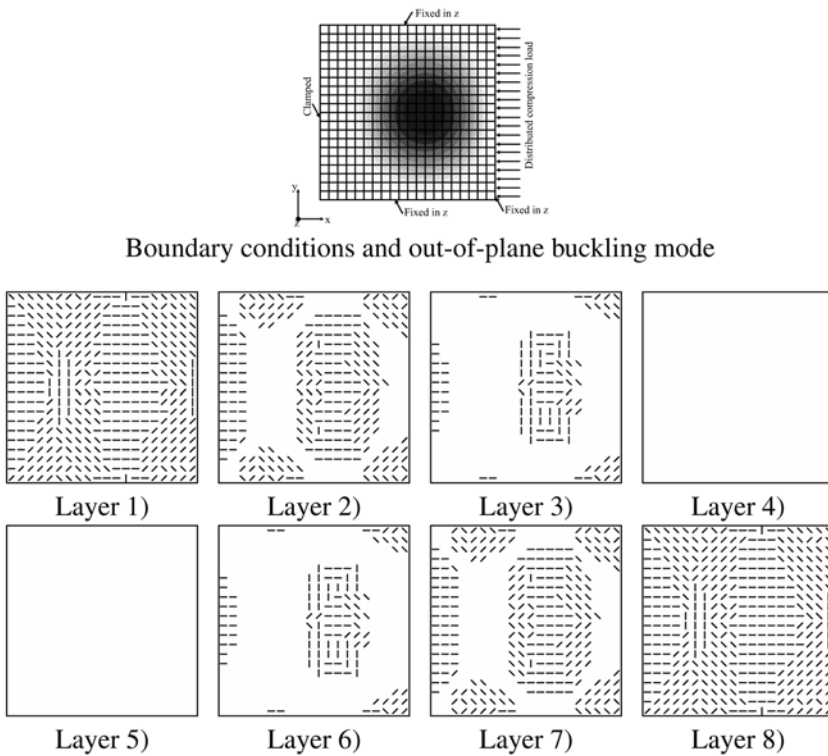


Figure 2. Optimized material directions (fiber angles) for maximum buckling load factor design of 8-layer simply supported plate when 5 DMO variables per element are used (soft material together with orthotropic material oriented at 0° , $\pm 45^\circ$, and 90°). White means that the isotropic soft material has been selected. The lowest eigenfrequency is distinct for the optimized design. No eigenmode mode switching appeared during the optimization.

The fiber directions for the orthotropic material in the upper and lower layers are quite similar to results published by other people for single layer plates made of unidirectional composites using continuous fiber angles, see e.g. [12]. For the remaining 14 interior layers the DMO method suggests to put soft material in the middle of the plate as expected. Furthermore, the orthotropic material available should be put at the middle of the clamped edges, oriented perpendicular to the boundary.

6. BUCKLING LOAD DESIGN OF 8-LAYER PLATE

Next a plate with dimension 0.5×0.5 m is considered. It has 8 layers of equal thickness 0.000125 m, yielding a total thickness of 0.001 m. The plate is clamped at the left edge, simply supported at the other three edges and subjected to a distributed compression load of 100 N/m at the right edge.

The same two candidate materials are used as in the previous example, and now the mass constraint is set such that half of the domain should be filled with soft material. The objective is to maximize the lowest buckling load factor, and the topology and fiber orientations of the orthotropic material for all 8 layers can be seen in Figure 2.

7. SUMMARY

In this paper the Discrete Material Optimization approach has been applied with the purpose of maximizing the lowest eigenfrequency or buckling load factor of laminated hybrid composite shell structures, and several examples have documented the potential of the parametrization method for multi material optimization. The parametrization used may not converge to a distinct 0/1 design everywhere in the domain but still the method provides much insight into the optimal solution to the material distribution problem.

REFERENCES

- [1] J. Stegmann, *Analysis and Optimization of Laminated Composite Shell Structures*, Ph.D. Thesis, Institute of Mechanical Engineering, Aalborg University, Denmark (2004). Special report no. 54, available at www.ime.aau.dk/~js.
- [2] J. Stegmann and E. Lund, Discrete material optimization of general composite shell structures, *International Journal for Numerical Methods in Engineering*, 62(14), 2009–2027 (2005).
- [3] O. Sigmund and S. Torquato, Design of materials with extreme thermal expansion using a three-phase topology optimization method, *Journal of the Mechanics and Physics of Solids*, 45, 1037–1067 (1997).
- [4] L.V. Gibiansky and O. Sigmund, Multiphase composites with extremal bulk modulus, *Journal of the Mechanics and Physics of Solids*, 48, 461–498 (2000).
- [5] R. Courant and D. Hilbert, *Methods of mathematical physics*, Vol. 1, Interscience Publishers, New York (1953).
- [6] W.H. Wittrick, Rates of change of eigenvalues, with reference to buckling and vibration problems, *Journal of the Royal Aeronautical Society*, 66, 590–591 (1962).
- [7] A.P. Seyranian, E. Lund and N. Olhoff, Multiple eigenvalues in structural optimization problems, *Structural Optimization*, 8, 207–227 (1994).
- [8] E. Lund, *Finite Element Based Design Sensitivity Analysis and Optimization*, Ph.D. Thesis, Institute of Mechanical Engineering, Aalborg University, Denmark (1994). Special report no. 23, available at www.ime.aau.dk/~el.
- [9] M.P. Bendsøe, N. Olhoff and J.E. Taylor, A variational formulation for multicriteria structural optimization, *Journal of Structural Mechanics*, 11, 523–544 (1983).
- [10] K. Svanberg, The method of moving asymptotes – A new method for structural optimization, *Numerical Methods in Engineering*, 24, 359–373 (1987).
- [11] E. Lund and J. Stegmann, On structural optimization of composite shell structures using a discrete constitutive parameterization, *Wind Energy*, 8(1), 109–124 (2005).
- [12] N.L. Pedersen, On design of fiber-nets and orientation for eigenfrequency optimization of plates, Report 703, DCAMM, 2005.

EFFECT OF INTERNAL LENGTH SCALE ON OPTIMAL TOPOLOGIES FOR COSSERAT CONTINUA

Massimiliano Gei, Marco Rovati and Daniele Veber

*Department of Mechanical and Structural Engineering, University of Trento,
Via Mesiano 77, I-38050 Trento, Italy*

massimiliano.gei@unitn.it, marco.rovati@ing.unitn.it, daniele.veber@ing.unitn.it

Abstract: Micropolar field theory represents an extension of the classical Cauchy continuum theory. In this paper, a topology optimization procedure for maximum stiffness is applied to two dimensional structural elements described in terms of micropolar (Cosserat) solids. The role of the characteristic length of bending on the optimal configurations is highlighted in the applications.

Keywords: Topology optimization, micropolar continua, Cosserat theory, internal length scale.

1. INTRODUCTION

Conventional continuum mechanics approaches do not incorporate any intrinsic characteristic length. However, real materials often exhibit a number of important length scales, which must be included in any realistic model: grains, particles, fibers, cellular solids, biological tissues [1]. So called nonlocal theories can be used to account for size effects in the mechanical behaviour of materials. The departure from local theories begins with the micropolar (or Cosserat) continuum models where rotational degrees of freedom of the material particles are considered. As a consequence, their associated stress quantities (couple stresses) enter the formulation and dimensional arguments lead to the introduction of an internal characteristic length.

The goal of this paper is to analyze the influence of this parameter on optimal shapes of micropolar solids obtained by imposing the maximum stiffness criterion with a defined amount of material [2, 3]. In the two-dimensional context, the internal length scale is identified as the characteristic length for bending, because the role of couple stresses is similar to that of bending moment in plane beam-like structures.

2. GOVERNING EQUATIONS FOR COSSERAT SOLIDS

In micropolar continua the deformation is described in terms of displacement field u_k and microrotations ϕ_k . The micropolar strain tensor ε_{kl} is defined as [4, 5]

$$\varepsilon_{kl} = e_{kl} + e_{klm}(w_m - \phi_m), \quad (1)$$

where e_{kl} denotes the macro-strain tensor

$$e_{kl} = \frac{1}{2}(u_{k,l} + u_{l,k}), \quad (2)$$

and e_{klm} the permutation tensor, whereas w_k is the particle macrorotation, $w_k = e_{klm}u_{m,l}/2$.

In a Cartesian co-ordinate system the equilibrium equations read

$$\sigma_{ji,j} + b_i = 0, \quad m_{ji,j} + e_{ilk}\sigma_{lk} + m_i = 0, \quad (3)$$

where σ_{ji} is the non-symmetric stress tensor and m_{ji} is the couple stress tensor; b_i and m_i are, respectively, body forces and body couples.

The constitutive equations for a micropolar linear (in general anisotropic) elastic solid are given by [6]

$$\sigma_{ij} = E_{ijkl}\varepsilon_{kl} + B_{ijkl}\phi_{l,k}, \quad m_{ij} = B_{klij}\varepsilon_{kl} + K_{ijkl}\phi_{l,k}, \quad (4)$$

where E_{ijkl} , B_{ijkl} and K_{ijkl} are the micropolar fourth-order constitutive tensors. E_{ijkl} couples strains with stresses, whereas K_{ijkl} associates microcurvatures ($\phi_{l,k}$) to couple stresses. B_{ijkl} is often called ‘‘pseudo-tensor’’ [6], as it vanishes in the relevant case of isotropic behaviour. The constitutive equations for a linear, elastic, isotropic micropolar solid are

$$\sigma_{kl} = \lambda e_{nn}\delta_{kl} + (2\mu + \kappa)e_{kl} + \kappa e_{klm}(w_m - \phi_m), \quad (5)$$

$$m_{kl} = \alpha\phi_{n,n}\delta_{kl} + \gamma\phi_{l,k} + \beta\phi_{k,l}, \quad (6)$$

where λ and μ correspond to the classical Lamè constants, while κ , α , β and γ are micropolar constants. The quantity $\mu^* = \mu - \kappa/2$ is the micropolar shear modulus.

Limit conditions in terms of static and/or kinematic quantities should be imposed on the boundary of the body Ω . By assuming that $\partial\Omega = \partial\Omega_{\text{static}} \cup \partial\Omega_{\text{kinematic}}$, we may write

$$t_j = \sigma_{ij}n_i, \quad s_j = m_{ij}n_i \quad \text{on } \partial\Omega_{\text{static}}, \quad (7)$$

where, in addition to surface tractions t_j , the expression for the surface couples s_j has been added, and

$$\phi_j = \phi_j^0, \quad u_j = u_j^0 \quad \text{on } \partial\Omega_{\text{kinematic}}, \quad (8)$$

where ϕ_j^0 and u_j^0 are, respectively, prescribed microrotation and displacement vectors.

2.1 Two-Dimensional Case

For a plane problem, the kinematics of a micropolar body is described through the components u_1 and u_2 of the displacement vector \mathbf{u} taken with respect to a Cartesian co-ordinate system $[O; x_1, x_2]$, together with the normal component (ϕ_3) of the microrotation vector $\boldsymbol{\phi}$, as follows

$$\begin{aligned} \varepsilon_{11} &= u_{1,1}, & \varepsilon_{22} &= u_{2,2}, \\ \varepsilon_{12} &= u_{2,1} - \phi_3, & \varepsilon_{21} &= u_{1,2} + \phi_3. \end{aligned} \tag{9}$$

Equilibrium equations reduce to

$$\begin{aligned} \sigma_{11,1} + \sigma_{21,2} + \mathbf{b}_1 &= 0, & \sigma_{12,1} + \sigma_{22,2} + \mathbf{b}_2 &= 0, \\ \sigma_{12} - \sigma_{21} + m_{13,1} + m_{23,2} + \mathbf{m}_3 &= 0. \end{aligned} \tag{10}$$

The specialization of the constitutive equations (4) to plane problems requires the distinction between plane-strain and plane-stress conditions. In the case of plane strain we have

$$\begin{aligned} \sigma_{11} &= (\lambda + 2\mu + \kappa) e_{11} + \lambda e_{22}, \\ \sigma_{22} &= (\lambda + 2\mu + \kappa) e_{22} + \lambda e_{11}, \\ \sigma_{12} &= (2\mu + \kappa) e_{12} + \kappa (w_3 - \phi_3), \\ \sigma_{21} &= (2\mu + \kappa) e_{21} - \kappa (w_3 - \phi_3), \\ m_{13} &= \gamma \phi_{3,1}, & m_{23} &= \gamma \phi_{3,2}, \end{aligned} \tag{11}$$

while in the plane-stress case

$$\begin{aligned} \sigma_{11} &= e_{11} (\lambda + 2\mu + \kappa) + \lambda (e_{22} + e_{33}), \\ \sigma_{22} &= e_{22} (\lambda + 2\mu + \kappa) + \lambda (e_{11} + e_{33}), \\ \sigma_{12} &= e_{12} (2\mu + \kappa) + \kappa (w_3 - \phi_3), \\ \sigma_{21} &= e_{21} (2\mu + \kappa) - \kappa (w_3 - \phi_3), \\ m_{13} &= \gamma \phi_{3,1}, & m_{23} &= \gamma \phi_{3,2}, \end{aligned} \tag{12}$$

where

$$e_{33} = -(e_{11} + e_{22}) \frac{\lambda}{(\lambda + 2\mu + \kappa)}. \quad (13)$$

It is however more useful to introduce generalized engineering constants (which are six in 3-D and four in 2-D); in plane problems these are: the Young's modulus [7, 8]

$$E = \frac{(2\mu + \kappa)(3\lambda + 2\mu + \kappa)}{2\mu + 2\lambda + \kappa}, \quad (14)$$

the Poisson's ratio

$$\nu = \frac{\lambda}{2\mu + 2\lambda + \kappa}, \quad (15)$$

the characteristic length for bending

$$\ell_m = \left(\frac{\gamma}{4\mu + 2\kappa} \right)^{1/2} = \left(\frac{\gamma(1 + \nu)}{2E} \right)^{1/2}, \quad (16)$$

and the coupling number

$$N_m = \left(\frac{\kappa}{2\mu + 2\kappa} \right)^{1/2} = \left(\frac{\kappa(1 + \nu)}{E + \kappa(1 + \nu)} \right)^{1/2}. \quad (17)$$

In order to fulfill thermodynamics requirements, these constants must satisfy the following bounds:

$$0 < \ell_m^2 < \infty, \quad 0 < E < \infty, \quad (18)$$

and

$$0 < N_m^2 < 1. \quad (19)$$

The constant κ couples the rotation of particles to shear stresses. If $\kappa = 0$ ($N_m = 0$) the Cauchy stress does not depend on the rotational degree of freedom. The equilibrium equation (10)₃ reduces to an equilibrium of couple stresses (as $\sigma_{12} = \sigma_{21}$) that are null if body couples (m_3) are absent. The limit $\kappa \rightarrow \infty$ is a condition energetically admissible, similar to "incompressibility" in classical elasticity, and corresponds to $N_m = 1$. The modulus γ sets the intensity of couple stresses in the problem and is proportional to the characteristic length for bending ℓ_m [7]. In Cauchy solids, the internal characteristic length is of the order of the atomic distance and moments of forces at this scale do not produce any macroscopic effect. However, in microstructured solids such as biological hard tissues, cellular and fibre-reinforced materials, where an intrinsic internal length at least of the order of microns may be detected (steel: $\ell_m \cong 0.05$ mm; graphite: $\ell_m \cong 2.8$ mm; cancellous bone: $\ell_m \cong 1$ mm; masonry $\ell_m > 100$ mm), couple stresses may influence the macroscopic behaviour. In the limit $\gamma = 0$ ($\ell_m = 0$) Cauchy elasticity is recovered.

3. THE TOPOLOGY OPTIMIZATION PROBLEM

The classical problem of maximum global stiffness [9] (or minimum compliance \mathcal{C}) is solved for a micropolar solid. It reads: find

$$\min_{\rho, \mathbf{u}, \bar{\boldsymbol{\phi}}} \mathcal{C}(E_{ijkl}(\rho), K_{ijkl}(\rho)) \quad (E_{ijkl} \in \mathcal{E}_{\text{adm}}, K_{ijkl} \in \mathcal{K}_{\text{adm}}), \quad (20)$$

subject to

$$\int_{\Omega} \rho \, d\Omega \leq \mathcal{V}, \quad 0 < \rho_{\min} < \rho \leq 1, \quad (21)$$

$$a_E(\mathbf{u}, \bar{\mathbf{u}}) + a_B(\mathbf{u}, \bar{\mathbf{u}}) + a_K(\mathbf{u}, \bar{\mathbf{u}}) = l(\bar{\mathbf{u}}) + g(\bar{\boldsymbol{\phi}}), \quad \mathbf{u} = \begin{bmatrix} \mathbf{u} \\ \boldsymbol{\phi} \end{bmatrix}, \quad (22)$$

for all $\bar{\mathbf{u}} \in U$ and $\bar{\boldsymbol{\phi}} \in S$. Sets \mathcal{E}_{adm} and \mathcal{K}_{adm} are those of thermodynamically admissible micropolar stiffness tensors, ρ is the material density and ρ_{\min} its lower limit, introduced in order to avoid singularities in the finite element procedure to obtain the solution. \mathcal{V} is an upper bound on the total amount of material available, whereas U and S denote the space of the kinematically admissible displacements and the space of the kinematically admissible microrotation field, respectively. Terms in the weak form of equilibrium (22) correspond to:

$$\begin{aligned} a_E(\mathbf{u}, \bar{\mathbf{u}}) &= \int_{\Omega} E_{ijkl} \varepsilon_{ij}(\mathbf{u}) \varepsilon_{kl}(\bar{\mathbf{u}}) \, d\Omega, \\ a_B(\mathbf{u}, \bar{\mathbf{u}}, \boldsymbol{\phi}, \bar{\boldsymbol{\phi}}) &= \int_{\Omega} B_{ijkl} \varepsilon_{ij}(\bar{\mathbf{u}}) \chi_{kl}(\boldsymbol{\phi}) \, d\Omega + \int_{\Omega} B_{klij} \varepsilon_{kl}(\mathbf{u}) \chi_{ij}(\bar{\boldsymbol{\phi}}) \, d\Omega, \\ a_K(\boldsymbol{\phi}, \bar{\boldsymbol{\phi}}) &= \int_{\Omega} K_{ijkl} \chi_{ij}(\boldsymbol{\phi}) \chi_{kl}(\bar{\boldsymbol{\phi}}) \, d\Omega, \\ l(\mathbf{u}) &= \int_{\Omega} \mathbf{b}_i u_i \, d\Omega + \int_{\partial\Omega} \mathbf{t}_i u_i \, dS, \\ g(\boldsymbol{\phi}) &= \int_{\Omega} \mathbf{m}_i \phi_i \, d\Omega + \int_{\partial\Omega} \mathbf{s}_i \phi_i \, dS. \end{aligned} \quad (23)$$

Henceforth, \mathbf{b}_i and \mathbf{m}_i will be taken to be null vectors for simplicity.

The constrained minimization problem (20) is solved by means of the SIMP method with different material interpolation laws for the stiffness tensors E_{ijkl} and K_{ijkl} , namely

$$E_{ijkl}(\mathbf{x}) = \rho(\mathbf{x})^p E_{ijkl}^0 \quad (p \geq 1), \quad K_{ijkl}(\mathbf{x}) = \rho(\mathbf{x})^q K_{ijkl}^0, \quad (24)$$

where E_{ijkl}^0 and K_{ijkl}^0 are the constitutive tensors of the base material. The solutions of maximum stiffness correspond to $q = 0$. In this case the penalization acts only on the translational part.

4. RESULTS

A couple of examples are illustrated in order to describe the role of the characteristic length for bending ℓ_m . The first is the standard “cantilever problem”, solved for micropolar materials (in plane strain). A parametric analysis in terms of ℓ_m is reported, with coupling number (N_m) fixed to 0.8. The ranging of ℓ_m from 0 to a value of the order of the dimension of the design domain (case of optimal design of a representative volume element of a periodic continuum) allows to investigate the influence of the length scale on the optimal shape of structures. Some interesting phenomena may be noted. First, the lost of connectivity in the optimal configurations as long as the characteristic length for bending increases to become comparable to the dimension of the domain. Second, the evolution from truss-like shapes to hierarchical configurations where different order of structures, able to transmit couple stresses in addition to normal tractions, cooperate to transfer the load from the point of application to the constraints (see [10] for additional examples).

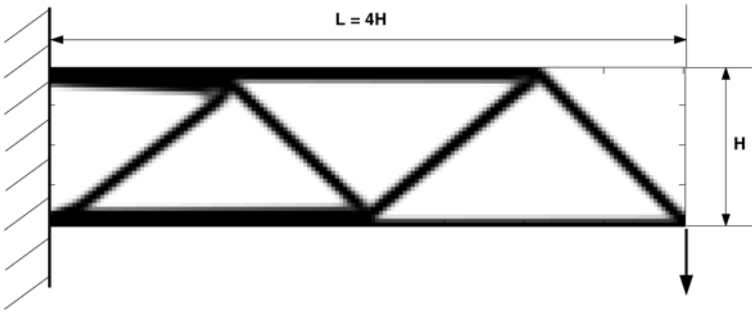


Figure 1. Optimal solution for the cantilever problem: Cauchy material.

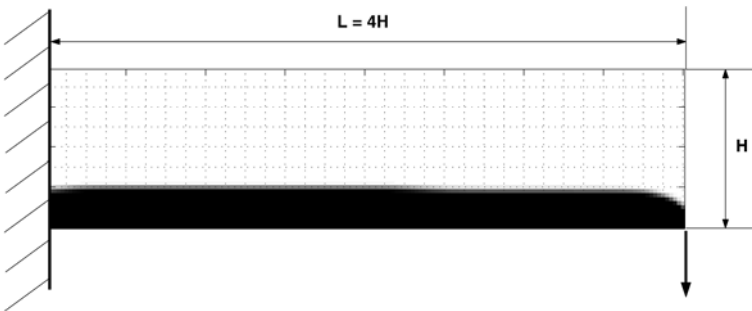


Figure 2. Optimal solution for the cantilever problem: Cosserat material with $\ell_m = H$.

In Figure 1 the optimal layout for Cauchy material, which corresponds to truss-like solution, is reported. Figure 2 displays the material distribution in

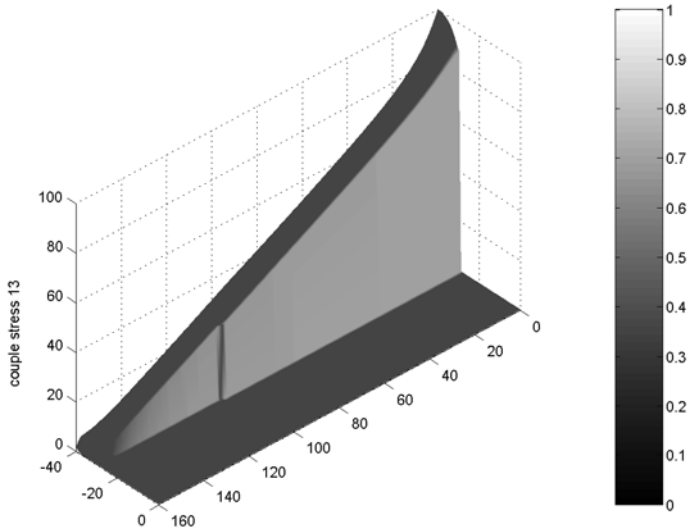


Figure 3. Couple stress m_{13} in optimal solution for Cosserat material with $\ell_m = H$.

the case of characteristic length for bending of the order of the design domain ($\ell_m = H$). It coincides with a thin cantilever subject mainly to couple stresses (Figure 3), whereas normal tractions are almost absent.

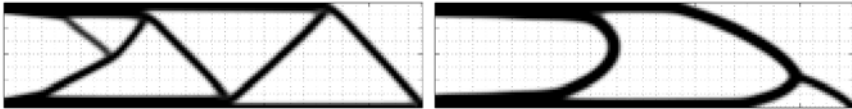


Figure 4. Optimal solution for the cantilever problem: Cosserat material with $\ell_m = H/40$ (left) and $\ell_m = H/8$ (right).

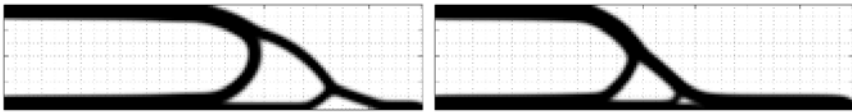


Figure 5. Optimal solution for the cantilever problem: Cosserat material with $\ell_m = H/4$ (left) and $\ell_m = H/2$ (right).

Another example where the role of the internal length scale can be appreciate is that of a structure consisting of two rectilinear elements, loaded with a vertical force in the free joint C (Figure 6). The oblique bar (index 1), of length L_1 , reacts only to axial load, while the horizontal rod (index 2, length $L_2 = L$)

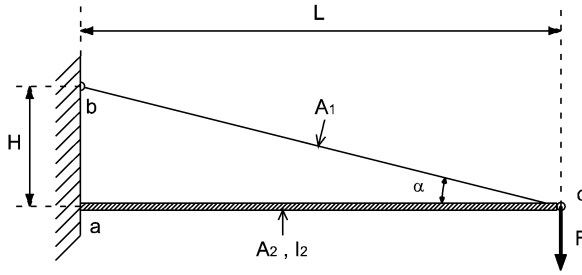


Figure 6. Truss optimal problem.

possesses both bending and axial stiffnesses. Two dimensionless parameters x_1 and x_2 (which serve as optimization variables) may be introduced in order to parametrize the areas of the two cross sections, namely

$$A_1(x_1) = x_1 A^0, \quad x_1 \in [0, 1], \tag{25}$$

$$A_2(x_2) = x_2 A^0, \quad x_2 \in [0, x_2^u], \tag{26}$$

where A^0 is a reference area and x_2^u is the upper limit of x_2 set by the constraint on the total volume V of the structure

$$V(x_1, x_2) = \sum_{k=1}^2 (A_k(x_k) L_k) = (x_1 L_1 + x_2 L_2) A^0 = \overline{\text{Vol}}, \tag{27}$$

where $\overline{\text{Vol}}$ is assigned. When $x_1 = 0$, it follows that $x_2^u = \overline{\text{Vol}} / (A^0 L_2)$; on the other hand, if the whole amount of material is distributed on bar 1 ($x_1 = 1, x_2 = 0$), then $\overline{\text{Vol}} = L_1 A^0$, so that $x_2^u = L_1 / L_2$. Equation (27) define also the dependence of x_2 on x_1 which becomes the independent variable of the problem. The cross-sectional inertia of the rod may be written as

$$I_2(x_2) = A_2(x_2) \rho_2^2 = A_2(x_2) (iL)^2, \tag{28}$$

where ρ_2 is the radius of gyration and $i = \rho_2 / L$ its dimensionless counterpart.

The object function is the compliance of the system, defined as

$$C(x_1) = F u_C = \sum_{k=1}^2 \frac{N_k^2 L_k}{E_k A_k(x_k)} + \int_{\text{rod 2}} \frac{M_2^2}{E_2 I_2} ds. \tag{29}$$

The optimization problem is to minimize the compliance $C(x_1)$, subject to the volume constraint (27). In Figure 7 the function $C(x_1)$ is plotted for different values of the parameter i and for $H = L/4$. When $i = 0$ the bending stiffness of rod 2 is absent, then the optimal solution (minimum of each curve) corresponds to classical truss-like structure with $x_1 = 0.515$. A similar result is obtained for $i = 1/8$. However in the cases $i = 1/4, 1/2$ the optimal

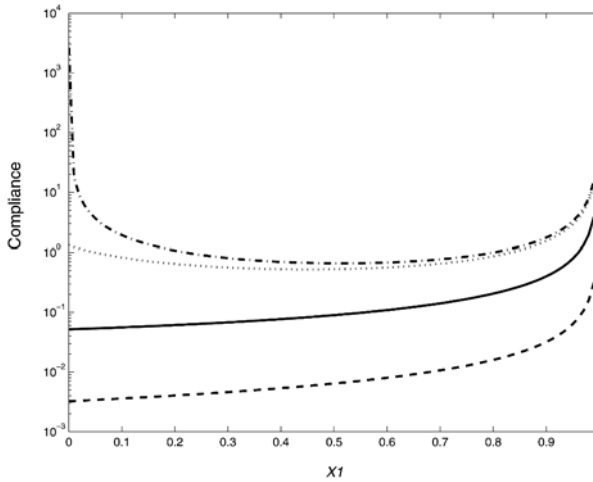


Figure 7. Plots of compliance C for different values of i as functions of the optimization parameter x_1 for the truss problem. From the top: $i = 0, 1/8, 1/4, 1/2$.

solution corresponds to a null value of x_1 , which means that the bar 1 has vanishing area: the load is carried by the cantilever 2 which is subject to bending moment.

These results suggest an analogy between the characteristic length for bending (ℓ_m) in micropolar solids and the radius of gyration (ρ_2) of the example,

$$\ell_m^2 \longleftrightarrow \rho_2^2 = (iL)^2. \tag{30}$$

Beam theory may be interpreted as a monodimensional Cosserat continuum theory. When ℓ_m is of the order of the dimension of the design domain, the material is subject to high couple stresses which are prominent with respect to normal tractions.

ACKNOWLEDGMENT

Financial support from grant MIUR-PRIN 2004: “Problemi e Modelli Microstrutturali: Applicazioni in Ingegneria Strutturale e Civile” is gratefully acknowledged.

REFERENCES

- [1] Pasternak, E. and Mühlhaus, H.-B., Generalised homogenisation procedures for granular materials, *J. Engng. Mathematics*, 52(1), 199–229 (2005).
- [2] Bendsoe, M.P. and Sigmund, O., *Topology Optimization: Theory, Methods and Applications*, Springer, Berlin (2002).
- [3] Cheng, K.T. and Olhoff, N., Regularized formulation for optimal design of axisymmetric plates, *Int. J. Solids Struct.*, 18, 153–169 (1982).

- [4] Eringen, A.C. *Microcontinuum Field Theories*, Vol. 1. Springer, Berlin (1999).
- [5] Novacki, W. *Theory of Asymmetric Elasticity*, Pergamon Press, New York (1986).
- [6] Fatemi, J., Van Keulen, F. and Onck, P.R., Generalized continuum theories: application to stress analysis in bone, *Meccanica*, 37, 385–396 (2002).
- [7] Lakes, R.S., Experimental methods for study of Cosserat elastic solids and other generalized elastic continua, in *Continuum Models for Materials with Microstructure*, H. Mühlhaus (ed.), Wiley, New York, pp. 1–25 (1995).
- [8] Lakes, R.S. and Benedict, R.L., Noncentrosymmetry in micropolar elasticity, *Int. J. Engng. Sci.*, 20, 1161–1167 (1982).
- [9] Eschenauer, H.A. and Olhoff, N., Topology optimization of continuum structures: A review, *Appl. Mech. Rev.*, 54, 331–390 (2001).
- [10] Rovati, M. and Veber, D., Optimal topologies for micropolar continua, submitted (2006).

Mathematical Programming and Modelling

CELLULAR AUTOMATA PARADIGM FOR TOPOLOGY OPTIMISATION

Mostafa M. Abdalla, Shahriar Setoodeh and Zafer Gürdal

*Chair of Aerospace Structures, Delft University of Technology,
2629 HS Delft, The Netherlands*

m.m.abdalla@lr.tudelft.nl, s.setoodeh@lr.tudelft.nl, z.gurdal@lr.tudelft.nl

Abstract: Cellular Automata (CA) is an emerging paradigm for the combined analysis and design of complex systems using local update rules. Several algorithms based on of the CA paradigm have recently been demonstrated successfully for the topology optimisation of structures. In the present paper, the elements of a CA paradigm for topology optimisation are discussed. A framework for a biologically inspired CA topology optimisation is proposed and an initial effort to fit existing CA topology optimisation studies within this basic framework.

Keywords: Cellular automata, biomemetics, topology optimisation.

1. INTRODUCTION

Use of Cellular Automata (CA) paradigm for modelling complex systems is finding widespread applications in science and engineering. CA uses a *lattice* of regularly spaced cells to model the physical domain (e.g., a continuum structure). Each cell contains all the information needed to update its state. This includes both field variables (e.g., displacements or stresses) as well as local design variables (e.g., local cross-sectional area or thickness). The only external information to the cell comes directly from the adjacent cells, which along with the cell forms a *neighbourhood*. The attraction of CA comes from two facts. First, the iterative application of simple *local* CA rules at the cell level can be used to generate *global* complex behavior. Second, by limiting computations to neighbourhoods and using identical update rules for cell variables in the entire lattice, CA proves to be an inherently massively parallel algorithm. The local CA rules can come from a variety of sources: heuristic, biomemetic, optimality based, or a mixture of these.

Several algorithms for structural analysis and/or design of structures based on the CA paradigm are presented in the literature. One of the early applications is the work in Hajela (1998) where CA rules for the solution of two-

dimensional elasticity problems are sought. This work was further extended in Hajela and Kirn (2000) and Hajela and Kim (2001). A CA topology optimisation algorithm based on the method of evolutionary structural optimisation (ESO) is presented in Kita and Toyoda (2000). The method relied on using finite element analysis to perform analysis and constructed CA design rule for updating the topology design variables. A similar approach is implemented in Tovar et al. (2004a) where the CA design rule is based on the uniform strain energy condition and the Solid Isotropic Microstructure with Penalisation (SIMP) material interpolation scheme. This work is further extended in Tovar et al. (2004b, 2005).

The use of the CA paradigm for addressing the automated combined analysis and design of two-dimensional elastic systems is implemented in Gürdal and Tatting (2000). The basic elements of the methodology are demonstrated using a simple two-dimensional domain occupied by a ground truss structures. CA rules are used both to update the displacements, the so-called analysis update rule, and to update the cross-sectional areas, the so-called design update rule. The design rule is limited to fully stressed design. The analysis and design rules are nested such that the analysis rule is applied several times before the design rule is invoked. Other extensions to include geometric and material non-linear behaviour and multiple load cases for truss topology design are presented in Missoum et al. (2003a, 2003b), while the nesting strategy of analysis and design is investigated in detail in Missoum et al. (2005). Parallel implementation of the method and basic stability analysis is carried out in Slotta et al. (2002), while a more refined parallel implementation is presented in Setoodeh et al. (2005b). The method is extended in Tatting and Gürdal (2000) to a two-dimensional continuum representation using an equivalent truss approach that was further refined in Canyurt and Hajela (2004). Continuum CA topology design algorithm is developed in Abdalla and Gürdal (2002) and Setoodeh et al. (2005a) using rigorous models for the analysis rule and optimality conditions for the design rule.

In this paper, we review the basic components of CA and describe a framework for a biologically inspired CA formalism for structural optimisation. The model problem considered is two-dimensional minimum compliance topology optimisation, but the approach can be easily generalised for other performance functionals. The different existing approaches to CA models for topology optimisation are discussed in relation to the proposed formalism. In particular, we discuss the role of cell definition in suppressing numerical instabilities such as checkerboard patterns and mesh dependency.

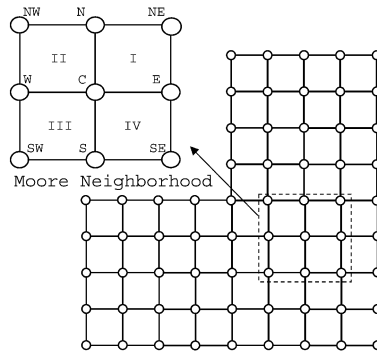


Figure 1. CA Lattice for 2D topology optimisation (Abdalla and Gürdal, 2002).

2. ELEMENTS OF CELLULAR AUTOMATA

Cellular automata are generally attributed to Ulam (1952) and von Neumann (1966) who introduced the concept in the late forties to provide a realistic model for the behaviour of complex systems. Cellular automata is a regular lattice of logical entities called cells which are updated synchronously in discrete time steps. Each cell can update its state based on the state of the cell itself and its lattice neighbours in the previous step. Moreover, the update (transition) rules and the neighbourhood structure are the same for all sites. Commonly, cells are defined to have a discrete set of states, while a variant of the cellular automata uses continuous lattice site values. In their modern engineering implementation, cellular automata are simple mathematical idealizations of natural systems, and are used successfully to represent a variety of phenomena (Wolfram, 1994). A typical CA algorithm is defined by few basic elements which are explained in the following subsections.

2.1 CA Lattice

The form of the cellular space directly reflects the physical dimensions of the problem being solved. Rectangular lattices (Figure 1) of uniform spacing are the simplest and for topology optimisation they are almost universally used. The lattice structures, however, are not limited to be rectangular and non uniform lattices have been used in CA algorithms for structural analysis such as the work of Hajela and Kim (2001). When CA algorithms are based on uniform lattices, they are highly suitable for massively parallel calculations. Preliminary results on parallel performance of CA for structural optimisation applications on standard clusters (Slotta et al., 2002; Setoodeh et al., 2005b) and on reconfigurable computers (Hartka et al., 2004) demonstrate the ease of parallelisation and the good scalability of the method.

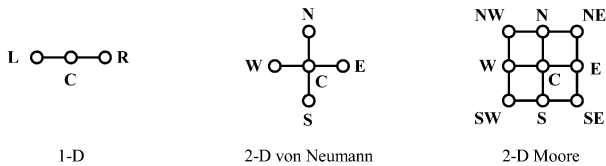


Figure 2. Traditional CA neighborhoods.

2.2 The Neighbourhood

The neighbourhood structure is one of the most important characteristics of a CA lattice. In updating the values of a site, it is necessary to consider the site's own value and the values of the sites in its neighbourhood. The set of sites that is utilized for the update is highly problem dependent, and relies heavily on the nature of the physical phenomenon that is being modelled. Some common examples of neighbourhood structures used in the literature are shown in Figure 2. The cell to be updated is labelled as C, and the adjacent ones are labelled with letters representing the East, West, North, and South directions.

CA algorithms that rely on finite element analysis to determine the displacement field identify CA cells with the elements of the rectangular mesh. This approach is consistent with the traditional practice of associating topology variables with elements. In these approaches (e.g., Kita and Toyoda, 2000; Tovar et al., 2004a), the neighbourhood structure is based on element adjacency. Other CA methods identify CA cells with nodes and the neighbourhood structure is based on node connectivity. In these methods, the topology variables are associated with nodes and element values need to be properly interpolated from nodal values.

2.3 Boundaries

Since every cell has the same neighbourhood structure, even the cell at the boundary of a physical domain has neighbouring cells that are outside the domain. For structural analysis applications, displacement boundary conditions may be modelled by using preset values of the cell displacements for the boundary cells. Traction boundary conditions can be avoided by using a variationally consistent update rule.

2.4 CA Update Rules

In a computer implementation, the update rules that are applied to every cell of the lattice are like function subroutines. The arguments for the function subroutine are the values of the sites of the neighbourhood, and the value returned by the function is the new value of the cell at which the function is being applied. For example, for the von Neumann neighbourhood, the function has

5 arguments, $f(C, E, W, N, S)$ which returns the value of the site C at the time/iteration $t + 1$. Since the update rule is applied to all the cells simultaneously, the incoming arguments are the values of all the cells in the previous cycle (t), and at the new cycle ($t + 1$) all the cells have new values.

CA update rules are at the heart of any CA algorithm. For structural applications, two types of update rules can be identified. Rules that alter structural displacements to satisfy local equilibrium are called analysis update rules. Rules that alter the design variables are called design update rules. One or both types may be devised depending on whether the CA algorithm is constructed to perform analysis only, design only or combined analysis and design. Classification of CA rules will be guided by the development of a biologically inspired CA formalism based on an interpretation of the variational formulation of the minimum compliance topology optimisation problem.

3. VARIATIONAL FORMULATION OF MINIMUM COMPLIANCE DESIGN

Minimum compliance design attempts to find the optimal distribution of material in a given domain Ω to minimize the compliance of the structure under given loads with constraints on material availability. The distribution of the material throughout the domain is described by certain design functions $b(x)$, that determine the local stiffness of the material and the local use of resources at any point x in the domain. An example is the topology design of variable stiffness panels considered in Setoodeh et al. (2005a), where the local design functions are the local material density and local fibre angle.

The compliance of the structure is measured by the complementary work done by the external loads. Compliance minimisation takes the form (Setoodeh et al., 2005a)

$$\max_b \min_u \Pi, \quad (1)$$

where Π is the total potential energy of the system,

$$\Pi = \int_{\Omega} \Phi(x, \gamma; b) d\Omega - \int_{\Gamma_1} t \cdot u \partial\Omega, \quad (2)$$

where t is the applied surface traction, and Φ is the strain energy density of the structure, and $\gamma(x, u)$ is the, generalized, strain vector.

Material availability becomes a constraint on functionals of the design functions (e.g., material volume). These integral constraints take the form

$$\int_{\Omega} [f(b) - f_0] d\Omega \leq 0. \quad (3)$$

Additionally, local point by point by constraints (e.g., maximum thickness) can be applied in the form

$$g(x, b(x)) \leq 0. \quad (4)$$

The optimality conditions for the minimum compliance problem can be shown (Setoodeh et al., 2005a) to be equivalent to the following local optimisation problem:

$$\min_{\mathbf{b}} \hat{\Phi}_{(x, \sigma)} + \boldsymbol{\mu} \cdot \mathbf{f}_x, \quad \text{subject to, } g_x(b) \leq 0, \quad (5)$$

where the generalised stress σ and the complementary energy $\hat{\Phi}$ are given by

$$\sigma = \frac{\partial \Phi}{\partial \gamma} \quad \text{and} \quad \hat{\Phi}(x, \sigma; b) = \sigma \cdot \gamma - \Phi(x, \gamma; b), \quad (6)$$

and $\boldsymbol{\mu}$ is a vector of Lagrange multipliers. In the optimisation problem (5), the subscripts under different functions indicate variables that are held constant during minimisation.

4. BIOLOGICALLY-INSPIRED CELLULAR AUTOMATA

In the previous section, the minimum compliance problem is reduced to a local mathematical optimization problem. In CA terms, the optimisation problem can be solved by the application of a local design rule. Note, however, that the local optimization problem presented above (5) contains an unknown vector of Lagrange multipliers associated with the global integral constraints. Values of these Lagrange multipliers, therefore, are dependent on the global integral constraints. The Lagrange multipliers associated with the integral constraints, $\boldsymbol{\mu}$, are obtained by solving the active integral constraints of (3), while the Lagrange multipliers associated with the inactive integral constraints will be zero. In this fashion, the minimum compliance design problem is split into a set of local design rules (5), and a global iteration to obtain the Lagrange multipliers.

The relation between the local design rule and the Lagrange multipliers parallels adaptation processes in nature where cells *respond* and *adapt* to external stimuli guided by their genetic code. The genetic code is not itself defined by the environment and is fixed for the lifetime of the cell. The adaptation of the genetic code is a separate process driven by interaction with the environment through survival of the fittest. The genetic code of the cell regulates both the way it responds to stimuli and the way it adapts its function over longer time scales. The adaptation of the genetic code itself occurs at a much slower time scale than adaptation which occurs at a slower time scale than response.

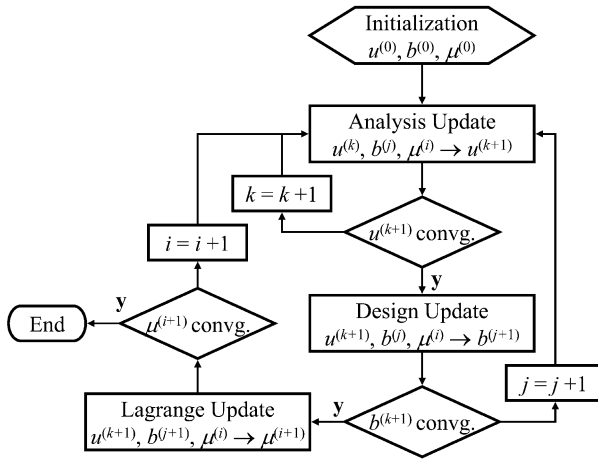


Figure 3. Biologically inspired CA paradigm.

The above view enables us to identify three nested processes in biologically inspired CA topology optimisation as illustrated in Figure 3. The innermost loop comprises an *analysis update*, where the state of a cell is iteratively updated to maintain equilibrium with neighbouring cells through the application of an *analysis rule*. The intermediate loop comprises a *design update* where the stress state of the cell is used together with the current value of the Lagrange multipliers to update the design of the cell through a *design rule*. Finally, the outermost loop is where the Lagrange multipliers are updated to satisfy the global integral constraints.

The proposed general paradigm depicted in Figure 3 is only one variant of a wide possibility of interpretation of biological processes and how they relate to structural analysis and design optimisation. One possibility not included is for the outer loop to adapt not only the Lagrange multipliers which appear in the design update, but to also adapt parameters in the analysis update. This possibility was explored by Hajela and Kim (2001) where the analysis rule was encoded using a Genetic Algorithm (GA) and optimised to give the best possible structural response. The main disadvantage of such an approach is that there are well known methods to discretise the structure for analysis purposes. However, the idea of using GA for the outer iteration, in a design context, is quite attractive and requires further investigation.

5. HYBRID CELLULAR AUTOMATA

One problem with the approach presented in Section 4 is that when the innermost loop is executed on serial computer architecture or medium sized parallel clusters, the analysis iterations converge poorly and the deterioration in con-

vergence rate increases when denser lattices are used. This phenomena can be addressed using acceleration techniques such as multigrid (Maar and Schulz, 2000; Abdalla et al., 2004). Another attractive option is to use standard finite elements for performing the analysis. Tovar et al. (2004b) terms this approach hybrid cellular automata (HCA). In their approach, the same paradigm as Section 4 is used except for the replacement of the innermost loop by a finite element analysis. It might be argued that this approach is inherently wasteful, since fully converged designs are obtained again and again that do not satisfy the integral constraints. The computational cost is large especially because of the finite element calculation is in the innermost loop. These designs, however, are physically meaningful. The integral constraints limit the availability of global resources and it is often interesting to investigate the optimal design as the amount available resources are parametrically varied, and this is effectively accomplished by parametrically varying the Lagrange multipliers. An instance of these trade-off studies is the trade-off between optimal compliance and available material volume in Setoodeh et al. (2005a).

6. CLASSIFICATION OF CA UPDATE RULES

There seems to be a basic dividing line of CA methods for structural analysis and design. There are hybrid methods that rely on finite element analysis and pure CA methods which use local rules either for analysis only or for combined analysis and design. In the following we review the basic features of these methods. A major issue with optimisation of structural topology is the suppression of numerical instabilities such as checkerboard patterns and mesh dependency (Sigmund and Petersson, 1998). While, traditionally, sensitivity filtering is applied (e.g., Diaz and Sigmund, 1995), different approaches to instability suppression are used in CA algorithms. These features will be highlighted.

An early hybrid method is the topology design algorithm considered in Kita and Toyoda (2000) where the optimal thickness distribution of a two-dimensional continuum (plate) under inplane loads is sought. The basic methodology advocated therein consists has finite elements identified as CA cells, the cell neighborhood is identified as the elements sharing a common edge with the cell (for the rectangular FEM mesh used, this is a Moore neighborhood), and an update rule is devised, based on stresses in the neighborhood, to update cell thickness. This work contained some far-reaching features. The CA design rule is formulated, for the first time, as a local optimization problem at the cell (element) level. The local update rule is based on the value of stress resultants in the neighbourhood. The main drawback of their method is that they depended on the evolutionary structural optimization (ESO) method. In ESO, the von Mises stress is used as a measure to eliminate elements in the

domain that are not contributing to the load carrying capacity of the structure. This method is essentially heuristic is not guaranteed to converge to optimal topologies. Another disadvantage of this CA algorithm is the large number of iterations (in excess of a thousand) required to reach a converged topology. Given that each CA design iteration required a full finite element analysis of the structure, the overall computational cost proved to be excessive. Additionally, the method does not have a mechanism for suppressing numerical instabilities such as checkerboard patterns.

An improved hybrid method is proposed in Tovar et al. (2004a). The design rule is based on the optimality condition of uniform strain energy. Instead of formulating the design rule as a local optimisation problem, the design rule is formulated as a control law. The method also included an averaging algorithm of the design variables over the cell neighbourhood to eliminate numerical instabilities. By optimising the parameters of the control law, convergence to optimal topologies could be achieved in a reasonable number of iterations. One drawback of the method is that the volume constraint was not explicitly reinforced and the method relied on changing the target value of strain energy density to generate designs with different volume fractions. The optimality condition is improved in Tovar et al. (2005) where a multi-objective formulation based on assigning different costs to the volume and the energy of the structure is used.

Pure CA approaches such as the work of Abdalla and Gürdal (2002) and Setoodeh et al. (2005a) identify CA cells with nodes and use optimality conditions for the design rule. By nesting the analysis and the design and directly addressing the issue of the determination of the Lagrange multipliers, these methods are the most general CA approaches available. Additionally, associating the design variables with nodes leads to a simple approach to suppress numerical instabilities by smoothly interpolating element densities (Maar and Schulz, 2000; Rahmatalla and Swan, 2003). The cell neighbourhood (Figure 1) is partitioned into four quadrants and when the popular SIMP model is used, the following *compliance averaging* is used to assign a constant average density to each quadrant:

$$\frac{1}{\bar{\rho}^p} = \frac{1}{4} \sum_{\text{cells}} \frac{1}{\rho_i^p}, \quad (7)$$

where ρ_i 's are the density measures of the four cells surrounding the quadrant.

This compliance averaging interpolation scheme is chosen so that any cell with a low density would turn-off (force the assigned density to zero) all four quadrants in which that cell participates. This makes cells in white (void) regions have a negligible (or no) effect on the equilibrium equations of cells in the black regions. Moreover, the interpolation scheme (7) does not allow checker board patterns to be representable on the lattice, thus, suppressing

checkerboard patterns automatically. Numerical experience with this scheme (Abdalla and Gürdal, 2002; Setoodeh et al., 2005a) also indicates that mesh independent topologies are obtained. A satisfactory explanation of this is a point that requires further research. The major drawback of pure CA methods is that the convergence of the analysis update can be extremely slow especially for dense lattices. Acceleration techniques such as multigrid offer one solution to this problem (Abdalla et al., 2004). Thus, the choice between pure CA or hybrid CA is not conclusive. Further comparison of these approaches requires careful computational experiments designed for a parallel environment.

7. CONCLUDING REMARKS

The paper discusses the elements of cellular automata (CA) and presents a biologically inspired CA paradigm for topology optimisation problems. The basic features of the proposed paradigm are explained and related to the existing literature on CA for structural optimisation. The proposed paradigm is shown to provide a unifying framework for the existing literature on the subject. There has been a substantial progress made in demonstrating the feasibility of the Cellular Automata (CA) paradigm for the analysis and design of two-dimensional structural systems under static loads as witnessed by the work reviewed herein. The set of applications considered so far is not exhaustive of the potential of CA in structural and multidisciplinary design optimization. Further development of CA algorithms for topology optimisation can be achieved in two main areas. The first area is extending the optimality conditions for general objectives and for multiple load cases including vibration and buckling. The second area where further work is needed is parallelisation studies. The value of CA as a topology optimisation tool lies mainly in its parallel capabilities. A careful investigation of the parallel performance of CA methods especially for three-dimensional problems is needed.

REFERENCES

- Abdalla, M. and Gürdal, Z. (2002) Structural design using optimality based cellular automata, In *43th AIAA/ASME/ AHS/ASC Structures, Structural Dynamics and Material Conference*, Denver, CO, AIAA-2002-1676.
- Abdalla, M., Kim, S. and Gürdal, Z. (2004) Multigrid accelerated cellular automata for structural design optimization: A 1-d implementation, in *45th AIAA/ASME/ ASCE/AHS/ASC Structures, Structural Dynamics and Materials Conference*, Palm Springs, CA, AIAA Paper 2004-1644.
- Canyurt, O. and Hajela, P. (2004) A sand approach based on cellular computation models for analysis and optimization, in *45th AIAA/ASME/ASCE/AHS/ASC Structures, Structural Dynamics & Materials Conference*, Palm Springs, CA.
- Diaz, A. and Sigmund, O. (1995) Checkerboard patterns in layout optimization, *Structural and Multidisciplinary Optimization*, 10, 40–45.

- Gürdal, Z. and Tatting, B. (2000) Cellular automata for truss structures with linear and nonlinear response, in *41st AIAA/ASME/ AHS/ASC Structures, Structural Dynamics and Material Conference*, AIAA-2000-1580.
- Hajela, P. (1998) Implications of artificial life simulations in structural analysis and design, in *39th AIAA/ASME/ AHS/ASC Structures, Structural Dynamics and Material Conference*, Long Beach, CA, AIAA-1998-1775.
- Hajela, P. and Kim, B. (2001) On the use of energy minimization for ca based analysis in elasticity, *Structural and Multidisciplinary Optimization*, 23, 24–33.
- Hajela, P. and Kirn, B. (2000) On the use of energy minimization for ca based analysis in elasticity, in *41st AIAA/ASME/ AHS/ASC Structures, Structural Dynamics and Material Conference*, Atlanta, GA, AIAA-2000-2003.
- Hartka, T., Jones, M., Gürdal, Z. and Abdalla, M. (2004) A reconfigurable approach to structural engineering design computations, in *IEEE Conference on Reconfigurable Computing*.
- Kita, E. and Toyoda, T. (2000) Structural design using cellular automata, *Structural and Multidisciplinary Optimization*, 19, 64–73.
- Maar, O. and Schulz, V. (2000) Interior point multigrid methods for topology optimization, *Structural and Multidisciplinary Optimization*, 19, 214–224.
- Missoum, S., Abdalla, M.M. and Gürdal, Z. (2003a) Nonlinear design of trusses under multiple loads using cellular automata, in *5th World Congress in Structural and Multidisciplinary Optimization*, Lido diJesolo, Italy.
- Missoum, S., Abdalla, M.M. and Gürdal, Z. (2003b) Nonlinear topology design of trusses using cellular automata, in *44th AIAA/ASME/ AHS/ASC Structures, Structural Dynamics and Material Conference*, Norfolk, VA, AIAA-2003-1445.
- Missoum, S., Gürdal, Z. and Setoodeh, S. (2005) Study of a new local update scheme for cellular automata in structural design, *Structural and Multidisciplinary Optimization*, 29, 103–112.
- Rahmatalla, S. and Swan, C.C. (2003) Continuum topology optimization of buckling-sensitive structures, *AIAA Journal*, 41, 1180–1189.
- Setoodeh, S., Abdalla, M. and Gürdal, Z. (2005a) Combined topology and fiber path design of composite layers using cellular automata, *Structural and Multidisciplinary Optimization*, 30, 413–421.
- Setoodeh, S., Adams, D.B., Gürdal, Z. and Watson, L.T. (2005b) Pipeline implementation of cellular automata for structural design on message-passing multiprocessors, *Mathematical and Computer Modelling*.
- Sigmund, O. and Petersson, J. (1998) Numerical instabilities in topology optimization: A survey on procedures dealing with checkerboards, mesh-dependencies and local minima, *Structural Optimization*, 16, 68–75.
- Slotta, D.J., Tatting, B., Watson, L.T., Gürdal, Z. and Missoum, S. (2002) Convergence analysis for cellular automata applied to truss design, *Engrg. Comput.*, 19, 953–969.
- Tatting, B. and Gürdal, Z. (2000) Cellular automata for design of two-dimensional continuum structures, Presented at the *8th AIAA/ISSMO Symposium on Multidisciplinary Analysis and Optimization*, AIAA-2000-4832.
- Tovar, A., Patel, N., Renaud, J. and Agarwal, H. (2005) Optimality of the hybrid cellular automata, in *46th AIAA/ASME/ASCE/AHS/ASC Structures, Structural Dynamics and Materials Conference*, Austin, TX, AIAA 2005-1898.
- Tovar, A., Niebur, G.L., Sen, M. and Renaud, J.E. (2004a) Bone structure adaptation as a cellular automaton optimization process, in *45th AIAA/ASME/ASCE/AHS/ASC Structures, Structural Dynamics & Materials Conference*, Palm Springs, CA.

- Tovar, A., Patel, N., Kaushik, A.K., Letona, G.A. Renaud, J.E. and Sanders, B. (2004b) Hybrid cellular automata: A biologically-inspired structural optimization technique, in *10th AIAA/ISSMO Multidisciplinary Analysis and Optimization Conference*, Albany, NY, AIAA 2004-4558.
- Ulam, S. (1952) Random processes and transformations, in *Proceedings of the International Congress of Mathematics*, Vol. 2, pp. 85–87.
- von Neumann, J. (1966) *Theory of Self-Reproducing Automata*, University of Illinois Press.
- Wolfram, S. (1994) *Cellular Automata and Complexity: Collected Papers*, Addison-Wesley Publishing Company.

A ONE SHOT APPROACH TO TOPOLOGY OPTIMIZATION WITH LOCAL STRESS CONSTRAINTS

Roman Stainko¹ and Martin Burger²

¹*Special Research Project SFB F013, University of Linz, Austria*

²*Industrial Mathematics Institute, University of Linz, Austria*

roman.stainko@jku.at, martin.burger@jku.at

Abstract: We consider the topology optimization problem with local stress constraints. In the basic formulation we have a pde-constrained optimization problem, where the finite element and design analysis are solved simultaneously. Here we introduce a new relaxation scheme based on a phase-field method. The starting point of this relaxation is a reformulation of the constraints of the optimization problem involving only linear and 0–1 constraints. The 0–1 constraints are then relaxed and approximated by a Cahn–Hillard type penalty in the objective functional. As the corresponding penalty parameter decreases to zero, it yields convergence of minimizers to 0–1 designs. A major advantage of this kind of relaxation opposed to standard approaches is a uniform constraint qualification that is satisfied for any positive value of the penalization parameter.

After the relaxation we end up with a large-scale optimization problem with a high number of linear inequality constraints. Discretization is done by usual finite elements and for solving the resulting finite-dimensional programming problems an interior-point method is used. Numerical experiments based on different stress criteria attest the success of the new approach.

To speed up computational times we investigated the construction of an optimal solver for the arising subproblem in the interior-point formulation.

Keywords: Topology optimization, local stress constraints, phase-field methods, one-shot methods, KKT-system.

1. INTRODUCTION

In comparison to maximization of material stiffness at given mass, the treatment of minimization of mass while keeping a certain stiffness is by far less understood. Until now there seems to be no approach that is capable of computing reliable (global) optima with respect to local stress constraints within reasonable computational effort.

In our work we use a different approach to the relaxation of the local constraints. Starting point of our analysis is a reformulation of the equality constraints describing the elastic equilibrium and the local inequality constraints for stresses and displacements into a system of linear inequality constraints. The main difficulty is that the arising problem also involves 0–1 constraints in addition to the linear inequalities. Instead of solving mixed linear programming problems, we propose to use a phase-field relaxation of the reformulated problem. The phase-field relaxation consists in using an interpolated material density ρ , similar to material interpolation schemes. In addition, a Cahn–Hilliard type penalization functional (cf. [3]) of the form

$$P^\epsilon(\rho) = \frac{\epsilon}{2} \int_{\Omega} |\nabla \rho|^2 \, dx + \frac{1}{\epsilon} \int_{\Omega} W(\rho) \, dx \quad (1)$$

is used to approximate the perimeter, where $W : \mathbb{R} \rightarrow \mathbb{R} \cup \{+\infty\}$ is a scalar function with exactly two minimizers at 0 and 1 satisfying $W(0) = W(1) = 0$. The second term of the penalty functional ensures that the values of the material density ρ converge to 0 or 1 as $\epsilon \rightarrow 0$, while the first term controls the perimeter of level sets of ρ .

2. REFORMULATION OF CONSTRAINTS AND PHASE-FIELD RELAXATION

We consider the following problem formulation as a starting point of our reformulation:

$$\begin{array}{ll} \int_{\Omega} \chi \, dx & \rightarrow \min_{\chi, \mathbf{u}} \\ \operatorname{div} \boldsymbol{\sigma} = 0 & \text{in } \{\chi = 1\} \\ \boldsymbol{\sigma} = \mathbf{C} : \mathbf{e}(\mathbf{u}) & \text{in } \Omega \\ \mathbf{u} = \mathbf{0} & \text{on } \Gamma_u \subset \partial\Omega \\ \boldsymbol{\sigma} \cdot \mathbf{n} = \mathbf{t} & \text{on } \Gamma_t \subset \partial\Omega \\ \boldsymbol{\sigma} \cdot \mathbf{n} = \mathbf{0} & \text{on } \partial\{\chi = 1\} \cup (\partial\Omega - \Gamma_u - \Gamma_t) \\ \chi \in \{0, 1\} & \text{a.e.} \\ \boldsymbol{\sigma}^{\min} \leq \boldsymbol{\sigma} \leq \boldsymbol{\sigma}^{\max} & \text{in } \{\chi = 1\} \\ \mathbf{u}^{\min} \leq \mathbf{u} \leq \mathbf{u}^{\max} & \text{in } \Omega. \end{array}$$

In the following we briefly summarize a reformulation, due to Stolpe and Svanberg [6], of constraints on subsets of locally bounded stresses, i.e., $\beta|\sigma_{ij}| \leq 1$, in Ω , $i, j = 1, \dots, d$, for some (small) $\beta > 0$. Next we introduce an additional artificial stress variable \mathbf{s} such that $\mathbf{s} = \boldsymbol{\sigma}$ if $\chi = 1$ and $\mathbf{s} = \mathbf{0}$ if $\chi = 0$, i.e., $\mathbf{s} = \chi \boldsymbol{\sigma} = \chi \cdot \mathbf{C} : \mathbf{e}(\mathbf{u})$. Then, (χ, \mathbf{u}) satisfying the original constraints

$$\begin{array}{ll} \boldsymbol{\sigma} = \mathbf{C} : \mathbf{e}(\mathbf{u}) & \text{in } \Omega \\ \boldsymbol{\sigma}^{\min} \leq \boldsymbol{\sigma} \leq \boldsymbol{\sigma}^{\max} & \text{in } \{\chi = 1\} \end{array}$$

is equivalent to $(\chi, \mathbf{u}, \mathbf{s})$ satisfying the following additional constraints (with the matrix $\mathbf{1} = (1)_{ij}$):

$$\begin{aligned} -(1 - \chi)\mathbf{1} &\leq \beta(\mathbf{C} : \mathbf{e}(\mathbf{u}) - \mathbf{s}) \leq (1 - \chi)\mathbf{1} && \text{in } \Omega \\ \chi \boldsymbol{\sigma}^{\min} &\leq \mathbf{s} \leq \chi \boldsymbol{\sigma}^{\max} && \text{in } \Omega \end{aligned}$$

Note that (except $\chi \in \{0, 1\}$) the constraints are now linear with respect to the new vector of unknowns $(\chi, \mathbf{u}, \boldsymbol{\sigma}, \mathbf{s})$, in particular all constraints are formulated on Ω and not on the unknown set $\{\chi = 1\}$. We would like to mention that the drawback of the reformulation is an increase in the number of unknowns and a high number of inequality constraints. On the other hand, this seems to be a reasonable price for the linear reformulation of the complicated original constraints.

We now turn our attention to the relaxation of the stress constrained topology optimization problem. For this sake it has been proposed in [5] to replace the indicator function χ by a density $\rho : \Omega \rightarrow [0, 1]$ and add the Cahn–Hilliard term (1) to the objective. The resulting relaxation in the case of total stress constraints is given by

$$\begin{aligned} \gamma \int_{\Omega} \rho \, d\mathbf{x} + P^\epsilon(\rho) &\rightarrow \min, \\ \operatorname{div} \mathbf{s} &= 0 && \text{in } \Omega, \\ \boldsymbol{\sigma} &= \mathbf{C} : \mathbf{e}(\mathbf{u}) && \text{in } \Omega, \\ \mathbf{u} &= \mathbf{0} && \text{on } \Gamma_D, \\ \mathbf{s} \cdot \mathbf{n} &= \mathbf{t} && \text{on } \Gamma_N, \\ \mathbf{s} \cdot \mathbf{n} &= \mathbf{0} && \text{on } \partial\Omega - \Gamma_D - \Gamma_N, \\ -(1 - \rho)\mathbf{1} &\leq \beta(\boldsymbol{\sigma} - \mathbf{s}) \leq (1 - \rho)\mathbf{1} && \text{in } \Omega, \\ \boldsymbol{\sigma}^{\min} \rho &\leq \mathbf{s} \leq \boldsymbol{\sigma}^{\max} \rho && \text{in } \Omega, \\ 0 &\leq \rho \leq 1 && \text{a.e. in } \Omega, \\ \mathbf{u}^{\min} &\leq \mathbf{u} \leq \mathbf{u}^{\max} && \text{in } \Omega. \end{aligned} \tag{2}$$

It is now possible to show for the relaxed problem the existence of a solution, and that the discretized problem satisfies the linear constraint qualification condition.

3. NUMERICAL REALIZATION

Usual finite element discretization with linear elements for ρ and \mathbf{u} and constant elements for \mathbf{s} lead to a very large scale optimization problem. In [5], we solve the discretized problem with IPOPT used as a black-box routine, which is realizing a primal-dual interior point method. Nevertheless, the algorithm behaves robust and produces reliable results. One test example shows the following picture where the left part shows the load condition, bearings and geometry and the left one the optimal design with respect to local von Mises constraints.



Here set $\gamma = 2$ and started the ϵ -continuation with $\epsilon^0 = 1$ where decreased ϵ over 4 levels as $\epsilon^{l+1} = \epsilon^l/4$. A mesh with 17291 elements results finally in a problem with 355097 unknowns and 242502 constraints (including slack variables).

One possibility to speed up the calculation is to construct a solver for the linear KKT-system, which results from the interior-point formulation, with optimal complexity. This can be done using a multi-grid approach with a multiplicative Schwarz-type smoother (see e.g. [4]). Here we list the numerical results for $\epsilon = \mu = 0.1$ with a W-cycle and 1 pre- and post-smoothing step, error reduction by a factor of 10^{-8} :

Level	Unknowns	Iterations	Conv. Factor
4	725	18	0.35
5	2853	10	0.14
6	11333	11	0.17
7	45189	11	0.18
8	180485	11	0.18

REFERENCES

- [1] G.D. Cheng and Z. Jiang, Study on topology optimization with stress constraints, *Engineering Optimization*, 20, 129–148 (1992).
- [2] G.D. Cheng and X. Gou, ϵ -relaxed approach in topology optimization, *Structural Optimization* 13, 258–266 (1997).
- [3] J.W. Cahn and J.E. Hilliard, Free energy of a nonuniform system. I. Inter-facial free energy, *J. Chem. Phys.*, 28, 258–267 (1958).
- [4] J. Schöberl and W. Zulehner, On Schwarz-type smoothers for saddle point problems, *Numer. Math.*, 95, 377–399 (2003).
- [5] R. Stainko and M. Burger, Phase-field relaxation of topology optimization with local stress constraints, SFB-Report 04-35 (SFB F013, University Linz) (2004), and submitted.
- [6] M. Stolpe and K. Svanberg, Modeling topology optimization problems as linear mixed 0-1 programs, *Int. J. Numer. Methods Eng.*, 57, 723–739 (2003).

A CONCEPT FOR GLOBAL OPTIMIZATION OF TOPOLOGY DESIGN PROBLEMS

Mathias Stolpe¹, Wolfgang Achtziger² and Atsushi Kawamoto³

¹*Department of Mathematics, Technical University of Denmark (DTU), Denmark*

²*Institute of Applied Mathematics, University of Dortmund, Germany*

³*Toyota Central Research and Development Laboratories Inc., Nagakute Aichi, Japan*

M.Stolpe@mat.dtu.dk, Wolfgang.Achtziger@uni-dortmund.de, Kawamoto@mosk.tytlabs.co.jp

Abstract: We present a concept for solving topology design problems to proven global optimality. We propose that the problems are modeled using the approach of simultaneous analysis and design with discrete design variables and solved with convergent branch and bound type methods. This concept is illustrated on two applications. The first application is the design of stiff truss structures where the bar areas are chosen from a finite set of available areas. The second considered application is simultaneous topology and geometry design of planar articulated mechanisms. For each application we outline a convergent nonlinear branch and bound method and present a numerical example.

Keywords: Stiffness optimization, mechanism design, global optimization, branch and bound.

1. INTRODUCTION

We propose a concept for solving certain classes of topology design problems to proven global optimality. The concept consists of a suitable choice of problem formulation and global optimization method. We propose that the topology design problems are formulated using the approach of simultaneous analysis and design. In these formulations continuous state variables and equilibrium equations are explicitly included. Furthermore, we require that the design variables are discrete. As a special case this includes the important situation that the design variables are binary to indicate presence or absence of material. The choice of optimization method falls on special purpose implementations of branch and bound type methods.

One of the main advantages of this modeling approach is that the objective function and the constraint functions are given as polynomials of low order, generally with only linear or quadratic terms. This is achieved at the expense

of an increased number of variables and constraints compared to a nested formulation stated in the design variables only. In a nested formulation, these functions are often rational functions in which the nominator and denominator are polynomials of high order. Our choice of modeling gives the possibility to take advantage of the particular mathematical structure of the optimization problem. It is possible to tailor global optimization methods, in particular branch and bound methods, and solve large-scale instances to proven global optimality. The concept is illustrated on two applications, design of stiff truss structures and the design of planar articulated mechanisms.

1.1 Reformulations of Topology Design Problems

In Grossman et al. (1992) a special class of discrete truss topology design problems are formulated as linear mixed integer programs. As a direct result of these formulations a special purpose branch and bound method for minimum weight design of linearly elastic trusses with stress and displacement constraints is presented in Bollapragada et al. (2001). Many topology design problems can be modeled as convex mixed 0–1 problems, see Stolpe and Svanberg (2003) and Stolpe (2004). The reformulation results hold for problems arising in a wide range of recent applications of topology optimization of continuum structures and materials. The cornerstone in all these reformulations is the use of simultaneous analysis and design with discrete design variables. In this model the non-convex terms which appear in the problems are bilinear terms involving a binary variable and a continuous variable. It is possible after introducing additional state variables and linear constraints to remove this non-convexity.

Similar reformulation techniques can also be used to construct convex continuous relaxations of the considered discrete problems. This possibility is used extensively when solving the mechanism design problem.

2. BRANCH AND BOUND METHODS

Branch and bound is a deterministic global optimization method based on the concept of divide and conquer and was first introduced for general integer programs in Land and Doig (1960). Branch and bound methods for mixed integer linear programs are described in Nemhauser and Wolsey (1999) and for general global optimization problems in Horst and Tuy (1993). Today methods based on branch and bound are de facto standard for solving large-scale linear and convex quadratic mixed integer programs.

In branch and bound algorithms the feasible set of the problem is partitioned into subsets (branching). For each subset a lower and an upper bound on the objective function value are determined (bounding). The lower bound is often found by solving a continuous relaxation of the problem over the subset.

A relaxation can be obtained by relaxing difficult constraints such as integer requirements. Upper bounds are given as the objective function values for solutions which are feasible to the problem. The partition of the feasible set is represented by an enumeration tree in which the sons of a given node represent a partition of the feasible region of the father. One of the key features of branch and bound methods is the ability to delete sets in the partition (pruning or fathoming) on which it can be shown that a global minimizer is not located. This corresponds to excluding entire subtrees from further consideration and thus avoid complete enumeration. Associated with the enumeration tree is the global lower bound lb defined as the lowest lower bound over all unpruned (active) nodes in the enumeration tree and the global upper bound ub given as the optimal objective function value of the best found feasible solution (the incumbent). Using the global bounds lb and ub it is possible to obtain a measure of the closeness from the incumbent to the global optimal solution by computing either the absolute gap $ub - lb$ or the relative gap $(ub - lb)/lb$ if $lb > 0$.

Many factors influence the behavior of branch and bound methods. Two of the most important are the quality and the mathematical structure of the relaxation. The relaxation should be a good approximation of the original problem. The strength of a relaxation is often measured by comparing the optimal objective function value of the relaxation and the optimal objective function value of the original problem (once this has been found). The relaxation should also be tractable and therefore the relaxations are often smooth and convex problems. The choice of method for solving the relaxation should preferably benefit from good starting information since this is almost always available. Another factor which can greatly influence the convergence of branch and bound methods is the generation of good feasible solutions by heuristics.

We next present the two applications from the field of topology optimization for which it is possible to tailor the different parts of a branch and bound method such that large-scale instances can be solved to global optimality.

3. APPLICATIONS

The first of the two applications is the classical problem of finding the stiffest truss subject to a volume constraint. The design variables are the cross section areas of the bars in the ground structure which are chosen from a finite set of available areas. The second application is simultaneous geometry and topology optimization of planar articulated mechanisms. The mechanism is modeled using a truss representation and the binary design variables indicate presence or absence of the bars in the ground structure. In both applications the state variables are the nodal displacements.

3.1 Design of Stiff Truss Structures

We consider the following single load minimum compliance problem where the bar areas a are to be chosen from a finite set of available areas.

$$\begin{aligned} & \underset{a,u}{\text{minimize}} && \frac{1}{2} f^T u && \text{(P)} \\ & \text{subject to} && K(a)u = f, && \sum_{j=1}^n a_j l_j \leq V, \\ & && a_j \in \{a_j^1, \dots, a_j^{m_j}\}, && j = 1, \dots, n. \end{aligned}$$

The elastic equilibrium of a truss subject to a static external nodal load vector $f \in \mathbb{R}^d$ is assumed to be given by $K(a)u = f$, where $u \in \mathbb{R}^d$ denotes the nodal displacement vector, and d denotes the number of degrees of freedom of the ground structure. The stiffness matrix $K(a) \in \mathbb{R}^{d \times d}$ in global coordinates may be written as

$$K(a) = \sum_{j=1}^n a_j K_j = \sum_{j=1}^n a_j \frac{E_j}{l_j} \gamma_j \gamma_j^T = \sum_{j=1}^n a_j b_j b_j^T.$$

Here, l_j is the bar length, E_j is the Young's modulus of the material used for the j th bar, γ_j is a vector of direction cosines, and $b_j = \sqrt{(E_j/l_j)} \gamma_j$. The available areas are assumed to satisfy $0 \leq a_j^1 < \dots < a_j^{m_j} < +\infty$.

A "natural" continuous relaxation of the discrete minimum compliance problem (P) is obtained if the requirements $a_j \in \{a_j^1, \dots, a_j^{m_j}\}$ are relaxed to $a_j^1 \leq a_j \leq a_j^{m_j}$. We study here relaxations of (P) with arbitrary box-constraints on the design variables. The relaxation is the non-convex continuous minimum compliance problem

$$\begin{aligned} & \underset{a,u}{\text{minimize}} && \frac{1}{2} f^T u && \text{(R)} \\ & \text{subject to} && K(a)u = f, && \sum_{j=1}^n a_j l_j \leq V, \\ & && L_j/l_j \leq a_j \leq U_j/l_j, && j = 1, \dots, n. \end{aligned}$$

This covers the relaxation of (P) with the constraints $a_j^1 \leq a_j \leq a_j^{m_j}$ if $L_j = a_j^1 l_j$ and $U_j = a_j^{m_j} l_j$. There exist numerous equivalent reformulations of the continuous minimum compliance problem (R), see e.g. Achtziger et al. (1992), Ben-Tal and Bendsøe (1993), and Ben-Tal and Nemirovski (1994, 1997). One such reformulation is the indefinite quadratic program

$$\begin{aligned}
 & \underset{u,s,\mu}{\text{minimize}} && \frac{1}{2}(u^T, s^T, \mu)C(u^T, s^T, \mu)^T - f^T u && \text{(QP)} \\
 & \text{subject to} && -\tilde{B}^T u - s - \mu e \leq 0, \\
 & && \tilde{B}^T u - s - \mu e \leq 0, \\
 & && s \geq 0, \mu \geq 0,
 \end{aligned}$$

where $e \in \mathbb{R}^n$ is a vector of all ones, the symmetric indefinite matrix

$$C = \begin{pmatrix} \sum_{j=1}^n \frac{L_j}{l_j} K_j & 0 & 0 \\ 0 & \text{diag}(U - L) & U - L \\ 0 & (U - L)^T & V - \sum_{j=1}^n L_j \end{pmatrix} \in \mathbb{R}^{(d+n+1) \times (d+n+1)}$$

and the matrix $\tilde{B} = \left(\frac{1}{\sqrt{l_1}}b_1 \quad \frac{1}{\sqrt{l_2}}b_2 \quad \cdots \quad \frac{1}{\sqrt{l_n}}b_n \right) \in \mathbb{R}^{d \times n}$. The relaxation (R) and the quadratic program (QP) are closely related.

PROPOSITION 1 *The following statements are equivalent:*

- (i) *Problem (R) possesses a solution.*
- (ii) *Problem (R) is feasible.*
- (iii) *Problem (QP) possesses a solution.*
- (iv) *Problem (QP) is bounded.*

In any case, $\inf(R) = -\inf(QP)$.

Given a Karush–Kuhn–Tucker (KKT) point of the quadratic program (QP), a global minimizer of the non-convex relaxation (R) can be constructed.

THEOREM 2 *Let (u, s, μ) be a KKT-point of (QP) with multipliers σ^-, σ^+, ρ and κ . If $\mu > 0$ then (a, u) is a global optimizer of (R) where*

$$a_j = \begin{cases} \frac{L_j}{l_j} + \frac{1}{\mu l_j} \left[(\sigma_j^- + \sigma_j^+) - (U_j - L_j)s_j \right] & \text{if } U_j > L_j, \\ L_j/l_j & \text{if } U_j = L_j. \end{cases}$$

In view of the branch and bound method we must solve the relaxation (R) repeatedly for different choices of bounds L and U . Now observe the following crucial effect when (QP) is solved instead of (R). The bounds L and U appear *solely in the objective function* of (QP), and the feasible set of (QP) remains identical for all choices of L and U . Hence, independent of the choice of L and U a feasible point of (QP) is immediate. In a branch and bound context, a good feasible solution to the relaxation is given by the optimal solution of the relaxation at the father node in the enumeration tree.

The branch and bound method. A strong lower bound on the optimal compliance is given by an optimal solution to the non-convex relaxation (R) which in turn is obtained by solving the indefinite quadratic program (QP). Upper bounds, i.e. feasible solutions, are found by a fast heuristic based on rounding. Given a globally optimal solution to the non-convex relaxation (R) the optimal bar areas are rounded to the nearest area in $\{a_j^1, \dots, a_j^{m_j}\}$ for all j while satisfying the volume constraint. This gives a candidate topology. If a displacement vector satisfying the equilibrium equations can be found for this candidate design a feasible solution is found. Every tenth iteration the node chosen for further refinement in the enumeration tree is the one where the least lower bound is attained (the best-bound-first rule). From this node we resort to a depth-first search strategy. The feasible set is partitioned using variable dichotomy branching on the discrete area variables. The design variable for branching is chosen according to the maximum integer infeasibility rule. With these choices of relaxation, node selection rule, and branching rule the branch and bound method is finitely convergent. Hence, a global optimal solution is obtained after solving a finite number of relaxations. The branch and bound method is implemented in MATLAB. The MATLAB code controls the overall program flow as well as constructs and maintains the branch and bound search tree. The indefinite quadratic programs (QP) are solved by the sparse sequential quadratic programming package SNOPT described in Gill et al. (2002).

Numerical example. The design domain, boundary conditions, and external load for a cantilever beam example are shown in Figure 1(a). A ground structure with $n = 72$ potential bars and $d = 48$ degrees of freedom is shown in Figure 1(b). The available volume $V = 60$ and the area variables are to be chosen from the set $\{0, 1, 3, 5, 7, 9\}$. The optimal topology to the continuous relaxation (R) is shown in Figure 1(c) and the optimal topology to the discrete minimum compliance problem (P) is shown in Figure 1(d). In this example the optimal topologies of the relaxed and the mixed discrete problem are identical and the heuristic found the optimal solution in the root node of the enumeration tree. The initial relative gap for this example is merely 2%. Global optimality of the solution was assured after processing 4211 nodes (= relaxations solved) of the enumeration tree.

3.2 Design of Planar Articulated Mechanisms

In the second application we consider an optimization model and a method for the design of planar articulated mechanical mechanisms. The mechanism design problem is modeled as a non-convex mixed integer program in which the optimal topology and geometry of the mechanism are determined simultaneously. Details of the problem formulation and the method together with several numerical examples are found in Stolpe and Kawamoto (2005).

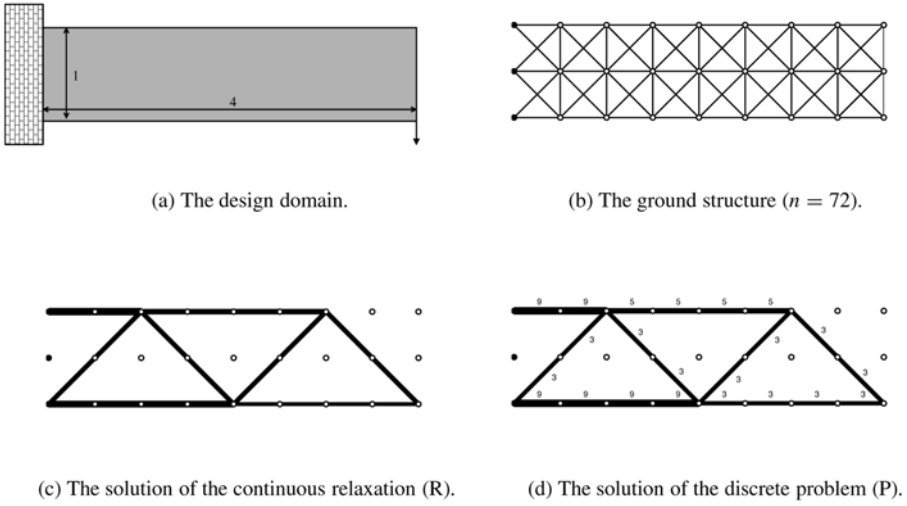


Figure 1. A cantilever beam example.

A mechanism consists of links which are connected by joints. An articulated mechanism is a mechanism which gains all of its mobility from its joints. Instead of using rigid bars and revolute joints in the analysis of the mechanism we propose to use an elastic truss representation. The use of a truss model is an approximation of the rigid bars and revolute joints. Therefore the modulus of elasticity is chosen sufficiently large such that the articulated mechanisms cannot rely on the elasticity of the bars to function. In the mechanical model we assume that large displacements are allowed but the strains are small. The strains are given by the Green–Lagrange strain measure. We also assume and that the material is linearly elastic and the material properties remain constant.

The topology of the mechanism is described by the binary vector $a \in \mathbb{B}^n$ indicating presence or absence of the bars in the ground structure. The geometry is described by the vector $\chi \in \mathbb{R}^{2N}$ containing the coordinates of the nodes. For a given topology and geometry the displacement vector $u \in \mathbb{R}^d$ should be a minimizer of the potential energy. In order to find a stable equilibrium, we need to find a local minimizer or at least a stationary point of the potential energy $\Pi(a, u, \chi)$ such that the Hessian of Π with respect to u is positive semidefinite. The first order necessary optimality conditions for this problem, in the form of equilibrium equations, are given by

$$\nabla_u \Pi(a, u, \chi) = 0. \tag{1}$$

The second order conditions are given by the nonlinear matrix inequality

$$\nabla_{uu}^2 \Pi(a, u, \chi) \succeq 0. \tag{2}$$

Since we want the optimal design to be able to perform its task repeatedly and with certainty, the elastic stability of the mechanism must be assured. We therefore include a constraint on the global stability of the mechanism in the problem formulation. A commonly used model for the stability analysis of trusses is the linear buckling model, see e.g. Bathe (1982). The condition on the truss stability can, in the linear buckling model, be stated as a nonlinear matrix inequality, see e.g. Ben-Tal et al. (2000). The stability condition is given by the non-linear matrix inequality

$$K(a, \chi) + G(a, u_0, \chi) \succeq 0, \quad (3)$$

where $u_0 \in \mathbb{R}^d$ is a solution to the small-deformation equilibrium equations

$$K(a, \chi)u_0 = p. \quad (4)$$

The matrices $K(a, \chi)$ and $G(a, u_0, \chi)$ are the linear stiffness matrix and the geometry matrix of the truss, respectively. The global stability condition (3) guarantees that the mechanism is stable in the initial configuration, while the condition (2) guarantees that the mechanism is stable in the final configuration.

The problem under consideration is to design a stable mechanism consisting of V_n bars with exactly one mechanical degree of freedom. Given an input force $p \in \mathbb{R}^d$, the output port displacement in the desired direction $c \in \mathbb{R}^d$ should be maximized. The (essential parts of the) mechanism design problem is stated as the non-convex mixed integer optimization problem

$$\begin{aligned} & \underset{a, u, u_0, \chi}{\text{minimize}} && -c^T u \\ & \text{subject to} && \nabla_u \Pi(a, u, \chi) = 0, \nabla_{uu}^2 \Pi(a, u, \chi) \succeq 0, \\ & && K(a, \chi)u_0 = p, K(a, \chi) + G(a, u_0, \chi) \succeq 0, \\ & && d_m(a) = 1, e^T a = V_n, a \in \{0, 1\}^n, \end{aligned}$$

where $d_m(a)$ denotes the number of mechanical degrees of freedom. Included in the mechanism design formulation (but not shown here) are also constraints on the member stresses and bounds on the geometry and displacement variables.

The branch and bound method. A mixed integer non-convex relaxation is obtained after temporarily removing the nonlinear matrix inequalities (2) and (3). This relaxation is then rewritten by introducing additional continuous state variables representing bar forces, strains, lengths, and disaggregating the equilibrium equations (1) and (4). The resulting problem consists of linear, bilinear, and quadratic terms. The nonlinear terms are then replaced by their convex envelopes. Finally, the integer requirements $a \in \{0, 1\}^n$ are relaxed to $a \in [0, 1]^n$. The final relaxation is a convex all-quadratic program. The node chosen for further refinement is the one where the least lower bound is

attained. Branching is first performed on the discrete design variables. Once all discrete variables are fixed, branching is done on the continuous displacement and geometry variables. The removed stability conditions (2) and (3) are reintroduced once a candidate topology has been found in the form of feasibility tests. The stability constraints are thus enforced to hold for all candidate designs. The choices of node selection rule, branching rule, and relaxation guarantee convergence (but not finite convergence) of the branch and bound method, see e.g. Horst and Tuy (1993). The branch and bound method is implemented in MATLAB. The MATLAB code controls the overall program flow and the branch and bound tree. The convex all-quadratic relaxations are solved using the package SNOPT.

Numerical example. A ground-structure consisting of $n = 66$ potential bars and $d = 18$ degrees of freedom for the example is shown in Figure 2(a). The bounds on the nodal positions are depicted by black boxes in the figure. In this example the design domain is a two dimensional square with width and height equal to one. The requested number of active bars in the mechanism is 10. The modulus of elasticity is in all examples set to $E_j = 10$ for all j . The stiffnesses of the linear springs at the input and output ports are denoted by $k_{in} = 2.0$ and $k_{out} = 0.02$, respectively. The external load vector p and the output direction vector c have $+1$ or -1 entries in the positions corresponding to the degrees of freedom for the input and output port displacements and zero entries otherwise. In Figure 2(b) the optimal design to the simultaneous topology and geometry design problem is shown in black. The optimal design with initial nodal positions is shown in grey in Figure 2(b). The optimal objective function value for the simultaneous topology and geometry problem is $c^T u = 0.993$. Global optimality of the solution was assured after processing 163 nodes of the enumeration tree.

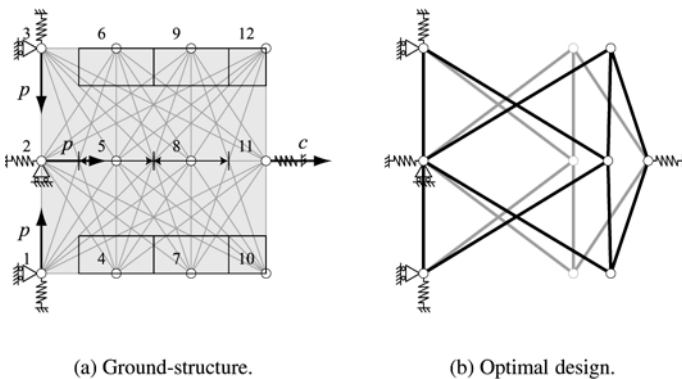


Figure 2. Ground-structure and optimal design for the example.

REFERENCES

- Achtziger, W., Bendsøe, M.P., Ben-Tal, A. and Zowe, J. (1992) Equivalent displacement based formulations for maximum strength truss topology design, *Impact of Computing in Science and Engineering*, 4, 315–345.
- Bathe, K.-J. (1982) *Finite Element Procedures in Engineering Analysis*, Prentice-Hall, Englewood Cliffs, NJ.
- Ben-Tal, A. and Bendsøe, M.P. (1993) A new method for optimal truss topology design, *SIAM Journal on Optimization*, 3(2), 322–358.
- Ben-Tal, A. and Nemirovski, A. (1994) Potential reduction polynomial time method for truss topology design. *SIAM Journal on Optimization*, 4(3), 596–612.
- Ben-Tal, A. and Nemirovski, A. (1997) Robust truss topology design via semidefinite programming, *SIAM Journal on Optimization*, 7(4), 991–1016.
- Ben-Tal, A., Jarre, F., Kočvara, M., Nemirovski, A. and Zowe, J. (2000) Optimal design of trusses under a nonconvex global buckling constraint, *Optimization and Engineering*, 1, 189–213.
- Bollapragada, S., Ghattas, O. and Hooker, J.N. (2001) Optimal design of truss structures by logical-based branch and cut. *Operations Research*, 49(1), 42–51.
- Gill, P.E., Murray, W. and Saunders, M.A. (2002) SNOPT: An SQP algorithm for large-scale constrained optimization, *SIAM Journal on Optimization*, 12(4), 979–1006.
- Grossman, I., Voudouris, V.T. and Ghattas, O. (1992) Mixed-integer linear programming formulations of some nonlinear discrete design optimization problems, in *Recent Advances in Global Optimization*, C.A. Floudas and P.M. Pardalos (eds), Princeton University Press.
- Horst, R. and Tuy, H. (1993) *Global Optimization: Deterministic Approaches*, Springer-Verlag.
- Land, A.H. and Doig, A.G. (1960) An automatic method for solving discrete programming problems, *Econometrica*, 28, 497–520.
- Nemhauser, G. and Wolsey, L. (1999) *Integer and Combinatorial Optimization*, Wiley.
- Stolpe, M. (2004) On the reformulation of topology optimization problems as linear or convex quadratic mixed 0-1 problems, Technical Report, Department of Mathematics, Technical University of Denmark (DTU). MAT-Report No. 2004-13. Submitted.
- Stolpe, M. and Kawamoto, A. (2005) Design of planar articulated mechanisms using branch and bound. *Mathematical Programming, Series B*, 103, 357–397.
- Stolpe, M. and Svanberg, K. (2003) Modeling topology optimization problems as linear mixed 0-1 programs, *International Journal for Numerical Methods in Engineering*, 57(5), 723–739.

Image Processing Ideas and Level Sets

IMPEDANCE IMAGING FOR INHOMOGENEITIES OF LOW VOLUME FRACTION

Yves Capdeboscq

Université de Versailles Saint-Quentin-en-Yvelines, 78035 Versailles Cedex, France

Yves.Capdeboscq@uvsq.fr

Abstract: We first review some recent representation formulas for the boundary voltage perturbation arising as a result of the presence of low volume fraction inhomogeneities, and then discuss the attainability of the limit set of possible polarization tensors by simply connected domains.

Keywords: Impedance imaging, polarization tensors.

1. INTRODUCTION

Impedance imaging uses measurements of boundary voltage potentials and associated boundary currents to obtain informations about the internal conductivity profile of an object. Without any a priori assumptions about the conductivity profile, impedance imaging is known to be extremely ill-conditioned [1]. The conditioning may be drastically improved in several practical important cases by the introduction of a priori information on the nature of the conductivity profile to be identified. One such case is that of a known background medium with low volume fraction inhomogeneities, the volume, locations and shapes of which one should like to estimate.

Over the last two decades, a considerable amount of work has been dedicated to the imaging of such low volume fraction inhomogeneities. This presentation does not attempt to give an exhaustive survey of all the work of this nature. Here, the focus shall be on certain representation formulas that have emerged [3, 5, 12–14]. After introducing these formulas in the general case, some properties of the polarization tensors that appear will be reviewed. Finally, the question of the attainability of the optimal bounds by simply connected sets will be discussed.

For simplicity, the focus of this talk is on the problem of electrical conduction. However, most of the results that are presented exist both for conduction and elasticity.

2. REPRESENTATION FORMULA

Let $\Omega \subset \mathbf{R}^n$ be a bounded smooth domain representing the entire object being imaged. Let K_0 be a compact subset of Ω and let $\omega_\epsilon \subset K_0 \subset \Omega$ represent the unknown set of inhomogeneities. The subscript ϵ on ω_ϵ is used to indicate that the focus is on “small” sets (in the sense of Lebesgue measure). A concrete example could be

$$\omega_\epsilon = \cup_{k=1}^N (z_k + \epsilon B_k),$$

where the “centers” z_k are points in Ω , and the “shapes” B_k are bounded, smooth domains. Another example could be

$$\omega_\epsilon = \cup_{k=1}^N \omega_\epsilon^k,$$

where each of the ω_ϵ^k has the form

$$\omega_\epsilon^k = \{x' + \eta n(x') : x' \in \sigma_k, \eta \in (-\epsilon, \epsilon)\}.$$

Here all σ_k are smooth non intersecting surfaces, and $n(x')$ denotes a smooth unit normal vector field to σ_k . Let γ_ϵ denote the conductivity in the presence of the inhomogeneities. It is given by $\gamma_\epsilon(x) = \gamma_0(x)$ for $x \in \Omega \setminus \omega_\epsilon$ and $\gamma_\epsilon(x) = \gamma_1(x)$ for $x \in \omega_\epsilon$, the functions $\gamma_0(\cdot)$ and $\gamma_1(\cdot)$ being smooth, and such that

$$0 < c < \gamma_0(x)\gamma_1(x) < C < \infty, x \in \Omega.$$

The background voltage potential u_0 and the voltage potential in the presence of inhomogeneities u_ϵ are the solutions of

$$\left\{ \begin{array}{l} \nabla \cdot (\gamma_0(x)\nabla u_0) = 0 \quad \text{in } \Omega, \\ \gamma_0 \frac{\partial u_0}{\partial n} = \psi \quad \text{on } \partial\Omega, \end{array} \right. \quad \text{and} \quad \left\{ \begin{array}{l} \nabla \cdot (\gamma_\epsilon(x)\nabla u_\epsilon) = 0 \quad \text{in } \Omega, \\ \gamma_\epsilon \frac{\partial u_\epsilon}{\partial n} = \psi \quad \text{on } \partial\Omega. \end{array} \right.$$

Here $\psi \in H^{1/2}(\partial\Omega)$ and $\int_{\partial\Omega} \psi = 0$ is the prescribed boundary current. The voltage potential is normalized by the assumption that $\int_{\partial\Omega} u_0 d\sigma = \int_{\partial\Omega} u_\epsilon d\sigma = 0$. The available data is the trace on the boundary of the voltage potential u_ϵ . The asymptotic limit of u_ϵ is straightforward: the sequence u_ϵ converges strongly in $H^1(\Omega)$ to u_0 . Informations on the inclusion can be extracted from the boundary voltage difference $u_\epsilon - u_0$. An integration by parts shows that, for all $w \in H^1(\Omega)$,

$$\begin{aligned} \int_{\Omega} \gamma_0 \nabla(u_\epsilon - u_0) \cdot \nabla w dx &= \int_{\Omega} (\gamma_0 - \gamma_\epsilon) \nabla u_\epsilon \cdot \nabla w dx, \\ &= |\omega_\epsilon| \int_{\Omega} (\gamma_0 - \gamma_1) \nabla u_\epsilon \cdot \nabla w \frac{1}{|\omega_\epsilon|} 1_{\omega_\epsilon}(x) dx. \end{aligned} \tag{1}$$

Since the function $|\omega_\epsilon|^{-1} 1_{\omega_\epsilon}(x)$ is bounded in $L^1(\Omega)$ we may extract a subsequence (also denoted by ϵ) such that it converges to a regular Borel measure μ , in the sense of measures

$$|\omega_\epsilon|^{-1} 1_{\omega_\epsilon}(x) dx \rightarrow d\mu \text{ as } |\omega_\epsilon| \rightarrow 0. \tag{2}$$

Introducing the Neumann function of the unperturbed problem

$$\begin{cases} \nabla_x \cdot (\gamma_0(x) \nabla_x N(x, y)) = 0 & \text{in } \Omega, \\ \gamma_0(x) \frac{\partial u_0}{\partial n_x} = -\delta_y + \frac{1}{|\partial\Omega|} & \text{on } \partial\Omega, \end{cases}$$

We deduce from (1) that

$$u_\epsilon(y) - u_0(y) = |\omega_\epsilon| \int_\Omega (\gamma_0 - \gamma_1)(x) \nabla u_\epsilon \cdot \nabla N(x, y) \frac{1}{|\omega_\epsilon|} 1_{\omega_\epsilon}(x) dx.$$

In order to state the general representation result, we need to introduce the following family of auxiliary problems

$$\begin{cases} \nabla \cdot (\gamma_\epsilon(x) \nabla v_\epsilon^j) = \frac{\partial \gamma_0}{\partial x_j}(x) & \text{in } \Omega, \\ \gamma_\epsilon \frac{\partial u_\epsilon}{\partial n} = \gamma_0(x) n_j & \text{on } \partial\Omega, \end{cases}$$

normalized as before by $\int_{\partial\Omega} v_\epsilon^j d\sigma = 0$. It is proved in [10] that up to the extraction of a subsequence (still indexed by ϵ),

$$\lim_{|\omega_\epsilon| \rightarrow 0} \frac{1}{|\omega_\epsilon|} \int_{\omega_\epsilon} \frac{\partial}{\partial x_i} v_\epsilon^j \phi(x) dx = \int_\Omega M_{ij}(x) \phi(x) d\mu, \tag{3}$$

for any $\phi \in C^0(\overline{\Omega})$. The following representation result for all possible leading terms of the boundary voltages $u_\epsilon - U$ was established in [10].

Theorem 2.1. *Given a family of measurable sets $\omega_\epsilon \subset K_0 \subset \Omega$, containing sets of arbitrarily small Lebesgue measure, let ω_ϵ be a subsequence such that $|\omega_\epsilon| \rightarrow 0$ and such that (2) and (3) hold. Then*

$$\begin{aligned} &u_\epsilon(y) - u_0(y) \\ &= |\omega_\epsilon| \int_\Omega (\gamma_0 - \gamma_1)(x) M \nabla u_0 \cdot \nabla N(x, y) d\mu(x) + o(|\omega_\epsilon|), \quad y \in \partial\Omega. \end{aligned}$$

The term $o(|\omega_\epsilon|)$ is such that $\|o(|\omega_\epsilon|)\|_{L^\infty(\partial\Omega)} / |\omega_\epsilon|$ converges to 0 for any fixed $\psi \in H^{-1/2}$ and uniformly on $\{\psi : \int_{\partial\Omega} \psi d\sigma = 0, \|\psi\|_{L^2(\partial\Omega)} \leq 1\}$.

Special instances of this representation formula were derived for specific collections of inhomogeneities [7, 8, 13, 14] and can be used to very effectively

reconstruct the support of μ [3, 9]. In the case of inhomogeneities of small diameter, i.e. when $\omega_\epsilon = \cup_{k=1}^N (z_k + \epsilon B_k)$ it is possible to obtain an asymptotic expansion to any order in ϵ ; this is explained in [3], also in the elasticity case, originally published in [4] (see also [19]). In that case, assuming for simplicity that $\omega_\epsilon = z + \epsilon B_\epsilon$, the expansion for the displacement u_ϵ starts by

$$u_\epsilon(x) = u_0(x) + \epsilon^m \sum_{i,j,p,q=1}^m \partial_i u^j(z) \partial_p N_{kq}(x-z) m_{pq}^{ij} + O(\epsilon^{2m}),$$

where $M = (m_{pq}^{ij})$ is the elastic moment tensor, and N is the Neumann function associated with the Lamé operator $\mathcal{L}_{\lambda,\mu}$.

Remark 2.2. The concept of polarization tensor is not new, neither in conduction nor in elasticity (see e.g. [3, 16, 17, 19–22, 24, 25]), and has been introduced either as the trace at infinity of an inclusion (or a cavity) inside an infinite domain, or as the small volume fraction limit of an homogenized operator, in a periodic setting. Here, the only assumption on the set ω_ϵ is that its measure tends to zero with ϵ , and no intermediate homogenization step is required.

3. BOUNDS FOR THE POLARIZATION TENSOR

In the spirit of effective media theory, it is possible to characterize the set of matrices M that may occur as polarization tensors. This characterization is in terms of the eigenvalues, more specifically in terms of bounds for the expression $\text{Trace}(M)$ and $\text{Trace}(M^{-1})$. While these bounds may be formulated point wise, they have only been rigorously verified in the following average sense [11, 12].

Theorem 3.1. *Suppose that the conductivities γ_0 and γ_1 are constants, with $\gamma_0 \neq \gamma_1$. Then*

$$\text{Trace} \left(\int_{\Omega} M d\mu \right) \leq m - 1 + \frac{\gamma_0}{\gamma_1} \quad (4)$$

and

$$\text{Trace} \left(\int_{\Omega} M d\mu \right)^{-1} \leq m - 1 + \frac{\gamma_1}{\gamma_0}. \quad (5)$$

Remark 3.2. Bounds (4)–(5) are very related to the so-called Hashin-Strikman bounds in Homogenization Theory [18, 23], and the proof relies on the Hashin-Strikman variational technique as described in [15]. These bounds were derived as dilute limits of effective tensors in [6, 17].

In the case $m = 2$, the trace and inverse trace bounds are optimal in the sense that every pair (λ_1, λ_2) in the set

$$\mathcal{E} = \left\{ (\lambda_1, \lambda_2) \in (\mathbf{R}_+)^2 \text{ s.t. } \lambda_1 + \lambda_2 \leq 1 + \frac{\gamma_0}{\gamma_1} \text{ and } \lambda_1^{-1} + \lambda_2^{-1} \leq 1 + \frac{\gamma_1}{\gamma_0} \right\}$$

arises as the eigenvalues of a polarization tensor in the presentation formula from Theorem 2.1. The polarization tensor of corresponding to the set

$$\left\{ (x_1, x_2) \in (\mathbf{R}_+)^2 \text{ s.t. } \frac{x_1^2}{a^2} + \frac{x_2^2}{b^2} \leq 1 \right\}$$

is given by [9]

$$M = \begin{pmatrix} \frac{\gamma_0(a+b)}{\gamma_1 b + \gamma_0 a} & 0 \\ 0 & \frac{\gamma_0(a+b)}{\gamma_1 a + \gamma_0 b} \end{pmatrix},$$

and this shows that the lower bound (5) is attained by elliptic inclusions. It is possible to show that the full set is obtained with “washers”, i.e., confocal ellipses [12]. In terms of diameter of the inclusion (at constant volume), “washers” are natural candidates for an upper estimate. It is however reasonable to suppose that in many cases the inclusions would be simply connected. The attainability of the full set \mathcal{E} by simply connected objects as been the subject of recent work [2]. Shapes are created by convex combinations of crosses C and ellipses E of unit area. Numerical simulations show that as the cross grows longer and thinner, it tends to the upper bound (4). Longer and thinner ellipses tend to the intersection of the two bounds, that is, $\lambda_1 = 1$ and $\lambda_2 = \gamma_0/\gamma_1$ (or vice-versa). Numerical simulation show that the convex combinations of these shapes

$$sE + (1 - s)C$$

fill in the rest of the interior of the domain. The next section is devoted to the attainability of the upper bound.

4. ATTAINABILITY OF THE UPPER BOUND

In the following proposition, we compute the limit of the sequence of polarization tensor M_n^H corresponding to a thin rectangular horizontal beams $H_n = [-\theta\delta_n^{-1}, \theta\delta_n^{-1}] \times [-\frac{1}{4}\delta_n, \frac{1}{4}\delta_n]$ where

$$\lim_{n \rightarrow \infty} \delta_n = 0.$$

Note that polarization tensor for similar structures or more complex thin structures have already been derived [8] together with precise regularity estimates for the corresponding correctors. It is very likely that the result below is a

consequence of these more general results. However, since we only need limited informations on the limit polarization tensor, and the structure we consider rather simple, it is possible to provide a independent proof.

Given $\lambda \in \mathbf{R}^2$, we denote by w_n^λ the unique in $D^{1,2}(\mathbf{R}^2)$ of the problem

$$\Delta w_n^\lambda = \frac{\gamma_0 - \gamma_1}{\gamma_0} \operatorname{div} (1_{X_n} (\nabla w_n^\lambda + \lambda)). \tag{6}$$

The domain X_n is a cross, given by $X_n = H_n \cup B_n$, where $H_n = [-\theta\delta_n^{-1}, \theta\delta_n^{-1}] \times [-\frac{1}{4}\delta_n, \frac{1}{4}\delta_n]$ is a thin horizontal beam, whereas B_n is the thin vertical beam $V_n = [-\frac{1}{4}\tilde{\delta}_n, \frac{1}{4}\tilde{\delta}_n][-(1 - \theta)\tilde{\delta}_n^{-1}, (1 - \theta)\tilde{\delta}_n^{-1}]$ rotated of an angle $\varphi \in]0, \pi[$.

$$\lim_{n \rightarrow \infty} \delta_n = \lim_{n \rightarrow \infty} \tilde{\delta}_n = 0.$$

We denote by h_n (resp. b_n) the unique solution in $D^{1,2}(\mathbf{R}^2)$ of the problem

$$\Delta h_n^\lambda \text{ (resp. } b_n^\lambda) = \frac{\gamma_0 - \gamma_1}{\gamma_0} \operatorname{div} (1_{H_n} \text{ (resp. } 1_{B_n}) (\nabla h_n^\lambda \text{ (resp. } b_n^\lambda) + \lambda)), \tag{7}$$

which tends to zero at infinity. In all the sequel, the superscript λ will be dropped.

Proposition 4.1. *The polarization tensor M_n^H for the horizontal beam H_n satisfies*

$$M_n^H = \theta \begin{pmatrix} 1 & 0 \\ 0 & \frac{\gamma_0}{\gamma_1} \end{pmatrix} + o(1). \tag{8}$$

As a consequence, we can derive the following estimates for h_n^λ , solution of (7)

$$\left\| \nabla h_n^\lambda + \lambda_2 1_{H_n} \frac{\gamma_0 - \gamma_1}{\gamma_1} \right\|_{L^2(\mathbf{R}^2)} = o(1) \tag{9}$$

with the notation $\lambda = \lambda_1 e_1 + \lambda_2 e_2$.

Let us first note that, asymptotically, beams H_n and B_n uncouple.

Proposition 4.2. *If w_n is unique the solution in $D^{1,2}(\mathbf{R}^2)$ of problem (6), then*

$$\lim_{n \rightarrow \infty} \|\nabla w_n - \nabla h_n - \nabla b_n\|_{L^2(\mathbf{R}^2)} = 0. \tag{10}$$

As a consequence, the polarization tensor M_n corresponding to the cross X_n satisfies

$$\lim_{n \rightarrow \infty} M_n = \lim_{n \rightarrow \infty} M_n^H + \lim_{n \rightarrow \infty} M_n^B, \tag{11}$$

where M_n^H and M_n^B are the polarization tensors corresponding to H_n and B_n respectively.

A consequence of (11) is that the Polarization tensor of X_n tends to

$$\theta \begin{pmatrix} 1 & 0 \\ 0 & \frac{\gamma_0}{\gamma_1} \end{pmatrix} + (1 - \theta) \begin{pmatrix} \cos \varphi & \sin \varphi \\ -\sin \varphi & \cos \varphi \end{pmatrix} \begin{pmatrix} \frac{\gamma_0}{\gamma_1} & 0 \\ 0 & 1 \end{pmatrix} \begin{pmatrix} \cos \varphi & -\sin \varphi \\ \sin \varphi & \cos \varphi \end{pmatrix}.$$

By varying θ between 0 and 1 or φ between 0 and π , we see that the bound (4) is described entirely.

We shall show that for all test function ϕ ,

$$\left| \int_{\mathbf{R}^2} \gamma_{X_n} \nabla (w_n - h_n - b_n) \cdot \nabla \phi \right| \leq \|\nabla \phi\|_{L^2(\mathbf{R}^2)} \times o(1), \tag{12}$$

where $o(1)$ is a sequence converging to zero with n , independently of ϕ , and $\gamma_{X_n} = \gamma_0 + 1_{X_n}(\gamma_1 - \gamma_0)$. The conclusion then naturally follows by coercivity of the left-hand side.

Proof of Proposition 4.1. It is sufficient to consider the case $\theta = 1$. We Let us start by noticing that, because of the symmetries of the structure, we have for all n

$$M_n^H e_1 \cdot e_2 = 0.$$

Secondly, M_n^H must satisfy (4) and (5), we only need to prove that

$$M_n^H e_2 \cdot e_2 = \frac{\gamma_0}{\gamma_1} + o(1). \tag{13}$$

Let us now prove (13). Note that, by definition,

$$(\gamma_1 - \gamma_0)M_n^H e_2 \cdot e_2 = \frac{\gamma_1 - \gamma_0}{\gamma_1} \gamma_0 + \min_{\phi \in D_0^{1,2}(\mathbf{R}^2)} \int_{\mathbf{R}^2} \gamma_{H_n} \left| \nabla \phi + 1_{H_n} \frac{\gamma_1 - \gamma_0}{\gamma_1} e_2 \right|^2.$$

It is therefore sufficient to provide a construct ϕ_n such that

$$\lim_{n \rightarrow \infty} \int_{\mathbf{R}^2} \gamma_{H_n} \left| \nabla \phi_n + 1_{H_n} \frac{\gamma_1 - \gamma_0}{\gamma_1} e_2 \right|^2 = 0.$$

Let $f_m(x)$ be the linear function $f_m(x) = 1 - x/m$, where m is a parameter. We define ϕ_n by $\phi_n(-x, y) = \phi_n(x, y)$, $\phi_n(x, -y) = -\phi_n(x, y)$,

$$\phi_n(x, y) = \gamma_1 \begin{cases} y & \text{if } (x, y) \in [0, \theta \delta_n^{-1}] \times [0, \frac{1}{4} \delta_n] \\ \frac{1}{4} \delta_n f_m(y - \frac{1}{4} \delta_n) & \text{if } (x, y) \in [0, \theta \delta_n^{-1}] \times [\frac{1}{4} \delta_n, \frac{1}{4} \delta_n + m] \\ y f_m(x - \theta \delta_n^{-1}) & \text{if } (x, y) \in [\theta \delta_n^{-1}, \theta \delta_n^{-1} + m] \times [0, \frac{1}{4} \delta_n] \end{cases}$$

and if we write $r = \sqrt{(x - \theta \delta_n^{-1})^2 + (y - \frac{1}{4} \delta_n)^2}$ for $r \in [0, m]$ and for $\theta \in [0, \pi/2]$, $\theta = \arctan((y - \frac{1}{4} \delta_n)/(x - \theta \delta_n^{-1}))$, $\phi_n(x, y) = \frac{1}{4} \delta_n f_m(r)$. A straightforward computation shows that $\int_{\mathbf{R}^2} \gamma_{H_n} |\nabla \phi_n + 1_{H_n} \gamma_1 e_2|^2 = o(1)$, if for example $m = \sqrt{\delta_n}$.

Finally, to prove (9), note that h_n is a linear function of λ , and that $M_n^H e_1 \cdot e_1 = 1 + o(1)$ means from

$$(\gamma_1 - \gamma_0)M_n^H e_1 \cdot e_1 = \frac{\gamma_1 - \gamma_0}{\gamma_1}\gamma_0 + \min_{\phi \in D_0^{1,2}(\mathbf{R}^2)} \int_{\mathbf{R}^2} \gamma_{H_n} \left| \nabla \phi + 1_{H_n} \frac{\gamma_1 - \gamma_0}{\gamma_1} e_1 \right|^2,$$

that the gradient of the minimizer tends to zero. □

Proof of Proposition 4.2. The proof relies on the following results, direct consequences of (9)

$$\lim_{\epsilon \rightarrow 0} \|\nabla h_n\|_{L^2(B_n)} = 0, \quad \lim_{\epsilon \rightarrow 0} \|\nabla b_n\|_{L^2(H_n)} = 0, \quad (14)$$

$$\lim_{\epsilon \rightarrow 0} \|\nabla h_n\|_{L^2(H_n \cap B_n)} = 0, \quad \lim_{\epsilon \rightarrow 0} \|\nabla b_n\|_{L^2(H_n \cap B_n)} = 0, \quad (15)$$

By simple algebra, we obtain

$$\begin{aligned} & \operatorname{div} \left((\gamma_0 + 1_{C_n} (\gamma_1 - \gamma_0)) \nabla (w_n - h_n - b_n) \right) \\ &= (\gamma_1 - \gamma_0) \operatorname{div} (1_{B_n} \nabla h_n + 1_{H_n} \nabla b_n) \\ &- (\gamma_1 - \gamma_0) \operatorname{div} (1_{H_n \cap B_n} (\nabla h_n + \nabla b_n + \lambda)). \end{aligned}$$

Thanks to (14) and (15), the last two terms tend to zero strongly in H^{-1} and we have obtained (12).

Let us now prove (11). Note that the polarization tensor M_n is given by [12]

$$\begin{aligned} (\gamma_1 - \gamma_0)M_n \lambda \cdot \lambda &= \int_{\mathbf{R}^n} \gamma_{X_n} \left| \nabla w_n + 1_{X_n} \frac{\gamma_1 - \gamma_0}{\gamma_1} \lambda \right|^2 \\ &+ \frac{\gamma_1 - \gamma_0}{\gamma_1} \gamma_0 |\lambda|^2. \end{aligned}$$

Furthermore, since w_n is a minimizer of the above energy, we have

$$\int_{\mathbf{R}^n} \gamma_{X_n} \left| \nabla w_n + 1_{X_n} \frac{\gamma_1 - \gamma_0}{\gamma_1} \lambda \right|^2 = - \int_{\mathbf{R}^n} \gamma_{X_n} |\nabla w_n|^2 + \int_{\mathbf{R}^n} \gamma_{X_n} \left| \frac{\gamma_1 - \gamma_0}{\gamma_1} \lambda \right|^2. \quad (16)$$

Note that the second integrand is a constant. Using (10) we deduce that up to a sequence ϵ_n converging to zero as n tends to infinity,

$$\begin{aligned} (\gamma_1 - \gamma_0)M_n \lambda \cdot \lambda &= (\gamma_1 - \gamma_0) |\lambda|^2 \theta - \int_{\mathbf{R}^n} \gamma_{H_n} |\nabla h_n|^2 \\ &+ (\gamma_1 - \gamma_0) |\lambda|^2 (1 - \theta) - \int_{\mathbf{R}^n} \gamma_{B_n} |\nabla b_n|^2 \\ &+ \epsilon_n, \end{aligned}$$

where $\gamma_{H_n} = \gamma_0 + 1_{H_n}(\gamma_1 - \gamma_0)$, $\gamma_{V_n} = \gamma_0 + 1_{V_n}(\gamma_1 - \gamma_0)$. Using identities similar to (16), we see that we have in fact obtained

$$(\gamma_1 - \gamma_0)M_n\lambda \cdot \lambda = (\gamma_1 - \gamma_0)M_n^H\lambda \cdot \lambda + (\gamma_1 - \gamma_0)M_n^{VB}\lambda \cdot \lambda + \epsilon_n.$$

□

REFERENCES

- [1] G. Alessandrini, Examples of instability in inverse boundary value problems, *Inverse Problems*, 13, 887–897 (1997).
- [2] H. Ammari, Y. Capdeboscq, H. Kang, E. Kim and M. Lim, Attainability by simply connected domains of optimal bounds for the polarization tensor, *European J. Appl. Math.*, to appear (2006).
- [3] H. Ammari and H. Kang, *Reconstruction of Small Inhomogeneities from Boundary Measurements*, Lecture Notes in Mathematics, Vol. 1846, Springer (2004).
- [4] H. Ammari, H. Kang, G. Nakamura and K. Tanuma, Complete asymptotic expansions of solutions of the system of elastostatics in the presence of an inclusion of small diameter and detection of an inclusion, *J. Elasticity*, 67(2), 97–129 (2002).
- [5] H. Ammari and J.K. Seo, An accurate formula for the reconstruction of conductivity inhomogeneities, *Adv. in Appl. Math.*, 30, 679–705 (2003).
- [6] A.Y. Belyaev and S.M. Kozlov, Hierarchical structures and estimates for homogenized coefficients. *Russian J. Math. Phys.*, 1(1), 5–18 (1993).
- [7] E. Beretta, A. Mukherjee and M.S. Vogelius, Asymptotic formulas for steady state voltage potentials in the presence of conductivity imperfections of small area, *Z. Angew. Math. Phys.*, 52, 543–572 (2001).
- [8] E. Beretta, E. Francini and M.S. Vogelius, Asymptotic formulas for steady state voltage potentials in the presence of thin inhomogeneities. A rigorous error analysis, *J. Math. Pures Appl. (9)*, 82(10), 1277–1301 (2003).
- [9] M. Brühl, M. Hanke and M.S. Vogelius, A direct impedance tomography algorithm for locating small inhomogeneities, *Numer. Math.*, 93(4), 635–654 (2003).
- [10] Y. Capdeboscq and M.S. Vogelius, A general representation formula for boundary voltage perturbations caused by internal conductivity inhomogeneities of low volume fraction, *M2AN Math. Model. Numer. Anal.*, 37(1), 159–173 (2003).
- [11] Y. Capdeboscq and M.S. Vogelius, Optimal asymptotic estimates for the volume of internal inhomogeneities in terms of multiple boundary measurements, *M2AN Math. Model. Numer. Anal.*, 37(2), 227–240 (2003).
- [12] Y. Capdeboscq and M.S. Vogelius, A review of some recent work on impedance imaging for inhomogeneities of low volume fraction, in *Partial Differential Equations and Inverse Problems*, Contemp. Math., Vol. 362, pp. 69–87, Amer. Math. Soc., Providence, RI (2004).
- [13] D.J. Cedio-Fengya, S. Moskow and M.S. Vogelius, Identification of conductivity imperfections of small diameter by boundary measurements. continuous dependence and computational reconstruction, *Inverse Problems*, 14, 553–595 (1998).
- [14] A. Friedman and M.S. Vogelius, Identification of small inhomogeneities of extreme conductivity by boundary measurements: A theorem on continuous dependence, *Arch. Rat. Mech. Anal.*, 105, 299–326 (1989).

- [15] R.V. Kohn and G.W. Milton, On bounding the effective conductivity of anisotropic composites, in *Homogenization and Effective Moduli of Materials and Media* (Minneapolis, MN, 1984/1985), IMA Vol. Math. Appl., Vol. 1, pp. 97–125, Springer, New York (1986).
- [16] V. Kozlov, V. Maz'ya and A. Movchan, *Asymptotic Analysis of Fields in Multi-Structures*, Oxford Mathematical Monographs, Oxford University Press (1999).
- [17] R. Lipton, Inequalities for electric and elastic polarization tensors with applications to random composites, *J. Mech. Phys. Solids*, 41(5), 809–833 (1993).
- [18] K.A. Lurie and A.V. Cherkaev, Exact estimates of conductivity of composites formed by two isotropically conducting media taken in prescribed proportion, *Proc. Roy. Soc. Edinburgh Sect. A*, 99(1–2), 71–87 (1984).
- [19] V. Maz'ya, S. Nazarov and B. Plamenevskij, *Asymptotic Theory of Elliptic Boundary Value Problems in Singularly Perturbed Domains*, of Operator Theory: Advances and Applications, Vols (I) 111, (II) 112, Birkhäuser Verlag, Basel (2000) [translated from German, first published in 1991].
- [20] G.W. Milton, *The Theory of Composites*, Cambridge Monographs on Applied and Computational Mathematics, Cambridge University Press (2002).
- [21] A.B. Movchan, Integral characteristics of elastic inclusions and cavities in the two-dimensional theory of elasticity, *European J. Appl. Math.*, 3(1), 21–30 (1992).
- [22] A.B. Movchan and S.K. Serkov, The Pólya and Szegő matrices in asymptotic models of dilute composites, *European J. Appl. Math.*, 8(6), 595–621 (1997).
- [23] F. Murat and L. Tartar, Calcul des variations et homogénéisation, in *Les Méthodes de l'Homogénéisation Théorie et Applications en Physique*, Coll. Dir. Etudes et Recherches EDF, pp. 319–369, Eyrolles (1985).
- [24] G. Pólya and G. Szegő, *Isoperimetric Inequalities in Mathematical Physics*, Annals of Mathematics Studies, No. 27, Princeton University Press, Princeton, NJ (1951).
- [25] M. Schiffer and G. Szegő, Virtual mass and polarization, *Trans. Amer. Math. Soc.*, 67, 130–205 (1949).

THE PHASE-FIELD METHOD IN OPTIMAL DESIGN

Blaise Bourdin¹ and Antonin Chambolle²

¹*Department of Mathematics, Louisiana State University, Baton Rouge, LA 70803, U.S.A.*

²*CMAF, École Polytechnique, CNRS (UMR 7641), 91128 Palaiseau Cedex, France*

bourdin@math.lsu.edu, chambolle@cmap.polytechnique.fr

Abstract: We describe the phase-field method, a new approach to optimal design originally introduced in Bourdin and Chambolle (2000, 2003). It is based on the penalization of the variation of the properties of the designs, and its variational approximation (in the sense of Γ -convergence). It uses a smooth function, the phase-field, to represent all materials involved.

We describe our approach, and detail its application to two problems.

Keywords: Phase-field, multi-physics optimal design, perimeter penalization.

1. INTRODUCTION

Consider the following generic optimal design problem: given a *reference domain* Ω in \mathbf{R}^N , some $D_0 \subset \Omega$, and two volume fractions $0 \leq \theta_1 \leq \theta_2 \leq 1$, the *admissible designs* are subsets D of Ω , such that

$$\begin{aligned} D_0 &\subseteq D \subseteq \Omega, \\ \theta_1 |\Omega| &\leq |D| \leq \theta_2 |\Omega|. \end{aligned} \tag{1}$$

An optimal design problem is to find an admissible design D minimizing some *objective function*, F , that is:

$$\inf_{D \text{ admissible}} F(D). \tag{2}$$

In this form, optimal designs problems are very likely to be ill-posed. The geometric constraints are not enough to ensure the compactness and closedness of the set of feasible designs. Over the years, several theoretical and numerical workaround have been proposed. In the *homogenization*-based methods, one considers generalized designs, microperforated or laminated materials for example (see Kohn and Strang, 1986; Bendsøe and Kikuchi, 1988; Allaire and Kohn, 1993a, 1993b, 1994; Cherkaev and Kohn, 1997; Allaire et al., 1997;

Cherkaev, 2000, Allaire, 2002, among others). Another class of numerical methods relies on heuristic “filtering” techniques (Diaz and Sigmund, 1995; Sigmund and Petersson, 1998). It was rigorously studied in Bourdin (2001). Lastly, various penalization methods have also been suggested, where one adds an additional term to the objective function, in order to gain compactness.

Among all these choice of penalizations, “perimeter-controlled” optimization has a special place (Haber et al., 1996). It has been long understood that adding a surface term proportional to the perimeter of the designs prevents from sequences of solutions wit rapid oscillations, and makes the problems well posed. This was indeed formalized in Ambrosio and Buttazzo (1993), where (2) is replaced with the following free discontinuity problem:

$$\inf_{D \text{ admissible}} F(D) + \lambda \mathcal{H}^{N-1}(\partial D), \quad (3)$$

where λ is an arbitrary parameter and \mathcal{H}^{N-1} represents the $N - 1$ -dimensional Hausdorff measure *i.e.* the length of ∂D in two dimensions, or its area in three dimensions (see Federer, 1969; Evans and Gariepy, 1992, for instance).

In the absence of an efficient numerical implementation, this method has not been widely accepted. The phase-field approach introduced in Bourdin and Chambolle (2000, 2003) provides such a thing.

2. THE PHASE-FIELD METHOD

The numerical implementation of (3) and in particular the approximation of the perimeter term are challenging. If D is a *set of finite perimeter*, then $\mathcal{H}^{N-1}(\partial D)$ is equal to the *total variation* of χ_D . If one uses *material interpolation schemes*, and replaces the characteristic function with a smooth material density ρ , with values in $[0, 1]$, then the total variation of ρ is given by

$$TV(\rho) = \int_{\Omega} |\nabla \rho| dx, \quad (4)$$

which raises two issues. Numerical minimization of an equivalent of (3) replacing the perimeter term with $TV(\rho)$ is challenging. If one tries to avoid intermediate material densities, using material penalization, for instance, then (4) becomes very stiff, and its numerical approximation non-isotropic (see Petersson et al., 1999; Chambolle, 1999).

Our approach is different. We consider a small parameter ε and introduce the functional

$$\mathcal{P}_{\varepsilon}(\rho) = \frac{1}{c_W} \int_{\Omega} \frac{\varepsilon}{2} |\nabla \rho(x)|^2 + \frac{1}{\varepsilon} W(\rho(x)) dx \quad (5)$$

where W is a l.s.c potential such that $W(0) = W(1) = 0$, $W(x) > 0$ if $x \notin \{0, 1\}$, $W(x) \geq c_1|x|^2 - c_2$ for some $c_1 > 0$ and c_2 , and $c_W = \int_0^1 \sqrt{2W(t)} dt$.

We also extend the objective function F by a \mathcal{F} , defined for any density field $\rho(x) \in L^1(\Omega)$, and such that

$$\mathcal{F}(\chi_D) = F(D), \quad (6)$$

for any set D of finite perimeter, and such that $\mathcal{F}(\rho)$ depends continuously on ρ . Then, we consider the following regularization of the optimal design problem:

$$\inf_{\rho \in \mathcal{D}_A} \mathcal{F}(\rho) + \lambda \mathcal{P}_\varepsilon(\rho), \quad (7)$$

where the set of admissible designs is

$$\mathcal{D}_A = \left\{ \rho \in H^1(\Omega), \rho(x) = 1 \text{ a.e. in } D_0, \text{ and } \theta_1 |\Omega| \leq \int_{\Omega} |\rho(x)| dx \leq \theta_2 |\Omega| \right\}.$$

It is well known (see Alberti, 2000; Modica and Mortola, 1977a, 1977b; Dal Maso, 1993; Braides, 2002, for instance) that if for any small ε there exists a subsequence ρ_{ε_j} of the sequence ρ_ε of minimizers of (7) and a subset $D \in \Omega$, such that $\rho_{\varepsilon_j} \rightarrow \chi_D$ almost everywhere in Ω , then D is a solution of (3). Practically, this means that solving the regularized problem (7) for a “small enough” ε will lead to a good approximation of the solution of (3).

This approach has several advantages over the classical ones. It is independent of the choice of \mathcal{F} , provided that condition (6) is satisfied. In the case of structural optimization, for instance, this means that the debate over the mechanical soundness of various material interpolation law is irrelevant in our case (although it might be used in the numerical implementation as in Bourdin and Chambolle, 2003). From the expression of \mathcal{P}_ε , it is clear that for a given ε , the minimizing sequences of designs are bounded in $H^1(\Omega)$. Classical numerical methods, finite elements or finite differences can be applied without fear of mesh-dependency, checkerboards, or anisotropy for instance.

One of the drawbacks of the method, which is indeed true of all perimeter controlled optimal design method, is that the solution of (3) may not be an open set and regular set. Optimal sets for the penalized problems are sets of finite perimeter, a very wide class of sets that contains very “pathological” sets. If one wishes to carry out a very rigorous analysis of the method applied to a specific objective function, one has to study the regularity of the solutions. This is done in Ambrosio and Buttazzo (1993) for the thermal conductivity problem and in Chambolle and Larsen (2003) in the case of compliance optimization, for instance.

Lastly, the penalization term in (7) takes into accounts only the part of the perimeter of D inside the computational domain. In other words, it does not account for the part of the boundary of D that lies along $\partial\Omega$. This can easily be addressed (see Bourdin and Chambolle, 2003 or Bourdin et al., 2000, for a

similar problem in fracture mechanics). For the sake of simplicity, we do not discuss this issue in this paper.

In the following section, we describe the application of the phase field in the classical context of compliance optimization, then extend it to a multi-phase problem with design-dependent loads. Note that it has already been used in more complicated problems (Burger and Stainko, 2003) and that extension to more general problems involving multiple materials and multiple physics are in progress.

3. A CLASSICAL EXAMPLE: COMPLIANCE OPTIMIZATION

We consider here the classical problem of the design of structure with maximal stiffness under given loads. Let Γ_0 and $\Gamma_f \in \partial\Omega$ be disjoint subsets of the boundary of Ω standing at strictly positive distance from each other. Let f , be a given force on Γ_f , and \mathbf{A} be the linear Hooke's law of an elastic material occupying a subset $D \subset \Omega$. The compliance of D under the load f is defined by

$$F(D) = - \inf_{u=0 \text{ on } \Gamma_0} \int_D \mathbf{A}e(u) : e(u) dx - 2 \int_{\Gamma_f} f \cdot u dx, \quad (8)$$

where $e(u)$ is the symmetrized gradient of u . It is easy to show that the perimeter-controlled optimal design associated with this objective function is well-posed, in the class of sets of finite perimeter. A little more care has to be taken while applying the phase-field regularization, however. Indeed, the straightforward extension of F to characteristic functions χ_D is not continuous. Following a now classical approach, we introduce an arbitrarily weak fictitious material with Hooke's law $\delta\mathbf{A}$ ($\delta > 0$), and extend the compliance as

$$F_\delta(D) = - \inf_{u=0 \text{ on } \Gamma_0} \int_\Omega ((1 - \delta)\chi_D + \delta) \mathbf{A}e(u) : e(u) dx - 2 \int_{\Gamma_f} f \cdot u dx. \quad (9)$$

Note that this step is not strictly related to the phase-field method, but simply about gaining continuity of the objective function with respect to design changes. In Bourdin and Chambolle (2003), it is shown using Γ -convergence, that when $\delta \rightarrow 0$, the minimizers of $F_\delta(D) + \lambda\mathcal{P}(D)$ converges to that of $F(D) + \lambda\mathcal{P}(D)$.

A trivial way to extend F_δ to arbitrary density functions $\rho(x)$ is to consider *any* function continuous monotonous function S such that $S(0) = 0$ and $S(1) = 1$, and

$$\mathcal{F}_\delta(\rho) = - \inf_{u=0 \text{ on } \Gamma_0} \int_\Omega ((1 - \delta)S(\rho) + \delta) \mathbf{A}e(u) : e(u) dx - 2 \int_{\Gamma_f} f \cdot u dx. \quad (10)$$

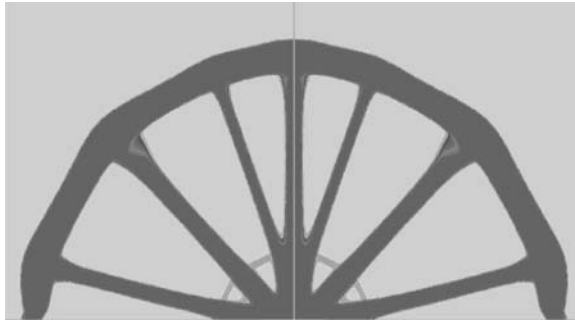


Figure 1. Optimal design of a beam using the phase field method.

Once again, it is shown in Bourdin and Chambolle (2003) that when $\varepsilon \rightarrow 0$, the minimizer $\rho_{\delta_\varepsilon}$ of $\mathcal{F}_\delta(\rho) + \lambda\mathcal{P}_\varepsilon(\rho)$ converge to a χ_{E_δ} , where E_δ minimizes $F_\delta(D) + \lambda\mathcal{P}(D)$ among all admissible designs D . Sending then δ to 0, one obtains convergence of $v_{\delta,\varepsilon}$ to the minimizers of $F(D) + \lambda\mathcal{P}(D)$.

Figure 1 presents a numerical example obtained by Arnaud Anantharaman and Alain Griveau under Antonin Chambolle's supervision, at École Polytechnique. It corresponds to a beam clamped on its lower-left and lower-right corners, and loaded in its center. The density of gray corresponds to the value of the phase field ρ . The function W used here is

$$W(t) = \begin{cases} t(t-1)/2 & \text{if } 0 \leq t \leq 1 \\ +\infty & \text{otherwise,} \end{cases}$$

and the material interpolation law is $S(t) = t^2$.

Note that the density function ρ , has very little intermediate values. Indeed, the second term in (5) penalizes them. The transition of ρ from 0 to 1 along the edges of the designs is still smooth, meaning that piecewise linear finite element, for instance, will provide a good interpolation. It is known indeed that the width of the transition layer around the edges of the designs is of the order of $\varepsilon\pi$, for any $\varepsilon > 0$. This gives an estimate on how small shall one set the regularization parameter, in relation with the mesh size, for example.

4. EXTENSION TO DESIGN-DEPENDENT LOADS

Another strength of our approach is that the phase field also provides a simple way to represent the edges of the designs, and is easy to extend to the case of more than two phases.

In Bourdin and Chambolle (2003), we consider the problem of the minimization of the compliance of structures submitted to fixed pressure loads on parts of their boundary. We consider a domain Ω partitioned in three subsets S (the structure), L (some liquid under a give pressure p), and V the void. The

compliance of this system is given by

$$F(S, L, V) = \inf_u \int_S Ae(u) : e(u) dx - 2 \int_{\partial L} pu(x) \cdot \nu_L(x) d\mathcal{H}^{N-1}(x), \quad (11)$$

where ν_L is the outer normal to the set L , and u varies among kinematically admissible displacement fields which we do not explicit here. A generalization of the perimeter energy to this three phase case would is

$$\Lambda(S, L, V) = \mathcal{H}^{N-1}(\partial S \cap \partial L) + \mathcal{H}^{N-1}(\partial S \cap \partial V) + \mathcal{H}^{N-1}(\partial L \cap \partial V). \quad (12)$$

Intuitively, however, it is clear that if the interface in between the liquid and the void sets has length > 0 , then the compliance (11) is infinite. Indeed, we show (in 2D only) that if $F(S, L, V) < \infty$ then $\mathcal{H}^{N-1}(\partial L \cap \partial V) = 0$, in which case we have

$$\Lambda(S, L, V) = \mathcal{H}^{N-1}(\partial L) + \mathcal{H}^{N-1}(\partial V). \quad (13)$$

Another consequence of that is that it allows the use of a *scalar* phase field: following the analysis of the previous section, we introduce a fictitious material of Hooke's law δA , a phase field ρ , and three material interpolation functions S, L, V such that

$$\begin{cases} V(-1) = 1, V(0) = V(1) = 0 \\ S(-1) = 0, S(0) = 1, S(1) = 0 \\ L(-1) = L(0) = 0, L(1) = 1 \end{cases} \quad (14)$$

In this case, one can approximate $F(S, L, V)$ by a function $F_\varepsilon(\rho)$ similar to (5) where W is now a three-well function such that $W(-1) = W(0) = W(1) = 0$ and $W(x) > 0$ if $x \notin \{-1, 0, 1\}$. Lastly, the compliance $F(S, L, V)$ becomes

$$\begin{aligned} \mathcal{F}_{\delta, \varepsilon}(S, L, V) = \inf_u \int_{\Omega} ((1 - \delta)S(\rho) + \delta) Ae(u) : e(u) dx \\ - 2 \int_{\Omega} pu(x) \cdot \nabla L(\rho) dx. \end{aligned} \quad (15)$$

Note in particular how the surface intergral over ∂L was approximated in terms of $\nabla L(\rho)$. Again using Γ -convergence with respect to δ first and then ε , one can show that the minimizers of $\mathcal{F}_{\delta, \varepsilon} + \lambda \mathcal{P}_\varepsilon$ converge to that of $F(S, L, V) + \lambda \Lambda(S, L, V)$.

Figure 2 represents the design of a piston subject to pressure forces in its lower side, and clamped along the black rectangle on the top left corner. The black colored region correspond to $\rho = 1$, *i.e.* the liquid, the gray area to $\rho = 0$ (the structure), and the white are to the void ($\rho = -1$). The white line correspond to the level line $1/3$ of ρ and the black one to $\rho = -1/3$. The three design correspond to decreasing parameters λ . As expected, the complexity of the topology of the designs increases when λ decreases.

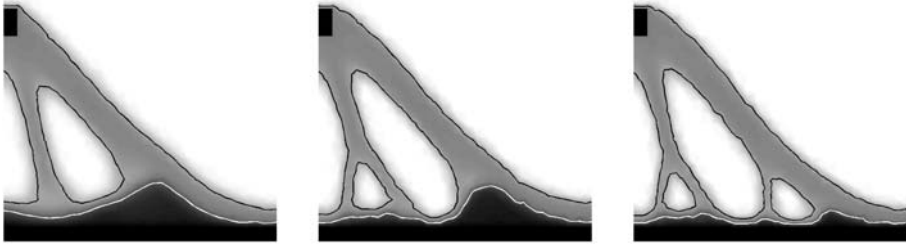


Figure 2. Optimal design of a piston.

5. NUMERICAL IMPLEMENTATION

The issues linked with the implementation of the phase field are a combination of typical difficulties in optimal design and in free discontinuity problems. We give here a short survey and refer the reader to Bourdin and Chambolle (2003), Burger and Stainko (2003) and Wang and Zhou (2004) for more details.

In order to correctly represent the perimeter term (5), it is necessary to use a discretization scheme for the phase field ρ which converges in $W^{1,2}$. This means in particular that piecewise constant approximation is not possible. Typically, one would use piecewise linear finite elements for the density and the displacement field, for example. Another solution, if one relies on structured meshed would be to use offset grids for u and ρ , in such a way that ρ is approximated at the center of the elements for u .

Another issue is the stiffness of the regularized perimeter (5). It is well known that a steepest-descent based algorithm for (5) will converge only if the descent step r_n is of the order of εh^4 , where h is the discretization size. This is of course not acceptable.

A steepest descent step would be

$$\rho^{(n+1)} = \rho^{(n)} - r_n \left(D_\rho \mathcal{F}_\delta(\rho^{(n)}) - \frac{\lambda \varepsilon}{c_W} \Delta \rho^{(n)} + \frac{\lambda}{\varepsilon c_W} W'(\rho^{(n)}) \right), \quad (16)$$

where $D_\rho \mathcal{F}_\varepsilon(\rho^{(n)})$ denotes the Frechet derivative of the objective function with respect to the phase field, evaluated at the point $\rho^{(n)}$. In Bourdin and Chambolle, 2003, a semi-implicit approach is used. The term $\Delta \rho^{(n)}$ is dealt with explicitly and the descent iteration is performed solving the problem:

$$\left(\mathbf{I} - \frac{r_n \lambda \varepsilon}{c_W} \Delta \right) \rho^{(n+1)} = \rho^{(n)} - r_n \left(D_\rho \mathcal{F}_\delta(\rho^{(n)}) + \frac{\lambda}{\varepsilon c_W} W'(\rho^{(n)}) \right). \quad (17)$$

This can even be improved by decomposing W as the sum of a quadratic and a concave function, and treating the quadratic term explicitly. Another approached, used in Burger and Stainko (2003) is to use an interior point minimization algorithm, which seems to also address the stiffness issue.

The last issue is related to the non-convexity of the problem, a typical problem in topology optimization which is emphasized here by the term $\frac{1}{\varepsilon}W(\rho)$ in the regularized perimeter. Once again, this is a common issue in the implementation of the Modica–Mortola functional. Typical methods rely on gradually reducing the regularization parameter ε , noticing that for “large” ε , the term (5) is convex. In Bourdin and Chambolle (2003), we combined this approach with an gradual increase of the descent step r_n , which is essentially equivalent to gradually increasing the weight on the non-convex term in \mathcal{P}_ε .

ACKNOWLEDGEMENT

Part of this work was supported by the Louisiana Board of Regent under the contract LEQSF (2003-06)-RD-A-05.

REFERENCES

- Alberti, G. (2000) Variational models for phase transitions, an approach via Γ -convergence, in G.B. et al. (eds), *Calculus of Variations and Partial Differential Equations*, Springer-Verlag, pp. 95–114 (also available at <http://cvgmt.sns.it/papers/>).
- Allaire, G. (2002) *Shape Optimization by the Homogenization Method*, Springer-Verlag, New York.
- Allaire, G. and Kohn, R. (1993a) Explicit optimal bounds on the elastic energy of a two-phase composite in two space dimensions, *Quart. Appl. Math.*, 51(4), 675–699.
- Allaire, G. and Kohn, R. (1993b) Optimal bounds on the effective behavior of a mixture of two well-ordered elastic materials, *Quart. Appl. Math.*, 51(4), 643–674.
- Allaire, G. and Kohn, R. (1994) Optimal lower bounds on the elastic energy of a composite made from two non-well-ordered isotropic materials, *Quart. Appl. Math.*, 52(2), 311–333.
- Allaire, G., Bonnetier, É., Francfort, G. and Jouve, F. (1997) Shape optimization by the homogenization method, *Numer. Math.*, 76(1), 27–68.
- Ambrosio, L. and Buttazzo, G. (1993) An optimal design problem with perimeter penalization, *Calc. Var. Partial Differential Equations*, 1(1), 55–69.
- Bendsøe, M. and Kikuchi, N. (1988) Generating optimal topologies in structural design using a homogenization method, *Comput. Methods Appl. Mech. Engrg.*, 71(2), 197–224.
- Bendsøe, M. and Sigmund, O. (2002) *Topology Optimization*, Springer, Berlin.
- Bourdin, B. (2001) Filters in topology optimization, *Int. J. Numer. Meth. Engrg.*, 50, 2143–2158.
- Bourdin, B. and Chambolle, A. (2000) *Optimisation topologique de structures soumises à des forces de pression*. Actes du 32ème Congrès National d’Analyse Numérique, SMAI (ed.).
- Bourdin, B. and Chambolle, A. (2003) Design-dependent loads in topology optimization *ESAIM: Control, Optimisation and Calculus of Variations*, 9, 19–48.
- Bourdin, B., Francfort, G.A. and Marigo, J.-J. (2000) Numerical experiments in revisited brittle fracture, *J. Mech. Phys. Solids*, 48(4), 797–826.
- Braides, A. (2002) *Γ -Convergence for Beginners*, Oxford Lecture Series in Mathematics and its Applications, Vol. 22, Oxford University Press, Oxford.
- Burger, M. and Stainko, R. (2005) Phase-field relaxation of topology optimization with local stress constraints, to appear.

- Chambolle, A. (1999) Finite differences discretizations of the Mumford-Shah functional, *M2AN Math. Model. Numer. Anal.*, 33(2), 261–288.
- Chambolle, A. and Larsen, C. (2003) C^∞ regularity of the free boundary problem for a two-dimensional optimal compliance problem, *Calc. Var. Partial Differential Equations*, 18(1), 77–94.
- Cherkaev, A. (2000) *Variational Methods for Structural Optimization*, Springer-Verlag, New York.
- Cherkaev, A. and Kohn, R. (eds) (1997) *Topics in the Mathematical Modelling of Composite Materials*, Birkhäuser, Boston, MA.
- Dal Maso, G., (1993) *An Introduction to Γ -Convergence*, Birkhäuser.
- Diaz, A. and Sigmund, O. (1995) Checkerboard patterns in layout optimization, *Struct. Optim.*, 10, 40–45.
- Evans, L. and Gariepy, R. (1992) *Measure Theory and Fine Properties of Functions*, CRC Press, Boca Raton, FL.
- Federer, H. (1969) *Geometric Measure Theory*, Springer-Verlag, New York.
- Haber, R.B., Jog C.S. and Bendsøe, M.P. (1996) A new approach to variable-topology shape design using a constraint on the perimeter, *Struct. Optim.*, 11, 1–12.
- Kohn, R. and Strang, G. (1986) Optimal design and relaxation of variational problems: I–III, *Comm. Pure Appl. Math.*, 39(3), 113–137, 139–182, 353–377.
- Modica, L. and Mortola, S. (1977a) Il limite nella Γ -convergenza di una famiglia di funzionali ellittici, *Boll. Un. Mat. Ital. A (5)*, 14(3), 526–529.
- Modica, L. and Mortola, S. (1977b) Un esempio di Γ^- -convergenza, *Boll. Un. Mat. Ital. B (5)*, 14(1), 285–299.
- Petersson, J. Beckers M., and Duysinx, P. (1999) Almost isotropic perimeters in topology optimization: Theoretical and numerical aspects, in *Proceedings of the Third World Congress on Structural and Multidisciplinary Optimization*, Amherst, NY.
- Sigmund, O. and Petersson, J. (1998) Numerical instabilities in topology optimization: A survey on procedures dealing with checkerboards, mesh-dependencies and local minima, *Struct. Opt.*, 16(1), 68–75.
- Wang, M.Y. and Zhou, S.W. (2004) Phase transition: A variational method for structural topology optimization, *CMES: Computer Modeling in Engineering & Sciences*, 6(6), 547–566.

LEVEL SET BASED SHAPE OPTIMIZATION OF GEOMETRICALLY NONLINEAR STRUCTURES

Seonho Cho, Seung-Hyun Ha and Min-Geun Kim

Department of Naval Architecture and Ocean Engineering and Research Institute of Marine and Systems Engineering, Seoul National University, San 56-1, Sillim-Dong, Kwanak-Gu, Seoul, Korea

Abstract: Using the level set method and topological derivatives, a topological shape optimization method that is independent of initial topology is developed for geometrically nonlinear structures in Total Lagrangian framework. In nonlinear topology optimization, response analysis may not converge due to relatively sparse material distribution driven by the conventional topology optimization such as homogenization and density methods. In the level set method, the initial domain is kept fixed and its boundary is represented by an implicit moving boundary embedded in the level set function, which facilitates to handle complicated topological shape changes. The “Hamilton–Jacobi” (H–J) equation and computationally robust numerical technique of “up-wind scheme” lead the initial implicit boundary to an optimal one according to the normal velocity field while both minimizing the objective function of instantaneous structural compliance and satisfying the required constraint of allowable material volume. In this paper, based on the obtained level set function, structural boundaries are actually represented in the response analysis. The developed method is able to create holes whenever and wherever necessary during the optimization and minimize the compliance through both shape and topological variations at the same time. The required velocity field in the initial domain to update the H–J equation is determined from the descent direction of Lagrangian derived from optimality conditions. The rest of velocity field is determined through a velocity extension method. Since the homogeneous material property and explicit boundary are utilized, the convergence difficulty is effectively prevented.

Keywords: Shape optimization, topological derivative, adjoint sensitivity analysis, geometric nonlinearity, level set method, velocity extension method, explicit boundary.

1. INTRODUCTION

In conventional topology optimization method for the geometrically nonlinear structures, the response analysis often experiences convergence difficulty due to relatively sparse material distribution driven by the conventional topo-

logy optimization methods [1, 2]. For the geometrically nonlinear problems, all the efforts seem not to work satisfactorily as long as we perform the topology optimization based on the variations of material distribution. However, in the level set approach, the difficulty can be significantly relieved by using homogeneous material and implicit boundary. Nevertheless, this approach incurs another convergence problem caused by the approximation of implicit functions [3]. In this paper, to prevent this difficulty, the explicit boundary determined from the level set function is utilized in the response analysis in total Lagrangian framework.

Osher et al. [4] have devised a level set method for numerically tracking fronts and free boundaries, which is used in many applications as motion by mean curvature. Allaire et al. [5] proposed a structural optimization method based on a combination of shape derivative and the level set method for front propagation. Wang et al. [6] developed a topology optimization method for linear elastic structures using implicit function. Kwak and Cho [3] proposed a level set based topology optimization method for geometrically nonlinear problems, which significantly relieve the existing convergence difficulty. Sokolowski et al. [7] defines a topological derivative for an arbitrary shape functional that can provide the information on the infinitesimal variation of the shape functional if a small hole is created. To obtain the topological derivative expression, C ea et al. [8] derives some optimality conditions using shape and topological gradients simultaneously. Novotny et al. [9] defines topological derivative as the limit of shape derivative when the radius of small hole approaches to zero.

The shape optimization is to move the boundary, according to the obtained sensitivity with respect to the boundary variations, while the allowable volume is kept constant. It is crucial to find an appropriate normal velocity field such that it will iteratively lead the design boundary to the optimal shape. The normal velocity is determined in the descent direction of Lagrangian function using its sensitivity. However, if the explicit boundary is employed, the normal velocity field can be computed only inside the domain. To solve the H–J equation, we should have the velocity field at least in narrow band region around the boundary. Thus, we employ a fast extension method [10], which extends the velocity field in an upwind fashion using the level set functions.

2. LEVEL SET METHOD

Given a closed d -dimensional hyper-surface Γ at zero level, we come up with a formulation for the motion of hyper-surface propagating Γ_τ along its normal direction with V_n at time τ . Let Γ_I and Ω_I be an initial reference boundary and domain, respectively, which include all the possible boundary and domain. At time $\tau = 0$, assume the existence of a zero level set function $\phi(\mathbf{x}, 0)$ that is

Lipschitz continuous and defined on Ω_I , satisfying

$$\phi(\mathbf{x}, \tau = 0) \begin{cases} +\zeta(\mathbf{x}, \Gamma) & \mathbf{x} \in \Omega, \\ = 0 & \mathbf{x} \in \Gamma, \\ -\zeta(\mathbf{x}, \Gamma) & \mathbf{x} \in \Omega_I \setminus \bar{\Omega}, \end{cases} \quad (1)$$

where $\zeta(\mathbf{x}, \Gamma)$ is a distance from a point \mathbf{x} to the boundary Γ , for all $\mathbf{x} \in R^d$. Using the level set function, an outward unit vector \mathbf{n} normal to the boundary Γ and a curvature κ are expressed as

$$\mathbf{n} = -\frac{\nabla\phi}{|\nabla\phi|}, \quad \kappa = \operatorname{div} \mathbf{n} = -\nabla \cdot \left(\frac{\nabla\phi}{|\nabla\phi|} \right). \quad (2)$$

Taking the material derivative of level set function in Equation (1) with respect to arbitrary time leads to the H–J equation [4] as

$$\frac{\partial\phi}{\partial\tau} = V_n|\nabla\phi|, \quad \frac{\partial\phi}{\partial n} \Big|_{\Gamma_I} = 0. \quad (3)$$

Note that given a normal velocity field V_n , repeated attempts to solve the first order partial differential equation leads to the optimal implicit boundary of the structures. In the level set approach, the boundary is varying to meet the optimization requirements, which significantly relieves the existing convergence difficulty. Nevertheless, this approach incurs another convergence problem caused by the approximation of implicit boundary. To prevent this difficulty, the explicit boundary determined from the level set function is utilized in the nonlinear response analysis. Since the response and sensitivity analyses are performed in the domain with explicit boundary, the necessary velocity field to integrate the H–J equation is available only in the domain with explicit boundary. To obtain the velocity field outside the domain, we use the velocity extension method proposed by Adalsteinsson et al. [10].

3. DESIGN SENSITIVITY ANALYSIS

Since the level set function is defined on the initial reference domain at undeformed configuration, the total Lagrangian formulation is an obvious choice for the response analysis. At the current configuration ($n + 1$), the linearized equilibrium equation is written, in incremental form, as

$$a^*({}^n\mathbf{z}; \Delta\mathbf{z}, \bar{\mathbf{z}}) = \ell^*({}^n\mathbf{z}; \bar{\mathbf{z}}), \quad \forall \bar{\mathbf{z}} \in Z, \quad (4)$$

$$\begin{aligned} a^*({}^n\mathbf{z}; \Delta\mathbf{z}, \bar{\mathbf{z}}) \equiv & \int_{0\Omega} S_{ij}({}^n\mathbf{z}) \hat{\eta}_{ij}(\Delta\mathbf{z}; \bar{\mathbf{z}}) \, d^0\Omega \\ & + \int_{0\Omega} c_{ijkl} \hat{\varepsilon}_{kl}({}^n\mathbf{z}; \Delta\mathbf{z}) \hat{\varepsilon}_{ij}({}^n\mathbf{z}; \bar{\mathbf{z}}) \, d^0\Omega, \end{aligned} \quad (5)$$

$$\ell^*({}^n\mathbf{z}; \bar{\mathbf{z}}) \equiv {}^{n+1}R - \int_{0\Omega} S_{ij}({}^n\mathbf{z}) \hat{\varepsilon}_{ij}({}^n\mathbf{z}; \bar{\mathbf{z}}) d^0\Omega. \quad (6)$$

${}^0\Omega$ and ${}^0\Gamma^t$ are the structural domain and traction boundary at initial configuration, respectively; \mathbf{z} , $\bar{\mathbf{z}}$, and Z are the displacement, virtual displacement, and variational space, respectively; $S_{ij}(\mathbf{z})$, $\hat{\varepsilon}_{ij}(\mathbf{z}; \bar{\mathbf{z}})$, and R_i are the second Piola–Kirchhoff stress tensor, virtual Green–Lagrange strain tensor, and external load, respectively. The constitutive relation for isotropic Kirchhoff material is used.

$$\hat{\varepsilon}_{ij}(\mathbf{z}; \bar{\mathbf{z}}) = \frac{1}{2} \left(\frac{\partial \bar{z}_i}{\partial^0 x_j} + \frac{\partial \bar{z}_j}{\partial^0 x_i} + \frac{\partial \bar{z}_m}{\partial^0 x_i} \frac{\partial z_m}{\partial^0 x_j} + \frac{\partial z_m}{\partial^0 x_i} \frac{\partial \bar{z}_m}{\partial^0 x_j} \right), \quad (7)$$

$$\hat{\eta}_{ij}(\Delta\mathbf{z}; \bar{\mathbf{z}}) \equiv \frac{1}{2} (\Delta z_{m,i} \bar{z}_{m,j} + \Delta z_{m,j} \bar{z}_{m,i}), \quad (8)$$

$$S_{ij}(\mathbf{z}) = c_{ijkl} \varepsilon_{kl}(\mathbf{z}). \quad (9)$$

Define a Lagrangian for instantaneous compliance at configuration $(n+1)$ and the corresponding adjoint equation as

$$\begin{aligned} L_\rho({}^{n+1}\mathbf{z}, \boldsymbol{\lambda}) &= \int_{0\Omega_\rho} {}^{n+1}\mathbf{b} \cdot ({}^{n+1}\mathbf{z} + \boldsymbol{\lambda}) d^0\Omega_\rho \\ &\quad + \int_{0\Omega_t \cup \partial\omega_\rho} {}^{n+1}\mathbf{t} \cdot ({}^{n+1}\mathbf{z} + \boldsymbol{\lambda}) d^0\Omega_\rho \\ &\quad - \int_{0\Omega_\rho} \mathbf{S}({}^{n+1}\mathbf{z}) : \hat{\boldsymbol{\varepsilon}}({}^{n+1}\mathbf{z}; \boldsymbol{\lambda}) d^0\Omega_\rho, \end{aligned} \quad (10)$$

$$a^*({}^{n+1}\mathbf{z}; \boldsymbol{\lambda}, \bar{\boldsymbol{\lambda}}) = \ell(\bar{\boldsymbol{\lambda}}), \quad \forall \bar{\boldsymbol{\lambda}} \in Z, \quad (11)$$

$$\begin{aligned} a^*({}^{n+1}\mathbf{z}; \boldsymbol{\lambda}, \bar{\boldsymbol{\lambda}}) &\equiv \int_{0\Omega} \mathbf{S}({}^{n+1}\mathbf{z}) : \bar{\boldsymbol{\eta}}(\bar{\boldsymbol{\lambda}}; \boldsymbol{\lambda}) d^0\Omega \\ &\quad + \int_{0\Omega} \hat{\boldsymbol{\varepsilon}}({}^{n+1}\mathbf{z}; \boldsymbol{\lambda}) : \mathbf{C} : \hat{\boldsymbol{\varepsilon}}({}^{n+1}\mathbf{z}; \bar{\boldsymbol{\lambda}}) d^0\Omega, \end{aligned} \quad (12)$$

$$\ell(\bar{\boldsymbol{\lambda}}) \equiv \int_{0\Omega} {}^{n+1}\mathbf{b} \cdot \bar{\boldsymbol{\lambda}} d^0\Omega + \int_{0\Omega_t} {}^{n+1}\mathbf{t} \cdot \bar{\boldsymbol{\lambda}} d^0\Gamma. \quad (13)$$

Taking the shape derivative of Equation (10) in the direction of \mathbf{V} and using the fact that $\mathbf{V} = \mathbf{0}$ for $\mathbf{x} \in \Gamma_d$, we have the following expression:

$$\begin{aligned} \dot{L}_S({}^{n+1}\mathbf{z}, \boldsymbol{\lambda}) &= \int_{0\Omega_{rho}} \nabla \cdot \left[\left\{ \begin{aligned} &{}^{n+1}\mathbf{b} \cdot ({}^{n+1}\mathbf{z} + \boldsymbol{\lambda}) + {}^{n+1}\mathbf{t} \cdot (\nabla({}^{n+1}\mathbf{z} + \boldsymbol{\lambda}) \cdot \mathbf{n}) \\ &+ \kappa ({}^{n+1}\mathbf{t} \cdot ({}^{n+1}\mathbf{z} + \boldsymbol{\lambda})) - \mathbf{S}({}^{n+1}\mathbf{z}) : \hat{\boldsymbol{\varepsilon}}({}^{n+1}\mathbf{z}; \boldsymbol{\lambda}) \end{aligned} \right\} \mathbf{V} \right] d^0\Omega_\rho \\ &= \int_{0\Omega_\rho} \nabla \cdot \{ \Pi({}^{n+1}\mathbf{z}, \boldsymbol{\lambda}) \mathbf{V} \} d^0\Omega_\rho. \end{aligned} \quad (14)$$

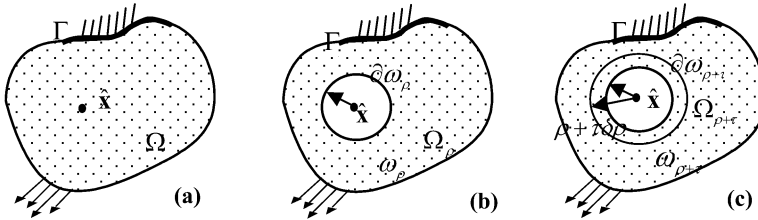


Figure 1. Domains and boundaries.

3.1 Topological Derivative

Consider a two-dimensional problem for simplicity as shown in Figure 1. Let $\Omega \subset R^2$ be an original domain without holes (Figure 1a). Its boundary is denoted by $\Gamma = \Gamma_D \cup \Gamma_N$. Also, let $\Omega_\rho = \Omega \setminus \bar{\omega}_\rho$ be an open domain with holes (Figure 1b). Its boundary is denoted by $\Gamma_\rho = \Gamma \cup \partial\omega_\rho$. $\bar{\omega}_\rho = \omega_\rho \cup \partial\omega_\rho$ is a complete circular domain of radius $\rho(\hat{\mathbf{x}})$ centered at the point $\hat{\mathbf{x}} \in \Omega$. Let $\Omega_{\rho+\tau} = \Omega \setminus \bar{\omega}_{\rho+\tau}$ be a perturbed domain (Figure 1c). Its boundary is denoted by $\Gamma_{\rho+\tau} = \Gamma \cup \partial\omega_{\rho+\tau}$. $\bar{\omega}_{\rho+\tau} = \omega_{\rho+\tau} \cup \partial\omega_{\rho+\tau}$ is a complete circular domain of radius $\rho(\hat{\mathbf{x}}) + \tau\delta\rho(\hat{\mathbf{x}})$ centered at the point $\hat{\mathbf{x}} \in \Omega$.

When a hole is created during the topology optimization, it is impossible to build a homeomorphic map between the domains Ω and Ω_ρ . Using the asymptotical regularization concept, the topological variation $\psi'_T(\hat{\mathbf{x}})$ is defined as the limit of shape variation when the radius of the hole $\rho(\hat{\mathbf{x}})$ approaches to zero.

$$\begin{aligned} \psi'_T(\hat{\mathbf{x}}) &= \lim_{\rho \rightarrow 0} \left\{ \lim_{\tau \rightarrow 0} \frac{\Psi(\Omega_{\rho+\tau}) - \Psi(\Omega_\rho)}{|\omega_{\rho+\tau}|} \right\} \delta|\omega_{\rho+\tau}| \Big|_{\tau=0} \\ &= \left\{ \lim_{\rho \rightarrow 0} \frac{1}{|\Omega_\rho|_\tau} \dot{\psi}_s(\mathbf{x}) \right\} \delta|\omega_\rho| \equiv \dot{\psi}_T(\hat{\mathbf{x}}) \delta|\omega_\rho|, \end{aligned} \tag{15}$$

where $|\cdot|$ denotes the negative function of Lebesgue measure of the set. $\dot{\psi}_T(\hat{\mathbf{x}})$ denotes the topological derivative. To calculate the topological derivative in total Lagrangian framework from the concept above, we need the shape derivative around the ball centered at $\hat{\mathbf{x}}$. To this end, the perturbation is made only on the boundary of hole that has homogenous Neumann boundary condition as $n^{+1}\mathbf{S} \cdot n^1\mathbf{n} = 0$ on $\partial\omega_\rho$. The Lagrangian for the instantaneous compliance in the domain ${}^0\Omega_\rho = {}^0\Omega \setminus {}^0\bar{\omega}_\rho$ has the same form as Equation (10). Note that since only the boundary of hole is perturbed, the design velocity vanishes on the other boundary. Using the following relations:

$$\delta|\omega_\rho| = 2\pi\rho\delta\rho = -2\pi\rho V_n,$$

$$|\omega_\rho|_{,\tau} = -\frac{d}{d\tau} \int_{\omega_{\rho+\tau}} d\omega_{\rho+\tau} \Big|_{\tau=0} = - \int_{\partial\omega_\rho} V_n \partial\omega_\rho, \quad (16)$$

the topological variation for the instantaneous compliance can be written, in the absence of body force for simplicity of problem, as

$$L'_T({}^{n+1}\mathbf{z}, \lambda)(\hat{\mathbf{x}}) = \left\{ \lim_{\rho \rightarrow 0} \frac{1}{\int_{\partial^0\omega_\rho} V_n \partial^0\omega_\rho} \int_{\partial^0\omega_\rho} \Pi({}^{n+1}\mathbf{z}_\rho, \lambda_\rho) V_n d^0\Omega_\rho \right\} 2\pi\rho V_n, \quad \forall \hat{\mathbf{x}} \in \Omega. \quad (17)$$

To calculate this limit in order to obtain the final expression of the topological derivative, we use an asymptotic analysis to know the behavior of the solution $\mathbf{S}({}^{n+1}\mathbf{z}_\rho)$ when $\rho \rightarrow 0$. This behavior may be obtained from the analytical solution for a stress distribution around a circular void in two-dimensional elastic body in polar coordinates [11]. Finally, the topological variation is expressed as

$$L'_T = ({}^{n+1}\mathbf{z}, \lambda)(\hat{\mathbf{x}}) = -2\pi\rho V_n \Sigma({}^{n+1}\mathbf{z}, \lambda)(\hat{\mathbf{x}}), \quad (18)$$

$$\Sigma = \begin{cases} \frac{\lambda+2\mu}{2\mu(\lambda+\mu)} [4\mu\mathbf{S}({}^{n+1}\mathbf{z}) : \hat{\boldsymbol{\varepsilon}}({}^{n+1}\mathbf{z}; \lambda) + (\lambda - \mu)\text{tr}\mathbf{S}({}^{n+1}\mathbf{z})\text{tr}\hat{\boldsymbol{\varepsilon}}({}^{n+1}\mathbf{z}; \lambda)] \\ \text{plane strain} \\ \frac{\lambda+\mu}{\mu(3\lambda+2\mu)} \left[8\mu\mathbf{S}({}^{n+1}\mathbf{z}) : \hat{\boldsymbol{\varepsilon}}({}^{n+1}\mathbf{z}; \lambda) + \frac{2\mu(\lambda-2\mu)}{(\lambda+2\mu)} \text{tr}\mathbf{S}({}^{n+1}\mathbf{z})\text{tr}\hat{\boldsymbol{\varepsilon}}({}^{n+1}\mathbf{z}; \lambda) \right] \\ \text{plane stress} \end{cases} \quad (19)$$

The topological variation is always positive when the hole is created since the topological derivative and the velocity on the boundary of hole is always negative. This means that the compliance increases when the hole is created.

4. TOPOLOGICAL SHAPE OPTIMIZATION

The objective of topological shape optimization is to find the optimal layout that minimizes the instantaneous compliance of the system under prescribed loadings. Considering the domain and boundary before nucleation, the topological shape optimization problem is stated as

$$\text{Minimize } \psi = \int_{\Omega} {}^{n+1}\mathbf{b} \cdot {}^{n+1}\mathbf{z} d^0\Omega + \int_{\Gamma_N} {}^{n+1}\mathbf{t} \cdot {}^{n+1}\mathbf{z} d^0\Gamma, \quad (20)$$

$$\text{Subject to } m = \int_{\Omega} d^0\Omega \leq M_{\max}, \quad (21)$$

where M_{\max} is an allowable volume. The velocity field $\mathbf{V}(\mathbf{x})$ defines the propagation speed of all level sets along outward normal direction. The velocity should be determined such that it reduces the instantaneous compliance while satisfying the requirement of allowable material volume.

To identify the location and time for nucleation, consider the velocity field \mathbf{V}^ω when only the boundary of hole centered at $\hat{\mathbf{x}}$ is perturbed. Since $V_n < 0$ on the hole, the topological variation in Equation (18) is always positive. However, the corresponding shape variation is occurring at the same time. If the topological variation is smaller than the shape variation at $\hat{\mathbf{x}}$ during the optimization process, the position $\hat{\mathbf{x}}$ and the optimization step are most appropriate for the nucleation.

$$\psi'_s - \psi'_T(\hat{\mathbf{x}}) = 2 \int_s \Pi^{(n+1)}(\mathbf{z}, \boldsymbol{\lambda}) V_n ds \delta\tau + \Sigma^{(n+1)}(\mathbf{z}, \boldsymbol{\lambda})(\hat{\mathbf{x}}) \delta|\omega_\rho| > 0, \quad (22)$$

where s denotes the circular path along the boundary of the hole. Introducing the ratio of shape to topological variations as $\alpha = V_n \delta\tau / \delta|\omega_\rho|$, we can define an indicator function as

$$\hat{H}(\Theta) = \begin{cases} 1 & \text{if } \Theta > 0, \\ 0 & \text{if } \Theta \leq 0, \end{cases} \quad \Theta \equiv \Sigma^{(n+1)}(\mathbf{z}, \boldsymbol{\lambda})(\hat{\mathbf{x}}) - 2\alpha \int_s \Pi^{(n+1)}(\mathbf{z}, \boldsymbol{\lambda}) ds. \quad (23)$$

Next, define the Lagrangian function Λ for the constrained optimization problems as

$$\Lambda(\tau, \mu, s) = \psi + \mu\{m + s^2 - M_{\max}\}, \quad (24)$$

where M_{\max} , s , and μ are the allowable material volume, a slack variable to convert the inequality constraint to the equality one, and a Lagrange multiplier, respectively. Using the indicator function to selectively introduce the topological variations, the application of the Kuhn–Tucker optimality conditions leads to the following optimality conditions.

$$\begin{aligned} \left. \frac{d\Lambda(\tau, \xi, s)}{d\tau} \right|_{\tau=0} &= \int_{0\Omega} \nabla \cdot \{\Pi^{(n+1)}(\mathbf{z}, \boldsymbol{\lambda}) + \xi\} \mathbf{n} V_n d^0\Omega + \hat{H}(\Theta) \\ &\quad \times \{\Sigma^{(n+1)}(\mathbf{z}, \boldsymbol{\lambda}) + \xi\}(\hat{\mathbf{x}}) = 0, \\ \xi &= \begin{cases} 0 & \text{if } \int_{0\Omega} d^0\Omega < M_{\max}, \\ \mu & \text{if } \int_{0\Omega} d^0\Omega \geq M_{\max}, \end{cases} \end{aligned} \quad (25)$$

where the Lagrange multiplier and velocity are determined by [3]

$$\xi = -\frac{\int_{0\Omega} \nabla \cdot \{\Pi^{(n+1)}(\mathbf{z}, \boldsymbol{\lambda}) \mathbf{n}\} d^0\Omega}{\int_{0\Omega} \nabla \cdot \mathbf{n} d^0\Omega}, \quad V_n = -\{\Pi^{(n+1)}(\mathbf{z}, \boldsymbol{\lambda}) + \xi\}. \quad (26)$$

5. NUMERICAL EXAMPLES

5.1 Example 1: Linear vs Nonlinear Formulations

Consider the simply supported plate as shown in Figure 2. The simply supported plate model is subjected to a concentrated force of $F = 10^7$ N. The

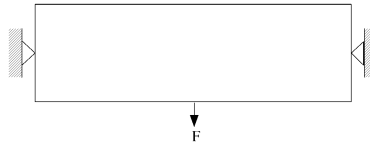


Figure 2. Simply supported plate.

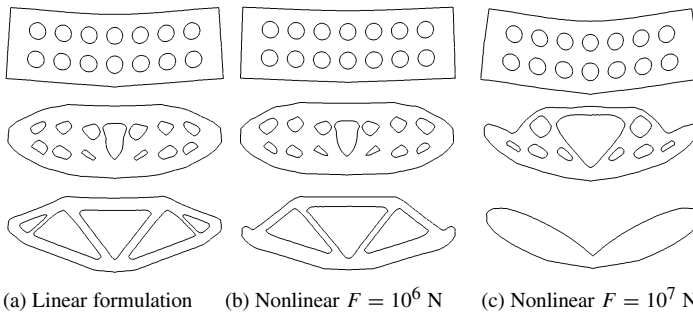


Figure 3. Optimization histories for various conditions.

objective is to obtain the optimal layout of the structure while minimizing the instantaneous compliance of the structure while satisfying the requirement of allowable volume, 40% of the original one.

Figure 3 shows the evolution of the optimal shapes for various conditions. According to the corresponding normal velocity, the explicit boundary determined from velocity extension scheme evolves to the optimal shape. Figure 3a shows the optimization history for linear formulation, Figure 3b for nonlinear formulation with $F = 5 \times 10^6$ N, and Figure 3c for nonlinear formulation with $F = 10^7$ N. It turns out that depending on the formulations, different optimal shapes are obtained (Figures 3a and 3b) and also it has dependence on the magnitude of loading (Figures 3b and 3c).

5.2 Example 2: Nucleation Using Topological Derivative

For the same model as Example 1, the topological shape optimization incorporating with topological derivative is carried out. Using the topological derivative concept, nucleation is made depending on the indicator function given in Equation (23). Moreover, the optimization is less dependent on the initial condition. Figures 4b and 4c show the evolution of the optimal shape under the different loading conditions.

Figure 5 shows the convergence history for linear (Figure 4a) and nonlinear (Figure 4c). Due to the volume constraint, compliance functional is increasing until volume constraint, which is 40% of original one, is satisfied. After that,

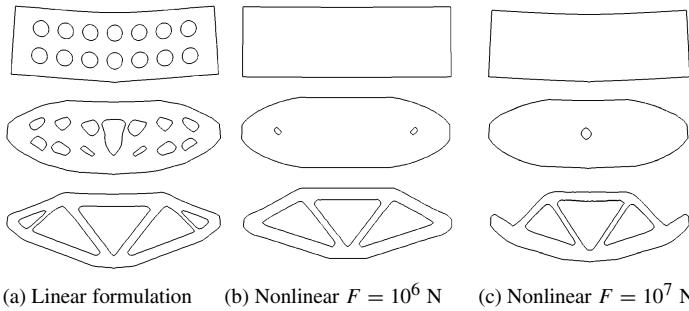
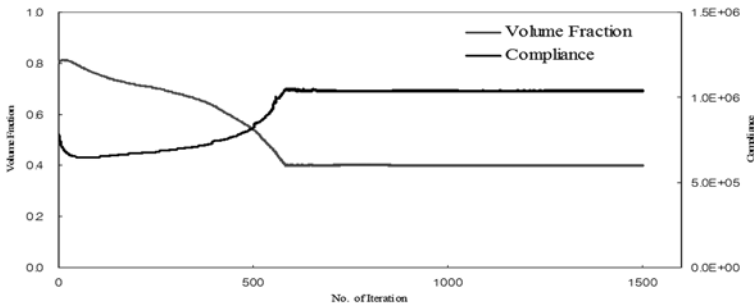
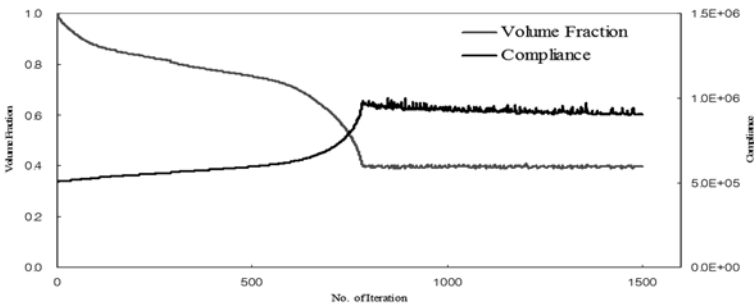


Figure 4. Optimization history for various loadings.



(a) Linear without Topological Derivative



(b) Nonlinear with Topological Derivative

Figure 5. Convergence history.

compliance is minimized while holding constraint. For the same model, the compliance of nonlinear formulation with topological derivative is less than that of linear one without topological derivative. It means that the nonlinear formulation with topological derivative can yield stiffer design using the same material volume.

6. CONCLUSION

A topological shape optimization method for geometrically nonlinear structures is developed using the level set method and topological derivative approach. To avoid convergence difficulty during the nonlinear response analysis, explicit boundary converted from the implicit one is utilized. For the optimization process, the required velocity field to integrate the Hamilton–Jacobi equation is obtained from the Kuhn–Tucker optimality condition for the Lagrangian function. The velocity field outside the domain is obtained using the extension method. The necessity of geometrically nonlinear topology optimization and the applicability to large deformation problems are demonstrated. The convergence difficulty is significantly relieved by using the level set method with explicit boundary. It turns out that the initial holes in the domain is not required to get the optimal result since this method creates holes whenever and wherever necessary during the optimization using the indicator function obtained from topological derivative.

REFERENCES

- [1] M.P. Bendsøe and O. Sigmund, *Topology Optimization: Theory, Methods, and Applications*, Springer-Verlag (2003).
- [2] S. Cho and H. Jung, Design sensitivity analysis and topology optimization of displacement-loaded nonlinear structures, *Computer Methods in Applied Mechanics and Engineering*, 192(22–24), 2539–2553 (2003).
- [3] J. Kwak and S. Cho, Topological shape optimization for geometrically nonlinear structures using level set method, *Computers & Structures*, 83(27), 2257–2268 (2005).
- [4] S. Osher and J.A. Sethian, Front propagating with curvature dependent speed: Algorithms based on Hamilton–Jacobi formulations, *Journal of Computational Physics*, 78, 12–49 (1988).
- [5] G. Allaire, F. Jouve and A.-M. Toader, Structural optimization using sensitivity analysis and a level-set method, *Journal of Computational Physics*, 194, 363–393 (2004).
- [6] M.Y. Wang, X. Wang and D. Guo, A level set method for structural topology optimization, *Computer Methods in Applied Mechanics and Engineering*, 192, 227–246 (2003).
- [7] J. Sokolowski and A. Zochowski, On topological derivative in shape optimization, *SIAM Journal of Control and Optimization*, 37, 1251–1272 (1999).
- [8] J. Céa, S. Garreau, P. Guillaume and M. Masmoudi, The shape and topological optimization connection, *Computer Methods in Applied Mechanics and Engineering*, 188, 713–726 (2000).
- [9] A.A. Novotny, R.A. Feijóo, E. Tarroco and C. Padra, Topological sensitivity analysis, *Computer Methods in Applied Mechanics and Engineering*, 188, 713–726 (2000).
- [10] D. Adalsteinsson and J. A. Sethian, The fast construction of extension velocities in level set methods, *Journal of Computational Physics*, 148, 2–22 (1999).
- [11] A.A. Novotny, C. Padra, R.A. Feijoo and E. Taroco, Topological-shape sensitivity method, in *European Congress on Computational Methods in Applied Sciences and Engineering, ECCOMAS* (2004).

Industry and Software

INDUSTRIAL IMPLEMENTATION AND APPLICATIONS OF TOPOLOGY OPTIMIZATION AND FUTURE NEEDS

Claus B.W. Pedersen and Peter Allinger

FE-DESIGN GmbH, Haid-und-Neu-Str. 7, 76131 Karlsruhe, Germany

Claus.Pedersen@FE-Design.de, Peter.Allinger@FE-Design.de

Abstract: This paper deals with topology optimization seen from an industrial and a manufacturing point of view. What the industrial users see as key issues when implementing topology optimization are frequently not the topics that the academic environments consider when implementing topology optimization. One of the key issues is that topology optimization should be integrated into an existing CAD and CAE environment (example of FE-solvers: ABAQUS, ANSYS, CATOPO, NX Nastran, MSc Nastran, MSc Marc and Permas). Here, it is of importance to note that the models analyzed in the industrial CAE environments often consist of many finite elements (can be more than 2 million elements) and different types of elements (continuum, beam, membrane, shell, bar and rigid elements) which all can be employed in the same model. Furthermore, symmetry and manufacturing constraints are important for ensuring that the results of the topology optimized are manufacturable. Several examples will be given of how structural topology optimization can be used as an add-on module in existing CAE environments. However, from an academic point of view an add-on module including topology optimization for commercial FE-solvers is also of interest because the latest finite element and solver technology can be applied in the modeling for the topology optimization. Furthermore, the aim is also to show where the industry is today and which demands exist for the future. The results reported here are based upon the work done by FE-Design and their industrial partners using the topology optimization module (TOSCA.topo) and smooth module (TOSCA.smooth) of the program TOSCA.

Keywords: Industrial integration, industrial applications, large scale optimization, CAD, CAE.

1. IMPLEMENTATION OF TOPOLOGY OPTIMIZATION IN EXISTING CAD AND CAE ENVIRONMENTS

For industry it is important that the topology optimization method can be integrated into an existing CAD and CAE environment. Several reasons exist for why it is important to integrate the topology optimization into an existing CAD and CAE environment. First, all the features and functionalities of proven and reliable CAE solvers should also be accessible for the topology optimization. Second, the optimization should utilize existing investments in software and hardware. Third, one should take advantage of the existing knowledge of the staff regarding the CAD and CAE when applying topology optimization. Hence, it is important that the topology optimization module work as an add-on module for the existing commercial finite element solvers (ABAQUS, ANSYS, CATOPO, NX Nastran, MSc Nastran, MSc Marc and Permas), see Figure 1.

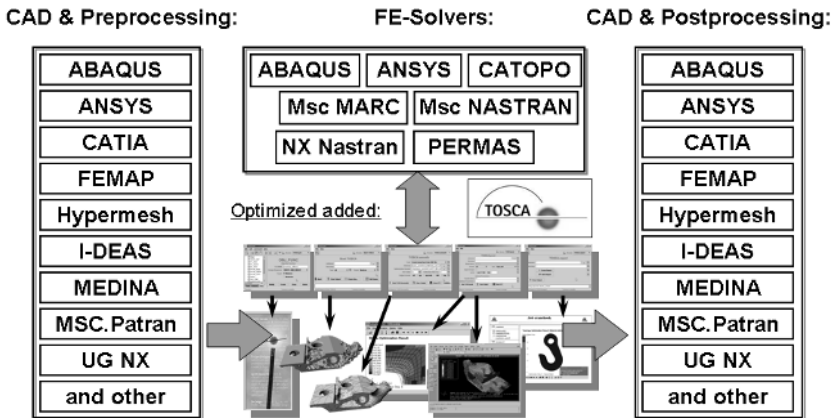


Figure 1. Integrating topology optimization in an established CAD and CAE environment. Initially, the preprocessing is conducted using existing preprocessing modules. Secondly, the topology optimization is an add-on module based upon the results obtained from the existing FE-solvers. Thirdly, the results can be evaluated and further modified in a postprocessor.

Some of the advantages of using the results of commercial FE-solvers for topology optimization are listed in the following subsection.

1.1 Advances of Using the Results of Existing CAE Solvers for Topology Optimization

Some main advances of using the result of proven and reliable CAE solvers in connection with topology optimization:

- Possible to use existing FE-models.
- Possible to use large 3D models (at the present feasible: more than 3 million elements).
- Possible to use different advanced FE-solver types. Both sparse direct solvers and iterative solves.
- Possible to apply different kind of elements in the model (continuum, shell, beam, membrane, shear and rigid elements). Parts can also be modeled as superelements¹ if the specific solver supports this ability.
- Boundary conditions with advanced kinematics, e.g. applied through rigid elements. Coupling between different components and parts.
- The models should also be compatible for other types of FE-analysis, e.g. static and frequency analysis, linear and non-linear analysis.

However, from an academic point of view the integration with commercial FE-solvers is also of interest because the latest finite element and solver technology can be applied in the modeling for the topology optimization for showing special effects and features.

1.2 Response Types for Objective and Constraints

The responses and constraint types applied in a topology optimization can often be characterized as following:

- Linear static analyze:
 1. Compliance of structure for specific loadcases (measure for stiffness of given loadcase).
 2. Displacements for specific loadcases (deflections and rotations).
 3. Reaction forces for specific loadcases (forces and moments).
- Modal eigenfrequencies:
 1. Single eigenfrequencies.
 2. Sum of eigenfrequencies.
- Mass of structure:
 1. The structural weight of the design space.
- Manufacturing restrictions (the mesh does not have to be regular):
 1. Stamping (straight sides of structure in stamping direction)

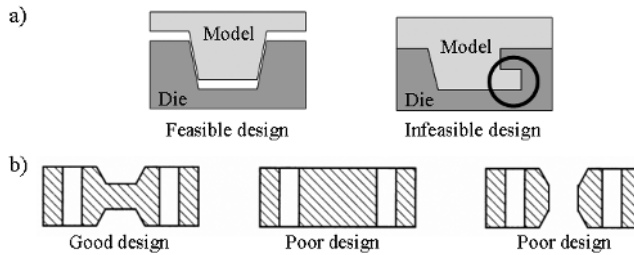


Figure 2. Manufacturing constraints. (a) Ensure manufacturing direction including avoiding no undercuts or cavities. (b) No material accumulation otherwise problems with cooling can occur. An additional constraint can also ensure that the mid plan has no holds ensuring a good material flow when molding.

2. Casting for avoiding under cuts as shown in Figure 2a. The mid plane can be fixed by user or determined automatically during the optimization. The mid plan can also be constraint to contain no holds as shown in Figure 2b.
3. Symmetry constraints (plane, point, rotational and cyclic symmetry and linked symmetry between different subdomains).

For the optimization the user has the free choice of combining the above listed response types in the objective function and in the constraints including the results of an eigenfrequency analysis and a static analysis using ones preferred CAE solver. Furthermore, the user can specify if the objective function should be minimized and maximized or if a Min-Max formulation should be applied.

1.3 Choice of Optimization Algorithm

In the literature (Bendsøe and Sigmund, 2003), several optimization algorithms can be found. Three algorithm types are implemented in TOSCA (TOSCA.topo) for topology optimization, FE-Design (2005). The manufacturing constraints can be applied in all three algorithm types. The type of algorithm has to be chosen according to the character of the optimization task and for minimizing the CPU-time. The three algorithms have some advantages and disadvantages:

- *The controller algorithm* can be used for stiffness optimization having material constraints. The controller algorithm is a modified optimality criteria algorithm based upon stresses and the algorithm optimizes for an even stress distribution. The algorithm has the advantage that it obtains very clear solid/void designs in 15 optimization iterations. The algorithm also converges for large models including non-linearities like

contact. However, the objective function and constraint is limited to be the compliance and the material volume, respectively.

- *The optimality criteria algorithms* can be used for stiffness or frequency optimization having material constraints. The optimality criteria algorithms optimize for average strain energy distribution. Usually, more than 15 optimization iterations are needed, however, the number is normally under 25 optimization iterations. The objective function is limited to be compliance or frequency and the constraint must be the material volume.
- *The mathematical programming algorithm* (Svanberg, 1987) converges normally in 25–50 optimization iterations. The mathematical programming algorithm is useful when more complicated optimization formulations are applied where compliance, frequencies, displacements and reaction forces are combined in the objective function and the constraints. The sensitivities are based on the theory in Bendsøe and Sigmund (2003).

Due to the large FE-models often applied in industrial applications the number of optimization iterations is of importance. Hence, a key issue when selecting an algorithm is often the number of optimization iterations.

1.4 Post Processing Using Smoothing Techniques

When the final topology optimized design is achieved, it consists of a large amount of data (fine meshes where each element has a density) and these FE-data are no standard input CAD. Consequently, an important issue is that the topology optimization data from the optimization should be converted (TOSCA.smooth) into a CAD-compatible format including a smoothing, calculation of isosurfaces and data reduction as shown in Figure 3. In this process the design is smoothed to a complete solid/void design for being directly remeshed or transferred into a CAD system for further changes and maybe afterwards the structure is reanalyzed in the CAE system.

2. EXAMPLES OF TOPOLOGY OPTIMIZATION USING EXISTING CAE SOLVERS

2.1 Manufacturing Constraints with the Controller Algorithm

The present design problem deals with a stiffness optimization of an engine mount including mass and manufacturing constraints as shown in Figure 4. However, for comparison the structure is also optimized without manufac-

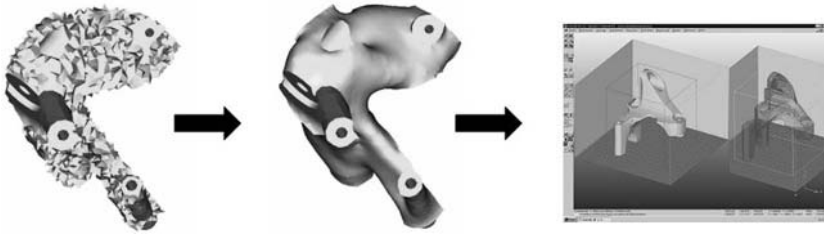


Figure 3. Transferring the optimized structure back into the CAD system using smoothed isosurfaces and data reduction.

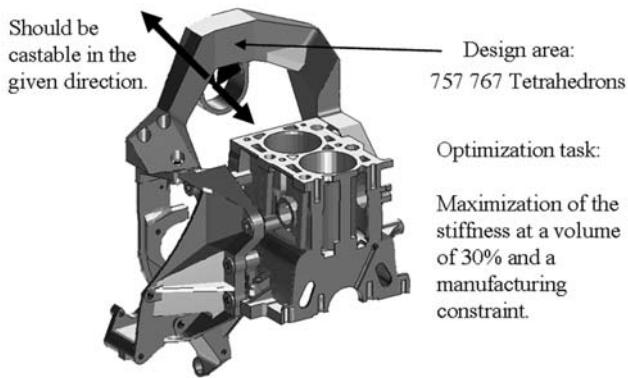


Figure 4. The design space for the stiffness optimization. The optimized structure should be castable in the given direction.

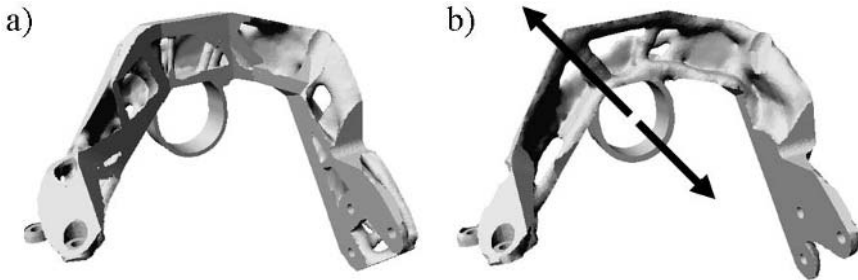


Figure 5. The optimized solutions. (a) Optimized without manufacturing constraint. (b) Optimized with manufacturing constraint.

turing constraint. The present solutions are obtained using the controller algorithm in TOSCA and the finite element solver Nastran.

The optimized solution without manufacturing constraint (see Figure 5a) is similar to a truss structure containing undercuts and therefore not castable. As expected the solution optimized with manufacturing constraint (see Figure 5b)

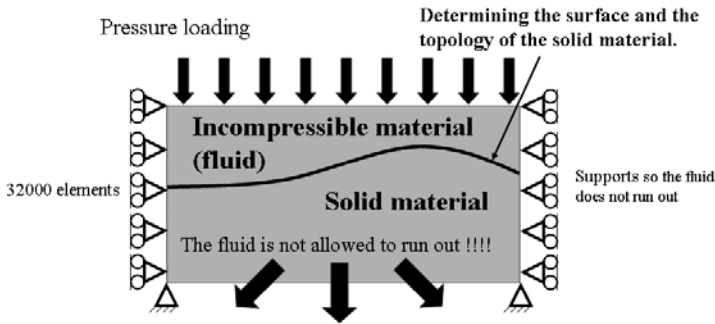


Figure 6. The design domain for the pressure loads. The domain is discretized in 3D using 32000 elements.

is castable. Consequently, the cost of adding the manufacturing constraint is that the maximal displacement increases from 1.45 mm to 1.73 mm. The model contains 3 loadcases and it is meshed with more than 750.000 theta continuum elements and several beam elements leading to a total of 511689 degrees of freedom. Still the total run time for the optimization was under 24 hours on a Windows PC.

2.2 Pressure Loads with the OC Algorithm

The present design problem deals with pressure loads as shown in Figure 6 where the stiffness should be maximized for a given amount material. The present example relates directly to the work by Sigmund and Clausen (2005). The idea is to use incompressible elements when designing for pressure loads because these elements can transfer forces when they are void due to their incompressibility. The present solutions are obtained using the optimality criteria in TOSCA and the finite element solver ABAQUS where the nodal pressure can be introduced as a degree of freedom.

The optimization problem is initially solved using standard compressible finite elements with a Poisson ratio of 0.3, see Figure 7a. Afterwards, the optimization problem is solved using the compressible finite elements with a Poisson ratio of 0.5, see Figure 7b. Figure 8 shows a mechanical interpretation of the two solutions. When the elements are incompressible the surface forces can be transferred by the void elements, which is not case when the elements are compressible. Meaning that the solution obtained using the incompressible elements do not only determine the topology but also locates where the loaded surface should be positioned. Opposite, the solution obtained using compressible elements has the loaded surface given by the initial pressure distribution defined by the user.

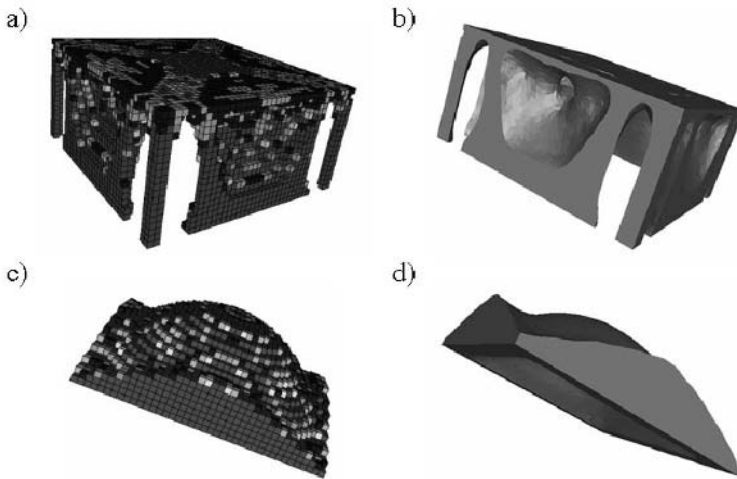


Figure 7. The optimized solutions and their equivalent smoothed solutions. (a) and (b) For compressible material, Poisson ratio of 0.3. (c) and (d) For incompressible material, Poisson ratio of 0.5.

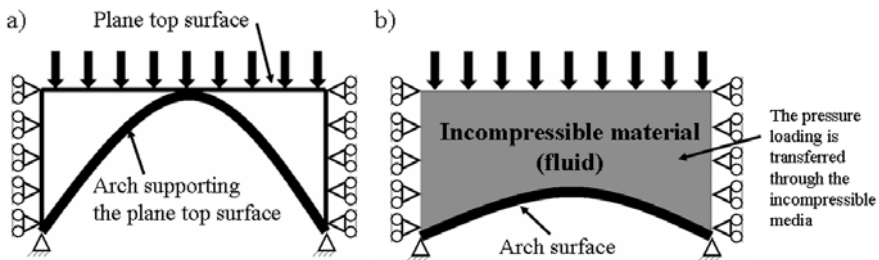


Figure 8. Interpreting the optimized solutions in Figure 7. (a) Compressible material, Poisson ratio 0.3. (b) Incompressible material, Poisson ratio 0.5.

2.3 Mechanisms with the Sensitivity Based Algorithm

The present problem will deal with so called hinge problem (Poulsen, 2002; Yin and Ananthasuresh, 2003) which occurs in mechanism design (Bendsøe and Sigmund, 2003; Pedersen et al., 2001). The hinges occur because the lower-order elements often used in topology optimization approximate inadequately the stresses and strains in the regions of the elements near to the nodes. For avoiding hinges the idea of the present study is to include the rotational degrees of freedom about the normal to the plane of the 2D element as shown in Figure 9.

As an example the inverter is designed using 20% material. The mechanism is applied to an actuator where the inverse output displacement is maximized as shown in Figure 10a. The example is solved using the element type shown in

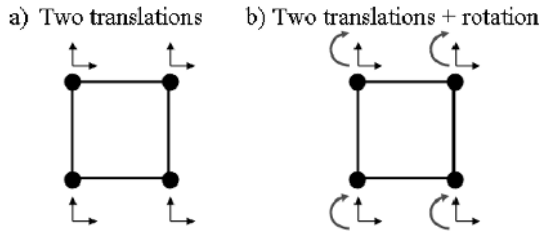


Figure 9. Four node elements. (a) Two translation degrees of freedom. (b) Two translation degrees of freedom plus the rotational degrees of freedom about the normal to the plane of the element.

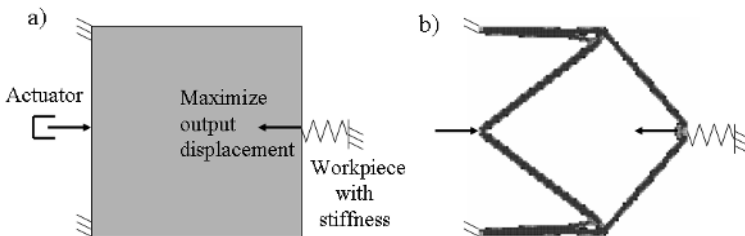


Figure 10. (a) Design space for inverter mechanism. (b) Optimized inverter mechanism modeled used elements including rotational degrees of freedom about the normal to the plane of the element as shown in Figure 9b.

Figure 9b obtained in ABAQUS or Nastran combined with the sensitivity based algorithm in TOSCA. The filter suggested by Sigmund and Petersson (1998) is applied with a filter size corresponding to 1.5 elements. Normally, the filter does not prevent hinges in mechanism designs. Nevertheless, the design in Figure 10b does not contain hinges when the filter is combined with elements including rotational degrees of freedom due to the more accurate physical description by the elements around the nodes. Both solution methods concerning hinges suggested in Poulsen (2002) and Yin and Ananthasuresh (2003) lead to a significant higher number of optimization iterations which was not observed in the present optimization. Thus, the discussions regarding hinges in the literature for mechanisms can be solved using a more accurate FE-modeling and a filter. Additional numerical experiments indicated that this conclusion is valid as long as the ground structure is stiff. However, when the ground structure is flexible some hinges could be observed. As shown here one of the main advantage of using commercial FE-solvers for topology optimization is that one can use the enormous element library and functionalities which the commercial solvers provide.

3. FUTURE NEEDS

These and other examples show that topology optimization and the features which can be found in the literature to a large extent can be and are integrated into existing CAD and CAE environments used in industry. However, some key issues are still unsolved and believed to be interesting also from an academic point of view. Especially, to include stress constraints in topology optimization would be desirable from an industrial point of view. Among highly nonlinear problems the possibility of combining crashworthiness and topology optimization is wanted, especially for the automotive industry. Due to the large FE-models frequently applied in these optimizations, the maximum number of allowed optimization iterations is 30–50 which is an important restriction.

NOTES

1. A superelement is a substructure which is condensed by eliminating its degrees of freedom.

REFERENCES

- Bendsøe, M.P. and Sigmund, O. (2003) *Topology Optimization: Theory, Methods and Applications*, Springer-Verlag, Berlin.
- FE-Design (2005) *TOSCA User's Manual*, FE-Design GmbH, Karlsruhe, Germany.
- Pedersen, C.B.W., Buhl, T. and Sigmund, O. (2001) Topology synthesis of large-displacement compliant mechanisms, *International Journal for Numerical Methods in Engineering*, 50(12), 2683–2706.
- Poulsen, T.A. (2002) A simple scheme to prevent checkerboard patterns and one-node connected hinges in topology optimization, *Structural and Multidisciplinary Optimization*, 24(5), 396–399.
- Sigmund, O. and Clausen, P. (2005) Topology optimization using a mixed formulation: An alternative way to solve pressure load problems, submitted.
- Sigmund O. and Petersson J. (1998) Numerical instabilities in topology optimization: A survey on procedures dealing with checkerboards, mesh-dependencies and local minima, *Structural Optimization*, 16(1), 68–75.
- Svanberg, K. (1987) The method of moving asymptotes – A new method for structural optimization, *International Journal for Numerical Methods in Engineering*, 24, 359–373.
- Yin, L. and Ananthasuresh, G.K. (2003) Design of distributed compliant mechanisms, *Mechanics Based Design of Structures and Machines*, 31(2), 151–179.

RECENT DEVELOPMENTS IN THE COMMERCIAL IMPLEMENTATION OF TOPOLOGY OPTIMIZATION

Uwe Schramm and Ming Zhou

Altair Engineering Inc., 2445 McCabe Way, Irvine, CA 92614, U.S.A.

schramm@altair.com

Abstract: Topology optimization has matured to be a practical design tool. After several years of success in the automotive industry, topology optimization has been introduced in other industries with great success. Design processes in the consumer products and aerospace industry benefit greatly from the use of topology optimization. The introduction of manufacturing constraints made the technology even more appealing. The paper will discuss recent developments in the implementation of topology optimization in commercial software and the use in a digital engineering environment.

Keywords: Topology optimization, software, design.

1. INTRODUCTION

The last decade has seen tremendous progress in the application of structural optimization. Many finite element based algorithms have matured and have been implemented into software packages applicable to day-to-day practical problems. Designs are created in an iterative process where computational simulation of the structural behavior is the basis for making design decisions. It is very common that design modifications are derived using a trial and error approach. However, the use of optimization technology would change the design process into a process driven directly by computational analysis.

Until the early 1990s, the use of structural optimization has been limited to improve designs with predetermined topology using sizing and shape optimization. Intuition and experience of the designer played the central role in defining the initial layout of a design. It has been shown that substantial further improvement of the design can be achieved by altering the initial design concept of the arrangement of cavity distribution inside a structure.

Bendsøe and Kikuchi pioneered the theoretical foundation of today's modern finite element based topology optimization methodology in 1988 [1]. Altair OptiStruct[®], first released in 1994 [2], appeared to be the first commercial software that utilizes this technology. It has found immediate overwhelming response from the automotive industry at the first place owing to its significant impact to designs at a very low effort for design engineers. Using such a tool, engineers are now able to generate efficient design concepts even before creating the first CAD model. The integration of topology optimization into the design process has been proven successful through a large number of industrial applications.

2. DESIGN PROCESS

Designing is optimization. The design is derived from a set of requirements. Knowing early in the design process what the design targets are makes it easy to apply computational means already in the definition of the design concept [3]. Generally, the design process is an iterative procedure consisting of the following phases: Conceptual design; Design; Testing; Optimization.

Changes to the design are introduced in all phases of the process. At a certain stage of this process changes to the concept become prohibitive. Hence the concept phase plays a fundamental role concerning the overall efficiency of the design and the cost of the overall development process.

This view of the process is quite theoretical. However, it can be used to define the use of computational methods to create and verify a design. These days, using topology optimization preceding the design can even extend this process. In each stage of the process computational methods are available. Depending on the character of the problem, the design optimization is performed using integrated or general optimization tools. Hence, computational means can be used to automate the design process as a whole.

In the concept phase of a design process, the freedom of the designer is just limited by the specifications of the design. Today, the decision on how a new design should look like is mostly based on a benchmark design or on previous designs. The decision-making is based on the experience of those involved in the design process. However, preliminary design tools such as topology and topography optimization can be introduced to enhance the process [4]. Topography optimization is methodology for preliminary sheet metal design [5]. This method is an application of shape optimization and allows the design of draw beads in sheet metal.

The concept can be based on results of a computational optimization rather than guessing by using topology and topography optimization. The initial design step is then already based on input generated using computational analysis. This way topology and topography optimization redefines the role of

computational analysis and simulation in the design process. Computational analysis has matured from a testing tool to a design tool.

3. TOPOLOGY OPTIMIZATION

The initial implementation of topology optimization in OptiStruct followed the original theory of [1]. The topology optimization problem is stated as

$$\begin{aligned} \text{Minimize} \quad & W(\boldsymbol{\rho}) \\ \text{Subject to} \quad & V = \sum \rho_i v_i \leq \bar{V}, \quad \eta \leq \rho_i \leq 1, \quad i = 1, \dots, n. \end{aligned} \quad (1)$$

Here, the quantity $W(\boldsymbol{\rho})$ represents the objective function. The quantities ρ_i and v_i are element densities and volumes, respectively, \bar{V} is the target volume, n is the total number of elements, and η is a small number that prevents the stiffness matrix being singular.

To enforce the design to be close to a black-and-white-solution, a penalty is introduced to reduce the efficiency of elements with intermediate density. This is achieved by a power law formulation

$$\hat{\mathbf{K}}_i(\rho_i) = \rho_i^p \mathbf{K}_i. \quad (2)$$

The matrices $\hat{\mathbf{K}}_i$ and \mathbf{K}_i represent the penalized and the real stiffness matrix of the i th element, respectively. The power p is the penalization factor that is larger than one. This method is frequently referred to as Density Method or Single Isotropic Material with Penalty (SIMP) Method.

A common objective function is the weighted sum of compliance across all load cases or a weighted sum of natural frequencies or any combination thereof.

For many practical applications a general formulation of the topology optimization problem is suitable, i.e.

$$\begin{aligned} \text{Minimize} \quad & W(\boldsymbol{\rho}) \\ \text{Subject to} \quad & g_j(\boldsymbol{\rho}) - \bar{g}_j \leq 0, \quad j = 1, \dots, m, \\ & \eta \leq \rho_i \leq 1, \quad i = 1, \dots, n. \end{aligned} \quad (3)$$

The functions g_j and \bar{g}_j are the j -th constraint and its upper bound, respectively, and m is the total number of constraints. To solve this problem dual optimization methods based on separable approximations are best suited [6, 7]. This is due to the fact that the number of design variables in a topology optimization problem is usually far too big for general nonlinear programming algorithms. The advantage of this formulation is that general optimization problems with constraints can be solved. Other methods such as the Method of Moving Asymptotes [8] or Interior Point methods with similar characteristics as the dual methods are applicable too.

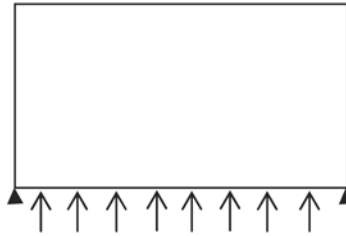


Figure 1. Rectangular design space with pressure boundary.

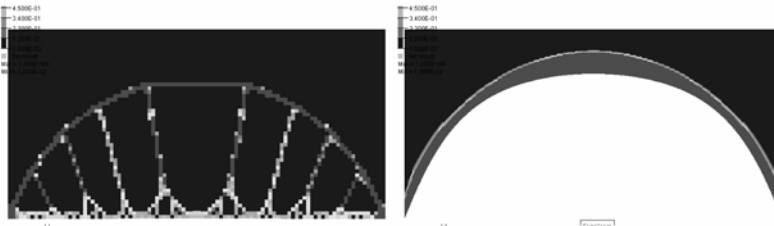


Figure 2. Rectangular design space with pressure boundary. Results.

4. SOFTWARE IMPLEMENTATION

In the software implementation the density method can be treated in the same manner as a typical sizing and shape optimization problem. Advanced approximation techniques using intermediate design variables and response are applied in the solution procedure [9]. Using such unified approach a wide variety of problems that have been off limits for topology optimization can be solved [10].

One example is the treatment of design space under pressure load. The best material distribution for the problem in Figure 1 is not the typical bridge design obtained with topology optimization, but a pressure vessel.

In a unified implementation of topology and shape optimization shape variables can be define on the pressure boundary. The problem solved is then to minimize the compliance with a volume constraint. Figure 2 shows the results obtained.

The pressure vessel is the much stiffer design. Its compliance is only about 50% of that of the bridge type structure with both having the same volume.

5. MANUFACTURABILITY

One of the major problems in topology optimization that needs to be addressed is the manufacturability of the optimization result. The transfer of a topology optimization result into a design still needs a lot of manual interference. The

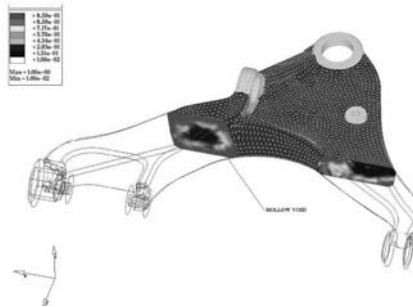


Figure 3. Control arm with enclosure due to torsion load.

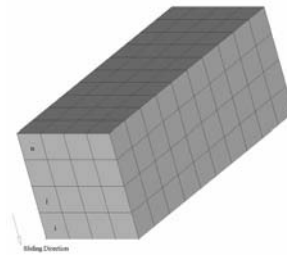


Figure 4. Defining a draw direction constraint.

design needs to include manufacturing consideration and practically recreates the optimization result in a CAD system. There is some help like geometry recovery tool such as OSSmooth, which is part of Altair OptiStruct [2]. But sometimes due to an unclear topology optimization result this involves much creativity, which may lead to a loss of performance of the design compared to the optimization result. Methods pioneered by Altair Engineering, such as minimum member size control [11] help already to improve the process. But still, in parts that are mainly under torsion load, large enclosures define the optimum structure, and these are difficult to manufacture (Figure 3).

The solution would be to develop a technology that defines a draw direction to open up the design into one direction only. This allows for better casting and milling manufacturability.

Harzheim [12] developed such a method using a Soft-Kill-Option method for topology optimization. The draw direction was determined based on a regular mesh with hexahedral elements. Zhou [13] suggests a similar method that would be valid for arbitrary meshes and is based on the computational optimization method described above. An efficient implementation has been found.

The following optimization problem is being solved (Figure 4):

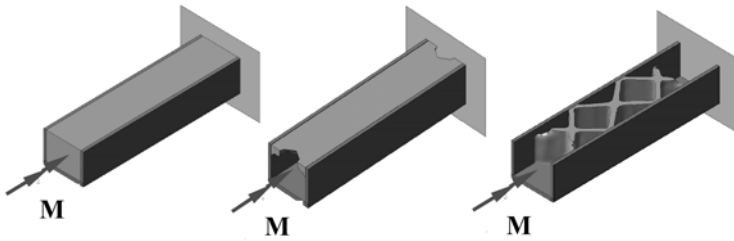


Figure 5. (a) Design, non-design space and loading. (b) Design without draw direction constraints. (c) Design with draw direction constraint.

$$\begin{aligned}
 & \min W(\boldsymbol{\rho}) \\
 & g_j(\boldsymbol{\rho}) - \bar{g}_j \leq 0 \\
 & 0 \leq \rho_i \leq \rho_{i+1} \leq \rho_{i+2} \leq \dots \leq \rho_M.
 \end{aligned} \tag{4}$$

For the user this method is hidden behind an efficient GUI. The user starts by defining the package volume (Figure 5a) for the part that has to be designed. The geometry of the design package volume is meshed and appropriate loading and constraints are applied. The user can then identify and impose performance constraints such as stiffness, frequencies, displacement, and weight thresholds that the resulting design has to meet. Also, to force the concept design to develop ribs in a C-channel, the user can specify the draw directions to pull out the part from the dies. Based on this information OptiStruct analyzes and optimizes the model to predict the optimum material layout that meets the performance constraints and also the manufacturability constraints. Below is an example of a torsion beam, optimized with and without casting constraints. Without any casting constraint imposed on the design space, it produces a hollow structure (Figure 5b). Although this structure is mathematically optimal, it cannot be manufactured by casting. Applying draw direction produces a design that can be manufactured by casting (Figure 5c) while optimally re-orienting the material to conform to the draw directions.

Entirely new approaches to manufacturing constraints are extrusion constraints [12]. These are intended to enforce constant cross sections in a largely prismatic design spaces. Figure 6 shows a simple example of that. It is a rail loaded on top with several load cases. It is compared to the design without extrusion constraints.

Here the optimization problem is defined as follows:

$$\begin{aligned}
 & \min W(\boldsymbol{\rho}) \\
 & g_j(\boldsymbol{\rho}) - \bar{g}_j \leq 0 \\
 & 0 = \rho_i = \rho_{i+1} = \rho_{i+2} = \dots = \rho_M.
 \end{aligned} \tag{5}$$

Similarly symmetry and patterns of repetition can be enforced for a design.

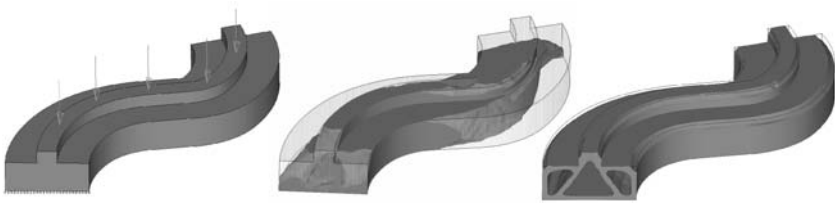


Figure 6. (a) Topology design space and loading. (b) Optimum design without extrusion constraints. (c) Optimum design with extrusion constraint.

6. LINEAR BUCKLING CONSTRAINTS

The issues of linear buckling constraints for topology optimization have been widely discussed [15]. Major obstacles for their robust implementation are:

1. The existence of singular designs;
2. The effect of low density elements on the buckling factors;
3. The absence of rules for stress calculation for semi-dens elements;
4. The computational effort for buckling sensitivity.

It is fairly straightforward to implement such constraints. For particular problems the solutions are of practical meaning. That is if a ribbing pattern on shell structures needs to be determined. For such cases topology solutions can be obtained.

In the general case an approach using compliance based topology optimization to find the stiffest design followed by a sizing and shape optimization to include buckling constraints needs to be employed [16].

7. SHELL AND COMPOSITE LAY-UP DESIGN

Using the density method for topology optimization of shells usually yields truss designs. Even more so if minimum member size control is employed. However, in many design applications it has been proven that shear web designs perform better [17].

Instead of using a density approach with penalty element-wise shell thickness as design variables has been implemented. It can be shown that this way shear panels can emerge in the design concept. Depending on the design target either the truss or the shear web design performs better. The term Free Sizing Optimization has been coined for this approach.

A trade-off study between the results of a density approach and a free sizing approach are shown below. The topology design always yields a truss structure while the free sizing design may yield a shear web if it is the best design.

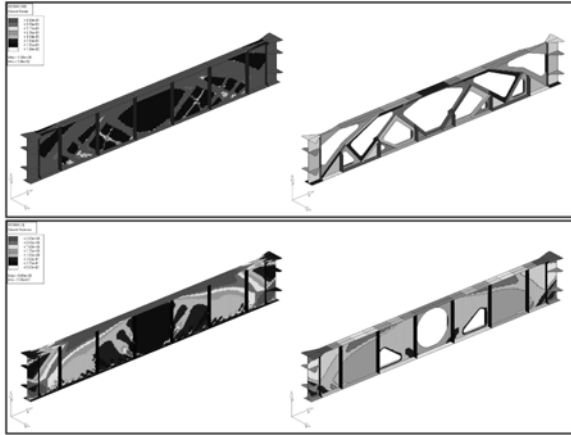


Figure 7. (a) Topology – Truss structure. (b) Free Sizing – Shear panels.

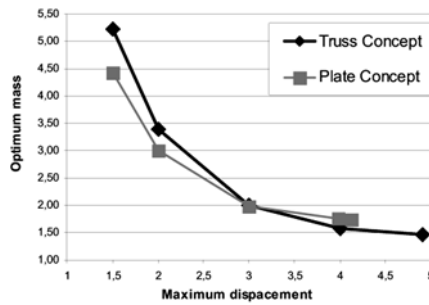


Figure 8. Comparison of truss and shear web designs.

It turns out that for a design target of lower stiffness (higher displacement) the truss yields a lighter design and for a higher stiffness the shear web design is of lower weight.

The free sizing approach can also be applied to the conceptual design of composite lay-ups. The approach is to fix the fiber angle in each ply and then to apply free sizing to the ply thickness in each element.

8. EXAMPLE 1: LEADING EDGE

This example resulted from a project at Airbus UK Ltd [18]. It showcases the advanced application of 2D topology optimization to a complex design problem such as the design of the A380 leading edge (Figure 9). The topology optimization was performed under consideration of a stiffness-based design. The design concept derived from it was then sized using size and shape optimization. In this final phase, stress and buckling constraints have been introduced.



Figure 9. Leading edge design.

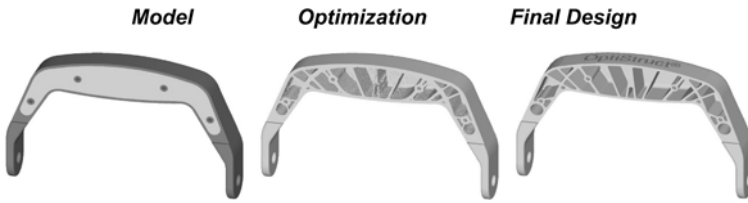


Figure 10. Handle design using draw direction constraints.



Figure 11. Impact of draw direction constraints.

Only the very final result of this entirely CAE based design process was then put into a CAD drawing.

9. EXAMPLE 2: INJECTION MOLDED PART

This example shows the application of the draw direction constraints [19]. The design is an injection molded handle. In order to be able to manufacture it, no die locking must be allowed. The use of manufacturing constraints directly produces a design that can be put into a prototype (Figure 10). Figure 11 compares the optimization with and without draw direction constraints. Without the constraint the part cannot be molded because of internal voids.

REFERENCES

[1] Bendsøe, M. and Kikuchi, N., Generating optimal topologies in optimal design using a homogenization method, *Computer Methods in Applied Mechanics and Engineering*, 71, 197–224 (1988).

[2] Altair OptiStruct, *User’s Manual v7.0*, Altair Engineering Inc., Troy, MI (2003).

- [3] Schramm, U., Structural optimization – An efficient tool in automotive design. *ATZ – Automobiltechnische Zeitschrift*, 100, Part 1: 456–462, Part 2: 566–572 (1998) [in German].
- [4] Schramm, U., Thomas, H.L., Zhou, M. and Voth, B., Topology optimization with Altair OptiStruct, in *Proceedings of the Optimization in Industry II Conference*, Banff, CAN (1999).
- [5] Voth, B., Using automatically generated shape variables to optimize stamped plates, Altair Internal Report, (1999).
- [6] Fleury, C., Structural weight optimization by dual methods of convex programming, *Int. J. for Num. Meth. Engn.*, 14, 1761–1783 (1979).
- [7] Fleury, C. and Braibant, V., Structural optimization: A new dual method using mixed variables, *Int. J. for Num. Meth. Engn.*, 23, 409–428 (1986).
- [8] Svanberg, K., Method of moving asymptotes – A new method for structural optimization, *Int. J. for Num. Meth. Engn.*, 24, 359–373 (1987).
- [9] Thomas, H.L., Vanderplaats, G.N. and Shyy, Y.-K., A study of move limit adjustment strategies in the approximation concepts approach to structural synthesis, in *Proceedings of the 4th AIAA/USAF/NASA/OAI Symposium on Multidisciplinary Design Optimization*, Cleveland, OH, pp. 507–512 (1992).
- [10] Zhou, M., Pagaldipti, N., Thomas, H.L. and Shyy, Y.K., An integrated approach for topology, sizing, and shape optimization, in *Proceedings of the 8th AIAA MDO Conference*, Long Beach, CA, AIAA-2000-4946 (2000).
- [11] Zhou, M., Shyy, Y.K. and Thomas, H.L., Checkerboard and minimum member size control in topology optimization, in *Proceedings of the 3rd WCSMO*, Buffalo, NY (1999).
- [12] Harzheim, L. and Graf, G., TopShape: An attempt to create design proposals including manufacturing constraints, in *Proceedings of OptiCon2000*, Irvine, CA (2000).
- [13] Zhou, M., Shyy, Y.K. and Thomas, H., Topology optimization with manufacturing constraints, in *Proceedings of the 4th World Congress of Structural and Multidisciplinary Optimization*, Dalian, China (2000).
- [14] Zhou, M., Fleury, R., Shyy, Y.K., Thomas, H.L. and Brennan, J., Progress in topology optimization with manufacturing constraints, in *Proceedings of the 9th AIAA MDO Conference*, Atlanta, GA, AIAA-2002-4901 (2002).
- [15] Zhou, M., Pagaldipti, N. and Shyy, Y.K., Topology optimization with linear buckling responses – Software and applications, in *Proceedings of the 5th WCSMO*, Venice, Italy (2003).
- [16] Schramm, U., Zhou, M., Tang, P.-S. and Harte, C.G., Topology layout of structural designs and buckling, in *Proceedings of the 10th AIAAMDO Conference*, Albany, NY, AIAA-2004-4636 (2004).
- [17] Cervellera, P., Zhou, M. and Schramm, U., Optimization driven design of shell structures under stiffness, strength and stability requirements, in *Proceedings of the 6th WCSMO*, Rio de Janeiro, Brasil (2005).
- [18] Krog, L., Tucker, A. and Rollema, G., Application of topology, sizing and shape optimization methods to optimal design of aircraft components (2003).
- [19] Nelson, E., Draw direction constraints in topology optimization – A practical example, in *Proceedings of the SAE World Congress*, Detroit, SAE Paper 2003-01-1306 (2003).

Mechanisms and Multiphysics

CONFIGURATION DESIGN OF RIGID LINK MECHANISMS BY AN OPTIMIZATION METHOD: A FIRST STEP*

Yoon Young Kim¹, Gang Won Jang², Jung Hun Park³, Jin Seup Hyun⁴ and Sang Jun Nam⁴

¹*School of Mechanical and Aerospace Engineering, and National Creative Research Initiatives Center for Multiscale Design, Seoul National University, Seoul, Korea*

²*Department of Mechanical Engineering, Kunsan University, Kunsan, Korea*

³*Brooks Automation Asia, Kyungki-Do, Korea*

⁴*School of Mechanical and Aerospace Engineering, Seoul National University, Seoul, Korea*

Abstract: This work is concerned with the automatic configuration design or synthesis of mechanisms consisting of rigid links and joints. The specific design goal is to configure a rigid-link mechanism that converts a given input motion at a certain location to a desired output motion at an end-effector location without any initial information on mechanism configuration. To the authors' knowledge, the automatic synthesis or design envisioned in this investigation has not been reported. In this respect, this investigation may open a door to rigid-body mechanism synthesis. For the synthesis, two-dimensional mechanisms consisting of rigid links and revolute joints will be considered. The synthesis is formulated as a problem to minimize the difference between the prescribed output motion and the actual output motion. The key to the success of the mechanism synthesis lies in the development of a single unified model that can represent all possible rigid-body mechanisms. Our idea is to represent rigid link mechanisms by *spring-connected rigid blocks*; by adjusting the real-valued spring stiffness, any rigid link mechanism can be simulated and a desired mechanism can be synthesized by varying the spring stiffness. In this investigation, only the kinematics of a mechanism will be considered. Numerical examples are presented to demonstrate the effectiveness of the proposed method.

Keywords: Rigid link mechanism, automatic design, synthesis, spring-connected blocks.

*The underlying concepts of some automatic synthesis methods, including the one given here, were presented as the plenary lecture under the same title at the 3rd China-Japan-Korea Joint Symposium on Optimization of Structural and Mechanical Systems (Kanazawa, Japan, October 30–November 2, 2004).

1. RESEARCH DIRECTION

Mechanism synthesis has been a subject of numerous investigations [1–11]. Since good reviews [8–11] on the subject can be found in the literature, we will mainly focus on the difference between existing investigations and the present investigation. The goal of this research is to develop a new computational method to automatically design or synthesize a planar linkage mechanism without using any initial baseline linkage. Most existing mechanism synthesis methods use a candidate mechanism layout such as an equal-length four-bar linkage and vary its link lengths and joint locations until a desired mechanism is obtained. If the desired linkage cannot be configured by the adjustment of the joint location and link size of the baseline linkage, the synthesis must be repeated with a new candidate linkage. Therefore, a synthesis method to determine the linkage type (the numbers of links and joint conditions) and specific dimensions in a single synthesis process will be extremely useful, but no such method has been developed so far.¹ In this work, the kinematic synthesis of planar linkages consisting of rigid links and revolute joints will be investigated.

The main criteria in developing the automatic synthesis method are (1) that the synthesis process should not require a specific initial mechanism and (2) that the synthesis process should be determined in reasonable computation time. To satisfy the two criteria, the idea of using a unified model for the topology optimization [15] of continuum bodies may be borrowed for the present investigation. Here, we should develop a single unified rigid-link mechanism model that can represent various candidate linkage configurations by the adjustment of some parameters or variables. The crucial step in this research is the development of a spring-connected block model (SBM); this model is shown to be capable of simulating the kinematic motion of any rigid-link mechanism connected by revolute joints by adjusting the spring stiffness. By means of SBM, the problem of the rigid link mechanism synthesis can become a minimization problem to determine the stiffness values. By formulating the problem with real-valued design variables that control the spring stiffness, numerically efficient gradient-based algorithms are applicable in searching the desired linkage configuration.

The automatic design or synthesis problem considered in this investigation is schematically depicted in Figure 1. To clarify the scope of the present investigation, the problem definition and assumptions are summarized as (OBJ: objective, G: Given condition; A: Assumption):

¹During the conference (topoptSYMP 2005), some related research works on the automatic mechanism synthesis were brought to our attention: articulated mechanism design approaches [12, 13] using deformable ground trusses and topology optimization of rigid body mechanisms using relaxed kinematic constraint equations [14].

OBJ: Without a baseline linkage, find a linkage mechanism producing the desired motion at a designated location.

- G1: Input motion (say, simple circular or linear motion at a designated location);
- G2: Desired output motion at a designated location such as the end-effector location;
- G3: Configuration domain within which a planar linkage is synthesized;
- A1: The desired linkage consists of rigid links and revolute joints;
- A2: The link number and the revolution joint number are not known in advance although the maximum numbers are constrained;
- A3: If necessary, revolute joints should be fixed to the ground;
- A4: No initial linkage type or configuration is available;
- A5: Only kinematics will be considered, i.e., dynamics will not be considered in this investigation.

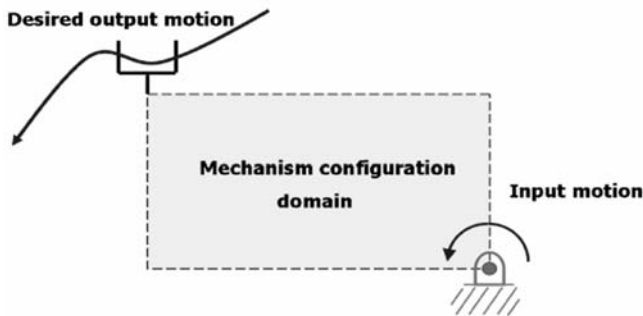


Figure 1. Problem definition: for given input and output motions, find a planar linkage mechanism without relying on any baseline linkage.

The following is the summary of the automatic synthesis procedure developed in this work:

- Step 1: The given mechanism configuration domain is discretized by a number of rigid rectangular blocks (see Figure 2(a)).
- Step 2: Rigid blocks are connected by zero-length one-dimensional elastic springs with varying stiffness (see Figure 2(b)). It will be shown that as far as the kinematics is concerned, a set of the developed

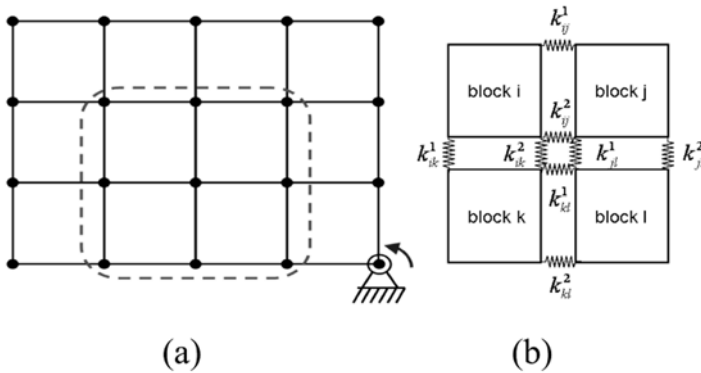


Figure 2. Spring-connected block model: (a) discretization of a mechanism configuration domain by a number of rigid rectangular blocks, and (b) a set of zero-length elastic springs with varying stiffness connecting adjacent rigid blocks.

spring-connected blocks can accurately simulate the movement of actual linkages composed of rigid links and revolute joints. The spring stiffness should be properly selected.

Step 3: Solve the following optimization problem to find the desired mechanism configuration:

$$\underset{\xi \in R^N}{\text{minimize}} F = \max_{t_0 \leq t \leq t_f} (\mathbf{r}_Q(t) - \hat{\mathbf{r}}_Q(t))^2, \tag{1}$$

where \mathbf{r}_Q is the motion of the end-effector at Q , and $\hat{\mathbf{r}}_Q$ the prescribed motion. In (1), time is denoted by t and subscripts 0 and f denote the initial and final stages. The symbol ξ denotes the design or decision variables controlling the stiffness of the springs attached to the rigid blocks.

Step 4: Identify the actual linkage mechanism consisting of rigid links and revolute joints from the spring-connected block model having the obtained values of ξ .

Step 5: If necessary, carry out the size/shape optimization (i.e., vary joint locations and link sizes) for the linkage obtained at Step 4) in order to decrease the value of F .

In Section 2, we propose a unified spring-connected block model to facilitate the automatic mechanism synthesis. In Section 3, the validity the proposed automatic synthesis method using the block model is examined by several numerical examples.

2. LINKAGE MECHANISM MODELING FOR AUTOMATIC SYNTHESIS

Since there is no given initial linkage layout, the following decision (or design) variables must be determined by the automatic mechanism synthesis if a typical rigid-link mechanism model is used for the synthesis:

- n_{link} : number of rigid links; L_i : link length, $i = 1, \dots, n_{\text{link}}$;
- n_{joint} : number of revolute joints;
- $\mathbf{r}_j \in R^2$: joint position vector ($j = 1, \dots, n_{\text{joint}}$);
- g_j : state variable indicating whether the j -th revolute joint is fixed in space or not (if $g_j = 0$, not fixed, else if $g_j = 1$, fixed).

The minimization problem in Equation (1) is nearly impossible to solve for n_{link} , L_i , n_{joint} , \mathbf{r}_j and g_j because different values of n_{link} and n_{joint} change the linkage types of the mechanism, say, from a four-bar linkage to a six-bar linkage. Whenever different values of n_{link} and n_{joint} are considered, new kinematic models should be built and analyzed. Even if the allowed maximum numbers of n_{link} and n_{joint} are moderate, solving Equation (1) as a minimization problem involving both integer and real variables would require impractically large computation time. Thus developing one universal model that can represent different linkage types may be the key to the success of the automatic mechanism synthesis.

The spring-connected block model shown in Figure 2(b) is the proposed model for the synthesis. Because spring elements are introduced, the pure kinematic problem of rigid-link mechanisms becomes the problem to solve both kinematics and statics. Instead of the block model shown in Figure 2(b), we also considered using a set of rigid links connected by translational and rotational springs. The adjustment of the rotational springs was problem-dependent so that the spring-connected rigid-link model could not be used as a single unified model.

In the proposed SBM, two neighboring blocks sharing a common edge are connected by a pair of elastic springs. In particular, each spring has only the translational stiffness (both in the horizontal and vertical components as before), and no rotational spring is considered for the connection. Symbols k_{ij}^1 and k_{ij}^2 in Figure 2(b) correspond to the two springs connecting the i -th and j -th blocks. When the interfacing edge of two blocks is horizontal, subscripts 1 and 2 are associated with the left and right springs, respectively, whereas if the edge is vertical, subscripts 1 and 2, the upper and lower springs, respectively. For actual numerical implementation, the values of k_{ij}^p ($p = 1, 2$) will be bound as $k_{\min} \leq k_{ij}^p \leq k_{\max}$. (For all numerical problems, $k_{\max} = 1$ and

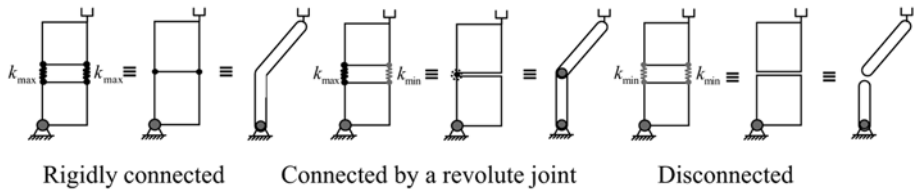


Figure 3. Representation of various joints by adjusting the spring stiffness of SBM.

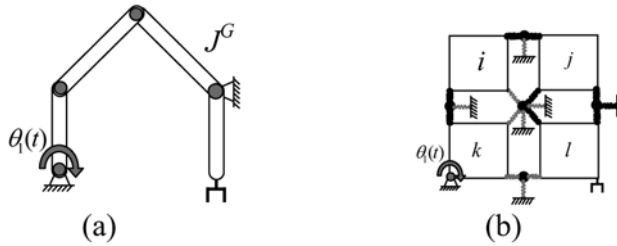


Figure 4. (a) A given rigid-link mechanism having an anchored revolute joint (J^G), (b) equivalent mechanism simulated by G-SBM.

$k_{\min} = 0.001 \sim 0.01$ are used.) Figure 3 illustrates how various joint statuses of rigid links are simulated by SBM.

Now let us consider the modeling of a more general linkage having an anchored revolute joint on the ground. The anchored revolute joint (denoted by J^G) is a revolute joint whose translation motion is constrained. To be able to express J^G in addition to the three joint statuses illustrated in Figure 3, we are modifying SBM; the modified model will be called the Generalized Spring-connected rigid Block Model (G-SBM). To give an idea of G-SBM, Figure 4 shows the application of G-SBM for the simulation of a rigid link having J^G .

In G-SBM, blocks α ($\alpha = i, j, k, l$) are supported by zero-length elastic (translational) springs $k_{p,\alpha}$ ($\alpha = i, j, k, l$) connecting nodes p_α in blocks α and a generic node p located at the common interfaces of the blocks (see Figure 4(b)). The generic node p is also connected to the ground by a zero-length anchoring spring $k_{p,A}$. The anchoring spring also has the translational stiffness only. If $k_{p,A}$ approaches zero, the resulting model is equivalent to the earlier SBM. On the other hand, if $k_{p,A}$ approaches infinity, the translational motions of node p become restrained. If $k_{1,A} \rightarrow 0, k_{2,A} \rightarrow \infty$ and $k_{p,\alpha} \rightarrow \infty$ ($p = 1, 2; \alpha = 1, 2$), the G-SBM simulates a rigid link with an anchored revolute joint. To avoid numerical singularity in solving kinematics and statics for G-SBM, the values of $k_{p,\alpha}$ and $k_{p,A}$ are also bound as $k_{\min} \leq k_{p,\alpha}, k_{p,A} \leq k_{\max}$.

When the minimization (1) is solved by a gradient-based approach, the stiffness should be as close as possible to either k_{\min} or k_{\max} ; otherwise, it is not possible to identify a physically-configurable rigid-link mechanism. Thus, the stiffness k can be made to approach k_{\min} or k_{\max} at the end of the minimization

process by relating k and the design variable ξ as:

$$k_{p,\alpha} = f(\xi_{p,\alpha}); \quad k_{p,A} = g(\xi_{p,A}), \quad (2)$$

where f and g are chosen as

$$f(\xi) = g(\xi) = \frac{k_{\max} - k_{\min}}{1 - \exp(-t\xi)} + k_{\min} \quad (t \in R^+). \quad (3)$$

For the numerical problems considered below, the use of the S-shaped function in (3) worked satisfactorily, but other functional forms may be considered. Successful applications of the S-shaped function in pushing design variables to their limits may also be found in the literature [16–18]. To check how closely SBM or G-SBM simulates the motions of various rigid-link mechanisms, several tests were conducted. Unless the motion duration was very large, SBM and G-SBM simulated the desired motions satisfactorily. (Due to space limitation, the simulated motions will not be included here.)

3. MECHANISM SYNTHESIS BY SBM AND G-SBM

In this section, the proposed method using SBM and G-SBM will be applied to synthesize or design a few rigid-link mechanisms. All numerical simulations were carried out by using ADAMS [19]. The solution of (1) was found by SQP [20] provided in ADAMS. The required sensitivity was calculated by finite difference.

As the first problem, we will check if the known mechanism can be synthesized by the proposed approach using SBM. Referring to Figure 5(a), the objective is to synthesize a rigid-link mechanism giving $\hat{\mathbf{r}}_Q(t)$ at Q if the link connecting $(0, 0)$ and $(0.033, 0.303)$ is rotated by the angle $\phi(t) = \pi t/6$. Figure 5(b) shows the discretized configuration design domain by 9 rigid blocks connected by 24 block-connecting springs. (To facilitate drawing, zero-length springs will not be shown.) For the synthesis, the initial values of $k_{ij}^\alpha = 0.5$ were used. Figure 5(c) shows the snapshots of the final motions of the converged SBM at $t = t_f$ and the identified rigid-link mechanism from the SBM. The iteration histories are shown in Figure 6. (If necessary, the joint coordinates of the identified rigid link mechanism can be updated by shape optimization.)

As the next problem, the synthesis of a vertical-line mechanism shown in Figure 7(a) is considered. The specific objective is to synthesize a mechanism converting a rotation motion ($\phi_A(t) = \pi t/6, 0.0 \leq t \leq 0.3$) at A to an upward motion at Q , the end-effector location. This problem will be solved by using G-SBM, which is the generalized form of SBM. The synthesis domain is discretized by 3×3 blocks that are connected by 32 block-connecting springs and 12 anchoring springs. For the synthesis, the design variables corresponding to $k_{p,\alpha} = 0.5$ and $k_{p,A} = 0.001$ were used as the initial values for

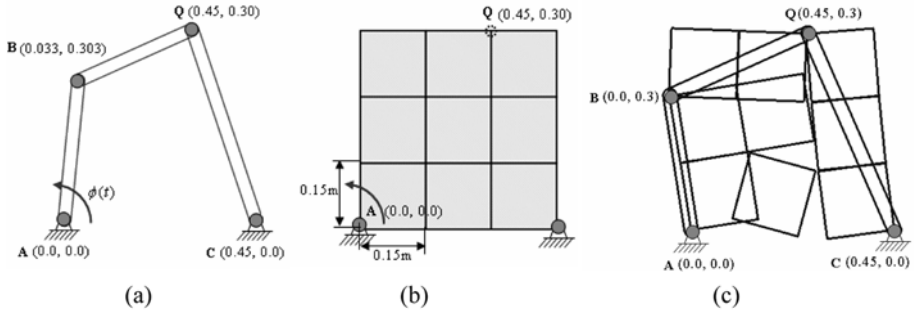


Figure 5. Mechanism synthesis by SBM. (a) The given four-bar mechanism (Q : end-effector location), (b) discretized configuration design domain, (c) snapshots of the final motion of the converged SBM at $t = t_f$ and the identified rigid link mechanism.

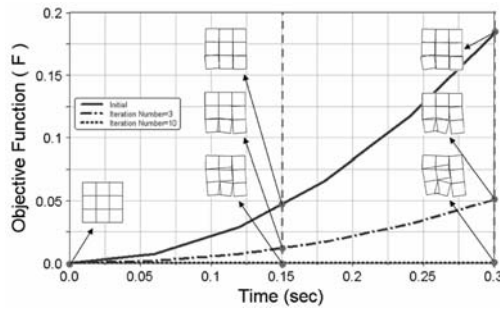


Figure 6. Iteration history for the problem depicted in Figure 5.

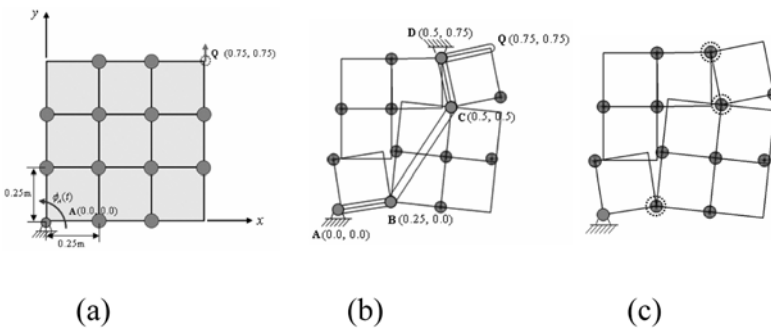


Figure 7. Synthesis of a straight-line mechanism by the proposed method based on G-SBM. (a) Problem definition and configuration design domain discretization, (b) snapshot of the converged G-SBM as the solution of Equation (1), (c) the identified rigid-link mechanism.

the synthesis. Figure 7(b) shows the snapshot of the motion of the converged G-SBM at $t = t_f$ and Figure 7(c) shows the identified link mechanism. To improve the straightness of the output motion, the coordinates of the revolute joints at B , C and D are updated by shape optimization. Not shown here is that the shape optimization changed the coordinates of B , C and D , which helped improve the straightness of the motion of the end-effector.

REFERENCES

- [1] J. Denavit and R.S. Hartenberg, Approximate synthesis of four-bar linkages, *Transactions of ASME*, 77 (August), 853–861 (1955).
- [2] D.P. Naik and C. Amarnath, Synthesis of adjustable planar 4-bar mechanism, *Mechanism and Machine Theory*, 24(6), 523–526 (1989).
- [3] R.L. Fox and K.C. Gupta, Optimization technology as applied to mechanism, *ASME Journal of Engineering for Industry*, 95, 657–663 (1973).
- [4] R.R. Roots and K.M. Ragesdell, A survey of optimization methods applied to the design of mechanisms, *Transactions of the ASME Series B, Journal of Engineering for Industry*, 98(3), 1036–1041 (1976).
- [5] J.A. Cabrera, A. Simon and M. Prado, Optimal mechanisms with genetic algorithms, *Mechanism and Machine Theory*, 37, 1165–1177 (2002).
- [6] C.F. Chang, Synthesis of adjustable four-bar mechanisms generating circular arcs with specified tangential velocities, *Mechanism and Machine Theory*, 36(3), 387–395 (2001).
- [7] T.M. Wu and C.K. Chen, Mathematical model and its simulation of exactly mechanism synthesis with adjustable link, *Applied Mathematics and Computation*, 160, 309–316 (2005).
- [8] D. Sen, S. Chowdhury and S.R. Pandey, Geometric design of interference-free planar linkages, *Mechanism and Machine Theory*, 39, 737–759 (2004).
- [9] P.S. Shiakolas, D. Koladiya and J. Kebrle, On the optimum synthesis of four-bar linkages using differential evolution and the geometric centroid of precision position, *Journal of Inverse Problem in Engineering*, 10(6), 485–502 (2002).
- [10] P.S. Shiakolas, D. Koladiya and J. Kebrle, On the optimum synthesis of six-bar linkages using differential evolution and the geometric centroid of precision positions technique, *Mechanism and Machine Theory*, 40, 319–335 (2005).
- [11] S.J. Chiou and S. Kota, Automated conceptual design of mechanisms, *Mechanism and Machine Theory*, 34, 467–495 (1999).
- [12] A. Kawamoto, M.P. Bendsøe and O. Sigmund, Articulated mechanism design with a degree of freedom constraints, *International Journal for Numerical Methods in Engineering*, 61, 1520–1545 (2004).
- [13] A. Kawamoto, Path-generation of articulated mechanism by shape and topology variations in non-linear truss representation, *International Journal for Numerical Methods in Engineering*, 64, 1557–1574 (2005).
- [14] C.L. Felter, Topology optimization of rigid body mechanisms, M.S. Thesis, Technical University of Denmark, Department of Mechanical Engineering (2003).
- [15] M.P. Bendsøe and N. Kikuchi, Generating optimal topologies in structural design using a homogenization method, *Computer Methods in Applied Mechanics and Engineering*, 71, 197–224 (1988).

- [16] Y.Y. Kim, and G.H. Yoon, Multi-resolution multi-scale topology optimization – A new paradigm, *International Journal of Solids and Structures*, 37, 5529–5559 (2000).
- [17] G.H. Yoon, and Y.Y. Kim, The role of S-shaped mapping functions in the SIMP approach for topology optimization, *KSME International Journal*, 15, 1496–1506 (2003).
- [18] Y.Y. Kim, G.W. Jang and S.J. Nam, Inverse kinematics of binary manipulators by using the continuous-variable-based optimization method, *IEEE Transactions on Robotics*, 2005, accepted.
- [19] ADAMS/View Manual (version 12.0), MSC Software (2002).
- [20] G.N. Vanderplaats, *Numerical Optimization Techniques for Engineering Design with application*, McGraw-Hill (1984).

THE PRESSURE LOAD PROBLEM RE-VISITED

Peter Michael Clausen* and Ole Sigmund

Department of Mechanical Engineering, Solid Mechanics, Technical University of Denmark, Nils Koppels Alle, Building 404, DK-2800 Lyngby, Denmark

peter.clausen@fe-design.de, sigmund@mek.dtu.dk

Abstract: A weak point of the density based approach to topology optimization has been its disability to handle design dependent surface loads like pressure loads without introducing special parameterizations of the load surfaces. In this paper we suggest a way to resolve the problem. Based on a mixed pressure-displacement finite element model we impose the pressure load through an incompressible hydrostatic fluid. One continuous design variable per element interpolates between solid elastic material and incompressible fluid. The method is straightforward to implement and applies to two as well as three dimensions.

Keywords: Pressure loads, mixed formulation, density method, incompressibility, SIMP.

1. INTRODUCTION

In pressure load problems, the position of the loads depend on the topology. Such problems are encountered in hydrostatics and dynamics of wind, water and snow loaded mechanical and civil structures such as ships, submerged structures, airplanes, combustion engines, pumps, etc.

Previous works on topology optimization with pressure load embrace several approaches (Hammer and Olhoff, 2000; Du and Olhoff, 2004a, 2004b; Chen and Kikuchi, 2001; Fuchs and Shemesh, 2004; Bourdin and Chambolle, 2003), all involving alternative parametrization schemes or shape parameterizations of the loading surfaces. Alternatively one may use the level-set method where it is fairly straight forward to implement pressure loads since the load surface is well-defined (Allaire et al., 2004; Liu et al., 2005).

In this paper we introduce a new way to solve the pressure load problem based on a mixed displacement-pressure (incompressible) formulation but using the standard density approach to topology optimization. Thus, the scheme can be implemented in existing topology optimization softwares based on the

*Now FE-design GmbH, Karlsruhe, Germany.

density approach. In fact, the only necessary changes to the code lies in the interpolation scheme, the boundary conditions and possibly the linear system solver.

The idea of the method is the following. Instead of defining the equilibrium equations in the typical FE displacement formulation, we define it in mixed form by including the pressure as a separate variable. This makes it possible to define the void phase in the topology optimization formulation as an incompressible hydrostatic fluid, thus allowing for transfer of pressure from the external boundary conditions to the structure – independent of its shape or topology.

2. MODELLING

Linear elasticity problems may be stated in a mixed pressure-displacement form by introducing a pressure variable

$$p = -K \varepsilon_{kk}, \quad (1)$$

where K is the bulk modulus and ε_{ij} the Cauchy strain tensor and double indices means summation.

The constitutive law for the mixed form is

$$\sigma_{ij} = 2G e_{ij} - \delta_{ij} p \quad (2)$$

where G is the shear modulus, σ_{ij} is the stress tensor, e_{ij} is the deviatoric strain tensor

$$e_{ij} = \varepsilon_{ij} - \frac{1}{2} \delta_{ij} \varepsilon_{kk} \quad (3)$$

and δ_{ij} is Kronecker's delta. Here we assumed planar elasticity but the idea applies to three dimensions as well.

In weak form, the equilibrium conditions for the mixed formulation can be written as

$$\int_{\Omega} \delta \varepsilon_{ij} 2G e_{ij} d\Omega - \int_{\Omega} \delta \varepsilon_{ij} \delta_{ij} p d\Omega - \int_{\Omega} \delta u_i F_i d\Omega - \int_{\Gamma_T} \delta u_i T_i^* d\Gamma = 0, \quad (4)$$

and additionally

$$\int_{\Omega} \delta p (p/K + \varepsilon_{kk}) d\Omega = 0, \quad (5)$$

which have to hold for all kinematically admissible displacement variations δu_i and pressure variations δp . In (4), F_i is the volume force tensor and T_i^* is the surface traction tensor.

The mixed form described by (4)–(5) is implemented in a standard finite element form using the commercial code FEMLAB which is a MATLAB add-on.

For stability reasons it is important to use the right element field interpolations schemes. Here we use rectangular 4-node elements with bi-linear displacement interpolation and element-wise constant pressures for computational efficiency. These elements are known only to be partially stable, however, in our optimizations we did not experience any problems with pressure oscillations.

3. INTERPOLATION SCHEME

Depending on the choices of the bulk and shear moduli, we can model different material behaviours. An infinite bulk modulus gives incompressibility and a shear modulus close to zero corresponds to a (hydrostatic) fluid whereas standard elastic materials have finite bulk and shear moduli. The simplest scheme is obtained for interpolation between a hydrostatic incompressible fluid and an incompressible elastic material

$$\left. \begin{aligned} K &= K_{\text{fluid}} = K_0 = \infty \\ G(\mu) &= G_{\text{fluid}} + \mu^\eta (G_0 - G_{\text{fluid}}) \end{aligned} \right\} \quad (6)$$

where μ is the density design variable and K_{fluid} , K_0 , G_{fluid} and G_0 are the fluid bulk modulus, elastic bulk modulus (both set to infinity), fluid shear modulus and elastic shear modulus, respectively. The penalization factor η is well-known from the standard SIMP approach.

4. NUMERICAL IMPLEMENTATION

Apart from the interpolation scheme and the mixed formulation, the implementation of the pressure load problem follows that of standard compliance minimization problems. The objective function is still to minimize compliance. Note that since the fluid domain is incompressible and has negligible shear stiffness, the strain energy stored in the fluid domain will be diminutive compared to the elastic domain. Therefore, we can stick to the usual compliance objective function.

The topology optimization problem is solved using Matlab scripts calling the FE-package FEMLAB. As demonstrated in Olesen et al. (2005), the Matlab script can be formulated very compactly using FEMLAB calls and the derivation of sensitivity information can be performed (semi-)automatically. This is obtained by defining the design variable field μ as an extra field in the FE model. The solver only solves for the original displacement and pressure fields.

Since the emphasis in this paper is on the physical concept and not the implementation, no further details about the FEMLAB implementation will be given here. However, it is noted that the automatically calculated sensitivities have been confirmed by finite differences checks. The optimization problems is solved by the Method of Moving Asymptotes (MMA, Svanberg, 1987). Finally, as with most other density formulations, the proposed topology optim-

ization scheme is prone to numerical problems like checkerboards and mesh-dependencies (Sigmund and Petersson, 1998). In order to avoid this problem we use the mesh-independency filtering scheme proposed by the first author (Sigmund, 1997).

5. INTERNALLY PRESSURIZED LID EXAMPLE

To demonstrate the method we use an example that has previously been used in the literature to demonstrate schemes for pressure load problems (Hammer and Olhoff, 2000; Du and Olhoff, 2004a, 2004b; Chen and Kikuchi, 2001; Liu et al., 2005). The design domain with indication of boundary conditions corresponding to a simply supported stubby beam of length 1 and height $1/2$ is shown in Figure 1a. The pressure load may for the mixed formulation be introduced by different boundary conditions. Common for all cases, however, is that a narrow fixed fluid region is introduced below the design domain. The fluid region is put under pressure either by removing the supports on the lower edge and applying a vertically distributed traction load, by prescribing the vertical displacements of the lower edge or by prescribing the pressure on the left, right and lower edges of the fixed fluid region. For the following case we used the latter approach, however, it has been tested that the other two formulations result in essentially the same responses and topologies. For this case, we use rectangular elements with bi-linear displacement interpolation and element-wise constant pressure interpolation but for the design field we use a bi-linear interpolation, i.e. a Q-4/1/4 element. In the following examples only half the design domain is discretized and there are 1681 nodal design variables. A volume fraction of $f_0 = 0.5$ may be filled with solid material with $E = 1$ and $\nu = 0.3$. The mesh-independency filter size is equal to 1.5 times the element size.

As a reference we first optimize the structure for fixed unit tractions on the lower edge of the design domain and non-fluid void regions, i.e. a standard SIMP approach. The optimized topology is seen to be the well-known bridge-like solution (Figure 1b) which has a compliance of $W_{\text{final}} = 1.12$. As a check we can also analyze this optimized structure with an incompressible fluid region with boundary conditions corresponding to prescribed $p = 1$ on the lower, left and right boundaries of the fixed fluid region. Also in this case the compliance is $W = 1.12$, confirming that it is possible to transmit surface loads through an incompressible fluid.

Next we optimize the structure with the incompressible fluid model. The optimized topology is seen in Figure 1c and is seen to be an arch-like structure known from the previous works on pressure load problems. The final compliance of the arch-like structure is $W_{\text{final}} = 0.94$, i.e. 16% better than for the fixed traction problem. This result corresponds well with the 17.67% improvement

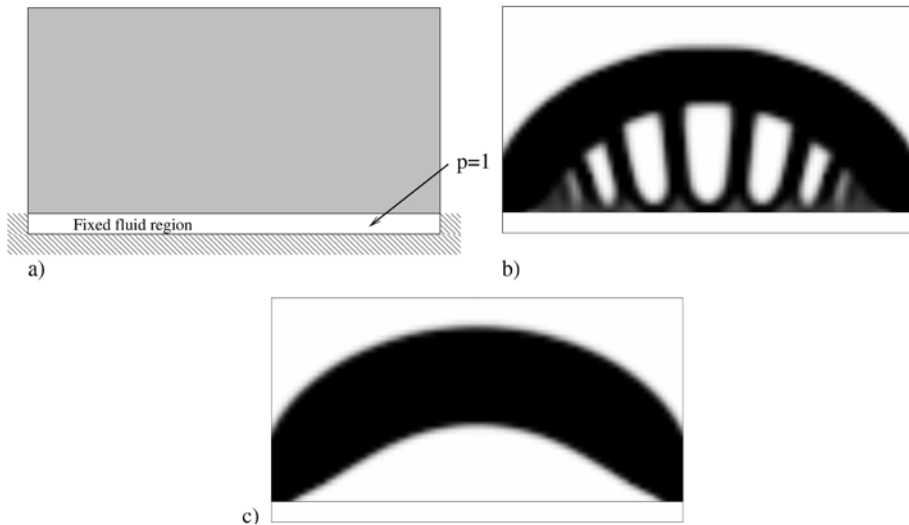


Figure 1. (a) Design domain and boundary conditions for internally loaded lid. The white region below the design domain indicates a region fixed to be fluid. (b) Reference case with optimized topology for pressure load fixed to the lower edge of the design domain. (c) Optimized topology with pressure load.

reported in Du and Olhoff (2004a) which was obtained for a coarser discretization (400 elements) and an iso-density curve for imposing the pressure load surface.

This example was done for the case of incompressible material and fluid. It is also possible to solve problems with small compressibility of the fluid phase and compressible elastic material. Here, however, it is important that the bulk modulus of the fluid does not exceed approximately 20 times that of the elastic material. This is to avoid numerical instabilities associated with spurious but numerically favorable mixtures of elastic material with incompressible fluid inclusions.

6. CONCLUSIONS

In this proceedings paper we have only shown a few details of the method and we have demonstrated its efficiency with only one example. However, the procedure immediately applies to three dimensions and by small modifications of the interpolation scheme, one may model cases with other material behaviours such as for example compressible elastic material.

A potentially weak point of method is that internal “void” regions in the structures also become incompressible (fluid-filled) – a possibility the optimization algorithm may take advantage of by using the void regions as “incom-

pressible cavities". This possibility, that may or may not be physically relevant for a particular problem, can be avoided by introducing an extra (compressible) void phase in the design problem. If one now puts a constraint on the available amount of fluid, it is possible to eliminate fluid filled cavities by a trial and error approach or alternatively by the method suggested by Chen and Kikuchi (2001). Also, the idea may be applied to design of water loaded structures like dams or water towers by introducing mass density and gravity loads on the fluid and structural regions.

More details about the method and several examples in two and three dimensions including dam design problems are given in a full paper (Sigmund and Clausen, 2005). An extension to dynamic problems (acoustic-structural interaction) can be found in these proceedings (Yoon et al., 2006).

REFERENCES

- Allaire, G., Jouve, F. and Toader, A.-M. (2004) Structural optimization using sensitivity analysis and a level-set method, *Journal of Computational Physics*, 194(1), 363–393.
- Bourdin, B. and Chambolle, A. (2003) Design-dependent loads in topology optimization, *ESAIM: Control, Optimisation and Calculus of Variations*, 9, 19–48.
- Chen, B. and Kikuchi, N. (2001) Topology optimization with design-dependent loads, *Finite Element in Analysis and Design*, 37, 57–70.
- Du, J. and Olhoff, N. (2004a) Topological optimization of continuum structures with design-dependent surface loading – Part I: New computational approach for 2D problems, *Structural and Multidisciplinary Optimization*, 27, 151–165.
- Du, J. and Olhoff, N. (2004b) Topological optimization of continuum structures with design-dependent surface loading – Part II: Algorithm and examples for 3D problems, *Structural and Multidisciplinary Optimization*, 27, 166–177.
- Fuchs, M.B. and Shemesh, N.N.Y. (2004) Density-based topological design of structures subjected to water pressure using a parametric loading surface, *Structural and Multidisciplinary Optimization*, 28(1), 11–19.
- Hammer, V.B. and Olhoff, N. (2000) Topology optimization of continuum structures subjected to pressure loading, *Structural and Multidisciplinary Optimization*, 19, 85–92.
- Liu, Z., Korvink, J.G. and Huang, R. (2005) Structure topology optimization: Fully coupled level set method via FEMLAB, *Structural and Multidisciplinary Optimization*, 29(6), 407–417.
- Olesen, L.H., Okkels, F. and Bruus, H. (2005) A high-level programming-language implementation of topology optimization applied to steady-state Navier–Stokes flow, *International Journal for Numerical Methods in Engineering*, to appear.
- Sigmund, O. (1997) On the design of compliant mechanisms using topology optimization, *Mechanics of Structures and Machines*, 25(4), 493–524.
- Sigmund, O. and Clausen, P.M. (2005) The pressure load problem revisited, submitted.
- Sigmund, O. and Petersson, J. (1998) Numerical instabilities in topology optimization: A survey on procedures dealing with checkerboards, mesh-dependencies and local minima, *Structural Optimization*, 16(1), 68–75.

- Svanberg, K. (1987) The Method of Moving Asymptotes – A new method for structural optimization. *International Journal for Numerical Methods in Engineering*, 24, 359–373.
- Yoon, G.H., Jensen, J.S. and Sigmund, O. (2006) Topology optimization for acoustic structure interaction problems, in *IUTAM Symposium on Topological Design Optimization of Structures, Machines and Materials: Status and Perspectives*, M.P. Bendsøe, N. Olhoff and O. Sigmund (eds), Springer, Dordrecht, pp. 355–364.

TOPOLOGY OPTIMIZATION IN MAGNETIC FIELDS

Jeonghoon Yoo

School of Mechanical Engineering, Yonsei University, 134 Sinchon-dong, Seodaemoon-ku, Seoul, Korea 120-749

Abstract: Topology optimization in magnetic fields has been studied based on the HDM (homogenization design method) and SIMP (Solid Isotropic Material with Penalization). Recently, the modified density approach that accepts the concept of the homogenization design method has been suggested. In this study, the results of topology optimization based on the objective functions such as maximizing magnetic force as well as maximizing the magnetic mean compliance are reviewed. Especially, the modified density approach is studied to obtain the improved final topology comparable to the results by HDM focusing on the hole-shape of the unit element structure considering the directional properties of the magnetic flux.

Keywords: Topology optimization, magnetic fields, homogenization design method, solid isotropic material with penalization, modified density approach.

1. INTRODUCTION

The studies on topology optimization in magnetic fields have been focused on the obtaining the optimal structure affected by magnetic fields. Two kinds of methods are used in ordinary topology optimization: density method such as SIMP (Bendsøe, 1989) and the homogenization design method (HDM) suggested by Bendsøe and Kikuchi (1988). The density method has been used in the name of the optimal material distribution method (OMD) from the late 1990s (Lowther et al., 1998) and HDM has been applied in 2000 (Yoo and Kikuchi, 2000; Yoo et al., 2000). Topology optimization has been also applied in the design of electromagnetic component or system such as coil and motor (Wang et al., 2004a, 2004b). The governing equation of magnetic field problems is very similar to that of elastic field problems. The shear terms in the material property tensor are very important in elasticity problems: on the other hand, those in magnetic problems are often ignored except in special cases. In

that sense, the density approach such as SIMP seems to be more attractive in topology optimization in magnetic fields than HDM.

During the topology optimization process using the density approach, the magnetic permeability value is penalized in magnetic field problems while the Young's modulus value is penalized in elastic field problems. The value of the penalization parameter in elasticity problems can be constrained by the Hashin–Strikman bounds (Bendsøe and Sigmund, 1999): therefore, it is selected as 3 for 1/3 Poisson's ratio in 2-D cases. In the magnetic field topology optimization, similar penalization values are used for the permeability calculation (Byun et al., 1999) without any theoretical supports. Recent study shows that for the topology optimization in magnetic fields, the results with small penalization parameter are superior to the results with large penalization parameter not only in the performance but also in the CPU time and the convergence rate (Yoo and Hong, 2004).

In this study, the results of topology optimization based on different objective functions such as maximizing magnetic force or maximizing the magnetic mean compliance are reviewed. Also, the study on the modified density approach is expanded to obtain the topology optimization results comparable to the HDM results by fixing the hole-shape of the unit element in specific directions considering the directional properties of the magnetic flux.

2. OPTIMIZATION PROBLEM

Two optimization problems are considered in this study. First one is the maximizing the magnetic energy in a design domain and the other is maximizing the force generated by magnetic flux. In both cases, the magnetic permeability is obtained using HDM or the density method. In the former method, the macro-micro scale analysis is required to obtain the homogenized permeability value meanwhile the penalization based on the element density is used to get the permeability in the latter method.

2.1 Magnetic Permeability Calculation

In HDM, the magnetic permeability is homogenized and used to compute the magnetic energy. Assuming μ_{ij}^0 as the original magnetic permeability, the homogenized permeability can be calculated as (Yoo and Kikuchi, 2000)

$$\mu^H = \int_Y \mu_{ij}^0 dY + \int_Y \mu_{ij}^0 \frac{\partial \gamma_i}{\partial y_j} dY, \quad (1)$$

where the characteristic function γ represents the magnetic field strength of a unit-cell and y represents the micro-scale coordinate. In the ordinary density method as SIMP, the magnetic permeability is penalized as follows (Byun et

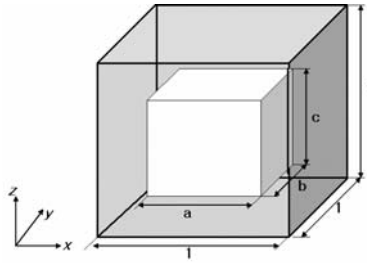


Figure 1. Element structure for the modified density approach.

al., 1999)

$$\mu = \mu_0[1 + (\mu_r - 1)\rho^p], \tag{2}$$

where μ_0 and μ_r represent the magnetic permeability in free space and relative magnetic permeability, respectively. The element density ρ has the value between 0 and 1 and the penalization parameter is valued as 2 to 4.

The modified density approach has been suggested by Yoo and Hong (2004) using the concept of HDM where each element has a hole as shown in Figure 1 and the element density is determined by the hole-size as

$$\mu = \mu_0[1 + (\mu_r - 1)(1 - abc)^p]. \tag{3}$$

According to the study by Yoo and Hong (2004), it is recommended to take the value of the penalization parameter as a small value different to the cases in elasticity problems. Without any restrictions, the hole-shape is changing as a square type: therefore, the modified density approach works as the ordinary density method. It is expected to control the flux density or improve the topology optimization result by fixing the hole-shape with a particular rectangular one. During the optimization process, the magnetic permeability is computed either by Equations (1)–(3) based on the optimization method used.

2.2 Formulation of the Optimization Problems

With the permeability values obtained and considering the saturation effect, the magnetic energy in the design domain Ω can be defined as

$$W_m = \frac{1}{2} \int_{\Omega} \int_0^B \frac{1}{\mu(\mathbf{B})} \mathbf{B} \, d\mathbf{B} \, dv = \frac{1}{2} \int_{\Omega} \mathbf{B}^T \frac{1}{\mu(\mathbf{B})} \mathbf{B} \, dv. \tag{4}$$

Using the relation between the magnetic flux density \mathbf{B} , inductance L , current I and the magnetic flux ψ , Equation (4) can be simplified as follows:

$$W_m = \frac{1}{2} LI^2 = \frac{1}{2} NI\psi. \tag{5}$$

As an example for topology optimization in magnetic fields, the objective function is defined as maximizing the magnetic mean compliance I_{MMC} that is the same as the maximizing magnetic flux because N and I are constant during the optimization process.

$$\begin{aligned} & \underset{\mathbf{D}}{\text{Maximize}} && I_{MMC} = NI\psi \\ & \text{Subject to} && \sum_{e=1}^N v_e \geq V_0, \end{aligned} \quad (6)$$

where \mathbf{D} stands for the design variable matrix and V_0 is the specified volume ratio.

Another example is maximizing the force generated by magnetic fields and it can be obtained by minimizing the magnetic energy in the design domain considering the force-energy relation (Yoo and Soh, 2005).

$$\begin{aligned} & \text{Minimize} && I_{MMC} = NI\psi \\ & \text{Subject to} && \sum_{e=1}^N v_e \leq V_0. \end{aligned} \quad (7)$$

The design variable is defined as the size of the hole in micro-cells when HDM is used or as the density of each element in the density approach. As explained previously, the magnetic permeability is updated according to the change of the design variables. The sequential linear programming (SLP) is used for the optimization algorithm.

3. APPLICATIONS

Figure 2 displays two structures where topology optimization is applied. Figure 2(a) shows a C-core excited by the current density by the wire coil around the air-gap portion. The design domain is fixed only at the tip end of the iron-core part and it is discretized as $15 \times 9 \times 1$ elements. The design objective for the structure is to maximize the magnetic energy that is maximizing the magnetic flux of the design domain. Figure 2(b) shows a solenoid type magnet actuator composed of an armature, a case and coil. The armature is a moving part made of ferrous material and the case is a ferrous structure surrounding the coil. The armature part is defined as the design domain to maximize the actuating force that is same as minimizing the magnetic mean compliance of the design domain. Figures 3(a) and (b) show the topology optimization results. In case of (b), the boundary of the optimal result is not clear and the response surface method is applied to determine the clear boundary contour (Yoo and Soh, 2005).

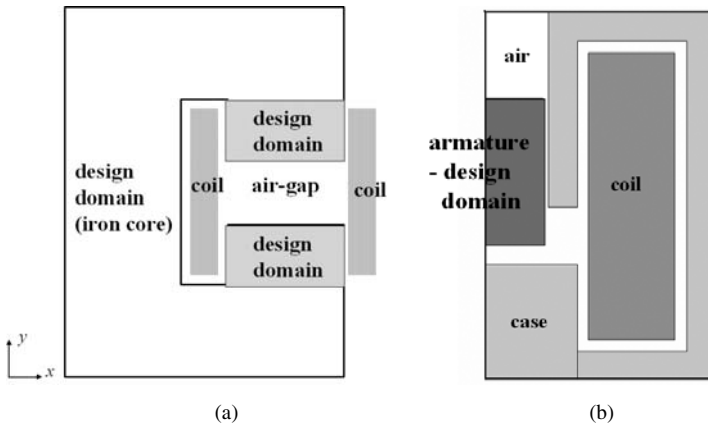


Figure 2. Schematic structures for topology optimization: (a) C-core and (b) magnetic actuator.

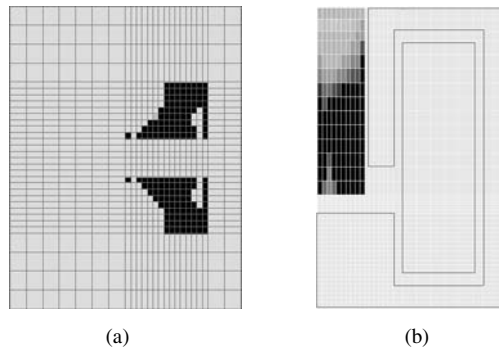


Figure 3. Topology optimization results by HDM: (a) C-core and (b) magnetic actuator.

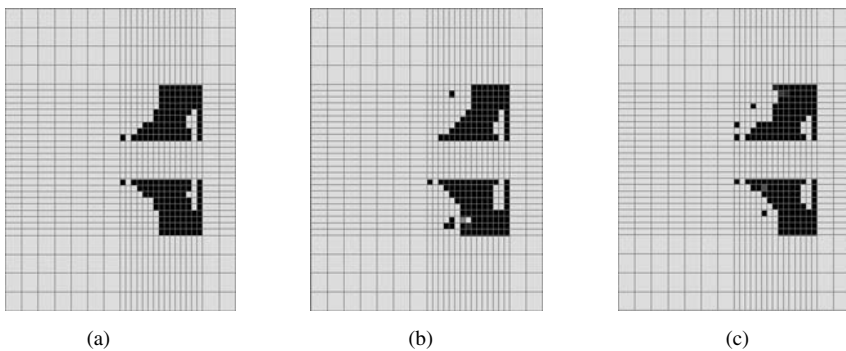


Figure 4. Topology optimization results by the modified density approach with (a) penalization parameter is 1.0, (b) penalization parameter is 2.0 and (c) penalization parameter is 3.0.

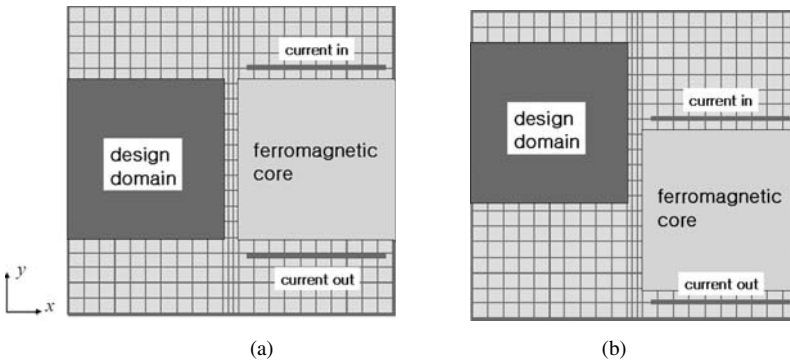


Figure 5. Simple core and design domain model when (a) the design domain is aligned and (b) the design domain is misaligned.

Figure 4 shows the application results for the C-core by applying the modified density approach with various penalization parameter values. The final figures are similar compared to the result by HDM shown in Figure 3(a). However, it requires more CPU time and iteration number if the penalization value is selected as a large number such as 2 or 3 (Yoo and Hong, 2004).

4. EXTENSION OF THE MODIFIED DENSITY METHOD

Another simple example shown in Figure 5 is considered for topology optimization. The purpose of the optimal design is to maximize the magnetic flux in the ferromagnetic design domain that is adjacent to the iron-core wired around. An air-gap exists in between and the core and the design domain are aligned with the core in Figure 5(a) and misaligned in Figure 5(b). In both cases, not only HDM but also the modified density approach with different penalization parameter is used for the comparison. Figures 6 and 7 show the topology optimization results for the aligned position and for the misaligned position, respectively. As shown in the figures, the results by the modified density method with penalization parameter 0.5 or 2 are similar to the results by HDM: however, many gray-scale representation can be found in the results by the modified density methods compared to the results by HDM even though there is no severe difference in the density method according to the change of the penalization parameter.

Considering the concept for a unit element shown in Figure 1, it is extended by fixing the hole-shape to specific directions to improve the results by the modified density method. Since the magnetic flux generated from the actuating core is mostly to the x -direction, it is assumed that the hole length to x and z -

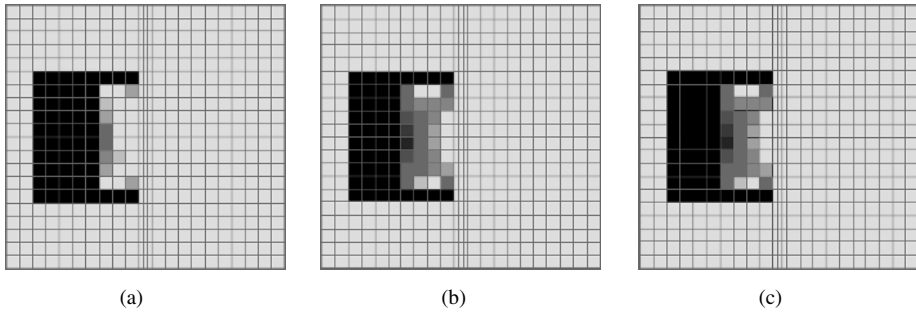


Figure 6. Topology optimization results for the aligned design domain by (a) HDM, (b) modified density method ($p = 0.5$) and (c) modified density method ($p = 2.0$).

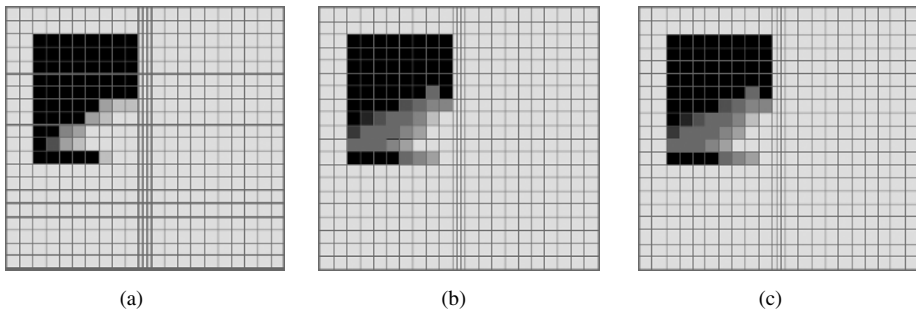


Figure 7. Topology optimization results for the misaligned design domain by (a) HDM, (b) modified density method ($p = 0.5$) and (c) modified density method ($p = 2.0$).

directions are 0.995 that is almost 1 . Therefore, only the length of the hole to y -direction is the only design variable for an element.

Figure 8 displays the optimal shape for the design domains designated in Figure 5 by fixing the element hole length to x and z -directions. Compared to the results by the modified density methods without any directional pre-setting, it can be verified that the final topology becomes more clear and comparable to the results by HDM.

5. CONCLUDING REMARKS

In this study, topology optimization for the structures in magnetic fields are reviewed focused on HDM and the modified density method. Especially, a new technique to obtain the better results by fixing the hole-length to specific directions is suggested when the modified density method is used. That kind of extension is only possible in the modified density approach due to its unique characteristic that the element density is defined base on the inner hole-size in the method.

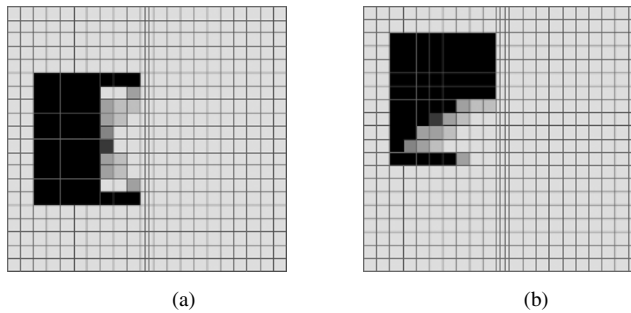


Figure 8. Topology optimization results with fixed hole length to x and z -directions by the modified density method ($p = 0.5$) for (a) aligned design domain and (b) misaligned design domain.

However, there are large rooms to study in topology optimization in magnetic fields. In the density method, the appropriate selection of the penalization parameter has not been supported by any theoretical researches and in HDM, it is required to test various micro-structures according to the characteristics dependent on the problem by problem.

REFERENCES

- Bendsøe, M.P. (1989) Optimal shape design as a material distribution problem, *Struct. Optim.*, 17, 193–202.
- Bendsøe, M.P. and Kikuchi, N. (1988) Generating optimal topologies in structural design using a homogenization method, *Comput. Methods Appl. Mech. Engrg.*, 71, 197–224.
- Bendsøe, M.P. and Sigmund, O. (1999) Material interpolation schemes in topology optimization, *Arch. of Applied Mechanics*, 69, 635–654.
- Byun, J., Lee, J., Park, I., Lee, H., Choi, K. and Hahn, S. (2000) Inverse problem application of topology optimization method with mutual energy concept and design sensitivity, *IEEE Trans. on Magnetics*, 36(4), 1144–1147.
- Lowther, D.A., Mai, W. and Dick, D.N. (1998) Automated design of magnetic devices by optimizing material distribution, *IEEE Trans. on Magnetics*, 34(5), 2885–2888.
- Wang, S., Kang, J. and Noh, J. (2004a) Topology optimization of a single-phase induction motor for rotary compressor, *IEEE Trans. on Magnetics*, 40(3), 1591–1596.
- Wang, S., Park, S., Kang, J. (2004b) Multi-domain topology optimization of electromagnetic systems, *COMPEL*, 23(4), 1036–1044.
- Yoo, J. and Hong, H. (2004) A modified density approach for topology optimization in magnetic fields, *Int. J. of Solids and Structures*, 41, 2461–2477.
- Yoo, J. and Kikuchi, N. (2000) Topology optimization in magnetic fields using the homogenization design method, *Int. J. for Numerical Methods in Engineering*, 48(10), 1463–1479.
- Yoo, J. and Soh, H.J. (2005) An optimal design of magnetic actuators using topology optimization and the response surface method, *Microsystem Technologies*, 11(12), 1252–1261.
- Yoo, J., Kikuchi, N. and Volakis, J.L. (2000) Structural optimization in magnetic devices by the homogenization design method, *IEEE Trans. on Magnetics*, 36(3), 574–580.

ELECTRO-MECHANICAL TOPOLOGY OPTIMIZATION CONSIDERING NON-MATCHING MESHES

Michael Raulli

*Department of Mechanical Engineering, Villanova University, 800 Lancaster Avenue,
Villanova, PA 19085, U.S.A.*

michael.raulli@villanova.edu

Abstract: A methodology for topology optimization of fully-coupled electro-mechanical systems is developed in this study, considering non-matching meshes. In order to develop a technique for parameterizing the electrostatic mesh, based on the solid-void state of the structural elements, the case of electrostatic forces is discussed in detail. High-fidelity analysis models are used in both the structural and electrostatic fields. The parameterization scheme is successfully applied to minimum compliance and compliant mechanism design.

Keywords: Topology optimization, electro-mechanical, non-matching meshes, MEMS.

1. INTRODUCTION

Since its modern inception, topology optimization has become an advanced design tool for many engineering applications. One area that has been largely unaccounted for is the development of topology optimization schemes for fully coupled multi-field systems that interact through a surface or interface. Examples of this type of interaction include fluid-structure and electro-mechanical systems. The coupling of the physical fields occur through stresses generated on the structure by the fluid or electrostatic fields, and the displacement of the structure. In this study, the topology optimization of fully coupled electro-mechanical systems is explored, in particular for the case in which the structural and electrostatic meshes do not match.

Electro-mechanical systems are an ideal application for topology optimization due to the development of a class of devices called micro-electro-mechanical systems (MEMS). This is because MEMS are (a) often used in new contexts and applications, demanding conceptually new designs and (b) fabric-

ated by a process that allows for arbitrary planar geometries without increase in manufacturing cost.

Based on the material formulation, topology optimization has been extended for various multi-physics problems. For example, Rodrigues and Fernandes [9] considered thermal loading. Sigmund [10–12] studied the design of electrothermo actuated MEMS, as did Yin and Ananthasuresh [13], including the use of multiple materials. These problems have in common that all physical fields involved are defined for the entire design space and the coupling results in mechanical forces due to thermal strains only. The structural, thermal, and all other fields evolve automatically along with the material distribution in the course of the optimization process.

Multi-physics topology optimization problems with loads acting on the surface of the structure, however, are less adaptable to material topology optimization as the surface is not known in advance. The surface evolves in the course of the optimization process and is not explicitly defined using the material formulation of the topology optimization problem. Topology optimization with design dependent surface loads has been studied by Hammer and Olhoff [6], Chen and Kikuchi [2], Bourdin and Chambolle [1] and Du and Olhoff [3, 4]. However, in these studies the magnitude of the surface load is given rather than being governed by other physical fields. Additionally, the use of parametric surfaces [3, 4, 6] to represent the topology of the interface is limiting. An electro-mechanical topology optimization scheme was developed by Raulli and Maute [8] that allows arbitrary interface locations and uses high-fidelity solution methods for the fully-coupled multiphysics solution of the electro-mechanical system.

The downside to the method in [8] is that it requires exactly matching electrostatic and structural meshes, a shortcoming which is addressed in the current study. For topology optimization problems, the design spaces are often simple, geometrical shapes, since the complexity of the structure is developed by the optimization procedure, therefore a simple, regular mesh is sufficient. The same arguments can be made for coupled problems with separate computational domains, however this puts an unnecessary limitation on the solution of the coupled optimization problem. Since the electrostatic and structural discretizations are of different spatial domains, forcing meshes to match exactly becomes a potentially more difficult and time consuming process for mesh generation. With the methods proposed herein, arbitrary meshes can be generated and parameterized with little user input in a preprocessing step that takes a few seconds. Therefore, the parameterization algorithms proposed can replace significant amounts of time spent in mesh generation. Another reason for the importance of this functionality is the eventuality that a complex geometrical feature limits the structural or electrostatic domain. A mesh to capture such a feature would (a) be difficult to match exactly to another mesh and (b) perhaps

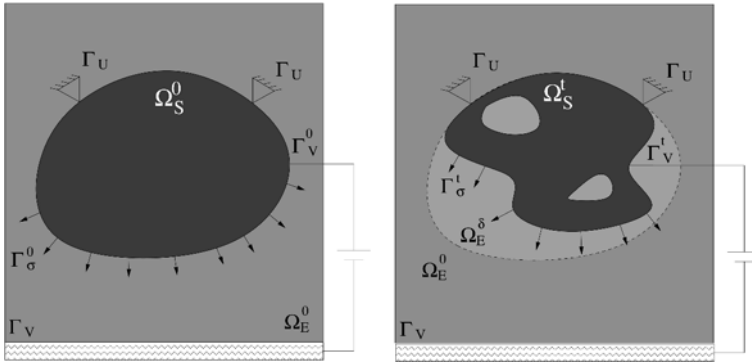


Figure 1. Topology optimization issues for electro-mechanical systems.

be meshed with a different fidelity in order to capture the behavior of this effect or (c) be meshed with an unstructured mesh generator. Therefore, the requirement of matching meshes presents a limitation on the problem formulation, which is overcome through the proposed methods.

2. ELECTRO-MECHANICAL TOPOLOGY OPTIMIZATION

Figure 1 illustrates the difficulties involved in topology optimization of electro-mechanical systems, and interface coupled systems in general. These issues include the fact that (A) as the initial structural domain (Ω_S^0) changes due to topology optimization, the electrostatic field must conform to the voids in the new structural domain (Ω_S^1). This entails the expansion of the initial electrostatic domain (Ω_E^0) to include the newly void areas (Ω_E^δ). (B) The electrostatic pre-pressure (Γ_σ) generated on the interface between the structure and the electrostatic domain changes magnitude and location as the solid-void state of the structure evolves. (C) The application of the voltage boundary condition (Γ_v) must also conform to the changing topology.

These matters are discussed in detail in [8] and are omitted here in interest of space. The electrostatic force computation and parameterization through the structural optimization variables is discussed in detail in Section 3 in order to illustrate the general technique used for the parameterization of non-matching meshes. A simple way to approach this problem is to fix the interface topology, however, a free interface allows greater flexibility in the optimal design. Details regarding electro-mechanical analysis and adjoint sensitivity analysis are omitted due to space. Please see [8] for further discussion of these issues.

3. PARAMETERIZATION OF LOAD TRANSFER FOR NON-MATCHING MESHES

The physics of the coupled system form the basis for the parameterization scheme. For electro-mechanical problems, the main source of coupling is through the electrostatic/structure interface. At the interface, electrostatic forces are generated, which cause the structure to deform. These deformations, in turn, affect the distribution of the electrostatic field by altering the physical domain in which it is computed. These interface coupled quantities are handled through an algorithm developed initially for aeroelastic applications [5], and extended to electro-mechanical applications [7]. The goal of the algorithm is the transfer of loads and motion between computational domains in a manner that conserves energy.

Since the structural and electrostatic problems are solved in separate numerical discretizations, a method for transferring loads from the electrostatic discretization (where they are computed) to the structural mesh is necessary. The transfer of loads can be summarized by the following equation:

$$\mathbf{f}_i = \sum_{j=1}^{n_e} \left(\int_{\Gamma^{\mathcal{E}/\mathcal{S}}} [\varepsilon \hat{\sigma}_e \cdot \mathbf{n} N_j \, d\Gamma^{\mathcal{E}/\mathcal{S}}] \right) N_i(\chi_j), \quad (1)$$

where n_e is the number of electrostatic nodes, $\Gamma^{\mathcal{E}/\mathcal{S}}$ represents the electrostatic structure interface, ε is the permittivity, $\varepsilon \hat{\sigma}_e$ is the Maxwell stress tensor, N_j and N_i are shape functions corresponding to electrostatic and structural nodes, respectively, χ_j represents the natural coordinate in a structural element to which an electrostatic node is matched and \mathbf{f}_i is the force on a structural node. In the case of material topology optimization with a free interface, the effect of the optimization variables on the structural *and* electrostatic material parameters must be considered.

The electrostatic force calculation exemplifies the proposed parameterization method. Physically, electrostatic stresses are generated on a conducting surface, therefore, if there is not a structure (conductor), then there cannot be any electrostatic stresses. Since the electrostatic/structural interface is free to evolve, the effect of the material distribution is factored into the force calculation in Equation (1) in the following manner: *contribution to a nodal force in the structure should only come from solid elements*. Since the force computation is carried out in the electrostatic mesh, which overlaps the structural design space in order to allow for new voids, the permittivity of an electrostatic element should be altered to correspond to the solid-void state of the structural elements with which it is associated.

If the meshes matched, this would be a simple task, as there would be a one-to-one correspondence between the overlapped structural and electrostatic elements and the following parameterization could be used: $\varepsilon_k = \varepsilon_0 s_i$, where

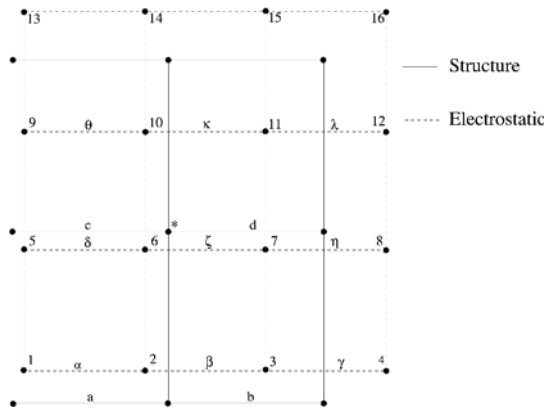


Figure 2. Example of interface. Electrostatic mesh: dotted lines, Greek letters for elements, numbers for nodes. Structural mesh: solid lines, Roman letters for elements.

ε_k is the permittivity in electrostatic element k , ε_0 is the base permittivity and s_i is the optimization variable that represents the solid-void state of the corresponding structural element, and can have values between zero and one. A void structural element will result in a zero force contribution from the corresponding electrostatic element. However, as illustrated in Figure 2, there are potentially multiple structural elements that are associated with a given electrostatic element. In order to properly parameterize the structural force, two effects need to be considered (a) which electrostatic elements contribute to the force calculation and (b) how does the solid-void state of the structural elements influence the force calculation in the electrostatic elements.

The first issue is illustrated by Equation (1). The latter issue is discussed below. Figure 2 illustrates the two-dimensional projection of the electrostatic interface on a two-dimensional structural domain. In order to compute the force on the structural node marked with an asterisk (*), Equation (1) is expanded, *considering only the contribution of electrostatic node 6*, for simplicity:

$$f_* = \left[\int \varepsilon_\alpha \hat{\sigma}_e \mathbf{n} N_6^\alpha d\Gamma^\alpha + \int \varepsilon_\beta \hat{\sigma}_e \mathbf{n} N_6^\beta d\Gamma^\beta + \int \varepsilon_\delta \hat{\sigma}_e \mathbf{n} N_6^\delta d\Gamma^\delta + \int \varepsilon_\zeta \hat{\sigma}_e \mathbf{n} N_6^\zeta d\Gamma^\zeta \right] N_*^a(\chi_6). \quad (2)$$

The superscript a on the shape function (N_*) indicates which structural element the electrostatic node 6 is matched to. In reality, the contribution from electrostatic nodes 1, 2, 3, 5, 6, 7, 9, 10 and 11 would effect f_* . Equation (2) exposes the difficulties of parameterizing the permittivity in the force calculations with the state of the matched structural element. The integration underlined in (2) over the electrostatic element ζ (neglecting the shape function) is a good example of this.

The element ζ is actually associated with all four structural elements, therefore the permittivity (ε_ζ), which is a constant, would ideally be piecewise con-

stant over Γ^ζ :

$$\int_{\Gamma^\zeta} \varepsilon_\zeta \hat{\sigma}_e \mathbf{n} d\Gamma^\zeta = \int \varepsilon_a \hat{\sigma}_e \mathbf{n} d\Gamma^{\zeta/a} + \int \varepsilon_b \hat{\sigma}_e \mathbf{n} d\Gamma^{\zeta/b} + \int \varepsilon_c \hat{\sigma}_e \mathbf{n} d\Gamma^{\zeta/c} + \int \varepsilon_d \hat{\sigma}_e \mathbf{n} d\Gamma^{\zeta/d}, \quad (3)$$

where $\varepsilon_a = \varepsilon(s_a)$ and indicates that the permittivity depends on the optimization variable that controls the state of structural element a and $\Gamma^{\zeta/a}$ represents the region of overlap between the electrostatic element ζ and the structural element a . The theoretically correct parameterization based on the load transfer algorithm is represented by rearranging Equation (3) and solving for ε_ζ :

$$\varepsilon_\zeta = \frac{\varepsilon_a \int \hat{\sigma}_e \mathbf{n} d\Gamma^{\zeta/a} + \varepsilon_b \int \hat{\sigma}_e \mathbf{n} d\Gamma^{\zeta/b} + \varepsilon_c \int \hat{\sigma}_e \mathbf{n} d\Gamma^{\zeta/c} + \varepsilon_d \int \hat{\sigma}_e \mathbf{n} d\Gamma^{\zeta/d}}{\int \hat{\sigma}_e \mathbf{n} d\Gamma^\zeta} \quad (4)$$

Equation (4) represents an intractable solution to the problem of preprocessing the parameterization of the permittivity in element ζ , due to the dependence of the parameterization on the physical response of the system, which is constantly changing with topology. Therefore, the simplification is made that the electrostatic stress tensor ($\hat{\sigma}_e$) is constant in an element (ζ), which is accurate in the limit of mesh refinement. This assumption is only made for the parameterization of the electrostatic elements, not for any numerical calculations. With this assumption, (4) reduces as follows:

$$\varepsilon_\zeta = \frac{\varepsilon_a \int d\Gamma^{\zeta/a} + \varepsilon_b \int d\Gamma^{\zeta/b} + \varepsilon_c \int d\Gamma^{\zeta/c} + \varepsilon_d \int d\Gamma^{\zeta/d}}{\int d\Gamma^\zeta}, \quad (5)$$

$$\varepsilon_\zeta = \varepsilon_a \frac{A^{\zeta/a}}{A^\zeta} + \varepsilon_b \frac{A^{\zeta/b}}{A^\zeta} + \varepsilon_c \frac{A^{\zeta/c}}{A^\zeta} + \varepsilon_d \frac{A^{\zeta/d}}{A^\zeta}; \quad \varepsilon_a = \varepsilon_0 \frac{(s_a - s_{\min})}{1 - s_{\min}}. \quad (6)$$

The permittivity parameterization is weighted by the area of overlap ($A^{\zeta/a}$) between an electrostatic (ζ) and structural (a) element, or their projections, normalized by A^ζ . The actual relation between ε_ζ and the optimization variables is formulated as follows:

$$\begin{aligned} \varepsilon_\zeta &= \frac{\varepsilon_0}{A^\zeta (1 - s_{\min})} \sum_{i=a}^d [(s_i - s_{\min}) A^{\zeta/i}] \\ &= \frac{\varepsilon_0}{1 - s_{\min}} \left[\frac{1}{A^\zeta} \left(\sum_{i=a}^d s_i A^{\zeta/i} \right) - s_{\min} \right]. \end{aligned} \quad (7)$$

The variable s_{\min} in Equation (6) represents the minimum value the variable can take on, in order to avoid singularities in the structural solver. It is included in the permittivity parameterization to ensure that the permittivity is

zero when the structural variables (s_a-s_d) are equal to s_{\min} . The denominator term $(1 - s_{\min})$ is used to ensure that the base permittivity (ϵ_0) is achieved if variables s_a-s_d are all unity. In order to encourage fully solid-void distributions, a penalization exponent is applied to Equation (7). The parameterization of any element in the electrostatic mesh (k) is given as follows:

$$\epsilon_k = \frac{\epsilon_0}{1 - s_{\min}} \left[\frac{1}{A^k} \left(\sum_{i=1}^{n_o} s_i A^{k/i} \right) - s_{\min} \right]^{p_f}, \quad p_f \geq 3.0, \quad (8)$$

where n_o is the number of structural elements overlapping the electrostatic element k and p_f is the exponent for penalizing the permittivity in force calculations. Equation (8) represents the parameterization of the force computation in the case of an evolving interface in electro-mechanical topology optimization, which preserves the conservative properties of the load transfer algorithm. The electrostatic sub-problem is parameterized in a pre-processing step to the topology optimization problem.

For other physical properties that are parameterized, such as the voltage boundary condition enforcement and the permittivity of the elements used to build the electrostatic stiffness matrix, a similar development can be followed. Therefore, all parameterization of electrostatic properties is accomplished through a normalized area weighting of overlapped elements. In the interest of space, these developments are omitted.

4. NUMERICAL EXAMPLES

Two and three-dimensional examples of free interface topology optimization were presented in the initial work on electro-mechanical topology optimization by Raulli and Maute [8]. Efforts were made to demonstrate the effectiveness of the methodology for automatically synthesizing optimal topologies which (a) performed well and (b) were almost completely solid-void in the final design and (c) avoided checkerboard modes. In order to achieve these optimal results, there was careful consideration of the filtering techniques.

In this paper, there will not be a general evaluation of the quality and performance of the topology optimization scheme *per se*, since this has already been carried out. This section will aim to demonstrate that results obtained with non-matching meshes are consistent with those obtained with matching meshes. In order to demonstrate this, two examples are shown: (1) a compliance problem with a two-dimensional structural mesh and a three-dimensional electrostatic mesh and (2) a completely two-dimensional compliant mechanism force-inverter, as in [8]. They are considered in Sections 4.1 and 4.2, respectively. Schematics for the three and two-dimensional problems are given in Figure 3.

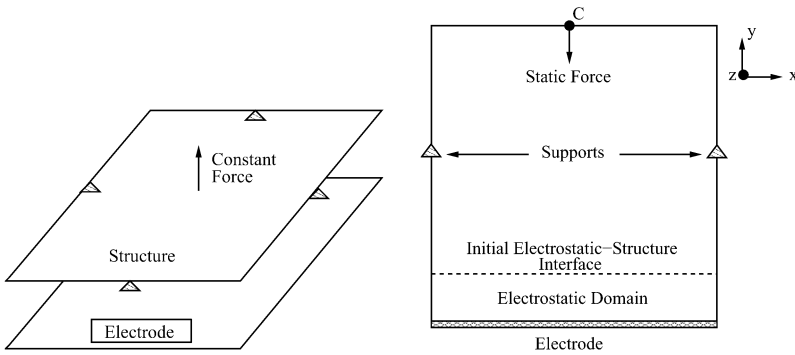


Figure 3. Three-dimensional compliance (left) and force inverter schematics.

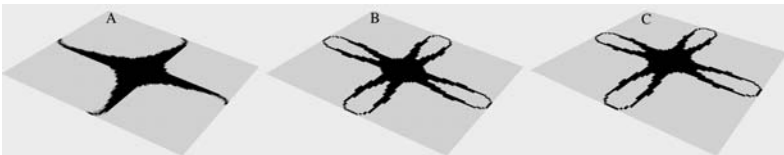


Figure 4. Comparison of topology results for varying electrostatic mesh sizes. The ratio of electrostatic to structural mesh density is given for each result in Table 1. Increasing letters indicate increasing electrostatic mesh refinement. Result B is for matching meshes.

4.1 Three-Dimensional Minimum Compliance

Using the simpler implementation and parameterization involved for matching meshes, an optimal topology was generated (Figure 4, center), given the setup in Figure 3. Using this as the benchmark, two additional topology optimization problems were run, one with an electrostatic mesh finer than the benchmark, and one with a coarser electrostatic mesh. The structural mesh was kept constant, in order to compare the final material designs, and how the fidelity of the electrostatic mesh affected the results, thus decoupling the problem from the structural mesh density.

A summary of the objective and constraint values is provided in Table 1. Figure 4, left and right, show the topology optimization results for the coarser and finer meshes, respectively. For the non-matching meshes, the only points at which there are matching nodes are the mesh boundaries.

The results are encouraging for the finer mesh and discouraging, but not unexpected, for the coarser mesh. The finer mesh achieves the same optimal design, visually, even though the values of the objective functions are somewhat different. The coarser mesh achieves a completely different, unsymmetric design. The reasons for the poor performance of the coarse mesh can be attributed to two reasons: (a) a decline in accuracy due to the need of a finer electrostatic mesh in the load and motion transfer algorithm [5] and (b) a coarser

Table 1. Three-dimensional compliance results.

	A (0.825)	B (1.0)	C (1.175)
$\Pi^{\text{init}} \times 10^{-17}$	9.71	9.71	9.71
$\Pi^{\text{final}} \times 10^{-17}$	0.117	0.0786	0.103

parameterization, which leads to unsymmetry in the parameterized response, and hence to the poor outcome of the coarser electrostatic mesh.

4.2 Two-Dimensional Force Inverter

Using the simpler implementation and parameterization involved for matching meshes, an optimal topology was generated given the setup in Figure 3. Using this as the benchmark, five additional topology optimization problems were run, three with an electrostatic mesh finer than the benchmark, and two with a coarser electrostatic mesh. As in Section 4.1 the structural mesh density was kept constant. The optimization problem is defined as follows:

$$\max_{\mathbf{s}} z(\mathbf{s}) = u_c \quad \text{subject to:} \quad (9)$$

$$g_1 : \text{Mass} \leq 10\% \text{ of total} \quad g_2 : \Pi \leq \Pi_0, \quad (10)$$

where Π_0 represents the initial strain energy and u_c is the displacement at point c in Figure 3.

The force inverter is a complicated problem and prone to checkerboard modes. In the previous study [8], careful attention was paid to the filter such that checkerboard modes were avoided. In this study, however, less attention is devoted to this matter to illustrate how non-matching meshes can lead to consistent topology optimization results, with less user input. Therefore, some of the results presented in this section, including the one for matching meshes, exhibit some small amount of checkerboard pattern. This is not to suggest that this is the best design obtainable with matching meshes, as superior results have been obtained in [8], but is simply used as a benchmark to compare different electrostatic mesh densities.

Table 2 summarizes the results for the six different electrostatic mesh sizes and Figure 5 shows the final designs. The constraints are active at the optimum for all examples. The number in the top row of Table 2 indicates the ratio of electrostatic to structural mesh densities. All six examples should produce the same value for initial displacements, but this is not the case for A and B because of the fact that the load transfer algorithm depends on the electrostatic mesh being finer than the structural mesh. Meshes C–F are all in good agreement for the initial displacement.

Table 2. Results from topology examples.

	A (0.717)	B (0.75)	C (1.0)	D (1.25)	E(1.72)	F(1.75)
$u_c^{\text{init}} \times 10^{-12}$	-1.01	-1.22	-1.30	-1.30	-1.30	-1.30
$u_c^{\text{final}} \times 10^{-12}$	619	567	498	514	500	497

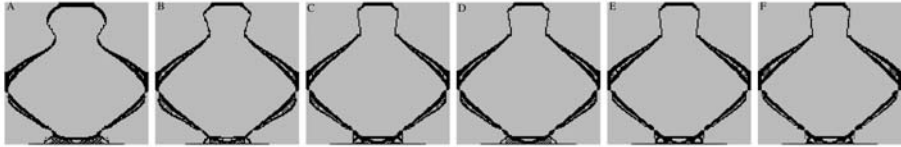


Figure 5. Comparison of topology results for varying electrostatic mesh sizes. The ratio of electrostatic to structural mesh density is given for each result in Table 2. Increasing letters indicates increasing electrostatic mesh refinement. Result C is for matching meshes.

Figure 5 demonstrates that all the examples achieve similar final designs, even though the numerical results for the coarser electrostatic meshes (A,B) are rather inconsistent with the equivalent (C) and finer electrostatic meshes (D–F). Symmetry is enforced in this example.

The two and three-dimensional examples illustrate that the proposed method is able to achieve similar designs to exactly matching meshes. Differences in numerical results naturally arise due to the fineness of the discretization and the effect this has on the gradients of the system, though the results are also quite consistent numerically for finer electrostatic meshes.

5. SUMMARY

The possibility of non-matching computational meshes is considered in this study when developing computational techniques for topology optimization in multifield, interface coupled problems, such as electro-mechanical systems. This study has developed a method for parameterization of non-matching meshes for use in a computational topology optimization procedure. These techniques were successfully applied to the design of micro-actuators in order to demonstrate the feasibility of the method.

REFERENCES

- [1] B. Bourdin and A. Chambolle, Design-dependent loads in topology optimization, *ESAIM: Control, Optimisation and Calculus of Variations*, 9, 19–48 (2003).
- [2] B.-C. Chen and N. Kikuchi, Topology optimization with design-dependent loads. *Finite Elements in Analysis and Design*, 37, 57–70 (2001).

- [3] J. Du and N. Olhoff, Topological optimization of continuum structures with design-dependent surface loading – part i: new computational approach for 2d problems. *Structural and Multidisciplinary Optimization*, 27, 151–165 (2004).
- [4] J. Du and N. Olhoff, Topological optimization of continuum structures with design-dependent surface loading – part ii: algorithm and examples for 3d problems. *Structural and Multidisciplinary Optimization*, 27, 166–177 (2004).
- [5] C. Farhat, M. Lesoinne and P. LeTallec, Load and motion transfer algorithms for fluid/structure interaction problems with non-matching discrete interfaces: Momentum and energy conservation, optimal discretization and application to aeroelasticity. *Computer Methods in Applied Mechanics and Engineering*, 157, 95–114 (1998).
- [6] V.B. Hammer and N. Olhoff, Topology optimization of continuum structures subjected to pressure loading, *Structural and Multidisciplinary Optimization*, 19, 85–92 (2000).
- [7] J.S. Kong, D.M. Franngopol, M. Raulli, K. Maute, R.A. Saravanan, L.-A. Liew and R. Raj, A methodology for analyzing the variability in the performance of a mems actuator made from a novel ceramic, *Sensors and Actuators A: Physical*, 116(2), 336–344 (2004).
- [8] M. Raulli and K. Maute, Topology optimization of electrostatically actuated microsystems, *Structural and Multidisciplinary Optimization*, published online (2005) in press.
- [9] H. Rodriques and P. Fernandes, A material based model for topology optimization of thermoelastic structures, *International Journal for Numerical Methods in Engineering*, 38, 1951–1965 (1995).
- [10] O. Sigmund, Topology optimization in multiphysics problems, in *Proceedings of the 7th AIAA/USAF/NASA/ISSMO Symposium on Multidisciplinary Analysis and Optimization, St. Louis, USA*, AIAA 98-4905, pp. 1492–1500 (1998).
- [11] O. Sigmund, Design of multiphysics actuators using topology optimization – Part I: One-material structures, *Computer Methods in Applied Mechanics and Engineering*, 190(49–50), 6577–6604 (2001).
- [12] O. Sigmund, Design of multiphysics actuators using topology optimization – Part II: Two-material structures, *Computer Methods in Applied Mechanics and Engineering*, 190(49–50), 6605–6627 (2001).
- [13] L. Yin and G.K. Ananthasuresh, A novel topology design scheme for the multi-physics problems of electro-thermally actuated compliant micromechanisms, *Sensors and Actuators A*, 97–98, 599–609 (2002).

Waves

STRUCTURAL TOPOLOGY OPTIMIZATION OF MECHANICAL RESONATORS, ACTUATORS AND SENSORS

Shinji Nishiwaki¹, Emilio C.N. Silva², Kazumi Matsui³, Kenjiro Terada⁴, Kazuhiro Izui¹ and Masataka Yoshimura¹

¹*Department of Aeronautics and Astronautics, Kyoto University, Yoshida Honmachi Sakyo, Kyoto 606-8501, Japan*

²*Department of Mechatronics and Mechanical Systems Engineering Escola Politécnica da Universidade de São Paulo, Av. Prof. Mello Moraes 2231, São Paulo-SP 05508-900, Brazil*

³*Graduate School of Environment and Information Science, Yokohama National University, 79-7 Tokiwadai, Hodogaya, Yokohama 240-8501, Japan*

⁴*Department of Civil Engineering, Tohoku University, Aramaki-Aza 06, Aoba, Sendai 980-8579, Japan*

Abstract: This research presents a structural topology optimization method for the design of mechanical resonators, and smart structures, such as mechanical actuators and sensors, that are composed of flexible structures and mechanical energy conversion devices. First, the concept of the topology optimization method is briefly discussed. Next, we clarify the mechanical design specifications of mechanical resonators, actuators and sensors, and construct objective functions that aim to satisfy design specifications. Based on these formulations, an optimization algorithm is constructed using Sequential Linear Programming (SLP). Finally, several numerical examples are presented in order to confirm that the method presented here can provide optimized structures applicable to the design of mechanical resonators, mechanical actuators and sensors.

Keywords: Topology optimization, vibration, smart structures, actuators, sensors, finite element method.

1. INTRODUCTION

This research presents a structural topology optimization method for the design of mechanical resonators, and smart structures such as mechanical actuators and sensors, that are composed of flexible structures and mechanical energy conversion devices.

First, the concept of the topology optimization method [1] is briefly discussed. Next, we clarify the mechanical design specifications of mechanical

resonators, actuators and sensors, and construct objective functions that aim to satisfy design specifications.

Finally, several numerical examples are presented in order to confirm that the method presented here can provide optimized structures applicable to the design of mechanical resonators, mechanical actuators and sensors.

2. TOPOLOGY OPTIMIZATION

Consider the design problem of determining the boundary of the design domain Ω_d by minimizing or maximizing objective functions. The key idea of the topology optimization method is the introduction of a fixed, extended design domain D that includes the original design domain Ω_d , *a priori*, and the utilization of the following characteristic function [1]:

$$\chi_{\Omega}(\mathbf{x}) = \begin{cases} 1 & \text{if } \mathbf{x} \in \Omega_d \\ 0 & \text{if } \mathbf{x} \in D \setminus \Omega_d, \end{cases} \quad (1)$$

where \mathbf{x} denotes a position in the extended design domain D . Since this characteristic function can be very discontinuous, i.e., resides in $L^{\infty}(D)$, some regularization or smoothing technique should be introduced for the numerical treatment. A homogenization method is utilized to deal with this extreme discontinuity of material distribution and to provide the material properties viewed in a global sense as homogenized properties. This method, called the Homogenization Design Method (HDM) [1, 2], has been applied to a variety of design problems, and the density approach [3], also called the SIMP (Solid Isotropic Material with Penalization) method [4], is another currently used method. The basic idea of SIMP is the use of a fictitious isotropic material whose elasticity tensor is assumed to be a function of penalized material density, expressed by an exponent parameter. In this research, both relaxation methods are examined for three design problems. That is, the HDM is employed for the design of mechanical resonators, and the SIMP method is employed for the design of mechanical actuators and sensors.

3. DESIGN SPECIFICATIONS AND OBJECTIVE FUNCTIONS

In order to design mechanical resonators and smart structures, two types of design specifications must be considered. One is a comprehensive motional specification that determines the performance concerning the vibration characteristics of mechanical resonators [5], the deformation characteristics of the flexible structure of mechanical actuators [6, 7], and the sensing characteristics of mechanical sensors [8]. The other is a structural specification that determines the structural stiffness of the target structure. Here, we discuss only the motional specification and the corresponding objective function. The structural

specification can be achieved by implementing an appropriate stiffness that is formulated as the minimization of the mean compliance.

3.1 Mechanical Resonator

Consider that an elastic and vibrating structure occupying a design domain Ω_d is fixed at boundary Γ_u . Body forces applied to this elastic body and damping effects are ignored for simplicity of the formulation. Here, we intend to control the amplitudes of vibrations for all the excitation frequencies from 1 to m_s . That is, we intend to maximize the amplitude of vibration of the j -th excitation frequency ($j = 1, \dots, m_s$) along the direction of a unit load vector $\mathbf{t}_j^{\text{Outmax}}$ at boundary $\Gamma_{ij}^{\text{Outmax}}$ and minimize the amplitude of vibration of the j -th excitation frequency ($j = 1, \dots, m_s$) along the direction of a unit load vector $\mathbf{t}_j^{\text{Outmin}}$ at boundary $\Gamma_{ij}^{\text{Outmin}}$ simultaneously when a harmonic exciting traction \mathbf{t}_j^{In} is applied at boundary Γ_{ij}^{In} , in order to specify the desired vibration mode where the j -th excitation frequency is assumed to be ω_j^{In} . Instead of directly specifying the amplitude of vibration of the excitation eigen-frequencies explained above, we control the structure's resonance eigen-frequencies and specified portions of eigen-modes, which yields sufficient deformation in the desired direction.

Suppose that the j -th eigen-frequency and its corresponding eigen-mode of the vibrating structure are ω_j and ϕ_j , respectively. To satisfy the above goals concerning the control of the amplitudes of the specified eigen-frequency vibrations, first, one of the eigen-frequencies must match the excitation frequency ω_j^{In} . Here, we intend to match the j -th eigen-frequency ω_j with the j -th excitation frequency ω_j^{In} ($j = 1, \dots, m_s$). Furthermore, other eigen-frequencies may also have to be specified to avoid changing the sequence in which the eigen-frequencies and eigen-modes are dealt with during the optimization process. In cases where such reordering must be avoided, an appropriate number, m ($m > m_s$), of eigen-frequencies, $\omega_{m_s+1}^{\text{In}}, \omega_{m_s+2}^{\text{In}}, \dots, \omega_m^{\text{In}}$, must be given fictitious and sufficiently large values. Therefore, the objective function concerning the eigen-frequencies can be formulated as:

$$\underset{r}{\text{minimize}} f_j^V = \left| \frac{\omega_j(r)^2 - \omega_j^{\text{In}2}}{\omega_j^{\text{In}2}} \right| = \left| \frac{\lambda_j(r) - \lambda_j^{\text{In}}}{\lambda_j^{\text{In}}} \right| \quad \text{for } j = 1, \dots, m, \quad (2)$$

where r is a design variable, $\lambda_j(r)$ is the j -th eigen-value, and $\lambda_j^{\text{In}} = \omega_j^{\text{In}2}$.

In order to satisfy the design requirements, the shape of the eigen-modes must also be controlled. The important design specifications are to determine the portions of the eigen-mode shape where the desired dynamic response is maximized, and other portions where undesirable dynamic response is minimized. Using this specification method, sufficient eigen-mode control can then be achieved for the design of vibrating structures and mechanical resonators.

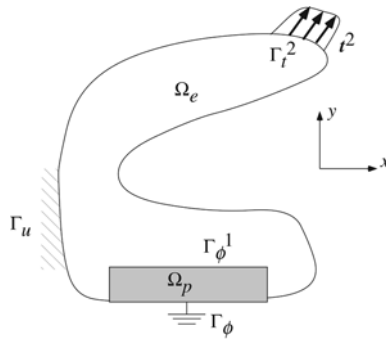


Figure 1. Motional performance of mechanical actuator.

Thus, the following objective functions are formulated to satisfy the above specifications:

$$\begin{aligned} \text{maximize}_r f^M = & \sum_{j=1}^{m_s} \{ w_j^{m, \text{In}} (\mathbf{t}_j^{\text{In}T} \boldsymbol{\phi}_j(r))^2 + w_j^{M, \text{Outmax}} (\mathbf{t}_j^{\text{Outmax}T} \boldsymbol{\phi}_j(r))^2 \\ & - w_j^{M, \text{Outmin}} (\mathbf{t}_j^{\text{Outmin}T} \boldsymbol{\phi}_j(r))^2 \}, \end{aligned} \quad (3)$$

where $w_j^{M, \text{In}}$, $w_j^{M, \text{Outmax}}$, and $w_j^{M, \text{Outmin}}$ are the weighting coefficients for the maximization of the j -th eigen-mode in the direction of \mathbf{t}_j^{In} , the maximization of the j -th eigen-mode in the direction of $\mathbf{t}_j^{\text{Outmax}}$, and the minimization of the j -th eigen-mode in the direction of $\mathbf{t}_j^{\text{Outmin}}$, respectively.

3.2 Mechanical Actuator

Here, we consider a piezoelectric actuator composed of a flexible and elastic structure Ω_e and piezoceramic device Ω_p as a mechanical actuator, and only the flexible structure is a design domain, Ω_d , as shown in Figure 1. Suppose that the flexible structure is fixed at boundary Γ_u , and the electric potential is set to zero at Γ_ϕ in the piezoceramic device. The piezoceramic device is also subjected to a specified electric potential ϕ^1 at boundary Γ_ϕ^1 , and the displacement vector of the flexible structure due to this potential ϕ^1 is \mathbf{u}^1 . Now, we intend to design a flexible structure that starts to deform in the direction specified by the unit vector \mathbf{t}^2 at Γ_t^2 in order to function as an actuator when electric potential ϕ^1 is applied. A sufficient and specified deformation can be obtained by maximizing the following linear form defined as the mean transduction:

$$L(\mathbf{t}^2, \mathbf{u}^1) = \int_{\Gamma_{t^2}} \mathbf{t}^2 \cdot \mathbf{u}^1 d\Gamma \quad (4)$$

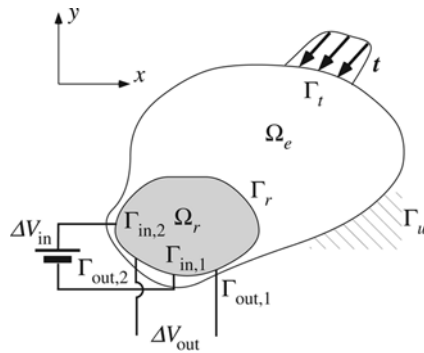


Figure 2. Motional performance of mechanical sensor.

3.3 Mechanical Sensor

Here, we consider a piezoresistive sensor composed of a flexible and elastic structure Ω_e and piezoresistive device Ω_r , and only the flexible structure is also a design domain, Ω_d , as shown in Figure 2. Suppose that the flexible structure is fixed at boundary Γ_u and is subjected to surface traction \mathbf{t} at boundary Γ_t . The change in resistivity of the piezoresistive device due to \mathbf{t} is measured as the change in electric potential ΔV_{out} using a Wheatstone bridge.

Now, we intend to design a flexible structure that maximizes electric potential ΔV_{out} when surface traction \mathbf{t} at boundary Γ_t is applied. In this problem, ΔV_{out} is a performance measure, and sufficient performance is obtained by maximizing ΔV_{out} . In order to calculate ΔV_{out} , the following equations must be solved:

$$\int_{\Omega_r} \nabla \phi : \mathbf{k} : \nabla \phi d\Omega = \int_{\Gamma_r} \mathbf{J} \cdot \mathbf{n} \phi d\Gamma \tag{5}$$

$$\boldsymbol{\rho} = \boldsymbol{\rho}_0(\mathbf{I}_m + \boldsymbol{\Pi} : \boldsymbol{\sigma}) = \boldsymbol{\rho}_0(\mathbf{I}_m + \boldsymbol{\Pi} : \mathbf{D}_r : \boldsymbol{\varepsilon}(\mathbf{u})) \tag{6}$$

$$\int_{\Omega} \boldsymbol{\varepsilon}(\mathbf{v}) : \mathbf{D} : \boldsymbol{\varepsilon}(\mathbf{u}) d\Omega = \int_{\Gamma_t} \mathbf{t} \cdot \mathbf{v} d\Gamma, \tag{7}$$

where $\nabla \phi$ and ϕ are the electric potentials, \mathbf{J} is the current density, \mathbf{n} is the normal vector defined at boundary Γ_r , $\boldsymbol{\rho}$ is the resistivity tensor, \mathbf{k} is the conductivity tensor such that $\mathbf{k} = \boldsymbol{\rho}^{-1}$, \mathbf{I}_m is the identity matrix, $\boldsymbol{\Pi}$ is the piezoresistive coefficient tensor, and \mathbf{D}_r is the elasticity tensor of the piezoresistive material. $\nabla \mathbf{v}$ and \mathbf{u} are displacement vectors, $\boldsymbol{\varepsilon}(\mathbf{u})$ is the strain tensor due to the displacement \mathbf{u} , and \mathbf{D} is the elasticity tensor of the flexible structure.

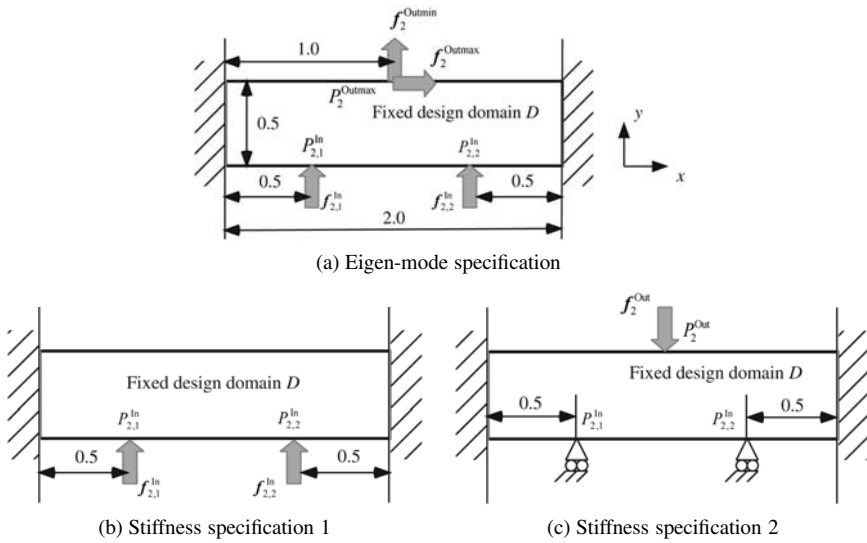


Figure 3. Design specifications of mechanical resonator.

4. NUMERICAL EXAMPLES

4.1 Mechanical Resonator

Figure 3 shows the design specifications of a mechanical resonator. As shown in this figure, the second eigen-mode along the direction f_2^{Outmax} at point P_2^{Outmax} , along the direction $f_{2,1}^{In}$ at point $P_{2,1}^{In}$, and along the direction $f_{2,2}^{In}$ at point $P_{2,2}^{In}$ is to be maximized, and the second eigen-mode along the direction f_2^{Outmin} at point P_2^{Outmin} is to be minimized, according to the eigen-mode specification shown in Figure 3(a), while the lowest and second eigen-frequencies are required to conform to target values, 350 Hz and 500 Hz, respectively, according to the eigen-frequency specification. Further, the static stiffness along the direction of $f_{2,1}^{In}$ at point $P_{2,1}^{In}$ and along the direction of $f_{2,2}^{In}$ at point $P_{2,2}^{In}$ is to be maximized to resist the applied force as shown in Figure 3(b), and the static stiffness along the direction of f_2^{Out} at point P_2^{Out} is to be maximized while point $P_{2,1}^{In}$ is fixed along the direction of $f_{2,1}^{In}$, and point $P_{2,2}^{In}$ is fixed along the direction of $f_{2,2}^{In}$ to resist the reaction force imposed by a workpiece, as shown in Figure 3(c). The total volume constraint Ω_s is set to 20% of the volume of the whole design domain. Figure 4(a) shows the optimal configuration. Figure 4(b) shows the eigen-mode shape corresponding to the second eigen-frequency. As shown in this figure, the optimal configuration satisfies the eigen-mode specification.

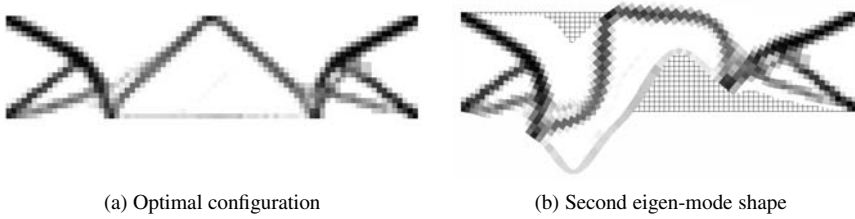


Figure 4. Optimal configuration and second eigen-mode of mechanical resonator.

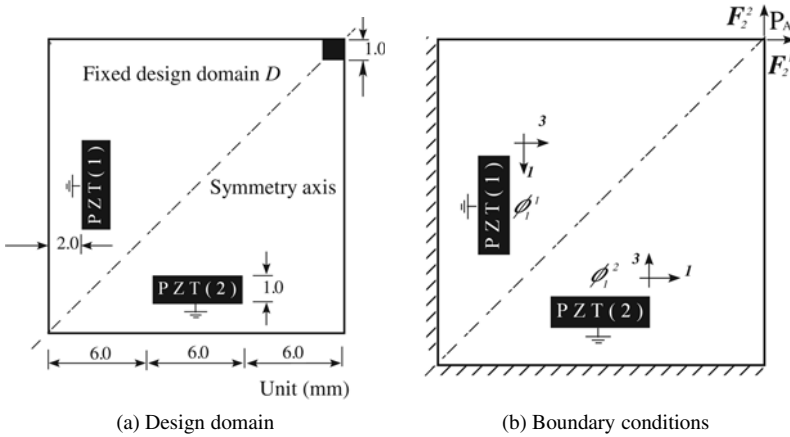


Figure 5. Design specifications of mechanical actuator.

4.2 Mechanical Actuator

Figure 5 shows the design specifications of a mechanical actuator. As shown in this figure, two rectangular shapes of PZT5A piezoceramic material are set in a square domain. The dark regions including the two piezoceramic shapes are set as non-design domains, with the remaining area set as a design domain whose material is assumed to be aluminum. Here, two deformations are to be maximized: the deformation at point P_A in the direction of F_2^1 is to be maximized when the electric potential ϕ_1^1 is applied to PZT(1), and the deformation at point P_A in the direction of F_2^2 is to be maximized when the electric potential ϕ_1^2 is applied to PZT(2), while the stiffness in the directions of $-F_2^1$ and $-F_2^2$ at point P_A are to be maximized. The total volume constraint Ω_s is set to 25% of the volume of the whole design domain. Figure 6 shows the optimal configuration. As shown in this figure, a clear optimal configuration is obtained.

4.3 Mechanical Sensor

Figure 7 shows the design domain of a mechanical sensor. As shown in this figure, the electric potential ΔV_{out} of the piezoresistive device is to be maximized

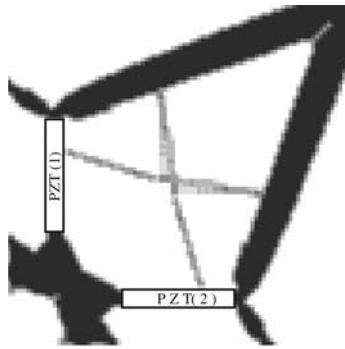


Figure 6. Optimal configuration of mechanical actuator.

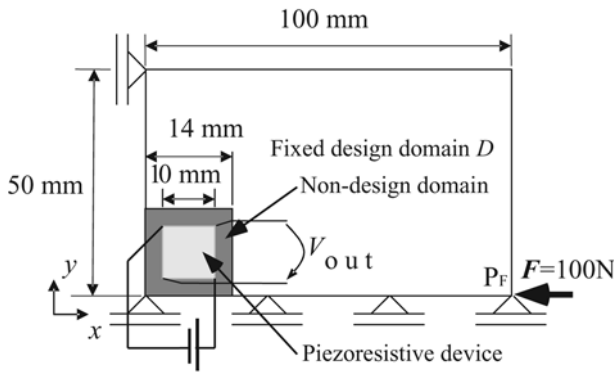


Figure 7. Design domain of mechanical sensor.

when an external force F of 100 N is applied at point P_F while the stiffness in the direction F at point P_F is to be maximized. The material of the design domain is assumed to be aluminum. The material properties of the piezoresistive device are shown in Table 1. The total volume constraint Ω_s is set to 50% of the volume of the whole design domain. Figure 8 shows the optimal configuration. ΔV_{out} of the optimal configuration is obtained as 31.2 mV whereas ΔV_{out} of the entire design domain of aluminum is 2.7 mV. Thus, the sensing performance is improved 12-fold using the obtained optimal configuration.

Table 1. Material properties of piezoresistive device.

Component	ρ_0 ($\Omega \cdot m$)	π_{11} ($10^{-11} m^2/N$)	π_{12} ($10^{-11} m^2/N$)	π_{14} ($10^{-11} m^2/N$)
	0.117	-102.2	53.4	-13.6
Component	D_{11} (GPa)	D_{12} (GPa)	D_{14} (GPa)	
	165.7	63.9	79.6	



Figure 8. Optimal configuration of mechanical sensor.

5. CONCLUSION

This research presented a structural topology optimization method for the design of mechanical resonators, and smart structures such as mechanical actuators and sensors, that are composed of flexible structures and mechanical energy conversion devices. It was confirmed, using several numerical examples, that the method presented here can provide optimized structures applicable to the design of mechanical resonators, mechanical actuators and sensors.

REFERENCES

- [1] M.P. Bendsøe and N. Kikuchi, Generating optimal topologies in structural design using a homogenization method, *Comput. Meth. Appl. Mech. Engrng.*, 71, 197–224 (1988).
- [2] K. Suzuki and N. Kikuchi, A homogenization method for shape and topology optimization, *Comput. Meth. Appl. Mech. Engrng.*, 93, 291–318 (1991).
- [3] R.J. Yang and C.H. Chung, Optimal topology design using linear programming, *Comput. & Struct.*, 53, 265–275 (1994).
- [4] M.P. Bendsøe and O. Sigmund, Material interpolation schemes in topology optimization, *Arch. Appl Mech.*, 69, 635–654 (1999).
- [5] Y. Maeda, S. Nishiwaki, K. Izui, M. Yoshimura, K. Matsui and K. Terada, Structural topology optimization of vibrating structures with specified eigen-frequencies and eigen-mode shapes, *Int. J. Numer. Meth. Engrg.*, to appear.
- [6] E.C.N. Silva, S. Nishiwaki and N. Kikuchi, Topology optimization design of flextensional actuators, *IEEE Trans. Ultrasonics, Ferroelectrics, and Frequency Control*, 47(3), 657–671 (2000).
- [7] R.C. Carbonari, E.C.N. Silva and S. Nishiwaki, Design of piezoelectric multiactuated microtools using topology optimization, *J. Smart Mater. Struct.*, 14, 1431–1447 (2005).
- [8] E.C.N. Silva and S. Nishiwaki, Piezoresistive sensor design using topology optimization, in *SPIE 12th Annual International Symposium on Smart Structures and Materials* (2005).

TOPOLOGY OPTIMIZATION OF WAVE TRANSDUCERS

Eddie Wadbro¹ and Martin Berggren^{1,2}

¹*Department of Information Technology, Uppsala University, Box 337, SE-751 05 Uppsala, Sweden*

²*Division of Systems Technology, FOI, Swedish Defence Research Agency, SE-164 90 Stockholm, Sweden*

Eddie.Wadbro@it.uu.se, Martin.Berggren@it.uu.se

Abstract: We apply topology optimization in order to design an acoustic horn that radiates sound as efficiently as possible. At the same time, we wish to monitor and control also the directivity properties of the horn. Topology optimization provides a rational approach to difficult design problems, such as finding the complex shape required for efficient transmission of sound at frequencies that are too low to efficiently transmit in a short straight horn.

Keywords: Topology optimization, material distribution, Helmholtz equation, acoustic horn, efficiency, radiation properties.

1. INTRODUCTION

The so-called material distribution method has demonstrated its effectiveness for topology optimization of linearly elastic structures. In this method, a scalar function $0 \leq \rho \leq 1$, which can be interpreted as a local density, is used to model presence or lack of material. The monograph by Bendsøe and Sigmund [2] contains a comprehensive discussion of the method and shows many applications.

A recent trend is to attempt a similar strategy to applications in fluid mechanics and wave propagation. Our interest is to design an acoustic horn to transmit sound waves as efficiently as possible. Previously, the second author and coworkers applied boundary shape optimization to this design problem [1, 3]. Recently, we have finished a manuscript [7] applying instead topology optimization using the material distribution method. Here, we summarize our findings and present an extension in which we also consider the directional characteristics of the horn in the far field.

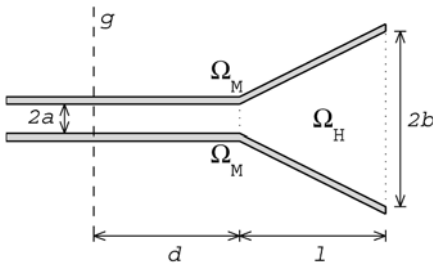


Figure 1a. The wave transducer to be optimized.

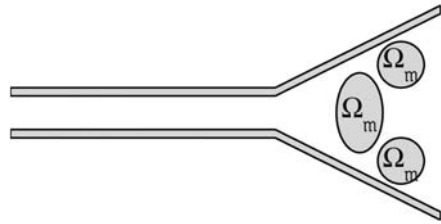


Figure 1b. Material is placed in the region Ω_m in order to improve the transducers radiation properties.

1.1 Problem Description

We consider the planar symmetric wave transducer depicted in Figure 1a. The waveguide has infinite extension to the left and its termination is denoted the horn. The gray shaded region above and below the waveguide and the horn is assumed to consist of sound-hard material.

The horn is fed by planar waves from the waveguide. When such a wave reaches the horn parts of it will propagate into free air, while other parts get reflected. For the horn to function as an effective loudspeaker this reflection needs to be low. We are also interested in the behavior of the wave in the far-field of the horn; in other words, how the wave evolves in different directions far away from the horn.

To optimize the horn we allow an arbitrary distribution of material Ω_m to be placed symmetrically with respect to the axis of the horn (Figure 1b), within the interior horn region Ω_H .

1.2 Geometry Modeling

We use the finite element method to solve the wave propagation problem numerically and thus need to truncate the domain and the waveguide. The computational domain Ω is illustrated in Figure 2. The inflow boundary Γ_{in} corresponds to the cross section g of the waveguide in Figure 1a and Γ_{sym} is a symmetry boundary. The radius of the computational domain is denoted R_Ω . The boundary of the *ground structure* (the portion of the wave guide plus horn contained in Figure 2) is denoted Γ_n .

1.3 The State Equation

Let Ω_d to be the subset of Ω occupied by air, that is $\Omega_d = \Omega - \Omega_m$, and let $\Gamma_{\bar{n}}$ be the boundary between the sound-hard material (ground structure plus Ω_m) and air. We consider time harmonic acoustic wave propagation governed by the Helmholtz equation. Seeking a solution for the complex amplitude function p

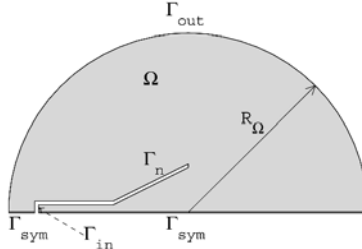


Figure 2. The computational domain.

and a single frequency ω and adding appropriate boundary conditions – for details, see the discussion by Bångtsson et al. [1] – yields

$$\begin{aligned} c^2 \Delta p + \omega^2 p &= 0 \quad \text{in } \Omega_d, & \frac{\partial p}{\partial n} &= 0 \quad \text{on } \Gamma_{\bar{n}} \cup \Gamma_{\text{sym}}, \\ \left(i\omega + \frac{c}{2R_\Omega} \right) p + c \frac{\partial p}{\partial n} &= 0 \quad \text{on } \Gamma_{\text{out}}, & i\omega p + c \frac{\partial p}{\partial n} &= 2i\omega A \quad \text{on } \Gamma_{\text{in}}, \end{aligned} \tag{1}$$

where n is the outward directed normal of the boundary of Ω_d , c is the speed of sound and A is the amplitude of the incoming wave at Γ_{in} .

The shape of Ω_d can be described by a material indicator function $\alpha : \mathbf{R}^2 \rightarrow \{0, 1\}$ such that α is equal to the characteristic function of Ω_d . Making use of α , the state equation (1) can be written as a variational problem over Ω :

Find $p \in H^1(\Omega)$ such that

$$\begin{aligned} c^2 \int_{\Omega} \alpha \nabla \bar{q} \cdot \nabla p \, d\Omega - \omega^2 \int_{\Omega} \alpha \bar{q} p \, d\Omega \\ + i\omega c \int_{\Gamma_{\text{in}} \cup \Gamma_{\text{out}}} \bar{q} p \, d\Gamma + \frac{c^2}{2R_\Omega} \int_{\Gamma_{\text{out}}} \bar{q} p \, d\Gamma = 2i\omega c A \int_{\Gamma_{\text{in}}} \bar{q} \, d\Gamma, \quad \forall q \in H^1(\Omega). \end{aligned}$$

In order to obtain a unique solution of this variational problem in Ω , we redefine α such that $\alpha(x) \in \{\varepsilon, 1\}$ for all $x \in \Omega_H$, where ε is a small positive number.

1.4 Optimization Problem

We are interested in the efficiency and the far-field behavior of the horn. In order to study the efficiency, the mean complex amplitude $\langle p \rangle_{\text{in}}$ on Γ_{in} ,

$$\langle p \rangle_{\text{in}} = \frac{1}{|\Gamma_{\text{in}}|} \int_{\Gamma_{\text{in}}} p \, d\Gamma,$$

is observed. The mean complex amplitude of the reflected wave at Γ_{in} can then be expressed as $\langle p \rangle_{\text{in}} - A$.

The behavior of the complex amplitude function far away from the horn can be described in the following manner. For details in the three dimensional case, see chapter 3 in [4] (current section contains a discussion about the modifications needed to treat the two dimensional case).

Let \hat{x} be a vector such that $|\hat{x}| = 1$, that is $\hat{x} = (\cos \theta, \sin \theta)$ and let ρ be a scalar. Assuming that all sources are located in a bounded region and that ρ is sufficiently large, the far-field behavior of the complex amplitude function is given by

$$p(\rho\hat{x}) = \frac{e^{-i\omega\rho}}{\sqrt{\rho}} \left\{ p_\infty(\theta) + O\left(\frac{1}{\rho}\right) \right\}.$$

We call the function $p_\infty(\theta)$ the *far-field pattern*.

Making use of the boundary conditions given in (1) and the fact that there are no sources located outside Ω and its mirror image on the other side of Γ_{sym} , the far-field pattern is given by

$$p_\infty(\theta) = \frac{1 - i}{4\sqrt{\pi k}} \int_{\hat{\Gamma}_{\text{out}}} e^{ik\hat{x}\cdot x} \left(\frac{ik\hat{x}\cdot x}{R_\Omega} + ik + \frac{1}{2R_\Omega} \right) p(x) d\Gamma(x),$$

where $\hat{\Gamma}_{\text{out}}$ is the closed path described by Γ_{out} and its mirror image on the other side of Γ_{sym} , $k = \omega/c$ is the wavenumber and $\hat{x}\cdot x$ is the scalar product of \hat{x} and x .

Remark 1. There is a sign difference depending on whether the ansatz $P(x, t) = \Re\{p(x)e^{i\omega t}\}$ (our choice) or $P(x, t) = \Re\{p(x)e^{-i\omega t}\}$ (Colton and Kress) is used. This choice affect the sign ($\pm i\omega$) in the boundary conditions at Γ_{in} and Γ_{out} as well as the sign in the expression for the far-field pattern.

In order to use gradient based optimization we relax the variable $\alpha(x)$ to attain values in the continuum $[\varepsilon, 1]$ for $x \in \Omega_{\text{H}}$. In order to obtain a purely solid–fluid final design we define a penalty function, J_p to promote α towards ε or 1 at all points in Ω_{H} . The penalty function we use have the form

$$\gamma \int_{\Omega} (\alpha - \varepsilon)(1 - \alpha) d\Omega,$$

where γ is the penalty constant.

Unfortunately the use of the penalty appears to make the problem ill posed [7]. In order to regularize the problem we use a filtering technique. Hence we define a new design variable $\tilde{\alpha}$ and let $\alpha(x)$ for x in Ω_{H} indirectly be defined by

$$\alpha(x) = \int_{\mathbf{R}^2} \sigma(x) \max\left(0, 1 - \frac{|x - y|}{\tau}\right) \tilde{\alpha}(y) dy,$$

where τ is the filter radius and $\sigma(x)$ is a normalization constant such that

$$\int_{\mathbf{R}^2} \sigma(x) \max\left(0, 1 - \frac{|x - y|}{\tau}\right) dy = 1.$$

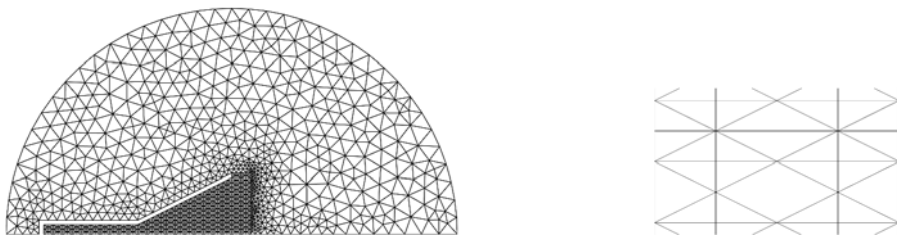


Figure 3. To the left: a coarse version ($h_{\max} = 0.119$) of the hybrid mesh used in our numerical experiments. To the right: a closeup on the structured part.

We define the set of all admissible designs,

$$\mathcal{U} = \left\{ \tilde{\alpha} \in L^\infty(\mathbf{R}^2); \begin{array}{l} \tilde{\alpha} \equiv 0 \text{ in } \Omega_M, \\ 0 < \tilde{\varepsilon} \leq \tilde{\alpha} \leq 1 \text{ a.e. in } \Omega_H, \\ \tilde{\alpha} \equiv 1 \text{ otherwise} \end{array} \right\},$$

and state the general form of our optimization problem as

$$\min_{\tilde{\alpha} \in \mathcal{U}} \left[\sum_{w_j} |\langle p^{(\omega_j)} \rangle_{\text{in}} - A|^2 + \sum_{w_j, \theta_l} \beta_{j,k} |p_\infty^{(\omega_j)}(\theta_k)|^2 + J_p \right],$$

where the constants $\beta_{j,k}$ stipulate whether the optimization should minimize, maximize or do nothing with the value of the far-field pattern for frequency ω_j at angle θ_k .

2. THE DISCRETE SETTING: SETUP AND IMPLEMENTATION

We apply the finite element method to numerically solve the variational form of the state equation. The computational domain Ω is triangulated using a hybrid mesh. The structured part of the mesh contains the waveguide, the horn and some of their surroundings (Figure 3). The triangles in the structured part are right triangles with a ratio of 1:2 between the two catheti.

In our numerical experiments we use second order Lagrangian elements. The function α is approximated with a function $\alpha_h : \Omega \rightarrow [\varepsilon, 1]$, constant on each element. The filtered version of α is approximated similarly. The dimensions of the horn and data about the mesh used for the finite element discretization of the problem can be found in Tables 1a and 1b respectively.

We use the software Femlab for the initial assembly of state matrices and the construction of the unstructured part of the mesh. In each step of the optimization algorithm the linear systems resulting from the discretization of the state and adjoint equations are solved using the sparse direct solver UMFPACK [5].

Table 1a. The dimensions of the horn in the numerical experiments, with the parameters defined in Figs. 1a and 2.

$a(\text{m})$	$b(\text{m})$	$l(\text{m})$	$d(\text{m})$	$R_{\Omega}(\text{m})$
0.05	0.3	0.5	0.5	1.2

Table 1b. Top row: data for the finite element mesh used in the numerical experiments optimizing the horn, bottom row: (as a reference) data for the mesh in Figure 3. M is the total number of elements, n is the degrees of freedom, N is the number of design variables, h_{\max} is the maximum edge length and h_{Ω_H} is the edge length in the x_1 direction in the structured part of the mesh.

M	n	N	h_{\max}	h_{Ω_H}
28104	56907	8960	0.03423	0.00625
2142	4463	560	0.11942	0.025

The objective functions are discretized by replacing the variables with their approximations. The necessary gradients are computed using the solution of the associated adjoint equations. The material distribution is updated using the *method of moving asymptotes*, MMA [6]. Afterwards the state matrices are updated, due to the changes in material distribution.

When optimizing the efficiency of the transducer we use $\alpha \equiv 1$ (all air) as a starting guess of the material distribution and a *continuation approach* for the penalization. That is, the optimization problem is first solved with $\gamma = 0$, then γ is increased and a new round of optimization is performed. The process is then repeated.

When optimizing both the efficiency and some far-field properties of the transducer we use the shape optimized only with respect to efficiency as start guess for the material distribution and a *reduced continuation approach* for the penalization. That is, we use the continuation approach but starting with a positive value of γ instead of 0.

3. RESULTS

For all numerical results below, we have used $\tilde{\varepsilon} = 10^{-6}$ and filter radius $\tau = 0.0125$ whenever filtering is being used.

The *reflection coefficient* R is the quotient between the amplitude of the reflected wave and the incoming wave at Γ_{in} , that is $R = (\langle p \rangle_{\text{in}} - A)/A$. The *reflection spectrum* is the absolute value of the reflection coefficient as a function of frequency. The shapes of the optimized horns are presented together with their reflection spectra, and the far-field behavior of the horns will be illustrated, for some frequencies, by polar plots of $|p_{\infty}(\theta)|^2$ as a function of θ .

Here we apply the same type of postprocessing as in our manuscript [7], that is when the optimization (using filtering) has converged at the highest penalty level the filter is removed and the optimization process is continues using a high penalty. For more results on accuracy, mesh dependency for the case

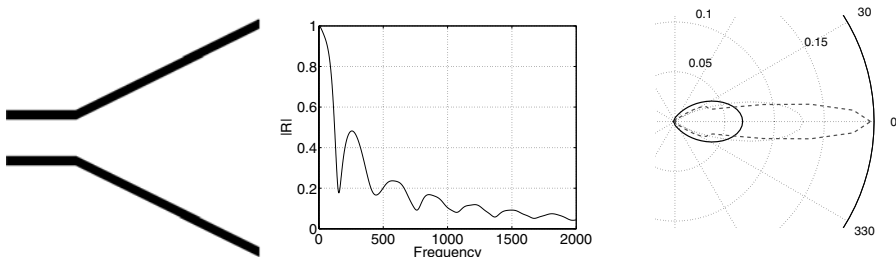


Figure 4. From the left: the initial horn, its spectrum and its far-field behavior for the frequencies 400 Hz (solid line), 800 Hz (dotted line) and 1600 Hz (dashed line).

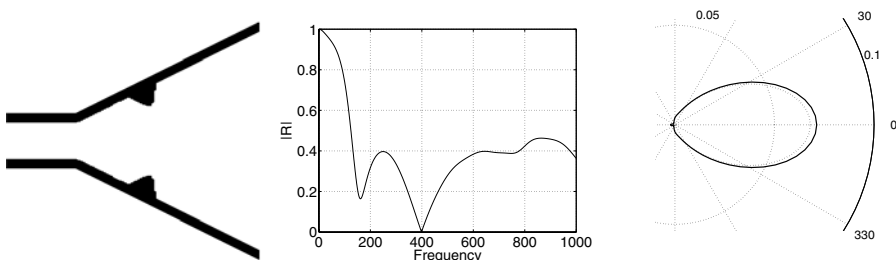


Figure 5. Left: horn optimized for a single frequency of 400 Hz, middle: its spectrum and right: its far-field behavior for the frequency 400 Hz (solid line) together with the far-field behavior for the initial horn at 400 Hz (dotted line).

when the horn is optimized with respect to efficiency we refer to our studies presented in [7].

3.1 Optimizing for Efficiency

First, we compute the reflection spectrum and the far-field behavior for the initial horn. The results presented in Figure 4 shows that the simple funnel-shaped horn is a fairly inefficient transmitter, particularly for the lower frequencies. The horn also exhibits a marked *beaming effect*. That is, the wave propagation becomes more concentrated right in front of the horn for higher frequencies.

At a single frequency the horn can be optimized to almost perfect transmission. There is no uniqueness in such designs; there are many different shapes that may provide good transmission. The horns computed by our topology optimization tends to have piles of material at different locations, depending on the frequency of optimization, along the walls of the funnel. These shapes differ substantially from the ones obtained by boundary shape optimization [1]. A horn optimized using topology optimization for a single frequency of 400 Hz is shown in Figure 5.

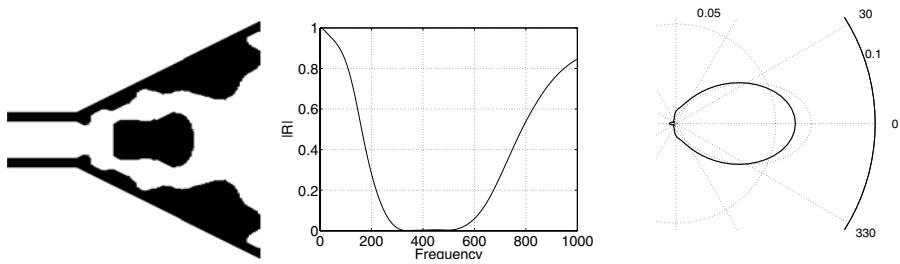


Figure 6. Left: horn optimized for the frequencies 400 Hz, 410 Hz, . . . , 500 Hz, middle: its spectrum and right: its far-field behavior for the frequency 400 Hz (solid line) together with the far-field behavior for the initial horn at 400 Hz (dotted line).

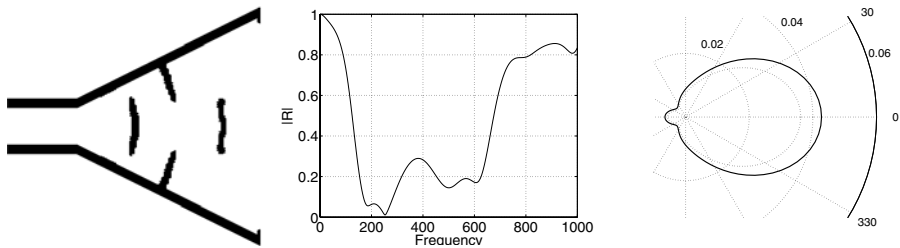
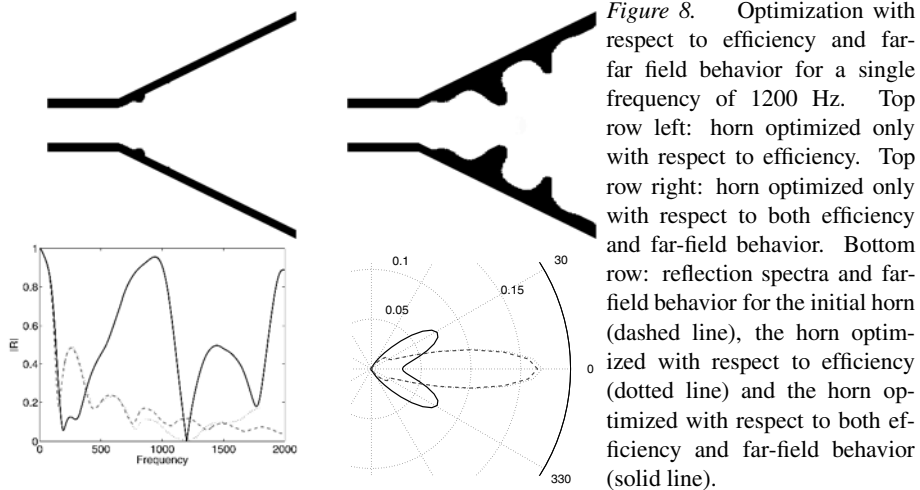


Figure 7. Left: horn optimized for the frequencies 150 Hz, 160 Hz, . . . , 300 Hz, middle: its spectrum and right: its far-field behavior for the frequency 200 Hz (solid line) together with the far-field behavior for the initial horn at 200 Hz (dotted line).

The horn shapes become more complicated when a larger frequency range is considered in the optimization. A horn optimized using topology optimization for eleven frequencies in the range 400–500 Hz is shown in Figure 6. This horn has almost perfect transmission properties throughout the frequency range considered in the optimization. The horns in Figs. 5 and 6 transmit almost perfectly at 400 Hz and illustrate the fact that many different horn shapes show almost perfect transmission at a single frequency.

From the far-field behaviors at 400 Hz presented in Figures 5 and 6 the following observation can be made. In comparison with the initial horn the horn optimized for a single frequency tends to concentrate the wave propagation around the symmetry axis while the horn optimized for the multi frequency case tends to spread the sound. Hence for the frequency 400 Hz both horns are much more efficient than the initial horn, but there is a significant difference in what influence these horns have on the behavior of the wave in the far field.

Horns tuned for low frequencies tend to be large and bulky since it is difficult to obtain good performance from a straight horn shorter than half the wavelength. Performing topology optimization for a frequency range of 150–300 Hz results in the horn presented in Figure 7. In this case the horn is shorter



that a quarter of the wavelength for the lowest frequency in the optimization. The material distribution serves as an effective elongation of the horn.

A comparison of the far-field patterns at 200 Hz between the initial horn and the horn optimized for frequencies in the range 150–300 Hz shows that the optimized horn has gained far-field intensity in all directions.

3.2 Optimizing for Efficiency and Directivity

As a second experiment, we optimize at a single frequency of 1200 Hz trying to maximize the efficiency of the horn, and at the same time minimize the far-field intensity right in front of the horn. In a sense the two objectives work in different directions. Since, the absolute value of the far-field pattern is zero when the incoming wave is totally reflected back into the waveguide.

The first step in this optimization is to optimize the horn only with respect to efficiency. The shape of the horn optimized for efficiency at a single frequency of 1200 Hz is shown at the top left side of Figure 8. Compared to the 400 Hz horn shown in Figure 5 we note that the piles of material at the funnel sides have moved closer to the throat of the horn and decreased in size.

The second step is to include the far-field behavior in the optimization problem and use the horn optimized only with respect to efficiency as a starting guess. The resulting horn is shown at the top right side of Figure 8. The shape of this horn is much more complex than the shape of the horn optimized only with respect to efficiency. However near the throat of the horn the two horns are similar in shape.

The horn optimized only with respect to efficiency is also efficient in a region around 1200 Hz. The horn optimized both with respect to transmission

efficiency and minimizing the far-field wave propagation right in front of the horn has only good transmission properties at the frequency subject to optimization.

Finally there is a vast difference in the far-field behavior at 1200 Hz for the two optimized horns indicating that it could be worthwhile to take the far-field behavior into account when performing optimization for acoustical devices.

4. CONCLUSIONS AND OUTLOOK

The dimensions of the horns considered here are in the order of the wavelength. Design problems in that parameter regime are difficult to solve by intuitive physical reasoning, since physical intuition typically relies on asymptotic theory that does not apply, such as long wavelength transmission line or short wavelength ray theory. We believe that there are many such design problem in acoustics and electromagnetics that would benefit from the use of numerical design optimization. Topology optimization is an attractive alternative to boundary-shape optimization particularly for cases like the one illustrated in Figure 7, when the device is too small for a simple shape modification to yield sufficient performance improvement.

We intend to extend the present study to three space dimensions and also to explore further the combined optimization of efficiency and directivity.

ACKNOWLEDGMENTS

The authors thank Stefan Jakobsson for discussions about the far-field and Daniel Noreland for sharing his knowledge in acoustics.

REFERENCES

- [1] E. Bängtsson, D. Noreland and M. Berggren, Shape optimization of an acoustic horn, *Comput. Methods Appl. Mech. Engrg.*, 192, 1533–1571 (2003).
- [2] M.P. Bendsøe and O. Sigmund, *Topology Optimization. Theory, Methods, and Applications*, Springer (2003).
- [3] M. Berggren, E. Bängtsson and D. Noreland, Multifrequency shape optimization of an acoustic horn, in *Computational Fluid and Solid Mechanics*, K.J. Bathe (ed.), pp. 2204–2207, Elsevier Science (2003).
- [4] D. Colton and R. Kress, *Integral Equation Methods in Scattering Theory*, John Wiley & Sons (1983).
- [5] T.A. Davis, Algorithm 832: UMFPACK – An unsymmetric-pattern multifrontal method, *ACM Transactions on Mathematical Software*, 30(2), 196–199 (2004).
- [6] K. Svanberg, The method of moving asymptotes – A new method for structural optimization, *Internat. J. Numer. Methods Engrg.*, 24, 359–373 (1987).
- [7] E. Wadbro and M. Berggren, Topology optimization of an acoustic horn, in review (2005).

OPTIMAL MODE COUPLING IN SIMPLE PLANAR WAVEGUIDES*

David C. Dobson

Department of Mathematics, University of Utah, Salt Lake City, UT 84112-0090, U.S.A.

dobson@math.utah.edu

Abstract: The problem of coupling electromagnetic or acoustic waves into a dielectric waveguide with minimal energy loss is formulated as a structural (topology) optimization problem. Optimal solutions are shown to attain at least one material constraint, almost everywhere in the design domain. A numerical optimization procedure using a level set method is proposed, and results from numerical experiments are described.

Keywords: Waveguide coupler, mode matching, optimal design.

1. INTRODUCTION

Dielectric channel and strip waveguides are simple devices for localizing and moving optical signals in integrated photonic structures. These waveguides are low-loss and relatively easy to fabricate. A fundamental engineering problem arising with these structures is how to efficiently couple energy into and out of the waveguide, particularly when the cross section of the waveguide is on the order of the wavelength of the incoming signal. This can be viewed as a classical problem of “mode-matching” which has been widely studied since early investigations in acoustics, and also in antenna design. Recent applications of optimization for photonic waveguides can be found in [2, 11]. Shape and topology optimization for waveguides has been studied in [1, 6].

We describe an approach for designing efficient waveguide couplers using the general techniques of topology optimization. The approach assumes very little about the general form that a solution should take, however we argue that optimal solutions generally attain at least one material constraint, almost everywhere in the design domain. Additional constraints can be added to the problem to enforce fabrication or performance requirements. Similar methods

*Research partially supported by NSF grant number DMS-0537015.

have been developed for other topology optimization problems in photonics and phononics, see for example [3, 4, 12].

2. MODEL PROBLEM

Consider time-harmonic electromagnetic wave propagation in two spatial dimensions, modeled by the Helmholtz equation

$$\Delta u + \omega^2 \epsilon u = 0, \quad \text{in } \mathbb{R}^2, \quad (1)$$

where ω represents the frequency, and $\epsilon \in L^\infty(\mathbb{R}^2)$, $\epsilon(x) \geq 1 > 0$ is the dielectric coefficient, and $x = (x_1, x_2) \in \mathbb{R}^2$. This is the underlying model for all wave propagation considered here.

A simple waveguide structure can be defined by

$$\epsilon(x) = \begin{cases} \epsilon_0, & |x_1| \leq \frac{h}{2}, \\ 1, & \text{otherwise,} \end{cases} \quad (2)$$

where $\epsilon_0 > 1$, and $h > 0$.

We are interested in coupling waves exterior to such a waveguide to particular solutions known as “guided modes” within the waveguide. Next we briefly describe the guided modes. A much more detailed discussion of waveguide modes can be found in [7].

Solutions to (1), (2) which decay exponentially as $|x_1| \rightarrow \infty$ can be sought in the form

$$u_0(x) = \begin{cases} ce^{-i(\alpha_0 x_1 + \beta x_2)}, & x_1 < -h/2, \\ ae^{-i(\alpha_1 x_1 + \beta x_2)} + be^{i(\alpha_1 x_1 - \beta x_2)}, & |x_1| \leq h/2, \\ de^{i(\alpha_0 x_1 - \beta x_2)}, & x_1 > h/2. \end{cases} \quad (3)$$

Here, β is a real propagation constant, chosen such that $\omega^2 < \beta^2 < \epsilon_0 \omega^2$, and a, b, c, d are unknown constants. We define $\alpha_0 = \sqrt{\omega^2 - \beta^2}$, $\alpha_1 = \sqrt{\epsilon_0 \omega^2 - \beta^2}$. Note that α_0 is purely imaginary, and α_1 is real and positive. By choosing the channel width h appropriately, modes which propagate along the $-x_2$ direction are supported. With β (and hence α_0 and α_1) fixed, allowable values of h are

$$h = \frac{1}{\alpha_1} (\pi n - \arg((\alpha_1 - \alpha_0)^2)), \quad (4)$$

where $n \geq 0$ is any integer which makes $h > 0$. Conversely, if h is specified large enough, there exist finitely many propagating modes (each corresponding to a different value of β), with the number of modes growing with h . Figure 1 illustrates typical dependence of h versus β .

For each pair h, β which satisfy (4), there exists a one-dimensional linear subspace of solutions proportional to

$$a = b = 1, \quad c = d = 2e^{-i\alpha_0 h/2} \cos(\alpha_1 h/2).$$

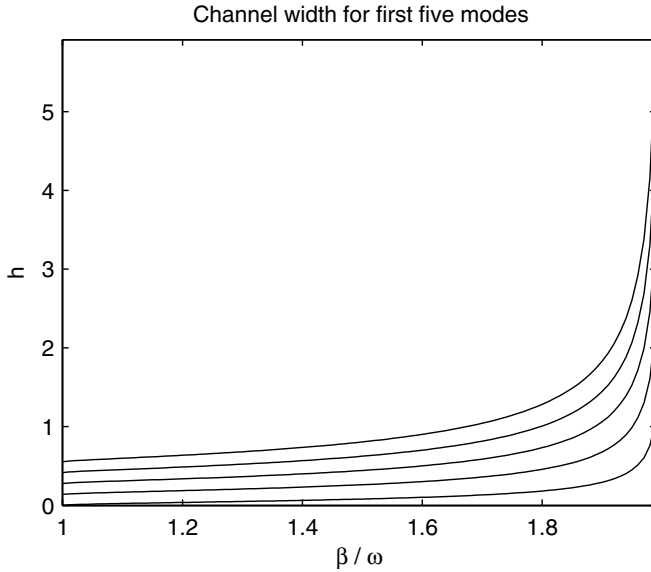


Figure 1. Typical channel width h versus propagation constant β .

From now on, u_0 will denote the solution (3) where a, b, c, d are defined above. The parameters h, β are assumed to be fixed.

Above the waveguide (for large x_2), consider an incoming wave propagating through an empty half-space. In particular, choosing some positive constant b and another slightly smaller constant b' such that $0 < b' < b$, assume that the dielectric coefficient $\epsilon(x)$ satisfies $\epsilon(x_1, x_2) = \epsilon_1$ for $x_1 \geq b'$, where $\epsilon_1 \geq 1$ is constant. The line $\Gamma_b = \{(x_1, x_2) : x_2 = b\}$ will denote the boundary between the homogeneous region above and the inhomogeneous region below.

In the homogeneous region $x_2 > b$, separate the solution u to (1) into an incident and scattered field: $u = u_i + u_s$. Taking the Fourier transform of u_s in the x_1 variable, and insisting that the scattered field is *outgoing*, one can derive from (1) that

$$\frac{\partial u_s}{\partial x_2}(x_1, b) = \int_{\mathbb{R}} i\gamma(\xi)\hat{u}_s(\xi, b)e^{i\xi x_1} d\xi \equiv (T(u_s|_{\Gamma_b}))(x_1),$$

where $\gamma(\xi) = \sqrt{\omega^2\epsilon_1 - \xi^2}$, and $\hat{u}_s(\cdot, b)$ is the Fourier transform of $u_s(x_1, b)$. The linear map T (Dirichlet-to-Neumann operator) then defines the relationship between the traces $u_s|_{\Gamma_b}$ and $\partial_2 u_s|_{\Gamma_b}$: $T(u_s|_{\Gamma_b}) = (\partial_2 u_s)|_{\Gamma_b}$. On the boundary Γ_b , the solution $u = u_i + u_s$ should then satisfy $\partial_2 u - Tu = \partial_2 u_i - Tu_i$. Thus given the incident wave u_i , one can calculate $q = \partial_2 u_i - Tu_i$ on Γ_b , and enforce the boundary condition $\partial_2 u - Tu = q$ on Γ_b .

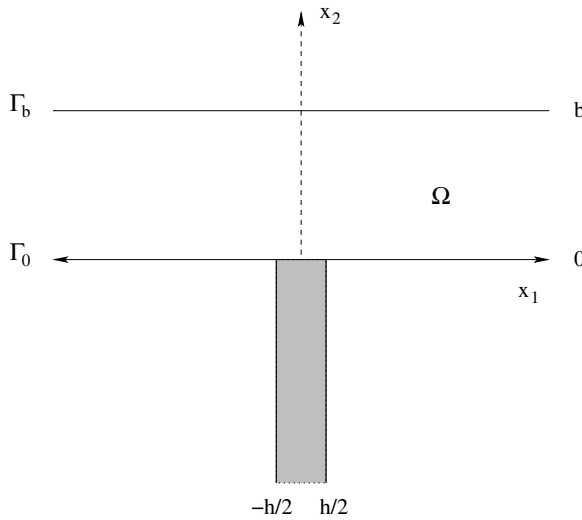


Figure 2. Problem geometry.

2.1 Ideal Waveguide Coupler

An ideal waveguide coupler (for our purposes) would consist of a material structure $\epsilon(x)$ in the slab $\Omega = \{x \in \mathbb{R}^2 : 0 < x_2 < b\}$ such that a given incident wave u_i coming in from $x_2 > b$ couples perfectly to particular waveguide channel mode u_0 situated in the half-space $x_2 < 0$ (see Figure 2). Perfect coupling means that all of the energy flux from u_i across the upper boundary Γ_b is transferred into the chosen waveguide mode.

For a given incident wave u_i , one can easily find a real constant t such that the energy flux of the channel mode tu_0 across Γ_0 matches that of u_i ,

$$t = \frac{\int_{\Gamma_b} \epsilon \operatorname{Re}\{u_i \overline{(\partial_2 u_i)}\}}{\int_{\Gamma_0} \epsilon \operatorname{Re}\{u_0 \overline{(\partial_2 u_0)}\}}.$$

Since the phase of the waveguide mode does not affect its energy flux, we may write the desired waveguide mode as $te^{i\theta}u_0$, where θ is an arbitrary real phase.

In the hypothetical situation where an ideal coupling structure $\epsilon(x)$ exists, the following overdetermined Cauchy problem must be satisfied:

$$\begin{aligned} \Delta u + \omega^2 \epsilon u &= 0, && \text{in } \Omega, \\ \left(\frac{\partial}{\partial x_2} - T\right) u &= q, && \text{on } \Gamma_b, \\ \frac{\partial u}{\partial x_2} &= e^{i\theta} f, && \text{on } \Gamma_0, \\ u &= e^{i\theta} g, && \text{on } \Gamma_0, \end{aligned} \tag{5}$$

where $f = t \frac{\partial u_0}{\partial x_2} |_{\Gamma_0}$ and $g = tu_0 |_{\Gamma_0}$. Even with the flexibility to choose an arbitrary function $\epsilon(x)$ in Ω and phase $\theta \in \mathbb{R}$, there is no reason to expect that a solution to this problem exists. Our goal will be to find a structure $\epsilon(x)$ such that this problem is *approximately* satisfied, in the sense described below.

3. OPTIMIZATION PROBLEM

Physically realizable structures must be of finite extent. We therefore define an admissible design set consisting of mixtures of two materials

$$\mathcal{A} = \{\rho \in L^\infty(\Omega') : \omega^2 \leq \text{Re}\{\rho(x)\} \leq \omega^2 \epsilon_1, 0 \leq \text{Im}\{\rho(x)\} \leq \delta_1, \text{ a.e.}\},$$

where Ω' is a bounded open set whose closure is contained in Ω . For each $\rho \in \mathcal{A}$, define the extension to Ω

$$\tilde{\rho}(x) = i\delta + \begin{cases} \rho(x), & x \in \Omega', \\ \omega^2 \epsilon_1, & \text{otherwise.} \end{cases}$$

The small absorption term $\delta > 0$ is included to facilitate estimates on the solution. In the numerical experiments (which take place on bounded domains), we set $\delta = 0$.

Define $F(\rho, \theta) = u|_{\Gamma_0}$, where u is the weak solution to the problem

$$\Delta u + \tilde{\rho}u = 0, \quad \text{in } \Omega, \tag{6}$$

$$\left(\frac{\partial}{\partial x_2} - T \right) u = q, \quad \text{on } \Gamma_b, \tag{7}$$

$$\frac{\partial u}{\partial x_2} = e^{i\theta} f, \quad \text{on } \Gamma_0. \tag{8}$$

LEMMA 1 *For each $\rho \in \mathcal{A}$, problem (6)–(8) admits a unique weak solution $u \in H^2(\Omega)$. Furthermore, there exists a constant C depending on $\delta > 0$, such that $\|u\|_{H^2(\Omega)} \leq C$, independent of $\rho \in \mathcal{A}$.*

The proof is an application of the Lax–Milgram theorem, and closely follows the similar result in [5].

Reformulate the overdetermined Cauchy problem as a minimization

$$\inf_{\substack{\rho \in \mathcal{A}, \\ \theta \in \mathbb{R}}} J(\rho, \theta) = \frac{1}{2} \|F(\rho, \theta) - e^{i\theta} g\|_2^2. \tag{9}$$

Finding ρ, θ for which $J(\rho, \theta) = 0$ would enforce condition (5), and consequently yield a solution to the overdetermined Cauchy problem (attaining ideal mode coupling). Again, we make no claim that such an *ideal* solution exists, however, the following proposition holds:

PROPOSITION 1 *Problem (9) has a solution $(\rho_0, \theta_0) \in \mathcal{A} \times \mathbb{R}$.*

The proof is a simple application of the Direct Method of the calculus of variations, using Lemma 1 to obtain a weakly convergent subsequence of solutions. Details for a similar problem can be found in [5].

In the following sections, solutions to (9) are characterized and numerically approximated. Numerical results indicate that one can in practice come quite close to achieving ideal coupling.

4. CHARACTERIZATION OF MINIMIZERS

Let $\rho \in \mathcal{A}$ and $\delta\rho \in L^\infty(\Omega')$ be given such that $\rho + \delta\rho \in \mathcal{A}$. The directional derivative of $J(\rho, \theta)$ in direction $\delta\rho$ is formally

$$\begin{aligned} DJ(\rho, \theta)(\delta\rho) &= \operatorname{Re}\langle DF(\rho, \theta)(\delta\rho), F(\rho, \theta) - e^{i\theta}g \rangle_{L^2(\Gamma_0)} \\ &= \operatorname{Re}\langle \delta\rho, DF^*(\rho, \theta)(F(\rho, \theta) - e^{i\theta}g) \rangle_{L^2(\Omega')}. \end{aligned}$$

One can calculate directly that

$$\langle DF(\rho, \theta)(\delta\rho), F(\rho, \theta) - e^{i\theta}g \rangle_{L^2(\Gamma_0)} = \int_{\Omega'} \delta\rho u \bar{w},$$

where w is the solution to the adjoint problem

$$\begin{aligned} \Delta w + \bar{\rho}w &= 0, && \text{in } \Omega, \\ \left(\frac{\partial}{\partial x_2} - T^*\right)w &= 0, && \text{on } \Gamma_b, \\ \frac{\partial w}{\partial x_2} &= F(\rho, \theta) - e^{i\theta}g, && \text{on } \Gamma_0, \end{aligned}$$

and T^* is the $L^2(\Gamma_b)$ adjoint of T . Identifying separate gradients for the real and imaginary parts of $\rho = \rho_r + i\rho_i$, we find $\nabla_{\rho_r}J(\rho, \theta) = \operatorname{Re}\{u\bar{w}|_{\Omega'}\}$, $\nabla_{\rho_i}J(\rho, \theta) = -\operatorname{Im}\{u\bar{w}|_{\Omega'}\}$, so that

$$DJ(\rho, \theta)(\delta\rho) = \langle \operatorname{Re}\{\delta\rho\}, \nabla_{\rho_r}J(\rho, \theta) \rangle + \langle \operatorname{Im}\{\delta\rho\}, \nabla_{\rho_i}J(\rho, \theta) \rangle.$$

The formal derivative of $J(\rho, \theta)$ with respect to θ is also easily calculated, $\partial_\theta J(\rho, \theta) = \operatorname{Re}\langle \partial_\theta F(\rho, \theta) - ie^{i\theta}g, F(\rho, \theta) - e^{i\theta}g \rangle_{L^2(\Gamma_0)}$, where $\partial_\theta F(\rho, \theta) = v|_{\Gamma_0}$ and v solves a perturbed problem.

Because of the constraint $\rho \in \mathcal{A}$, necessary conditions include a Lagrange multiplier rule. Consequently, if (ρ_0, θ_0) is a minimizer, it must hold that $\nabla_{\rho_r}J(\rho_0, \theta) = \nabla_{\rho_i}J(\rho_0, \theta) = 0$ on the set

$$\mathcal{V} = \{x \in \Omega' : \omega^2 < \operatorname{Re}\{\rho_0(x)\} < \omega^2\epsilon_1, 0 < \operatorname{Im}\{\rho_0(x)\} < \delta_1\}$$

upon which the constraints are not active. Suppose that \mathcal{V} contains an open set \mathcal{U} . The real and imaginary gradient fields are both zero on \mathcal{U} . In other words, the product $u\bar{w} = 0$ on \mathcal{U} , where u and w are solutions of the direct and adjoint scattering problems, respectively. Since both fields are in $H^2(\Omega)$ and hence continuous, one of the two fields must also be zero on some open set contained in \mathcal{U} . By the unique continuation property of solutions (see e.g. [8]), the field must then be zero everywhere. By uniqueness of solutions, this can only occur when the boundary data is zero, which is only possible for w , and only then when the residual $F(\rho_0, \theta_0) - e^{i\theta} g = 0$. The following proposition must then hold:

PROPOSITION 2 *If (ρ_0, θ_0) is a solution of the minimization problem (9) for which $J(\rho_0, \theta_0) > 0$, then $\rho_0(x)$ attains at least one of the bound constraints in the admissible class \mathcal{A} , for almost every $x \in \Omega'$.*

A slightly closer look at regularity estimates shows that u and w are C^1 functions. It then follows from the necessary conditions that boundaries separating regions in which the material constraints are active are C^1 .

5. OPTIMIZATION METHOD

The derivative calculations in the previous section lead directly to the following projected gradient descent method. For simplicity, it is assumed henceforth that the upper bound δ_1 on the imaginary part of ρ is zero. Note that Proposition 2 above does *not* then guarantee that the constraints on $\text{Re}\{\rho\}$ are attained, since the constraints on $\text{Im}\{\rho\}$ are automatically active everywhere.

For the initial step $k = 0$, choose an initial structure ρ_0 , phase angle θ_0 , and step parameters $s_\rho, s_\theta > 0$.

Algorithm 1.

```

while (necessary conditions are not satisfied),
   $G := \nabla_{\rho_r} J(\rho_k, \theta_k)$ ;
   $p := \partial_\theta J(\rho_k, \theta_k)$ ;
  if  $J(P(\rho_k - s_\rho G), \theta_k - s_\theta p) < J(\rho_k, \theta_k)$  then
     $\rho_{k+1} = P(\rho_k - s_\rho G)$ ;
     $\theta_{k+1} = \theta_k - s_\theta p$ ;
     $k := k + 1$ ;
  else
     $(s_\rho, s_\theta) := \frac{1}{2}(s_\rho, s_\theta)$ ;
  end if
end while
    
```

The map $P : L^\infty(\Omega') \rightarrow \mathcal{A}$ is simply pointwise projection onto \mathcal{A} .

For optical applications, designs which utilize only two materials are highly preferable to those using intermediate indexes. It makes sense to use an al-

gorithm which enforces this condition. The level-set method [9] is readily adapted and combined with Algorithm 1 for this situation. We follow the approach in [10].

The idea is to represent $\rho(x)$ through an auxiliary *level set* function $\phi(x)$ through the formula

$$\rho(x) = \begin{cases} \omega^2, & \phi(x) < 0, \\ \omega^2 \epsilon_1, & \phi(x) > 0. \end{cases} \quad (10)$$

The zero set of ϕ encodes the boundary between one material and the other. For our purposes, the primary advantages of this approach are that changes in the topology of the design are handled effortlessly, and that all computations can be done on a fixed grid. The only modification necessary to Algorithm 1 is that the level set function ϕ must be updated in the gradient step, rather than modifying ρ directly. One can calculate in a straightforward way that an appropriate update is

$$\phi_{k+1} = \phi_k - s_\phi G.$$

All references to ρ are made through its definition (10) with respect to ϕ , and the projection operator P is no longer necessary.

6. NUMERICAL EXPERIMENTS

The algorithm was implemented by discretizing problem (6)–(8), along with the adjoint problem, with piecewise bilinear finite elements on a fixed, uniform rectangular grid. To truncate the x_1 -direction, periodic boundary conditions were enforced, usually with an absorptive layer near the computational boundaries. The nonlocal boundary condition (7) results in a full subblock in the finite element matrix, however the number of nonzero elements is still on the order of the number of grid points, for relatively square domains. The matrix is complex symmetric, but non-Hermitian, resulting in poor performance from standard iterative matrix solvers. Also, acceptable performance of the gradient descent algorithm often requires extremely accurate solutions and gradients. For these reasons, solution of the finite element problem is accomplished with a direct sparse solver.

Figures 3–5 illustrate the results of some preliminary numerical experiments. The examples in Figures 3 and 4 use $\epsilon_0 = \epsilon_1 = 4$, while that in Figure 5 uses $\epsilon_0 = \epsilon_1 = 6$. In this last example, additional constraints were added to enforce the connectedness of the high-index region. The resulting structure has similar characteristics to those produced in [2]. Note that when coupling into symmetrical modes, symmetrical structures are generated. Coupling efficiency (the proportion of incident energy coupled into the waveguide) in some of our experiments exceeded 99%, far in excess of the performance typically obtained with conventional structures.

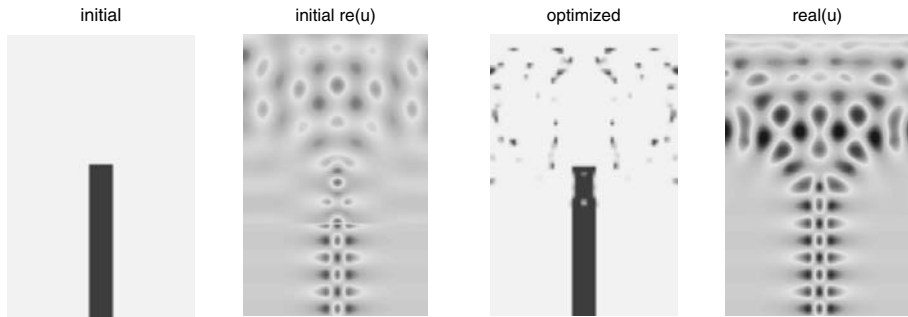


Figure 3. Coupling from air into a symmetrical waveguide mode. Initial guess and real part of initial field is on the left, optimized solution and real part of resulting field is on the right.

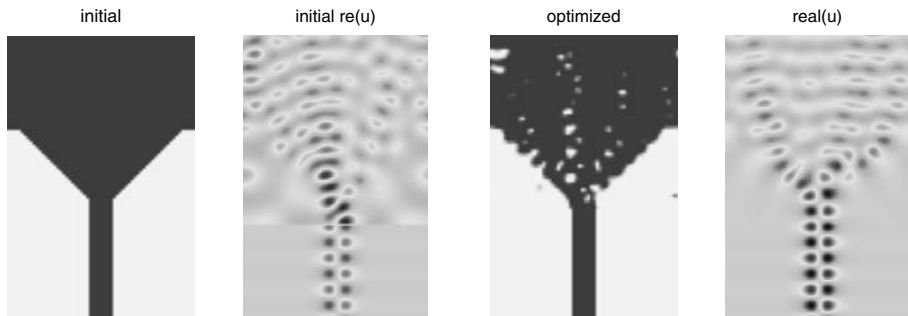


Figure 4. Coupling from a high-index medium into an antisymmetric waveguide mode.

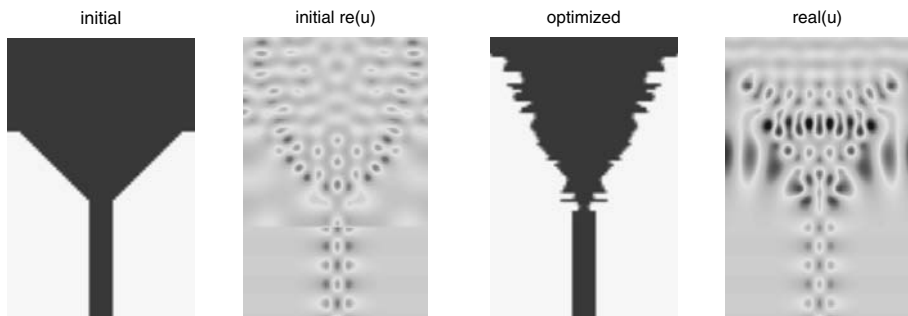


Figure 5. Coupling from a high-index medium into a symmetrical waveguide mode, with interface constraints on the design.

The numerical optimizations require three PDE solves for each gradient descent step. Convergence is generally very slow (typically requiring thousands of steps), meaning the method is computationally intensive. Essentially no attempt was made to improve the efficiency of the optimization, for example by implementing a step length control strategy. A more sophisticated optimization

algorithm could alleviate the situation considerably. The point here is merely to indicate that the general design approach is plausible.

The approximate “optimal” designs generated here lack some desirable features. First, the designs tend to be very sensitive to perturbations. Nothing in the objective functional enforces robustness, and it turns out that small changes in the solutions can have a drastic effect on the coupling efficiency. Second, the designs can be quite complicated. Simpler designs may exist which perform equally well (and are perhaps more robust). Either or both of these drawbacks might be addressed with modifications to the objective, or through better optimization strategies.

REFERENCES

- [1] Bangtsson, E., Noreland, D. and Berggren, M., Shape optimization of an acoustic horn, *Comput. Methods Appl. Mech. Engrg.*, 192, 1533–1571 (2003).
- [2] Bogaerts, W., Taillaert, D., Luyssaert, B., Dumon, P., Van Campenhout, J., Bienstman, P., Van Thourhout, D., Baets, R., Wiaux, V. and Beckx, S., Basic structures for photonic integrated circuits in silicon-on-insulator, *Optics Express*, 12(8), 1583–1591 (2004).
- [3] Cox, S.J. and Dobson, D.C., Maximizing band gaps in two-dimensional photonic crystals, *SIAM J. Appl. Math.*, 59, 2108–2120 (1999).
- [4] Dobson, D.C., Optimal design of periodic antireflective structures for the Helmholtz equation, *Euro. J. Appl. Math.*, 4, 321–340 (1993).
- [5] Dobson, D.C. and Simeonova, L.B., Optimal design of periodic micro-composite lenses, in preparation.
- [6] Jensen, J.S. and Sigmund, O., Topology optimization of two-dimensional waveguides, in *5th World Congress on Structural and Multidisciplinary Optimization*, May 19–23, 2003, C. Cinquini, M. Rovati, P. Venini and R. Nascimbene (eds), Italian Polytechnic Press, Milano, pp. 125–126 (2003).
- [7] Marcuse, D., *Theory of Dielectric Optical Waveguides*, Academic Press, New York (1974).
- [8] Miranda, C., *Partial Differential Equations of Elliptic Type*, Second revised edition, Springer-Verlag, New York (1970).
- [9] Osher, S.J. and Fedkiw, R.P., *Level Set Methods and Dynamic Implicit Surfaces*, Springer-Verlag, New York (2003).
- [10] Osher, S. and Santosa, F., Level set methods for optimization problems involving geometry and constraints I. Frequencies of a two-density inhomogeneous drum, *J. Comp. Phys.*, 171, 272–288 (2001).
- [11] Sanchis, P., Marti, J., Blasco, J., Martinez, A. and Garcia, A., Mode matching technique for highly efficient coupling between dielectric waveguides and planar photonic crystal circuits, *Optics Express*, 10(24), 1391–1397 (2002).
- [12] Sigmund, O. and Jensen, J.S., Systematic design of phononic band-gap materials and structures by topology optimization, *Phil. Trans. Royal Soc.: Math. Phys. and Eng. Sci.*, 361, 1001–1019 (2003).

Geometry Modelling

TOPOLOGY OPTIMIZATION BY PENALTY (TOP) METHOD

T.E. Bruns

Beckman Institute for Advanced Science and Technology, University of Illinois at Urbana-Champaign, Urbana, IL 61801, U.S.A.

tbruns@uiuc.edu

Abstract: In traditional structural topology optimization (TO), the material properties of continuum finite elements of fixed form and coupling are varied to find the optimal topology that satisfies the design problem. We develop an alternative, fundamental formulation where the design space search is dependent on the coupling, and the goal of the topology optimization by penalty (TOP) method is to determine the optimal finite element coupling constraints. By this approach, seemingly disparate topology design problems, e.g. the design of structural supports, topology optimization for fluid mechanics problems, and topology optimization by the element connectivity parameterization (ECP) method, can be understood as related formulations under a common topology optimization umbrella, and more importantly, this general framework can be applied to new design problems. For example, in modern multibody dynamics synthesis, the geometric form of finite elements of fixed material properties and interconnectivity are varied to find the optimal topology that satisfies the mechanism design problem. The a priori selection of coupling, e.g. by revolute or translational joints, severely limits the design space search. The TOP method addresses this limitation in a novel way. We develop the methodology and apply the TOP method to the diverse design problems discussed above.

Keywords: Topology optimization, penalty methods, structures, fluids and mechanisms.

1. INTRODUCTION

The goal of topology optimization [1] is to determine the optimal material distribution that satisfies a design objective and design constraints. In a discrete or continuum setting, the physical design domain is discretized by finite elements. Each finite element is distinguished by its material properties, its shape or form, and its coupling with other finite elements. The mixture of these finite elements defines the overall topology. In traditional structural topology optimization, the material properties of a collection of finite elements of fixed form,

e.g. a 4-node quadrilateral element or 2-node truss element, and interconnectivity are varied to find the optimal topology that satisfies the design problem. In traditional rigid or flexible multibody dynamics synthesis, the shape of a collection of finite elements of fixed material properties and interconnectivity are varied to find the optimal topology that satisfies the design problem. We note that the a priori selection of coupling, e.g. by revolute or translational joints in mechanism design, can severely limit the design space search, and this issue is the motivation for the method developed here.

We develop an alternative topology optimization formulation where the design space search is dependent on the coupling. The main idea behind the topology optimization by penalty (TOP) method is that design-dependent kinematic constraint equations can be appended to the conventional finite element methodology by a penalty method. The degree of enforcement of the constraint equations is then dependent on the design variables associated with the kinematic constraints. We demonstrate that the idea of design-dependent constraint equations can be applied to a wide range of different problems.

In Section 2, we briefly describe the Lagrange multiplier and penalty methods, and the TOP method is defined in Section 3. In the presentation, the approach is applied to support design, fluid mechanics, convection-dominated (top and side surface) heat transfer, structural mechanics, and mechanism design problems to demonstrate its wide application. Of particular note, the goal of mechanism design is the ability to systematically synthesize the coupling topology, and for the first time in the literature, this issue can be addressed by the TOP method because the method utilizes design-dependent constraint equations with a continuously variable degree of enforcement **and** admits redundant constraints. However, due to space constraints here, we illustrate the basic concept by only presenting the material and support design problem in Section 4. More detailed information about the other design problems are provided in references [2] and [3].

2. LAGRANGE MULTIPLIER AND PENALTY METHODS

Lagrange multiplier and penalty methods, e.g. see [4], can be used to enforce constraints on the finite element equations that we derive from variational formulations. Without loss of generality, we briefly describe both approaches for a steady-state, discrete, linear structural system with (potential energy) functional Π^* expressed by

$$\Pi^* = -\frac{1}{2}\mathbf{U}^T \mathbf{K} \mathbf{U} + \mathbf{U}^T \mathbf{F}. \quad (1)$$

The displacement response \mathbf{U} of the structural system with (symmetric) stiffness matrix \mathbf{K} subjected to external load \mathbf{F} is found for conditions which make

the variation of Π^* stationary, i.e.

$$\delta \Pi^* = \delta \mathbf{U}^T (-\mathbf{K}\mathbf{U} + \mathbf{F}) = 0 \quad (2)$$

with respect to all admissible virtual displacements $\delta \mathbf{U}$. Since $\delta \mathbf{U}$ are arbitrary, Equation (2) yields residual

$$\mathbf{R}^*(\mathbf{U}) = -\mathbf{K}\mathbf{U} + \mathbf{F} = \mathbf{S}(\mathbf{U}) + \mathbf{F} = \mathbf{0}, \quad (3)$$

where we define the internal force $\mathbf{S}(\mathbf{U}) = -\mathbf{K}\mathbf{U}$ for the linear problem, and we recover the familiar linear finite element equations

$$\mathbf{K}\mathbf{U} = \mathbf{F}. \quad (4)$$

Now, assume that the unconstrained variational formulation is subject to a set of discrete, linear constraint equations of the form

$$\Phi(\mathbf{U}) = \mathbf{C}\mathbf{U} - \mathbf{D} = \mathbf{0}, \quad (5)$$

e.g. the x -displacement U_i^x of node i is constrained to fixed value \hat{U}^x by $U_i^x - \hat{U}^x = 0$. By the Lagrange multiplier method, we modify the unconstrained functional Π^* by

$$\Pi = \Pi^* - \lambda^T \Phi(\mathbf{U}), \quad (6)$$

where λ are the Lagrange multipliers and invoke the stationarity of the constrained functional Π , i.e.

$$\delta \Pi = \delta \Pi^* - \delta \mathbf{U}^T (\mathbf{C}^T \lambda) - \delta \lambda^T (\mathbf{C}\mathbf{U} - \mathbf{D}) = 0, \quad (7)$$

which yields, for arbitrary $\delta \mathbf{U}$ and $\delta \lambda$, the familiar equation

$$\begin{bmatrix} \mathbf{K} & \mathbf{C}^T \\ \mathbf{C} & \mathbf{0} \end{bmatrix} \begin{Bmatrix} \mathbf{U} \\ \lambda \end{Bmatrix} = \begin{Bmatrix} \mathbf{F} \\ \mathbf{D} \end{Bmatrix}. \quad (8)$$

By the penalty method, we modify the unconstrained functional Π^* by

$$\Pi = \Pi^* - \frac{\alpha}{2} \Phi(\mathbf{U})^T \Phi(\mathbf{U}) \quad (9)$$

with penalty parameter α and again invoke the stationarity of the constrained functional Π (and drop the \mathbf{U} dependencies), i.e.

$$\delta \Pi = \delta \Pi^* + \delta \mathbf{U}^T (-\alpha \Phi_{\mathbf{U}}^T \Phi), \quad (10)$$

where Jacobian $\Phi_{\mathbf{U}} \equiv \frac{\partial \Phi}{\partial \mathbf{U}}$. Assuming the linear FEA of Equation (3) and linear constraints of Equation (5), the modified residual \mathbf{R} is

$$\begin{aligned} \mathbf{R}(\mathbf{U}) &= \mathbf{R}^*(\mathbf{U}) - \alpha \mathbf{C}^T (\mathbf{C}\mathbf{U} - \mathbf{D}) = \mathbf{0} \\ &= -\mathbf{K}\mathbf{U} + \mathbf{F} - \alpha \mathbf{C}^T (\mathbf{C}\mathbf{U} - \mathbf{D}) = \mathbf{0} \end{aligned} \quad (11)$$

which leads to the modified linear finite element equations

$$(\mathbf{K} + \alpha \mathbf{C}^T \mathbf{C}) \mathbf{U} = \mathbf{F} + \alpha \mathbf{C}^T \mathbf{D}. \quad (12)$$

An advantage of the Lagrange multiplier method is that the constraints are satisfied exactly, but this is accomplished at the expense of a larger set of equations. On the other hand, an advantage of the penalty method is that the size of the set of equations is preserved, but the enforcement of the constraints relies on the proper penalty parameter α selection that is large enough to fully enforce the constraints but not too large to cause numerical difficulties. The augmented Lagrangian penalty method can iteratively correct for the constraint violation and, therefore, is less dependent on the α selection. For analysis, each approach has trade-offs that should be weighed for an effective incorporation of constraints. However, in the context of topology optimization, the variable degree of enforcement of the constraints is a feature of the penalty method that we can exploit. When $\alpha = 0$ in Equation (9), the constraints are not enforced, but when α is sufficiently large, the constraints are fully enforced, and intermediate α values impose a continuously varying degree of constraint enforcement. This concept is the essence of the topology optimization by penalty (TOP) method approach.

Although we imposed linear constraints on discrete variables \mathbf{U} above, the penalty method can be generalized to constraints on continuous variables \mathbf{u} , e.g. through

$$\Pi = \Pi^* - \frac{\alpha}{2} \int_{\Omega} \Phi(\mathbf{u})^T \Phi(\mathbf{u}) dv, \quad (13)$$

to constraints that impose continuity requirements, and to constraints that enforce specific values, e.g. recall $U_i^x - \hat{U}^x = 0$, or that impose conditions between solution variables. Furthermore, constraints can be applied to more diverse and complex quantities than the primal discrete and continuous state variables, e.g. by $\phi = \Phi(\mathbf{u}, \mathbf{f}, \mathbf{f}(\mathbf{u}), \mathbf{p}, \mathbf{p}(\mathbf{u}), \sigma(\mathbf{u}), w(\mathbf{u}))$ where the structural constraints may depend on the continuous displacement states \mathbf{u} , dead and live loads \mathbf{f} and $\mathbf{f}(\mathbf{u})$, pressure loads \mathbf{p} and $\mathbf{p}(\mathbf{u})$, stress measures $\sigma(\mathbf{u})$, or work/energy measures $w(\mathbf{u})$.

A particular case that we encounter is a nonlinear (structural) finite element analysis (FEA) constrained by nonlinear constraints. We generalize the penalty method to enforce nonlinear, discrete constraint equations of the form

$$\Phi(\mathbf{U}) = \mathbf{0}, \quad (14)$$

and with nonlinear internal force \mathbf{S} , the nonlinear residual that arises due to the penalty method is

$$\mathbf{R}(\mathbf{U}) = \mathbf{S}(\mathbf{U}) + \mathbf{F} - \alpha \Phi_{\mathbf{U}}^T \Phi = \mathbf{0}. \quad (15)$$

By the Newton Raphson method, we solve Equation (15) for \mathbf{U} by iteratively computing $\mathbf{U}^{i+1} = \mathbf{U}^i + \Delta \mathbf{U}$ at iteration $i + 1$ with update

$$-\frac{\partial \mathbf{R}}{\partial \mathbf{U}} \Delta \mathbf{U} = \mathbf{R} \tag{16}$$

until convergence. For nonlinear analysis and nonlinear constraints, Equation (16) reduces to

$$\left(\mathbf{K}_T + \alpha (\bar{\Phi}_U^T \bar{\Phi})_U + \alpha \bar{\Phi}_U^T \Phi_U \right) \Delta \mathbf{U} = \mathbf{R} \tag{17}$$

where $\mathbf{K}_T \equiv -\frac{\partial \mathbf{S}}{\partial \mathbf{U}}$ and $(\bar{\cdot})$ indicates a function of fixed \mathbf{U} . The constrained analysis by penalty method can now be embedded into the topology optimization problem.

3. TOPOLOGY OPTIMIZATION BY PENALTY METHOD

The optimization problem is stated as

$$\begin{aligned} &\text{minimize} && \Theta_0(\mathbf{d}) \\ &\text{subject to} && \Theta_i(\mathbf{d}) \leq 0 \\ &&& \underline{d}_j \leq d_j \leq \bar{d}_j \end{aligned} \tag{18}$$

where Θ_0 is the objective function, Θ_i for $i = 1, \dots, noc$ are the *noc* inequality optimization constraints and d_j for $j = 1, \dots, nd$ are the *nd* design variables that are bounded below and above by \underline{d}_j and \bar{d}_j . Here, the large design space is searched by the Method of Moving Asymptotes (MMA) [5], and the analytical sensitivities, i.e. $\frac{d\Theta_0}{d\mathbf{d}}(\mathbf{d})$ and $\frac{d\Theta_i}{d\mathbf{d}}(\mathbf{d})$, are efficiently calculated by the adjoint variable method. For topology optimization, we define density, or indicator, design variables bounded by $0 \leq \underline{d} \leq d \leq \bar{d} = 1$.

In traditional topology optimization, a density design variable d_i is assigned to every element i that ranges between its small lower bound $\underline{d}_i \approx 0$, e.g. $\underline{d}_i = 10^{-6}$, and upper bound $\bar{d}_i = 1$. Following [6], a first density measure η_{1i} is computed for every finite element i and is defined as a function of the density design variable field \mathbf{d} , i.e. $\eta_{1i} = \hat{\eta}_{1i}(\mathbf{d})$. In a manner consistent with the density design variable range, the density measure η_1 ranges from a small value to one representing void and solid material respectively, and therefore the variation in the first density measure field $\boldsymbol{\eta}_1 = \{\eta_{11}, \dots, \eta_{1i}, \dots, \eta_{1ne}\}^T$ for ne elements depicts the topology of the structure. The notion of topology is introduced into the analysis by weighting the material properties of the construction material by the first density measure field in some manner, e.g.

$$\mathbf{K}_i(\mathbf{d}) = \hat{\eta}_{1i}(\mathbf{d}) \hat{\mathbf{K}}_i \tag{19}$$

where $\hat{\mathbf{K}}_i$ is the stiffness matrix of solid construction material of element i , and stiffness matrix \mathbf{K}_i is used in the computations. To generalize, we can refer to

stiffness in a general sense independent of any particular discipline, i.e. not limited to structural stiffness, as a representation of the behavior of the constituent material, e.g. elastic material properties, viscous fluid properties, heat conductivity properties, or electric conductivity properties, etc. Similarly, we refer to the displacement response which can be more generally described as the state response consistent with the particular discipline. Usually intermediate density design variables are penalized, e.g. by SIMP or SINH methods, and the effective volume v_m of material is constrained by its upper bound \bar{v}_m through

$$\Theta_1(\mathbf{d}) = v_m(\mathbf{d}) - \bar{v}_m, \quad (20)$$

where the effective volume v_m is computed by

$$v_m(\mathbf{d}) = \sum_{i=1}^{ne} \int_{\Omega} \hat{\eta}_{2i}(\mathbf{d}) dv, \quad (21)$$

the second density measure η_{2i} for every element i is defined as a function of the density design variables \mathbf{d} , i.e. $\eta_{2i} = \hat{\eta}_{2i}(\mathbf{d})$, and the upper bound \bar{v}_m is defined as fraction $0 < \gamma_m < 1$ of the maximal volume, i.e. $\bar{v}_m = \gamma_m \int_{\Omega} dv$. A common objective function for structural topology optimization is minimal compliance, i.e. minimize $\Theta_0(\mathbf{d}) = \mathbf{U}(\mathbf{d})^T \mathbf{F}$, and a typical objective for compliant mechanism design is to extremize an output displacement component, e.g. minimize $\Theta_0(\mathbf{d}) = U_1^x$.

In the TOP method, we associate an indicator, or for convenience to be analogous with common topology optimization terminology, density design variable d_i with every constraint set i , i.e. Φ_i . In turn, each constraint set is assembled into a global vector Φ of constraint sets, i.e. $\Phi = \{\Phi_1^T, \dots, \Phi_i^T, \dots, \Phi_{nkc}^T\}^T$, for nkc kinematic constraint sets of any form, e.g. simple or complex, linear or nonlinear, discrete or continuous, and of specified value or between variables. In a manner consistent with the density design variable range, a third density measure η_{3i} is computed for every constraint set i and is defined as a function of the density design variable field \mathbf{d} , i.e. $\eta_{3i} = \hat{\eta}_{3i}(\mathbf{d})$. When $\eta_{3i} = \underline{\eta}_{3i}$, the third density measure indicates the (relative) absence of influence of its corresponding constraint set Φ_i . Likewise, $\eta_{3i} = 1$ indicates the full presence and enforcement of constraint set Φ_i . A penalty measure α_i for every constraint set i is computed, for example, by

$$\alpha_i(\mathbf{d}) = \alpha \hat{\eta}_{3i}(\mathbf{d}) \quad (22)$$

where α is a scalar penalty parameter. The notion of constraint topology is introduced into the analysis of the topology optimization by penalty method, e.g. for linear elastic analysis

$$\mathbf{R}(\mathbf{U}) = -\mathbf{K}\mathbf{U} + \mathbf{F} - \alpha(\mathbf{d}) \Phi_{\mathbf{U}}^T \Phi = \mathbf{0}. \quad (23)$$

where $\alpha(\mathbf{d}) = \text{diag}[\alpha_1(\mathbf{d}), \dots, \alpha_i(\mathbf{d}), \dots, \alpha_{nkc}(\mathbf{d})]$, and the constraint topology is depicted by η_3 . Note that $\alpha(\mathbf{d}) \Phi_U^T \Phi$ can be systematically assembled by the summation of each $\alpha_i(\mathbf{d}) \Phi_{U_i}^T \Phi_i$ by looping over each constraint set i in the same manner as global \mathbf{K} is assembled by $\mathbf{K} = \sum_{i=1}^{ne} \mathbf{K}^i$ for each element i by traditional finite element methodology. Analogous to the constrained effective volume of material of Equations (20) and (21), the effective constraint “volume” v_c is restricted by its upper bound \bar{v}_c and computed, for example, by

$$v_c(\mathbf{d}) = \sum_{i=1}^{nkc} \hat{\eta}_{4i}(\mathbf{d}), \tag{24}$$

where the fourth density measure η_{4i} for every constraint set i is defined as a function of the density design variables \mathbf{d} and the upper bound \bar{v}_c is defined as fraction $0 < \gamma_c < 1$ of the number of kinematic constraints, i.e. $\bar{v}_c = \gamma_c nkc$.

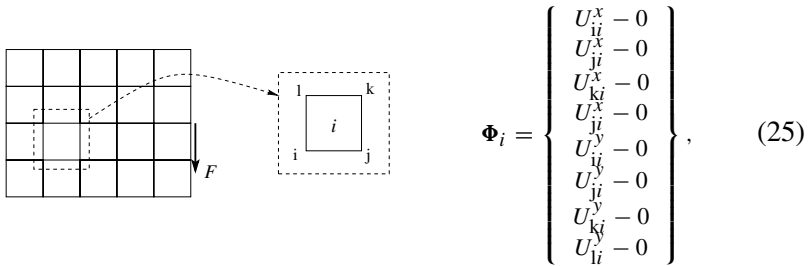
We do not explicitly define the density measures here to generalize the formulation, to accommodate the many variants that have appeared in the literature, and to admit alternative schemes that may be required for different topology problems, e.g. structural topology optimization vs. fluidic topology optimization. However, as examples, the first and second density measures are defined in stiffest structural topology design to penalize intermediate density values by $\hat{\eta}_{1i}(\mathbf{d}) = d_i^p$ and $\hat{\eta}_{2i}(\mathbf{d}) = d_i$ with penalty parameter p , by $\hat{\eta}_{1i}(\mathbf{d}) = \hat{\phi}_i^p$ and $\hat{\eta}_{2i}(\mathbf{d}) = \hat{\phi}_i$, or by $\hat{\eta}_{1i}(\mathbf{d}) = d_i$ and $\hat{\eta}_{2i}(\mathbf{d}) = 1 - (1 - \hat{\phi}_i(\mathbf{d}))^p$ with $\phi_i = \hat{\phi}_i(\mathbf{d}) = \sum_j \omega_{ij} d_j$ where the filtered density design variable field ϕ is computed using blurring filter kernel weights ω_{ij} for every element i . The main point here is that the density measures, i.e. η_1, η_2, η_3 , and η_4 , are defined as some smooth and continuous functions of the density design variables \mathbf{d} or a filtered function ϕ thereof, and they are defined based on the underlying mechanics problem.

The key concept of the TOP method is that we associate a density-weighted penalty with every constraint set, and therefore we can search the design space for an optimized constraint topology. We note that the effectiveness of penalization is dependent on the magnitude of penalty α which should be just large enough to enforce the constraints when $\eta_{3i} = 1$ and should not be too large to cause numerical conditioning problems. A particularly interesting feature is that the methodology can easily accommodate redundant constraints. The methodology can be applied to problems with discrete or continuum, linear or nonlinear finite elements and discrete or continuous, linear or nonlinear constraints. The approach can be combined with traditional topology optimization techniques to simultaneous design for material properties and coupling constraints. Most importantly, the TOP method is a fundamental topology optimization formulation that can be applied to a wide range of topology design problems.

4. TOP METHOD FOR SUPPORT DESIGN

In most structural topology design problems, we search for the optimal material distribution within a given design domain with given external loads and prescribed boundary support conditions. This a priori selection of the support conditions can greatly limit the design space for optimal designs.

By the TOP method, we can introduce the notion of spatially variable supports into the topology design problem. For example, in a planar design domain discretized by 4-noded quad elements connected by nodes denoted by $i, j, k,$ and $l,$ we define a discrete, linear constraint set Φ_i for every element i by



$$\Phi_i = \begin{Bmatrix} U_{ii}^x - 0 \\ U_{jj}^x - 0 \\ U_{kk}^x - 0 \\ U_{ll}^x - 0 \\ U_{ii}^y - 0 \\ U_{jj}^y - 0 \\ U_{kk}^y - 0 \\ U_{ll}^y - 0 \end{Bmatrix}, \quad (25)$$

where U^x and U^y are nodal x - and y -displacement components, and we notice that Equation (25) can be readily formulated into Equation (5) form, i.e. $\Phi_i = C_i U_i$ where $D_i = 0$.

For linear elastic structural mechanics, the governing equation for the constrained finite element analysis of the TOP method is

$$(\mathbf{K}(\dot{\mathbf{d}}) + \alpha(\ddot{\mathbf{d}}) \mathbf{C}^T \mathbf{C}) \mathbf{U} = \mathbf{F}, \quad (26)$$

where we distinguish between the material density design variable field $\dot{\mathbf{d}}$ and the support or indicator density design variable field $\ddot{\mathbf{d}}$. The density design variable field \mathbf{d} is partitioned by $\mathbf{d} = \{\dot{\mathbf{d}}^T, \ddot{\mathbf{d}}^T\}^T$. For generality, the $\dot{\mathbf{d}}$ and $\ddot{\mathbf{d}}$ design variables could be linked, but they are treated separately here.

We demonstrate the approach by the structure and support design of a tip-loaded micro-cantilever beam. The design domain with prescribed support boundary conditions on the left edge is shown in Figure 1(a). The stiffest structural topology design, i.e. minimum compliance subject to a limited volume of distributable material, found by traditional topology optimization is shown in Figure 1(b). Next, we apply the TOP method for structure and support design. The design domain of a tip-loaded cantilever beam without prescribed support boundary conditions is shown in Figure 1(c). The stiffest structural and support topology design found by minimal compliance subject to the same limited volume of distributable material as above and a limited volume of support material is shown in Figure 1(d). The elements of the optimized support conditions are encircled. Note that we generate the same optimized mater-

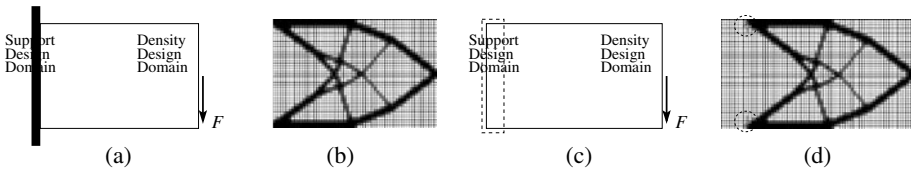


Figure 1. Design domain of tip-loaded cantilever beam (a) with prescribed support and (c) without prescribed support conditions. Optimized topology (b) with prescribed support and (d) without prescribed support conditions.

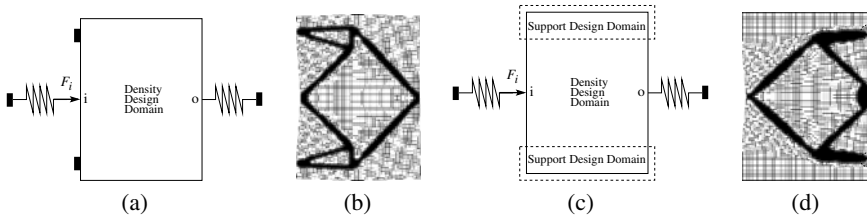


Figure 2. Design domain of inverter mechanism (a) with prescribed support and (c) without prescribed support conditions. Optimized topology (b) with prescribed support and (d) without prescribed support conditions.

ial distribution for both cases, and the supports are located at the appropriate locations by the TOP method.

In a similar manner, the TOP method is applied to the material and support design for an inverter mechanism depicted in Figure 2. We note that this approach is particularly beneficial for compliant mechanism design where the optimal support locations are less intuitive.

5. CONCLUSION

We developed the TOP method where design-dependent constraints are appended to the FEA by a penalty method and the degree of enforcement depends on the design variables associated with each constraint. We applied the fundamental concept to a wide range of design problems which are illustrated in Figures 1, 2 and 3 and are more fully described in [2] and [3]. It was our intent to show that the TOP method is a fundamental counterpart to the common density-based stiffness matrix approach, that many diverse design problems that have been previously handled can be reinterpreted under this common TOP method umbrella, and, more importantly, that the approach can be applied to new and more complex design problems.

In future work, we will more fully develop and tailor the TOP method to particular mechanics problems, particularly for mechanism topology design within large ground structures. To illustrate the methodology, we concentrated on design problems with constraints that are simply dependent on the

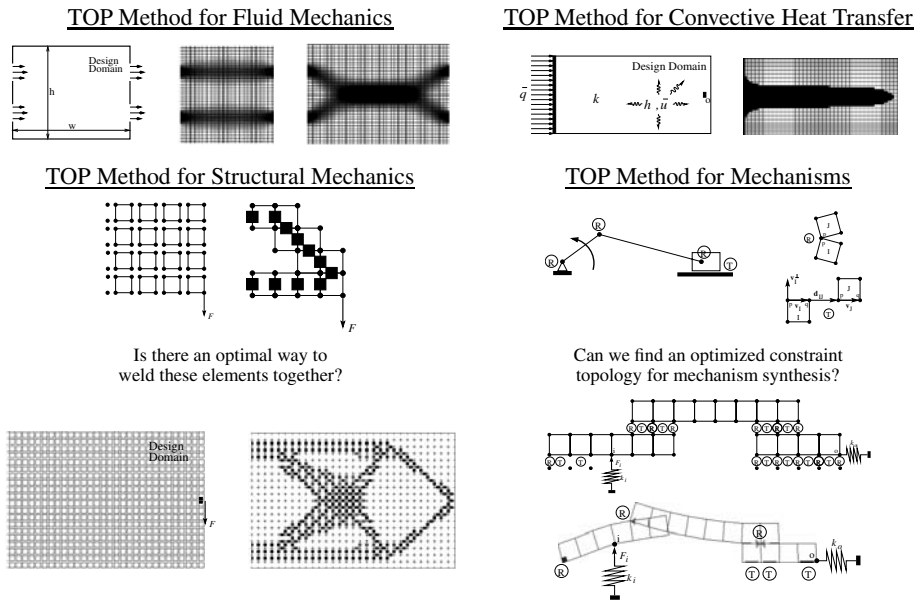


Figure 3. Overview of the TOP method applied to diverse design problems.

discrete or continuous state variables, but we emphasize that the approach can be applied to more diverse constraint types. We will investigate how the (non)convexity of the constraints of the penalty method affects the topology optimization. Also, we are investigating the selective application of the augmented Lagrangian penalty method to constraints where $\alpha_i(\mathbf{d})$ approaches penalty parameter α in value.

REFERENCES

- [1] M.P. Bendsøe and O. Sigmund, *Topology Optimization: Theory, Methods and Applications*, Springer-Verlag, New York (2003).
- [2] T.E. Bruns, Topology optimization by penalty (TOP) method, in *Proceedings of the 6th World Congress of Structural and Multidisciplinary Optimization*, Rio de Janeiro, Brazil, May 30–June 3 (2005).
- [3] T.E. Bruns, Topology optimization by penalty (TOP) method, submitted (2005).
- [4] O.C. Zienkiewicz and R.L. Taylor. *The Finite Element Method, Fourth Edition, Volume 1: Basic Formulations and Linear Problems* and *Volume 2: Solid and Fluid Mechanics, Dynamics, and Non-linearity*, McGraw-Hill, New York (1989) and (1991).
- [5] K. Svanberg, Method of moving asymptotes – A new method for structural optimization, *Int. J. Num. Meth. Engrg.*, 24(2), 359–373 (1987).
- [6] T.E. Bruns, A re-evaluation of the SIMP method with filtering and an alternative formulation for solid-void topology optimization, *Struct. Multidisc Optim.* (2005).
- [7] T. Buhl, Simultaneous topology optimization of structure and supports, *Struct. Multidisc Optim.*, 23, 336–346 (2002).

TOPOLOGY OPTIMIZATION WITH CAMD FOR STRUCTURES UNDERGOING FINITE DEFORMATION

K. Matsui¹, K. Terada² and S. Nishiwaki³

¹*Department of Artificial Environment and Information, Yokohama National University, Japan*

²*Department of Civil Engineering, Tohoku University, Japan*

³*Department of Precision Engineering, Kyoto University, Japan*

kzm@ynu.ac.jp, tei@civil.tohoku.ac.jp, shinji@prec.kyoto-u.ac.jp

Abstract: A new method for topology optimization (CAMD method) is extended to the stiffness design problem of a structure undergoing finite deformation. In this methodology, the continuous distribution of microstructures, or equivalently, design variables, is approximated using the nodal design variables and standard shape functions, in the context of FE discretization. After summarizing the basic settings for the finite deformation stiffness optimization problem and the CAMD method, we formulate a stiffness design problem for nonlinear solids. A representative numerical example is presented to show the validity and efficiency of the proposed method. In particular, we clarified the mechanism that generates optimal structures while inhibiting structural instabilities such as snap-through.

Keywords: Topology optimization, finite deformation, homogenization design method.

1. INTRODUCTION

Recent years have been seen great developments in topology optimization, since Bendsøe and Kikuchi [1] originally proposed the homogenization design method (HDM) for the practical applications. This methodology is based on the concept of the fixed design domain and the homogenization method to relax the domain and to change the material distribution problem into a sizing problem in the micro-scale. Suzuki and Kikuchi [2] applied the methodology to the stiffness design problem using a microstructure with a rectangular void and succeeded to obtain mesh independent topologies by rotating it. Contrastly, Bendsøe [3] also proposed a simplified methodology using a fictional isotropic material elasticity tensor which is assumed to be a function of the penalized material density with an exponent parameter. This is nowadays known as the SIMP method (Solid Isotropic Microstructures with Penalization) [4, 5]. Since

these pioneering works, a considerable number of theoretical and computational studies have been made on the area of topology optimization [6].

Although it has been argued that there is no physical interpretation of the assumptions in the latter approach, Bendsøe and Sigmund [7] demonstrated its validity under a certain conditions. Thanks to this demonstration and to inherent simplicity for implementation, the SIMP method has been widely accepted by researchers and applied to various optimization problems. However in some cases, over simplified SIMP method causes complications which significantly influence the optimized results. In such cases, the problem of checkerboard patterns and the mesh dependency of the results occur. These problems have generated an enormous amount of interest, with many different solutions made possible by the SIMP method. That different optimized solutions are obtained for different sizes or discretizations of the finite element is a matter of concern.

To avoid these kinds of numerical instabilities, including the appearance of gray-scale (intermediate density), a variety of techniques have been proposed [8, 9]. For example, there are material interpolation schemes which can be used to solve gray-scale problems [7], checkerboard-free topologies are successfully obtained by means of higher-order finite elements [10], and there are a variety of filtering schemes to avoid checkerboard patterns or mesh-dependencies (see, e.g., [11, 12]). In addition, a perimeter control method was proposed by Haber et al. [13] to resolve the issues of mesh dependency. Since the use of high-order elements requires significant computational cost, the filtering schemes and perimeter controls are commonly used to avoid numerical instabilities, having provided clear or fine topologies in the above-cited literatures. The basic idea of the filtering schemes is to restrict the solution space by defining some additional constraints on either the perimeter or the distribution modes of the material.

On the other hand, the authors have proposed a checkerboard free topology optimization method without introducing any additional constraint parameters [14]. This is successfully achieved by assuming the continuous distribution of material in a fixed design domain, and by introducing the C^0 -continuous finite element approximation of the design variables, we refer to our method as the CAMD method (Continuous Approximation of Material Distribution). By virtue of this continuous FE approximation of design variables, discontinuous material distributions, like checkerboard patterns, disappear without the need for any filtering schemes.

In this paper, we extend the CAMD method to the stiffness design in the finite deformation problem, and demonstrate its efficiency and capability. At the end of the 20th century, some authors began to address the stiffness design problem with geometrical nonlinearities [15–19] using the conventional element-based discretization. In addition, Pedersen et al. extended their method to the design of compliant mechanisms [20]. Most of the literature

has concluded that the consideration of geometrical nonlinearity in topology optimization gives quite different topologies from cases where small strain is assumed.

In the following, we first briefly review the formulation for the stiffness design problem at finite deformation in general form. Then we formulate the CAMD method for stiffness design with finite deformation, and also present a sensitivity analysis. Representative numerical example shows how capable this method is and also shows the difference between optimized structures with linear elasticity and those with finite deformation.

2. STIFFNESS DESIGN PROBLEM AT FINITE DEFORMATION

In this section, we formulate the stiffness optimization problem for the structures in the framework of hyperelasticity. Our emphasis is placed on the fact that the problem of topology optimization should be recognized as a problem of finding distribution of the material in the fixed design domain, but not the configuration of finite elements.

Let $\mathcal{B}_0 \subset \mathcal{R}^{n_{\text{dim}}}$ be the reference configuration of a design domain with smooth boundary $\partial\mathcal{B}_0$. It is assumed that the elastic body is subjected to dead loading with the body force per unit mass defined by \mathbf{b} and that the nominal traction vector is also prescribed as $\hat{\mathbf{T}}$ for Γ_t of the boundary. In addition, the deformation is prescribed as $\mathbf{u} = \mathbf{0}$ for $\Gamma_u \subset \partial\mathcal{B}_0$ of the boundary. Then the equilibrium equation for the elastic body is given in the following weak form:

$$\int_{\mathcal{B}_0} \mathbf{P} : (\boldsymbol{\eta}_0 \otimes \nabla_X) dV - \int_{\mathcal{B}_0} \rho_0 \mathbf{B} \cdot \boldsymbol{\eta}_0 dV - \int_{\partial\mathcal{B}_0} \hat{\mathbf{T}} \cdot \boldsymbol{\eta}_0 d\Gamma = 0. \quad (1)$$

Generally speaking in the topology optimization problems, from \mathcal{B}_0 we are able to find the optimal distribution of material, which is occupied by the domain of a designed structure, \mathcal{B}_0^m . Buhl et al. [16] have introduced the following end compliance as a simple extension of the mean compliance in linear elasticity to large deformation problems, that is, the mean compliance in the deflected configuration at the design load level.

$$C_{\text{end}} := \int_{\mathcal{B}_0} \rho_p \mathbf{b} \cdot \mathbf{u} dV + \int_{\partial\mathcal{B}_0} \hat{\mathbf{T}} \cdot \mathbf{u} d\Gamma. \quad (2)$$

Then the general form of the stiffness design problem for nonlinear solids can be defined as

$$\begin{aligned} & \min_{\substack{\text{(material distribution for } \mathcal{B}_0)}} C_{\text{mean}} \\ & \text{subject to} \\ & \text{equilibrium equation (1),} \\ & \text{volume constraint for domain } \mathcal{B}_0^m. \end{aligned} \quad (3)$$

To express the material distribution, the following indicator function $\chi(\mathbf{x})$ is usually introduced:

$$\mathcal{C}_{IJKL}(\mathbf{x}) = \chi(\mathbf{x})\bar{\mathcal{C}}_{IJKL}, \quad \chi(\mathbf{x}) = \begin{cases} 1 & \text{if } \mathbf{x} \in \mathcal{B}_0^m, \\ 0 & \text{if } \mathbf{x} \in \mathcal{B}_0 \setminus \mathcal{B}_0^m, \end{cases} \quad (4)$$

where \mathcal{C}_{IJKL} are the components of the elastic tensor of the material distributed in the fixed design domain \mathcal{B}_0 , and $\bar{\mathcal{C}}_{IJKL}$ are those of the actual material in \mathcal{B}_0^m . However, this setting gives the discrete optimization problem (black-and-white design) with 0-1 integer parameterization, which tends to be difficult to solve unless some regularization or smoothing is performed for the material distribution. That is, as first demonstrated by Bendsøe and Kikuchi [1], the ON-OFF problem of macro-scale material can be transformed into a continuous sizing problem for microstructures by means of the homogenization method. However, in these developments, the designed structures were formed by the arrangement of discrete *finite elements* rather than the continuous distribution of *material*. In the following formulation of CAMD method, the emphasis is placed on the concept of continuous material distribution.

3. CAMD METHOD FOR TOPOLOGY OPTIMIZATION

In this section, we extend the method of continuous approximation of material distribution to the finite deformation problems. After briefly reviewing the CAMD method, we accomplish the formulation of the stiffness design problem with finite deformation using the methodology.

3.1 Continuous FE Approximation of Material Distribution

As pointed out in the literature [14], the continuous distribution of material, or equivalence of microstructure is consistent with the mathematical assumptions of the homogenization theory, have been introduced in the original formulation by Suzuki and Kikuchi [2]. The CAMD method can maintain consistency during its optimization process and can avoid rboading without requiring any special treatment, such as, the use of filtering schemes or perimeter controls. In the following, we summarize the basic concept of the CAMD method in the context of the FE-analysis, and accomplish the formulation of the stiffness design problem.

In the standard displacement-based FEM, the displacement field \mathbf{u} in the domain \mathcal{B}_0 is approximated by nodal interpolation such that

$$\mathbf{u} \approx \mathbf{u}^h = \mathbf{N}(\mathbf{X})\mathbf{d}, \quad (5)$$

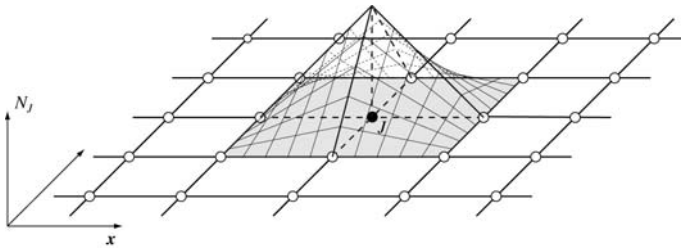


Figure 1. Global shape function N_J associated with node J .

where $\mathbf{N}(\mathbf{x})$ is a matrix of global shape functions and \mathbf{d} is the corresponding nodal displacement vector. Here, the parameter h is the representative size of elements for spatial discretization of the domain, and designates the discretized quantities when attached as a super- or subscript. Note that the components of the shape function matrix, $N_J(\mathbf{x})$, are non-zero only in elements associated with the J -th node as shown in Figure 1. Employing the same interpolation function for variations of $\boldsymbol{\eta}$, we can obtain the discretized form of the governing equation (1) or linearized equation.

To maintain mathematical consistency, the CAMD method approximates the distribution of the design variable $r(\mathbf{X})$ continuously in space. That is, using the same shape functions as those for displacement fields, we approximate the design variable as

$$r(\mathbf{X}) \approx r^h(\mathbf{X}) = \mathbf{M}(\mathbf{X})\mathbf{R} = \sum_{J=1}^n N_J(\mathbf{X})R_J, \tag{6}$$

where \mathbf{M} is a vector whose components are $N_J(\mathbf{X})$ ($J = 1, \dots, n$), \mathbf{R} is a vector of nodal (discrete) design variables R_J ($J = 1, \dots, n$) and n the total number of nodes (and of design variables). The design variable can be C^0 -continuous over the domain due to the partition-of-unity property of $N_J(\mathbf{X})$ and also continuously distributed in an element. Consequently, the topology optimization problem yields the following discretized alternative:

$$\begin{aligned} \min_{\mathbf{R}} C_{\text{end}}^h &= \min_{\mathbf{R}} \left[\left(\int_{\mathcal{B}_0} (\rho^H \mathbf{B}) \mathbf{N} \, dV + \int_{\partial \mathcal{B}_0} \hat{\mathbf{T}} \mathbf{N} \, d\Gamma \right) \mathbf{d} \right] \\ &\text{subject to} \\ &\text{discretized version of the equilibrium equation (1),} \\ &\mathcal{B}_0^m := \int_{\mathcal{B}_0} (1 - (r^h)^2) \, dV \leq \Omega_{\text{des}}, \\ &0 \leq R_J \leq 1 \quad (J = 1, \dots, n). \end{aligned} \tag{7}$$

3.2 Sensitivity Analysis

To solve the above optimization problem by mathematical programming, we need to compute its sensitivity. As the final step of our formulation, the sensitivity analysis using the adjoint method is presented under the assumption that the external load is independent of design.

Introducing a vector of Lagrangian multipliers λ , the objective function is modified as

$$C_{\text{end}}^* = C_{\text{end}} + R(\mathbf{P}, \lambda), \quad (8)$$

where we define

$$R(\mathbf{P}, \lambda) := \int_{\mathcal{B}_0} \mathbf{P} : \nabla_X \lambda \, dV - \int_{\mathcal{B}_0} \rho_0^H \mathbf{B} \cdot \lambda \, dV - \int_{\partial \mathcal{B}_0} \hat{\mathbf{T}} \cdot \lambda \, d\Gamma. \quad (9)$$

When the state variables are in the equilibrium state, $R(\mathbf{P}, \lambda) = 0$ is achieved for all λ and the sensitivity of the objective function does not change,

$$\frac{dC_{\text{end}}}{dr} = \frac{dC_{\text{end}}^*}{dr}. \quad (10)$$

Using the modified objective function, the sensitivity becomes the following:

$$\begin{aligned} \frac{dC_{\text{end}}^*}{dr} &= \int_{\mathcal{B}_0} \rho_0^H \mathbf{B} \cdot \frac{d\mathbf{u}}{dr} \, dV + \int_{\partial \mathcal{B}_0} \hat{\mathbf{T}} \cdot \frac{d\mathbf{u}}{dr} \, d\Gamma + \frac{\partial R(\mathbf{P}, \lambda)}{\partial \mathbf{u}} \cdot \frac{d\mathbf{u}}{dr} \\ &\quad + \int_{\mathcal{B}_0} \frac{d\rho_0^H}{dr} \mathbf{B} \cdot \mathbf{u} \, dV + \frac{\partial R(\mathbf{P}, \lambda)}{\partial r}. \end{aligned} \quad (11)$$

Since the vector of Lagrangian multipliers λ is arbitrary, we choose λ^* such that

$$\int_{\mathcal{B}_0} \rho_0^H \mathbf{B} \cdot \frac{d\mathbf{u}}{dr} \, dV + \int_{\partial \mathcal{B}_0} \hat{\mathbf{T}} \cdot \frac{d\mathbf{u}}{dr} \, d\Gamma + \frac{\partial R(\mathbf{P}, \lambda^*)}{\partial \mathbf{u}} \cdot \frac{d\mathbf{u}}{dr} = 0. \quad (12)$$

With the solution of the above adjoint system λ^* , the sensitivity of the objective function is computed as

$$\frac{dC_{\text{end}}^*}{dr} = \int_{\mathcal{B}_0} \frac{d\rho_0^H}{dr} \mathbf{B} \cdot \mathbf{u} \, dV + \frac{\partial R(\mathbf{P}, \lambda^*)}{\partial r}. \quad (13)$$

Here, if we set $d\mathbf{u}/dr = \boldsymbol{\eta}$, Equation (12) would be similar to the linearized version of equilibrium equation. In addition, we are able to obtain the sensitivity very easily, since $\partial R/\partial \mathbf{u}$ corresponding to the tangential stiffness.

4. NUMERICAL EXAMPLE

To show the validity and the efficiency of the CAMD method for topology optimization problems with finite deformation, we would like to present some

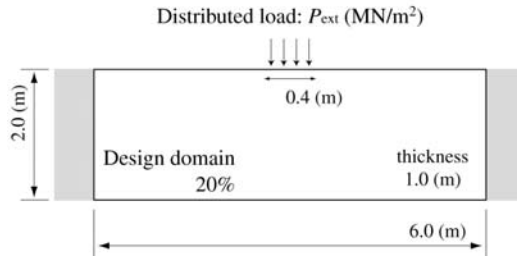


Figure 2. Design domain for topology optimization.

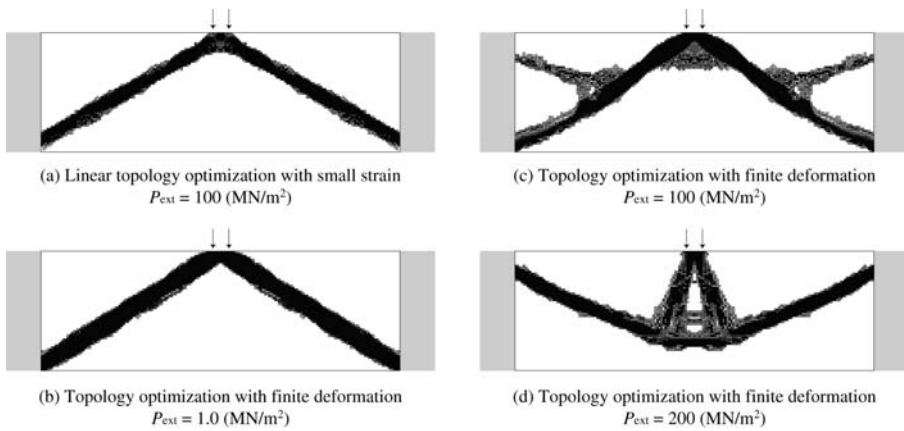


Figure 3. Optimal topologies for small strain and finite deformation.

illustrative numerical example. Note that no filtering scheme to avoid checkerboarding or mesh dependent design in topology optimization.

The optimization problem for hyperelasticity shown in Figure 2 is solved for three different loading conditions ($P_{ext} = 1.0, 100, 200 \text{ (MN/m}^2\text{)}$). The optimized topology obtained from these analyses are shown in Figure 3, and the result of the linear elasticity is also shown for comparison. In the small strain problem, very similar topologies are obtained when the magnitude of the external load is changed (Figure 3(a)). As can be seen, the resulting topology for a small load is similar to the result of linear elasticity (Figure 3(b)). However, the topologies change according to the increment of the external load (Figures 3(c), (d)). The topology shown in Figure 3(d) is very similar to that Buhl et al. [16] showed and explained by buckling effect in which “the topology consists of two longer beams in tension and two short beams in compression”.

In order to discuss the validity of the above topologies and the proposed optimization method, we make the computations with sufficient large load for the optimized topologies. Figure 4 shows the load-displacement curves at the cen-

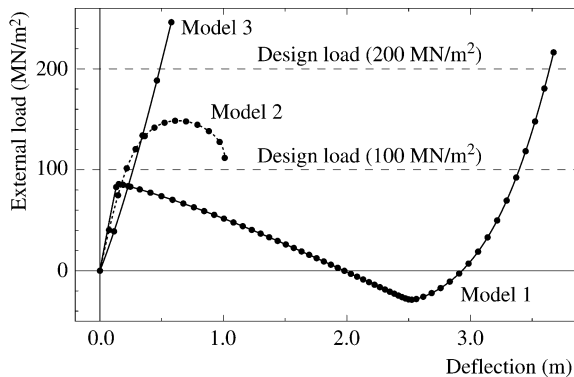


Figure 4. Force-displacement diagram for optimum design.

ter of the design domain obtained from the computation. As can be seen in the figure, Model (b) is the stiffest structure when the applied load is small. However, this structure snaps through at a certain load level and the stiffness of the whole structure decreases. As a result, after Model (b) has snapped through, Model (c) becomes the stiffest of the three structures. Then Model (c) also snaps through and loses its stiffness. Finally, Model (d) which has low stiffness becomes the stiffest when a maximum external load is applied. That is, when we consider loading level applied to each model, each structure obtained by the topology optimization is the stiffest at a certain level. Consequently we could conclude that the proposed method is valid not only for linear elasticity but also for finite deformation problems.

According to the above computations, the explanation by Buhl et al. [16] seems to be correct. However, their optimization started from the horizontal straight bar, which never buckles under such loading conditions, and the objective function, or end compliance could not explicitly take into account the buckling. Thus, the interpretation is not sufficient to clarify the mechanism. That is, it failed to explain why the topologies are different depending on the magnitude of the external load.

Figure 5 shows the change of topology during the optimization process for two load cases. Especially here shows topologies at the beginning of the optimization where a large change of topology was occurred. As can be seen from the figure, they begin to converge to quite different topologies from the first optimization step, and the convergence tendency observed in the small loading case being very similar to that in the optimization in cases with small strain. In addition, we have observed that there is no buckling during the optimization process nor at any of the loading steps. This means that the topology shown in Figure 3(d) is not affected by any unstable mechanical behavior such as buckling or snap-through, and is governed only by the large deformation at

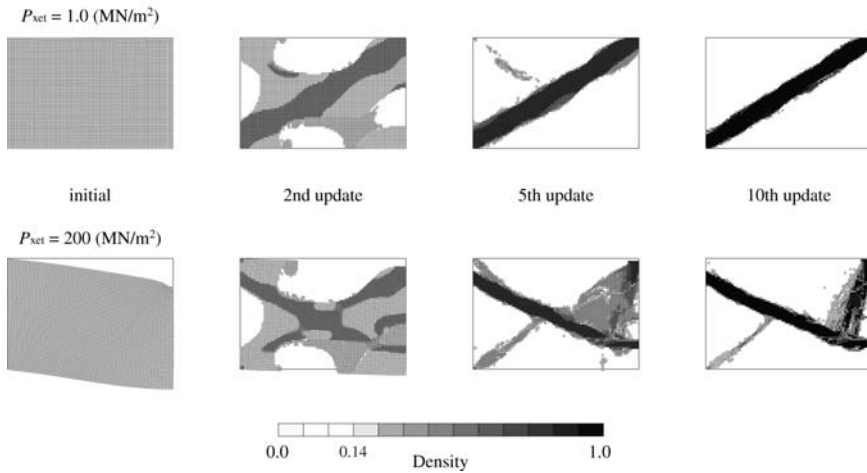


Figure 5. Change of topology (and its deformation) during optimization.

the initial state of optimization. In other words, we could obtain the topology using a nonlinear finite element analysis not because it enables us to treat the unstable mechanical behavior, but because it simulates the large deformations in the design domain more accurately. Therefore we should recognize that the topology happens to be stiff so that buckling or snap-through do not occur.

5. CONCLUDING REMARKS

In this paper, we extended the CAMD method to the stiffness design problem undergoing finite deformation. Owing to the mathematically consistent approximation of material distribution, the optimum topologies obtained by this methodology are free from checkerboard patterns.

In the illustrative optimization example in the context of finite deformation, we were able to obtain quite different topologies from those with a linear elasticity. We gave some consideration to how different topologies are generated, especially to those which seem to be against instable mechanical behavior, such as buckling or snap-through. That is, it is not because we take such behavior into account, but because we could describe the large deformation in the design domain at the beginning of the optimization process. Thus another kind of the objective functions is needed, which take into account the geometrical instabilities explicitly.

REFERENCES

- [1] Bendsøe, M.P. and Kikuchi, N., Generating optimal topologies in structural design using a homogenization method, *Comput. Methods in Appl. Mech. Engrg.*, 71, 197–224 (1988).

- [2] Suzuki, K. and Kikuchi, N., A homogenization method for shape and topology optimization, *Comput. Methods in Appl. Mech. Engrg.*, 93, 291–318 (1991).
- [3] Bendsøe, M.P., Optimal shape design as a material distribution problem, *Structural Optimization*, 1, 193–202 (1989).
- [4] Rozvany, G.I.N., Zhou, M. and Sigmund, O., Topology optimization in structural design, in *Advances in Design Optimization*, H. Adeli (ed.), Chapman and Hall, London, pp. 340–399 (1994).
- [5] Rozvany, G.I.N., Aims, scope, methods, history and unified terminology of computer-aided topology optimization in structural mechanics, *Structural and Multidisciplinary Optimization*, 21, 90–108 (2001).
- [6] Bendsøe, M.P. and Sigmund, O., *Topology Optimization*, Springer-Verlag, Berlin (2003).
- [7] Bendsøe, M.P. and Sigmund, O., Material interpolation schemes in topology optimization, *Archive of Applied Mechanics*, 69, 635–654 (1999).
- [8] Sigmund, O. and Petersson, J., Numerical instabilities in topology optimization: A survey on procedures dealing with checkerboards, mesh-dependencies and local minima, *Structural Optimization*, 16, 68–75 (1998).
- [9] Bourdin, B., Filters in topology optimization, *Int. J. Numer. Meth. Engrg.*, 50, 2143–2158 (2001).
- [10] Diaz, J. and Sigmund, O., Checkerboard patterns in layout optimization, *Structural Optimization*, 10, 40–45 (1995).
- [11] Petersson, J. and Sigmund, O., Slope constrained topology optimization, *Int. J. Numer. Meth. Engrg.*, 41, 1417–1434 (1998).
- [12] Fujii, D. and Kikuchi, N., Improvement of numerical instabilities in topology optimization using the SLP method, *Structural Optimization*, 19, 113–121 (2000).
- [13] Haber, R.B., Jog, C.S. and Bendsøe, M.P., A new approach to variable-topology shape design using a constraint on perimeter. *Structural Optimization*, 11, 1–12 (1996).
- [14] Matsui, K. and Terada, K., Continuous approximation of material distribution for topology optimization, *Int. J. Numer. Meth. Engrg.*, 59, 1925–1944 (2004).
- [15] Burns, T.E. and Tortorelli, D.A., Topology optimization of non-linear elastic structures and compliant mechanisms, *Comput. Methods in Appl. Mech. Engrg.*, 190, 3443–3459 (2001).
- [16] Buhl, T., Pedersen, C.B.W. and Sigmund, O., Stiffness design of geometrically nonlinear structures using topology optimization, *Structural and Multidisciplinary Optimization*, 19, 93–104 (2001).
- [17] Gea, H.C. and Luo, J., Topology optimization of structures with geometrical nonlinearities, *Computers & Structures*, 79, 1977–1985 (2001).
- [18] Kemmler, R., Schwarz, S. and Ramm, E., Topology optimization including geometrically nonlinear response, in *Proceedings of the 3rd World Congress of Structural and Multidisciplinary Optimization* pp. 17–21 (1999).
- [19] Swan, C.C. and Kosaka, I., Voigt–Reuss topology optimization for structures with non-linear material behaviors, *Int. J. Numer. Meth. Engrg.*, 40, 3785–3814 (1997).
- [20] Pedersen, C.B.W., Buhl, T. and Sigmund, O., Topology synthesis of large-displacement compliant mechanisms, *Int. J. Numer. Meth. Engrg.*, 50, 2683–2705 (2001).

SPECTRAL LEVEL SET METHODOLOGY IN THE DESIGN OF A MORPHING AIRFOIL

Alexandra A. Gomes and Afzal Suleman

IDMEC, Instituto Superior Técnico, Av. Rovisco Pais, 1049-001 Lisboa, Portugal

magoncal@dem.ist.utl.pt, suleman@alfa.ist.utl.pt

Abstract: In this paper, we consider the design of a morphing airfoil for improved aileron effectiveness using the spectral level set methodology. This methodology is a framework to formulate topology optimization of interfaces based on the level set methods, which represent the interface as the zero level set of a function. As this function evolves, during the optimization process, topological changes of the interface are easily described. According to our formulation, the Fourier coefficients of the level set function are the design variables of the optimization problem. An advantage of the proposed methodology, for a sufficiently smooth interface, is to admit an error asymptotically smaller than the one for non-adaptive spacial discretizations of the level set function. In this case, the methodology could lead to a reduction of the design space dimension. Another advantage is the nucleation of holes in the interior of the interface.

As an application, we consider an airfoil with a system of actuators distributed along its chord. This system provides morphing capability to the airfoil by operating on its camber to increase lift generation. The optimization problem consists in determining the camber profile that minimizes the actuation power while improving the airfoil effectiveness. The sign of the level set function determines which actuators are activated.

Keywords: Topology optimization, level set methods, Fourier series, morphing airfoil, aileron control reversal.

1. INTRODUCTION

In this paper, we consider the design of a morphing airfoil for the improvement of its aileron effectiveness [4]. To this end, we formulate the topology optimization problem using the spectral level set methodology.

The topology optimizer searches for minimizing configurations among topologically distinct classes. Consequently, in structural optimization for instance, holes may appear or disappear from the initial design, and breakages and merges of the structure may occur.

The main approach to structural boundary design is the homogenization method [5–7], in which the initial design is composed of a repeated base cell made of an arrangement of solid material and void space. The design variables of the optimization problem define that arrangement. Another important approach is SIMP [19]. In this case, the stiffness is multiplied by a density-like function with values between zero and one, which becomes the design variable of the optimization problem. Other theories include the evolutionary algorithm [23], in which solid elements are deleted from a fixed mesh to decrease the objective function, and the bubble method [8], in which holes are positioned along the structure, thus changing its initial topology.

The spectral level set methodology is based on the level set methods introduced in [16]. According to these methods, the relevant boundary or interface is the zero level set of a function. As this function evolves during the optimization, so does the boundary. In this way, an interface can easily sustain topological changes, establishing the level set approach as an adequate tool in topology optimization problems. Classic level set methods use the nodal values of the level set function as design variables of the optimization problem. The spectral level set methodology expands this function into a finite Fourier series and uses its coefficients as the design variables.

Sethian and Wiegmann [20] use the level set approach to achieve fully stressed structures. Osher and Santosa [17] and Allaire and co-workers [2, 3] have also applied the level set methods to structural optimization.

The application of topology optimization to aeroservoelasticity is very recent, of which the studies in [13–15] are good examples. In particular, in [15], the authors propose the integration of mechanisms in the aeroelastic optimization of adaptive airfoils, considering both aerodynamic and structural constraints and using a level set approach.

In this work, the spectral level set methodology is used to design a morphing airfoil which enhances the performance of its aileron effectiveness. A system of actuators provides morphing capability by operating on the camber to increase lift. The optimization problem consists in determining the airfoil profile which minimizes the actuation power while improving the aileron effectiveness. The sign of the level set function establishes the set of driving actuators and its Fourier coefficients constitute the design variables.

This paper is divided into two main parts: the discussion of the key ideas behind the spectral level set methodology and the analysis of an application of the proposed methodology to the design of an aircraft structure with improved roll maneuvering performance.

2. SPECTRAL LEVEL SET METHODOLOGY

The spectral level set methodology inherits from the level set formulation [16], the idea of embedding the evolution of an interface into the evolution of a function during the optimization. However, instead of defining this function using its nodal values, the spectral level set methodology uses the coefficients of its Fourier series expansion for its definition. The Fourier coefficients become the design variables of the optimization problem assigned to the interface definition.

The proposed formulation does not consider the level set function to be a solution of an Hamilton–Jacobi equation. As a result, the spectral level set methodology is able to nucleate new holes in the interior of the interface in a two-dimensional setting. Therefore, the formation of new holes is possible, making it less likely for the optimization algorithm to settle in a non-global solution. Other solutions to avoid the lack of nucleation mechanism have been addressed in [1, 21].

In the following, we present the key ideas of the spectral level set methodology. A detailed description may be found in [11].

Let $\psi : \mathbb{T}^n \rightarrow \mathbb{R}$ be the level set function. The Fourier coefficients of ψ are

$$\hat{\psi}(k) = \frac{1}{(2\pi)^n} \int_{\mathbb{T}^n} \psi(\theta) e^{-ik \cdot \theta} d\theta. \quad (1)$$

The Fourier inversion formula is given by

$$\psi(\theta) = \sum_{k \in \mathbb{Z}^n} \hat{\psi}(k) e^{ik \cdot \theta} \quad (2)$$

for ψ defined as a function of θ , with $\theta \in [0, 2\pi]^n$. In general, we wish to identify $\mathbb{T}^n = [0, 2\pi]^n$ with the physical space defined by the variable $x \in \mathbb{R}^n$. Assume $x \in [a_1, b_1] \times \dots \times [a_n, b_n]$. Then, each component of θ is linearly related to the corresponding component of x , through $\theta_i = \frac{2\pi}{p_i} (x_i - a_i)$, in which $p_i = b_i - a_i$ is the period corresponding to coordinate $i = 1, \dots, n$.

Consider the set of functions constructed using a finite Fourier series. A key question in the spectral level set methodology consists in determining estimates on the error committed in this approximation of the interface. For the sake of completeness, we provide in the following an upper bound for this error.

The existence of an infinite number of functions with the same zero level set implies the lack of uniqueness of the level set function in the description of an interface. Our goal is to choose one of these functions and then see if its zero level set is adequately represented by the zero level set of a finite Fourier expansion.

One candidate is the signed distance to the interface which is Lipschitz continuous independently of the degree of regularity of the interface, and therefore

can be uniformly approximated by Fourier series. However, further results from the theory of the Fourier series [22] determine that we must increase the regularity of the signed distance to the interface to guarantee the convergence of its Fourier series.

The smoothing, or mollification [9], results in a smooth function very similar to the original except at sharp corners. At these points, the original function undergoes an averaging operation. Gomes and Suleman [11] provides an upper bound for the error committed in the smoothing procedure, estimating the difference between the original and the smoothed level set functions.

Given the smoothed signed distance to the interface, an estimate of the error committed in using a finite Fourier series expansion, with an *a priori* specified number of Fourier coefficients, is also given in [11] as the truncation error.

The total error bound involved in the proposed methodology, which is the sum of the smoothing and truncation error bounds, is asymptotically proportional to $1/N$, in which N is a measure of the number of Fourier modes in the expansion. This error is of the same order as the one in classic non-adaptive spacial discretizations of ψ considering N nodes. However, if the level set function is sufficiently smooth, we can prove asymptotically in N , that the proposed methodology achieves the same error with less design variables than spacial discretizations [11]. That is, under certain circumstances, the spectral level set methodology could lead to the reduction of the design space dimension.

3. MORPHING AIRFOIL

3.1 Problem Setting

Consider an airfoil equipped with an aileron deflected downwards to provide additional lift. The flow acting on the aileron generates a moment of force which twists the airfoil nose down, thus reducing the angle of attack and the aileron incidence. Consequently, the net lift generation is decreased and for the same aileron deflection, the rolling moment for an elastic wing is less than that for a rigid wing. This loss of aileron effectiveness is a consequence of the elastic properties of the wing and is dependent on the flight condition. If not accounted for, this condition can lead to a reduction of the vehicle's performance in roll maneuvers. In case the aileron produces no lift, we say the aileron has reversed.

Consider the lift coefficient produced by an aileron deflection on the airfoil of a real wing, Δc_l^e , and the lift coefficient produced in a similar way on a rigid wing, Δc_l^r . A way to measure aileron effectiveness consists in evaluating the ratio $\Delta c_l^e / \Delta c_l^r$ [4]. Ideally, this ratio should be one. However, the elastic proprieties of the wing add a negative contribution to Δc_l^r . Considering strip

theory [4], Δc_l^e can be written as

$$\Delta c_l^e = \Delta c_l^r + \frac{\partial c_l^r}{\partial \alpha} \theta, \quad (3)$$

in which θ is airfoil twist, α is the angle of attack, $\partial \Delta c_l^r / \partial \alpha > 0$ and $\theta < 0$.

Suppose the airfoil is equipped with a system of actuators capable of generating an additional lift coefficient Δc_l^a such that the negative twist contribution is counteracted. The designer is satisfied as long as

$$\Delta c_l^a \geq -\frac{\partial c_l^r}{\partial \alpha} \theta. \quad (4)$$

The actuation system is comprised of a setup of actuators, each with two possible states, activated or deactivated, distributed along the airfoil chord. To generate Δc_l^a , the system changes the airfoil mean camber line. Moreover, Δc_l^a depends on the flight condition through θ and $\partial c_l^a / \partial \alpha$. As this condition changes, the airfoil mean camber line adapts itself to produce the required Δc_l^a .

The specific characteristics of the actuators as well as the actuation mechanism are not of concern in this study. The requirement is that each actuator is able to increase the camber at its location by a positive value h_z .

The optimization problem is to minimize the fraction of active actuators, thus minimizing the actuation power, constrained by inequality (4). In the framework of the spectral level methodology, the sign of the level set function ψ defines the state of each actuator. The Fourier coefficients of ψ constitute the set of design variables of the optimization problem.

3.2 Problem Statement

The effect of camber line change on the airfoil lift coefficient is determined using general thin airfoil theory [12]. Given a point on the airfoil chord, the mean camber line is defined as halfway between the upper and lower surfaces describing the airfoil geometry at that point. The general thin airfoil theory assumes the mean camber line stays close to the chord line and that the maximum airfoil thickness is small compared to the chord length.

Consider an airfoil with a mean camber line given by the graph of z_c , which is a function of the coordinate along the chord direction, x . The lift coefficient at a zero angle of attack, c_{l_0} , is a function of z_c . In fact, neglecting the effect of the aileron deflection as an additional camber line shape variation, we have

$$c_{l_0} = 2 \int_0^c \frac{dz_c}{dx} \frac{[\cos \tau(x) - 1]}{c/2 \sin \tau(x)} dx, \quad (5)$$

in which $x = c(1 - \cos \tau)/2$, $\tau \in [0, \pi]$ and c represents the airfoil chord. The convergence of this integral requires $z_c = 0$ at $x = 0$ and $x = c$.

Let $z_{c_{\text{nom}}}$ describe the nominal camber configuration. Each active actuator modifies the camber at its location by increasing the local $z_{c_{\text{nom}}}$ by a positive value h_z . The actuation state is regulated by the sign of the level set function ψ : at chord locations where ψ is negative, the actuators are not activated, and the camber coincides with the nominal camber; at positions where ψ is positive, the camber is incremented by h_z . Consequently, the zero level set of ψ determines the distribution pattern of active actuators along the airfoil chord. Accordingly,

$$z_c(x) = z_{c_{\text{nom}}}(x) + h_z \left\{ \frac{\arctan[a_{\text{act}}\psi(x)]}{\pi} + 0.5 \right\}, \quad (6)$$

in which h_z is multiplied by a relaxed indicator function. The larger the a_{act} , the fastest are the changes from $z_{c_{\text{nom}}}$ to $z_{c_{\text{nom}}} + h_z$ and vice-versa.

The additional amount of lift, Δc_l^a , is the difference between the lift produced by the nominal camber and the lift provided by the new camber line, that is,

$$\Delta c_l^a = \frac{2h_z}{\pi} \int_0^c \frac{d}{dx} \{ \arctan[a_{\text{act}}\psi(x)] \} \frac{[\cos \tau(x) - 1]}{c/2 \sin \tau(x)} dx. \quad (7)$$

Finally, the optimization problem is

$$\begin{aligned} \min_{\text{Fourier coeff.}} \quad & \frac{V(\psi)}{V_{\text{total}}} & (8) \\ \text{subject to} \quad & -\frac{2h_z}{\pi} \int_0^c \frac{d}{dx} \{ \arctan[a_{\text{act}}\psi(x)] \} \frac{[\cos \tau(x) - 1]}{c/2 \sin \tau(x)} dx \leq \frac{\partial c_l^r}{\partial \alpha} \theta, \end{aligned}$$

in which V stands for the volume of active actuation and V_{total} stands for the total volume of actuators.

Typically, in subsonic regime, z_c has a maximum value of 5% of c , [12]. In our case, suppose the airfoil has a z_c maximum of 2.5% of c , and assume the increase in camber, h_z , is 1.0% of c . Let $c = 1.0$ m. Then $h_z = 0.01$ m. Also, let $\partial c_l^r / \partial \alpha \theta = -0.1$, which for $\partial c_l^r / \partial \alpha = 2\pi$ corresponds, approximately, to a twist angle of 1° . These values were found to be adequate to satisfy the constraint in (8) and the hypothesis of the thin airfoil theory.

The initial design is a fully activated actuation system, that is, $\psi \equiv 1.0$.

The airfoil chord was discretized into 5000 elements. The optimization problem (8) was solved for $a_{\text{act}} = 10000.0$.

The optimization algorithm is composed of two steps: a quick random search of the design space followed by a local search with COBYLA [18], a derivative-free optimization tool.

3.3 Results and Discussion

In previous work [10, 11], the iteration approach in the number of design variables proved to be a good strategy to find an optimal design. In this case, we also follow this approach. For $n = 1$, the number of design variables corresponding to $N + 1$ Fourier coefficients is $2N + 1$. The initial value was chosen to be $N = 3$. For this value, we preceded COBYLA with a random search in the design space. The resulting Fourier coefficients were consecutively used to initialize simulations $N = 6, 9$, without random search.

The optimal configuration of active actuators applied on a real airfoil results in a smooth displacement vector field, and, consequently, in a smooth variation of the mean camber line. To simulate the effects of elasticity and digital actuation mode on the airfoil geometry, we have convolved the relaxed indicator function in (6), restricted to $[0, c]$, with a Gaussian function with zero mean and variance $\sigma^2 = 0.03$. The variance can be considered a measure of the net elastic properties of the airfoil materials and internal arrangement.

For visualizing the evolution of the morphing airfoil geometry during the optimization procedure, we applied the actuation system to a nominal airfoil based on the NACA four-digit family of wing sections [12]. In particular, we have consider a value of 0.1 for the maximum thickness expressed as a fraction of c , a value of 0.025 for the maximum value of $z_{c_{\text{nom}}}$ attained at position $0.25c$. In the following figures, the nominal airfoil is represented by a dashed line. Moreover, the depicted airfoils are graphic representations of the results attained with the spectral level set formulation of optimization problem (8). There is no relation between the value used for $\theta \partial c'_i / \partial \alpha$ and the represented airfoils.

Table 1 shows the values of the optimal objective function J and the maximum constraint violation for the corresponding optimal configuration, MAXCV. The value of J decreases with increasing N , corresponding to a progressive reduction of the width of the set of active actuators, as depicted in Figure 1.

The results in Figure 1 show that the set of active actuators is being drawn to $x = c$. From the constraint in (8), we deduce that a way to minimize the actuation, while still provide additional lift, would be to concentrate all the

Table 1. Quantitative results for an all-active initial design.

	J	MAXCV
Initial	9.99937E-01	9.99990E-01
$N = 3$	2.27479E-01	0.0
$N = 6$	1.88164E-01	6.70552E-08
$N = 9$	1.45582E-01	1.11759E-07

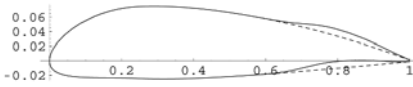


Figure 1a. All active initial configuration: $N = 3$.

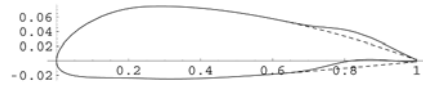


Figure 1b. All active initial configuration: $N = 6$.

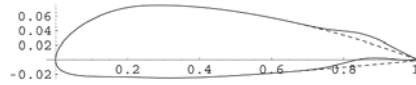


Figure 1c. All active initial configuration: $N = 9$.

active actuators near the trailing edge, that is, $x = c$. In fact, the closer to the trailing edge, the less active actuators are needed. A limiting case would be to set a spike-type of actuation very close to the trailing edge, since we cannot have actuation at $x = c$ because of constraint $\psi(x = c) \leq 0.0$. Therefore, the interface is evolving according to our predictions.

Another experiment starts from the configuration in Figure 2a, which has a different topology from those considered in the first example. The value of the initial objective function is 0.5, with verified constraints, and the final value for the objective function, obtained with $N = 6$, is $J = 3.89045E-02$, also with verified constraints. The spectral level set formulation was capable of achieving the one-spike configuration depicted in Figure 2b.

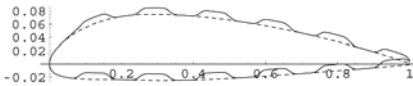


Figure 2a. Initial configuration.

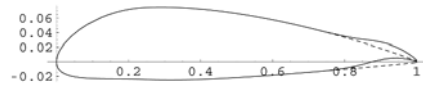


Figure 2b. Optimal design for $N = 6$.

We can conclude that for topologically different initial configurations, the spectral level set methodology was able to produce a very narrow set of active actuators close to $x = c$ using a very small number of Fourier modes.

4. CONCLUSIONS

In this paper we proposed the optimization of an airfoil aeroelastic response using the spectral level set methodology. According to this formulation, an interface is described as a level set of a function. As this function evolves, during the optimization process, topological changes of the interface may occur. An advantage of the spectral level set methodology is to provide, asymptotically in the number of degrees of freedom design variables and for a sufficiently

regular boundary, a lower error bound than non-adaptive classical approaches to structural topology optimization. Under this circumstances, the proposed methodology could lead to a reduction of the design space dimension.

An application of the proposed methodology, consisting in the design of a morphing airfoil minimizing the actuation power while improving the aileron effectiveness, was discussed. This problem showed the spectral level set methodology can adequately handle the occurrence of spike-like functions during the optimization process, starting from different topologies and with a very small number of Fourier coefficients.

ACKNOWLEDGEMENTS

The first author acknowledges the financial support of Fundação para a Ciência e a Tecnologia, Programa PRAXIS XXI, and of the European Social Fund under Community Support Framework III.

REFERENCES

- [1] G. Allaire, F. De Gournay, F. Jouve and A.-M. Toader, Structural optimization using topological and shape sensitivity via a level set method, *Control and Cybernetics* (2004) to appear.
- [2] G. Allaire, F. Jouve and A.-M. Toader, A level-set method for shape optimization. *Comptes Rendus de l'Académie des Science Paris, Series I*, 334, 1125–1130 (2002).
- [3] G. Allaire, F. Jouve and A.-M. Toader, Structural optimization using sensitivity analysis and a level set method, *Journal of Computational Physics*, 194(1), 363–393 (2004).
- [4] R.L. Bisplinghoff, H. Ashley, and R.L. Halfman, *Aeroelasticity*, Dover Publications, Mineola, NY (1996).
- [5] M.P. Bendsøe, A.R. Diaz and N. Kikuchi, Topology and generalized layout optimization of elastic structures, in *Topology Design of Structures*, M.P. Bendsøe and C.A. Mota Soares (eds), NATO ASI Series, Series E, Vol. 227, Kluwer Academic Publishers, Dordrecht, pp. 159–205 (1993).
- [6] M.P. Bendsøe, *Optimization of Structural Topology, Shape and Material*, Springer, Berlin (1995).
- [7] M.P. Bendsøe and N. Kikuchi, Generating optimal topologies in structural design using a homogenization method, *Computer Methods in Applied Mechanics and Engineering*, 71, 197–224 (1988).
- [8] H.A. Eschenauer, V.V. Kobelev and A. Schumacher, Bubble method for topology and shape optimization of structures, *Structural Optimization*, 8, 42–51 (1994).
- [9] L.C. Evans, *Partial Differential Equations*, Graduate Studies in Mathematics, Vol. 19, American Mathematical Society, Providence, RI (1998).
- [10] A.A. Gomes, *Spectral Level Methodology in Optimization*, Ph.D. Thesis, IST, Technical University of Lisbon, in preparation.
- [11] A.A. Gomes and A. Suleman, Application of the spectral level set methodology in topology optimization, *Structural and Multidisciplinary Optimization*, accepted for publication.

- [12] E.L. Houghton and P.W. Carpenter, *Aerodynamics for Engineering Students*, 4th edn, Edward Arnold (1993).
- [13] K. Maute and M. Allen, Conceptual design of aeroelastic structures by topology optimization, *Structural and Multidisciplinary Optimization*, 27(1–2), 27–42 (2004).
- [14] K. Maute, M. Nikbay and C. Farhat, Conceptual layout of aeroelastic wing structures by topology optimization, in *43rd AISS/ASME/ASCE/AHS/ASC Structures, Structural Dynamics, and Materials Conference*, Denver, CO, April 22–25, AIAA 2002-1480 (2002).
- [15] K. Maute and G.W. Reich, An aeroelastic topology optimization approach for adaptive wing design, AIAA 2004-1805 (2004).
- [16] S.J. Osher and J.A. Sethian, Fronts propagating with curvature dependent speed: Algorithms based on the Hamilton–Jacobi formulation, *Journal of Computational Physics*, 79, 12–49 (1988).
- [17] S. Osher and F. Santosa, Level set methods for optimization problems involving geometry and constraints. I. Frequencies of a two-density inhomogeneous drum, *Journal of Computational Physics*, 171, 272–288 (2001).
- [18] M.J.D. Powell, A direct search optimization method that models the objective and constraint functions by linear interpolation, in *Advances in Optimization and Numerical Analysis*, S. Gomez and J.P. Hennart (eds), Kluwer Academic Publishers, Dordrecht, pp. 51–67 (1994).
- [19] G.I.N. Rozvany and M. Zhou, Applications of the COC algorithm in layout optimization, in *Engineering Optimization in Design Processes*, Proc. Int. Conf., Karlsruhe, Germany, September 1990, C. Mattheck, H. Eschenauer and N. Olhoff (eds), Springer-Verlag, Berlin, pp. 59–70 (1991).
- [20] J.A. Sethian and A. Weigmann, Structural boundary design via level set and immersed interface methods, *Journal of Computational Physics*, 163, 489–528 (2000).
- [21] J. Sokolowski and A. Zochowski, On the topological derivative in shape optimization, *SIAM Journal on Control and Optimization*, 37, 1251–1272 (1999).
- [22] M.E. Taylor, *Partial Differential Equations I – Basic Theory*, chapter on Fourier Analysis, Distributions, and Constant-Coefficient Linear PDE, Springer-Verlag (1997).
- [23] Y.M. Xie and G.P. Steven, *Evolutionary Structural Optimization*, Springer (1997).

Acoustics and Fluids and Actuators

TOPOLOGY OPTIMIZATION FOR ACOUSTIC-STRUCTURE INTERACTION PROBLEMS

Gil Ho Yoon, Jakob Søndergaard Jensen and Ole Sigmund

*Department of Mechanical Engineering, Technical University of Denmark,
DK-2800 Lyngby, Denmark*

ghy@mek.dtu.dk, jsj@mek.dtu.dk, sigmund@mek.dtu.dk

Abstract: We propose a gradient based topology optimization algorithm for acoustic-structure (vibro-acoustic) interaction problems without an explicit interfacing boundary representation. In acoustic-structure interaction problems, the pressure field and the displacement field are governed by the Helmholtz equation and the linear elasticity equation, respectively, and it is necessary that the governing equations should be properly evolved with respect to the design variables in the design domain. Moreover, all the boundary conditions obtained by computing surface coupling integrals should be properly imposed to subdomain interfaces evolving during the optimization process. In this paper, we propose to use a mixed finite element formulation with displacements and pressure as primary variables (u/p formulation) which eliminates the need for explicit boundary representation. In order to describe the Helmholtz equation and the linear elasticity equation, the mass density as well as the shear and bulk moduli are interpolated with the design variables. In this formulation, the coupled interface boundary conditions are automatically satisfied without having to compute surface coupling integrals. Two-dimensional acoustic-structure interaction problems are optimized to show the validity of the proposed method.

Keywords: Mixed formulation, acoustic-structure interaction, dynamics, harmonic loading, coupled problems.

1. INTRODUCTION

Topology optimization has been applied to a variety of engineering problems and extensions to multiphysics systems seems to be a promising future direction [1]. In this paper, the computational framework for topology optimization of acoustic-structure interaction problems is proposed.

First, however, we are required to address the following issues. During the optimization process, two distinct governing equations – Helmholtz equation and the linear elasticity equation – should be modeled without explicit bound-

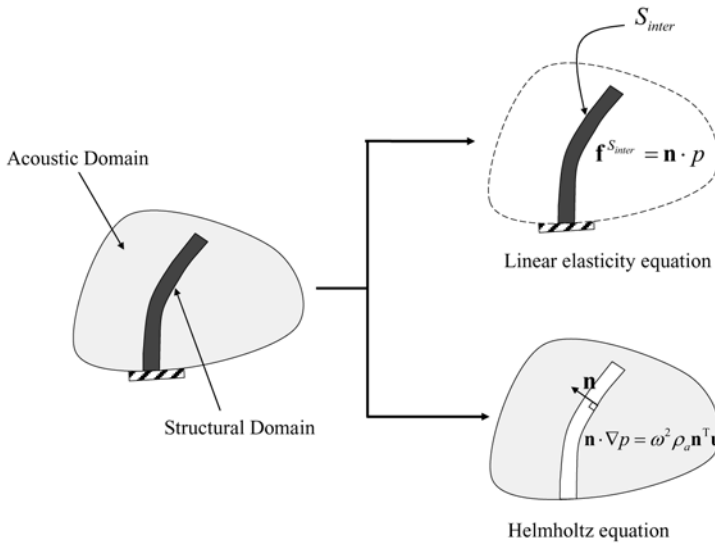


Figure 1. The interaction boundary conditions between acoustic and structure (where \mathbf{n} : the normal vector from the fluid to the solid, p : the pressure, \mathbf{u} : the displacement, ω : the angular speed, ρ_s : the structural density, and S_{inter} : the interfacing boundary).

ary representation to allow for free topological variations. Because the pressure and the displacements are the primal variables for the acoustic and the linear elasticity equation, respectively, alternating these two equations during optimization is difficult. Moreover, at the evolving interfacing boundaries, some conditions, illustrated in Figure 1, coming from the conservation of mass and the equation of motion should be properly imposed. This implies that positions and parameters of boundary conditions depend on a given topology. This explicit boundary issue is also observed in hydrostatics and electromagnetic structures [2]. To make it possible to compute these design dependent boundary conditions, an explicit boundary representation as known from shape optimization must be used. However, in topology optimization relying on the localized density, this is not possible.

2. u/p MIXED FORMULATION FOR THE ACOUSTIC-STRUCTURE INTERACTION PROBLEM

In this paper, instead of separately solving the Helmholtz equation and the linear elasticity equation, we propose to adopt the mixed displacement/pressure (u/p) finite element formulation, in which the displacements as well as the pressure are the primal variables for both physical regions [3, 4]. Moreover,

the material interpolation scheme based on the SIMP (Solid Isotropic Material with Penalization) method [1] must account for the interpolation between the material properties of air (fluid) and solid.

2.1 The Mixed Finite Element Formulation for the Acoustic-Structure Interaction Problem

Rather than using only the displacements of nodes as the primal variables, in the mixed finite element procedure, pressure is added as an additional primal variable and the constitutive equation involving pressure and displacements is implemented in a finite element context.

2.1.1 Basic Principle of the Mixed Finite Element Formulation. In the mixed finite element formulation, the (2D) governing equation, without consideration of body force, and the constitutive equation are formulated as follows:

$$\text{Frequency domain equilibrium equation: } \nabla \boldsymbol{\sigma} = -\omega^2 \rho \mathbf{u} \quad \text{on } \Omega, \quad (1)$$

$$\text{Stress and strain relationship: } \boldsymbol{\sigma} = K \varepsilon_v \boldsymbol{\delta} + 2G \mathbf{e}, \quad (2)$$

$$\text{Pressure and volumetric strain relationship: } p = -K \varepsilon_v \quad (3)$$

$$\mathbf{e} = \boldsymbol{\varepsilon} - \frac{\varepsilon_v}{2} \boldsymbol{\delta}, \quad \varepsilon_v = \frac{\Delta V}{V} = \varepsilon_{kk}, \quad (4)$$

where K , G and ρ are the bulk modulus, the shear modulus, and the density in the analysis domain Ω , respectively. The deviatoric strain components and the volumetric strain are denoted by \mathbf{e} and ε_v , respectively, and $\boldsymbol{\delta}$ is Kronecker's delta.

The basic approach of displacement/pressure finite element formulations is to interpolate the displacements and the pressure, simultaneously. This requires that we express the principle of virtual work in terms of the independent variables \mathbf{u} and p , which gives

$$\int_V \delta \mathbf{e}^T \mathbf{C} \boldsymbol{\sigma} \, dV - \int_V p \delta \varepsilon_v \, dV = \int_\Omega -\omega^2 \rho \delta \mathbf{u}^T \mathbf{u} \, d\Omega + \int_{S^f} \delta \mathbf{u}^T \mathbf{f}^{S^f} \, dS^f, \quad (5)$$

$$\int_V (p/K + \varepsilon_v) \delta p \, dV = 0, \quad (6)$$

$$(\boldsymbol{\sigma} + p\boldsymbol{\delta}) = \mathbf{C}' \left(\boldsymbol{\varepsilon} - \frac{1}{2} \varepsilon_v \boldsymbol{\delta} \right). \quad (7)$$

The virtual displacement and the corresponding strains are denoted by $\delta \mathbf{u}$ and $\delta \boldsymbol{\varepsilon}$, respectively, and \mathbf{C}' is the stress-strain matrix for the deviatoric stress and strain component.

In this mixed displacement/pressure finite element formulation, three involved material properties, the bulk modulus (K), the shear modulus (G), and the density (ρ) in Equations (1)–(7), are alternated with respect to the acoustic domain and the structural domain. For instance, if the analysis domain Ω is assumed to be divided into a structural domain Ω_s and an acoustic domain Ω_a , these three material properties are varying as follows:

$$\Omega = \Omega_s \cup \Omega_a, \quad \Omega_s \cap \Omega_a = \mathbf{0}, \quad (8)$$

$$\text{For structural domain: } K \equiv K_s, \quad G \equiv G_s, \quad \rho \equiv \rho_s \text{ on } \Omega_s, \quad (9)$$

$$\text{For acoustic domain: } K \equiv K_a, \quad G \equiv G_a = 0, \quad \rho \equiv \rho_a \text{ on } \Omega_a, \quad (10)$$

where the subscripts ‘s’ or ‘a’ on the bulk, the shear and the density denote whether the corresponding material properties are belonging to the structural domain or the acoustic domain, respectively.

2.1.2 The Derivation of the Wave Equation from the Mixed Displacement/Pressure Formulation. The analysis procedure for response of linear solid media by the mixed displacement/pressure finite element procedure is well understood. However, in case of the acoustic domain, it requires some algebra to derive the Helmholtz equation from the mixed displacement/pressure formulation by assigning the appropriate material properties.

Setting the shear modulus to zero makes it possible to derive the Helmholtz equation on the acoustic domain from the mixed displacement/pressure formulation.

$$K \equiv K_a, \quad G = G_a = 0, \quad \rho \equiv \rho_a. \quad (11)$$

The governing equation (1) and the constitutive equation (3) may then be simplified as follows:

$$\nabla p - \omega^2 \rho_a \mathbf{u} = 0, \quad (12)$$

$$\nabla \cdot \mathbf{u} + \frac{p}{K_a} = 0. \quad (13)$$

Note that Equations (12) and (13) can be regarded as the *linearized Euler’s equation* and the *linear continuity equation*, respectively, which together constitute the basis of the linear wave equation [5]. Substituting the displacement in (12) into Equation (13), the Helmholtz equation (the frequency dependent wave equation for the pressure variable) can be derived:

$$\nabla \cdot \left(\frac{1}{\rho_a} \nabla p \right) + \omega^2 \frac{1}{K_a} p = 0. \quad (14)$$

This shows that we can imitate the wave equation (or Helmholtz equation) using the mixed displacement/pressure finite element problems with the proper

bulk, shear modulus, and the fluid density corresponding to air or fluid domain as well as the proper boundary conditions for the pressure and displacements. (This can be conceptually understood because the acoustic pressure is in fact generated by the harmonic movement of the fluid element.)

2.2 Parameterization Method for Topology Optimization

For the mixed finite element governing equation to alternate between the Helmholtz equation and the linear elasticity equation, the involved material properties, i.e., the bulk modulus, the shear modulus, and the mass density, should be properly interpolated with respect to the design variables following Equations (8)–(10) [2]. In this paper, the nodal design variable method based on the SIMP (Solid Isotropic Material with Penalization) is used:

$$K(\gamma) = K_s \gamma^{n_1} + (1 - \gamma^{n_1}) K_a, \quad (15a)$$

$$G(\gamma) = G_s \gamma^{n_1} + G_a (1 - \gamma^{n_1}) = G_s \gamma^{n_1}, \quad (15b)$$

$$\rho(\gamma) = \rho_s \gamma^{n_2} + (1 - \gamma^{n_2}) \rho_a, \quad (15c)$$

$$0 \leq \gamma \leq 1, \quad (15d)$$

where γ is the nodal design variable. The penalty factors for the bulk modulus, the shear modulus, and the density are denoted by n_1 and n_2 , respectively. In these interpolation functions, the solid media can be represented when γ is one and the acoustic media when γ is zero. Positive values between 1 and 3 are used for n_1 and $n_2 = 1$.

3. TOPOLOGY OPTIMIZATION OF ACOUSTIC-STRUCTURE INTERACTION PROBLEMS

In this section, an analysis example as well as topology optimization problems for the acoustic-structure interaction structures will be solved with the developed mixed displacement/pressure (\mathbf{u}/p) finite element procedures and the method of moving asymptotes [6].

Case 1: The pressure calculation by the mixed finite element formulation

In order to verify the analysis code we first solve the simple wave propagation problem shown in Figure 2(a) by the Helmholtz equation as well as the mixed finite element formulation with the same discretization. Figure 2(b) shows the pressure distributions along cross-section AA' obtained by the mixed finite element formulation and the Helmholtz equation, respectively. It is hereby shown

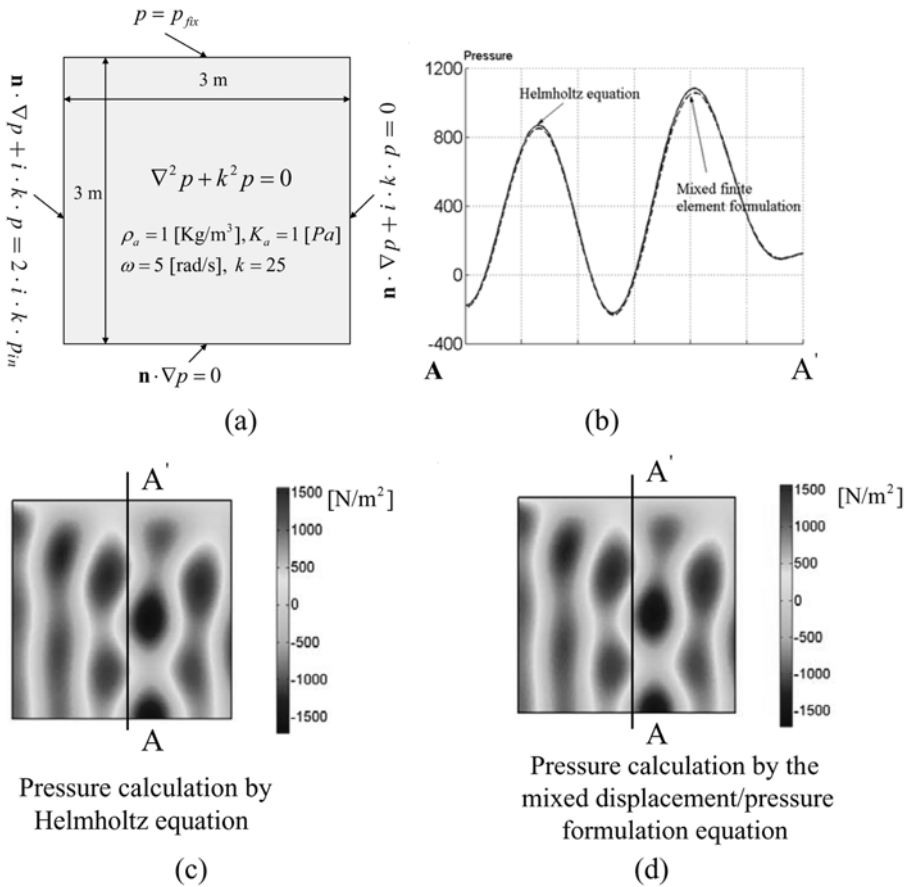


Figure 2. Analysis example 1: Acoustic domain analysis with the mixed formulation with various boundary conditions. (a) Problem definition (where $p_{fix} = 123$ Pa and $p_{in} = 1000$ Pa), (b) the pressure distribution of the cross section, (c) the pressure distribution by the Helmholtz equation, and (d) the pressure distribution by the mixed finite element procedure.

that it is possible to implement the Helmholtz equation by the studied mixed finite element formulation.

Case 2: Topology optimization for flexible partition

For an illustrative topology optimization example, a design problem shown in Figure 3 is considered. By designing a structure inside the structural (design) domain, the noise level in a defined domain should be minimized. The objective function is defined as the minimizing of the integral of the pressure.

$$\text{Minimize}_{\gamma} \quad \phi = \int_{\Omega_0} |p| \, d\Omega \quad (\text{where the objective domain is defined by } \Omega_0). \tag{16}$$

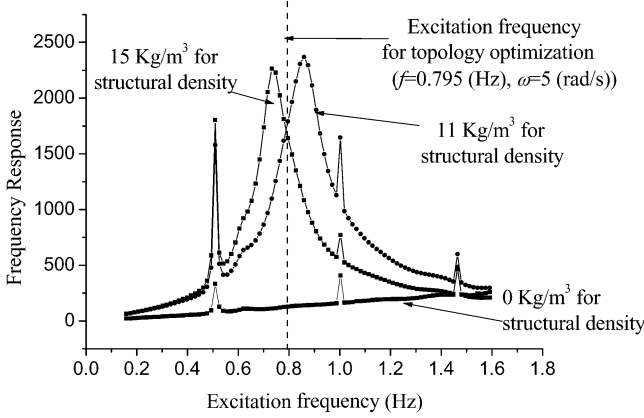
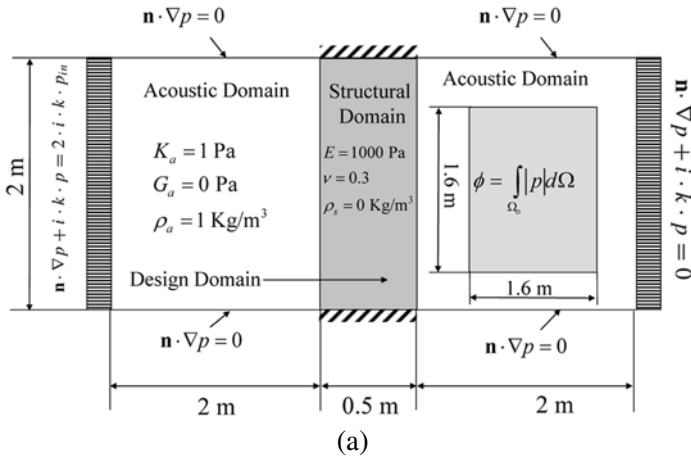


Figure 3. Topology optimization for a flexible partition. (a) The definition of optimization problem (where E , ν , and ρ_s are Young’s modulus, the Poisson’s ratio, and the structural density, respectively. p_m is set to -1.0×10^3 Pa), (b) the initial frequency response functions of the objective function with two different mass densities.

At first, the initial frequency response functions of the defined objective function for two different mass densities ($\rho = 11$ and 15 kg/m^3) are presented in Figure 3(b) with the whole design domain filled with solid. Important differences between these two frequency response functions can be observed. As expected, the eigenfrequencies for $\rho = 11 \text{ kg/m}^3$ are higher than those for $\rho = 15 \text{ kg/m}^3$. Setting the excitation frequency to $5/2\pi$ between two hills in Figure 3(b) and minimizing the objective function, one can imagine the different behaviors of these frequency response functions during optimization. In Figures 4 and 5, the optimized results and the frequency response func-

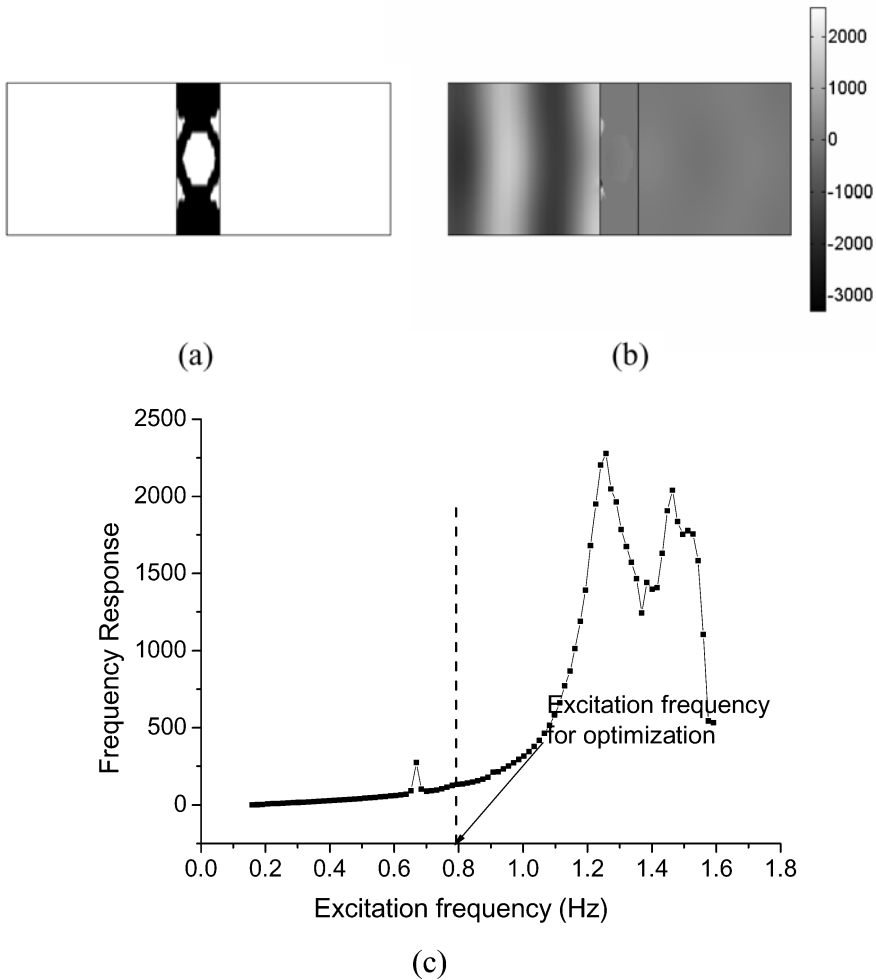


Figure 4. Optimization results with $\rho = 11 \text{ kg/m}^3$. (a) An optimized result ($\phi_{\text{optimized}} = 250.93 \text{ N}$), (b) the pressure distribution, and (c) the frequency response.

tions are plotted. When the heavier mass density ($\rho = 15 \text{ kg/m}^3$) is used, the second eigenfrequency is placed to the left of the excitation frequency. Thus, to minimize the objective function, the optimized result will be one having low fundamental eigenfrequency. Oppositely, with the lighter structural density $\rho = 11 \text{ kg/m}^3$, the fundamental eigenfrequency is placed to the right of the excitation frequency. This leads to an optimized result having larger fundamental eigenfrequency as Figure 4 shows. Some observations can be made here. First, it can be postulated that optimization topology for frequencies between eigenfrequencies will have similar topologies. Second, minimizing

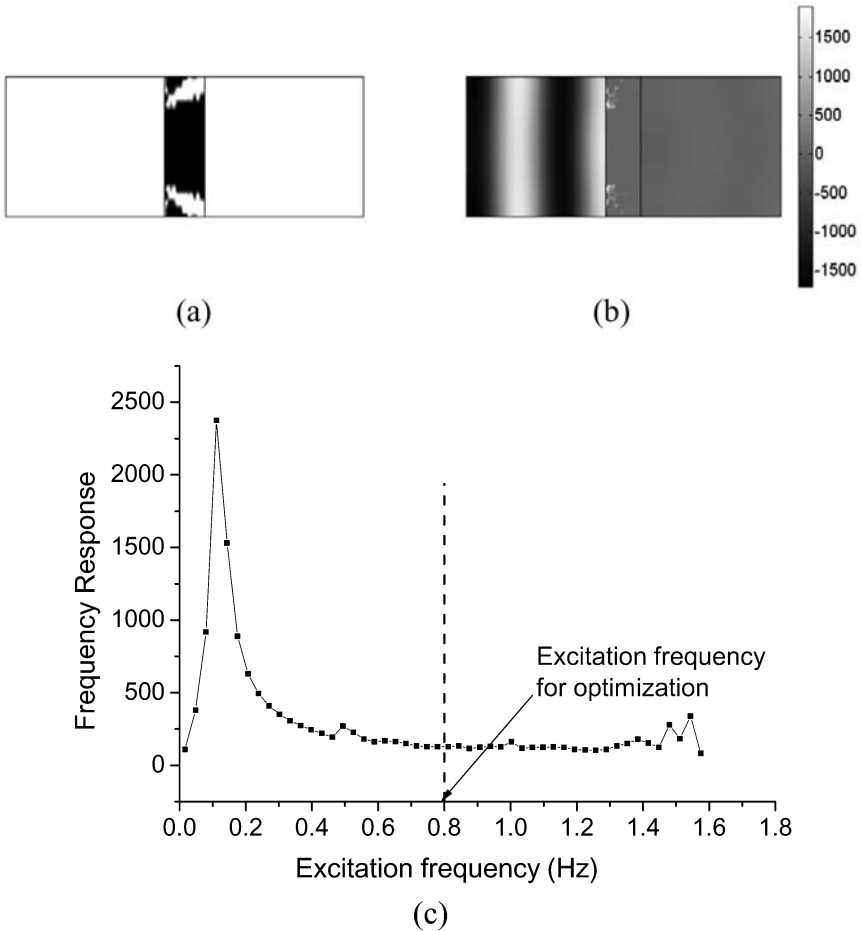


Figure 5. An optimization result with $\rho = 15 \text{ kg/m}^3$. (a) An optimized result ($\phi_{\text{optimized}} = 129.27 \text{ N}$), (b) the pressure distribution, and (c) the frequency response function.

the response below the fundamental frequency is very similar to maximizing the fundamental eigenfrequency as seen in Figure 4. It should also be noted that the sharp peaks seen at regular intervals in the response function correspond to acoustical eigenmodes with little influence on the structural behaviour.

4. CONCLUSION

Using a mixed displacement/pressure formulation, we can solve acoustic-structure interaction problems using a standard density based topology optimization approach. By changing the bulk modulus, the shear modulus, and the density in the mixed displacement/pressure formulation, the Helmholtz equa-

tion and the linear elasticity equation can be recovered. Topology optimization of acoustic-structure interaction structures is demonstrated and the behavior of the optimized designs was interpreted.

REFERENCES

- [1] Bendsøe, M.P. and Sigmund, O., *Topology Optimization Theory, Methods and Applications*, Springer-Verlag, Berlin (2003).
- [2] Sigmund, O. and Clausen, P.M., Topology optimization using a mixed formulation: An alternative way to solve pressure load problems, submitted (2005).
- [3] Bathe, K.J., *Finite Element Procedures*, Prentice Hall, Englewood Cliffs, NJ (1996).
- [4] Wang, X. and Bathe, K.J., Displacement/pressure based mixed finite element formulations for acoustic fluid-structure interaction problems, *International Journal for Numerical Methods in Engineering*, 40, 2001–2017 (1997).
- [5] Kinsler, L.E., Frey, A.R., Coppens, A.B. and Sanders, J.V., *Fundamentals of Acoustics*, John Wiley & Sons, New York (2000).
- [6] Svanberg, K., The method of moving asymptotes – A new method for structural optimization, *International Journal for Numerical Methods in Engineering*, 24, 359–373 (1987).

TOPOLOGY OPTIMIZATION OF MASS DISTRIBUTION PROBLEMS IN STOKES FLOW

Allan Gersborg-Hansen¹, Martin Berggren² and Bernd Dammann³

¹*Department of Mathematics, Technical University of Denmark, DK-2800 Lyngby, Denmark*

²*Department of Information Technology, Uppsala University, Box 337, SE-751 05 Uppsala, Sweden*

³*Informatics and Mathematical Modelling, Technical University of Denmark, DK-2800 Lyngby, Denmark*

agh@mek.dtu.dk

Abstract: We consider topology optimization of mass distribution problems in 2D and 3D Stokes flow with the aim of designing devices that meet target outflow rates.

For the purpose of validation, the designs have been post processed using the image processing tools available in FEMLAB. In turn, this has enabled an evaluation of the design with a body fitted mesh in a standard analysis software relevant in engineering practice prior to design manufacturing.

This work investigates the proper choice of a maximum penalization value during the optimization process that ensures that the target outflow rates are met in the validation test.

Keywords: Topology optimization, fluid dynamics, FEM, sensitivity analysis, FEMLAB, COMSOL.

1. INTRODUCTION

Shape optimization for fluid mechanics problems is now an established research field [9]. However, the application of topology optimization tools is quite recent. Topology optimization of fluid network problems was treated by Klarbring and Petersson [8], the concept of a topological derivative has been introduced as a new tool for shape optimization by Guillaume and Idris [7], and Borrvall and Petersson [2] investigated topology optimization of Stokes flow problems to design energy efficient fluid devices. The latter seminal work was extended including the effect of inertia in [4, 5, 11, 10]. New work on topology optimization of transport problems was presented in [14].

The present work elaborates on the idea of designing a fluid device that meets quantitative performance measures. Here we consider topology optim-

ization of mass distribution devices in 2D and 3D Stokes flow that meet a uniform target outflow rate. This is a new extension of topology optimization in fluid dynamics, since previous works in the field have focused on minimizing the rate of energy dissipation [2] or obtaining a special qualitative behavior of the fluid, see [5, 10].

Also, we are concerned with post processing of a design prior to manufacturing, i.e. the interpretation of the design that defines the optimized geometry. We investigate the value of the penalization that gives reasonable agreement between the finite element model used during the optimization process and the optimized geometry run in a standard analysis software. Finally we show how easily the post processing steps are done using FEMLAB¹ and thereby we suggest that such a check should be performed as a standard check by researchers in the field of topology optimization that have access to FEMLAB.

2. TOPOLOGY OPTIMIZATION IN STOKES FLOW

Topology optimization problems in Stokes flow was introduced in [2], which the present study extends by also including target outflow rates as part of the optimization problem. The topology optimization problem is stated in the generic form below, see [1] for more details

$$\begin{aligned}
 \min_{\hat{\mathbf{a}} \in \mathbb{R}^m} \quad & \Phi = \int_{\Omega} \nabla \mathbf{u} \cdot \nabla \mathbf{u} + \alpha \mathbf{u} \cdot \mathbf{u} & (1) \\
 \text{subject to} \quad & \int_{\Omega} a \leq V f_V & (2) \\
 & (f_i - 1)^2 \leq \epsilon^2, \quad i = 1, \dots, N_{\text{out}} & (3) \\
 & a = \sum_{j=1}^m \psi_j(\mathbf{x}) \hat{a}_j & (4) \\
 & 10^{-3} \leq \hat{a}_i \leq 1, \quad i = 1, \dots, m & (5) \\
 & \alpha = \bar{\alpha} + (\underline{\alpha} - \bar{\alpha}) a^{\frac{1+q}{a+q}} & (6) \\
 & \left. \begin{aligned} -\nabla^2 \mathbf{u} + \alpha(a) \mathbf{u} + \nabla p &= \mathbf{0} & \text{in } \Omega \\ \nabla \cdot \mathbf{u} &= 0 & \text{in } \Omega \\ \mathbf{u} &= \mathbf{g} & \text{on } \Gamma_D \\ \frac{\partial \mathbf{u}}{\partial n} - \mathbf{n} p &= 0 & \text{on } \Gamma_N \end{aligned} \right\} & (7)
 \end{aligned}$$

The problem is to choose the m -dimensional vector $\hat{\mathbf{a}}$ of design parameters such that the rate of energy dissipation (1) is minimized subject to box constraints (5), a volume constraint (2), and constraints (3) on the outflow rates of the device. Parameter f_i is the outflow rate at the i -th outlet channel scaled with the target flow rate, and ϵ is the relative tolerance on the outflow rate; in the present case $\epsilon = 0.005$ ensuring that the flow rates differ no more than 1%.

The effect of the design parameters $\hat{\mathbf{a}}$ is visible in the Stokes equations (7) as the control term α . Following standard topology optimization ideas $\hat{\mathbf{a}}$ is

interpolated through an interpolation function (6) which is based on a finite element interpolation (4). In turn this means that a large value of $\alpha \gg 1$ corresponds to a “solid” (porous material) and a small value of $\alpha \ll 1$ corresponds to a fluid obeying the Stokes equations. Using topology optimization with this interpretation we can determine an optimal fluid layout.

The first term in the cost function (1) measures the velocity gradients which is the mathematical link to energy dissipation. The second term plays a different role, it penalizes large velocities in “solid” areas. Furthermore, in order to obtain final designs with $|\log_{10} \alpha| > 1$ we have also added penalization of the form $\alpha(\bar{\alpha} - \alpha)$ when needed. When doing this an extra adjoint problem needs to be solved in the sensitivity analysis, however when the number of outlets is large this does not increase the computational effort significantly.

In the present problem the presence of the volume constraint (4) lacks a practical engineering motivation, because there is no economical cost of allowing more fluid to flow through the device. One could speculate that if the weight of the fluid device was to be minimized, such a constraint could be relevant. Nonetheless, numerical evidence suggest that the volume constraint is necessary in order to ensure a well-posed optimization problem.

Equation (7) is the Stokes equations given in the strong form where the incompressibility constraint has been used to decouple the velocity components such that the Laplacian appears. This is a well known trick in fluid mechanics [6] which makes the problem well suited for a parallel implementation. Note, however, that this alters the boundary conditions compared to [2]. For the boundary condition on Γ_N to be valid one needs a down stream (pipe type) flow, which requires inlets/outlets to be added to the design domain. This was also introduced in [10] and is relevant to include in the modeling since this boundary condition often occurs in experimental practice. For optimization purposes this has the consequence that the symmetry boundary condition – frequently used in optimization of solid mechanics problems – does not apply.

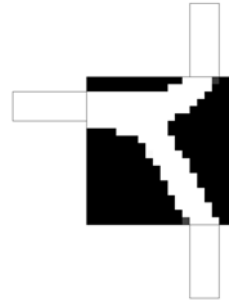
The optimization problem (1)–(7) is solved using the gradient driven MMA algorithm [12, 13] in combination with a finite element solver for equation (7). FEMLAB is used as a finite element library and also provides semi-analytical sensitivities. A continuation approach is used such that penalization parameter q is gradually increased to obtain a 0 – 1 design.

2.1 Investigation of Proper Penalization

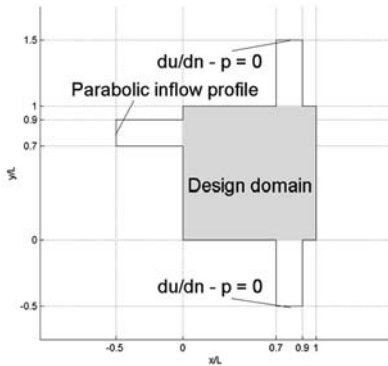
To illustrate the effect of the penalization parameter $\bar{\alpha}$ we consider a quantitative design problem. First, consider the example shown in Figures 1(a)–1(b) where the outflow rates are fixed through the choice of boundary conditions. This design problem is similar to designs that minimize the rate of energy dissipation subject to a low fluid volume fraction, see, e.g., [2]. Now, changing



(a) Boundary conditions (D). The velocity profile is prescribed at the boundary and the design domain is colored grey. At edges without a label the no-slip boundary condition is enforced.



(b) Using the BCs in Figure 1(a), the rate of energy dissipation is minimized.



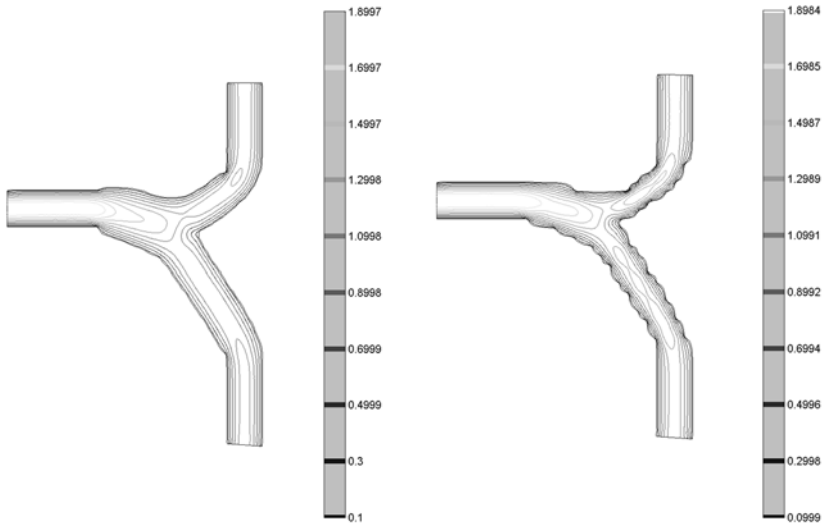
(c) Boundary conditions (D+N). The velocity profile is prescribed at the inlet and the pressure is fixed at the outlet. The design domain is colored grey and edges without a label have the no-slip boundary condition imposed.



(d) Using the BCs in Figure 1(c), the rate of energy dissipation is minimized with a constraint on the difference between the outflow rates.

Figure 1. Mass distribution example where the amount of fluid in the device is fixed. As expected, the outflow boundary makes a difference on the design.

the boundary conditions such that the outflow rates depend on the design gives a new problem, cf. Figures 1(c)–1(d). The result shown in Figure 1(d) is able to deliver uniform outflow rates within the 1% tolerance, a feature the design in Figure 1(b) does not have when subjected to the boundary conditions seen in



(a) Geometry created from the level curve of the velocity $|u| = 0.1$ in the design setting, cf. Figure 1(d).

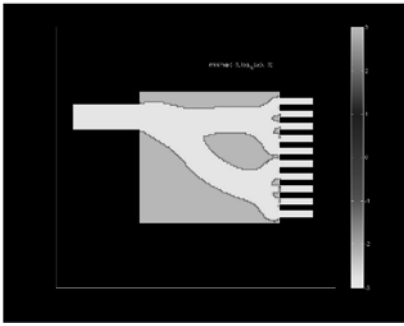
(b) Geometry created from the level curve of the velocity $|u| = 0.01$ in the design setting, cf. Figure 1(d).

Figure 2. Post processed designs. The values of the colored level curves, depicting the magnitude of the velocity, are seen in the color bar. The geometry in Figure 2(a) is smooth because the no-slip boundary condition is only loosely incorporated in the post processing procedure.

Figure 1(c). One problem remains, however, in engineering practice the credibility of above results would be low, since the design in Figure 1(d) has not been validated in standard software.

Different interpretations of the design in Figure 1(d) are possible. First, the design is a 0 – 1 design which is desirable since it has a clear physical meaning. Unfortunately, the corresponding level curve of α may be too rough such that the number of unknowns grows beyond what can be solved in practice. Secondly, for the optimized geometry the no-slip condition is enforced on channel walls. This motivates the use of a level curve of the magnitude of the velocity which also produces a smooth boundary, see Figure 2.

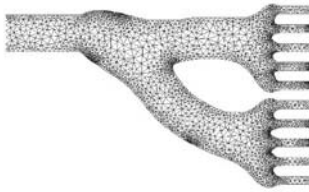
Although the procedure used in Figure 2 yields an optimized geometry that is smooth, it is required – in order to obtain a meaningful level curve in Figure 2(b) – to use a larger maximum value $\bar{\alpha}$ in (6) than the value used during the optimization process. The winks in this figure are due to the coarse design, but one would think that the no-slip condition is critical in reproducing the behavior seen in figure 1(d) for the optimized geometry. On the poster presented at the symposium, this was investigated in greater detail by a comparison of $\bar{\alpha}$ and the performance of the optimized geometries.



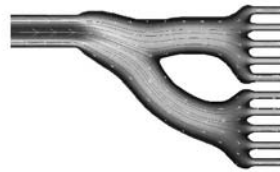
(a) Topology design.



(b) Interpretation given as a jpg picture: Level curve of the magnitude of the velocity.



(c) FEMLAB mesh of the optimized geometry.



(d) Standard run in FEMLAB.

Figure 3. Illustrations of FEMLAB as a post processing tool. Figure 3(a) is a typical picture seen in topology optimization from which an optimized geometry can be extracted. This is done using a post processing procedure (level curve of the control variable α , the magnitude of the velocity etc.), see Figure 3(b). This picture can be imported in FEMLAB and meshed (Figure 3(c)) which enables a validation run in standard software (Figure 3(d)).

2.2 Postprocessing Steps

Running FEMLAB with MATLAB one can create a mesh based on level curves of a standard picture, such as a jpg picture. This we find to be a valuable tool for developing topology design since it enables a validation check of planar designs produced important to engineering practice. Figure 3 shows as an example how this can be done as a supplement to the MATLAB code shown below.

MATLAB Code.

```

clear all
close all

% Get jpg file
[fn,pn]=uigetfile('*.jpg');

% Read image
pic=imread([pn fn]);

% Get coutours as a FEMLAB geometry object
[c_fl,r] = flim2curve(pic,{[],0:120:255},'KeepFrac',0.1);
% Fix FEMLAB bug
c = mirror(c_fl,[0 1] ,[0 1]);

% Plot using FEMLAB routine
figure(1)
geomplot(c,'Pointmode','off');

figure(2)
geomplot(c_fl,'Pointmode','off');
% Plot all small curves in a red color.
for j = 1:length(r)
    hold on, geomplot(r{j},'Pointmode','off','edgecolor','r','linewidth',2)
end

% In FEMLAB, use 'Import geometry objects'. Type 'c'

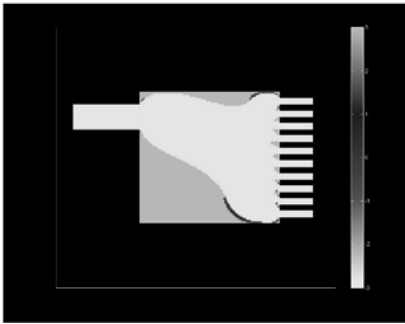
```

2.3 Ongoing Research

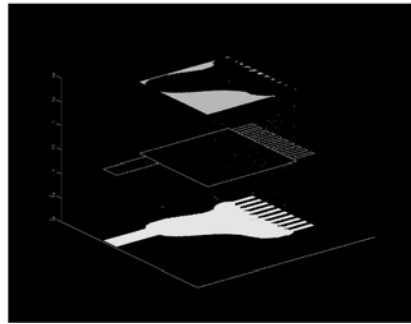
Advanced 2D Example. This design problem is an extension of the problem described in Section 2.1. It is more difficult due to the number of outlets, thus it requires a fine mesh and it yields 10 adjoint problems, one for each outlet. For this problem extra penalization was needed – giving one extra adjoint problem – to avoid intermediate densities near the outlets (a porous plug). The final design was obtained after 400 MMA iterations using UMFPAK as the direct sparse linear algebra solver, see Figure 4.

3D Simulations. Here we investigate the influence of the effects of 3D fluid modeling on the design. These effects are present even in Stokes flow (where the velocity components decouple) since the problem is posed on a finite domain. In Figure 5 we show preliminary 3D designs of the 3D version of the problem presented in Section 2.1.

The computations are substantially larger for the 3D problem. These investigations we carry out on a SUN computer using the parallized SUN Performance Library to solve the large sparse linear algebra problems.

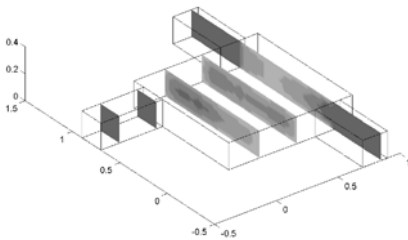


(a) Topology design. Intermediate values of the control term appear as black.

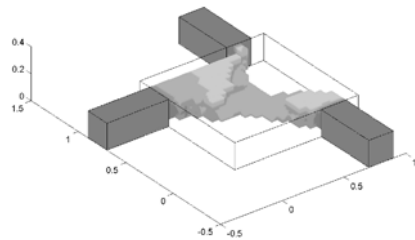


(b) Topology design. The height shows \log_{10} to the control term α . White areas should be filled with fluid and grey areas (at the top) should be filled with solid.

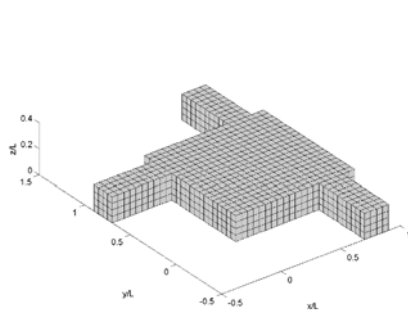
Figure 4. Advanced 2D design. The goal is to obtain uniform outflow rates in the 10 channels while minimizing the rate of energy dissipation and obeying a volume constraint. The numbers at the color bar are \log_{10} to the control term α .



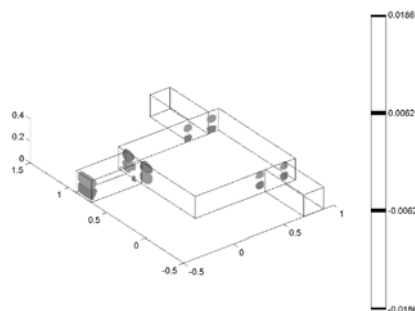
(a) 3D slice plot of the design field.



(b) 3D tetrahedron plot of the design field.



(c) Mesh used



(d) u_3 component of the velocity field. It is non-zero, but small.

Figure 5. Future research is directed towards investigating the effect of 3D fluid response on the design.

ACKNOWLEDGMENTS

The first author thanks Jukka Komminaho, Department of Information Technology, Uppsala University for initial help with the implementation on a SUN computer.

In addition the authors thank Martin P. Bendsøe and Ole Sigmund from the Technical University of Denmark for valuable discussions related to the material presented.

This work received support from the Danish Center for Scientific Computing through the SUN High Performance Computing System at the Technical University of Denmark.

NOTE

1. The work presented here is based on FEMLAB 3.1. Newer versions of the software is now called Comsol Multiphysics, see www.comsol.com

REFERENCES

- [1] Bendsøe, M.P. and Sigmund, O., *Topology Optimization – Theory, Methods, and Applications*, Springer-Verlag, Berlin (2004).
- [2] Borrvall, T. and Petersson, J., Topology optimization of fluids in Stokes flow, *Int. J. Num. Meth. Fluids*, 41, 77–107, DOI:10.1002/fld.426 (2003).
- [3] See homepage of Tim Davis, <http://www.cise.ufl.edu/research/sparse/umfpack/>
- [4] Evgrafov, A., Topology optimization of slightly incompressible fluids, in *Approximation of Topology Optimization Problems Using Sizing Optimization Problems*, Ph.D. Thesis, Department of Mathematics, Chalmers University of Technology, Göteborg, Sweden, ISBN 91-7291-466-1, pp. 55–81 (2004).
- [5] Gersborg-Hansen, A., Sigmund, O. and Haber, R.B., Topology optimization of channel flow problems, *Struct. Multidisc. Optim.*, 30(3), 181–192, DOI:10.1007/s00158-004-0508-7 (2005).
- [6] Glowinski, R., Finite element methods for the numerical simulation of incompressible viscous flow: Introduction to the control of the Navier–Stokes equations, in *Vortex Dynamics and Vortex Methods*, C.R. Anderson and C. Greengard (eds), Lectures in Applied Mathematics, Vol. 28, American Mathematical Society, pp. 219–301 (1991).
- [7] Guillaume, P. and Idris, K.S., Topological Sensitivity and Shape Optimization for the Stokes equations, *Siam Journal on Control and Optimization*, 43(1), 1–31, DOI:10.1137/S0363012902411210 (2005).
- [8] Klarbring, A., Petersson, J., Torstenfelt, B. and Karlsson, M., Topology optimization of flow networks, *Computer Methods in Applied Mechanics and Engineering*, 192(35–36), 3909–3932, DOI:10.1016/S0045-7825(03)00393-1 (2003)
- [9] Mohammadi, B. and Pironneau, O., Shape optimization in fluid mechanics, *Annu. Rev. Fluid Mech.*, 36, 255–279, DOI:10.1146/annurev.fluid.36.050802.121926 (2004).
- [10] Olesen, L.O., Okkels, F. and Bruus, H., A high-level programming–language implementation of topology optimization applied to steady-state Navier–Stokes flow, *Int. J. Numer. Meth. Engng.*, in press, DOI:10.1002/nme.1468 (2005)

- [11] Sigmund, O., Gersborg-Hansen, A. and Haber, R.B., Topology optimization for multiphysics problems: A future femlab application?, in *Nordic Matlab Conference (held in Copenhagen)*, L. Gregersen (ed.), Comsol, Søborg, Denmark, pp. 237–242 (2003).
- [12] Svanberg, K. The method of moving asymptotes – A new method for structural optimization, *Int. J. Numer. Meth. Eng.*, 24, 359–373 (1987).
- [13] Svanberg, K., A class of globally convergent optimization methods based on conservative convex separable approximations, *SIAM Journal on Optimization*, 12(2), 555–573, DOI:10.1137/S1052623499362822 (2002).
- [14] Thellner, M., Topology optimization of convection-diffusion problems, in *Multi-Parameter Topology Optimization in Continuum Mechanics*, Ph.D. Thesis, Linköping Studies in Science and Technology Dissertations No. 934, ISBN 91-85297-71-2, pp. 71–87 (2005).

TOPOLOGY OPTIMIZATION FOR ACOUSTIC PROBLEMS*

Maria Bayard Dühring

*Department of Mechanical Engineering, Solid Mechanics, Niels Koppels Allé,
Building 404, Technical University of Denmark, DK-2800 Kgs. Lyngby, Denmark*
s991010@student.dtu.dk

Abstract: In this paper a method to control acoustic properties in a room with topology optimization is presented. It is shown how the squared sound pressure amplitude in a certain part of a room can be minimized by distribution of material in a design domain along the ceiling in 2D and 3D. Nice 0-1 designs can be obtained when optimizing for low frequencies, but for higher frequencies the method results in complicated designs with porous material.

Keywords: Topology optimization, room acoustics, Helmholtz equation, 2D and 3D problems, Padé expansions.

1. INTRODUCTION

This paper presents a method to control acoustic properties in a room by means of topology optimization.

So far topology optimization has only been applied to a few problems in acoustics. In [1, 2] results are presented for an inverse acoustic horn and an acoustic horn, respectively. In [3] an example is shown where the shape of a reflection chamber is optimized to reflect waves, first for a single frequency and then for an entire frequency interval. The equation governing the wave propagation is the Helmholtz equation and in the article material interpolation functions for the inverse density and bulk modulus as function of the design variable are suggested to formulate the topology optimization problem. The model has resulted in nice optimized designs and is thus used as the basis for the model in this paper. See [4] for a detailed description of the general topo-

*This work is an overview of a master thesis carried out at Department of Mechanical Engineering, Solid Mechanics, Technical University of Denmark, during the period from the 2nd of May to the 15th of December 2005 with Professor Dr.techn. Ole Sigmund, Professor Dr.techn. Martin Bendsøe and Associate Professor, Ph.D. Jakob Søndergaard Jensen as supervisors.

logy optimization method and how it has been applied to problems in various engineering fields.

The problem considered here is a rectangular room in two or three dimensions bounded by rigid walls and with a source emitting sinusoidal sound waves. The task is to distribute material in a design domain along the ceiling, such that the squared sound pressure amplitude is minimized in a certain area of the room (the optimization domain). The problem of minimizing this quantity in a room is interesting for various applications for instance in car cabins where the noise from the motor can be reduced at the positions of the driver and passengers and in rooms where people are working at certain positions among noisy machinery.

2. THE ACOUSTIC MODEL

The governing equation of steady-state acoustic problems with sinusoidal sound waves is the Helmholtz equation

$$\nabla \cdot (\rho^{-1} \nabla \hat{p}) + \omega^2 \kappa^{-1} \hat{p} = 0. \quad (1)$$

Here \hat{p} is the complex pressure amplitude and depends on the position \mathbf{r} . ρ is the density and κ is the bulk modulus for the acoustic medium in which the sound propagates. ω is the angular frequency at which the acoustic system is driven. The real physical sound pressure p is found as the real part of \hat{p} . The optimized design found by the topology optimization is a distribution of air and solid material and the material properties ρ and κ must take values corresponding to either air or solid material depending on the position. For air the material properties are $(\rho, \kappa) = (\rho_1, \kappa_1)$ and for the solid material $(\rho, \kappa) = (\rho_2, \kappa_2)$, where large values of ρ_2 and κ_2 correspond to a reflecting, rigid material and smaller values correspond to an acoustic medium where the waves are partly reflected and partly transmitted. The material values used in the project are $\rho_1 = 1.204 \text{ kg/m}^3$ and $\kappa_1 = 141.921 \cdot 10^3 \text{ N/m}^2$ for air and $\rho_2 = 2643.0 \text{ kg/m}^3$ and $\kappa_2 = 6.87 \cdot 10^{10} \text{ N/m}^2$ for solid material (aluminum).

To introduce the design variable ξ in the following section it is convenient to use the two variables

$$\tilde{\rho} = \frac{\rho}{\rho_1} = \begin{cases} 1, & \text{air,} \\ \frac{\rho_2}{\rho_1}, & \text{solid,} \end{cases} \quad \tilde{\kappa} = \frac{\kappa}{\kappa_1} = \begin{cases} 1, & \text{air,} \\ \frac{\kappa_2}{\kappa_1}, & \text{solid.} \end{cases} \quad (2)$$

When Equation (1) is rescaled with these variables Helmholtz equation takes the form

$$\nabla \cdot (\tilde{\rho}^{-1} \nabla \hat{p}) + \tilde{\omega}^2 \tilde{\kappa}^{-1} \hat{p} = 0. \quad (3)$$

Here $\tilde{\omega} = \omega/c$ is a scaled angular frequency and $c = \sqrt{\kappa_1/\rho_1}$ is the speed of sound in air. To solve the problem the two boundary conditions are used

$$\mathbf{n} \cdot (\tilde{\rho}^{-1} \nabla \hat{p}) = 0, \quad \mathbf{n} \cdot (\tilde{\rho}^{-1} \nabla \hat{p}) = -i\tilde{\omega} \sqrt{\kappa_1 \rho_1} U. \tag{4}$$

The first boundary condition describes a perfectly reflecting surface and is employed for the rigid walls of the room. The second boundary condition expresses a vibrating surface with the vibrational velocity U and is used to imitate a point source emitting sinusoidal sound waves.

3. DESIGN VARIABLES AND MATERIAL INTERPOLATION

In topology optimization the task is to find a distribution of air and solid material in the design domain Ω_d for which the objective function is optimized. The way to find the optimal design in acoustic problems is to allow the material properties $\tilde{\kappa}$ and $\tilde{\rho}$ to take any value in between the values for air and solid material during the optimization process. To control the intermediate material properties a continuous material indicator field $0 \leq \xi \leq 1$ is introduced, where $\xi = 0$ corresponds to air and $\xi = 1$ to solid material. The material properties are now functions of ξ . Thus the two continuous property interpolation functions $\tilde{\rho}(\xi)$ and $\tilde{\kappa}(\xi)$ have to meet the conditions

$$\tilde{\rho}(\xi) = \begin{cases} 1, & \xi = 0, \\ \frac{\rho_2}{\rho_1}, & \xi = 1, \end{cases} \quad \tilde{\kappa}(\xi) = \begin{cases} 1, & \xi = 0, \\ \frac{\kappa_2}{\kappa_1}, & \xi = 1. \end{cases} \tag{5}$$

The final design is only allowed to contain material corresponding to $\xi = 0$ and $\xi = 1$ in order to be able to produce it. This can be obtained by choosing interpolation functions that somehow provide this property. In [3] it is suggested to find the interpolation functions by looking at a 1D acoustic system where a wave with an amplitude of unit magnitude propagates in air and hits an interface to an acoustic medium. The amplitudes R and T of the reflected and transmitted waves are

$$R = \frac{\sqrt{\tilde{\kappa}\tilde{\rho}} - 1}{\sqrt{\tilde{\kappa}\tilde{\rho}} + 1}, \quad T = \frac{2}{\sqrt{\tilde{\kappa}\tilde{\rho}} + 1}. \tag{6}$$

This means that $R \rightarrow 1$ and $T \rightarrow 0$ for $\tilde{\kappa}\tilde{\rho} \rightarrow \infty$ when the wave is reflected from a perfectly rigid surface, and $R \rightarrow 0$ and $T \rightarrow 1$ for $\tilde{\kappa}\tilde{\rho} \rightarrow 1$ when the wave just continuous in air. Experience shows that good 0-1 designs are obtained if the interpolation functions are chosen, such that the reflection from the acoustic medium is a smooth function of ξ with non-vanishing slopes at $\xi = 1$. According to [3] such functions are obtained if the inverse material

properties are interpolated between the two material phases as follows:

$$\tilde{\rho}(\xi)^{-1} = \left(1 + \xi^{q_1} \left(\left(\frac{\rho_2}{\rho_1} \right)^{-1} - 1 \right) \right) \cdot \left(1 + i\tilde{\omega}\nu_1\right), \quad (7)$$

$$\tilde{\kappa}(\xi)^{-1} = \left(1 + \xi^{q_2} \left(\left(\frac{\kappa_2}{\kappa_1} \right)^{-1} - 1 \right) \right) \cdot \left(1 + i\frac{\nu_2}{\tilde{\omega}}\right). \quad (8)$$

The factors ν_1 and ν_2 in the imaginary terms are small quantities below 1 which are introduced to incorporate material damping in the model. The term including ν_2 damps the lowest modes most, whereas the term with ν_1 damps the highest modes most. The two factors q_1 and q_2 are penalty factors which are used to penalize intermediate material properties.

4. THE OPTIMIZATION PROBLEM

The objective function Φ considered in this paper is the average of the squared amplitude of the sound pressure over the optimization domain, Ω_{op} . The formulation of the optimization problem then takes the form

$$\min_{\xi} \log(\Phi) = \log \left(\frac{1}{\int_{\Omega_{\text{op}}} \mathbf{d}\mathbf{r}} \int_{\Omega_{\text{op}}} |\hat{p}(\mathbf{r}, \xi)|^2 \mathbf{d}\mathbf{r} \right), \quad \text{Objective function} \quad (9)$$

$$\text{subject to } \frac{1}{\int_{\Omega_{\text{d}}} \mathbf{d}\mathbf{r}} \int_{\Omega_{\text{d}}} \xi(\mathbf{r}) \mathbf{d}\mathbf{r} - \beta \leq 0, \quad \text{Volume constraint} \quad (10)$$

$$0 \leq \xi(\mathbf{r}) \leq 1, \quad \text{Design variable bounds} \quad (11)$$

The optimization problem is solved using the Method of Moving Asymptotes (MMA) [5] and as this algorithm is performing best for moderate values of the objective function the logarithm is taken. A volume constraint is employed to put a limit on the amount of material distributed in the design domain Ω_{d} . Here β is a volume fraction of allowable material and takes values between 0 and 1, where $\beta = 1$ corresponds to no limit. To fulfil the constraint from the beginning of the optimization the initial guess for the optimized design is simply to have a uniform distribution of material in the design domain with the volume fraction β . The final design is dependent on both the initial guess and the allowable amount of material to be placed and is therefore dependent on β . Hence β can be varied to obtain good and usable designs.

5. DISCRETIZATION AND SENSITIVITY ANALYSIS

The mathematical model of the physical problem is given by the Helmholtz equation (3) and the boundary conditions (4) and to solve the problem finite element analysis is used. Hence the complex pressure amplitude field \hat{p} and

the design variable field ξ are discretized using sets of finite element basis functions $\{\phi_{i,n}(\mathbf{r})\}$

$$\hat{p}(\mathbf{r}) = \sum_{n=1}^N \hat{p}_n \phi_{1,n}(\mathbf{r}), \quad \xi(\mathbf{r}) = \sum_{n=1}^{N_d} \xi_n \phi_{2,n}(\mathbf{r}). \quad (12)$$

The values of the degrees of freedom (dofs) corresponding to the two fields are assembled in the vectors $\hat{\mathbf{p}} = \{\hat{p}_1, \hat{p}_2, \dots, \hat{p}_N\}^T$ and $\boldsymbol{\xi} = \{\xi_1, \xi_2, \dots, \xi_{N_d}\}^T$. For the model in 2D a triangular element mesh is used and tetrahedral elements are used in 3D to subdivide the domain. Quadratic Lagrange elements are used for the complex pressure amplitude \hat{p} to obtain high accuracy in the solution to the governing equation and for the design variable linear Lagrange elements are used.

The commercial program FEMLAB is employed to do the finite element analysis where the Helmholtz equation and the boundary conditions are written in general form and discretized by the standard Galerkin method, see [6]. This results in solving the discretized equation

$$\mathbf{K}_0(\hat{\mathbf{p}} - \hat{\mathbf{p}}_0) = \mathbf{L}_0, \quad (13)$$

where the stiffness matrix \mathbf{K} and the residual vector \mathbf{L} are evaluated for the linearization point $\hat{\mathbf{p}}_0$, which is indicated by the subscript 0.

To update the design variables in the topology optimization the derivatives with respect to the design variables of the objective and the constraint function are needed. First the derivative of the objective function is found. $\hat{\mathbf{p}}$ is an implicit function of the design variables, because a solution $\hat{\mathbf{p}}(\boldsymbol{\xi})$ can be found for any $\boldsymbol{\xi}$. Thus the derivative of the objective function $\Phi = \Phi(\hat{\mathbf{p}}(\boldsymbol{\xi}), \boldsymbol{\xi})$ is given by the following expression found by the chain rule:

$$\frac{d\Phi}{d\boldsymbol{\xi}} = \frac{\partial\Phi}{\partial\boldsymbol{\xi}} + \frac{\partial\Phi}{\partial\hat{\mathbf{p}}} \frac{\partial\hat{\mathbf{p}}}{\partial\boldsymbol{\xi}}. \quad (14)$$

As $\hat{\mathbf{p}}$ is an implicit function of $\boldsymbol{\xi}$ the derivative $\partial\hat{\mathbf{p}}/\partial\boldsymbol{\xi}$ is not directly known, so it is convenient to do the sensitivity analysis by use of the standard adjoint method. By this method the unknown derivative is eliminated at the expense of determining a set of Lagrange multipliers $\boldsymbol{\lambda}$ from the adjoint equation

$$\mathbf{K}^T \boldsymbol{\lambda} = \frac{\partial\Phi}{\partial\hat{\mathbf{p}}}. \quad (15)$$

The equation for the derivative of the objective function then reduces to

$$\frac{d\Phi}{d\boldsymbol{\xi}} = \frac{\partial\Phi}{\partial\boldsymbol{\xi}} + \boldsymbol{\lambda}^T \frac{\partial\mathbf{L}}{\partial\boldsymbol{\xi}}. \quad (16)$$

To do the optimization the derivative of the constraint function with respect to the design variable is also needed. The derivative with respect to one of the design variables is

$$\frac{\partial}{\partial \xi_n} \left(\frac{1}{\int_{\Omega_d} \mathbf{dr}} \int_{\Omega_d} \xi(\mathbf{r}) \mathbf{dr} - \beta \right) = \frac{1}{\int_{\Omega_d} \mathbf{dr}} \int_{\Omega_d} \phi_{2,n}(\mathbf{r}) \mathbf{dr}. \quad (17)$$

The vectors $\partial\Phi/\partial\xi$, $\partial\Phi/\partial\hat{\mathbf{p}}$ and $\int_{\Omega_d} \phi_{2,n}(\mathbf{r}) \mathbf{dr}$ as well as the matrix $\partial\mathbf{L}/\partial\xi$ are assembled in FEMLAB as described in [6]. As problems occur when the derivative of $|\hat{p}|^2$ is calculated by the symbolic differentiation available from FEMLAB (to get $\partial\Phi/\partial\xi$) it is instead calculated by hand as

$$\frac{d}{d\hat{p}}(|\hat{p}|^2) = 2(\text{Re}(\hat{p}) - i\text{Im}(\hat{p})). \quad (18)$$

As the logarithm is taken to the objective function the sensitivities are also modified as follows:

$$\frac{d(\log(\Phi(\xi)))}{d\xi} = \frac{1}{\Phi(\xi)} \frac{d\Phi(\xi)}{d\xi}. \quad (19)$$

6. OPTIMIZATION OF A RECTANGULAR ROOM IN 2D

The squared sound pressure amplitude is now minimized over the optimization domain Ω_{op} by distributing material in the design domain Ω_d in a rectangular room in 2D as shown in Figure 1. The volume fraction is chosen to $\beta = 0.15$, the vibrational velocity of the pulsating circle is $U = 0.01$ m/s and the angular frequency is $\omega = 217.125$ rad/s, which is chosen as it is a natural frequency for the room with the initial guess of the material distribution. The maximum

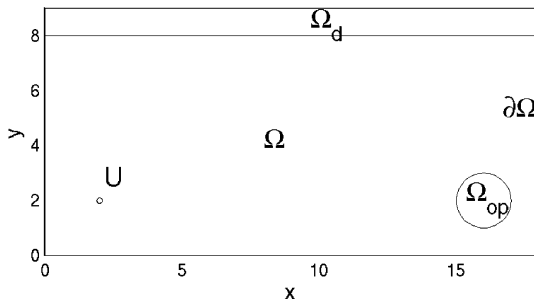


Figure 1. The dimensions of the rectangular room in 2D with the design domain Ω_d , the optimization domain Ω_{op} and the point source with the vibrational velocity U .

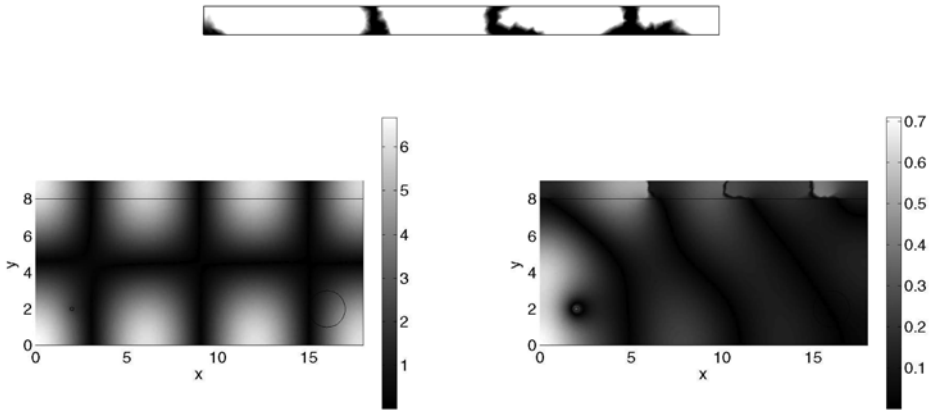


Figure 2. Top: the optimized design for a single frequency, bottom left: the sound pressure amplitude for the initial guess, bottom right: the sound pressure amplitude for the optimized design.

length of an element side hm is set to 0.3. An absolute tolerance of 0.01 on the maximal change of the design variables is used to terminate the optimization loop. The penalty factors are both equal to 1.5 and the damping factors are $\nu_1 = 0$ and $\nu_2 = 0.001$. The optimized design was found in 158 iterations and the objective function was reduced from 6.052 Pa^2 to $1.012 \cdot 10^{-3} \text{ Pa}^2$. Figure 2 shows the optimized design and the sound pressure amplitude for the initial guess and the optimized design, respectively. It is clearly seen that in comparison to the initial guess the redistributed material in the design domain is influencing the sound pressure in the room, so it is nearly zero in the optimization domain Ω_{op} , note the different scales on the color bars. Figure 3 shows the transfer function for the initial guess and the optimized design, where Φ is plotted as function of ω . It is seen that in comparison to the initial guess the

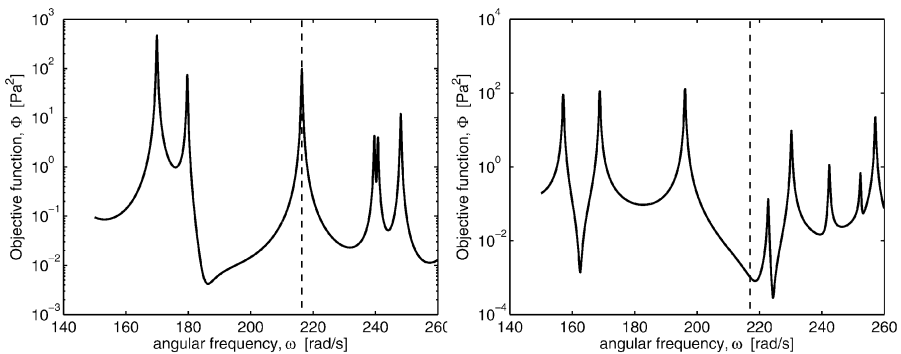


Figure 3. Transfer function for the rectangular room; left: for initial guess, right: for optimized design.

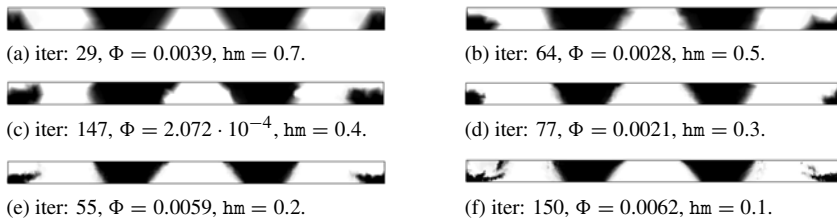


Figure 4. Optimized designs of the rectangular room for decreasing values of hm .

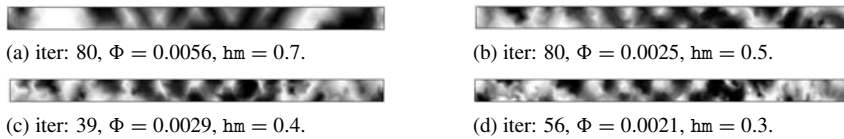


Figure 5. Optimized designs of the rectangular room for decreasing values of hm and $\omega = 4 \cdot 217.125$ rad/s.

natural frequencies for the optimized design have changed, and instead of a high response for $\omega = 217.125$ rad/s there is now a very low response for this frequency.

It is possible to get mesh-independent designs if the sensitivities are filtered as described in [4]. The idea is to modify the sensitivities $d\Phi/d\xi_n$ for each degree of freedom using a weighted average of the sensitivities in a fixed neighborhood of the actual degree of freedom. The radius of the neighborhood is given by r_{\min} . In Figure 4 the results are shown for decreasing hm and the quantities used are $r_{\min} = 0.6hm$, $q_1 = q_2 = 1.5$, $\nu_2 = 0.001$ and $\omega = 217.125$ rad/s. For this example nice 0-1 and mesh-independent designs are obtained.

In the previous examples a low frequency has been used resulting in nice optimized designs. In the next example the room is optimized for the quantities $\omega = 4 \cdot 217.125$ rad/s, $\beta = 0.5$, $q_1 = q_2 = 3$, $\nu_2 = 0.001$ and $r_{\min} = 1.0hm$. The optimized designs for decreasing hm are seen in Figure 5. The designs consist of complicated structures with a mixture of porous materials and they clearly indicate that it is difficult to get good 0-1 solutions for high angular frequencies. The reason is that for increasing angular frequency the distribution of the sound pressure amplitude in the room gets more complex and the design needed to minimize the objective function will naturally also consist of more complicated shapes and be more difficult to find.

The optimization problem is now changed such that the optimization is done for an entire frequency interval. The method is to minimize the sum of responses for a number of target frequencies ω_i in the interval considered. The critical frequencies in the interval are then updated at regular intervals during the optimization. The objective function Φ as function of the frequency is ap-

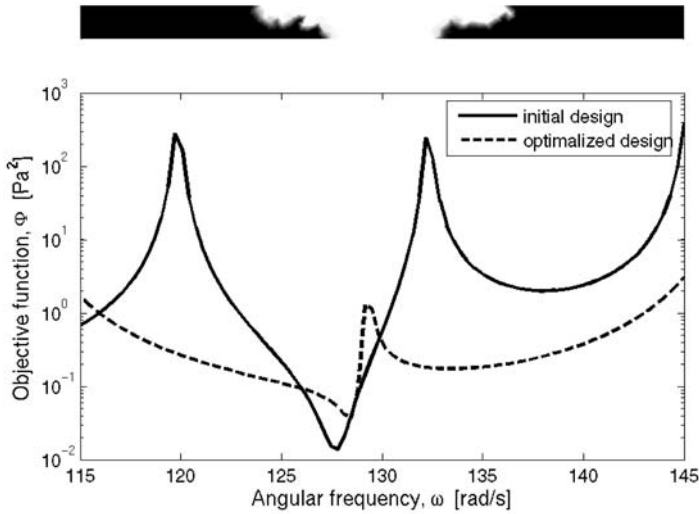


Figure 6. Top: the optimized design for the angular frequency interval [115;145] rad/s, bottom: the transfer function for the initial guess and the optimized design.

proximated using Padé expansions, see [7]. The room from Figure 1 is now optimized for the interval [115;145] rad/s using 5 target frequencies where the target frequencies are updated for each 25th optimization iteration. The quantities used in the optimization is $\beta = 0.9$, $hm = 0.3$, $q_1 = q_2 = 1.5$, $\nu_2 = 0.001$ and $r_{\min} = 0.7hm$. The optimized design obtained after 56 iterations is illustrated in Figure 6 together with the transfer function for the initial guess and the optimized design. It is seen from the two graphs that the objective function is minimized almost in the entire interval for the optimized design and that the high peaks have disappeared.

7. OPTIMIZATION OF A RECTANGULAR ROOM IN 3D

The optimization problem is now extended to 3D problems and a rectangular room with the geometry shown in Figure 7 is considered. The optimization is done for the interval [264;276] rad/s for a single target frequency which is updated for every 15th iteration. The quantities $\beta = 0.5$, $hm = 0.4$, $q_1 = q_2 = 1.5$, $\nu_2 = 0.001$ and $r_{\min} = 0.5hm$ are used. The optimized design obtained after 46 iterations is shown in Figure 8 as well as the transfer function for the initial guess and the optimized design. The material in the design has been placed along the two walls in the y -direction and the graphs show that the objective function is minimized in the entire interval for the optimized design compared to the initial guess.

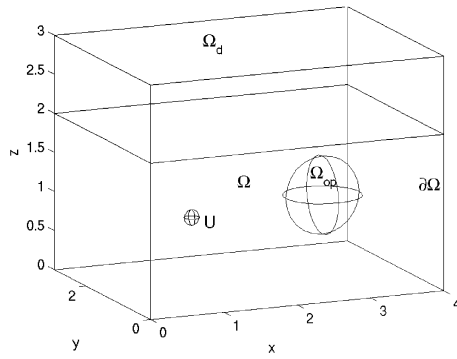


Figure 7. The dimensions of the rectangular room in 3D with the design domain Ω_d , the optimization domain Ω_{op} and the point source with the vibrational velocity U .

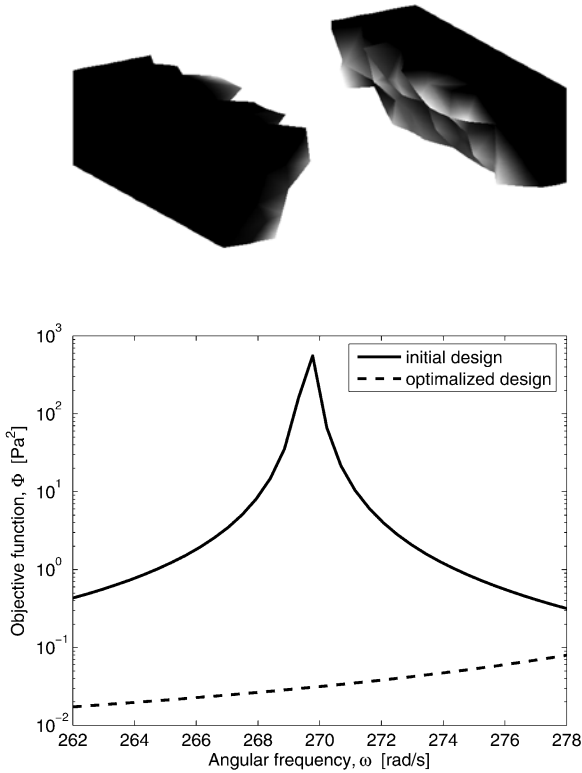


Figure 8. Top: the optimized design for the frequency interval $[262;278]$ rad/s, bottom: the transfer function for the initial guess and the optimized design.

8. CONCLUSION AND FURTHER WORK

In this paper the topology optimization method is employed to minimize the squared sound pressure amplitude in a certain part of a rectangular room with rigid walls by distribution of material in a design domain along the ceiling. The method is based on continuous material interpolation functions in the inverse density and bulk modulus and is developed for problems in 2D and 3D.

It is shown that for low frequencies nice mesh-independent, 0-1 designs can be obtained for a single frequency or a frequency interval for proper choices of penalty factors and when a mesh-independent filter is used. However, for higher frequencies the designs consist of complicated structures with a mixture of porous materials due to the more complex distribution of sound pressure amplitude in the room.

Further work includes optimization of rooms with more complicated geometries, with several sound sources and obstacles placed around the room. In addition the boundaries can have different reflecting and absorbing properties.

REFERENCES

- [1] O. Sigmund, J.S. Jensen, A. Gersborg-Hansen and R.B. Haber, Topology optimization in wave-propagation and flow problems, *Warsaw International Seminar on Design and Optimal Modelling*, WISDOM 2004, Warsaw, pp. 45–54 (2004).
- [2] O. Sigmund and J.S. Jensen, Design of acoustic devices by topology optimization, Short paper of the *5th World Congress on Structural and Multidisciplinary Optimization*, WC-SMO5 2003, pp. 267–268 (2003).
- [3] J.S. Jensen and O. Sigmund, Systematic design of acoustic devices by topology optimization, *Twelfth International Congress on Sound and Vibration*, Lisbon (2005).
- [4] M.P. Bendsøe and O. Sigmund, *Topology Optimization, Theory, Methods and Applications*, 2nd edn, Springer-Verlag, Berlin (2003).
- [5] K. Svandberg, The method of moving asymptotes – A new method for structural optimization, *International Journal for Numerical Methods in Engineering*, 24, 359–373 (1987).
- [6] L.H. Olesen, F. Okkels and H. Bruus, A high-level programming-language implementation of topology optimization applied to steady-state Navier–Stokes flow, *International Journal for Numerical Methods in Engineering*, in press, DOI: 10.1002/nme.1468 (2005).
- [7] J. Jin, *The Finite Element Method in Electromagnetics*, 2nd edn, John Wiley & Sons (2002).

TOPOLOGY OPTIMIZATION OF WAVE-PROPAGATION PROBLEMS

Jakob S. Jensen and Ole Sigmund

Department of Mechanical Engineering, Solid Mechanics, Technical University of Denmark, DK-2800 Kgs. Lyngby, Denmark

jsj@mek.dtu.dk, sigmund@mek.dtu.dk

Abstract: Topology optimization is demonstrated as a useful tool for systematic design of wave-propagation problems. We illustrate the applicability of the method for optical, acoustic and elastic devices and structures.

Keywords: Topology optimization, wave-propagation.

1. INTRODUCTION

We consider steady-state wave-propagation governed by the 2D Helmholtz equation:

$$\nabla \cdot (A(\mathbf{x})\nabla u(\mathbf{x})) + \omega^2 B(\mathbf{x})u(\mathbf{x}) = 0, \quad (1)$$

where ω is the wave frequency, $u(\mathbf{x})$ is some scalar and complex amplitude function, and $A(\mathbf{x})$ and $B(\mathbf{x})$ are position-dependent coefficients that depend on the problem. Table 1 lists the coefficients that can be applied to model acoustic, elastic and optical wave-propagation. A topology optimization algorithm [1] is applied based on a finite element discretization of Equation (1) with appropriate boundary conditions. The resulting optimization problems are solved using analytical sensitivity analysis and MMA [2].

Table 1. Choices of A and B for different 2D wave-propagation problems. Symbols: ρ (density), κ (bulk modulus), μ (shear modulus), ε (dielectric constant) and c (speed of light in vacuum).

2D wave problem	A	B
Acoustic	ρ^{-1}	κ^{-1}
Out-of-plane shear	μ	ρ
E-polarized light	1	εc^{-2}
H-polarized light	ε^{-1}	c^{-2}

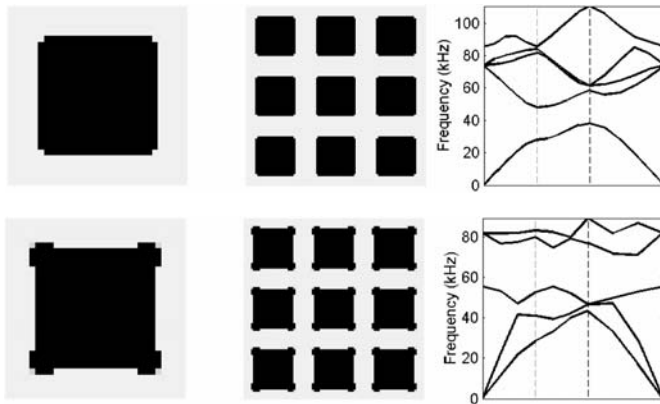


Figure 1. Optimized distribution of two elastic materials for maximizing relative bandgaps. Top figure: out-of-plane shear waves and bottom figure: in-plane waves (not governed by the Helmholtz equation). From [6].

2. MAXIMIZING BANDGAPS

Wave-propagation through an infinite material is characterized by its band diagram, relating the wave-length and -direction to the wave frequency. A periodic modulation of the material properties may introduce gaps in the diagram, the so-called band gaps.

A material layout algorithm was first used in [3, 4] to maximize bandgaps for E- and H-polarized light (photonic bandgaps), and in [5, 6] for plane elastic waves (phononic or sonic bandgaps). Figure 1 shows the optimized distribution of two elastic materials for maximizing the relative bandgap for out-of-plane shear waves (top figure) and in-plane waves (bottom figure.) An extension of the elastic problem is found in [7] dealing also with bending waves.

3. MAXIMIZING TRANSMISSION IN OPTICAL DEVICES

Using topology optimization to maximize the transmission through photonic crystal devices was suggested in [8, 9].

Topology optimized photonic crystal structures have recently been fabricated [10–13], and the optimized structures (two of them shown in Figure 2) display very good broadband performance in good agreement with 3D computations.

4. DESIGN OF ACOUSTIC DEVICES

In [14–16] topology optimization was used to design acoustic devices. Figure 3 shows an example of an optimized acoustic de-multiplexor. A broadband wave

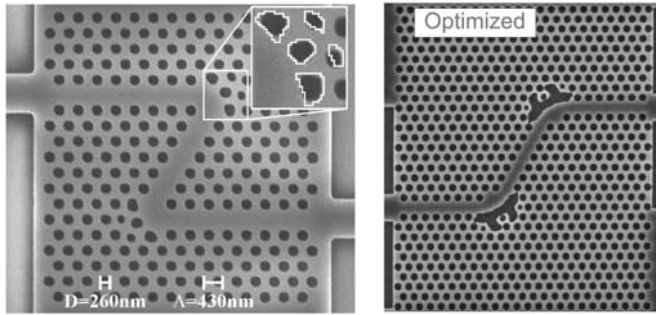


Figure 2. Optimized 120-degree and 60-degree bends in 2D photonic crystal waveguides. The fabricate structures display low transmission loss for large wavelength ranges in good agreement with 3D computations. From [10] and [11].

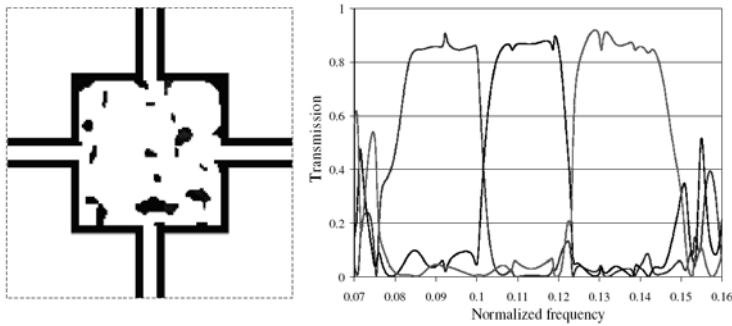


Figure 3. Topology optimized acoustic de-multiplexor. A broadband wave enters in the left channel and exits in the top, right or lower channel depending on the frequency. The transmission curves right show the fraction of the input energy that is transmitted through the three channels.

enters the chamber from the left channel and is transmitted into the other three channels depending on the frequency. As shown in the transmission plot, about 90% of the input energy is transmitted into the appropriate channel in quite large frequency ranges with very little cross-talk between channels.

5. CONCLUSION

We have demonstrated how topology optimization can be used as a tool for optimization of optical, acoustic and elastic wave-propagation problems. Further work in this direction deals with multi-physics applications, e.g. elasto-acoustic, fluid-structure and opto-elastic interaction problems.

REFERENCES

- [1] Bendsøe, M.P. and Sigmund, O., *Topology Optimization: Theory, Methods and Applications*, Springer Verlag, Berlin (2003).
- [2] Svanberg, K., The Method of Moving Asymptotes – A new method for structural optimization, *International Journal for Numerical Methods in Engineering*, 24, 359–373 (1987).
- [3] Cox, S.J. and Dobson, D.C., Maximizing band gaps in two-dimensional photonic crystals, *SIAM J. Appl. Math.*, 59, 2108–2120 (1999).
- [4] Cox, S.J. and Dobson, D.C., Band structure optimization of two-dimensional photonic crystals in *H*-polarization, *J. Comp. Phys.*, 158, 214–224 (2000).
- [5] Sigmund, O., Microstructural design of elastic band gap structures, in *Proceeding of the fourth World Congress of Structural and Multidisciplinary Optimization WCSMO-4*, on CD-Rom (2001).
- [6] Sigmund, O. and Jensen, J.S., Systematic design of phononic band-gap materials and structures by topology optimization, *Proc. R. Soc. London, Ser. A*, 361, 1001–1019 (2003).
- [7] Halkjær, S., Sigmund, O. and Jensen, J.S., Inverse design of phononic crystals by topology optimization, *Zeitschrift für Kristallographie*, 220, 895–905 (2005).
- [8] Jensen, J.S. and Sigmund, O., Systematic design of photonic crystal structures using topology optimization: Low-loss waveguide bends, *Applied Physics Letters*, 84, 2022–2024 (2004).
- [9] Jensen, J.S. and Sigmund O., Topology optimization of photonic crystal structures: A high-bandwidth low-loss T-junction waveguide, *J. Opt. Soc. Am. B*, 22(6), 1191–1198 (2005).
- [10] Borel, P.I., Harpøth, A., Frandsen, L.H., Kristensen, M., Shi, P., Jensen, J.S. and Sigmund, O., Topology optimization and fabrication of photonic crystal structures, *Optics Express*, 12(9), 1996–2001 (2004).
- [11] Frandsen, L.H., Harpøth, A., Borel, P.I., Kristensen, M., Jensen, J.S. and Sigmund, O., Broadband photonic crystal waveguide 60-degree bend obtained using topology optimization, *Optics Express*, 12(24), 5916–5921 (2004).
- [12] Borel, P.I., Frandsen, L.H., Harpøth, A., Kristensen, M., Jensen, J.S. and Sigmund, O., Topology optimised broadband photonic crystal Y-splitter, *Electron. Lett.*, 41(2), 69–71 (2005).
- [13] Jensen, J.S., Sigmund, O., Frandsen, L.H., Borel, P.I., Harpøth, A. and Kristensen, M., Topology design and fabrication of an efficient double 90-degree photonic crystal waveguide bend, *IEEE Photonics Technology Letters*, 17(6), 1202–1204 (2005).
- [14] Sigmund, O. and Jensen, J.S., Design of acoustic devices by topology optimization, in *Short Papers of the 5th World Congress on Structural and Multidisciplinary Optimization WCSMO5*, pp. 267–268 (2003).
- [15] Sigmund, O., Jensen, J.S., Gersborg-Hansen, A. and Haber, R.B., Topology optimization in wave-propagation and flow problems, in *Proceedings of Warsaw International Seminar on Design and Optimal Modelling WISDOM*, pp. 45–54 (2004).
- [16] Sigmund, O. and Jensen, J.S., Systematic design of acoustic devices by topology optimization, in *Proceedings of 12th International Congress on Sound and Vibration ICSV12* (2005).

TOPOLOGY OPTIMIZATION OF PIEZOELECTRIC ACTUATORS CONSIDERING GEOMETRIC NONLINEARITIES

Eduardo Lenz Cardoso¹ and Jun Sérgio Ono Fonseca²

¹*Department of Mechanical Engineering, UDESC, Joinville, Brazil*

²*Department of Mechanical Engineering, UFRGS, Porto Alegre, Brazil*

lenz@joinville.udesc.br, jun@ufrgs.br

Abstract: This work shows a methodology for the optimum design of piezoelectric actuators undergoing large deformations. An equilibrium formulation for the finite movement of a piezoelectric body is introduced, as well as its finite element discretization. The solution of the nonlinear finite element equations is accomplished through a new coupled-field arc-length algorithm. The optimization consists in the maximization of the output displacements subject to volume and displacement constraints. Sensitivities are derived with respect to mechanical displacements and electric potentials. The Generalized Method of Moving Asymptotes (GMAA) is used for the solution of the optimization problem. The results obtained with the proposed formulation are shown and the influence of the geometric nonlinearities is discussed.

Keywords: Topology optimization, piezoelectric actuators, geometric nonlinearities.

1. INTRODUCTION

Piezoelectric materials are usually fabricated in simple geometries and operate in simple deformation modes. Additionally, for the usual electric fields and dimensions, the displacements are quite small, requiring the use of some mechanical amplification mechanisms. Many of such devices are described in the literature, mostly small improvements of existing designs.

Recently, Topology Optimization was introduced as a tool for designing these mechanisms, with substantial improvements in their performance and allowing non-traditional actuation modes (Silva and Kikuchi, 1999; Bendsøe and Sigmund, 2003). Additionally, recent works on the design of compliant mechanisms (Buhl et al., 2000; Sigmund, 2001; Bruns and Tortorelli, 2001) have shown that considering geometric nonlinearities might lead to different topologies. These designs could be stable under other loading conditions, avoid

locking positions and avoid elastic instabilities. It is also possible to consider nonlinear springs and stress-stiffening/softening effects.

This text presents a methodology for the optimum design of piezoelectric transducers considering the geometric nonlinearities.

2. FINITE ELEMENTS FOR LARGE-DEFORMATION PIEZOELECTRICITY

A finite element formulation for the mechanics of large deformation piezoelectricity was recently published (Cardoso and Fonseca, 2004). It is a total Lagrangian incremental formulation, referring all variables at the instant $t + \Delta t$ to the initial ($t = 0$) domain Ω_0 and its initial boundary Γ_0 .

The incremental fields for the mechanical displacement and electrical potential fields $\Delta \mathbf{u}$ and $\Delta \phi$ are approximated inside each finite element e as

$$\Delta u_I^e \simeq N_{\alpha I}^u \Delta U_{\alpha I}^e, \quad (1)$$

$$\Delta \phi^e \simeq N_{\alpha}^c \Delta \Phi_{\alpha}^e, \quad (2)$$

where $\alpha \in [1, nen]$ and nen are the number of nodes of each finite element, $I \in [1, 3]$ are the Cartesian coordinates, $N_{\alpha I}^u$ are the shape functions for the displacement increments of the I direction of the α node and $\Delta U_{\alpha I}^e$ its corresponding nodal value, whereas N_{α}^c is the shape function for the electric potential increment of the α node and $\Delta \Phi_{\alpha}^e$ its nodal value. An 8-node serendipity plane stress finite element was chosen.

This discretization is used to define a finite element approximation to the Principle of the Minimum Total Potential Energy, which states that the variation ${}^{t+\Delta t} \delta_{a_n}$ at the time $t + \Delta t$ with respect to any component n of a vector field a of the internal energy minus the external work W_{ext} should vanish

$${}^{t+\Delta t} \delta_{a_n} \int_{\Omega_0} G \, d\Omega_0 + {}^{t+\Delta t} \delta_{a_n} W_{\text{ext}} = 0. \quad (3)$$

The internal energy is given by the Gibbs functional

$$G = \frac{1}{2} E_{ij} C_{ijkl} E_{kl} - \frac{1}{2} \varphi_i \epsilon_{ij} \varphi_j - \varphi_k e_{kij} E_{ij}, \quad (4)$$

where \mathbf{E} is the Green–Lagrange strain tensor, \mathbf{C} is the fourth-order elastic coefficient tensor, $\boldsymbol{\varphi}$ is the electric field vector, $\boldsymbol{\epsilon}$ is the second-order dielectric coefficient tensor, and \mathbf{e} is the third-order piezoelectric coefficient tensor. The work of the external loads is given by the mechanical body forces \mathbf{b} , the mechanical surface tractions \mathbf{t} , and the electric surface charges $\boldsymbol{\sigma}$.

$$W = \int_{\Omega_0} \mathbf{b} \cdot \mathbf{u} \, d\Omega_0 + \int_{\Gamma_0} \mathbf{t} \cdot \mathbf{u} \, d\Gamma_0 - \int_{\Gamma_0} \boldsymbol{\sigma} \phi \, d\Gamma_0. \quad (5)$$

After assembly, it yields the nonlinear finite element equations

$$\begin{bmatrix} \mathbf{K}_{uu} & \mathbf{K}_{u\phi} \\ \mathbf{K}_{\phi u} & -\mathbf{K}_{\phi\phi} \end{bmatrix} \begin{Bmatrix} \Delta \mathbf{U} \\ \Delta \Phi \end{Bmatrix} = \begin{Bmatrix} {}_0^{t+\Delta t} \mathbf{F}_{\text{ext}} \\ {}_0^{t+\Delta t} \mathbf{Q}_{\text{ext}} \end{Bmatrix} - \begin{Bmatrix} {}_0^t \mathbf{F}_{\text{int}} \\ {}_0^t \mathbf{Q}_{\text{int}} \end{Bmatrix} = \mathbf{R}, \quad (6)$$

where \mathbf{K}_{uu} is the nonlinear mechanical stiffness matrix, $\mathbf{K}_{\phi\phi}$ is the nonlinear electrical matrix, $\mathbf{K}_{u\phi}$ is the electromechanical coupling matrix, ${}_0^{t+\Delta t} \mathbf{F}_{\text{ext}}$ is the external mechanical force increment vector, and ${}_0^{t+\Delta t} \mathbf{Q}_{\text{ext}}$ is the external electric charges increment vector. It is convenient to rearrange Equation (6) as a simpler system

$$\mathbf{K}_t \Delta \mathbf{x} = {}_0^{t+\Delta t} \mathbf{P}_{\text{ext}} - {}_0^t \mathbf{F} = \mathbf{R}. \quad (7)$$

where \mathbf{K}_t is the coupled tangent matrix, \mathbf{x} is the state vector with the displacement increments and the electric potential increments. \mathbf{P}_{ext} is the external loading vector, and \mathbf{F} is the internal forces vector. \mathbf{R} is the residual which should vanish at the equilibrium.

This nonlinear system of equations is solved with a modified GDC (Generalized Displacement Control) algorithm described in Cardoso and Fonseca (2004, 2005). Additional care is taken to ensure that the exact load is applied (load multiplier is unitary) at the end of the nonlinear analysis, because this condition is not necessarily satisfied in arc-length algorithms. This is very important because the lack of consistence between successive analyses can prevent the GMMA optimization algorithm to build a good convex approximation.

3. DESIGN OF PIEZOELECTRIC TRANSDUCTORS

The formulation adopted here for the design of piezoelectric transducers is an extension of the formulation for the design of geometric nonlinear compliant mechanisms used by Buhl et al. (2000) and Brun and Tortorelli (2001). In a given admissible domain, some points are defined as output ports, to which output springs attached to simulate the stiffness of the external medium. The goal is to find the design that maximizes the displacement of the output port, subject to a volume constraint. Additionally, it is possible to impose displacement constraints, for instance to avoid the lateral movement of the output port.

$$\begin{aligned} & \text{Max} && u_{\text{out}} \\ & \text{Subject to} && V \leq \bar{V} \\ & && g(\mathbf{u}) = 0 \end{aligned} \quad (8)$$

where u_{out} is the output displacement, V is the volume of the mechanism, \bar{V} is the upper bound on the volume, $g(u) = 0$ expresses the optional displacement constraints. The extension proposed here imposes the input as an electric potential instead of a mechanical force.

The domain contains a fixed (non-design) regions of piezoelectric material whereas the design domains is assumed to be made of an isotropic material.

The design variable is the isotropic material density distribution, using a cubic relation between the elastic properties and the density (SIMP), so that the Youngs modulus is expressed as $E = \rho^3 E^0$. Densities are assumed constant within each finite element, so the number of design variables is equal the number of finite elements in the isotropic material domain.

Filtering is a well known technique to avoid numerical instabilities and to control the complexity of the topology optimization solution (Bendsøe and Sigmund, 2003). This work uses a moving limit filter, where neighborhood dependent box constraints for each variable are introduced in each optimization step, as described in Cardoso and Fonseca (2003).

3.1 Sensitivity Analysis

Volume Sensitivity to the Design Variables. In this work, the volume is used as a constraint in the optimization. The volume is expressed simply as

$$V = \sum_{i=1}^{n \text{ elems}} A_i * \rho_i, \quad (9)$$

where A_i and ρ_i are the element area and density. The derivative is given directly by

$$\frac{dV}{d\rho_i} = A_i * \rho_i. \quad (10)$$

Derivative of the State Vector with Respect to the Design Variables. Using the adjoint approach to the derivation of the derivative of the x_i component of the state vector, we start with

$$x_i = \mathbf{L}i^T \mathbf{x} + \boldsymbol{\lambda}_g^T \mathbf{R}, \quad (11)$$

where $\boldsymbol{\lambda}_g$ is the adjoint vector and the L_i is the localization vector. Differentiating x_i with respect to a design variable yields

$$\frac{dx_i}{d\rho_m} = \mathbf{L}i^T \frac{d\mathbf{x}}{d\rho_m} + \boldsymbol{\lambda}_g^T \left(\frac{d\mathbf{R}}{d\mathbf{x}} \frac{d\mathbf{x}}{d\rho_m} + \frac{\partial \mathbf{R}}{\partial \rho_m} \right). \quad (12)$$

Collecting the common terms results in

$$\frac{dx_i}{d\rho_m} = \frac{d\mathbf{x}}{d\rho_m} \left(\mathbf{L}i^T + \boldsymbol{\lambda}_g^T \frac{d\mathbf{R}}{d\mathbf{x}} \right) + \boldsymbol{\lambda}_g^T \frac{\partial \mathbf{R}}{\partial \rho_m}, \quad (13)$$

which is further developed by choosing $\boldsymbol{\lambda}_g$ such as the expression between parenthesis vanishes and thus eliminating the need to compute $d\mathbf{x}/d\rho_m$.

$$\mathbf{K}_i \boldsymbol{\lambda}_g = \mathbf{L}i. \quad (14)$$

As λ_g is now known, the sensitivity (13) can be expressed as

$$\frac{dx_i}{d\rho_m} = \lambda_g^T \frac{\partial \mathbf{R}}{\partial \rho_m}. \tag{15}$$

The solution of (14) is quite simple and costs only a backsubstitution. The inner product in Equation (15), is calculated element by element.

Special care was taken with the sensitivities for the boundary conditions, since the electric potentials are equivalent to non-homogeneous essential boundary conditions. The formulation presented by Cho and Jung (2003) for prescribed displacements was easily extended to this application, allowing the calculation of the sensitivities with prescribed Dirichlet conditions for both mechanical (displacements) and electrical (potentials) fields.

3.2 Optimization Algorithm

Optimization was performed by a implementation of the Generalized Method of Moving Asymptotes (GMA) shown in Zhang et al. (1996). The implementation uses a Conjugate Gradients algorithm for the dual problem. It also explicitly includes box constraints for each variable for the moving limit neighborhood filtering.

4. RESULTS

This formulation is suitable for the design of both actuators and sensors, although this work presents only applications to actuators.

In the following results, the fixed piezoelectric material is PZT-5, with elastic, dielectric and piezoelectric material properties given by

$$\mathbf{C} = \begin{bmatrix} 12.1 & 7.54 & 7.52 & 0.0 & 0.0 & 0.0 \\ 7.54 & 12.1 & 7.52 & 0.0 & 0.0 & 0.0 \\ 7.52 & 7.52 & 11.1 & 0.0 & 0.0 & 0.0 \\ 0.0 & 0.0 & 0.0 & 2.1 & 0.0 & 0.0 \\ 0.0 & 0.0 & 0.0 & 0.0 & 2.1 & 0.0 \\ 0.0 & 0.0 & 0.0 & 0.0 & 0.0 & 2.3 \end{bmatrix} * 10^{10} \text{ Pa}, \tag{16}$$

$$\frac{\epsilon}{\epsilon_0} = \begin{bmatrix} 1650 & 0.0 & 0.0 \\ 0.0 & 1650 & 0.0 \\ 0.0 & 0.0 & 1700 \end{bmatrix}, \tag{17}$$

$$\mathbf{e} = \begin{bmatrix} 0.0 & 0.0 & 0.0 & 0.0 & 12.3 & 0.0 \\ 0.0 & 0.0 & 0.0 & 12.3 & 0.0 & 0.0 \\ -5.4 & -5.4 & 15.8 & 0.0 & 0.0 & 0.0 \end{bmatrix} \text{ Cm}^{-2} \tag{18}$$

and the isotropic material to be designed is copper ($E = 110 \text{ GPa}$ and $\nu = 0.34$). Full geometry was modelled with finite elements, while symmetry was

enforced throughout the design variables. Densities ranged from the lower bound of 10^{-3} to one.

4.1 Moonie-Type Actuator

In this case, it is chosen a 60×60 mm domain with a 30×4 mm piezoelectric insert considering a 15 mm thickness, as shown in Figure 1. The PZT-5 is polarized upwards, and its submitted to a 100 V/mm electric field. An output spring is added to the output port. A regular mesh of 3600 elements was used, as well as a 20% constraint on the volume fraction.

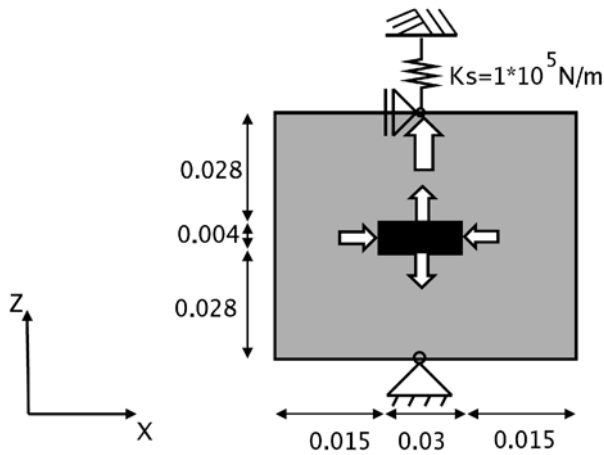


Figure 1. Design domain of a Moonie Actuator (dimensions in meters).

Without filtering, the optimization failed to yield meaningful results, stopping in most runs at some low performance local minima for both linear and nonlinear formulations. Once filtering was introduced, results as shown in Figure 2 were systematically obtained. The designs obtained by this formulation depend heavily on hinges to work; large deformation effects are mostly confined to the hinges, so there are almost no differences between the linear and nonlinear models, as shown in Table 1.

Table 1. Normalized displacement values for the designs shown in Figure 2.

Linear	Nonlinear	Diference between models
1.00	0.997	0.3%



Figure 2. Topologies obtained for the linear (left) and nonlinear (right) cases, using filtering.



Figure 3. Topologies obtained considering constant, linear, and quadratic output springs.

Table 2. Normalized displacements of the designs shown in Figure 3.

Stiffness	Constant	Linear	Quadratic
Displacement	1.00	0.514	0.654

Nonlinear stiffness of the output spring is possible only with the nonlinear model, and did influence the results, as shown in Figure 3 and in Table 2. In this case, the output spring stiffness was chosen to be constant (10^5 N/m), linear-stiffening ($10^5 + 4 * 10^1 u_{out}$ N/m), or softening-stiffening quadratic ($10^5 - 10^1 u_{out} + 10^1 7u_{out}^2$ N/m). The linear model can consider only constant stiffness.

4.2 Bridge Actuator

Another popular actuator is the bridge actuator (Figure 4) which uses two piezoelectric actuators to obtain a transverse displacements. Actuation is performed by six PZT-5. A regular mesh of five thousands elements was used. Three different output stiffnesses are considered.

As in the case of the Moonie actuator, only small details differ nonlinear and linear designs (Figure 5). With low rigidity of the output, the resulting designs uses hinges, whereas with high output force the designs have small output displacements. In both cases the nonlinear influence is small.

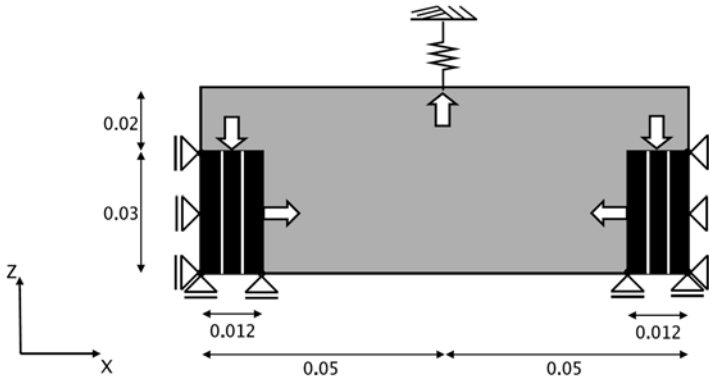


Figure 4. Design domain for the bridge actuator (dimensions in meters).

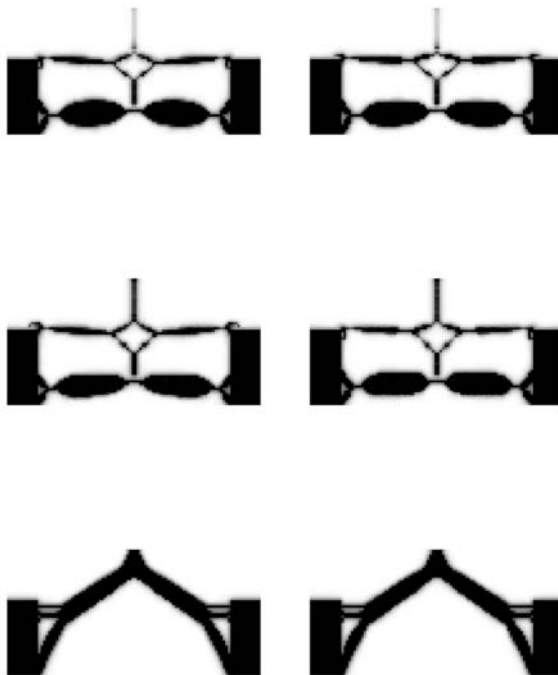


Figure 5. Topologies obtained for the linear (left) and nonlinear (right), for constant stiffness ouptup springs with $K_s = 1 * 10^2$ N/m (first line), $K_s = 1 * 10^5$ N/m (second line) and $K_s = 1 * 10^{10}$ N/m (third line), with 20% volume constraint.

The use of lower stiffness of the output spring, has also the side effect of the appearance of intermediate densities on the output region. The low-density material is sufficiently stiff to move the output, and the resulting designs become difficult to be interpreted.

5. CONCLUSIONS

A procedure for the topology design for geometric nonlinear piezoelectric structures was developed, together with its sensitivity analysis. The optimization problem is set as the maximization of the output port displacement against a spring. Tests show that filtering is essential to obtain meaningful designs. The results show no significant difference between the linear and nonlinear designs for this optimization setting in the case of linear springs.

The objective function of maximizing the output displacement favours designs with hinges, which reduces the influence of the geometric nonlinearities. Therefore the authors suggest the development of an alternative formulation for the optimization problem.

ACKNOWLEDGMENTS

The authors acknowledge the financial support provided by CAPES – Brasília and the useful contributions by Emílio C. N. Silva, Rogério J. Marczak, and Pablo A. Muñoz R.

REFERENCES

- Bendsøe, M.P. and Sigmund, O. (2003) *Topology Optimization: Theory, Methods and Applications*, Springer Verlag, Berlin.
- Bruns, T.E. and Tortorelli, D.A. (2001) Topology optimization of non-linear elastic structures and compliant mechanisms, *Computer Methods in Applied Mechanics and Engineering*, 150, 3443–3453.
- Buhl, T., Pedersen, C.B.W. and Sigmund, O. (2000) Stiffness design of geometrically nonlinear structures using topology optimization, *Structural and Multidisciplinary Optimization*, 19(2), 93–104.
- Cardoso, E.L. and Fonseca, J.S.O. (2003) Complexity control in the topology optimization of continuum structures, *Journal of the Brazilian Society of Mechanical Sciences and Engineering*, XXV(3), 293–301.
- Cardoso, E.L. and Fonseca, J.S.O. (2004) An incremental Lagrangian formulation to the analysis of piezoelectric bodies subjected to geometric non-linearities, *International Journal for Numerical Methods in Engineering*, 57(7), 895–1020.
- Cardoso, E.L. and Fonseca, J.S.O. (2005) The GDC method as an orthogonal arc-length method, submitted.
- Cho, S. and Jung, H.-S. (2003) Design sensitivity analysis and topology optimization of displacement-loaded non-linear structures, *Computer Methods in Applied Mechanics and Engineering*, 192, 2539–2553.

- Sigmund, O. (2001) Design of multiphysics actuators using topology optimization – Part I: One-material structures, *Computer Methods in Applied Mechanics and Engineering*, 190(49–50), 6577–6604.
- Silva, E.C.N. and Kikuchi, N. (1999) Design of piezoelectric transducers using topology optimization, *Smart Materials and Structures*, 8, 350–364.
- Zhang, W.H., Fleury, C., Duysinx, P., Nguyen, V.H. and Laschet, I. (1996) A generalized method of moving asymptotes (GMA) including equality constraints, *Structural Disciplinary Optimization*, 12, 143–165.

Mathematical Programming Issues

THE WORST-CASE MULTIPLE LOAD FMO PROBLEM REVISITED

Michal Kočvara¹ and Michael Stingl²

¹*Institute of Information Theory and Automation, Academy of Sciences of the Czech Republic, Pod vodárenskou věží 4, 18208 Prague; and Faculty of Electrical Engineering, Czech Technical University, Technická 2, 16627 Prague, Czech Republic*

²*Institute of Applied Mathematics, University of Erlangen, Martensstr. 3, 91058 Erlangen, Germany*

kocvara@utia.cas.cz, mstingl@am.uni-erlangen.de

Abstract: We propose a new formulation of the worst-case multiple-load problem of free material optimization. It leads to an optimization problem with bilinear matrix inequality constraints. The resulting problem can be solved by a recently developed code PENBMI. The new formulation is shown to be more computationally efficient than the recently used one.

Keywords: Free material optimization, semidefinite programming.

1. INTRODUCTION

We want to solve a worst-case multiple load formulation of the free material optimization (FMO) problem. The formulation used so far (for instance in the FMO code MOPED; Hörnlein et al., 2001) leads to a (large-scale) linear semidefinite programming (SDP) problem. This has two main disadvantages:

- the SDP problem is much more complex than a nonlinear program of the same dimension – consequently, we can only solve problems of much smaller dimension than in the single-load case;
- the result gives us just indirect information about the properties of the optimal material; the full material matrix can only be obtained by expensive postprocessing.

We propose to solve the multiple load problem by means of another formulation which was known for some time but which has never been used for the numerical solution. The reason for that was that it leads to an SDP problem with bilinear matrix inequality (BMI) constraints. Until now, there was no soft-

ware for this kind of problems available. We solve the problem by our recently developed code PENBMI. Using the BMI formulation, we can avoid the two difficulties mentioned above. Though nonlinear, the BMI formulation leads to problems with very sparse data that can be solved efficiently even for high dimensional problems. Further, the optimal material matrices can be obtained directly as Lagrangian multipliers of the BMI constraints, provided by PENBMI. Finally, the number and size of the constraints are independent of the number of load cases, contrary to the formulation used so far.

2. THE FMO MULTIPLE-LOAD PROBLEM

We study the optimization of the design of a *continuum* structure that is loaded by multiple independent forces. In order to deal with the problem in a very general form, we consider the *distribution of the material in space* as well as the *material properties at each point* as design variables. The idea to treat the material itself as a function of the space variable goes back to the work by Bendsoe et al. (1994) and has also been studied in various other contexts (see Bendsoe and Sigmund, 2002; Zowe et al., 1997).

We look for a structure within a domain Ω which can withstand a whole set of loads f^ℓ , $\ell = 1, \dots, L$, in the worst-case sense. This leads to the following multiple-load design problem, in which we seek the design function E which yields the smallest possible worst-case compliance¹

$$\inf_{E \in \mathcal{E}} \sup_{\ell=1, \dots, L} \sup_{u \in \mathcal{H}} \left\{ -\frac{1}{2} \int_{\Omega} \langle Ee(u), e(u) \rangle dx + F^\ell(u) \right\}. \quad (1)$$

Here

$$F^\ell(u) := \int_{\Gamma} f^\ell \cdot u dx \quad \text{for } \ell = 1, \dots, L, \quad (2)$$

and

$$\mathcal{E} := \left\{ E \in [L^\infty(\Omega)]^{3 \times 3} \mid E \succcurlyeq 0, \int_{\Omega} \text{tr}(E) dx \leq V, 0 \leq \text{tr}(E) \leq \bar{\rho} \right\}.$$

3. THE CURRENT APPROACH

Assume that Ω is partitioned into M finite elements Ω_m of volume ω_m and let N be the number of nodes. We approximate E by a function that is constant on each element Ω_m , i.e., E becomes a vector (E_1, \dots, E_M) of 3×3 matrices E_m . The feasible set \mathcal{E} is replaced by its discrete counterpart

$$\mathcal{E} := \left\{ E \in \mathbb{R}^{3 \times 3M} \mid \begin{array}{l} E_m = E_m^T \succcurlyeq 0 \text{ and } \text{tr}(E_m) \leq \bar{\rho}, \quad m = 1, \dots, M \\ \sum_{m=1}^M \text{tr}(E_m) \omega_m \leq V \end{array} \right\}.$$

To avoid merely technical details we neglect in the following the constraint $\text{tr}(E_m) \leq \bar{\rho}$. We further approximate the displacement vector by a piecewise bi-linear function $u^\ell(x) = \sum_{n=1}^N u_n^\ell \vartheta_n(x)$ where ϑ_n is the basis function associated with n th node; i.e., $u = (u_1, \dots, u_N) \in \mathbb{R}^D$, $D \leq 2N$.

For basis functions $\vartheta_n, n = 1, \dots, N$, we define matrices

$$B_n(x) = \begin{pmatrix} \frac{\partial \vartheta_n}{\partial x_1} & 0 \\ 0 & \frac{\partial \vartheta_n}{\partial x_2} \\ \frac{1}{2} \frac{\partial \vartheta_n}{\partial x_2} & \frac{1}{2} \frac{\partial \vartheta_n}{\partial x_1} \end{pmatrix}.$$

For an element Ω_m , let \mathcal{D}_m be an index set of nodes belonging to this element. The value of the approximate strain tensor e on element Ω_m is then (we add the space variable x as a subscript to indicate that $e_x(u^\ell)$ is a function of x)

$$e_x(u^\ell) = \sum_{n \in \mathcal{D}_m} B_n(x) u_n^\ell \quad \text{on } \Omega_m.$$

Finally, the linear functional $F^\ell(u^\ell)$ reduces to $(f^\ell)^T u^\ell$ with some $f^\ell \in \mathbb{R}^D$.

The discrete character of the “ sup ” in (1) is treated using a weight vector λ for the loads, which runs over the unit simplex

$$\Lambda := \left\{ \lambda \in \mathbb{R}^L \mid \sum_{\ell=1}^L \lambda_\ell = 1, \lambda_\ell \geq 0 \text{ for } \ell = 1, \dots, L \right\}.$$

Further we put $\mathbf{v} := (v^1, \dots, v^L)$,

$$\mathcal{V} := \{(\mathbf{v}; \lambda) \mid \mathbf{v} \in [\mathcal{H}]^L, \lambda \in \Lambda^0\}$$

and denote $(\mathbf{v}; \lambda) = (v^1, \dots, v^L; \lambda) \in \mathcal{V}$.

Denote by $x_{ms} \in \Omega_m$ the Gaussian points and by γ_{ms}^2 the corresponding weights; here $s = 1, \dots, S$. With the $(d \times LS)$ -matrix

$$Z_m := [\gamma_{m1} e_{x_{m1}}(v^1), \dots, \gamma_{ms} e_{x_{ms}}(v^1), \dots, \gamma_{m1} e_{x_{m1}}(v^L), \dots, \gamma_{ms} e_{x_{ms}}(v^L)]$$

and the $(LS \times LS)$ -matrix

$$\Lambda(\lambda) := \text{diag}(\lambda_1, \dots, \lambda_1, \dots, \lambda_L, \dots, \lambda_L)$$

the problem can be written as a linear *semidefinite program*:

$$\inf_{\substack{(\mathbf{v}; \lambda) \in \mathcal{V} \\ \tau \in \mathbb{R}}} \alpha \tau - 2 \sum_{\ell=1}^L (f^\ell)^T v^\ell \tag{3}$$

$$\text{subject to } \begin{pmatrix} \tau I_d & Z_m(\mathbf{v}) \\ Z_m(\mathbf{v})^T & \Lambda(\lambda) \end{pmatrix} \succcurlyeq 0 \quad \text{for } m = 1, \dots, M.$$

The question of recovering the optimal elasticity matrices E_1^*, \dots, E_M^* from the solution of (3) is a bit technical; we refer the reader to Ben-Tal et al. (1997).

This formulation is currently implemented in the computer program MOPED (Hörnlein et al., 2001). The linear SDP problem (3) is solved by a generalized augmented Lagrangian algorithm implemented in the general-purpose optimization code PENNON (Kočvara and Stingl, 2003). Although it allows us to solve real-world size problems, it has certain *disadvantages*:

- the constraint matrices in (3) are sparse but relatively large and, compared to the single-load problem, the solution time is considerably high for large problems;
- the size of the constraint matrices is linearly proportional to the number of load cases (see the dimension of $Z_m(\mathbf{v})$); that means, the solution time for problems with a higher number of load cases is rather high;
- the dimension of the constraint matrices in (3) increases considerably when switching from 2d to the 3d problems (from $8 \cdot 4 \cdot L$ to $24 \cdot 8 \cdot L$);
- the optimal elasticity matrices E_1^*, \dots, E_M^* are not readily available and their recovering requires solution of an auxiliary problem (see Ben-Tal et al., 1997).

4. THE NEW APPROACH

Recall the discretized single-load formulation of the FMO problem: For an element Ω_i , let \mathcal{D}_i be an index set of nodes belonging to this element.

$$A_m = \sum_{k, \ell \in \mathcal{D}_i} \int_{\Omega_i} B_k^T B_\ell dx. \quad (4)$$

The discretized single load problem can be reduced to a convex NLP

$$\min_{\alpha, u} \alpha V - f^T u \quad \text{s.t.} \quad \frac{1}{2} u^T A_m u \leq \alpha, \quad m = 1, \dots, M$$

(see Zowe et al., 1997). This formulation is extremely numerically efficient due to its convexity, simplicity and sparsity of the constraints.

It turns out that the multiple load problem can be formulated in a way mimicking the structure of the single-load problem (4) and thus sharing some of its advantages.

The multiple-load problem (1) is a Lagrange dual to the following problem

$$\begin{aligned} \min_{\alpha, \lambda^\ell, u^\ell} \quad & \alpha V - \sum_{\ell=1}^L \lambda^\ell (f^\ell)^T u^\ell \\ \text{s.t.} \quad & \sum_{\ell=1}^L \lambda^\ell e(u^\ell) e(u^\ell)^T \preceq \alpha I_{d \times d} \\ & \sum_{\ell=1}^L \lambda^\ell \leq 1, \quad \lambda^\ell \geq 0, \quad \ell = 1, \dots, L, \end{aligned}$$

where the material matrix E plays the role of the Lagrange multiplier to the matrix inequality constraint. The variable λ plays again the role of weights for the load cases.

After discretization, using the same symbols as in the previous section, we get the following nonlinear semidefinite programming problem

$$\begin{aligned} \min_{\alpha, \lambda^\ell, u^\ell} \quad & \alpha - \sum_{\ell=1}^L \lambda^\ell (f^\ell)^T u^\ell \\ \text{s.t.} \quad & \sum_{\ell=1}^L \lambda^\ell \sum_{s=1}^S e_{x_{ms}}(u^\ell) e_{x_{ms}}(u^\ell)^T \preceq \alpha I_{d \times d}, \quad m = 1, \dots, M \\ & \sum_{\ell=1}^L \lambda^\ell \leq 1, \quad \lambda^\ell \geq 0, \quad \ell = 1, \dots, L. \end{aligned}$$

With the change of variables

$$\lambda = \mu^2, \quad u^\ell = v^\ell / \mu$$

we arrive at the problem which, by its structure, reminds the discretized single-load problem (4):

$$\begin{aligned} \min_{\alpha, \mu^\ell, v^\ell} \quad & \alpha - \sum_{\ell=1}^L \mu^\ell (f^\ell)^T v^\ell \tag{5} \\ \text{s.t.} \quad & \sum_{\ell=1}^L \sum_{s=1}^S e_{x_{ms}}(v^\ell) e_{x_{ms}}(v^\ell)^T \preceq \alpha I_{d \times d}, \quad m = 1, \dots, M \\ & \sum_{\ell=1}^L (\mu^\ell)^2 \leq 1, \quad \mu^\ell \geq 0, \quad \ell = 1, \dots, L. \end{aligned}$$

The resulting problem is a semidefinite program with bilinear objective function and convex quadratic matrix inequality constraints. This kind of problems can be efficiently used by the recently developed code PENBMI (Kočvara

et al., 2004) that is built on the generalized augmented Lagrangian algorithm (Kočvara and Stingl, 2003). Note that this formulation was first proposed in the thesis of Werner (2000) who, however, did not consider it numerically important due to the lack of nonlinear SDP algorithm at that time.

The advantages of the new formulation are now obvious:

- like (3), problem (5) is a problem in displacements only;
- the convex quadratic matrix constraints are of much smaller dimension than in (3); further, the dimension (and the number of the constraints) does not increase with the number of load cases and only mildly increases when going from 2d to 3d problems (from 3×3 to 6×6);
- the material matrices are the multipliers to these constraints and are readily available in the PENBMI code.

5. COMPLEXITY ESTIMATES AND EXAMPLE

Recall first the original (primal) formulation of the problem, where we minimize the maximal (over load-cases) compliance subject to (nonlinear) equilibrium constraints and (semidefinite) constraints on the material:

$$\begin{aligned}
 & \min_{\alpha, E_1, \dots, E_M} \alpha & (6) \\
 & \text{subject to} \\
 & E_m \succeq 0, \quad \underline{\rho} \leq \text{tr} E_m \leq \bar{\rho}, \quad m = 1, \dots, M \\
 & (f^\ell)^T A(E)^{-1} f^\ell \leq \alpha, \quad \ell = 1, \dots, L \\
 & \sum_{m=1}^M \text{tr} E_m \leq V.
 \end{aligned}$$

This formulation is known to be quite inefficient, compared to the problem (3), as it is a nonlinear SDP problem with a difficult equilibrium constraint. It can be solved by the recent version of the code PENNON; however, because only first-order information is available, and because PENNON is based on a second-order algorithm, we have to approximate the second derivatives by finite differences and solve the Newton system by a conjugate gradient method. As a result, the whole approach is not that robust as the other two approaches, where the analytic second derivatives are available. In order to be able to work with the inverse of the stiffness matrix, we also have to relax the original constraint $0 \leq \text{tr} E_m$ to $0 < \underline{\rho} \leq \text{tr} E_m$.

It is now easy to see the dependence of the computational complexity of the three problems on the number of load-cases. While in the current formulation (3) this dependence is cubic, in the new formulation (5) it is only quadratic. Furthermore, the dependence is only linear in the primal formulation

(6). These complexity estimates will be clearly demonstrated in the following numerical example:

Example 1. We present preliminary results for the new formulation. The new formulation was recently implemented in our code MOPED for free material optimization.

We consider an academic two-dimensional problem with the number of load-cases increasing from two to ten. All problems are discretized using 5000 elements. In the next two figures we see the data (left) and optimal solution (right) for the problem with two and six load-cases, respectively.

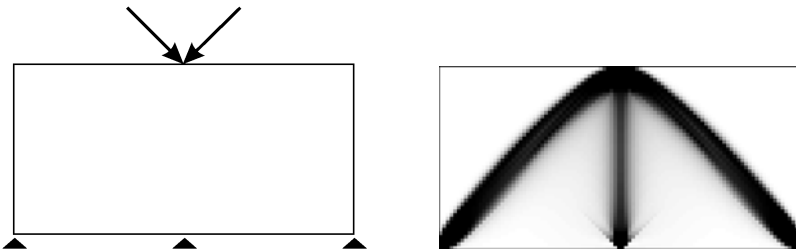


Figure 1. Example 1: initial design and optimal result for two load-cases.

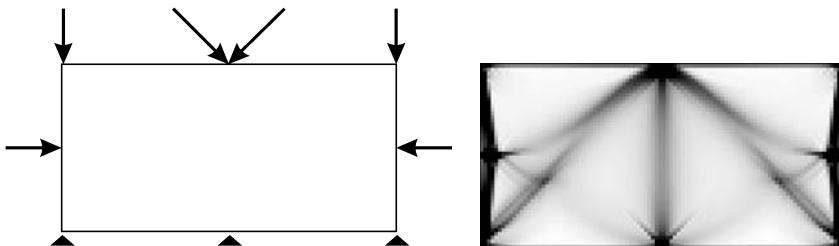


Figure 2. Example 1: initial design and optimal result for six load-cases.

Table 1 gives the dimensions of the problems: while the number of the primal variables (given just by the number of finite elements) stays the same, the number of dual variables (given by the displacement vectors) increases linearly with the number of load-cases.

Finally, Table 2 presents the results for the three approaches: the current formulation (linear SDP), the new formulation (dual nonlinear SDP) and also for the primal formulation of the problem (primal nonlinear SDP). We can clearly see the effect predicted by the complexity estimates. For small number of load-cases, the new formulation is clearly the best one. With increasing number of load-cases, it is better and better than the currently implemented

Table 1. Example 1: problem dimensions.

Elements	Loads	Dual variables	Primal variables
5000	2	20598	30001
5000	4	41205	30001
5000	6	61812	30001
5000	10	103122	30001

Table 2. Example 1: numerical results for 2-10 forces (process time in seconds).

Loads	Process time (linear SDP)	Process time (dual nl. SDP)	Process time (primal nl. SDP)
2	197	120	597
4	896	512	1171
6	2992	1473	1496
10	15356	5216	3012

formulation. The primal formulation, as expected, is by far the worst one for small number of load-cases. However, its complexity grows only linearly with this number, and we can see that for large number of load-cases it actually becomes the most efficient formulation; a rather unexpected effect. But recall that the (first-order) primal formulation is much less robust than the other two and, for large real-world problems, this effect may not be confirmed.

6. REMARKS

6.1 Weighted Multiple-Load

For *given* weights λ^ℓ , $\ell = 1, \dots, L$, we can directly derive the weighted multiple-load problem from (5):

$$\begin{aligned}
 \min_{\alpha, v^\ell} \quad & \alpha - \sum_{\ell=1}^L \mu^\ell (f^\ell)^T v^\ell \\
 \text{s.t.} \quad & \sum_{\ell=1}^L \sum_{s=1}^S e_{x_{ms}}(v^\ell) e_{x_{ms}}(v^\ell)^T \preceq \alpha I_{d \times d}, \quad m = 1, \dots, M
 \end{aligned} \tag{7}$$

using the same change of variables ($\lambda \rightarrow \mu, u \rightarrow v$) as above.

This problem can now be solved just as the worst-case multiple-load problem by the code PENBMI. Further, it is now a convex problem and, as before, the optimal material is directly available by means of the Lagrangian mul-

multipliers. Note that the weighted multiple-load problem has almost the same computational complexity as the worst-case formulation.

6.2 Truss Topology Problem

An analogous development can be done for the worst-case multiple-load truss topology problem. Due to the dimensional reduction, the resulting formulation, analogous to (5), is now a standard nonlinear optimization problem. The corresponding formulation appeared, e.g., in Kočvara et al. (1998).

ACKNOWLEDGMENT

This research was supported by the Academy of Sciences of the Czech Republic through grant No. A1075402.

NOTE

1. To simplify the notation, we present all formulations in two-dimensional space. Generalization to three dimensions is immediate.

REFERENCES

- Ben-Tal, A., Kočvara, M., Nemirovski, A., and Zowe, J. (1997). Free material design via semi-definite programming. The multi-load case with contact conditions. *SIAM J. Optimization*, 9:813–832.
- Bendsøe, M. and Sigmund, O. (2002). *Topology Optimization. Theory, Methods and Applications*. Springer-Verlag, Heidelberg.
- Bendsøe, M. P., Guades, J. M., Haber, R., Pedersen, P., and Taylor, J. E. (1994). An analytical model to predict optimal material properties in the context of optimal structural design. *J. Applied Mechanics*, 61:930–937.
- Hörnlein, H., Kočvara, M., and Werner, R. (2001). Material optimization: Bridging the gap between conceptual and preliminary design. *Aerospace Science and Technology*, 5:541–554.
- Kočvara, M., Zibulevsky, M., and Zowe, J. (1998). Mechanical design problems with unilateral contact. *M2AN Mathematical Modelling and Numerical Analysis*, 32:255–282.
- Kočvara, M., Leibfritz, F., Stingl, M., and Henrion, D. (2004). A nonlinear SDP algorithm for static output feedback problems in COMPlib. LAAS-CNRS research report no. 04508, LAAS, Toulouse.
- Kočvara, M. and Stingl, M. (2003). PENNON—a code for convex nonlinear and semidefinite programming. *Optimization Methods and Software*, 18(3):317–333.
- Werner, R. (2000). *Free Material Optimization. Mathematical Analysis and Numerical Solution*. PhD thesis, Inst. of Applied Mathematics, University of Erlangen.
- Zowe, J., Kočvara, M., and Bendsøe, M. (1997). Free material optimization via mathematical programming. *Mathematical Programming, Series B*, 79:445–466.

SIMULTANEOUS OPTIMIZATION OF TRUSS TOPOLOGY AND GEOMETRY, REVISITED

Wolfgang Achtziger

Institute of Applied Mathematics, University of Dortmund, Dortmund, Germany

wolfgang.achtziger@uni-dortmund.de

Abstract: The paper considers the problem of simultaneous truss geometry and topology optimization. We tackle the classical problem of minimal compliance subject to a volume constraint which alternatively can be regarded as a minimum volume problem subject to symmetric stress constraints. After the review of a bilevel approach of Kočvara et al. we propose three closely related approaches which, however, overcome the pitfall of vanishing potential bars for melting end nodes. This is achieved through the use of the data structure of the problem allowing a split of the dependence of the data on the geometry variable into a linear and a quadratic part. The paper closes with some numerical experiments based on the new problem formulations. In particular, we are interested in a relation of the number of potential bars needed in a pure topology approach and a simultaneous geo/topo approach, respectively, to achieve the same value of optimal compliance resp. volume.

Keywords: Truss optimization, geometry optimization, bilevel programming.

1. INTRODUCTION, NOTATIONS, AND REVIEW

We consider the problem of truss topology optimization on a given ground structure. One difficulty in this approach is the “good” definition of nodal points. When defining a ground structure one would like to choose the nodal points in way that the optimal structure can make profit of these choices. On the other hand, one would not like to predefine an optimal design by certain choices of nodal positions because, obviously, an optimal structure is not known.

One common attempt to escape from this dilemma is to set up a ground structure which is “dense”, i.e., possesses many nodes and potential bars. The optimization will then automatically select those nodes which are “needed” for the construction of a good structure. Usually, the nodal points are chosen on a rectangular grid. As a consequence, the optimization problem gets very large

scaled, and thus is hard to solve, at least, if all possible nodal connections are considered as potential bars. As a further consequence, the obtained solution usually consists of very many (thin) bars because the optimization can resort to a very rich design space.

A second approach is alternating optimization of topology and geometry. This means, for given nodal positions first the topology is optimized resulting in some vector of positive or zero cross-sectional areas. Then these areas are fixed and the geometry is optimized resulting in new nodal positions. Then these nodal positions are fixed, and the topology is optimized again, and so on. Such approaches often use heuristics, and it is hardly possible to guarantee (local) optimality of the calculated solutions in a given mathematical problem setting. We will come back to this approach below.

A third approach is the simultaneous optimization of topology and geometry. This means, both, cross-sections as well as nodal positions of the ground structure, are optimized. In this way, qualitative statements of the structure obtained are possible for a clearly defined mathematical problem statement, sparse structures are obtained because the set of potential bars can be kept “small”, and the nodal positions are optimized without a given “pre-justice” by the user. Of course, there is a high price to pay for these advantages. The numerical treatment of this optimization setting is very hard. The nonlinear dependence of the geometry data on the position of the nodal points screws up the successful numerical optimization of problems of larger size, at least, if a “straightforward” optimization problem formulation is tackled. Here it is necessary to exploit the mathematical structure of the problem data and to adjust the mathematical optimization method used. In this paper we review and propose new computational approaches to the problem. We note, however, that the development presented here does not only apply to the simultaneous geometry and topology optimization of trusses, but may be viewed as a more general study on how to numerically attack problems with certain linear and quadratic dependencies in the problem data.

For the further development in this paper we use the data structure of the stiffness matrix, and hence we will focus on the following well-known definitions and notations in more detail. In this paper we consider truss ground structures consisting of m potential bars and N nodal points in d spatial dimensions, i.e., $d \in \{2, 3\}$. For the moment being, let the nodal positions of the N nodal points be fixed, as usual. After the deletion of s displacement coordinates referring to support conditions, the degree of freedom of the (ground) structure is denoted by $n = N \cdot d - s$. For the i th potential bar, the so-called *geometry vector* $\gamma_i \in \mathbb{R}^n$ in the displacement coordinates referring to its two end nodes contains the cosines and sines w.r.t. the position of the bar in the ground structure. Moreover, ℓ_i denotes the length of the i th potential bar, and E_i refers to the Young’s modulus of the material used for this bar. Hence,

if for each index $i \in \{1, \dots, m\}$, respectively, the value $a_i \geq 0$ denotes the cross-sectional area (yet to be optimized) of the i th potential bar, we may state the global stiffness matrix of the structure $a \in \mathbb{R}^m$, $a \geq 0$, in global reduced coordinates as

$$K(a) := \sum_{i=1}^m a_i \frac{E_i}{\ell_i} \gamma_i \gamma_i^T \in \mathbb{R}^{n \times n}, \tag{1}$$

where we assume linear elastic material behavior, as usual. Hence, with a corresponding displacement vector $u \in \mathbb{R}^n$ the equations of elastic equilibrium can be written as $K(a)u = f$ where $f \in \mathbb{R}^n$ is a vector of a given external load applied to some nodal points expressed in global reduced coordinates.

With these notations we can formulate the (classical) problem of truss topology optimization on a ground structure where compliance is minimized s.t. a volume constraint:

$$\min_{a \in \mathbb{R}^m, u \in \mathbb{R}^n} \left\{ f^T u \mid K(a)u = f, \sum_{i=1}^m a_i \ell_i \leq V, a \geq 0 \right\}. \tag{2}$$

Here, $V > 0$ is a given bound on the total volume of the structure. This problem has been extensively studied, also for discrete and discretized structures other than trusses (cf., e.g., [1, 2, 4, 5], and the references therein). For truss structures, however, the construction of the element stiffness matrices from dyadic products $\gamma_i \gamma_i^T$ can be used to obtain the following linear programming formulation (LP) of (2) (cf. [1, 2, 10]).

$$\max_{u \in \mathbb{R}^n} \left\{ f^T u \mid -1 \leq \frac{\sqrt{E_i}}{\ell_i} \gamma_i^T u \leq 1 \quad \forall i \right\}. \tag{3}$$

With certain substitutions, the LP-dual of this problem can be written in the form

$$\min_{a \in \mathbb{R}^m, q \in \mathbb{R}^m} \left\{ \sum_{i=1}^m a_i \ell_i \mid Bq + f = 0, -\bar{\sigma}_i a_i \leq q_i \leq \bar{\sigma}_i \quad \forall i, a \geq 0 \right\}. \tag{4}$$

Here, the so-called *geometry matrix* (or *compatibility matrix*) B is defined by the geometry vectors γ_i through

$$B := (\gamma_1 \cdots \gamma_m) \in \mathbb{R}^{n \times m}.$$

Hence, q plays the role of a vector of internal forces, and (4) can be interpreted as a minimum volume problem subject to force equilibrium and stress constraints with the same absolute member stress bound $\bar{\sigma}_i$ for tension and for compression (cf. [2] for a summary).

Now we add the variation of geometry to the problem. Let us collect the initial spacial positions of the N nodal points of the ground structure in a vector

$\bar{y} \in \mathbb{R}^{N \cdot d}$. Similarly we may define a set $Y \subseteq \mathbb{R}^{N \cdot d}$ of admissible nodal positions where, of course, the connectivity of nodes through potential bars remains unchanged independently of y . We assume that $\bar{y} \in Y$.

By this additional variable y , the geometry vectors γ_i and the values of the bar lengths ℓ_i become dependent on y , i.e., in generalization to (1) the global stiffness matrix is written as

$$K(y, a) := \sum_{i=1}^m a_i \frac{E_i}{\ell_i(y)} \gamma_i(y) \gamma_i(y)^T \in \mathbb{R}^{n \times n}.$$

Problem (2) is generalized to

$$\min_{y \in Y, a \in \mathbb{R}^m, u \in \mathbb{R}^n} \left\{ f^T u \mid K(y, a)u = f, \sum_{i=1}^m a_i \ell_i(y) \leq V, a \geq 0 \right\}. \quad (5)$$

It turns out that the direct numerical treatment of this formulation is not efficient, and generally fails, even for moderate problem sizes. The background lies in the difficult treatment of local optimizers due to non-convexity and in the lack of satisfaction of constraint qualifications which are needed for algorithmic convergence.

As an “alternative” let us briefly discuss alternating optimization in y and a . This means, for fixed y solve (5) in (a, u) (cf. problem (2) above; as already outlined, this can be easily done). Then fix a and solve (5) in (y, u) (or, alternatively, fix (a, u) and solve (5) in y). Obviously, this methodology generates better and better feasible points (i.e., structures), and thus may be interpreted as a numerical descent method for the treatment of (5). Sometimes this methodology is also referred to as *coordinate-wise optimization*. Pedersen [13–15] proposed this methodology for the solution of (5) using the fact that, without restriction, the solution a of each topology optimization represents a statically determinate structure. Hence, u (locally) can be interpreted as a differentiable function of y (or of (a, y)), and thus gradients for the optimization w.r.t y (or w.r.t. to (a, y)) can be calculated. Since the existence of statically determinate solutions remains true if local buckling constraints are added to the problem [3], this calculation methodology may well be used also for the more complicated problem setting including buckling constraints. As the meanwhile famous examples in [15] prove, this methodology is able to end up in very good practical results. There are, however, some mathematical drawbacks of this methodology. First, the linear independency hidden in static determinacy only holds in a small neighborhood of the considered point (a, u) , and thus the optimization model used in each step may be wrong if one moves away from (a, u) . Second (more serious), it is known that coordinate-wise optimization usually gets stuck at points which may lack to be local optimizers. To understand this, think of a situation where locally an improvement is not possible,

neither if y is varied for fixed a , nor if a is varied for fixed y (and u depends on (a, y)). But it may well be the case that improvement is still possible if a and y are *simultaneously* varied! It is easy to construct examples showing this unpleasant behavior at almost every feasible point. Hence, convergence of coordinate-wise optimization to local optimizers cannot be proved in general without taking into account further properties of the problem. Having a look at the results of Pedersen, however, it may well be that such properties exist for our particular problem (5). To the knowledge of the author, however, mathematical results in this field are not yet known.

The simultaneous treatment of a and y is the keypoint in the following methodology. Kočvara et al. [7, 11, 12] (or, cf. [2]) propose a bilevel approach making use of the fact that for fixed geometry y , problem (5) can be easily solved as the LP (3) for fixed y ,

$$\max_{u \in \mathbb{R}^n} \left\{ f^T u \mid -1 \leq \frac{\sqrt{E_i}}{\ell_i(y)} \gamma_i(y)^T u \leq 1 \ \forall i \right\}. \tag{6}$$

With the function $\phi : Y \rightarrow \mathbb{R} \cup \{+\infty\}$,

$$\phi(y) := \inf_{a \in \mathbb{R}^m, u \in \mathbb{R}^n} \left\{ f^T u \mid K(y, a) = f, \sum_{i=1}^m a_i \ell_i(y) \leq V, a \geq 0 \right\}, \tag{7}$$

problem (5) becomes

$$\min_{y \in Y} \phi(y). \tag{8}$$

The function ϕ can be viewed as the so-called *optimal value function* of the inner problem in (7) where $y \in Y$ acts as a perturbation parameter. The behavior of such functions is well studied, e.g., for perturbed linear programming problems (as is here the case). Notice the strict coupling of y with (a, u) contrary to coordinate-wise optimization (cf. above). If y (“master variable”) is varied then the optimal variables (a, u) in the inner problem must compete (“follower variables”), i.e., must follow y . In this sense, a and u can be interpreted as (yet set-valued) functions of y .

As seen above, the inner problem in (7) in the variables (a, u) can be written as the LP (6). There are, however, serious difficulties when solving (8). The function ϕ lacks to be differentiable. Moreover, if Y is not appropriately chosen then ϕ attains infinite values. Even worse, if nodal points “melt”, i.e., have the same position, singularities occur in the definitions. For example, $K(y, a)$ is undefined because $\ell_i(y) = 0$ for some i , and the values of cosines and sines in $\gamma_i(y)$ become undefined as well. As a consequence, ϕ even needs not be locally Lipschitz-continuous. Nevertheless, with a careful definition of Y , e.g., as a small box around \bar{y} , a step-wise treatment of problem (8) can be performed by the use of algorithms of Nonsmooth Nonconvex Optimization. At each iteration point y^k these algorithms require the function value

$\phi(y^k)$ and the knowledge of one arbitrary so-called *subgradient* (in the sense of Clarke [8]). The function value $\phi(y^k)$ is obtained through the LP (6). The subgradient is a vector $g^k \in \mathbb{R}^{N \cdot d}$ generalizing the gradient of ϕ at y^k if ϕ lacks to be differentiable at y^k . Under certain technical assumptions, an explicit formula for g^k is available [12]. This formula can be simply evaluated when the Lagrange multipliers of problem (6) are available, i.e., when (6) has been solved for $y = y^k$. Several numerical examples in [12] show the practical use of this approach. In particular, also the optimization of positions of support nodes and of load nodes(!) is possible. Nevertheless, the serious drawbacks of this approach remain. In the following chapter we try to get rid of these difficulties. Moreover, we want to get more and general insight into the numerical treatment of bilevel formulations such as (8) because such an approach may be useful for very many other applications in Structural Optimization.

2. IMPROVED APPROACH

One of the difficulties in the approach of Kočvara et al. is the nonlinear dependence of the data on the nodal positions y . Another difficulty is that for certain geometries y the data is not defined, or, one needs to calculate with a modified ground structure after the removal of vanishing potential bars. In the following we use the data structure of γ_i and ℓ_i to get rid of these drawbacks.

Let $y \in \mathbb{R}^{N \cdot d}$ be an arbitrary geometry. Let $j_{i,1,k}, j_{i,2,k} \in \{1, \dots, N \cdot d\}$ denote two indices which correspond to the coordinates of the two end nodes of the i th potential bar in the same spatial dimension $k \in \{1, \dots, d\}$. Then the difference $y_{j_{i,2,k}} - y_{j_{i,1,k}}$ is obviously a linear function of y . Hence, we define a Matrix $C_i \in \mathbb{R}^{(N \cdot d) \times (N \cdot d)}$ such that the p th component of the vector $Cy \in \mathbb{R}^{N \cdot d}$ contains the value $y_{j_{i,2,k}} - y_{j_{i,1,k}}$ if $p = j_{i,2,k}$ for some k , and $y_{j_{i,1,k}} - y_{j_{i,2,k}}$ if $p = j_{i,1,k}$ for some k , and zero otherwise. A closer look shows that for $d = 2$ the matrix C_i has the structure

$$C_i = -v_i v_i^T - w_i w_i^T, \quad (9)$$

where each of the vectors $v_i, w_i \in \{-1, 0, +1\}^{N \cdot d}$ contains exactly one entry -1 and one entry $+1$ where

$$v_i^T v_i = w_i^T w_i = 2 \quad \text{and} \quad v_i^T w_i = 0. \quad (10)$$

(Analogous relations hold for $d = 3$ with three vectors v_i, w_i, z_i .)

Denote by $\bar{y}_0 \in \mathbb{R}^{N \cdot d}$ the vector containing the fixed coordinates of the original geometry \bar{y} , which may be given by the support conditions, and zeros otherwise. In the following we assume that all nodal coordinates with free degree of freedom w.r.t. displacements can also be freely varied w.r.t. geometry. Hence, for simplicity, the set Y of admissible geometries is given by

$$Y = \{ Py + \bar{y}_0 \mid y \in \tilde{Y} \} \subseteq \mathbb{R}^{N \cdot d},$$

where $\tilde{Y} \subseteq \mathbb{R}^n$ is a proper subset (like a box) or even the whole space, and $P \in \mathbb{R}^{n \times (N \cdot d)}$ is a simple projection matrix inserting zero components to y at the fixed nodal coordinates. Note that the meaning of y now slightly differs from above due to this definition. It is now $y \in \mathbb{R}^n$.

With these settings, for each $y \in \tilde{Y}$ the length $\ell_i(y)$ of the i th potential bar can be expressed as

$$\ell_i(y) = \|\frac{1}{2}C_i(Py + \bar{y}_0)\|_2 = \sqrt{\frac{1}{2}(Py + \bar{y}_0)^T(-C_i)(Py + \bar{y}_0)},$$

where we have used that C_i is symmetric and that $C_i^2 = -2C_i$ because of (9) and (10). Similarly, by simple arguments from elementary geometry in calculating sines and cosines, the vectors γ_i are given by

$$\gamma_i(y) = \frac{1}{\ell_i(y)}P^T C_i(Py + \bar{y}_0)$$

with $\ell_i(y)$ from above. Now, insert these expressions into problem (8):

$$\min_{y \in \tilde{Y}} \sup_{u \in \mathbb{R}^n} \left\{ f^T u \mid -\ell_i(y)^2 \leq \sqrt{E_i}(Py + \bar{y}_0)^T C_i P u \leq \ell_i(y)^2 \quad \forall i \right\}. \quad (11)$$

Here we have replaced the inner problem by (6) (Note that the relation of the optimal objective function value $f^T u^*$ in (6) and its counterpart $f^T u^{**} = \phi(y)$ in (7) is given by $(f^T u^*)^2 = f^T u^{**}$ [1],[2]. Hence, optimal geometries in (8) and in (11) are the same).

Notice that in formulation (11) the problem of singularities does not occur. If the nodal positions of two end points of a potential bar coincide then $\ell_i(y) = 0$ and $C_i(Py + \bar{y}_0) = 0$. Therefore, the corresponding constraints “ $-\ell_i(y)^2 \leq \sqrt{E_i}(Py + \bar{y}_0)^T C_i P u \leq \ell_i(y)^2$ ” in (11) become “ $0 \leq 0^T u \leq 0$ ”, and thus are trivially satisfied. Moreover, the inner supremum takes the value $+\infty$ if and only if the potential bar with $\ell_i(y) = 0$ is needed for the structure to carry the load (i.e., $\sum_j \alpha_j \gamma_j(y) = f \implies \alpha_i \neq 0$).

By LP-duality applied to the inner sup-problem in (11) we arrive at the formulation

$$\begin{aligned} & \min_{y \in \tilde{Y}, \rho^+, \rho^- \in \mathbb{R}^m} \sum_{i=1}^m (\rho_i^+ + \rho_i^-)(Py + \bar{y}_0)^T(-C_i)(Py + \bar{y}_0) & (12) \\ \text{s.t.} & \sum_{i=1}^m (\rho_i^+ - \rho_i^-)\sqrt{E_i}P^T C_i(Py + \bar{y}_0) + f = 0 \\ & \rho^+, \rho^- \geq 0. \end{aligned}$$

Again, the effect of vanishing potential bars due to melting end nodes does not cause difficulties. If $\ell_i(y) = 0$ then $C_i(Py + \bar{y}_0) = 0$, and the variables ρ_i^+, ρ_i^- become meaningless. Obviously, for fixed geometry y the inner problem in (12) is a version of problem (4) where $(\rho^+ - \rho^-)$ takes the role of the

vector q of internal member forces. Hence, problem (12) means simultaneous optimization of topology and geometry in a minimum volume setting.

Besides the effect for vanishing potential bars, notice the interesting mathematical problem structure of (12). As above, for fixed y the problem in (ρ^+, ρ^-) is a linear programming problem LP. Vice versa, for fixed (ρ^+, ρ^-) the remaining problem in y is a convex(!) quadratic optimization problem (QP) because the matrix C_i is symmetric and negative semi-definite due to (9). Hence, problem (12) may be numerically attacked in two ways. First, formulation (12) may be treated jointly in the variables (y, ρ^+, ρ^-) by any solver of Nonlinear Programming. It is a problem in $n + 2m$ variables where the objective function is a polynomial of degree 3 with a special structure. The equality constraints are bilinear. Second, we may treat the formulation

$$\min_{\rho^+, \rho^- \geq 0} \psi(\rho^+, \rho^-), \quad (13)$$

where the function ψ is the optimal value function for the convex quadratic optimization problem in y with (ρ^+, ρ^-) as perturbation parameters,

$$\psi(\rho^+, \rho^-) := \inf_{y \in \tilde{Y}} \left\{ \begin{array}{l} \sum_{i=1}^m (\rho_i^+ + \rho_i^-) (Py + \bar{y}_0)^T (-C_i) (Py + \bar{y}_0) \Big| \\ \sum_{i=1}^m (\rho_i^+ - \rho_i^-) \sqrt{E_i} P^T C_i (Py + \bar{y}_0) + f = 0 \end{array} \right\}.$$

Note that for fixed (ρ^+, ρ^-) the calculation of $\psi(\rho^+, \rho^-)$ is “simple” because it requires just the solution of a convex quadratic optimization problem for which very efficient solution procedures are available. Similarly to the approach described in Sec. 1, formulas for subgradients of ψ can be derived. Note also that the “perturbation” (ρ^+, ρ^-) enters the inner QP in a linear(!) way, which also simplifies the necessary theoretical considerations.

3. SOME NUMERICAL EXPERIMENTS

For the time being, we have made some first experiments with the new formulations (11), (12), and (13). It seems that (11) is still difficult to handle as a bilevel problem, since the behavior of the feasible set for u heavily changes with the outer variable y . A direct treatment of (12) with the solver SNOPT [9] shows good performance for problems up to several thousand bars (SNOPT is a well-established standard solver of Nonlinear Programming, realizing a method of Sequential Quadratic Programming). Note that in realistic examples the number m of potential bars in the ground structure needs not be excessively large because the geometry is varied as well (and, in view of practical realizations, we want to avoid structures consisting of very many thin bars). Figure 1 shows the result of an optimization run for a cantilever-like structure

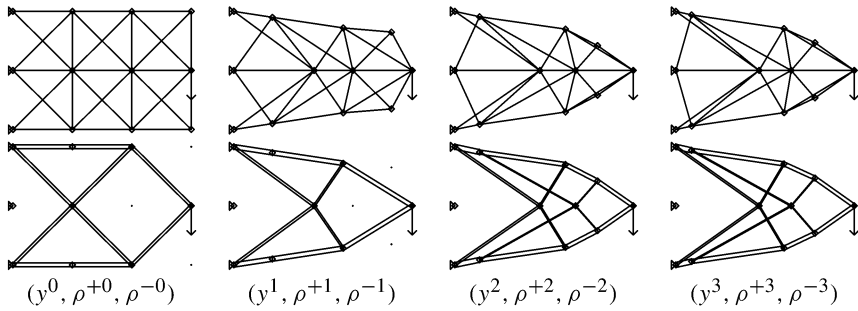


Figure 1. Optimization of a cantilever.

of academic size. For the calculation of a good starting point we first calculate a solution (ρ^{+0}, ρ^{-0}) of (12) with fixed $y := y^0$, i.e., for fixed geometry. Then SNOPT produces three iteration points $(y^k, \rho^{+k}, \rho^{-k})$, $k = 1, 2, 3$, until it terminates with the information that a local optimizer of (12) has been reached. Figure 1 displays the four structures given by the iteration points $(y^k, \rho^{+k}, \rho^{-k})$, $k = 0, 1, 2, 3$. For each k the underlying ground structure is shown (upper row; indicates y^k) as well as its material distribution on this ground structure (bottom row; indicates $\rho^{+k} + \rho^{-k}$).

Approach (13) is still under development, but first experiments are promising. The treatment of the non-convexity of ψ in a non-smooth problem setting, however, is still not easy.

We close with a brief view on a study which might be of more and of general interest. This leads back to the beginning of the paper. From a practitioner’s point of view it is the question whether one should solve the topology problem on a dense ground structure, or whether one should simultaneously optimize geometry as well while using a sparse ground structure. Hence, we compare formulation (2) for a dense ground structure (“topo”; solved through LP (3)) with formulation (5) for a sparser ground structure (“geo+topo”; solved through (12)). For a fixed number N of nodal points but for increasing “density” of the ground structure we have calculated the values of optimal compliance for different support and load scenarios [16]. Clearly, optimal compliance decreases in both problem formulations when the number m of potential bars is increased (See also the similar study in [6]). For example, the test for a 2D bridge scenario with $N = 50$ nodal points shows that the optimal compliance for the “pure” topology problem (2) on a ground structure with (\approx) 6000 potential bars results in almost the same value as for the geo+topo problem (5) on a ground structure with (\approx) 700 potential bars. This leads to the principal question of how to find a mathematical measure or formula for the difference of both approaches in terms of optimal compliance as well as in terms of resulting structures (Are they similar? What does “similar” mean?). Another

principal question is how to compare compliance values for ground structures of different size, in particular for a different number N of nodal points.

ACKNOWLEDGEMENT

This research was supported by the German-Czech DAAD–AV ČR project D–CZ 7/05–06.

REFERENCES

- [1] Achtziger, W., Bendsøe, M.P., Ben-Tal, A. and Zowe, J.m *Equivalent Displacement Based Formulations for Maximum Strength Truss Topology Design*, Impact of Computing in Science and Engineering 4, 1992, 315–345 (1992).
- [2] Achtziger, W., Topology optimization of discrete structures – An introduction in view of computational and nonsmooth aspects, in *Topology Optimization in Structural Mechanics*, G.I.N. Rozvany (ed.), CISM Courses and Lectures, No. 374, Springer, Vienna, pp. 57–100 (1997).
- [3] Barta, J., On the minimum weight of certain redundant structures, *Acta Technica Academiae Scientiarum Hungaricae*, 18, 67–76 (1957).
- [4] Bendsøe, M.P. and Sigmund, O., *Topology Optimization*, Springer, Berlin (2003).
- [5] Ben-Tal, A. and Bendsøe, M.P., A new method for optimal truss topology design, *SIAM Journal on Optimization*, 322–358 (1993).
- [6] Beckers, M. and Fleury, C., A primal-dual approach in truss topology optimization, in *Advances in Structural Optimization*, B.H.V. Topping and M. Papadrakakis (eds), Civil-Comp. Press, Edinburgh, pp. 91–101 (1994).
- [7] Ben-Tal, A., Kočvara, M. and Zowe, J., Two nonsmooth approaches to simultaneous geometry and topology design of trusses, in *Topology Optimization of Structures*, M.P. Bendsøe and C.A. Mota Soares (eds), Kluwer Academic Publishers, Dordrecht, pp. 31–42 (1993).
- [8] Clarke, F.H., *Optimization and Nonsmooth Analysis*, J. Wiley & Sons, New York (1983).
- [9] Gill, P.E., Murray, W. and Saunders, M.A., *SNOPT 5.3 User's Guide, Report NA 97-5*, Department of Mathematics, University of California, San Diego (1997, revised 1998).
- [10] Hemp, W.S., *Optimum Structures*, Clarendon Press, Oxford (1973).
- [11] Kočvara, M. and Zowe, J., How to optimize mechanical structures simultaneously with respect to geometry and topology, in *First World Congress of Structural and Multidisciplinary Optimization*, N. Olhoff and G.I.N. Rozvany (eds), Pergamon, Oxford pp. 135–140 (1995).
- [12] Kočvara, M. and Zowe, J., How mathematics can help in design of mechanical structures, in *Numerical Analysis 1995*, D. Griffiths and G. Watson (eds), Longman Scientific and Technical, Harlow, pp. 76–93 (1996).
- [13] Pedersen, P., On the minimum mass layout of trusses, in *Proc. AGARD Symposium on Structural Optimization*, Tarabya, Istanbul, Turkey, October, AGARD-CP-36-70 (1969).
- [14] Pedersen, P., On the optimal layout of multi-purpose trusses, *Computers & Structures*, 2, 695–712 (1972).

- [15] Pedersen, P., Optimal joint positions for space trusses, *Journal of the Structural Division, ASCE*, Vol. 99, No. ST12, Proc. Paper 10199, 2459–2476 (1973).
- [16] Plitman, Y., Simultane Geometrie- und Topologieoptimierung von Stabwerken – Mathematische Ansätze im Vergleich, Diplom Thesis, Institute of Applied Mathematics, University of Dortmund, Germany, (2004) [in German].

TOPOLOGY OPTIMIZATION BY SEQUENTIAL INTEGER LINEAR PROGRAMMING

Krister Svanberg and Mats Werme

Optimization and Systems Theory, Royal Institute of Technology, Sweden

Abstract: We present a new iterative approach for topology optimization of load-carrying structures. In each iteration an integer linear programming problem is generated and solved. The method is guaranteed to find a local optimum of the original problem, but not necessarily a global optimum. Numerical results for some stress constrained problems are presented.

Keywords: Topology optimization, stress constraints, sequential integer linear programming, first order sensitivities.

1. INTRODUCTION

This paper deals with optimal design of load-carrying structures. In continuum topology optimization a fixed design domain in a two or three dimensional space is given. The problem is then to determine which subdomains of the design domain that should be filled with material and which should be void. In practice the design domain is usually discretized into finite elements in order to obtain a finite dimensional problem with binary variables indicating presence or absence of material in the various finite elements. The following general form is often adopted:

$$\begin{aligned} & \text{minimize} && f_0(\mathbf{x}) \\ & \text{subject to} && f_i(\mathbf{x}) \leq f_i^{\max}, \quad i = 1, \dots, m \\ & && \mathbf{x} \in \{0, 1\}^n, \end{aligned} \tag{1.1}$$

where the design variable vector $\mathbf{x} = (x_1, x_2, \dots, x_n)^T$ is defined as $x_j = 1$ when the j th element is filled with material while $x_j = 0$ when the j th element is void. In most cases, the objective function f_0 and/or some of the constraint functions f_i are implicitly defined through the solution of the equilibrium equations of the structure. A common choice of objective is the weight of the structure and the constraints can be e.g. bounds on the displacements and stresses. Unfortunately, this gives rise to integer nonlinear programs, with a

non-convex NLP-relaxation, which are very hard to solve to a global optimum even for relatively small problems. In Stolpe and Svanberg (2003) a subclass of the nonlinear problems was reformulated to mixed integer linear programs but also these turned out to be very hard to solve to a global optimum, partly due to the large number of additional continuous variables needed to transform the nonlinear constraints to linear.

A common heuristic approach to tackle problem (1.1) is to relax the binary constraints on the variables and then model the stiffness matrix so that intermediate values between ε and one are given low stiffness in comparison to their weight. Here $\varepsilon > 0$ is an artificial lower bound on the design variables introduced in order to assure that the stiffness matrix never becomes singular. This approach is seen in interpolation models such as SIMP, see e.g. Bendsøe (1989) and Rozvany et al. (1992). For more information on topology optimization, see Bendsøe and Sigmund (1999) and the references therein.

In this paper we propose a sequential integer linear programming (SILP) method that solves a sequence of integer linear programs (ILP) where each subproblem is solved to a global optimum by a integer linear programming package. The SILP method uses the first order sensitivity of a function $f_i : \{0, 1\}^n \rightarrow \mathbb{R}$, which in a sense corresponds to a “discrete derivative”, to obtain a linearization of f_i . Since it is uncertain how good the linearization is “far away” from the current point, a neighbourhood constraint is added to the integer linear program restricting the number of design variables allowed to be changed at each iteration. Further, numerical experience indicate that a hierarchical approach should be used, where one starts with a coarse mesh, solves the problem by the SILP method, and then uses the obtained (locally optimal) solution to construct a starting point for the same problem on a refined mesh. In each refinement, every finite element is divided into four new finite elements.

The paper is organized as follows. In Section 2 the first order sensitivities are defined and their use in the SILP approach is presented. In Section 3 the mathematical formulation of the considered problems is given. More details on the SILP method are given in Section 4. In Section 5 we present some numerical results and conclusions are drawn in Section 6.

2. SENSITIVITIES WITH RESPECT TO BINARY VARIABLES AND THE SILP APPROACH

If the optimization problem (1.1) was posed for *continuous* variables a natural approach would be to generate and solve a sequence of approximating sub-problems. Many optimization methods, such as Sequential linear programming (SLP, see Griffith and Stewart, 1961), Convex linearization method (CONLIN, see Fleury, 1989; Fleury and Braibant, 1986), Method of moving asymptotes

(MMA, see Svanberg, 1987, 2002) and Sequential quadratic programming (SQP, see e.g. Nash and Sofer, 1996) use this approach. All of these methods require the first and in some cases the second order derivatives, i.e. gradients and Hessians, of the objective and constraint functions. Since (1.1) is posed in a “discrete universe” derivatives can not be defined. There is, however, a natural definition of the first order sensitivity for a function $f_i : \{0, 1\}^n \rightarrow \mathbb{R}$ with respect to a binary variable x_j , in a point $\mathbf{x} \in \{0, 1\}^n$ given by

$$\frac{\delta f_i}{\delta x_j}(\mathbf{x}) = \frac{f_i(\mathbf{x} + \xi_j \mathbf{e}_j) - f_i(\mathbf{x})}{\xi_j}, \tag{2.1}$$

where $\xi_j = 1 - 2x_j \in \{-1, 1\}$ and $\mathbf{e}_j = (0, \dots, 1, \dots, 0)^\top \in \mathbb{R}^n$.

In an earlier work, documented in Svanberg and Werme (2005a), we developed a fast method to calculate the quantities $f_i(\mathbf{x} + \xi_j \mathbf{e}_j)$ provided the structure corresponding to the point \mathbf{x} had already been analyzed and f_i stands for a displacement, a compliance or a stress. Thus we can efficiently calculate the *exact* changes in displacements, compliances and stresses when one variable x_j is changed from its current value to its opposite binary value. These changes can be calculated *without* any need for a refactorization of the stiffness matrix and *without* any need for the frequently used artificial lower bound $\varepsilon > 0$ on the variables x_j . This means that it is perfectly valid that the number of “active” degrees of freedom (i.e. degrees of freedom that are present in the finite element model used to compute the displacements) is changed when a design is changed.

The approach presented in this paper is a “Sequential integer linear programming method” (SILP), where a linear approximation is used to obtain integer linear programs (ILPs). The idea is to at the iteration point $\mathbf{x}^{(k)}$, where k is the iteration number, approximate the functions f_i for $i = 0, 1, \dots, m$ by the functions $\tilde{f}_i^{(k)}$ defined by

$$\begin{aligned} \tilde{f}_i^{(k)}(\mathbf{x}) &= f_i(\mathbf{x}^{(k)}) + \mathbf{g}_i(\mathbf{x}^{(k)})^\top (\mathbf{x} - \mathbf{x}^{(k)}) \\ \text{where } \mathbf{g}_i(\mathbf{x}^{(k)}) &= \left(\frac{\delta f_i}{\delta x_1}(\mathbf{x}^{(k)}), \dots, \frac{\delta f_i}{\delta x_n}(\mathbf{x}^{(k)}) \right)^\top. \end{aligned} \tag{2.2}$$

It can be noted that if $\mathbf{x} \in \{0, 1\}^n$ and $\|\mathbf{x}^{(k)} - \mathbf{x}\|_1 = 1$, the approximation is exact, i.e. $\tilde{f}_i^{(k)}(\mathbf{x}) = f_i(\mathbf{x})$.

Further, if $f_i \in C^1$ and the variables were continuous this would correspond to the first order Taylor expansion of f_i at the point $\mathbf{x}^{(k)}$, namely $f_i(\mathbf{x}) \approx f_i(\mathbf{x}^{(k)}) + \nabla f_i(\mathbf{x}^{(k)})^\top (\mathbf{x} - \mathbf{x}^{(k)})$, where $\nabla f_i(\mathbf{x}^{(k)})$ denotes the gradient of f_i at the point $\mathbf{x}^{(k)}$.

The next iteration point $\mathbf{x}^{(k+1)}$ in the SILP process is then obtained as the optimal solution to the ILP

$$\begin{aligned}
& \text{minimize} && \tilde{f}_0^{(k)}(\mathbf{x}) \\
& \text{subject to} && \tilde{f}_i^{(k)}(\mathbf{x}) \leq f_i^{\max}, \quad i = 1, \dots, m, \\
& && \mathbf{x} \in X^{(k)},
\end{aligned} \tag{2.3}$$

where $X^{(k)} \subset \{0, 1\}^n$ is a certain “neighbourhood” of $\mathbf{x}^{(k)}$ described by linear inequalities.

3. MATHEMATICAL FORMULATION OF THE CONSIDERED PROBLEMS

First of all it is assumed that the considered ground structure has been divided into n finite elements giving it a total of d degrees of freedom, *dofs*, corresponding to displacements of the non-fixed nodes. The design of a certain structure, within the ground structure, is then represented by the design variable vector $\mathbf{x} \in \{0, 1\}^n$. As already mentioned an element which is filled with material will have $x_j = 1$ while an element which is void has $x_j = 0$. The stiffness matrix $\mathbf{K}(\mathbf{x}) \in \mathbb{R}^{d \times d}$ corresponding to a given design $\mathbf{x} \in \{0, 1\}^n$ can be written as $\mathbf{K}(\mathbf{x}) = \sum_{j=1}^n x_j \mathbf{K}_j$, where each element stiffness matrix $\mathbf{K}_j \in \mathbb{R}^{d \times d}$ is symmetric and positive semidefinite. Further, an external load vector $\mathbf{p} \in \mathbb{R}^d$ is assumed to be given. The corresponding vector of nodal displacements $\mathbf{u} \in \mathbb{R}^d$ satisfies the equilibrium equations $\mathbf{K}(\mathbf{x})\mathbf{u} = \mathbf{p}$, provided that these equations have a solution. For ease of exposition we only consider a single load-case, but the generalization to multiple load-cases is straightforward.

If there are some white elements, i.e. variables with $x_i = 0$, the stiffness matrix $\mathbf{K}(\mathbf{x})$ may contain some rows in which all matrix elements are equal to zero, so called “zero rows”. Since $\mathbf{K}(\mathbf{x})$ is symmetric, the corresponding columns are “zero columns”. When analyzing the structure, it is possible to reduce $\mathbf{K}(\mathbf{x})$ by simply removing the zero rows and zero columns. This means that the corresponding *dofs*, which are from now on called “passive *dofs*”, are neglected. To get a unique solution of the equilibrium equations for the remaining *dofs*, which are from now on called “active *dofs*”, it is necessary and sufficient that this reduced stiffness matrix is non-singular (and thus positive definite) and that the external load vector $\mathbf{p} \in \mathbb{R}^d$ has no non-zero components among the passive *dofs*. This motivates the following definition of the set \mathcal{S} which characterizes the set of *stable designs*.

Definition: $\mathcal{S} = \{\mathbf{x} \in \{0, 1\}^n \mid \text{rank}(\mathbf{K}(\mathbf{x})) = \text{nzc}(\mathbf{K}(\mathbf{x})) \text{ and } \mathbf{p} \in \mathcal{R}(\mathbf{K}(\mathbf{x}))\}$.

Here, $\mathcal{R}(\mathbf{K}(\mathbf{x}))$ denotes the column space (or range) of $\mathbf{K}(\mathbf{x})$, $\text{rank}(\mathbf{K}(\mathbf{x}))$ denotes the dimension of this column space, and $\text{nzc}(\mathbf{K}(\mathbf{x}))$ denotes the number of non-zero columns in $\mathbf{K}(\mathbf{x})$.

We are now ready to state the three different problems that are considered in this paper. The first is a minimum volume problem with constraints on the maximum von Mises stress in all non-void elements. The second is the problem of minimizing the maximum von Mises stress with a volume constraint. Finally, for comparison, we consider the minimum compliance problem with a volume constraint.

3.1 Minimum Volume with Stress Constraints and an Additional Thickness Variable

One of the problems considered in this work is the following:

$$\begin{aligned}
 & \text{minimize} && t \cdot \mathbf{e}^T \mathbf{x} \\
 & \text{subject to} && \tilde{\mathbf{u}}(t \mathbf{x})^T \mathbf{S}_i \tilde{\mathbf{u}}(t \mathbf{x}) \leq C \text{ for all elements } i \text{ with } x_i = 1, \\
 & && \mathbf{A} \mathbf{x} \leq \mathbf{b}, \\
 & && \mathbf{x} \in \mathcal{S} \text{ and} \\
 & && t > 0,
 \end{aligned} \tag{3.1}$$

where \mathbf{x} is the vector of binary design variables, t is a continuous design variable denoting the common thickness of all non-void elements, $\mathbf{e} = (1, \dots, 1)^T \in \mathbb{R}^n$, the objective function $t \cdot \mathbf{e}^T \mathbf{x}$ is the volume of the structure, the displacement vector $\tilde{\mathbf{u}}(t \mathbf{x})$ is a solution to the equilibrium equations $\mathbf{K}(t \mathbf{x}) \mathbf{u} = \mathbf{p}$, the matrix \mathbf{S}_i is chosen such that $\tilde{\mathbf{u}}(t \mathbf{x})^T \mathbf{S}_i \tilde{\mathbf{u}}(t \mathbf{x})$ becomes the squared von Mises stress in the i th element (provided this element is non-void) and the constant $C > 0$ is a given upper bound on the squared von Mises stress in all non-void elements. The linear constraints $\mathbf{A} \mathbf{x} \leq \mathbf{b}$ are introduced to avoid some unwanted things like “checkerboards” and bar-like parts which are much too thin. Details on these linear constraints are given in Svanberg and Werbe (2005b).

Assuming that $\mathbf{K}(t \mathbf{x}) = t \mathbf{K}(\mathbf{x})$, the continuous variable t can be eliminated from the problem (3.1), and then the following equivalent problem in \mathbf{x} is obtained.

$$\begin{aligned}
 & \text{minimize} && \mathbf{e}^T \mathbf{x} \cdot \max_i \sqrt{x_i \mathbf{u}(\mathbf{x})^T \mathbf{S}_i \mathbf{u}(\mathbf{x})} \\
 & \text{subject to} && \mathbf{A} \mathbf{x} \leq \mathbf{b}, \\
 & && \mathbf{x} \in \mathcal{S},
 \end{aligned} \tag{3.2}$$

where the new displacement vector $\mathbf{u}(\mathbf{x})$ is a solution to $\mathbf{K}(\mathbf{x}) \mathbf{u} = \mathbf{p}$ (without any t). If $\hat{\mathbf{x}}$ is optimal to (3.2) then $(\hat{\mathbf{x}}, \hat{t})$, with $\hat{t} = \max_i \sqrt{\hat{x}_i \mathbf{u}(\hat{\mathbf{x}})^T \mathbf{S}_i \mathbf{u}(\hat{\mathbf{x}}) / C}$, is optimal to (3.1).

The problem (3.2) can in turn be written equivalently as the following problem in \mathbf{x} and z :

$$\begin{aligned} & \text{minimize} && z \\ & \text{subject to} && z \geq f_i(\mathbf{x}) \text{ for } i = 1, \dots, n, \\ & && \mathbf{Ax} \leq \mathbf{b}, \\ & && \mathbf{x} \in \mathcal{S} \text{ and } z \in \mathbb{R}, \end{aligned} \tag{3.3}$$

where $f_i(\mathbf{x}) = \mathbf{e}^T \mathbf{x} \cdot \sqrt{x_i \mathbf{u}(\mathbf{x})^T \mathbf{S}_i \mathbf{u}(\mathbf{x})}$.

3.2 Minimizing the von Mises Stress with a Volume Constraint

The second considered problem in this paper can be written as

$$\begin{aligned} & \min_{\mathbf{x}, \mathbf{u}} \max_i \sigma_i \\ & \text{s.t.} && \mathbf{K}(\mathbf{x})\mathbf{u} = \mathbf{p}, \\ & && \sigma_i = \sqrt{x_i \mathbf{u}^T \mathbf{S}_i \mathbf{u}}, \quad i = 1, 2, \dots, n, \\ & && \mathbf{Ax} \leq \mathbf{b}, \\ & && \mathbf{x} \in \mathcal{S}. \end{aligned} \tag{3.4}$$

In this problem the linear constraints $\mathbf{Ax} \leq \mathbf{b}$ include the volume constraint $\mathbf{e}^T \mathbf{x} \leq V$. With $f_i(\mathbf{x}) = \sqrt{x_i \mathbf{u}(\mathbf{x})^T \mathbf{S}_i \mathbf{u}(\mathbf{x})}$, where $\mathbf{u}(\mathbf{x})$ is a solution to $\mathbf{K}(\mathbf{x})\mathbf{u} = \mathbf{p}$, (3.4) may equivalently be written as the following problem in \mathbf{x} and z :

$$\begin{aligned} & \min && z \\ & \text{s.t.} && z \geq f_i(\mathbf{x}) \text{ for } i = 1, 2, \dots, n, \\ & && \mathbf{Ax} \leq \mathbf{b}, \\ & && \mathbf{x} \in \mathcal{S} \text{ and } z \in \mathbb{R}. \end{aligned} \tag{3.5}$$

3.3 Minimizing the Compliance with a Volume Constraint

As a comparison, the problem of minimizing compliance with a volume constraint is also treated in this paper. This problem can be stated as

$$\begin{aligned} & \min_{\mathbf{x}} && f_0(\mathbf{x}) \\ & \text{s.t.} && \mathbf{Ax} \leq \mathbf{b}, \\ & && \mathbf{x} \in \mathcal{S}, \end{aligned} \tag{3.6}$$

where $f_0(\mathbf{x}) = \mathbf{p}^T \mathbf{u}(\mathbf{x})$ and $\mathbf{u}(\mathbf{x})$ is the solution to $\mathbf{K}(\mathbf{x})\mathbf{u} = \mathbf{p}$. Note that the linear constraints $\mathbf{Ax} \leq \mathbf{b}$, as for (3.5), include the volume constraint $\mathbf{e}^T \mathbf{x} \leq V$.

4. THE SEQUENTIAL INTEGER LINEAR PROGRAMMING APPROACH

The suggested SILP approach for solving the problems (3.3) and (3.5) generates a sequence of iteration points $\mathbf{x}^{(1)}, \mathbf{x}^{(2)}, \mathbf{x}^{(3)} \dots$. A typical iteration, starting in $\mathbf{x}^{(k)}$ and ending in $\mathbf{x}^{(k+1)}$, goes as follows (the compliance case, i.e. (3.6) will be treated later).

First, the function values $f_i(\mathbf{x}^{(k)}) = \mathbf{e}^T \mathbf{x}^{(k)} \cdot \sqrt{x_i \mathbf{u}(\mathbf{x}^{(k)})^T \mathbf{S}_i \mathbf{u}(\mathbf{x}^{(k)})}$ or $f_i(\mathbf{x}^{(k)}) = \sqrt{x_i \mathbf{u}(\mathbf{x}^{(k)})^T \mathbf{S}_i \mathbf{u}(\mathbf{x}^{(k)})}$ and the first order sensitivities $\frac{\delta f_i}{\delta x_j}(\mathbf{x}^{(k)})$ are calculated for $i = 1, \dots, n$, the latter by using (2.1) with the appropriate $f_i(\mathbf{x})$ together with the sensitivity analysis method from Svanberg and Werme (2005a).

Next, the following integer linear programming problem in \mathbf{x} and z is solved (e.g. with the well known integer programming software CPLEX).

$$\begin{aligned}
 &\text{minimize } z \\
 &\text{subject to } z \geq \tilde{f}_i^{(k)}(\mathbf{x}) \text{ for } i = 1, \dots, n, \\
 &\quad \mathbf{Ax} \leq \mathbf{b}, \\
 &\quad \sum_{j=1}^n |x_j - x_j^{(k)}| \leq M \\
 &\quad \mathbf{x} \in \{0, 1\}^n \text{ and } z \in \mathbb{R},
 \end{aligned} \tag{4.1}$$

where $\tilde{f}_i^{(k)}(\mathbf{x})$ is defined by (2.2), and M is an given upper bound on the number of elements that are allowed to be simultaneously changed in the current iteration.

Assume that an optimal solution, denoted $\bar{\mathbf{x}}$, of this problem (4.1) has been obtained. If $\bar{\mathbf{x}} \in \mathcal{S}$ and $\max_i f_i(\bar{\mathbf{x}}) < \max_i f_i(\mathbf{x}^{(k)})$, the next iteration point is chosen as $\mathbf{x}^{(k+1)} = \bar{\mathbf{x}}$. Otherwise, the right hand side M is temporarily decreased by one, and (4.1) is solved again. This decrease in M is repeated until $\bar{\mathbf{x}} \in \mathcal{S}$ and $\max_i f_i(\bar{\mathbf{x}}) < \max_i f_i(\mathbf{x}^{(k)})$, in which case the next iteration point is chosen as $\mathbf{x}^{(k+1)} = \bar{\mathbf{x}}$ and M is reset to its original value, or until M has decreased down to 0, in which case the whole algorithm is stopped with the current point $\mathbf{x}^{(k)}$ being an (at least) local optimal solution of the original problem (3.3) or (3.5). For the compliance case, i.e. (3.6), the additional variable $z \in \mathbb{R}$ is not needed. Instead the objective function in (4.1) is simply chosen to be the linearization $\tilde{f}_0^{(k)}(\mathbf{x})$ of $f_0(\mathbf{x}^{(k)}) = \mathbf{p}^T \mathbf{u}(\mathbf{x})$ and the constraints $z \geq \tilde{f}_i^{(k)}(\mathbf{x})$ for $i = 1, \dots, n$ are omitted from the problem formulation (4.1).

Note that the constraint $\sum_{j=1}^n |x_j - x_j^{(k)}| \leq M$ can equivalently be written as the linear constraint

$$\sum_{j \in \mathcal{J}_0^{(k)}} x_j + \sum_{j \in \mathcal{J}_1^{(k)}} (1 - x_j) \leq M, \tag{4.2}$$

where $\mathcal{J}_0^{(k)} = \{j \mid x_j^{(k)} = 0\}$ and $\mathcal{J}_1^{(k)} = \{j \mid x_j^{(k)} = 1\}$.

The motivation for this constraint, which defines a certain “neighbourhood” of the current iteration point $\mathbf{x}^{(k)}$, is twofold. First, it makes the ILP problem (4.1) easier to solve since the number of possible solutions are decreased by this constraint. Second, the approximations $f_i(\mathbf{x}) \approx \tilde{f}_i^{(k)}(\mathbf{x})$ are likely to be better if \mathbf{x} is reasonably close to $\mathbf{x}^{(k)}$.

Numerical experience indicate that an hierarchical approach should be used, were one starts with a coarse mesh, solves the problem (3.3), (3.5) or (3.6) by the above SILP method, and then uses the obtained (locally optimal) solution to construct a starting point for the corresponding problem (3.3), (3.5) or (3.6) on a refined mesh. In each refinement, every finite element is divided into four new finite elements. This means that each new considered problem has four times as many binary variables as the previous problem. After several refinements, the number of binary variables has become so large that the ILP problem (4.1) gets very time consuming to solve, even if M is reasonably small. Then a possible simplification is to specify that a certain subset of the binary variables should be held fixed in the current iteration. If $\mathcal{F}(\mathbf{x}^{(k)})$ denotes the index set for these fixed variables, then the constraints $x_j = x_j^{(k)}$ for all $j \in \mathcal{F}(\mathbf{x}^{(k)})$ are included in (4.1). A natural way to generate this set $\mathcal{F}(\mathbf{x}^{(k)})$ for problem (3.3) is as follows. First, the number N of elements that should *not* be fixed is chosen, say $N = 100$. Next, the quantities $w_j = \max_i f_i(\mathbf{x}^{(k)} + \xi_j^{(k)} \mathbf{e}_j)$ are calculated for $j = 1, \dots, n$, where (as before) $\xi_j^{(k)} = 1 - 2x_j^{(k)}$ and $f_i(\mathbf{x}) = \mathbf{e}^T \mathbf{x} \cdot \sqrt{x_i \mathbf{u}(\mathbf{x})^T \mathbf{S}_i \mathbf{u}(\mathbf{x})}$. Finally, the indices j corresponding to the $n - N$ largest w_j define the set $\mathcal{F}(\mathbf{x}^{(k)})$, while the indices corresponding to the N smallest w_j define the set of non-fixed variables x_j in the current ILP problem (4.1). The set $\mathcal{F}(\mathbf{x}^{(k)})$ can be constructed in a similar way for problem (3.5) and (3.6).

5. NUMERICAL RESULTS

The method has been implemented in Matlab and the CPLEX 8.1 Callable Library (see ILOG, 2001) was used in order to solve the ILPs. The considered problems were solved for the ground structure, supports and load-case shown in Figure 1 where a distributed unit load is applied to a third of the right-most side. In the test example Young’s modulus was set to 100 and Poisson’s ratio was 0.3. Nine-node isoparametric finite elements were used. The initial (coarsest) mesh consisted of 27 finite elements. Three refinements were accomplished, so that the final (fourth) mesh consisted of $27 \times 64 = 1728$ elements.

The numbers M and N which define, respectively, the neighbourhood radius and the number of non-fixed elements in the ILP problem (4.1), were chosen as

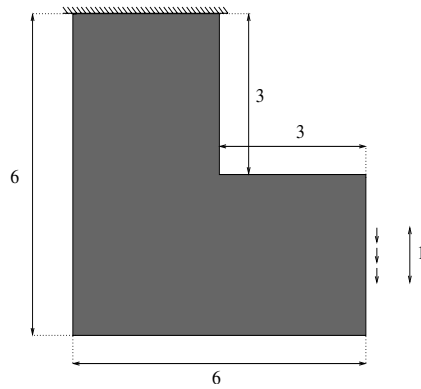


Figure 1. The test example.

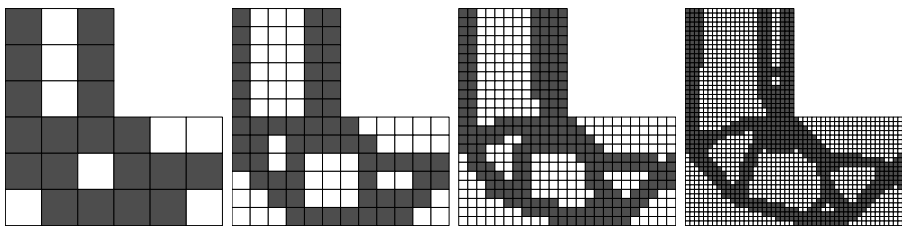


Figure 2. Obtained solutions for the load-case in Figure 1 for problem (3.3).

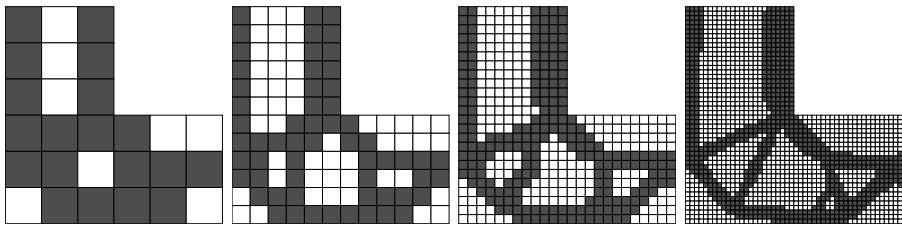


Figure 3. Obtained solutions for the load-case in Figure 1 for problem (3.5).

follows for the four different meshes: $(M, N) = (2, 27), (4, 108), (8, 108),$ and $(8, 108)$.

The obtained results for problem (3.3) are presented in Figure 2 and Table 1. Problem (3.5) was also solved and here the volume constraints for all meshes were set to the corresponding volumes obtained in the previous problem, i.e. (3.3). The obtained results for problem (3.5) are presented in Figure 3 and Table 2.

Table 1. The data for the initial structure and solutions given in Figure 2 All the numerical values have been computed after translating all the solutions to the finest mesh. \mathbf{x}_0 is the completely black structure.

\mathbf{x}	$\mathbf{e}^T \mathbf{x}$	$\max_i \sigma_i$	$\mathbf{p}^T \mathbf{u}$
\mathbf{x}_0	100	100	100
\mathbf{x}_1	70.4	123.8	155.1
\mathbf{x}_2	54.6	103.8	185.0
\mathbf{x}_3	50.5	90.7	198.9
\mathbf{x}_4	41.7	82.7	233.6

Table 2. The data for the initial structure and solutions given in Figure 3. All the numerical values have been computed after translating all the solutions to the finest mesh. \mathbf{x}_0 is the completely black structure.

\mathbf{x}	$\mathbf{e}^T \mathbf{x}$	$\max_i \sigma_i$	$\mathbf{p}^T \mathbf{u}$
\mathbf{x}_0	100	100	100
\mathbf{x}_1	70.4	123.8	155.1
\mathbf{x}_2	54.6	109.3	180.7
\mathbf{x}_3	50.5	81.6	187.8
\mathbf{x}_4	41.7	73.6	216.5

Table 3. The data for the initial structure and solutions given in Figure 4. All the numerical values have been computed after translating all the solutions to the finest mesh. \mathbf{x}_0 is the completely black structure.

\mathbf{x}	$\mathbf{e}^T \mathbf{x}$	$\max_i \sigma_i$	$\mathbf{p}^T \mathbf{u}$
\mathbf{x}_0	100	100	100
\mathbf{x}_1	70.4	114.3	152.5
\mathbf{x}_2	54.6	137.3	170.5
\mathbf{x}_3	50.5	123.5	158.8
\mathbf{x}_4	41.7	131.6	182.4

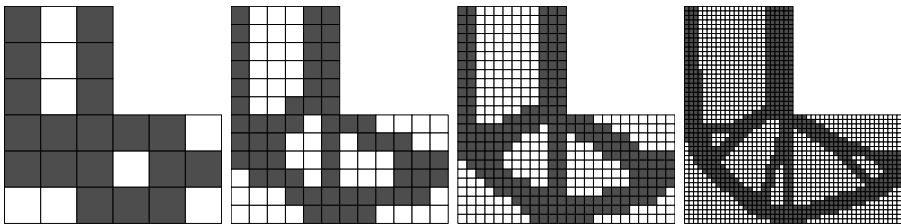


Figure 4. Obtained solutions for the load-case in Figure 1 for problem (3.6).

Finally, problem (3.6) was solved. The volume constraints were set to the corresponding volumes obtained for problem (3.3) and the results are given in Figure 4 and Table 3.

6. CONCLUSIONS

The numerical results indicate that the proposed method is able to find reasonable solutions to medium-scale topology optimization problems. Since a pure 0-1 setting is used no “grey” elements appear which means that no post-

processing is needed. Further advantages is that the method is able to reduce the volume while at the same time reduce the maximum von Mises stress, compared to the completely black starting solution, for both the problems involving stresses. The linear subproblems are solved to a global optimum and the obtained solutions to the original problem are guaranteed to be a local optimum in the sense that no binary variable can be changed to its opposite binary value while at the same time give a lower objective value. That the (fourth mesh) solution to (3.3) is just a local optima is apparent since the maximum von Mises stress for this solution is actually higher than the von Mises stress for the (fourth mesh) solution to (3.5). Both solutions have the same volume however, which implies that the obtained solution for (3.5) is actually better than the obtained solution for (3.3), even if the objective from (3.3) is used. Thus, the solution for the finest mesh in Figure 2 is not a global optimum of problem (3.3).

Another conclusion, based on the numbers in Tables 1–3, is that obtained solutions to a minimum compliance problem may be poor with respect to stresses.

ACKNOWLEDGMENTS

The authors are grateful to Mathias Stolpe at DTU for fruitful discussions on the method and valuable help concerning the integer programming solver CPLEX/8.1.

REFERENCES

- Bendsøe, M.P. (1989) Optimal shape design as a material distribution problem, *Structural Optimization*, 1, 193–202.
- Bendsøe, M.P. and Sigmund, O. (1999) Material interpolation schemes in topology optimization, *Archive of Applied Mechanics*, 69, 635–654.
- Fleury, C. (1989) Conlin: An efficient dual optimizer based on convex approximation concepts, *Structural Optimization*, 1, 81–89.
- Fleury, C. and Braibant, V. (1986) Structural optimization: A new dual method using mixed variables, *International Journal for Numerical Methods in Engineering*, 23, 409–428.
- Griffith, R.E. and Stewart, R.A. (1961) A nonlinear programming technique for the optimization of continuous processing system, *Management Science*, 7, 379–392.
- ILOG (2001) *ILOG CPLEX 8.0 User's manual*.
- Nash, S.G. and Sofer, A. (1996) *Linear and Nonlinear Programming*, McGraw-Hill, New York.
- Rozvany, G.I.N., Zhou, M. and Birker, T. (1992) Generalized shape optimization without homogenization, *Structural Optimization*, 4, 250–252.
- Stolpe, M. and Svanberg, K. (2003) Modelling topology optimization problems as linear mixed 0-1 programs, *International Journal for Numerical Methods in Engineering*, 57, 723–739.
- Svanberg, K. (1987) The method of moving asymptotes – A new method for structural optimization, *International Journal for Numerical Methods in Engineering*, 24, 359–373.

- Svanberg, K. (2002) A class of globally convergent optimization methods based on conservative convex separable approximations, *SIAM Journal on Optimization*, 12(2), 555–573.
- Svanberg, K. and Werme, M. (2005a) Sensitivities of displacements and stresses with respect to changes in shape and topology, *Proceedings of the WCSMO6 in Rio de Janeiro* (<http://www.wcsmo6.org/papers/1281.pdf>).
- Svanberg, K. and Werme, M. (2005b) Topology optimization by a neighbourhood search method based on efficient sensitivity calculations, submitted.

Bio

BIO-INSPIRED MATERIAL DESIGN AND OPTIMIZATION

Xu Guo^{1,2} and Huajian Gao²

¹*Department of Engineering Mechanics, State Key Laboratory of Structure Analysis for Industrial Equipment, Dalian University of Technology, 116023 China*

²*Max-Planck Institute for Metals Research, Heisenbergstr. 3, D-70569 Stuttgart, Germany*
hjgao@mf.mpg.de

Abstract: Natural materials such as bone, tooth, and nacre are nano-composites of proteins and minerals with superior stiffness and toughness. At the most elementary structure level, bio-composites exhibit a generic microstructure consisting of staggered mineral bricks wrapped by soft protein in nanoscale. Why does nature design building blocks of biological materials in this form? Can we reproduce this kind of structure from the structural optimization point of view? We believe that biological materials are designed with simultaneous optimization of stiffness and toughness for maximum structural support and flaw tolerance. With this philosophy, an optimization problem is formulated under the assumption of appropriate material constitutive models and failure criteria. It is shown that, within this optimization framework, the staggered microstructure of biological materials can be successfully reproduced at the nanometer length scale. This study may have at least partially provided an answer to the question whether the nanostructure of biological materials is an optimized structure and what is being optimized. The results suggest that we can draw lessons from the nature in designing nanoscale and hierarchically structured materials.

Keywords: Bio-inspired mimetic, material design, optimization, flaw tolerance.

1. INTRODUCTION

Natural materials such as bone, tooth, and nacre are nano-composites of proteins and minerals with superior stiffness and toughness (Jackson et al., 1988). Experimental results show that while the stiffness of bio-composites is close to that of its mineral constituent, its fracture strength and toughness are significantly higher than those of the mineral. This outstanding performance of bio-composites comes from their highly complex hierarchical structures at different length scales (Weiner and Wanger, 1998). For instance, sea shells have 2 to 3 orders of lamellar structure (Currey, 1997; Menig et al., 1998; Weiner and

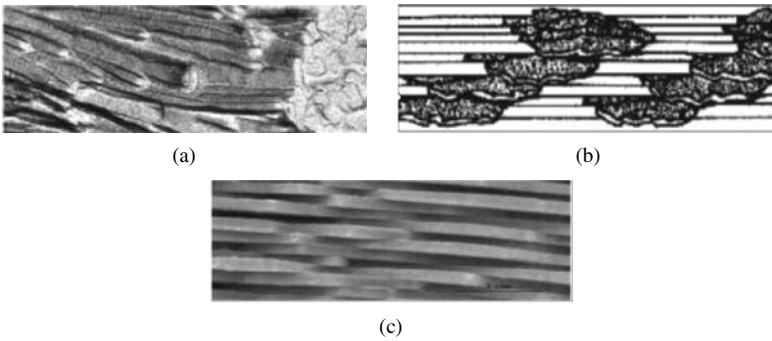


Figure 1. The nanostructure of some typical hard biological tissues; (a) tooth, (b) bone and (c) shell.

Wanger, 1998) and bone has 7 orders of hierarchy (Currey, 1984; Rho et al., 1998; Weiner and Wanger, 1998). Figure 1 shows the nanostructure of some typical bio-composites.

While the full hierarchical structure of bio-materials such as bone is extremely complex and variable, it is most interesting to observe that its basic building blocks, the mineralized collagen fibril are rather universal. They are generally designed at the nanoscale with nanometer sized hard mineral inclusions embedded in the soft protein matrix (Gao et al., 2003). For instance, at the lowest level of hierarchy, the nanostructure of bone (mineralized fibrils) is consisting of mineral platelets with thickness around a few nanometers aligned in a stagger pattern in a collagen matrix (Landis, 1995; Rho et al., 1998; Weiner and Wanger, 1998). Dentin is a calcified tissue somewhat similar to bone, where the collagen-rich matrix is reinforced by calcium phosphate crystals (Weiner et al., 1999; Tesch et al., 2001; Weiner and Wanger, 1998). Similarly, the cell walls of wood are made of cellulose fibrils embedded in a soft semicellulose-lignin matrix.

Because mineralized fibrils are the elementary unit of many complex bio-composites, it is important to understand how their mechanical properties depend on the properties of their constituents and the style of arrangement of different materials at the level of individual fibrils. The components of mineral fibril have extremely different mechanical properties. The mineral is stiff and brittle while the (wet) protein is much softer but also much tougher than the mineral. Increasing the amount of mineral particles will always increase the stiffness but also the brittleness of the bone tissue at the same time. How to make the bio-composite hard enough with high toughness? Nature solves this problem in an elegant way by the smart design of the size, shape and material distribution of the nanostructures of bio-composites.

Previous studies (Gao and Ji, 2003; Ji and Gao, 2004) show that large aspect ratios and the pattern of a staggered alignment of mineral platelets are the key factors contributing to the large stiffness of biomaterials. On the other hand, proteins between staggered mineral platelets play the essential role of absorbing and dissipating a large amount of fracture energy. Furthermore, as shown by Gao and Ji (2003), at the nanoscale, brittle mineral becomes insensitive to flaws which makes it possible for it to sustain large stress without brittle fracture and in turn enhance the toughness of biomaterials. In summary, it is apparent that both the organic and mineral components as well as their arrangement contribute equally to the strength of biomaterials. The bio-composite combines the optimal properties of its both components, the stiffness and the toughness. This rather unusual combination of material properties provides both rigidity and resistance against fracture. From the viewpoint of materials science, a better understanding of the underlying construction principles might help designing better composite materials.

Nature materials have been perfected by the evolution through millions of years. The essential idea of bio-inspired material design is to see how, in some cases at least, the forms of these “well designed” nature materials can be explained by physical and mathematical laws. Once we can abstract the principle and mechanism of good design from nature, we can therefore use them to make advanced synthetic materials. From example, if we know some of the methods that natural systems have evolved to increase toughness, we can realize that holes, carefully used, can improve strength while at the same time actually making the structure lighter.

It is generally believed that the complex hierarchical structure is optimized to achieve a remarkable mechanical performance (Weiner and Wanger, 1998; Aksay and Weiner, 2004; Fratzl, 2004). Among the key features of the biological systems, the organization of bio-structures at nano-scale is the prominent one. The amazing rationality of these biological constructions naturally excites the interest to analyze them by using mathematical tools developed in the theory of mechanics and structural optimization. Although the “result” of the “optimization problem” is known, until now, however it is still unclear what performance index is optimized when nature designs the building blocks of bio-composites, i.e. in what sense the structure is optimal.

In order to obtain more insight in bio-inspired material design from nano-scale and up, an optimization model is proposed in the present study to explain why nature designs building blocks of biological materials in the present form. We believe that biological materials are designed with simultaneous optimization of stiffness and toughness for maximum structural support and flaw tolerance. With this philosophy, an optimization problem is formulated under the assumption of appropriate material constitutive models and failure criteria. It is shown that, within this optimization framework, the staggered microstructure

of biological materials can be successfully reproduced at the nanometer length scale. This study may have at least partially provided an answer to the question whether the nanostructure of biological materials is an optimized structure and what is being optimized. The results suggest that we can draw lessons from the nature in designing hierarchically structured materials.

This paper is organized as follows. In Section 2, the mechanical properties of mineral and protein as well as their basic failure mechanisms will be discussed. Then in Section 3, an optimization model used for the design of nanostructure of bio-composites with appropriate objective and constraint functions is proposed. Optimization results obtained with the proposed optimization model will be given in Section 4. It is shown that the staggered pattern of the material distribution in the nanostructure of bio-composites can be successfully reproduced via the present optimization model. Finally, we end the paper with some concluding remarks.

2. MECHANICAL PROPERTIES AND FAILURE MECHANISMS OF THE BASIC COMPONENTS OF BIO-COMPOSITE AT NANOSCALE

2.1 Mechanical Property of Mineral and Its Flaw Tolerance Behaviour at Nanoscale

The present study focuses on the basic building block, the collagen-mineral composite, containing nano-sized mineral platelets (essentially carbonated hydroxyapatite), protein and water. These components have extremely different mechanical properties. The mineral is stiff and brittle, which can be considered as linear elastic material during the process of deformation in physiological conditions. It has a Young modulus as high as about 100 GPa with failure strain about 1–2%. The stiffness of the biomaterials, which provides skeletal rigidity, is mainly provided by the mineral crystals.

Although the theoretic strength of mineral material in bio-composites is about 1 GPa, it is, however, as fragile as a classroom chalk. It is very sensitive to the flaw in it at macroscopic length scale. The cracks in the mineral can always propagate at stresses much lower than its theoretical strength, which often leads to the catastrophe failure of structures. The high toughness of bio-materials, however, requires that the mineral constituent should sustain large stresses without brittle fracture. How does nature solve this problem?

This problem has been studied by Gao et al. (2003). They pointed out that there is a critical length scale of mineral material below which the mineral is insensitive to existing flaws, which can be expressed as:

$$h^{\text{cri}} \approx \alpha^2 \frac{\gamma E^M}{\sigma_{\text{th}}^2}, \quad (1)$$

where γ is the surface energy and E^m is the Young's modulus of mineral. α is a crack geometry dependent parameter and σ_{th} is the theoretical strength of mineral.

As the thickness of mineral crystal drops below this length scale, the strength of a perfect mineral platelet is maintained in spite of defects. In this circumstance, *the failure criterion is governed by theoretical strength rather than by the Griffith criterion*. For typical values of γ , E^M and σ_{th} , it can be estimated that h^{crit} is in the nanometer scale. This explains why the basic building blocks of bio-composites are always taken in nanometer sizes.

2.2 Mechanical Property of Protein and Its Failure Mechanism

Protein plays very important role in biomaterials. Although protein may have less effect on the biomaterial's stiffness than mineral, however, it has a profound effect on the biomaterial's toughness. While the toughness of bone results from its complex hierarchical microstructure with several contributing toughening mechanisms, at the level of mineralized collagen fibrils, the soft organic matrix between the hard but brittle mineral plays a crucial role because it is a primary arrestor of cracks and source of energy dissipation. Previous studies (Gao and Ji, 2003; Ji and Gao, 2004) show that the tensile stress on the bio-composite is transmitted through the organic matrix mainly by shear, therefore the shear stiffness, failure strength and post yielding deformation behaviour are the controlling factors for the toughness of the bio-composites. Furthermore, it has been shown that the geometric arrangement of the inorganic and organic materials in the nanostructure of bio-composites also plays an essential role for the toughening effect. This naturally leads to the question that whether the staggered pattern in which the mineral and the organic material are organized in bio-composites is good enough from optimization point of view? This issue will be addressed in the following sections.

Since the mechanical behaviour of protein is vital for the toughness of bio-composites, here we will discuss it in more details. Smith et al. (1999) used atomic force spectroscopy to test the axial force-extension behavior of organic matrix exposed on a fractured nacre surface. The axial force-extension behavior exhibited an irregular "saw-tooth" character, so named because of the repeating pattern of a nonlinear force increase with extension followed by abrupt load drops. This phenomenon is attributed to the unfolding of complicated domains along the bio-macromolecular chain and overcoming sacrificial bonds induced by Ca^{2+} ions in organic matrix sequentially. This behavior is speculated to play a significant role in the mechanical behavior of biomaterials. The protein molecules can undergo large deformation as the protein domains unfold, which in turn increases the amount of energy dissipated before frac-

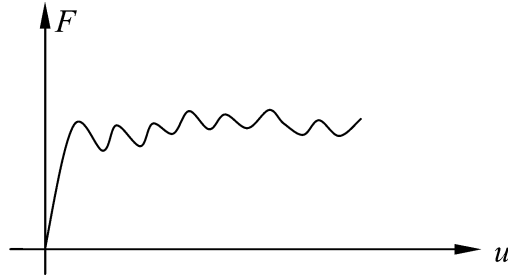


Figure 2. A schematic illustration of the force-extension curve of protein.

ture and results in a very long flat tail of the force-extension curve as shown in Figure 2. In this work, the mechanical behavior of protein is modeled as $\sigma_e = f(\epsilon_e) = \sigma_f^P(1 - e^{-\gamma\epsilon_e})$, where $\gamma = 5$ and $\sigma_f^P = 20$ MPa. σ_e and ϵ_e are equivalent stress and equivalent strain, respectively.

3. OPTIMIZATION PROBLEM

The present work aims at understanding the rationality of the existing brick and mortar form of the building blocks of bio-composites from optimization point of view. Mathematically speaking, bio-mimicking or bio-inspired material design can be formulating as an *inverse optimization* problem, i.e. finding a goal functional of an optimization problem with the inspiration that obtained from the analysis of existing forms of biomaterials. If the solution of this optimization problem can be in reasonable agreement with the reality, then the design principles embedded in the proposed optimization problem can be used to design high-performance man-made materials. This is just the essential idea of bio-mimicking research.

Here we have assumed implicitly that the building block of bio-composites is the “optimization result” of natural evolution, which is consistent with Neo-Darwin’s theory of natural selection. As for an optimization problem, the design variables, the objective as well as constraint functions (or functionals) are its three basic ingredients. In the following, these issues will be addressed respectively.

3.1 Design Variables

In this work, we will formulate the corresponding optimization problem in the framework of optimal topology design, i.e. finding the optimal distribution of hard and brittle inorganic as well as soft and ductile organic materials in a basic unit-cell (*RVE*) of the basic building blocks of bio-composites. To this end, an indicator function $\rho(\mathbf{x})$ defined on the unit cell Y is introduced, which can only take the values of 0 and 1. If $\rho(\mathbf{x}) = 0$, it is indicated that the current point \mathbf{x}

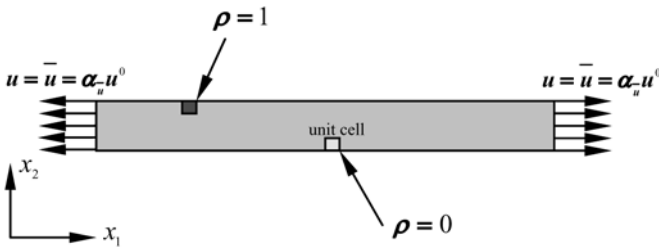


Figure 3. Illustration of the design variable and design domain.

is occupied by hard mineral material, otherwise it is occupied by soft protein like material (see Figure 3).

In order to use gradient based numerical algorithms for the solution of the proposed discrete valued design optimization problems, a conventional approach is to replace the integer variables with continuous variables and then introduce some form of penalty that steers the solution to discrete 0-1 values. This approach is also adopted in the present paper.

Another design variable is the displacement control factor $\alpha_{\bar{u}}$, which controls the process of deformation. Here we assume that the unit cell is loaded by prescribed displacements on the boundary of the unit cell, which takes the form of $\mathbf{u} = \bar{\mathbf{u}} = \alpha_{\bar{u}} \mathbf{u}^0$ on ∂Y_u .

3.2 Objective Function

The determination of a suitable objective functional is a crucial aspect for the solution of an inverse optimization problem. As for the present bio-mimicking problem, it should reflect the essential idea (if there is) that nature used to “design” the biomaterials. In the present work, we postulate that *biological materials are designed with simultaneous optimization of stiffness and toughness for maximum structural support and flaw tolerance*. With this philosophy, the following objective functional is proposed:

$$f = \left(\frac{E^{\text{eff}}}{E_0} \right) \left(\frac{\Gamma}{\Gamma_0} \right). \tag{2}$$

We use f as a measure of the ductility of the material. Here only one dimensional loading case (uni-axial tensile loading along principle deformation direction) is considered and E^{eff} is the effective stiffness along the loading direction. Γ is the energy dissipated during the process of deformation before any material point in the unit cell reaches its critical failure status. E^0 and Γ^0 are two parameters used for the dimensionless of the objective function.

3.3 Constraint Functions

Constraint function is another very important ingredient for an optimization problem, since it has vital influence on the final optimal solution. In a biomimicking problem, just like that of objective functional, the constraint functions should also reflect the basic challenges nature faced when designing biomaterials. From mechanics point of view, these constraint functions are closely related to the basic failure mechanisms of different materials as shown by Gao and Ji (2003). In the proposed optimization model, it requires that during the process of deformation, the effective strain of any material point in the unit cell should not exceed its critical value. According to the discussions in Section 2, in this work, the effective failure strain is set to be 1% for hard and brittle mineral material while 150% for soft and ductile organic material. This is consistent with the typical deformation and failure mechanisms of these materials as discussed thoroughly in the literatures.

It is worth noting that in the present work, we tacitly assumed that the interfaces between different materials are strong enough. This can be justified by the fact that special polymers such as proteoglycans at the interface of organic and inorganic materials in bio-composites are capable of making the binding between them tight enough (Fratzl et al., 2004). Another problem is that 1of mineral material, but if we take the unavoidable defects into consideration, is it still reasonable to use this theoretical strength value as the control parameter in the optimization problem?

This problem can be solved by restricting the size of the unit cell below the critical size of mineral derived from the argument of flaw tolerance. As pointed out in Section 2, when the mineral size drops below this critical length scale, the theoretical strength of mineral platelet can be maintained in spite of defects. From optimization point of view, this dimension restriction of the unit cell can also be seen as a result of fracture strength optimization, which is an essential part of the multidisciplinary optimization process of biomaterial design.

In summary, the optimization problem of bio-material design can be formulated as follows:

Find $\rho(\mathbf{x}) \in L^\infty(Y)$, $\alpha_{\bar{\mathbf{u}}}$

$$\min f = - \left(\frac{E^{\text{eff}}}{E_0} \frac{\Gamma}{\Gamma_0} \right) \quad (3)$$

S.t.

$$\iint_Y \mathbf{C}(\mathbf{x}) \boldsymbol{\varepsilon}(\mathbf{u}(\mathbf{x})) : \boldsymbol{\varepsilon}(\mathbf{v}(\mathbf{x})) dY = 0 \quad \text{in } Y \text{ for every } \mathbf{v} \in \mathbf{U}_{\text{ad}}, \quad (4)$$

$$\iint_Y \rho(\mathbf{x}) dY = \bar{V}, \quad 0 \leq \rho(\mathbf{x}) \leq 1, \quad (5)$$

$$\mathbf{u} = \bar{\mathbf{u}} = \alpha_{\bar{\mathbf{u}}}\mathbf{u}^0 \quad \text{on } \partial Y_{\bar{\mathbf{u}}}, \tag{6}$$

$$\boldsymbol{\varepsilon}^{\text{eq}}(\mathbf{x}) = \sqrt{\boldsymbol{\varepsilon}(\mathbf{u}(\mathbf{x})) : \boldsymbol{\varepsilon}(\mathbf{u}(\mathbf{x}))} \leq \rho^n(\mathbf{x})\boldsymbol{\varepsilon}_f^M + [1 - \rho^n(\mathbf{x})]\boldsymbol{\varepsilon}_f^P \quad \text{in } Y, \tag{7}$$

where $\mathbf{C}(\mathbf{x}) = \rho^n(\mathbf{x})\mathbf{C}^M + 1 - \rho^n(\mathbf{x})\mathbf{C}^P$ is the fourth order elasticity tensor at material point \mathbf{x} . It is obtained by interpolating between the elasticity tensors \mathbf{C}^M of mineral and \mathbf{C}^P of protein, respectively. $n > 1$ is an integer used for the penalization of the intermediate values of ρ . $\boldsymbol{\varepsilon}^{\text{eq}}(\mathbf{x})$ is the equivalent strain at \mathbf{x} . $\boldsymbol{\varepsilon}_f^M$ and $\boldsymbol{\varepsilon}_f^P$ denote the failure strain of mineral and protein, respectively. $\mathbf{u}^0 = (1, 0)^T$ is the displacement mode vector, which indicates that the structure is only loaded along x_1 direction. \mathbf{U}_{ad} is the space of admissible test functions appeared in the weak form of equilibrium equation. \bar{V} is the given amount of the available mineral material. For simplicity, only the 2-D case is considered, extensions to the 3-D case is straightforward.

For the calculation of E^{eff} , a homogenization approach based on asymptotic expansion is used. E^{eff} can be expressed as:

$$E^{\text{eff}} = \frac{1}{|Y|} \iint_Y \left[E_{1111}(\mathbf{x}) - E_{11pq} \frac{\partial \chi_p^{11}(\mathbf{x})}{\partial y_q} \right] dY, \tag{8}$$

where $\chi^{11} = \chi^{11}(\mathbf{x})$ is the characteristic function, which can be obtained by solving a boundary value problem defined on Y with periodic boundary conditions. $|Y|$ denotes the area of the unit cell.

In the present work, the measure of the toughness of the bio-composites corresponding to the considered loading condition is defined as:

$$\Gamma = \iint_Y [(1 - \rho(\mathbf{x})\boldsymbol{\sigma}(\mathbf{x}) : \boldsymbol{\varepsilon}(\mathbf{x}))] dY, \tag{9}$$

where $\boldsymbol{\sigma}(\mathbf{x})$ and $\boldsymbol{\varepsilon}(\mathbf{x})$ are stress and strain at point \mathbf{x} , respectively. An assumption is also made here that all of the work done on the soft material is dissipated as heat during the process of deformation.

3.4 Optimization Algorithms

For the nonlinear constitutive model, although the sensitivities used for numerical optimization can be obtained analytically (for the limitation of space, the detailed derivations are omitted here), numerical experiments show that the behavior of the solution process is unstable and often lead to non-convergent results. This is can be partially attributed to the inaccurate numerical calculation of the sensitivities since at some stages of the solution process, the condition number of tangent stiffness matrix is large for the high contrast of the material stiffness properties of different materials. Taking this into consideration and in order for dealing with the 0-1 constraints more directly, in the present work,

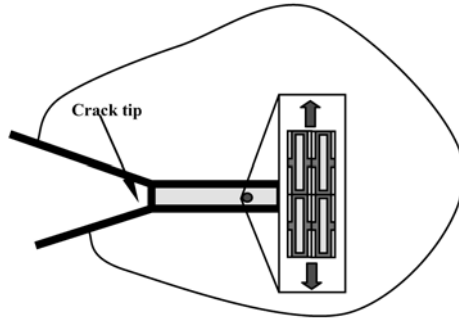


Figure 4. Loading condition in front of the tip of a propagating crack.

Genetic Algorithm (GA) is used to solve the corresponding optimization problem. A binary chain with $m + 9$ bits is used to represent one point in the design space. The first m bits represent the material type in m elements and the last 9 bits represent the value of the displacement control factor. Its value is varied in the interval of $[0.0, 5.1]$ with a resolution of 0.1.

4. RESULTS AND DISCUSSION

In this section, a numerical example will be given for illustration purpose. For the considered problem, the design domain is a rectangular one with an aspect ratio of 10:1. The length and width of the design domain are $\text{len } x = 100 \text{ nm}$ and $\text{len } y = 10 \text{ nm}$, respectively. The Young's modulus of mineral and protein like material are $E^M = 100 \text{ GPa}$ and $E^P = 100 \text{ MPa}$ (corresponding to $\gamma = 5$), respectively. The effective failure strains for mineral and protein like material are 1% and 150%, respectively. The yield stress for protein like material is $\sigma_f^P = 20 \text{ MPa}$. E^0 and Γ^0 in objective function used for dimensionless are $E^0 = E^M \bar{V}/|Y|$ and $\Gamma^0 = \sigma_f^P \epsilon_f^P \times \text{len } x \times \text{len } y/4$, respectively. The available volume percentage of mineral in the design domain is chosen as 57%. The prescribed displacements are imposed on the lateral boundary of the unit cell in the horizontal direction. This loading condition is used to simulate the pull out process in the process zone in the front of the propagating crack (see Figure 4).

We assume that the unit cell to be designed has one-quarter symmetry. Then only one quarter of the unit cell needs to be optimized. The design domain and the boundary conditions determined from both of the symmetry and periodic properties of the unit cell and loading condition are depicted in Figure 5. In this figure, the vertical displacement at the upper and lower boundaries and the horizontal displacements at the right boundary are set to zero values.

14×3 and 7×6 meshes are first used to solve the same optimization. The individuals in the initial population for GA algorithm are generated randomly.

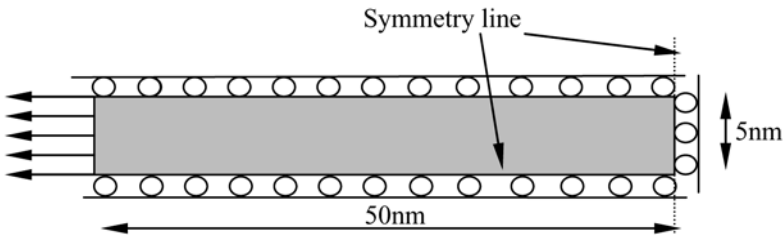


Figure 5. Design domain and boundary as well as loading conditions.

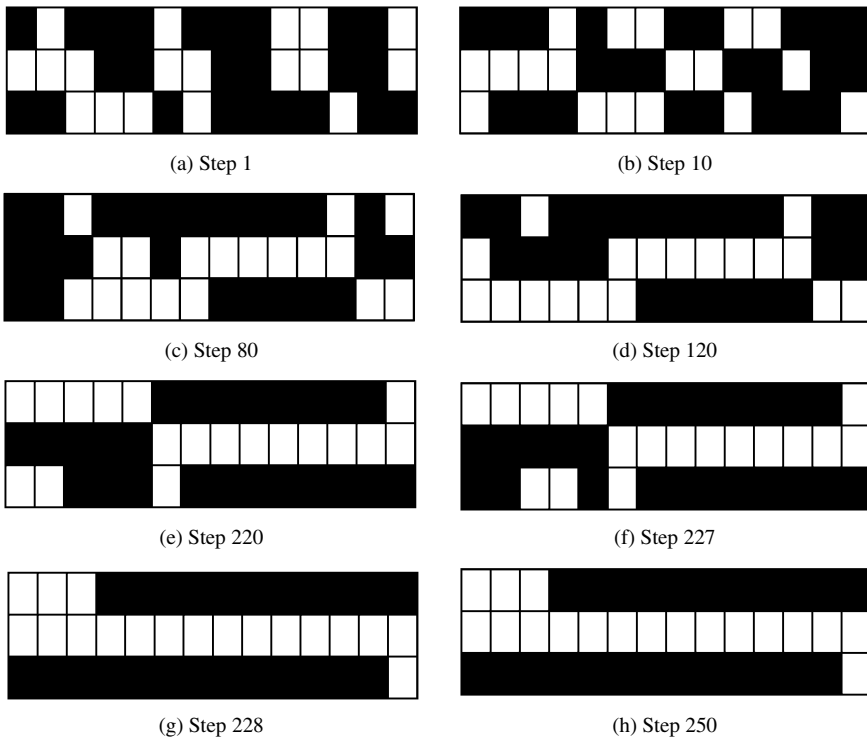


Figure 6. GA evolution history for 14×3 mesh (best individual in each generation).

The GA evolution histories are illustrated in Figures 6a–6h and Figures 7a–7l, respectively. The optimal values of the displacement control factor and objective function are 2.6 and -0.0386 for 14×3 mesh as well as 1.5 and -0.0946 for 7×6 mesh, respectively. It can be seen that for these meshes, the optimal distributions of the mineral and protein like material are also of staggered type.

In order to further examine the optimality of the staggered type material arrangement, refined finite element mesh should be used. In order to enhance the computational efficiency of GA algorithm, under these circumstance, we insert

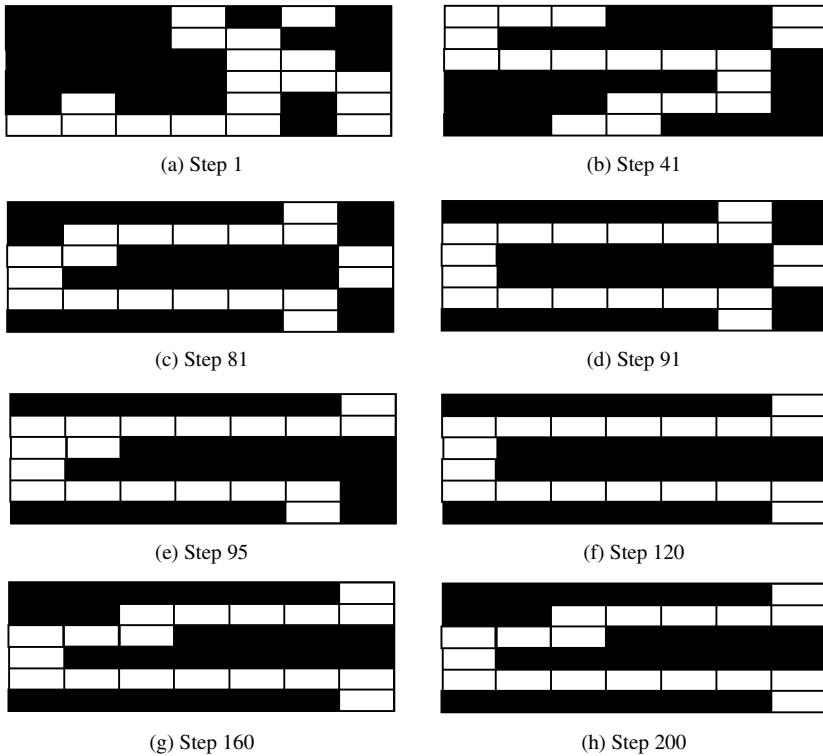
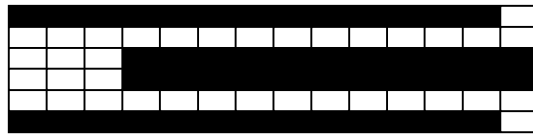


Figure 7. GA evolution history for 7×6 mesh (best individual in each generation).

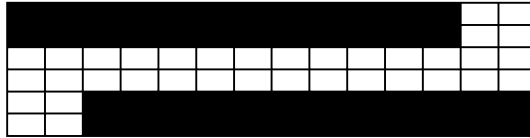
the specific individuals constructed based on the inspirations obtained from the optimization results for coarse mesh. In this way, a lot of computational efforts can be saved. Figures 8a–8d show several such specific individuals. Optimal topologies obtained by GA algorithm for different meshes are shown in Figure 9. Both are of staggered type.

Jager and Fratzl (2000) studied the mechanical properties of mineralized collagen and proposed a model with a staggered array of platelets that is in better agreement with results on molecular packing in collagen fibrils (see Figure 10). They showed this material arrangement leads to larger elastic modulus and fracture strain with the given amount of mineral in the fibril compared with a strictly parallel arrangement.

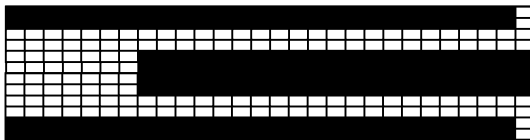
It can be seen that with the use of the proposed optimization model, the staggered arrangement of the hard and soft materials which is in reasonable agreement with that found in natural bio-composites can be reproduced (see Figures 1 and 10). Then it seems that a plausible explanation for the convergent evolution in biology can be given (at least partially) from the optimization point of view. The obtained encouraging results confirm the belief that a staggered



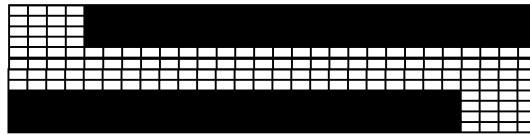
(a) Individual 1 for 14×6 mesh



(b) Individual 2 for 14×6 mesh

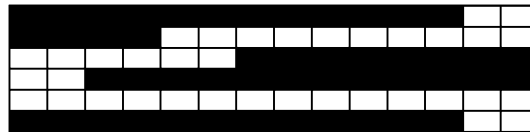


(c) Individual 1 for 28×12 mesh

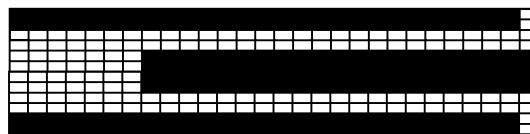


(d) Individual 2 for 28×12 mesh

Figure 8. Specific individuals used for GA algorithm for different meshes.



(a)



(b)

Figure 9. (a) Optimal topology for 14×6 mesh. (b) Optimal topology for 28×12 mesh.

arrangement of mineral particles in the fibrils is mechanically superior to a strictly parallel arrangement from optimization point of view.

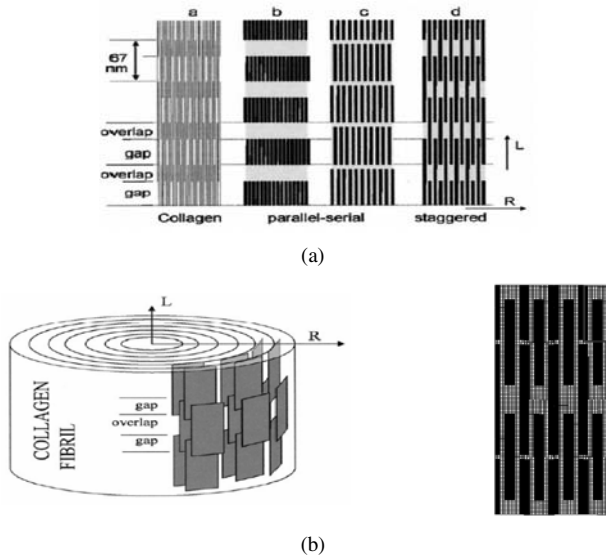


Figure 10. (a) Stagger model of mineralized collagen fiber (Jager and Fratzl, 2000) and (b) the optimal material distribution obtained by the proposed optimization model.

5. CONCLUDING REMARKS

The results of this study show that an optimization model with appropriate material constitutive models, failure criteria as well as objective and constraint functions can reproduce the realistic material distribution in the nanostructure of bio-composites. Although our approach to model the complex physical behaviour of biomaterials is certainly simplified, results obtained do show the independent roles played by mineral and soft protein like material and highlight the design principles used by the nature to produce the building blocks of bio-composites.

It seems that the maximization of ductility may be an objective of nature to design the basic building blocks of bio-composites. The insights gained from the present study are not only important for biological materials, but may also inspire novel ideas for the design of synthetic materials. From optimization point of view, bio-mimicking or bio-inspired material design can be formulated as an inverse optimization problem, i.e. finding a goal functional of an optimization problem under the condition that the solution to that problem is known. It is worth noting that the optimization problems in bio-inspired material design and engineering construction design are mutually inverse. In the former, the biological structure is *known*, but it is not clear what performance is optimized whereas the goal of the latter is to find an (*unknown*) optimal structure with the minimization (or maximization) of a *given* functional

(LeeLavanichkul and Cherkaev, 2004). Using optimization principles to reveal the strategies and mechanisms used by nature to design biomaterials is a promising research field. The present work is only a preliminary step along this direction, more work needs to be done in this promising research field.

ACKNOWLEDGEMENTS

This work is supported by the Max Planck Society of Germany; China National Science Foundation under the grants of No. 10332010, No. 10472022–No. 10421002; the Program for Changjiang Scholars and NCET Program provided by the Ministry of Education of China.

REFERENCES

- Aksay, I.A. and Weiner, S. (2004) Biomaterials. Is this really a field of research?, *J. Mater. Chem.*, 14, 2115–2123.
- Currey, J.D. (1984) *The Mechanical Adaptations of Bone*, Princeton University Press, Princeton, NJ, pp. 24–37.
- Currey, J.D. (1997) Mechanical properties of mother of pearl in tension, *Proc. R. Soc. London, Ser. B*, 196, 443–463.
- Fratzl, P., Burgert, I. and Gupta, H.S. (2004) On the role of interface polymers for the mechanics of nature polymeric composites, *Phys. Chem. Chem. Phys.*, 6, 5575–5579.
- Gao, H., Ji, B., Jager, I.L., Artz, E. and Fratzl, P. (2003) Materials become insensitive to flaws at nanoscale: lessons from nature, *Proc. Natl. Acad. Sci. USA*, 100, 5597–5600.
- Jackson, A.P., Vincent, J.F.V. Turner, R.M. (1988) The mechanical design of nacre, *Proc. R. Soc. London, Ser. B*, 234, 415–440.
- Jager, I.L. and Fratzl, P. (2000) Mineralized collagen fibrils: A mechanical model with a staggered arrangement of mineral particles, *Biophys. J.*, 79, 1737–1746.
- Ji, B. and Gao, H. (2004) Mechanical properties of nanostructure of biological materials, *J. Mech. Phys. Solids*, 52, 1963–1990.
- Landis, W.J. (1995) The strength of a calcified tissue depends in part on the molecular structure and organization of its constituent mineral crystals in their organic matrix, *Bone*, 16, 533–544.
- LeeLavanichkul, S. and Cherkaev, A. (2004) Why the grain in tree trunk spirals: A mechanical perspective, *Struct. Multidisc. Optimiz.*, 28, 127–135.
- Mening, R., Meyers, M.H., Meyers, M.A. and Vecchio, K.S. (2000) Quasi-static and dynamic mechanical response of *Haliotis rufescens* (abalone) shell, *Mater. Sci. Eng.*, A297, 203–211.
- Smith, B.L., Schaeffer, T.E., Viani, M., Thompson, J.B., Frederick, N.A., Kindt, J., Belcher, A., Stucky, G.D., Morse, D.E. and Hansma, P.K. (1999) Molecular mechanistic origin of the toughness of natural adhesive, fibers and composites, *Nature*, 399, 761–763.
- Tesch, W., Eidelman, N., Roschger P., Goldenberg, F., Klaushofer, K. and Fratzl, P. (2001) Graded microstructure and mechanical properties of human crown dentin, *Calcif. Tissue Int.*, 69, 147–157.
- Weiner, S. and Wanger, H.D. (1998) The material bone: Structure-mechanical function relations, *Annu. Rev. Mater. Sci.*, 28, 271–298.
- Weiner, S., Veis A., Beniash, E., Arad, T., Dillon, J.W., Sabsay, B. and Siddiqui, F. (1999) Per-tubular dentin formation: crystal organization and the macromolecular constituent in human teeth, *J. Struct. Biol.*, 126, 27–41.

PROTEIN SEQUENCE DESIGN ON THE BASIS OF TOPOLOGY OPTIMIZATION TECHNIQUES

Using Continuous Modeling of Discrete Amino Acid Types

G.K. Ananthasuresh

Mechanical Engineering, Indian Institute of Science, Bangalore 560012, India

suresh@mecheng.iisc.ernet.in

Abstract: The notion of optimization is inherent in protein design. A long linear chain of twenty types of amino acid residues are known to fold to a 3-D conformation that minimizes the combined inter-residue energy interactions. There are two distinct protein design problems, viz. predicting the folded structure from a given sequence of amino acid monomers (*folding problem*) and determining a sequence for a given folded structure (*inverse folding problem*). These two problems have much similarity to engineering structural analysis and structural optimization problems respectively. In the folding problem, a protein chain with a given sequence folds to a conformation, called a *native state*, which has a unique global minimum energy value when compared to all other unfolded conformations. This involves a search in the *conformation space*. This is somewhat akin to the principle of minimum potential energy that determines the deformed static equilibrium configuration of an elastic structure of given topology, shape, and size that is subjected to certain boundary conditions. In the inverse-folding problem, one has to design a sequence with some objectives (having a specific feature of the folded structure, docking with another protein, etc.) and constraints (sequence being fixed in some portion, a particular composition of amino acid types, etc.) while obtaining a sequence that would fold to the desired conformation satisfying the criteria of folding. This requires a search in the *sequence space*. This is similar to structural optimization in the design-variable space wherein a certain feature of structural response is optimized subject to some constraints while satisfying the governing static or dynamic equilibrium equations. Based on this similarity, in this work we apply the topology optimization methods to protein design, discuss modeling issues and present some initial results.

Keywords: Protein sequence design, continuous modeling of amino acid types, topology optimization, inverse folding.

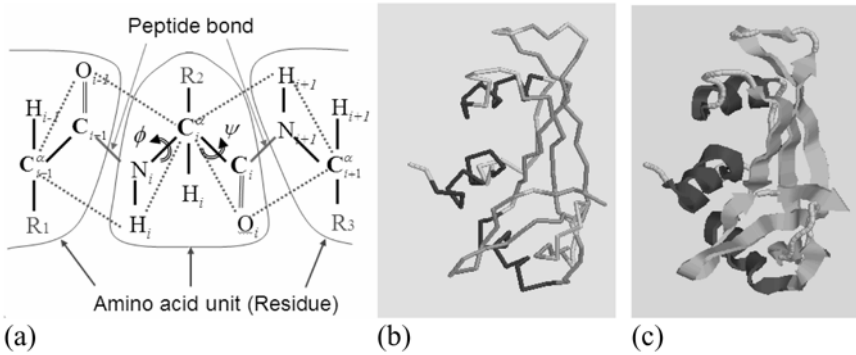


Figure 1. (a) Three amino acid residues connected by peptide bonds. The relative rotations are indicated by ϕ and ψ . (b) The representation of the backbone formed by the C_{α} atoms. (c) Ribbon representation highlighting the secondary structures, viz., α -helices, β sheets and loop regions.

1. INTRODUCTION

Proteins are heteropolymer linear chains consisting of 20 types of amino acid residues. Figure 1a shows how two adjacent residues in the chain are connected by a peptide bond and how they can rotate relative to each other. Additionally, the side chains that are denoted by R_i in Figure 1a can also assume different configurations. These mobilities allow protein chains to fold in numerous ways. The folded shape is often denoted by the backbone formed by the C_{α} atoms in the chain. As shown by the backbone in Figure 1b, proteins fold into their preferred three dimensional structures. The term “conformation” is also often used interchangeably with “structure”. The conformation of a protein has hierarchical structure: the linear chain is the primary structure; α -helices, β sheets and loop regions are secondary structures; and the compact three dimensional form is the tertiary structure [1]. The folded conformation has flexible regions and relatively rigid regions. The flexible motions allow conformation changes, which form the basis for the functionality of most proteins [2]. Proteins are thus nano-scale deformable structures.

There is a strong correlation between the function of a protein and its folded structure to the extent that predicting the biological function of a protein from its sequence without knowing its conformation is very difficult and may even be impossible [1]. However, it is the sequence of amino acids that entirely determines its folded conformation [3]. The folded conformation is called the “native state” of the protein. The protein of a given sequence is said to have the lowest free energy in its native state when compared with all other conformations. Thus, the notion of optimization is inherent in protein folding. The next section elaborates this view and briefly reviews previous approaches in computational studies on proteins. Section 3 includes a discussion of the continuous

modeling of a discrete problem to make it amenable to computationally efficient gradient-based local optimization methods. The continuous modeling brings out an analogy between structural topology optimization and protein design problems, as presented in Section 4 with some results. The paper ends with Section 5.

2. OPTIMIZATION IN PROTEIN DESIGN

Based on Anfinsen's thermodynamic hypothesis [3] and subsequent modeling and experimental observations, it is generally accepted that the linear chain of a protein folds to its native state because it has the lowest free energy in that state. Thus, computational prediction of the folded conformation is a minimization problem in the *conformation into space*. This space consists of all possible ways that a protein chain can fold. Given a sequence, the *folding problem* attempts to identify the folded conformation. Even after many decades of intensive research, this problem does not yet have a complete solution. Stochastic methods such as Monte Carlo methods (e.g., [4]), genetic algorithms (e.g., [5]) and simulated annealing (e.g., [6]) as well as somewhat deterministic methods such as dead end elimination (e.g., [7]) and mean field theories (e.g., [8]) have been applied to solve this problem. Template matching algorithms have also been developed. Among them, ROSETTA [9] is said to be the most reliable computer program/algorithm today [10]. Many of the above methods amount to semi-exhaustive searches. Experimental determination of folded conformation is an equally difficult problem. X-ray crystallography is the dominant method while the Nuclear Magnetic Resonance (NMR) method is the other. In the protein data bank (PDB), there are more than 30,000 proteins with determined conformations but there are already more than 1.3 million sequenced proteins whose structure is not known. Furthermore, it is remarked that while the number of determined conformations doubles every three years, the sequences with unknown folded conformations doubles every few months [10].

There is also an alternate criterion for protein folding. From the stability viewpoint, it is argued that proteins prefer a native conformation that is not necessarily the one with the lowest energy but the one with an energy that is separated by a large value from the average energy of unfolded conformations in its vicinity. That is, in the energy landscape in the conformation space, the native state is a minimum located in a deep and narrow valley rather than in a wide valley even if the latter is a global minimum. This view, for example, is explained using mean field theory by Wolynes [8]. Yet another criterion is the kinetic accessibility. That is, a protein should be able to fold to its native state rapidly and consistently. Molecular dynamics (MD) simulations help in this regard [11].

The *inverse folding problem* or *sequence-design problem*, i.e., determining the sequence for a given conformation, is a harder problem than the folding problem. Unlike the folding problem, it does not even have a conceptual basis such as the minimum free energy criterion. In other words, if we determine a sequence that has the lowest energy in a given conformation, there is no guarantee that this sequence will fold to this conformation. This is because this particular sequence may have even lower energy in another conformation. This is one difficulty with the inverse folding problem.

A second difficulty is the size and the nature of the sequence space. Consider a protein that has N residues. Since there are 20 amino acids and they can occur any number of times, the number of possible sequences are 20^N . For $N = 100$, the number of sequences is $20^{100} \approx 1.27 \times 10^{130}$. Therefore, exhaustive enumeration is completely ruled out in the foreseeable computational power. Furthermore, the sequence space is discrete which makes searching through this using continuous algorithms impossible.

In this work, we model the discrete, combinatorial sequence space as a continuous space and formulate a continuous optimization problem based on some assumed criteria for folding and simplified models of energetic interactions.

2.1 Criteria for Protein Folding

The criteria for protein folding can be summarized as follows. Let S^{C^*} denote the entire sequence space for a protein chain. Then, for a given conformation C^* , $S_{ns}^{C^*}$ represents a subset of S^{C^*} , the members of which have C^* as the native state. This is shown pictorially in Figure 2. Likewise, we can visualize $S_e^{C^*}$ and $S_\Delta^{C^*}$ as subsets in which the energy is a minimum or the energy gap is a maximum respectively. Based on the foregoing criteria, the designed sequence must belong to $S_{ns}^{C^*}$. Some researchers believe that it suffices if the sequence belongs to $S_\Delta^{C^*}$ [6, 8]. Some other researchers consider $S_e^{C^*}$ because it is easier to deal with computationally: only the sequence space needs to be searched here. They believe that when the composition of amino acid types is fixed, energy-minimizing sequences for a conformation also prefer that conformation as the native state. The mathematical basis for this is explained in [12]. In this work, we first search only in the sequence space subjected to above constraint and later extend the search to a limited portion of the conformation space as well.

2.2 Analogy with Structural Optimization

The two important criteria of protein folding lead to an optimization problem that assumes the following form:

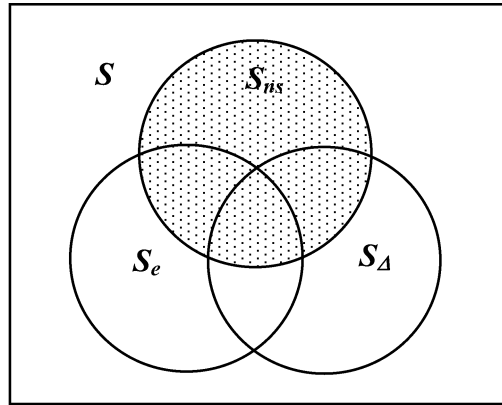


Figure 2. Subsets of the sequence space that have: a conformation C^* as the native state (S_{ns}), minimum energy in C^* (S_e) and maximum energy gap (S_Δ).

$$\begin{aligned}
 &\text{Minimize}_{x \in S} && E = \text{energy} \\
 &\text{Subject to} && x \text{ has a minimum } E \text{ for } C^* \text{ in the conformation space. (1)} \\
 &&& \text{Given amino acid residue composition for } x.
 \end{aligned}$$

The above optimization problem implies that the minimization of the energy in the sequence space is to be done in such a way that each considered sequence must have C^* as its native state (which in turn means a minimization of the energy in the conformation space) and it satisfies the composition constraint. If we compare $x \in S$ with the design variables in structural optimization, the variables defining the conformation can be thought of as the state variables, i.e., displacements. In other words, the minimizing sequence should be found in the sequence space in such a way that every one of them has the desired conformation as the native state in the conformation space. The composition constraint in Equation (1) is like a resource constraint, which is similar to volume constraint in multiple-material topology optimization.

3. CONTINUOUS MODELING

When we search in the sequence space in order to minimize energy for a given conformation, at each residue site there are 20 possibilities. Let us consider a simpler case. Amino acids can be grouped into two categories based on their hydrophobicity. Hydrophobic types (denoted by H) usually get buried inside the folded conformation hiding from water molecules in the environment whereas non-hydrophobic ones (denoted by P for polar) often get exposed on the outside. Since hydrophobicity plays an important role in protein folding, especially in the initial stages, a two-category HP modeling is quite justifiable

as a starting point. Now, if there are only two types, each residue site can be occupied by either H or P. This is a discrete binary problem leading to multiple combinations of N -tuples of 1s (for Hs) and 0s (for Ps) when there are N residues in the chain. This is similar to the structural topology optimization problem where occupation by material at a point (1 state) or not (0 state) leads to a binary problem. Just as in the topology optimization problem, here too it can be relaxed into a continuous model.

Following [13, 14], consider the unity-normalized Gaussian distribution function to denote the H (1) and P (0) states for the i th residue site.

$$S_i(\rho_i) = e^{-(\rho_i/\sigma)^2}, \quad -\infty < \rho_i < \infty. \quad (2)$$

It is easy to see that the H state is obtained when $\rho_i = 0$, and the P state for all other values of ρ_i . When the tuning parameter σ is very small, the above interpolation asymptotically approaches an almost discrete selection between 1 and 0 depending on whether ρ_i is equal to 0 or not. For all practical purposes, in numerical calculations the peak of the Gaussian distribution function becomes a Kronecker delta function. In numerical optimization, a moderately large σ is used initially and subsequently is driven to a small value.

A similar approach can also be followed for more number of amino acid types by expressing the interpolating function S_i in terms of two variables per each site, viz., ϕ_i, θ_i . Letting S_i^j denote the j th residue type at the i th site, we write

$$S_i^j(\phi_i, \theta_i) = \sum_{k=1}^2 P_j^k, \quad j = 1, \dots, m-1, \quad (3)$$

where

$$P_j^k = \exp \left[-\frac{\arccos^2(\langle \rho(\phi_i, \theta_i), \rho_k^j \rangle)}{\sigma^2} \right], \quad i = 1, \dots, m; \quad k = 1, 2.$$

Furthermore, for the “ground” (zero) state we have

$$S_i^m = 1 - \sum_{j=1}^{m-1} S_i^j. \quad (4)$$

The above equations can be understood by visualizing a sphere (see Figure 3a) on which “peaks” are arranged. The two variables per site ϕ_i, θ_i now denote the angular part of the spherical coordinates and point to a certain direction. If this direction coincides with the direction of a pre-specified peak, at that residue site the corresponding amino acid type will be assumed. The peaks are arranged on the sphere such that from each type of peak all others are equally accessible. Once again, σ allows tuning of the intermediate states.

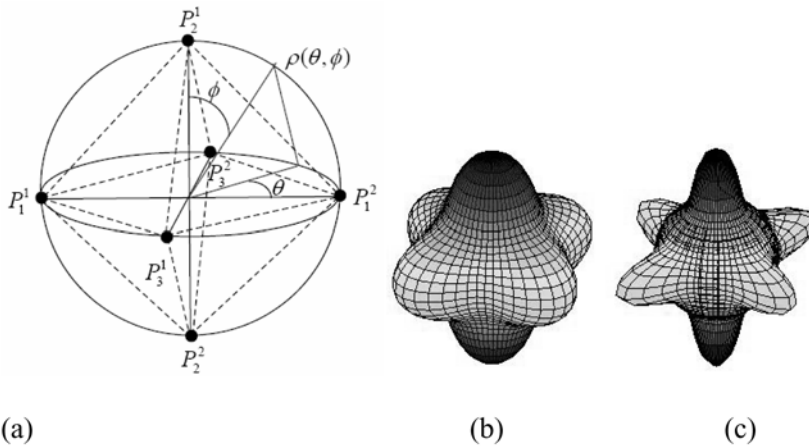


Figure 3. Continuous interpolation of multiple states: (a) arrangement of “peaks” on a sphere, (b) a large value of the tuning parameter σ , (c) a smaller value σ .

We also use another continuous modeling in which m variables are assigned to each site where there are m amino acid types. In this case, there will be mN variables for an N -residue chain. The m variables of each site individually determine each of the m amino acid states. Here, we let the interpolation function be linear but each variable is bounded between 0 and 1. Of course, we now need a constraint of the form shown below to ensure that no site is occupied by more than “one” combined state.

$$\sum_{j=1}^m x_i^j = 1. \quad (5)$$

As explained in [15], this leads to a quadratic programming problem. Any one of the above three continuous modeling schemes for the discrete amino acid types could be used as per the categorization of residue types.

3.1 Modeling of Energy

When the discrete amino acid types are continuously interpolated, a question naturally arises as to how the energy is computed using the interpolated states. To see this, let us consider the simplest case of HP modeling in which only three residue sites exist with the middle site fixed to be an H as shown on the left side in Figure 4. Now, by letting the state of the other two residues interpolated using Equation (2), we write [16]:

$$\begin{aligned} E &= e(S_1, S_2) \\ &= e_{\text{HH}}S_1S_2 + e_{\text{HP}}S_1(1 - S_2) + e_{\text{HP}}(1 - S_1)S_2 + e_{\text{PP}}(1 - S_1)(1 - S_2). \end{aligned} \quad (6)$$

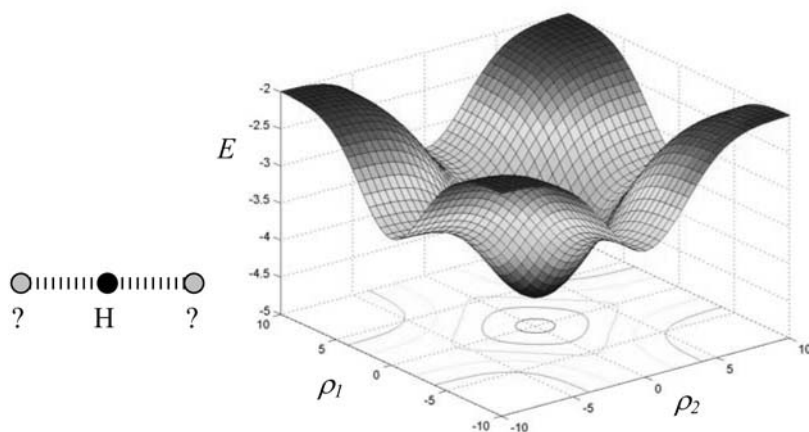


Figure 4. A simple three-residue example to show the energy calculation using continuous modeling of the amino acid types at two sites shown on the left side. The figure on the right is the interpolated energy as per Equation (6).

Here, all the four possible cases are considered and their corresponding inter-residue energy is included. It is easy to see that when the two residue sites are purely H or P, the energy is properly computed. The interpolated energy function is plotted on the right side in Figure 4.

In a general protein with N residue sites, we define an adjacency matrix \mathbf{A} in which A_{ij} element is 1 if i th and j th residue sites have an energetic interaction and 0 otherwise. This is shown below.

$$E = \frac{1}{2} \sum_{i=1}^N \sum_{\substack{j=1 \\ j \neq i}}^N A_{ij} e(S_i(\rho_i), S_j(\rho_j)). \quad (7)$$

The inter-residue energy $e_{m_1 m_2}$ is determined from the Miyazawa–Jernigan (MJ) potentials [17]. The MJ potentials are based on statistical analysis of occurrence of amino acid residues found in real proteins. It is one of the easiest ways to model energetic interactions in proteins.

3.2 Finite Modeling of the Conformation Space

A protein chain, whose backbone (see Figure 1b) can be considered as a curve in three dimensional space, can fold in infinitely many ways. Using a continuous curve has practical difficulties. For example, ensuring that this curve does not cross itself is difficult. Letting the curve take any shape would make the energy landscape rather difficult to deal with. Instead, in the literature the relative rotations between adjacent amino acid residues are varied to define the conformation space. Usually, the angles are fixed to a few positions (say, 10

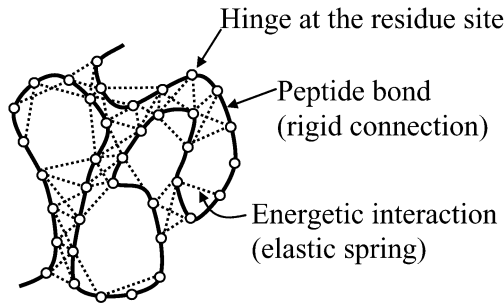


Figure 5. Elastic network model of a protein. The peptide-bonded neighbors are rigidly connected with hinges at the residues sites. Non-bonded neighbors within some cut-off distance are assumed to have energetic interaction, which is shown by a spring (dotted line).

positions separated by 36°). For stochastic approaches, this modeling is fine. However, since we want to optimize with respect to continuous variables related to varied angular positions, an alternative modeling is preferred. We use the following approach.

For visualizing the kinetic pathway for a conformational change, an elastic network model was used in [18]. This is valid even physically because the relative motion between adjacent residues is not without any resistance to motion. Here, we use such an elastic network but do not use all possible angles as variables because there will be too many. Instead, we perform an eigenanalysis of the elastic network to obtain the eigenmode shapes. Then, following the mode summation method, we select a few modes and consider their amplitudes to get local changes in the conformations.

Let $\mathbf{w}_i, i = 1, 2, \dots, N$ denote the eigenmode shapes of an elastic network, which consists of point masses and springs between adjacent residue sites that have an energetic interaction. Each energetic interaction is assigned a spring constant of unity. We do not count the interactions between peptide bonded adjacent pairs of residue sites. The peptide bonds are taken as hinges. Such an elastic network is shown in Figure 5. By multiplying a few selected mode shapes and taking a linear sum with mode shape amplitudes $q_j, j = 1, 2, \dots, n < N$, we get a variety of local conformation changes. By denoting the initial spatial positions of the residue sites by $\mathbf{x}_i^0, i = 1, 2, \dots, N$, we can write the changed positions as follows:

$$\mathbf{x}_i = \mathbf{x}_i^0 + \sum_{j=1}^{n < N} q_j \mathbf{w}_j, \quad i = 1, 2, \dots, N. \quad (8)$$

In exploring the conformation space, $q_j, j = 1, 2, \dots, n < N$ become the finite number of design variables. These variables decide the conformation. Any designed sequence should have a global minimum in the conformation

space. However, in this work we use only local optimization method. The energy modeling should now take into account the changing distance between pairs of interacting residue sites. This is taken as follows where d_{ij}^0 is the initial distance in the given conformation and d_{ij} in the changed conformation. This modulates the elements of the adjacency matrix, A_{ij} .

$$E = \frac{1}{2} \sum_{i=1}^N \sum_{\substack{j=1 \\ j \neq i}}^N \frac{A_{ij}}{1 + d_{ij} - d_{ij}^0} e(S_i(\rho_i), S_j(\rho_j)). \quad (9)$$

4. PROBLEM STATEMENT AND RESULTS

Using the modeling done so far, the problem is formulated as follows:

$$\begin{aligned} & \text{Minimize}_{\substack{\rho_i, i=1,2,\dots,N \\ q_j, j=1,2,\dots,n < N}} E = \frac{1}{2} \sum_{i=1}^N \sum_{\substack{j=1 \\ j \neq i}}^N \frac{A_{ij}}{1 + d_{ij} - d_{ij}^0} e(S_i(\rho_i), S_j(\rho_j)) \\ & \text{Subject to} \quad \sum_{i=1}^N S_i(\rho_i) - N_H = 0, \quad q^l \leq q_i \leq q^u, \quad -\infty \leq \rho_i \leq \infty. \end{aligned}$$

Other relationships

$$d_{ij} = \|\mathbf{x}_i - \mathbf{x}_j\|, \quad d_{ij}^0 = \|\mathbf{x}_i^0 - \mathbf{x}_j^0\| \quad (10)$$

$$S_i(\rho_i) = \exp\left(-\frac{\rho_i^2}{\sigma^2}\right)$$

$$e(S_i, S_j) = e_{HH}S_iS_j + e_{HP}S_i(1 - S_j) + e_{PH}(1 - S_i)S_j + e_{PP}(1 - S_i)(1 - S_j)$$

$$e_{HH} = -2.3, \quad e_{HP} = e_{PH} = -1, \quad e_{PP} = 0.$$

Here, the HP modeling is shown for simplicity. The objective function is the energy in the changed conformation as it depends on the eigenmode shape amplitudes. The constraint refers to a given number of H residue types, N_H . The HP potentials are taken from [19]. They are derived from the Miyajawa–Jernigan potentials. Two examples are shown in Figures 6a and 6b.

5. CLOSURE

Protein sequences for a given conformation are to be designed in such a way that the designed sequence would have the lowest energy in the given conformation among all the other conformations in the conformation space. This

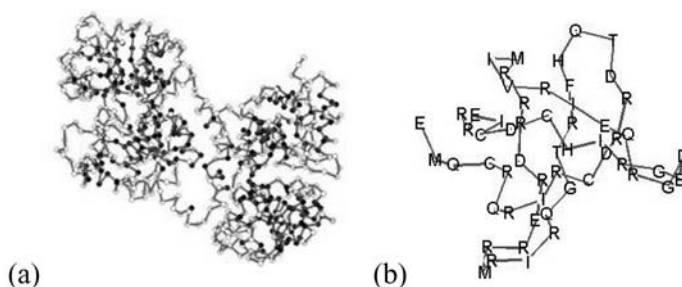


Figure 6. (a) Lactoferrin protein (PDB code: 1LFG) designed with only two types of amino acid monomers, H (hydrophobic; black dots) and P (polar; circles), (b) SRC Tyrosine Kinase transformation protein (PDB code: 1SRL) designed by considering all amino acid monomer types but in two stages using a combination of two methods using a procedure similar to the one described in [16].

can be done by simultaneously searching in the sequence and conformation spaces. Continuous modeling of the discrete sequence space and finite dimensional continuous modeling of the conformation space give rise to a problem structure that is similar to structural topology optimization. Thus, gradient-based methods are used to solve this problem for some protein models with simple energetic potentials. Future work will use more realistic modeling of the energy due to the changing conformations.

ACKNOWLEDGMENTS

Some parts of this work were done in collaboration with Dr. Sung Koh (MEAM, University of Pennsylvania), Professor Christopher Croke (Math., University of Pennsylvania), and Professor Saraswathi Vishveswara (Mol. Bio-Phys. Unit, Indian Institute of Science). NSF grant (DMI0200362) is also acknowledged.

REFERENCES

- [1] Branden, C. and Tooze, J., *Introduction to Protein Structure*, Garland Publishers, New York (1998).
- [2] Lie, M., Zavodszky, M.I., Kuhn, L.A. and Thorpe, M.F., *J. Comp. Chem.* (2003).
- [3] Anfinsen, C., *Science*, 181, 223–230 (1973).
- [4] Hinds, D.A. and Levitt, M., *J. Mol. Biol.*, 258, 201–209 (1996).
- [5] Jones, D.T., *Protein Science*, 3, 567–574 (1994).
- [6] Deutsch, J.M. and Kurosky, T., *Phys. Rev. Lett.*, 76(2), 323–326 (1996).
- [7] Desmet, J., De Maeyer, Hazes, B. and Lasters, I., *Nature*, 356, 539–542 (1992).
- [8] Onuchic, J.N., Luthey-Schulten, Z. and Wolynes, P.G., *Annu. Rev. Phys. Chem.*, 48, 545–600 (1997).
- [9] Roh, C.A., Strauss, C.E.M., Misura, K.M.S. and Baker, D., *Meth. in Enzy.*, 383, 66–93 (2004).

- [10] Kretsinger, R.H., Ison, R.E. and Hovmöller, S., *Meth. in Enzy.*, 383, 1–27 (2004).
- [11] Pitera, J.D. and Swope, W., *Proc. Nat'l Acad. Sci.*, 100, 7587–7592 (2003).
- [12] Shakhnovitch, E.I. and Gutin, A.M., *Protein Engineering*, 6, 793–800 (1993).
- [13] Yin, L. and Ananthasuresh, G.K., *Struc. and Multidisc. Optim.*, 23(1), 49–62 (2001).
- [14] Yin, L. and Ananthasuresh, G.K., *Sens. and Actu., A Phys.*, 97–98, 599–609 (2002).
- [15] Sung, K., Ananthasuresh, G.K. and Vishveshwara, S., *Int. J. of Robot. Res.*, 24(2–3), 109–130 (2005).
- [16] Koh, S.K., Ananthasuresh, G.K. and Croke, C., *J. Mech. Des.*, 127, 728–735 (2005).
- [17] Miyazawa, S. and Jernigan, R.L., *Macromolecules*, 18, 534–552 (1995).
- [18] Kim, M.K., Jernigan, R.L. and Chirikjian, G.S., *Biophys. J.*, 83, 1620 (2002).
- [19] Li, H., Tang, C. and Wingreen, N.S., *Phys. Rev. Lett.*, 79(4), 765–768 (1985).

**Topological Derivatives,
Reliability, and Other Features**

TOPOLOGICAL-SHAPE SENSITIVITY METHOD: THEORY AND APPLICATIONS

A.A. Novotny¹, R.A. Feijóo¹, E. Taroco¹ and C. Padra²

¹*Laboratório Nacional de Computação Científica LNCC/MCT,*

Av. Getúlio Vargas 333, 25651-075 Petrópolis – RJ, Brasil

²*Centro Atómico Bariloche, 8400 Bariloche, Argentina*

novotny@lncc.br, feij@lncc.br, etam@lncc.br, padra@cab.cnea.gov.ar

Abstract: The topological derivative allow us to quantify the sensitivity of a given cost function when the domain of definition of the problem is perturbed by introducing a hole or an inclusion. This concept has been successfully applied in the context of topology design and inverse problems. In order to find close expressions for the topological derivative several methods can be achieved in the literature. In particular, we have proposed the Topological-Shape Sensitivity Method, whose main feature is that all mathematical framework (and results), already developed for shape sensitivity analysis, can be used in the calculation of the topological derivative. In this paper we present the Topological-Shape Sensitivity Method and use it as a systematic methodology for computing the topological derivative for holes and inclusions in problems governed by Poisson's and Navier's equations.

Keywords: Topological derivative, shape sensitivity analysis, asymptotic expansion.

1. INTRODUCTION

The topological derivative [3, 5, 15] has been recognized as a promising tool to solve topology optimization problems (see [4] and references therein). In addition, extension of the topological sensitivity in order to include arbitrary shaped holes and its applications to Laplace, Poisson, Helmholtz, Navier, Stokes and Navier–Stokes equations were developed by Masmoudi and his co-workers and by Sokolowsky and his co-workers (see, for instance, [11]).

Although the topological sensitivity is extremely general, this concept may become restrictive due to mathematical difficulties involved in its calculation. However, several approaches to compute the topological derivative may be found in the literature [3, 14, 15]. In particular, we have proposed an alternative approach, called Topological-Shape Sensitivity Method [12], which is

based on classical shape sensitivity analysis. On the other hand, the topological derivative (TD) concept is wider. In fact, this same idea can also be used to calculate the sensitivity of the problem when, instead of a hole, a small inclusion is introduced at a point in the domain. In this last case, no topology change occurs, then we have called it as configurational derivative (CD). Despite the conceptual difference between TD and CD, we will show that this last one can also be computed using the Topological-Shape Sensitivity Method.

In this paper, we firstly present a brief description of the Topological-Shape Sensitivity Method. Next we apply this approach to obtain the TD for Poisson’s (considering both homogeneous and non-homogeneous Neumann and Dirichlet and also Robin boundary conditions on the hole) and Navier’s (plane-stress, plane-strain and three-dimensional linear elasticity problems) equations . Furthermore, we compute the CD for steady-state heat conduction and plane-stress linear elasticity. Finally, it is also shown that in general the CD cannot be used to obtain the TD for homogeneous Neumann boundary condition on the hole simply taking the limit when the material property associated to the inclusion vanishes.

2. TOPOLOGICAL-SHAPE SENSITIVITY METHOD

Let us consider an open bounded domain $\Omega \subset \mathbb{R}^N$ ($N = 2, 3$) with a smooth boundary $\partial\Omega$. If the domain Ω is perturbed by introducing a small hole B_ε of radius ε at an arbitrary point $\hat{\mathbf{x}} \in \Omega$, we have a new domain $\Omega_\varepsilon = \Omega - \overline{B_\varepsilon}$, whose boundary is denoted by $\partial\Omega_\varepsilon = \partial\Omega \cup \partial B_\varepsilon$. Then, considering a cost function ψ defined in both domains, its topological derivative for holes is given in [3], for $f(\varepsilon) > 0$, such that $f(\varepsilon) \rightarrow 0$ with $\varepsilon \rightarrow 0^+$, as

$$D_T (\hat{\mathbf{x}}) = \lim_{\varepsilon \rightarrow 0} \frac{\psi (\Omega_\varepsilon) - \psi (\Omega)}{f (\varepsilon)} . \tag{1}$$

We have proposed in [12] an alternative procedure to compute the topological derivative called Topological-Shape Sensitivity Method. This approach makes use of the whole mathematical framework (and results) developed for shape sensitivity analysis (see, for instance, the pioneer work of Murat and Simon [10]). The main result obtained in [12] is given by the following theorem:

THEOREM 1 *Let $f (\varepsilon)$ be a function chosen in order to $0 < |D_T (\hat{\mathbf{x}})| < \infty$, then the topological derivative given by Equation (1) can be written as*

$$D_T (\hat{\mathbf{x}}) = \lim_{\varepsilon \rightarrow 0} \frac{1}{f' (\varepsilon)} \frac{d}{d\varepsilon} \psi (\Omega_\varepsilon) , \tag{2}$$

where the derivative of the cost function with respect to the parameter ε may be seen as its classical shape sensitivity analysis.

In general the cost function $\psi(\Omega) := \mathcal{J}_\Omega(u)$ may depends explicitly and implicitly on the domain Ω . This last dependence comes from the solution of a variational problem associated to Ω : find $u \in \mathcal{U}(\Omega)$, such that

$$a(u, \eta) = l(\eta) \quad \forall \eta \in \mathcal{V}(\Omega) , \tag{3}$$

where $\mathcal{U}(\Omega)$ and $\mathcal{V}(\Omega)$ respectively are the sets of admissible functions and admissible variations defined on Ω and $a(\cdot, \cdot) : \mathcal{U} \times \mathcal{V} \rightarrow \mathbb{R}$ is a bilinear form and $l(\cdot) : \mathcal{V} \rightarrow \mathbb{R}$ is a linear functional, which will be characterized later according to the problem under analysis. Likewise, the state equation written in the original configuration Ω (without hole) may also be satisfied in the perturbed configuration Ω_ε (with the introduction of a hole at point $\hat{\mathbf{x}} \in \Omega$). Therefore, we have the following variational problem associated to function Ω_ε : find $u_\varepsilon \in \mathcal{U}_\varepsilon(\Omega_\varepsilon)$, such that

$$a_\varepsilon(u_\varepsilon, \eta) = l_\varepsilon(\eta) \quad \forall \eta \in \mathcal{V}_\varepsilon(\Omega_\varepsilon) , \tag{4}$$

where $a_\varepsilon(\cdot, \cdot) : \mathcal{U}_\varepsilon \times \mathcal{V}_\varepsilon \rightarrow \mathbb{R}$, $l_\varepsilon(\cdot) : \mathcal{V}_\varepsilon \rightarrow \mathbb{R}$ and $\mathcal{U}_\varepsilon(\Omega_\varepsilon)$ and $\mathcal{V}_\varepsilon(\Omega_\varepsilon)$ respectively are the sets of admissible functions and admissible variations defined on Ω_ε , which will be also defined later according to the problem under analysis and the boundary condition on the hole.

Formally, the shape derivative of the cost function $\psi(\Omega_\varepsilon) := \mathcal{J}_{\Omega_\varepsilon}(u_\varepsilon)$ in relation to the parameter ε reads

$$\left\{ \begin{array}{l} \text{Calculate : } \frac{d}{d\varepsilon} \mathcal{J}_{\Omega_\varepsilon}(u_\varepsilon) \\ \text{Subject to : } a_\varepsilon(u_\varepsilon, \eta) = l_\varepsilon(\eta) \quad \forall \eta \in \mathcal{V}_\varepsilon(\Omega_\varepsilon) \end{array} \right. . \tag{5}$$

Let us relax the constraint of the above problem, given by the state equation (Equation 5), by Lagrangian multipliers. Therefore, the Lagrangian is written as

$$\mathcal{L}_\varepsilon(v, \mu) = \mathcal{J}_{\Omega_\varepsilon}(v) + a_\varepsilon(v, \mu) - l_\varepsilon(\mu) \quad \forall \mu \in \mathcal{V}_\varepsilon(\Omega_\varepsilon) \text{ and } v \in \mathcal{U}_\varepsilon(\Omega_\varepsilon) . \tag{6}$$

Then, we have the following well-known result

$$\frac{d}{d\varepsilon} \mathcal{J}_{\Omega_\varepsilon}(u_\varepsilon) = \left. \frac{\partial}{\partial \varepsilon} \mathcal{L}_\varepsilon(v, \mu) \right|_{\substack{v=u_\varepsilon \\ \mu=\lambda_\varepsilon}} , \tag{7}$$

where u_ε is the solution of the state equation (Equation 4) and λ_ε is the solution of the *adjoint equation* given by: find $\lambda_\varepsilon \in \mathcal{V}_\varepsilon(\Omega_\varepsilon)$, such that

$$a_\varepsilon(\lambda_\varepsilon, \eta) = - \left\langle \frac{\partial}{\partial u_\varepsilon} \mathcal{J}_{\Omega_\varepsilon}(u_\varepsilon), \eta \right\rangle \quad \forall \eta \in \mathcal{V}_\varepsilon(\Omega_\varepsilon) . \tag{8}$$

It should be observed that only the part of the boundary $\partial\Omega_\varepsilon$ associated to ∂B_ε is submitted to a perturbation (a uniform expansion of the ball B_ε in

this case). Therefore, the shape derivative of the cost function results in an integral on the boundary ∂B_ε . In addition, considering the result of Theorem 1 (Equation 2), the topological derivative becomes

$$D_T(\hat{\mathbf{x}}) = -\lim_{\varepsilon \rightarrow 0} \frac{1}{f'(\varepsilon)} \int_{\partial B_\varepsilon} \boldsymbol{\Sigma}_\varepsilon \mathbf{n} \cdot \mathbf{n}, \tag{9}$$

where tensor $\boldsymbol{\Sigma}_\varepsilon$, that depends on u_ε and λ_ε , can be interpreted as a generalization of the Eshelby energy-momentum tensor [6]. As a consequence, this tensor plays a central role in the Topological-Shape Sensitivity Method and should be clearly identified according to the problem under consideration.

Finally, we need to calculate the limit $\varepsilon \rightarrow 0$ in Equation (9). Thus, we should know the behavior of the solutions u_ε and λ_ε when $\varepsilon \rightarrow 0$, which may be obtained from an asymptotic analysis around the neighborhood of the hole. For that, we can define a new function w_ε such as $u_\varepsilon = u + w_\varepsilon$ and, after making $\mathbf{y} = \mathbf{x}/\varepsilon$, we need to solve an exterior boundary value problem (define in $\mathbb{R}^N - \overline{B_1}$, where B_1 is a unit ball) associated to w_ε . At least for linear cases, this problem may be solved using separation of variables. From this result, we can choose a function $f(\varepsilon)$ in order to take the limit $\varepsilon \rightarrow 0$, obtaining the final expression of the topological derivative. Therefore, the Topological-Shape Sensitivity Method may be summarized in the following steps:

1. choose the cost function $\psi(\Omega) := \mathcal{J}_\Omega(u)$, where u is the solution of the state equation associated to the original domain Ω ;
2. define the associated cost function $\psi(\Omega_\varepsilon) := \mathcal{J}_{\Omega_\varepsilon}(u_\varepsilon)$, where u_ε is the solution of the state equation defined in the perturbed domain Ω_ε ;
3. compute the shape derivative of the cost function $\mathcal{J}_{\Omega_\varepsilon}(u_\varepsilon)$ using the Lagrangian Method, identifying tensor $\boldsymbol{\Sigma}_\varepsilon$ and writing the sensitivity expression as a boundary integral only defined on ∂B_ε ;
4. use the result of Theorem 1;
5. make an asymptotic analysis around the neighborhood of the hole B_ε in order to know the behavior of the solutions u_ε and λ_ε when $\varepsilon \rightarrow 0$;
6. finally, choose function $f(\varepsilon)$ and compute the final expression of the topological derivative taking the limit $\varepsilon \rightarrow 0$.

Now, let us apply the above method to compute the topological (holes) and configurational (inclusions) sensitivities for some classical problems.

REMARK 1 *For the sake of simplicity, we will choose a cost function that depends only implicitly on the domain of definition of the problem through the solution of the state equation. Therefore $\psi(\Omega) := \mathcal{J}(u)$ and $\psi(\Omega_\varepsilon) := \mathcal{J}(u_\varepsilon)$, where u is the solution of Equation (3), associated to Ω , and u_ε is the solution of Equation (4), associated to Ω_ε .*

3. TOPOLOGICAL DERIVATIVE (HOLES)

In this section we will compute the topological derivative for steady-state heat conduction (considering both homogeneous and non-homogeneous Neumann and Dirichlet and also Robin boundary conditions on the hole) and linear elasticity (plane-stress, plane-strain and three-dimensional problems).

3.1 Steady-State Heat Conduction

Let us state the following variational problem associated to the original domain Ω : given a constant excitation b in Ω and a Dirichlet data \bar{u} on $\partial\Omega$, find the temperature field $u \in \mathcal{U}(\Omega)$, such that

$$\int_{\Omega} k \nabla u \cdot \nabla \eta = \int_{\Omega} b \eta \quad \forall \eta \in \mathcal{V}(\Omega) , \tag{10}$$

where k is a material property and $\mathcal{U}(\Omega)$ and $\mathcal{V}(\Omega)$ are given, respectively, by

$$\mathcal{U} = \{ u \in H^1(\Omega) : u|_{\partial\Omega} = \bar{u} \} , \quad \mathcal{V} = \{ \eta \in H_0^1(\Omega) \} . \tag{11}$$

Now, let us state a new variational problem associated to the perturbed domain Ω_ε : considering that on ∂B_ε we have Dirichlet, Neumann or Robin boundary conditions, find the temperature field $u_\varepsilon \in \mathcal{U}_\varepsilon(\Omega_\varepsilon)$, such that

$$\int_{\Omega_\varepsilon} k \nabla u_\varepsilon \cdot \nabla \eta + \gamma \int_{\partial B_\varepsilon} u_\varepsilon \eta = \int_{\Omega_\varepsilon} b \eta + (\beta + \gamma) \int_{\partial B_\varepsilon} h \eta \quad \forall \eta \in \mathcal{V}_\varepsilon(\Omega_\varepsilon) , \tag{12}$$

where $\mathcal{U}_\varepsilon(\Omega_\varepsilon)$ and $\mathcal{V}_\varepsilon(\Omega_\varepsilon)$ are given, respectively, by

$$\mathcal{U}_\varepsilon = \{ u_\varepsilon \in \mathcal{U}(\Omega_\varepsilon) : \alpha(u_\varepsilon|_{\partial B_\varepsilon} - h) = 0 \} , \tag{13}$$

$$\mathcal{V}_\varepsilon = \{ \eta \in \mathcal{V}(\Omega_\varepsilon) : \alpha \eta|_{\partial B_\varepsilon} = 0 \} , \tag{14}$$

and $\alpha, \beta, \gamma \in \{0, 1\}$, with $\alpha + \beta + \gamma = 1$. This notation should be interpreted as follows: when $\alpha = 1$, $u_\varepsilon = h$ and $\eta = 0$ on ∂B_ε , and when $\alpha = 0$, u_ε and η are free on ∂B_ε , where h is a data. Considering Remark 1, the shape derivative of the cost function becomes

$$\frac{d}{d\varepsilon} \mathcal{J}(u_\varepsilon) = - \int_{\partial B_\varepsilon} \left(\boldsymbol{\Sigma}_\varepsilon \mathbf{n} \cdot \mathbf{n} - \frac{1}{\varepsilon} (\gamma(u_\varepsilon - h) - \beta h) \lambda_\varepsilon \right) , \quad \text{where} \tag{15}$$

$$\boldsymbol{\Sigma}_\varepsilon = (k \nabla u_\varepsilon \cdot \nabla \lambda_\varepsilon - b \lambda_\varepsilon) \mathbf{I} - k (\nabla u_\varepsilon \otimes \nabla \lambda_\varepsilon + \nabla \lambda_\varepsilon \otimes \nabla u_\varepsilon) . \tag{16}$$

Finally, from an asymptotic analysis of u_ε and λ_ε , we can choose function $f(\varepsilon)$ depending on each type of boundary condition on ∂B_ε , which allow us to compute the limit $\varepsilon \rightarrow 0$ in Equation (15). This procedure leads to the results presented in Table 1, where u and λ are the solutions of the state and adjoint equations, respectively, both defined in the original domain Ω (without hole).

See [12] for applications of the results shown in Table 1. We also observe that the exceptional case $h = h^*$ appears in the Saint-Venant theory of torsion of elastic shafts.

Table 1. Topological derivatives for Poisson’s problem in 2D domains.

Boundary conditions	$f(\varepsilon)$	$D_T(\hat{\mathbf{x}})$
$\beta = 1, \alpha = \gamma = 0$ and $h = 0$	$\pi \varepsilon^2$	$-2k \nabla u \cdot \nabla \lambda + b \lambda$
$\beta = 1, \alpha = \gamma = 0$ and $h \neq 0$	$2\pi \varepsilon$	$-h \lambda$
$\gamma = 1, \alpha = \beta = 0$	$2\pi \varepsilon$	$(u - h) \lambda$
$\alpha = 1, \beta = \gamma = 0$ and $h = h^*$	$\pi \varepsilon^2$	$2k \nabla u \cdot \nabla \lambda$
$\alpha = 1, \beta = \gamma = 0$ and $h \neq h^*$	$-\frac{2\pi}{\log(\varepsilon)}$	$(u - h) \lambda$

3.2 Linear Elasticity

The mechanical model associated to linear elasticity problem can be stated in its variational formulation as following: find the displacement vector field $\mathbf{u} \in \mathcal{U}(\Omega)$, such that

$$\int_{\Omega} \mathbf{T}(\mathbf{u}) \cdot \mathbf{E}(\boldsymbol{\eta}) = \int_{\Gamma_N} \bar{\mathbf{q}} \cdot \boldsymbol{\eta} \quad \forall \boldsymbol{\eta} \in \mathcal{V}(\Omega) , \tag{17}$$

where $\mathcal{U}(\Omega)$ and $\mathcal{V}(\Omega)$ are given by

$$\mathcal{U} = \{ \mathbf{u} \in H^1(\Omega) : \mathbf{u}|_{\Gamma_D} = \bar{\mathbf{u}} \}, \quad \mathcal{V} = \{ \boldsymbol{\eta} \in H^1(\Omega) : \boldsymbol{\eta}|_{\Gamma_D} = \mathbf{0} \} \tag{18}$$

and Ω represents a deformable body submitted to a set of surface forces $\bar{\mathbf{q}}$ on the Neumann boundary Γ_N and displacement constraints $\bar{\mathbf{u}}$ on the Dirichlet boundary Γ_D . In addition, $\mathbf{E}(\mathbf{u})$ is the linearized Green deformation tensor and $\mathbf{T}(\mathbf{u})$ is the Cauchy stress tensor respectively given by

$$\mathbf{E}(\mathbf{u}) = \frac{1}{2} (\nabla \mathbf{u} + \nabla \mathbf{u}^T) := \nabla \mathbf{u}^s \quad \text{and} \quad \mathbf{T}(\mathbf{u}) = \mathbf{C} \mathbf{E}(\mathbf{u}) , \tag{19}$$

where $\mathbf{C} = \mathbf{C}^T$ is the elasticity tensor for linear elastic isotropic material. The problem stated in the original domain Ω can also be written in the domain Ω_ε with a hole B_ε . Therefore, assuming null forces on the hole, we have the following variational problem: find the displacement vector field $\mathbf{u}_\varepsilon \in \mathcal{U}_\varepsilon(\Omega_\varepsilon)$, such that

$$\int_{\Omega_\varepsilon} \mathbf{T}_\varepsilon(\mathbf{u}_\varepsilon) \cdot \mathbf{E}_\varepsilon(\boldsymbol{\eta}) = \int_{\Gamma_N} \bar{\mathbf{q}} \cdot \boldsymbol{\eta} \quad \forall \boldsymbol{\eta} \in \mathcal{V}_\varepsilon(\Omega_\varepsilon) . \tag{20}$$

where $\mathcal{U}_\varepsilon(\Omega_\varepsilon) = \mathcal{U}(\Omega_\varepsilon)$ and $\mathcal{V}_\varepsilon(\Omega_\varepsilon) = \mathcal{V}(\Omega_\varepsilon)$. Observe that in accordance with the variational problem given by Equation (20), the natural boundary condition on ∂B_ε is $\mathbf{T}_\varepsilon(\mathbf{u}_\varepsilon) \mathbf{n} = \mathbf{0}$ (homogeneous Neumann condition). Considering Remark 1, the shape derivative of the cost function becomes

$$\frac{d}{d\varepsilon} \mathcal{J}(\mathbf{u}_\varepsilon) = - \int_{\partial B_\varepsilon} \boldsymbol{\Sigma}_\varepsilon \mathbf{n} \cdot \mathbf{n} , \quad \text{where} \tag{21}$$

$$\Sigma_\varepsilon = (\mathbf{T}_\varepsilon(\mathbf{u}_\varepsilon) \cdot \mathbf{E}_\varepsilon(\boldsymbol{\lambda}_\varepsilon)) \mathbf{I} - (\nabla \boldsymbol{\lambda}_\varepsilon)^T \mathbf{T}_\varepsilon(\mathbf{u}_\varepsilon) - (\nabla \mathbf{u}_\varepsilon)^T \mathbf{T}_\varepsilon(\boldsymbol{\lambda}_\varepsilon). \quad (22)$$

Finally, taking into account homogeneous Neumann boundary condition on the hole and considering a classical stress distribution around the void, we can choose function $f(\varepsilon)$ and take the limit $\varepsilon \rightarrow 0$ in Equation (21) to obtain the final expression for the topological derivative. Thus, for \mathbf{u} and $\boldsymbol{\lambda}$ solutions of the direct and adjoint problems, respectively, both associated to the original domain Ω (without hole) and with ν being the Poisson’s ratio, we have the following results (see also [8] and [9]):

- plane-stress linear elasticity, $f(\varepsilon) = \pi \varepsilon^2$

$$D_T(\hat{\mathbf{x}}) = -\frac{4}{1+\nu} \mathbf{T}(\mathbf{u}) \cdot \mathbf{E}(\boldsymbol{\lambda}) + \frac{1-3\nu}{1-\nu^2} \text{tr} \mathbf{T}(\mathbf{u}) \text{tr} \mathbf{E}(\boldsymbol{\lambda}); \quad (23)$$

- plane-strain linear elasticity, $f(\varepsilon) = \pi \varepsilon^2$

$$D_T(\hat{\mathbf{x}}) = -4(1-\nu) \mathbf{T}(\mathbf{u}) \cdot \mathbf{E}(\boldsymbol{\lambda}) + \frac{(1-4\nu)(1-\nu)}{1-2\nu} \text{tr} \mathbf{T}(\mathbf{u}) \text{tr} \mathbf{E}(\boldsymbol{\lambda}); \quad (24)$$

- three-dimensional linear elasticity, $f(\varepsilon) = (4/3)\pi \varepsilon^3$

$$D_T(\hat{\mathbf{x}}) = -\frac{3}{2} \frac{1-\nu}{7-5\nu} \left[10 \mathbf{T}(\mathbf{u}) \cdot \mathbf{E}(\boldsymbol{\lambda}) - \frac{1-5\nu}{1-2\nu} \text{tr} \mathbf{T}(\mathbf{u}) \text{tr} \mathbf{E}(\boldsymbol{\lambda}) \right]. \quad (25)$$

For applications of these results, see [7] for 2D and [13] for 3D problems.

4. CONFIGURATIONAL DERIVATIVE (INCLUSIONS)

In this section we will compute the configurational derivative in steady-state heat conduction and plane-stress linear elasticity. Therefore, let us consider that the domain Ω is now perturbed by introducing, instead a hole, a small inclusion represented by B_ε . Therefore, we have a perturbed domain $\Omega_\varepsilon \cup B_\varepsilon$, where $\Omega_\varepsilon = \Omega - B_\varepsilon$. Thus, considering a cost function ψ defined in both domains Ω and $\Omega_\varepsilon \cup B_\varepsilon$, its configurational derivative is defined as

$$D_C(\hat{\mathbf{x}}) = \lim_{\varepsilon \rightarrow 0} \frac{\psi(\Omega_\varepsilon \cup B_\varepsilon) - \psi(\Omega)}{|B_\varepsilon|}, \quad (26)$$

where $|B_\varepsilon|$ is the Lebesgue measure of the inclusion. It is important to observe that all the mathematical framework introduced in section 2 can also be applied in this context. See also [1] and references therein.

4.1 Steady-State Heat Conduction

Let us consider again the Poisson’s equation. Therefore, the problem formulation associated to the original domain Ω is given by Equation (10) and the state equation associated to the domain $\Omega_\varepsilon \cup B_\varepsilon$ is given by the following variational problem: find the temperature field $u_\varepsilon \in \mathcal{U}_\varepsilon(\Omega_\varepsilon \cup B_\varepsilon)$, such that

$$\int_{\Omega_\varepsilon \cup B_\varepsilon} k_\delta \nabla u_\varepsilon \cdot \nabla \eta = \int_{\Omega_\varepsilon \cup B_\varepsilon} b \eta \quad \forall \eta \in \mathcal{V}_\varepsilon(\Omega_\varepsilon \cup B_\varepsilon), \tag{27}$$

where, according to definitions of the set $\mathcal{U}(\Omega)$ and the space $\mathcal{V}(\Omega)$ given by Equation (11), we have $\mathcal{U}_\varepsilon(\Omega_\varepsilon \cup B_\varepsilon) = \mathcal{U}(\Omega_\varepsilon \cup B_\varepsilon)$ and $\mathcal{V}_\varepsilon(\Omega_\varepsilon \cup B_\varepsilon) = \mathcal{V}(\Omega_\varepsilon \cup B_\varepsilon)$. In addition, the material property k_δ is defined, for $\delta \in \mathbb{R}^+$, as

$$k_\delta = k \quad \forall \mathbf{x} \in \Omega_\varepsilon \quad \text{and} \quad k_\delta = \delta k \quad \forall \mathbf{x} \in B_\varepsilon. \tag{28}$$

Introducing the notation $[[\cdot]] := (\cdot)|_e - (\cdot)|_i$, where $(\cdot)|_e$ is associated to the bulk material e , represented by Ω_ε , and $(\cdot)|_i$ is associated to the inclusion i , represented by B_ε . Then the shape derivative of the cost function, according to Remark 1, results in

$$\frac{d}{d\varepsilon} \mathcal{J}(u_\varepsilon) = - \int_{\partial B_\varepsilon} [[\Sigma_\varepsilon \mathbf{n}]] \cdot \mathbf{n}, \tag{29}$$

where tensor Σ_ε is given by Equation (16) for $k = k_\delta$. Using the jump conditions associated to the normal derivatives of solutions u_ε and λ_ε , we can compute the limit $\varepsilon \rightarrow 0$ to get the configurational derivative, that is

$$D_C (\hat{\mathbf{x}}) = -2k \frac{1 - \delta}{1 + \delta} \nabla u \cdot \nabla \lambda, \tag{30}$$

where u and λ are the solutions of the state and adjoint equations, respectively, both defined in the original domain Ω (without inclusion).

4.2 Plane-Stress Linear Elasticity

In this section we compute the configurational derivative in plane-stress linear elasticity problem, whose variational formulation, associated to the original domain Ω , is given by Equation (17). On the other hand, the mechanical model associated to the domain $\Omega_\varepsilon \cup B_\varepsilon$ is given by the following variational problem: find the displacement vector field $\mathbf{u}_\varepsilon \in \mathcal{U}_\varepsilon(\Omega_\varepsilon \cup B_\varepsilon)$, such that

$$\int_{\Omega_\varepsilon \cup B_\varepsilon} \mathbf{T}_\varepsilon(\mathbf{u}_\varepsilon) \cdot \mathbf{E}_\varepsilon(\boldsymbol{\eta}) = \int_{\Gamma_N} \bar{\mathbf{q}} \cdot \boldsymbol{\eta} \quad \forall \boldsymbol{\eta} \in \mathcal{V}_\varepsilon(\Omega_\varepsilon \cup B_\varepsilon). \tag{31}$$

where, according to definitions of the set $\mathcal{U}(\Omega)$ and the space $\mathcal{V}(\Omega)$ given by Equation (18), we have $\mathcal{U}_\varepsilon(\Omega_\varepsilon \cup B_\varepsilon) = \mathcal{U}(\Omega_\varepsilon \cup B_\varepsilon)$ and $\mathcal{V}_\varepsilon(\Omega_\varepsilon \cup B_\varepsilon) =$

$\mathcal{V}(\Omega_\varepsilon \cup B_\varepsilon)$. In addition, the elasticity tensor is now defined, for $\delta \in \mathbb{R}^+$, as

$$\mathbf{C}_\delta = \mathbf{C} \quad \forall \mathbf{x} \in \Omega_\varepsilon \quad \text{and} \quad \mathbf{C}_\delta = \delta \mathbf{C} \quad \forall \mathbf{x} \in B_\varepsilon . \tag{32}$$

From Remark 1, the shape derivative of the cost function results in

$$\frac{d}{d\varepsilon} \mathcal{J}_\varepsilon(\mathbf{u}_\varepsilon) = - \int_{\partial B_\varepsilon} \llbracket \boldsymbol{\Sigma}_\varepsilon \mathbf{n} \rrbracket \cdot \mathbf{n} , \tag{33}$$

remembering that $\llbracket \cdot \rrbracket := (\cdot)|_e - (\cdot)|_i$ and that $\boldsymbol{\Sigma}_\varepsilon$ is the generalized Eshelby tensor, given in by Equation (22) for $\mathbf{C} = \mathbf{C}_\delta$. Finally, taking into account the jump condition on the boundary of the inclusion, we find $f(\varepsilon) = \pi \varepsilon^2$ and the configurational derivative, for $\alpha = (3 - \nu)/(1 + \nu)$, becomes

$$D_T(\hat{\mathbf{x}}) = - \frac{1 - \delta}{2} \frac{1 + \alpha}{1 + \delta \alpha} \left[2\mathbf{T}(\mathbf{u}) \cdot \mathbf{E}(\boldsymbol{\lambda}) - \frac{(1 - \delta)(\alpha - 2)}{2\delta + \alpha - 1} \text{tr}\mathbf{T}(\mathbf{u}) \text{tr}\mathbf{E}(\boldsymbol{\lambda}) \right] , \tag{34}$$

where \mathbf{u} and $\boldsymbol{\lambda}$ are solutions of the direct and adjoint problems, respectively, both associated to the original domain Ω (without inclusion).

5. FINAL REMARKS

In this paper, we have applied the Topological-Shape Sensitivity Method as a systematic procedure to compute the topological (holes) and configurational (inclusions) sensitivities for some classical problems in continuum mechanics.

We have observed that the CD in general doesn't converge in the limit case (for $\delta = 0$) to the TD for homogeneous Neumann boundary condition on the holes. In order to illustrate this issue, let us consider a cost function that also depends explicitly on the domain Ω as follows

$$\psi(\Omega) := \mathcal{J}_\Omega(u) = \int_\Omega w(u - u^*)^2 , \tag{35}$$

where u is the solution of Equation (10), u^* is a target temperature and w is a weighting factor defined, for a given subset $\varpi \subset \Omega$, as $w = 1$ if $\mathbf{x} \in \varpi$ and $w = 0$ if $\mathbf{x} \in \Omega - \overline{\varpi}$. From the Topological-Shape Sensitivity Method, we have respectively obtained the following results for holes and inclusions:

$$D_T(\hat{\mathbf{x}}) = -w(u - u^*)^2 - 2k \nabla u \cdot \nabla \lambda + b \lambda , \tag{36}$$

$$D_C(\hat{\mathbf{x}}) = -2k \frac{1 - \delta}{1 + \delta} \nabla u \cdot \nabla \lambda . \tag{37}$$

Observe that the result given by Equation (36) cannot be obtained taking the limit $\delta \rightarrow 0$ in Equation (37). Therefore, this fact suggests that in general the CD cannot be used to compute the TD for homogeneous Neumann boundary condition on the hole simply taking the limit when the material property associated to the inclusion vanishes.

Finally, we would like to point out that this paper only deals with linear problems. In addition, only linear problems or when the nonlinear term is a compact perturbation of the principal part of the operator have been considered in the current literature [2]. Therefore, we are now interested in the applications of the topological sensitivity for the cases in that the nonlinear term involves the principal part of the operator, like the p -Poisson's equation, plasticity, finite deformations and so on.

ACKNOWLEDGMENTS

This research was partly supported by CNPq (Brasil) and by CONICET (Argentina). The support from these Institutions is greatly appreciated.

REFERENCES

- [1] H. Ammari and H. Kang, *Reconstruction of Small Inhomogeneities from Boundary Measurements*, Lecture Notes in Mathematics, Vol. 1846, Springer (2004).
- [2] S. Amstutz, The topological asymptotic for the Navier–Stokes equations, *ESAIM J. Control Optimization and Calculus of Variations*, 11(3), 401–425 (2005).
- [3] J. Céa, S. Garreau, Ph. Guillaume and M. Masmoudi, The shape and topological optimizations connection, *Comput. Methods Appl. Mech. Engrg.*, 188, 713–726 (2000).
- [4] H.A. Eschenauer and N. Olhoff, Topology optimization of continuum structures: A review, *Applied Mechanics Review*, 54, 331–390 (2001).
- [5] H.A. Eschenauer, V.V. Kobelev and A. Schumacher, Bubble method for topology and shape optimization of structures, *Structural Optimization*, 8, 42–51 (1994).
- [6] J.D. Eshelby, The elastic energy-momentum tensor, *J. Elasticity*, 5, 321–335 (1975).
- [7] R.A. Feijóo, A.A. Novotny, C. Padra and E. Taroco, The topological-shape sensitivity method and its application in 2D elasticity, *J. Comput. Methods Sci. Engrg.*, to appear (2005).
- [8] S. Garreau, Ph. Guillaume and M. Masmoudi, The topological asymptotic for PDE systems: The elasticity case, *SIAM J. Control Optim.*, 39, 1756–1778 (2001).
- [9] T. Lewiński and J. Sokolowski, Energy change due to the appearance of cavities in elastic solids, *Int. J. Solids Struct.*, 40, 1765–1803 (2003).
- [10] F. Murat and J. Simon, *Sur le Contrôle par un Domaine Géométrique*, Thesis, Université Pierre et Marie Curie, Paris VI, France (1976).
- [11] P. Neittaanmäki et al. (eds.), *Mini-symposium on Topological Sensitivity Analysis: Theory and Applications*, Jyväskylä, Finland, ECCOMAS (2004).
- [12] A.A. Novotny, R.A. Feijóo, C. Padra and E. Taroco, Topological sensitivity analysis, *Comput. Methods Appl. Mech. Engrg.*, 192, 803–829 (2003).
- [13] A.A. Novotny, A. Labanowski and E.A. Fancello, Topological sensitivity analysis applied to three-dimensional elasticity topology design, *COBEM*, Brazil (2005).
- [14] B. Samet, S. Amstutz and M. Masmoudi. The topological asymptotic for the Helmholtz equation, *SIAM J. Control Optim.*, 42(5), 1523–1544 (2003).
- [15] J. Sokolowski and A. Żochowski, On the topological derivative in shape optimization, *SIAM J. Control Optim.*, 37(4), 1251–1272 (1999).

TOPOLOGICAL DERIVATIVES FOR CONTACT PROBLEMS

Conical Differentiability and Asymptotic Analysis

Jan Sokołowski and Antoni Żochowski

¹*Institut Elie Cartan, Laboratoire de Mathématiques, Université Henri Poincaré Nancy I, B.P. 239, 54506 Vandoeuvre lés Nancy Cedex, France, and Systems Research Institute of the Polish Academy of Sciences, ul. Newelska 6, 01-447 Warszawa, Poland*

²*Systems Research Institute of the Polish Academy of Sciences, ul. Newelska 6, 01-447 Warszawa, Poland*

sokolows@iecn.u-nancy.fr, zochowsk@ibspan.waw.pl

Abstract: Numerical methods of evaluation of topological derivatives are proposed for contact problems in two dimensional elasticity. Problems of topology optimisation are investigated for free boundary problems of boundary obstacle types. The formulae for the first term of asymptotics for energy functionals are derived. The precision of obtained terms is verified numerically. The topological differentiability of solutions to variational inequalities is established. In particular, the so-called *outer asymptotic expansion* for solutions of contact problems with respect to singular perturbation of geometrical domain depending on small parameter are obtained by an application of nonsmooth analysis. The topological derivatives can be used in numerical methods of simultaneous shape and topology optimisation, in particular, in the level set type methods.

Keywords: Shape optimization, topological derivative, contact problem, asymptotic expansion, energy functional, optimal design.

1. INTRODUCTION

The main idea we use to derive the topological derivatives for contact problems is the modification of the energy functional by an appropriate correction term and subsequent minimisation of the resulting energy functional over the cone of admissible displacements. Such an approach leads to the *outer* approximations of solutions to variational inequalities.

In this paper we derive useful formulae for the correction terms of the energy functionals. We restrict ourselves to two dimensional problems and to singular perturbations of geometrical domains in the form of small discs.

The correction terms are derived in such a form, that the numerical verification of its precision is straightforward. On the other hand, the terms are directly used to establish the topological differentiability of solutions to variational inequalities. As a result, the one term *outer* expansion of solutions is derived for a class of nonlinear problems. Outer expansion means that the expansion is precise far from the hole, the expansion precise near the hole is called *inner* expansion and usually the matching procedure is applied [7] to construct the global asymptotic approximation of solutions to boundary problems in singularly perturbed geometrical domains.

We provide a list of references, which includes in particular the results based on asymptotic analysis of singularly perturbed boundary value problems in the spirit e.g., of the monographs [7, 8], and of the paper [9]. The list is not complete, since the topic is under dynamical expansion, we refer the reader to the special issue on shape optimization of the journal *Control and Cybernetics* 34(1) (2005), which includes many related results. The notion of topological derivative for an arbitrary shape functional is introduced for the first time in the report [20], published in [21], and can be extended in many directions, for the most general study of interior topological derivatives for the elasticity system we refer the reader to [9]. Since the topological derivative is actually the first term of asymptotic expansion of the functional under study, the results for the energy functionals are already given, e.g., in [7] (the Russian version of the book is published in 1987), and used in [3] for numerical methods of shape optimization.

The outline of the paper is the following. In Section 1 the main result, on asymptotic expansion of solutions to the contact problem, is presented. The result uses the conical differentiability of solutions and the appropriate correction term of the energy functional. In Section 2 the correction term is derived in two dimensional case. Mathematical analysis of the problem considered here is performed in [27], where some numerical results are included.

1.1 Contact Problem in Elasticity

We establish the conical differentiability of solutions for two dimensional contact problem in the elasticity. We consider the bounded domain Ω with the boundary $\partial\Omega = \Gamma_0 \cup \Gamma_c$. On Γ_0 the displacement vector of the elastic body is given, on Γ_c the frictionless contact conditions are prescribed. To specify the weak formulation we need an expression for the symmetric bilinear form and for the convex set $K \subset H^1(\Omega)^2$.

The method of analysis is the same as in the case of Signorini problem. We start with the formulation of the free boundary problem in unperturbed domain Ω . The form of variational inequality is straightforward.

(1) Contact problem in Ω

Find $\mathbf{u} = \mathbf{u}(\Omega) = (u_1, u_2)$ and $\sigma = (\sigma)_{ij}, i, j = 1, 2$, such that

$$-\mathbf{div} \sigma = \mathbf{f} \quad \text{in } \Omega, \tag{1}$$

$$C\sigma - \epsilon(\mathbf{u}) = 0 \quad \text{in } \Omega, \tag{2}$$

$$\mathbf{u} = 0 \quad \text{on } \Gamma_0, \tag{3}$$

$$\mathbf{u}v \geq 0, \quad \sigma_\nu \leq 0, \quad \sigma_\nu \mathbf{u}v = 0 \quad \sigma_\tau = 0 \quad \text{on } \Gamma_c. \tag{4}$$

Here

$$\begin{aligned} \sigma_\nu &= \sigma_{ij} \nu_j \nu_i, \quad \sigma_\tau = \sigma_\nu - \sigma_\nu = \{\sigma_\tau^i\}_{i=1}^2, \quad \sigma_\nu = \{\sigma_{ij} \nu_j\}_{i=1}^2, \\ \epsilon_{ij}(\mathbf{u}) &= \frac{1}{2}(u_{i,j} + u_{j,i}), \quad i, j = 1, 2, \quad \epsilon(\mathbf{u}) = (\epsilon_{ij})_{i,j=1}^2, \\ \{C\sigma\}_{ij} &= c_{ijkl} \sigma_{kl}, \quad c_{ijkl} = c_{jikl} = c_{klij}, \quad c_{ijkl} \in L^\infty(\Omega). \end{aligned}$$

The Hooke's tensor C satisfies the ellipticity condition

$$c_{ijkl} \xi_{ji} \xi_{kl} \geq c_0 |\xi|^2, \quad \forall \xi_{ji} = \xi_{ij}, \quad c_0 > 0, \tag{5}$$

and we have used the summation convention over repeated indices.

When the topology of Ω is changed, we have the following contact problem in the domain Ω_ρ with the small hole $B(\rho)$.

(2) Contact problem in Ω_ρ

Find $\mathbf{u} = \mathbf{u}(\Omega_\rho) = (u_1, u_2)$ and $\sigma = (\sigma)_{ij}, i, j = 1, 2$, such that

$$-\mathbf{div} \sigma = \mathbf{f} \quad \text{in } \Omega_\rho, \tag{6}$$

$$C\sigma - \epsilon(\mathbf{u}) = 0 \quad \text{in } \Omega_\rho, \tag{7}$$

$$\mathbf{u} = 0 \quad \text{on } \Gamma_0, \tag{8}$$

$$\sigma_\nu = 0 \quad \text{on } \Gamma_\rho, \tag{9}$$

$$\mathbf{u}v \geq 0, \quad \sigma_\nu \leq 0, \quad \sigma_\nu \mathbf{u}v = 0 \quad \sigma_\tau = 0 \quad \text{on } \Gamma_c. \tag{10}$$

We assume for simplicity that the case of isotropic elasticity is considered, thus the symmetric bilinear form associated with the boundary value problem (1)–(4) is given by

$$a(\mathbf{u}, \mathbf{u}) = \int_\Omega [(\lambda + \mu)(\epsilon_{11} + \epsilon_{22})^2 + \mu(\epsilon_{11} - \epsilon_{22})^2 + \mu\gamma_{12}^2], \tag{11}$$

where the notation for isotropic elasticity is fixed in Section 2.

The problem (6)–(10) is approximated by the problem with modified bilinear form in the following way.

(3) Approximation of contact problem in Ω_ρ

We determine the modified bilinear form as a sum of two terms, as it is for the energy functional, the first term defines the elastic energy in the domain Ω , the second term is a correction term, determined in Section 2.3 by formula (42). The correction term is quite complicated to evaluate, and we do not provide its explicit form, such a form is actually defined by the formulae in Section 2. The values of the symmetric bilinear form $a(\rho; \cdot, \cdot)$ are given by the expression

$$a(\rho; \mathbf{v}, \mathbf{v}) = a(\mathbf{u}, \mathbf{u}) + \rho^2 b(\mathbf{v}, \mathbf{v}) . \tag{12}$$

The derivative $b(\mathbf{v}, \mathbf{v})$ of the bilinear form $a(\rho; \mathbf{v}, \mathbf{v})$ with respect to ρ^2 at $\rho = 0+$ is given by the expression

$$b(\mathbf{v}, \mathbf{v}) = -2\pi e_v(0) - \frac{2\pi\mu}{\lambda + 3\mu} (\sigma_{11}\delta_1 - \sigma_{12}\delta_2) , \tag{13}$$

where all the quantities are evaluated for the displacement field \mathbf{v} according to formulae (26), (27), (29), (42), (33), we provide the line integrals which defines all terms in (13) below.

Hence, we can determine the bilinear form $a(\rho; \mathbf{v}, \mathbf{w})$ for all \mathbf{v}, \mathbf{w} , from the equality

$$2a(\rho; \mathbf{v}, \mathbf{w}) = a(\rho; \mathbf{v} + \mathbf{w}, \mathbf{v} + \mathbf{w}) - a(\rho; \mathbf{w}, \mathbf{w}) .$$

In the same way the bilinear form $b(\mathbf{v}, \mathbf{w})$ is determined from the formula for $b(\mathbf{v}, \mathbf{v})$.

The convex set is defined in this case by

$$\mathbf{K} = \{ \mathbf{v} \in H^1(\Omega)^2 \mid \mathbf{v} \geq 0 \text{ on } \Gamma_c , \quad \mathbf{v} = \mathbf{g} \text{ on } \Gamma_0 \} . \tag{14}$$

Let us consider the following variational inequality which provides a sufficiently precise for our purposes approximation \mathbf{u}_ρ of the solution $\mathbf{u}(\Omega_\rho)$ to contact problem (6)–(10),

$$\mathbf{u}_\rho \in \mathbf{K} : \quad a(\rho; \mathbf{u}, \mathbf{v} - \mathbf{u}) \geq L(\rho; \mathbf{v} - \mathbf{u}) \quad \forall \mathbf{v} \in \mathbf{K} . \tag{15}$$

The result obtained is the following, for simplicity we assume that the linear form $L(\rho; \cdot)$ is independent of ρ .

THEOREM 1 *For ρ sufficiently small we have the following expansion of the solution u_ρ with respect to the parameter ρ at $0+$,*

$$\mathbf{u}_\rho = \mathbf{u}(\Omega) + \rho^2 \mathbf{q} + o(\rho^2) \quad \text{in } H^1(\Omega)^2 , \tag{16}$$

where the topological derivative \mathbf{q} of the solution $\mathbf{u}(\Omega)$ to the contact problem is given by the unique solution of the following variational inequality

$$\mathbf{q} \in \mathcal{S}_{\mathbf{K}}(\mathbf{u}) = \{ \mathbf{v} \in (H^1_{\Gamma_0}(\Omega))^2 \mid \mathbf{v} \leq 0 \text{ on } \Xi(\mathbf{u}) , \quad a(0; \mathbf{u}, \mathbf{v}) = 0 \} \tag{17}$$

$$a(0; \mathbf{q}, \mathbf{v} - \mathbf{q}) + b(\mathbf{u}, \mathbf{v} - \mathbf{q}) \geq 0 \quad \forall \mathbf{v} \in \mathcal{S}_{\mathbf{K}}(\mathbf{u}) . \tag{18}$$

The coincidence set $\Xi(\mathbf{u}) = \{x \in \Gamma_s | \mathbf{u}(x) \cdot \mathbf{v}(x) = 0\}$ is well defined [18] for any function $\mathbf{u} \in H^1(\Omega)^2$, and $\mathbf{u} \in \mathbf{K}$ is the solution of variational inequality (14) for $\rho = 0$.

REMARK 1.1 *In the linear case, it can be shown that $\|\mathbf{u}(\Omega_\rho) - \mathbf{u}_\rho\| = o(\rho^2)$ in the norm of appropriate weighted space. We refer the reader to [9] for the related error estimates in the Hölder weighted spaces. In general, we cannot expect that \mathbf{u}_ρ is close to $\mathbf{u}(\Omega_\rho)$ in the vicinity of B_ρ , therefore the weighted spaces should be used for error estimates.*

For the convenience of the reader we provide the explicite formulae for the terms in $b(\mathbf{v}, \mathbf{v})$ defined by (13), we refer to Section 2.2 for details. We have

$$2\pi e_{\mathbf{v}}(0) = \frac{\pi(\lambda + \mu)}{\pi^2 R^6} \left(\int_{\Gamma_R} (v_1 x_1 + v_2 x_2) ds \right)^2 + \quad (19)$$

$$+ \frac{\mu}{\pi^2 R^6} \left(\int_{\Gamma_R} \left[(1 - 9k)(v_1 x_1 - v_2 x_2) + \frac{12k}{R^2}(v_1 x_1^3 - v_2 x_2^3) \right] ds \right)^2 +$$

$$+ \frac{\mu}{\pi^2 R^6} \left(\int_{\Gamma_R} \left[(1 + 9k)(v_1 x_2 + v_2 x_1) - \frac{12k}{R^2}(v_1 x_2^3 + v_2 x_1^3) \right] ds \right)^2,$$

with

$$\sigma_{11} = \frac{\mu}{\pi R^3} \int_{\Gamma_R} \left[(1 - 9k)(v_1 x_1 - v_2 x_2) + \frac{12k}{R^2}(v_1 x_1^3 - v_2 x_2^3) \right] ds,$$

$$\sigma_{12} = \frac{\mu}{\pi R^3} \int_{\Gamma_R} \left[(1 + 9k)(v_1 x_2 + v_2 x_1) - \frac{12k}{R^2}(v_1 x_2^3 + v_2 x_1^3) \right] ds,$$

and

$$\delta_1 = \frac{9k}{\pi R^3} \int_{\Gamma_R} \left[(v_1 x_1 - v_2 x_2) - \frac{4}{3R^2}(v_1 x_1^3 - v_2 x_2^3) \right] ds,$$

$$\delta_2 = \frac{9k}{\pi R^3} \int_{\Gamma_R} \left[(v_1 x_2 + v_2 x_1) - \frac{4}{3R^2}(v_1 x_2^3 + v_2 x_1^3) \right] ds.$$

2. TRANSFORMATIONS OF THE ENERGY FUNCTIONAL FOR THE 2D ELASTICITY SYSTEM

2.1 Using Poisson Kernel for Computing Strain

As it turns out, similar reasoning may be carried out in case of the 2D elasticity system, even if it is much more complicated. In absence of volume forces such a system has a form

$$\begin{aligned} \mu \Delta u_1 + (\lambda + \mu)(u_{1/1,1} + u_{2/1,2}) &= 0, \\ \mu \Delta u_2 + (\lambda + \mu)(u_{1/1,2} + u_{2/2,2}) &= 0, \end{aligned} \quad (20)$$

where $\mathbf{u} = (u_1, u_2)^T$ denotes the displacement and λ, μ are Lamé constants. We shall use also the usual notation for the symmetric strain tensor $\epsilon = [\epsilon_{ij}]$, $\epsilon_{11} = u_{1/1}, \epsilon_{22} = u_{2/2}, \gamma_{12} = 2\epsilon_{12} = u_{1/2} + u_{2/1}$ as well as stress tensor $\sigma = [\sigma_{ij}]$. The Hooke's law

$$\sigma_{11} = (\lambda + 2\mu)\epsilon_{11} + \lambda\epsilon_{22}, \quad \sigma_{22} = \lambda\epsilon_{11} + (\lambda + 2\mu)\epsilon_{22}, \quad \sigma_{12} = \mu\gamma_{12} = 2\mu\epsilon_{12}$$

links both objects. In these terms (20) reduces to

$$\nabla \cdot \sigma(\mathbf{u}) = 0. \tag{21}$$

For such a system there exists an analog to the Poisson kernel, see [1]. It is a matrix $\mathbf{G}(\mathbf{x}, \mathbf{y})$ allowing us to express the values of the solution inside the circle $\Gamma_R(\mathbf{x}_0)$ by means of its values on the circumference:

$$\mathbf{u}(\mathbf{x}) = -\frac{1}{\pi} \int_{\Gamma_R(\mathbf{x}_0)} \mathbf{G}(\mathbf{x} - \mathbf{x}_0, \mathbf{y} - \mathbf{x}_0) \cdot \mathbf{u}(\mathbf{y}) ds_{\mathbf{y}}. \tag{22}$$

Let us denote \mathbf{I} – identity matrix and

$$k = \frac{\lambda + \mu}{\lambda + 3\mu}.$$

Then $\mathbf{G}(\mathbf{x}, \mathbf{y})$ has a form

$$\mathbf{G}(\mathbf{x}, \mathbf{y}) = \mathbf{\Gamma}(\mathbf{x}, \mathbf{y}) + \mathbf{A}(\mathbf{x}, \mathbf{y}), \tag{23}$$

where

$$\mathbf{\Gamma}(\mathbf{x}, \mathbf{y}) = \left((1 - k)\mathbf{I} + 2k \begin{bmatrix} \left(\frac{\partial d}{\partial x_1}\right)^2 & \frac{\partial d}{\partial x_1} \frac{\partial d}{\partial x_2} \\ \frac{\partial d}{\partial x_1} \frac{\partial d}{\partial x_2} & \left(\frac{\partial d}{\partial x_2}\right)^2 \end{bmatrix} \right) \frac{\partial}{\partial \mathbf{n}_{\mathbf{y}}} \log \frac{1}{d}, \tag{24}$$

$$\mathbf{A}(\mathbf{x}, \mathbf{y}) = \frac{1}{2R} \left((1 - k)\mathbf{I} - k \begin{bmatrix} \frac{x_1 y_1 - x_2 y_2}{R^2} - 1 & \frac{x_1 y_2 + x_2 y_1}{R^2} \\ \frac{x_1 y_2 + x_2 y_1}{R^2} & -1 - \frac{x_1 y_1 - x_2 y_2}{R^2} \end{bmatrix} \right), \tag{25}$$

and $d = d(\mathbf{x}, \mathbf{y}) = \|\mathbf{x} - \mathbf{y}\|$.

From now on we shall assume that $\mathbf{x}_0 = 0$. This greatly simplifies formulae without loss of generality.

Using the representation of displacement as given by (22) we may compute the values of its derivatives at 0. Before writing down the result, we must introduce some notation. Let us define $I_1(k, l)$ and $I_2(k, l)$ as

$$I_1(k, l) = \frac{1}{\alpha(k, l)} \int_{\Gamma_R} u_1 x_1^k x_2^l ds, \quad I_2(k, l) = \frac{1}{\beta(k, l)} \int_{\Gamma_R} u_2 x_1^k x_2^l ds, \tag{26}$$

where

$$\alpha(k, l) = R^{k+l+2} \int_0^{2\pi} \cos^{k+1} \phi \sin^l \phi \, d\phi ,$$

$$\beta(k, l) = R^{k+l+2} \int_0^{2\pi} \cos^k \phi \sin^{l+1} \phi \, d\phi ,$$

whenever these expressions make sense, i.e. if k is odd and l even or vice versa. Observe that $\alpha(k, 0) = \beta(0, k)$ and

$$\alpha(1, 0) = \pi R^3, \quad \alpha(3, 0) = \frac{3}{4}\pi R^5, \quad \alpha(1, 2) = \frac{1}{4}\pi R^5,$$

$$\alpha(5, 0) = \frac{5}{8}\pi R^7, \quad \alpha(3, 2) = \frac{1}{8}\pi R^7$$

and so on. Furthermore, let

$$\delta_1 = 9k ([I_1(1, 0) - I_2(0, 1)] - [I_1(3, 0) - I_2(0, 3)]),$$

$$\delta_2 = 9k ([I_1(0, 1) + I_2(1, 0)] - [I_1(0, 3) + I_2(3, 0)]). \tag{27}$$

In terms of these symbols one may obtain, after very lengthy calculations, the formulae for the values of strain components at the point $\mathbf{x}_0 = 0$ which will constitute the basis of our energy transformations:

$$\epsilon_{11} + \epsilon_{22} = I_1(1, 0) + I_2(0, 1) ,$$

$$\epsilon_{11} - \epsilon_{22} = I_1(1, 0) - I_2(0, 1) - \delta_1 ,$$

$$\gamma_{12} = I_1(0, 1) + I_2(1, 0) + \delta_2 . \tag{28}$$

Let us recall also the expression for the elastic energy density at the same point,

$$e_u(0) = \frac{1}{2} \boldsymbol{\sigma} : \boldsymbol{\epsilon} = \frac{1}{2} [(\lambda + \mu)(\epsilon_{11} + \epsilon_{22})^2 + \mu(\epsilon_{11} - \epsilon_{22})^2 + \mu\gamma_{12}^2]. \tag{29}$$

2.2 Distortion of the Stress Field Caused by Small Circular Hole

We shall recall here some formulae describing the stress field around circular hole in the infinite 2D elastic medium. If we assume that at infinity only σ_{11} is not zero, and the hole $B(\rho)$ is centered around origin, then the stresses for $r \geq \rho$ have the form

$$\sigma_{rr} = \frac{1}{2}\sigma_{11} \left[\left(1 - \frac{\rho^2}{r^2}\right) + \left(1 - 4\frac{\rho^2}{r^2} + 3\frac{\rho^4}{r^4}\right) \cos 2\phi \right],$$

$$\sigma_{\phi\phi} = \frac{1}{2}\sigma_{11} \left[\left(1 + \frac{\rho^2}{r^2}\right) - \left(1 + 3\frac{\rho^4}{r^4}\right) \cos 2\phi \right], \tag{30}$$

$$\sigma_{r\phi} = -\frac{1}{2}\sigma_{11} \left(1 + 2\frac{\rho^2}{r^2} - 3\frac{\rho^4}{r^4}\right) \sin 2\phi .$$

Here (r, ϕ) constitute the polar coordinate system around origin and the σ -components are given in the orthogonal coordinates defined by $\{\mathbf{e}_r, \mathbf{e}_\phi\}$, with base vectors at any given point directed along radius and perpendicularly to it, anticlockwise.

Using these expressions we may immediately construct the solution corresponding to nonzero σ_{22} at infinity, by substituting $\phi := \phi + \frac{\pi}{2}$, $\sigma_{11} := \sigma_{22}$ (exchange of axis):

$$\begin{aligned}\sigma_{rr} &= \frac{1}{2}\sigma_{22}\left[\left(1 - \frac{\rho^2}{r^2}\right) - \left(1 - 4\frac{\rho^2}{r^2} + 3\frac{\rho^4}{r^4}\right)\cos 2\phi\right], \\ \sigma_{\phi\phi} &= \frac{1}{2}\sigma_{22}\left[\left(1 + \frac{\rho^2}{r^2}\right) + \left(1 + 3\frac{\rho^4}{r^4}\right)\cos 2\phi\right], \\ \sigma_{r\phi} &= \frac{1}{2}\sigma_{22}\left(1 + 2\frac{\rho^2}{r^2} - 3\frac{\rho^4}{r^4}\right)\sin 2\phi.\end{aligned}\quad (31)$$

Furthermore, we may exploit the fact that the pure shear stress σ_{12} is equivalent to simultaneous stretching and compression with the same intensity σ_{12} and $-\sigma_{12}$, but along the axis rotated by the angle $\pi/4$. Thus we make substitutions $\phi := \phi + \frac{\pi}{4}$, $\sigma_{11} := \sigma_{12}$, then $\phi := \phi - \frac{\pi}{4}$, $\sigma_{11} := -\sigma_{12}$ in (30) and add both solutions together obtaining:

$$\begin{aligned}\sigma_{rr} &= \sigma_{12}\left(1 - 4\frac{\rho^2}{r^2} + 3\frac{\rho^4}{r^4}\right)\sin 2\phi, \\ \sigma_{\phi\phi} &= \sigma_{12}\left(1 + 3\frac{\rho^4}{r^4}\right)\sin 2\phi, \\ \sigma_{r\phi} &= \sigma_{12}\left(1 + 2\frac{\rho^2}{r^2} - 3\frac{\rho^4}{r^4}\right)\cos 2\phi.\end{aligned}\quad (32)$$

Let us now denote

$$\sigma_I = \frac{1}{2}(\sigma_{11} + \sigma_{22}), \quad \sigma_{II} = \frac{1}{2}(\sigma_{11} - \sigma_{22}).\quad (33)$$

Then adding (30), (31), (32) gives the solution corresponding to the general stress field at infinity:

$$\begin{aligned}\sigma_{rr} &= \sigma_I + \sigma_{II}\cos 2\phi + \sigma_{12}\sin 2\phi \\ &\quad - \sigma_I\frac{\rho^2}{r^2} - \sigma_{II}\left(4\frac{\rho^2}{r^2} - 3\frac{\rho^4}{r^4}\right)\cos 2\phi - \sigma_{12}\left(4\frac{\rho^2}{r^2} - 3\frac{\rho^4}{r^4}\right)\sin 2\phi, \\ \sigma_{\phi\phi} &= \sigma_I - \sigma_{II}\cos 2\phi - \sigma_{12}\sin 2\phi \\ &\quad + \sigma_I\frac{\rho^2}{r^2} - 3\sigma_{II}\frac{\rho^4}{r^4}\cos 2\phi - 3\sigma_{12}\frac{\rho^4}{r^4}\sin 2\phi, \\ \sigma_{r\phi} &= -\sigma_{II}\sin 2\phi + \sigma_{12}\cos 2\phi \\ &\quad - \sigma_{II}\left(2\frac{\rho^2}{r^2} - 3\frac{\rho^4}{r^4}\right)\sin 2\phi + \sigma_{12}\left(2\frac{\rho^2}{r^2} - 3\frac{\rho^4}{r^4}\right)\cos 2\phi.\end{aligned}\quad (34)$$

Recalling the rules for the transformation of stresses under rotation of the coordinate system, we get the distortion of the stress due to the circular hole:

$$\begin{aligned} \hat{\sigma}_{rr} &= -\sigma_I \frac{\rho^2}{r^2} - \sigma_{II} \left(4 \frac{\rho^2}{r^2} - 3 \frac{\rho^4}{r^4} \right) \cos 2\phi - \sigma_{12} \left(4 \frac{\rho^2}{r^2} - 3 \frac{\rho^4}{r^4} \right) \sin 2\phi, \\ \hat{\sigma}_{\phi\phi} &= \sigma_I \frac{\rho^2}{r^2} - 3\sigma_{II} \frac{\rho^4}{r^4} \cos 2\phi - 3\sigma_{12} \frac{\rho^4}{r^4} \sin 2\phi, \\ \hat{\sigma}_{r\phi} &= -\sigma_{II} \left(2 \frac{\rho^2}{r^2} - 3 \frac{\rho^4}{r^4} \right) \sin 2\phi + \sigma_{12} \left(2 \frac{\rho^2}{r^2} - 3 \frac{\rho^4}{r^4} \right) \cos 2\phi. \end{aligned} \tag{35}$$

2.3 Transformation of the Energy Functional

Now we shall consider the contribution, in the absence of volume forces, of the energy integral over the circle surrounding the origin (i.e. the potential location of the small hole)

$$e_R(\mathbf{u}) = \frac{1}{2} \int_{B(R)} (\boldsymbol{\sigma} : \boldsymbol{\epsilon}) \, dx = \frac{1}{2} \int_{\Gamma_R} \mathbf{u}^T (\boldsymbol{\sigma} \cdot \mathbf{n}) \, ds \tag{36}$$

to the global elastic energy. Similarly as in the case of Laplace equation, we shall leave the displacement as is and consider the distortion to the stress field caused by introducing the small hole. Due to (35) it may be expressed as

$$\delta e_R = \frac{1}{2} \int_{\Gamma_R} \mathbf{u}^T (\hat{\boldsymbol{\sigma}} \cdot \mathbf{n}) \, ds. \tag{37}$$

At every point on the Γ_R we shall use the same coordinate system $\{\mathbf{e}_r, \mathbf{e}_\phi\}$ as in the last section. In this system $\mathbf{u} = [u_r, u_\phi]^T$, $\mathbf{n} = [1, 0]^T$. As a result, we have to compute the integral

$$\delta e_R = \frac{1}{2} \int_{\Gamma_R} (\hat{\sigma}_{rr} u_r + \hat{\sigma}_{r\phi} u_\phi) \, ds. \tag{38}$$

Now we observe that $x_1^2 + x_2^2 = R^2$ on Γ_R and

$$\begin{aligned} u_r &= \frac{1}{R} (u_1 x_1 + u_2 x_2) & u_\phi &= \frac{1}{R} (-u_1 x_2 + u_2 x_1), \\ \sin \phi &= \frac{1}{R} x_2 & \cos \phi &= \frac{1}{R} x_1. \end{aligned}$$

To simplify the calculations we introduce notations:

$$\begin{aligned} f &= I(1, 0) + I(0, 1), & a &= I(1, 0) - I(0, 1), & b &= I(3, 0) - I(0, 3), \\ c &= I(0, 1) + I(1, 0), & d &= I(0, 3) - I(3, 0). \end{aligned}$$

In these terms

$$\begin{aligned}
 \int_{\Gamma_R} u_r ds &= \pi R^2 f, \\
 \int_{\Gamma_R} u_r \cos 2\phi ds &= \pi R^2 \left(\frac{3}{2}b - a\right), \\
 \int_{\Gamma_R} u_r \sin 2\phi ds &= \pi R^2 \left(2c - \frac{3}{2}d\right), \\
 \int_{\Gamma_R} u_\phi \cos 2\phi ds &= \pi R^2 \left(\frac{3}{2}b - 2a\right), \\
 \int_{\Gamma_R} u_r \cos 2\phi ds &= \pi R^2 \left(\frac{3}{2}d - c\right).
 \end{aligned}
 \tag{39}$$

Now, due to (27),(28),

$$\begin{aligned}
 f &= \epsilon_{11} + \epsilon_{22}, & a &= \epsilon_{11} - \epsilon_{22} + \delta_1, & b &= \epsilon_{11} - \epsilon_{22} + \left(1 - \frac{1}{9k}\right)\delta_1, \\
 c &= \gamma_{12} - \delta_2, & d &= \gamma_{12} - \left(1 + \frac{1}{9k}\right)\delta_2.
 \end{aligned}$$

Substituting this into (38) gives

$$\begin{aligned}
 \delta e_R &= -\frac{1}{2}\pi\rho^2 \left[\sigma_I(\epsilon_{11} + \epsilon_{22}) + \sigma_{II}(\epsilon_{11} - \epsilon_{22}) + \sigma_{12}\gamma_{12} + \right. \\
 &\quad \left. + \left(1 - \frac{1}{k} + \frac{\rho^2}{R^2} \frac{1}{k}\right)(\sigma_{II}\delta_1 - \sigma_{12}\delta_2) \right].
 \end{aligned}
 \tag{40}$$

Since from Hooke’s law follows

$$\sigma_I = (\lambda + \mu)(\epsilon_{11} + \epsilon_{22}), \quad \sigma_{II} = \mu(\epsilon_{11} - \epsilon_{22}), \quad \sigma_{12} = \mu\gamma_{12}$$

then, because of (29),

$$\delta e_R = -\pi\rho^2 e_u(0) - \frac{1}{2}\pi\rho^2 \left[\left(1 - \frac{1}{k} + \frac{\rho^2}{R^2} \frac{1}{k}\right)(\sigma_{II}\delta_1 - \sigma_{12}\delta_2) \right].
 \tag{41}$$

This makes it different from the Laplace equation case, where the additional term vanishes. Observe, that in order to solve the elasticity problem in the domain containing the hole with accuracy (outside Γ_R) up to $o(\rho^2)$, we don’t need, due to (41), the solution in the intact domain. Simultaneously all the terms in (41) are quadratic with respect to \mathbf{u} and introduce no difficulty into numerical procedures.

If we restrict ourself to the terms depending strictly on ρ^2 and take into account the value of k , the energy corrections take on the form

$$\delta e_R = -\pi\rho^2 e_u(0) - \pi\rho^2 \frac{\mu}{\lambda + 3\mu} (\sigma_{II}\delta_1 - \sigma_{12}\delta_2).
 \tag{42}$$

In order to make clear that the energy correction is indeed an integral bilinear form of \mathbf{u} defined over Γ_R , we collect below the dependences given by (27),(28),(29) and write down the explicit expression for the terms appearing in (42):

$$\begin{aligned}\epsilon_{11} + \epsilon_{22} &= \frac{1}{\pi R^3} \int_{\Gamma_R} (u_1 x_1 + u_2 x_2) ds, \\ \epsilon_{11} - \epsilon_{22} &= \frac{1}{\pi R^3} \int_{\Gamma_R} \left[(1 - 9k)(u_1 x_1 - u_2 x_2) + \frac{12k}{R^2}(u_1 x_1^3 - u_2 x_2^3) \right] ds, \\ \gamma_{12} &= \frac{1}{\pi R^3} \int_{\Gamma_R} \left[(1 + 9k)(u_1 x_2 + u_2 x_1) - \frac{12k}{R^2}(u_1 x_2^3 + u_2 x_1^3) \right] ds, \\ \delta_1 &= \frac{9k}{\pi R^3} \int_{\Gamma_R} \left[(u_1 x_1 - u_2 x_2) - \frac{4}{3R^2}(u_1 x_1^3 - u_2 x_2^3) \right] ds, \\ \delta_2 &= \frac{9k}{\pi R^3} \int_{\Gamma_R} \left[(u_1 x_2 + u_2 x_1) - \frac{4}{3R^2}(u_1 x_2^3 + u_2 x_1^3) \right] ds.\end{aligned}$$

These expressions are easy to compute numerically, but unfortunately the correction formula is not so compact as in the Laplace operator case.

ACKNOWLEDGEMENT

The research is performed in the framework of the cooperation between Centre National de la Recherche Scientifique and Polish Academy of Sciences, PECO-NEI, Projet 18282, and partially supported by the grant 4 T11A 01524 of the State Committee for the Scientific Research of the Republic of Poland.

REFERENCES

- [1] M.O. Bašeleišvili, An analog of the Poisson formula in elasticity, (Georgian, with Russian abstract), *Trudy Vyčislitel'noy Centra AN Gruzinskoy SSR*, 1, 97–101 (1960).
- [2] J. Cea, S. Garreau, Ph. Guillaume and M. Masmoudi, The shape and topological optimizations connection, *Comput. Methods Appl. Mech. Eng.* 188(4), 713–726 (2000).
- [3] H.A. Eschenauer, V.V. Kobelev and A. Schumacher, Bubble method for topology and shape optimization of structures, *Struct. Optimiz.*, 8, 42–51 (1994).
- [4] T. Lewinski and J. Sokolowski, Optimal shells formed on a sphere. The topological derivative method, RR-3495, INRIA-Lorraine (1998).
- [5] T. Lewinski and J. Sokolowski, Energy change due to appearing of cavities in elastic solids, *Int. J. Solids & Structures*, 40, 1765–1803 (2003).
- [6] T. Lewinski, J. Sokolowski and A. Żochowski, Justification of the bubble method for the compliance minimization problems of plates and spherical shells, in *3rd World Congress of Structural and Multidisciplinary Optimization (WCSMO-3)*, Buffalo/Niagara Falls, New York, May 17–21, CD-Rom (1999).

- [7] W.G. Mazja, S.A. Nazarov and B.A. Plamenevskii, *Asymptotic Theory of Elliptic Boundary Value Problems in Singularly Perturbed Domains*, Vols. 1, 2, Birkhäuser Verlag, Basel (2000).
- [8] S.A. Nazarov and B.A. Plamenevskii, *Elliptic Problems in Domains with Piecewise Smooth Boundaries*, De Gruyter Exposition in Mathematics, Vol. 13, Walter de Gruyter (1994).
- [9] S.A. Nazarov and J. Sokołowski, Asymptotic analysis of shape functionals, *Journal de Mathématiques pures et appliquées*, 82-2, 125–196 (2003).
- [10] S.A. Nazarov and J. Sokołowski, Self adjoint extensions for the Neumann Laplacian in application to shape optimization, *Acta Mathematica Sinica*, in press.
- [11] S.A. Nazarov and J. Sokołowski, The topological derivative of the Dirichlet integral due to formation of a thin ligament, *Siberian Math. J.*, 45(2), 341–355 (2004).
- [12] S.A. Nazarov and J. Sokołowski, Self adjoint extensions of differential operators in application to shape optimization, *Comptes Rendus Mécanique*, 331(10), 667–672 (2003).
- [13] S.A. Nazarov and J. Sokołowski, Selfadjoint extensions for elasticity system in application to shape optimization, *Bulletin of the Polish Academy of Sciences – Mathematics*, 52(3), 237–248 (2004).
- [14] S.A. Nazarov and J. Sokołowski, Modeling of topology variations in elasticity, in *System Modeling and Optimization*, J. Cagnol and J.-P. Zolésio (eds), IFIP Int. Fed. Inf. Process., Vol. 166, Springer, Boston, MA, pp. 147–158 (2005).
- [15] S.A. Nazarov, A.S. Slutskij and J. Sokołowski, Topological derivative of the energy functional due to formation of a thin ligament on the spatial body, Les prépublications de l’Institut Élie Cartan 14/2004; <http://www.iecn.u-nancy.fr/Preprint/publis/index.html>, *Folia Mathematica*, in press.
- [16] A.A. Novotny, R.A. Feijóo, C. Padra and E. Taroco, Topological sensitivity analysis applied to topology design of Kirchhoff’s plate bending problem, *Control and Cybernetics*, 34(1), 339–361 (2005).
- [17] M. Rao and J. Sokołowski, Non-linear balayage and applications, *Illinois J. Math.*, 44, 310–328 (2000).
- [18] M. Rao and J. Sokołowski, Tangent sets in Banach spaces and applications to variational inequalities, Les prépublications de l’Institut Élie Cartan 42/2000.
- [19] J. Sokołowski and J.-P. Zolesio, *Introduction to Shape Optimization. Shape Sensitivity Analysis*, Springer Verlag (1992).
- [20] J. Sokołowski and A. Żochowski, On topological derivative in shape optimisation, INRIA-Lorraine, Rapport de Recherche No. 3170 (1997).
- [21] J. Sokołowski and A. Żochowski, On topological derivative in shape optimization, *SIAM Journal on Control and Optimization*, 37(4), 1251–1272 (1999).
- [22] J. Sokołowski and A. Żochowski, Topological derivative for optimal control problems, *Control and Cybernetics*, 28(3), 611–626 (1999).
- [23] J. Sokołowski and A. Żochowski, Topological derivatives for elliptic problems, *Inverse Problems*, 15(1), 123–134 (1999).
- [24] J. Sokołowski and A. Żochowski, Topological derivatives of shape functionals for elasticity systems, *Mechanics of Structures and Machines*, 29, 333–351 (2001).
- [25] J. Sokołowski and A. Żochowski, Optimality conditions for simultaneous topology and shape optimization, *SIAM Journal on Control and Optimization*, 42(4), 1198–1221 (2003).

- [26] J. Sokółowski and A. Żochowski, Topology optimization for unilateral problems, in *Control and Boundary Analysis*, Lect. Notes Pure Appl. Math., Vol. 240, Chapman and Hall/CRC, Boca Raton, FL, pp. 97–105 (2005).
- [27] J. Sokółowski and A. Żochowski, Modelling of topological derivatives for contact problems, *Numerische Mathematik*, 102(1), 145–179 (2005).

RELIABILITY-BASED TOPOLOGY OPTIMIZATION (RBTO)

Semyung Wang¹, Heegon Moon¹, Chwail Kim¹, Jenam Kang² and Kyung K. Choi³

¹*Department of Mechatronics, Gwangju Institute of Science & Technology, 1 Oryongdong, Bukgu, Gwangju 500-712, Korea*

²*Digital Appliance Research Lab, LG Electronics, 327-23 Gasan-dong, Keumchun-gu, Seoul 153-802, Korea*

³*Department of Mechanical Engineering, University of Iowa, Iowa City, IA 52242, U.S.A.*

Abstract: Recently, topology optimization has been the subject of a significant amount of academic and industrial research due to its simplicity in implementation and impact on product design. In this paper, reliability-based topology optimization (RBTO) is introduced for structures, electromagnetics, heat transfer, and coupled systems with consideration of uncertainties in topology optimization. Continuum design sensitivity using the adjoint variable method, the density method, and optimization algorithm (SLP and MMA) are used for topology optimization. PMA is mainly used for reliability computations. Examples are given to validate the proposed method.

Keywords: Reliability, topology optimization, uncertainty, multi-physics.

1. INTRODUCTION

Conventional structural optimization techniques such as sizing or shape/configuration optimizations are aimed at the improvement of current designs. Conversely, topology optimization focuses on obtaining an initial conceptual design and does not require a sophisticated initial design. As such, any geometry within the boundaries for conditions and loads is sufficient for commencing an initial topology optimization. Starting from basic structural systems, topology optimization is now of an age where it extends throughout various physical systems including electromagnetic, acoustic, thermal, and even to coupled-physics systems.

Reliability-based design optimization (RBDO) together with topology optimization has received high attention from optimization societies [1]. The primary goal of probabilistic optimization is to consider the variations of per-

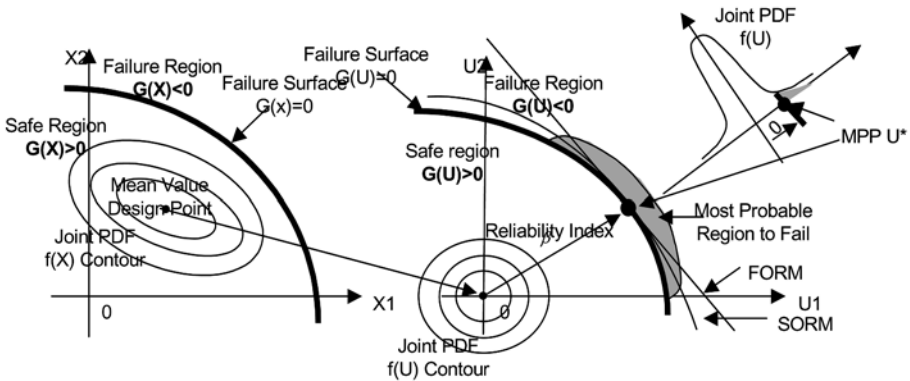


Figure 1. Concept of reliability-based design optimization.

performances caused by uncertainties. In deterministic optimization, these uncertainties are not considered and therefore the optimum design can be unreliable with respect to failures. On the other hand, in probabilistic optimization, minimizing the cost and bringing the probabilistic constraints on target should be done simultaneously.

In this research, the RBDO concept is applied to Topology Optimization and Reliability-Based Topology Optimization (RBTO) [2] is introduced. RBTO determines the optimal topology that satisfies the given probability in consideration of the variances of the uncertainties. RBTO is then applied to various multi-physics systems and numerical examples are presented.

2. RELIABILITY-BASED TOPOLOGY OPTIMIZATION

2.1 Concept of Reliability-Based Design Optimization

In general, engineering design problems are based on the control of the elements of a system such that they satisfy various criteria for performance, safety, serviceability, and durability under various demands. For example, a structure should be designed so that its strength or resistance is greater than the effects of the applied loads. However, there are numerous sources of uncertainty in system parameters. The goal of RBDO is to incorporate this uncertainty information into the actual design problems. The main idea for RBDO and its corresponding evaluations are shown in Figure 1.

RBDO has the same cost function as deterministic optimization, but it has probabilistic constraints used in the consideration of the probability of the satisfaction/failure potential of the constraints.

The general form of RBDO is described as follows:

$$\begin{aligned}
& \text{Minimize} && f(X) \\
& \text{subject to} && P_f(X) = P[G(x) < 0] \leq P_{ft} \\
& && x_i^L \leq x_i \leq x_i^U, \quad i = 1, \dots, n,
\end{aligned} \tag{1}$$

where P_{ft} is the target probability of failure. In RBDO, a limit state function, G , is formulated, and the system fails when $G < 0$.

2.2 General Formulation of Reliability-Based Topology Optimization (RBTO)

Conventional topology optimization is a deterministic method, so the RBDO concept was applied to topology optimization, resulting in the development of Reliability-Based Topology Optimization (RBTO) [2]. RBTO can be interpreted as a problem which finds an optimum topology under probabilistic constraints such that it becomes reliable for these uncertainties.

The general form of an RBTO problem is described as the following:

Find the design variable vector such that:

$$\begin{aligned}
& \text{Min/Max} && f(\eta_i) \\
& \text{Subject to} && P_s(X) = P[G(\eta_i, X_j) \geq 0] \geq P_t \\
& && 0 \leq \eta_i \leq 1 \\
& && i = 1, \dots, ndv \text{ and } j = 1, 2, \dots, \text{no. of uncertain variables,}
\end{aligned} \tag{2}$$

where X_j is the j th uncertain variable, P_s is the system probability of success, P_t is the target probability of success, and G is the limit state function (performance function). Design variables are density functions, η_i , in each finite element.

Applying the Performance Measure Approach (PMA) to Equation (2) yields:

$$\begin{aligned}
& \text{Min/Max} && f(\eta_i) \\
& \text{Subject to} && G^*(\eta_i, X_j) \geq 0 \\
& && \text{when } \beta_s = \beta_t \text{ for each evaluation} \\
& && 0 \leq \eta_i \leq 1 \\
& && i = 1, \dots, ndv \text{ and } j = 1, 2, \dots, \text{no. of uncertain variables,}
\end{aligned} \tag{3}$$

where β_s is the system reliability index for success, and β_t is the target reliability index for success.

In an RBTO problem, the performance (or limit-state) function should be defined, and each sensitivity analysis should be performed with respect to each uncertain variable.

2.3 RBTO for Structural Systems

Displacement is considered the limit-state function for a static problem. Young's modulus, thickness, and loading are considered uncertain variables.

The limit state function, G , is defined by:

$$\begin{aligned} G &= -\psi + \psi_{\max} \geq 0, \\ \psi &= z(\hat{x}) = \int_{\Omega} \hat{\delta}(x - \hat{x})z(x)d\Omega, \\ X &= [X_1, X_2, X_3]^T = [E, t, F]^T, \end{aligned} \quad (4)$$

where ψ is the displacement at an isolated point \hat{x} and $\hat{\delta}$ is the Dirac-Delta function, and X_j is the j th uncertain variable. The limit-state, Equation (4), implies that if the displacement, ψ , is larger than the limit value, ψ_{\max} , the system fails.

2.4 RBTO for Electromagnetic System

In RBTO for electromagnetic systems, in order to estimate the failure probability, the magnetic energy is considered the limit-state function for static problems. Design variables are density functions, η_i , in each finite element and the permeability, applied current density, and coercive force are uncertain variables [4–7].

The limit-state function G is defined by:

$$\begin{aligned} G &= \psi - \psi_{\min} \geq 0, \\ \psi &= \int_{\Omega} g(A, u)d\Omega = \frac{1}{2} \int_{\Omega} B \cdot Hd\Omega, \\ X &= [X_1, X_2, X_3]^T = [\mu, J_s, H_c]^T, \end{aligned} \quad (5)$$

where ψ is the magnetic energy. The limit-state implies that if the magnetic energy, ψ , is smaller than the limit value, ψ_{\min} , the system fails.

2.5 RBTO for Thermal System

For thermal systems, the temperature of the k th nodal point is chosen as the performance response, and the convection coefficient, h , is assumed to be an uncertain variable.

The limit-state function becomes:

$$G = \psi - \psi_{\min} \geq 0,$$

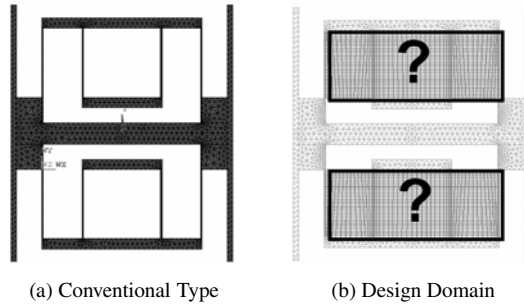


Figure 2. Basis model for topology optimization.

$$\begin{aligned} \psi &= \mathbf{u}^T \mathbf{T}, \\ X &= [X_1]^T = [h]^T, \end{aligned} \tag{6}$$

where \mathbf{u} is the vector which has 1 in the k th position and 0 elsewhere.

2.6 RBTO for Electric-Thermal-Structural Coupled System

For coupled systems, the objective function is to maximize the displacement of a target node. Since the example system is an actuator, the maximum displacement leads to a well-working device. The performance function is the total input current, I_m , and it should be less than a limit value. The electric conductivity, σ , is assumed to be an uncertain variable.

Then, the limit state function becomes:

$$\begin{aligned} \psi &= I_m, \\ G &= -\psi + \psi_{\max} \geq 0, \\ X &= [X_1]^T = [\sigma]^T. \end{aligned} \tag{7}$$

3. NUMERICAL EXAMPLES

3.1 Structural System: Double-Folded-Spring for MEMS

In this system [8], the spring is the most important part for the overall system performance (k_θ and k_x). Therefore, the spring is selected as the design domain for topology optimization. The conventional model is given in Figure 2(a) and the design domain from the conventional model is shown in Figure 2(b).

Three topology optimization problems are performed: (1) Deterministic Topology Optimization (DTO); (2) RBTO with $\beta = 1.0$; and (3) RBTO with $\beta = 1.5$. The number of design variables is 3400. The system should be

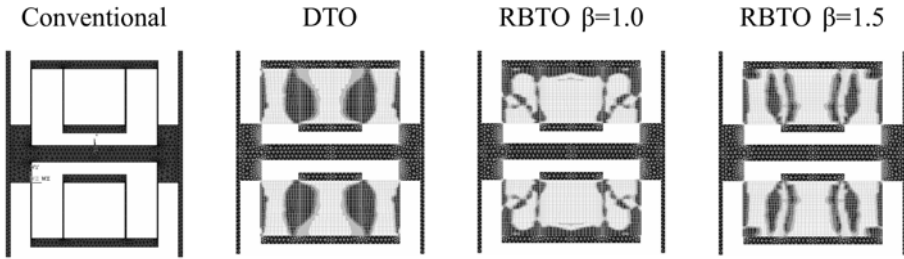


Figure 3. Summary of topology designs.

Table 1. Comparison of topology designs.

	Conventional	DTO	RBTO $\beta = 1.0$	RBTO $\beta = 1.5$
UX	0.02209	0.1473	0.03601	0.02270
UY	8.428E-06	7.974E-06	7.323E-06	6.951E-06
k_x	226.3	33.95	138.85	220.3
k_θ	4.878E+09	5.157E+09	5.615E+09	5.910E+09

symmetric, and a symmetric condition is internally imposed. The uncertain variables are Young’s modulus, thickness, and loading. The uncertain variables have a 5% standard deviation of the mean values and they have normal distributions.

In the following equations, UX is an x -directional displacement of the target node and is inversely proportional to k_x . This property is associated with the actuation of the device. Additionally, UY is a y -directional displacement of the target node and is inversely proportional to k_θ . This property is associated with the stability of the device. The target value of the constraint is selected from the analysis result of the conventional model (Figure 2(a)).

RBTO using PMA

$$\begin{aligned}
 \text{Max} \quad & UX, && \text{(Under Force Set 1: Translation)} \\
 \text{s.t.} \quad & UY < 8.0E - 6, && \text{(Under Force Set 2: Torsion)} \\
 & \text{when } \beta = \beta_i(1.0, 1.5) && (8) \\
 & X = [E, t, F], \sigma_i = 0.05 \times \mu_i, \quad i = 1, 2, 3.
 \end{aligned}$$

Figure 3 and Table 1 summarize the obtained results.

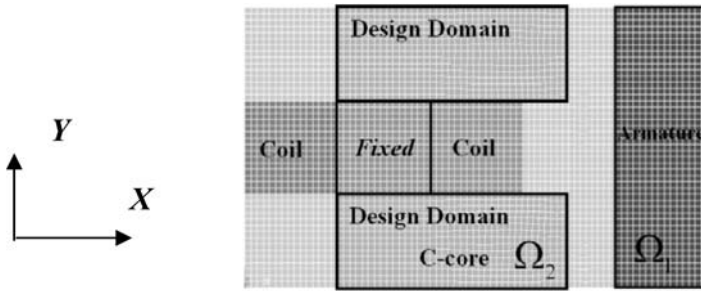


Figure 4. C-core actuator.

3.2 Electromagnetic System: C-Core Model

A numerical example [5] is a C-core model, as shown in Figure 4. The C-core actuator has three parts; an armature, a core, and a coil. The width of both the armature and the core is 20 mm. The length of the core and the blade are 60 mm and 50 mm, respectively. The relative permeability is 1000 at both the core and armature. The current density of the coil is 2.0 [A/mm²].

The limit-state function is the magnetic energy and should be larger than 140 [J/m], which is the target magnetic energy (ψ_t) in this example. The permeability and current density are the uncertain variables. The permeability and current density have 10% and 5% variance of the initial values, respectively, and they are assumed to be normal random variables.

If the PMA is used for RBTO, the RBTO problem is written as:

$$\begin{aligned} &\text{Minimize} && \text{Total Volume} \\ &\text{Subject to} && G = \psi - \psi_t \geq 0 \text{ when } \beta_s = 3, \quad \psi_t = 140, \end{aligned} \quad (9)$$

where ψ_t is the target magnetic energy.

The optimum results of several topology problems are shown in Figure 5 and Table 2. DTOSV is the Deterministic Topology Optimization with the Same Volume as the RBTO result. Since RBTO requires a reliability analysis, it needs a greater computational time than DTO. Empirically, RBTO needs about three times more computations than DTO. However, as shown in Table 2, RBTO gave a more reliable solution than DTOSV, while both methods used the same volume. Moreover, RBTO can satisfy the target reliability exactly as requested.

3.3 Thermal System: 2-D Cooling Fin

A 2-D cooling fin [9] is examined as a verification purpose. A $20 \times 50 \text{ mm}^2$ plate (Figure 6) is considered to have heat conditions such that $k = 0.2$. $h_f = 0.005$, $T_b = 25^\circ\text{C}$, $T^S = 300^\circ\text{C}$. Knowing that a larger temperature difference

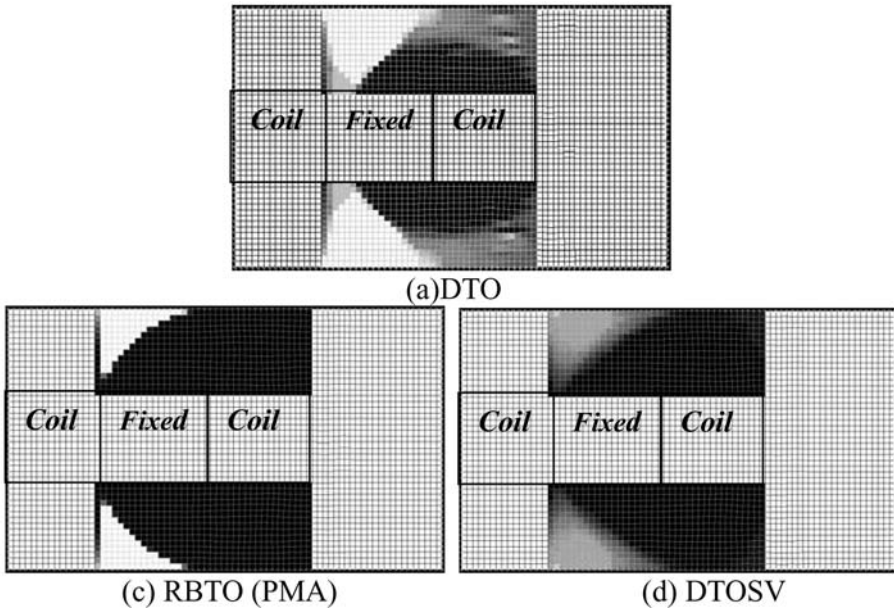


Figure 5. Topology results for electromagnetic systems.

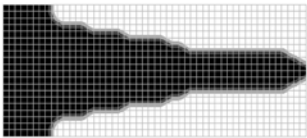
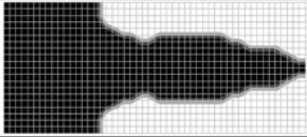
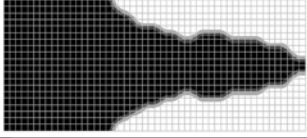
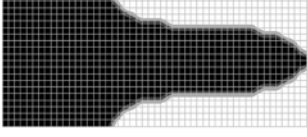
Table 2. Comparison between DTO and RBTO.

	Objective (volume)	Energy at mean value	Force (F_x) [Nm]	Reliability
DTO	59.03	139.96	-6048.5	-0.070274
RBTO with 3 uncertainties	86.40	140.81	-6110.6	3.00241
DTOSV (with the same volume of RBTO result)	86.40	140.73	-6102.9	2.40125



Figure 6. A simple heat transfer system illustrating energy balance.

Table 3. Optimal 2-D fin designs with consideration of different reliability indices.

DTO		Vol = 52.88 (%) $\beta = 0.0$ Mean Temp = 30.64
RBTO 1		Vol = 60.77 (%) $\beta = 1.0$ Mean Temp = 33.18
RBTO 2		Vol = 66.03 (%) $\beta = 2.0$ Mean Temp = 35.80
RBTO 3		Vol = 63.38 (%) $\beta = 3.0$ Mean Temp = 38.37

ensures a higher heat transfer rate by convection, an optimization problem is suggested that has a high temperature in the middle of the right side on the end.

$$\begin{aligned}
 &\text{Minimize} && \text{Total Volume} \\
 &\text{Subject to} && \Pr(T_p > 30.6) \leq \Pr(\beta_{tgt}). \tag{10}
 \end{aligned}$$

The convection coefficient, h , is assumed to be an uncertain variable which has 20% standard deviation of the mean value. Three different reliability indices (1.0, 2.0, 3.0) are used to test influences on the optimal results. PMA is used for RBTO in this example. As shown in Table 3, as the reliability index gets higher, the more volume is used, and the higher the mean temperature achieved. This result coincides with the fact that the rectangular fin (full material) has the highest temperature.

3.4 Electric-Thermal-Structural Coupled System: Electro-thermal Actuator

A switch with a bi-stable actuator for RF and optical applications is a useful device. The switch is electro-thermally actuated and it exhibits a clear bi-stable performance. The micro-switch mainly consists of a bi-stable actu-

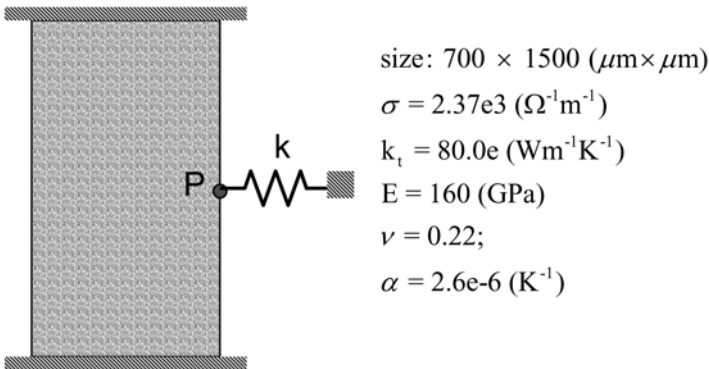


Figure 7. Initial design domain of the actuator for topology optimization.

ator enabling two separate transmission lines to connect physically, and a thermoelastic micro-actuator for making the bi-stable micro-actuator latch-up.

For this device, topology optimization is performed on the cascaded bent-beam area to obtain a more efficient structure in terms of displacement and power. The initial design domain is chosen as a simple rectangle, and then meshed into 30 *times* 60 finite elements. The leaf spring is replaced with a spring element [10].

Constraint on the total input current is considered to limit the overall power usage.

For the electro-thermal actuator RBTO is applied as:

$$\begin{aligned} & \text{Maximize} && \text{Displacement at } P (\delta_p) \\ & \text{Subject to} && \Pr(I_{\text{in}} < 50\text{mA}) \leq \Pr(\beta_t), \end{aligned} \quad (11)$$

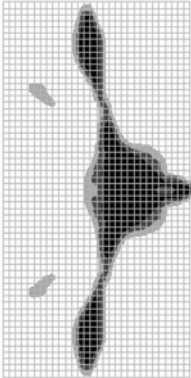
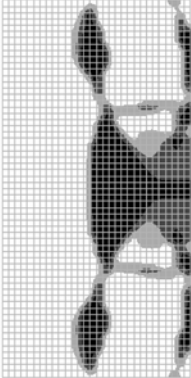
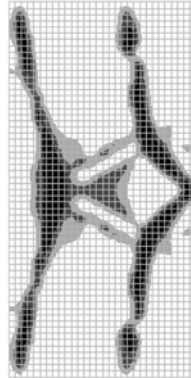
where I_{in} is the total input current.

Since an electric analysis works as a constraint, the uncertain variable is selected from one of the electric properties, i.e., the electric conductivity, σ . It is assumed that σ has a 10% standard deviation of the mean value. PMA is used for RBTO. The test proceeds with two different target reliability indices, i.e., $\beta_t = 1.0, 2.0$. As shown in Table 4, the objective function decreases when the target reliability index increases. The resulting input current decreases when the higher target reliability index is imposed, which explains that the limit of the constraint function (input current) is affected by the imposition of the reliability analysis.

4. CONCLUSION

In this research, the RBDO concept is applied to Topology Optimization and Reliability-Based Topology Optimization (RBTO) is introduced. RBTO de-

Table 4. Electro-thermal actuator design using RBTO.

DTO	RBTO1	RBTO2
-	$\beta_{igt} = 1.0$	$\beta_{igt} = 2.0$
$\delta_p = 72.4 \mu m$ $I_{in} = 50.0 mA$	$\delta_p = 69.2 \mu m$ $I_{in} = 45.4 mA$	$\delta_p = 63.6 \mu m$ $I_{in} = 41.5 mA$
		

termines an optimal topology that satisfies the given probability in consideration of the variances of the uncertainties. RBTO is then applied to multi-physics systems and each formulation is derived.

Structural displacement, magneto-static energy, thermal temperature, and electro-thermal actuator problems are solved using the RBTO methodology. RBTO is mainly compared to the deterministic Topology Optimization with the same volume of RBTO and the effectiveness of RBTO is shown.

ACKNOWLEDGMENT

This research was supported by the Center of Innovative Design Optimization Technology (iDOT), the Korea Science and Engineering Foundation.

REFERENCES

- [1] J. Tu, K.K. Choi and Y. Park, Design potential method for robust system parameter design, *AIAA Journal*, 39(4), 667–677 (2001).
- [2] K. Bae, S. Wang and K.K. Choi, Reliability-based topology optimization, in *9th AIAA MAO Conf.*, Atlanta, GA (2002).
- [3] G. Kharmanda, N. Olhoff, A. Mohamed and M. Lemaire, Reliability-based topology optimization, *Structural and Multidisciplinary Optimization*, 26(5), 295–307 (2004).
- [4] S. Wang and J. Kang, Topology optimization of nonlinear magnetostatics, *IEEE Transaction on Magnetics*, 38(2), 1029–1032 (2002).

- [5] J. Kang, C. Kim and S. Wang, Reliability-based topology optimization for electromagnetic systems, *COMPEL*, 23(3), 715–723 (2004).
- [6] S. Wang, S., Park and J. Kang, Multi-domain topology optimization of electromagnetic systems, *COMPEL*, 23(4), 1036–1044 (2004).
- [7] S. Wang, J. Kang and J. Noh, Topology optimization of single-phase induction motor, *IEEE Transactions on Magnetics*, 40(3), 1591–1596 (2004).
- [8] C. Kim, S. Wang, I. Hwang and J. Lee, Parallel computed reliability-based topology optimization using response surface method, in *WCSSMO6 Conf.*, Brazil, May (2005).
- [9] H. Moon, C. Kim and S. Wang, Reliability-based topology optimization of thermal systems considering convection heat transfer, *AIAA MA&O Conf.*, Albany, September (2004).
- [10] H. Moon, C. Kim and S. Wang, Reliability-based topology optimization of a thermoelastic actuator, in *WCSSMO6 Conf.*, Brazil, May (2005).

A FEATURE-BASED STRUCTURAL TOPOLOGY OPTIMIZATION METHOD

Gengdong Cheng¹, Yulin Mei¹ and Xiaoming Wang²

¹*State Key Laboratory of Structural Analysis of Industrial Equipment,
Dalian University of Technology, Dalian 116024, China*

²*Department of Mechanical Engineering, Dalian University of Technology,
Dalian 116024, China*

Abstract: Feature-based modeling has been widely studied in Computer Aided Design (CAD) and greatly facilitates mechanical design and manufacture. This paper incorporates the standard technology into topology optimization, and develops a feature-based structural topology optimization method. The method employs implicit models or level set models to represent complex structural boundaries; adopts R-function theory to handle set-theoretic operations; applies topological derivative analysis to determine the insertion position of geometric primitives; uses morphing technology and sensitivity analysis to choose the geometric primitives; employs the shape matching to merge the given geometric primitives for the further simplification of the final design.

Keywords: Topology optimization, feature-based, topological derivative, R-function, implicit representation, shape matching.

1. INTRODUCTION

Structural topology optimization has rapidly developed in the past two decades, and a number of methods have been proposed. In [4], Eschenauer and Olhoff divide them into two classes, the so-called material or Micro-approach, and the geometrical or Macro-approach. The Micro-approach uses fixed finite element meshes to describe the geometry and the mechanical response fields within the entire admissible design domain. The constitutive properties of finite elements are modeled based on the porous microstructures, whereas the Macro-approach assumes that the structure entirely consists of solid, isotropic or anisotropic material, and the topology of a solid body can be changed by growing or de-generating material. Since the topology optimization is always performed in conjunction with shape optimization, the finite element mesh cannot be a fixed one and must change with the changes of the structural boundaries [4].

Inspired by the level set method for topological optimization [1, 11], which can be regarded as a Macro-approach but can be implemented on the fixed meshes and need not track the boundaries of a structure explicitly, we realize that whether a topological optimization algorithm can be implemented easily on the fixed finite element meshes depends on whether the structure is described implicitly. For example, the SIMP method [2] describes the structure by means of the material density, and level set method employs the zero level set of a real valued function to represent the design, while the topology description function approach also defines the geometry of a structure by the level set of a summation of basis functions [3]. In fact, the description of a shape by a single real-valued function is a traditional approach of analytical geometry and has been exploited to define an arbitrary complex solid in computer-aided geometric modeling and in computer graphics [7]. Using the standard ideas from Constructive Solid Geometry (GSD), this paper presents a feature-based structural topology optimization method, which is based on the combination of topological derivative theory, sensitivity analysis, R-function theory, morphing technology, shape matching with the implicit structural representation. During the optimization process, we gradually construct a structure by Boolean operation of geometric primitives, which is directed by topological analysis and morphing technology, the topological derivative informs us where to subtract a simple geometric primitive, while morphing technology helps us to choose one among the given geometric primitives, and all the analyses can be conveniently implemented in the fixed Euler meshes, such as topological derivative analysis, morphing and Boolean operations. Certainly, the final design structure is composed of a finite set of simple geometric primitives so as to reduce manufacture cost.

2. BASIC APPROACHES

2.1 Problem Setting in Implicit Representation Frame

For the sake of realizing a feature-based optimization, we construct a structure by using some simple geometric primitives and set-theoretic operations, and the complex structure is described by Constructive Solid Geometry model and expressed by geometric tree in the topological optimization process. To guarantee that all the computation of the method can be implemented in a fixed Euler meshes, we apply a real valued function to implicitly represent complex material interfaces of a structure. We use Ω to denote the computational domain. The structure to be designed occupies a part of the domain Ω . If the structure is composed of one solid material, we consider the computational domain to be occupied by two materials, one is solid material, and another is void. In this case the structure can be represented implicitly by a real valued function $\phi(X)$ as closed subset of two-dimensional or three-dimensional Euc-

clidean space. The structure or solid material is represented by $\{X \mid \phi(X) < 0, X \in \Omega\}$, the void is represented by $\{X \mid \phi(X) > 0, X \in \Omega\}$, and the boundary of the structure can be described by the level set $\{X \mid \phi(X) = 0, X \in \Omega\}$ of the function $\phi(X)$. In this way, each geometric primitive is defined by a real valued function analytically or with tabulated values and an appropriate interpolation algorithm, and the major requirement to the function is to have at least C^0 continuity. A complex structure is a result of set operations on the simple geometric primitives, and typical set-theoretic operations include “or”, “and” and “subtract” operations. And these set-theoretic operations on functionally expressed object have been introduced and studied by Rvachev (1963, 1974) [7] for solving problems of mathematical physics on an area with complex shapes. By now, there is a rich set of functions to realize the set-theoretic operations, and they are characterized that their signs are completely defined by signs of their arguments and do not depend on arguments values, and are generally named after R-function.

Let us consider a structural topology optimization problem in the frame of linear elasticity. With implicit representation of structures, the problem can be formulated as

$$\begin{aligned}
 \text{Minimize}_{\phi(X)} \quad & J(u) = \int_{\Omega} F(u)H(\phi)d\Omega \\
 \text{subject to:} \quad & \int_{\Omega} E_{ijkl}\varepsilon_{ij}(u)\varepsilon_{kl}(v)H(\phi)d\Omega \\
 & = \int_{\Omega} p v H(\phi)d\Omega + \int_{\Omega} \tau v \delta(\phi)d\Omega, \quad \forall v \in U \\
 & u|_{\partial\Omega_u} = u_0, \\
 & R_i(u) \int_{\Omega} r_i(u)H(\phi)d\Omega \leq 0, \quad i = 1, 2, \dots, m, \quad (1)
 \end{aligned}$$

where $H(\cdot)$ is a Heaviside function, $\delta(\cdot)$ is a Dirac function, U stands for a space of kinematically admissible displacement fields, whereas u denotes the displacement field, E_{ijkl} the elasticity tensor, ε_{ij} the liberalized strain tensor, p the body forces, τ the tractions applied on the structure traction boundary, u_0 the prescribed displacement on the structure displacement boundary, and m the number of constraints. Assume that a given solid material may occupy the domain Ω , then the structural optimization problem is to find the optimal material distribution so that the objective function $J(u)$ is minimized while the constraints $R_i(u) \leq 0$ are satisfied.

2.2 Sensitivity Analysis

For clarity, it is assumed that a given solid material initially occupies the computational domain Ω , and that the optimum structure is achieved by subtracting some simple geometric primitives and changing their positions, sizes or orientations. In this case, the structure to be designed can be expressed by a series of Boolean “and” operation of some geometric primitive representation function, which can be formulated as

$$\phi(X) = \bigcap_{i=1}^n \left[c_i \phi_i \left(\frac{1}{c_i} R_i^T (X - b_i) \right) + L_i \right], \quad (2)$$

where \cap denotes the “and” operation; $\phi(X)$ is the representation function of the design structure, and results from the “and” operation of n simple geometric primitives; ϕ_i denotes the representation function of the i th geometric primitive; the superscript T expresses the matrix transpose, and R_i is the rotation matrix, which determines the orientation of the i th geometric primitive in the structure. For our purpose it is sufficient to think that R_k belongs to the group of 2×2 or 3×3 rotation matrices, and its derivative is the set of 2×2 or 3×3 real skew-symmetric matrices and can also be regarded as a vector in two- or three-dimensional Euclidean space, which is denoted by $d\omega_k$; c_i stands for the scale coefficient of the i th geometric primitive, which determines the geometric size of the i th geometric primitive, and it can also be substituted with an affine matrix for different scale coefficients in different coordinate directions; b_i expresses a vector in the computational domain, which determines the position of the i th geometric primitive; L_i is a constant, which determines the offset size of the i th geometric primitive. Therefore, the structural topology optimization problem aims to find the number n of the geometric primitives, their size scale coefficient c_i ($i = 1, 2, \dots, n$), the offset size L_i ($i = 1, 2, \dots, n$), and position vector b_i ($i = 1, 2, \dots, n$), as well as the orientation matrix R_i ($i = 1, 2, \dots, n$).

Differentiating the objective function in Equation (1) yields its sensitivity with respect to $\phi(X)$ in the direction $\psi(X)$ [11],

$$\left\langle \frac{dJ(u)}{d\phi}, \psi \right\rangle = \int_{\Omega} \nabla J(u, w) \psi(x) \delta(\phi) d\Omega, \quad (3)$$

where $\nabla J(u, w)$ stands for the boundary shape sensitivity of the objective function. For detailed formulae, the reader is referred to [11].

For brevity, we rewrite Equation (2) as follows:

$$\phi(X) = A \left(\Phi(X), c_k \phi_k \left(\frac{1}{c_k} R_k^T (X - b_k) \right) + L_k \right). \quad (4)$$

Here, $A(\cdot, \cdot)$ denotes the R-function of “and” operation; $\Phi(X)$ is a representation function resulting from “and” operations of the other $n - 1$ geometric primitives in Equation (2).

With this notation in mind, differentiating Equation (4) with respect to size scale coefficient c_k , offset size L_k , and position vector b_k as well as orientation matrix R_k of the k th geometric primitive, we can obtain

$$d\phi = A'_2 \left[-\nabla\phi_k \cdot \left(R_k^T (X - b_k) \frac{dc_k}{c_k} + d\omega_k \times R_k^T (X - b_k) + R_k^T db_k \right) + \phi_k dc_k + dL_k \right], \tag{5}$$

where A'_2 stands for the partial derivative of the “and” operation function $A(\cdot, \cdot)$ with respect to the second argument. Applying Equations (3) and (5), substituting $\psi(X)$ with $d\phi$ yields

$$\begin{aligned} \frac{dJ(u)}{dc_k} &= - \int_{\Omega} \nabla J(u, w) A'_2 \nabla\phi_k \cdot \frac{1}{c_k} R_k^T (X - b_k) \delta(\phi) d\Omega, \\ \frac{dJ(u)}{d\omega_k} &= - \int_{\Omega} \nabla J(u, w) A'_2 R_k^T (X - b_k) \times \nabla\phi_k \delta(\phi) d\Omega, \\ \frac{dJ(u)}{db_k} &= - \int_{\Omega} \nabla J(u, w) A'_2 R_k \nabla\phi_k \delta(\phi) d\Omega, \\ \frac{dJ(u)}{dL_k} &= - \int_{\Omega} \nabla J(u, w) A'_2 \delta(\phi) d\Omega. \end{aligned} \tag{6}$$

Equation (6) expresses the sensitivity of the objective function when changing the geometric and positional parameters of the k th geometric primitive.

2.3 Topological Derivative Analysis

As mentioned above for our purposes of machinability, the structure to be designed is modeled by using the constructive geometry method in the topological optimization, which leads to the resulting structure composed of a particularly simple set of geometric primitives. During the optimization process, the structure is begun with a block of the given solid material, which occupies the entire computational domain, and then some simple geometric primitives are subtracted from the structure gradually, meanwhile their characteristic parameters are updated in order to achieve a better design. With the helps of the topological derivative analysis, which characterizes the sensitivity of the objective of the optimization problem when a small hole is created at a point of the domain, we can find the proper position where a simple geometric primitive is subtracted in the current structure. The so-called topological derivative of an arbitrary shape functional is introduced by Garreau et al. [5] and Sokolowski and Zochowski [9] with applying asymptotic analysis in singularly perturbed

geometrical domains. Recently, an alternative way is proposed to compute the topological derivative based on the shape sensitivity analysis concepts [6], and the topological derivative of multi-material structures is also applied [11]. The topological derivative provides us for any point of the domain the sensitivity in creating a small hole in that point. By simple comparison, we can determine where a simple geometric primitive should be inserted in the current structure. The topological derivative formulae derived in [9] for the two-dimensional case is used here.

2.4 Morphing Technology

Although the contour or iso-surface of the topological derivative near the perforated point can offer us some information about which geometric primitive in the prescribed set is chosen to be subtracted from the current structure, a matching calculation of geometric graphs is needed. Here, we use an alternative way to choose the geometric primitive based on morphing technology in computer graphic, which is a method used to construct a smooth, natural sequence of images between an ordered pair of images [8].

Consider n geometric primitives $\phi_1, \phi_2, \dots, \phi_n$ we formulate each geometric primitive to be a vertex of an $(n - 1)$ -dimensional simplex. An in-between geometric primitive is considered a point in the simplex and expressed by barycentric coordinates $T = (t_1, t_2, \dots, t_n)$ subject to the constraints $t_i \geq 0$ and $\sum_{i=1}^n t_i = 1$. Thus, an in-between geometric primitive can be formulated as $\phi_T(X) = \sum_{i=1}^n t_i \phi_i$, and the sensitivities of the objective function with respect to barycentric coordinates are given as

$$\frac{dJ(u)}{dt_k} = \int_{\Omega} \nabla J(u, w) A'_2 \phi_k \delta(\phi) d\Omega, \quad k = 1, 2, \dots, n. \quad (7)$$

In sum, we first subtract the in-between geometric primitive from the current structure after topological derivative analysis and then continuously optimize its geometric and positional parameters according to Equation (6), while we gradually update the parameter to find the suitable basis geometric primitive by using the sensitivity information (7) and by penalizing the in-between shape during the optimization process.

2.5 Shape Matching Techniques

Numerical experiments show that the outcome of the topology optimization process is influenced by the initial dimension of the in-between geometric primitive that is inserted into the structure in iterations. In order to search for an optimum design, the inserted dimension of the in-between geometric primitive can not be too large, and it usually is chosen as 3–10% of the design domain area or volume, which results in the final structure consisted of dozens of the

basis geometric primitives as illustrated in the next section. For the sake of simplifications, before the topology optimization process is finished, the merging of the geometric primitives will be implemented with the helps of shape matching techniques, and the connected geometric primitives will be replaced by a basis geometric primitive.

Shape matching has been approached in a number of ways, which deals with transforming a shape, and measuring the resemblance with another one, and so on. Here the template metric is employed as the similarity measure, which is defined as the area of symmetric difference of two compared compact sets [10]. If we use $\phi(X)$ to implicitly represent a connected domain that is formed by the union of some geometric primitives, and $\phi_r(X)$ denotes the substituting geometric primitive, which is written in the form of in-between geometric primitive so that the appropriate basis geometric primitive can be found automatically in the matching process, the template metric can be formulated in the implicit notations as $\int_{\Omega} H(A(\phi, -\phi_r)) + H(A(-\phi, \phi_r))d\Omega$, its derivative with respect to the affine, rotation, displace and offset transform can be easily written out, here we omit it for brevity. Therefore, the structure simplification or matching can be implemented by a mathematical programming; here the steepest descent method is applied while the constraints and the penalty also are considered.

3. NUMERICAL EXAMPLES

Example 1: A Michell-type structure in Figure 1 is considered. Three concentrated forces are applied at the equally distanced points on the bottom with $P_1 = 300$ N and $P_2 = 150$ N. The design domain is occupied by one material with elasticity modulus 200 Gpa and Poisson ratio 0.3. The design aims to minimize structural energy under the material volume constraints 0.3. During the optimization process, only the right half is analyzed and discretized by 62×62 quadrilateral elements, and a circle, a square and a triangle are chosen as the basis geometric primitives. The iteration histories of the objective function and the constraint are shown in Figure 2. Figure 3 shows the evolution of structural topology during optimization, where Figure 3(a) is the initial structure, and during the optimization process 20 in-between geometric primitives are inserted and Figure 3(d) is the optimal topology constructed by the given quadrangle, 3 triangles and 17 circles. The example is recalculated while the shape matching algorithm is implemented to simplify the optimization result. In this case the iteration histories of the objective function and the constraint are shown in Figure 4. The iterative processes are illustrated in Figure 5, where Figure 5(a) is the initial structure and Figure 5(d) is the final result that is only constructed by the given quadrangle, 1 triangle, 2 rectangles as well as 1 ellipse.

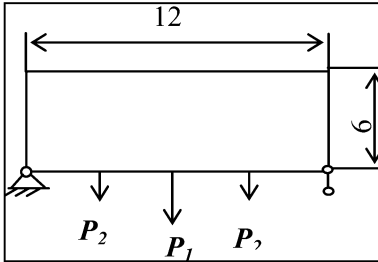


Figure 1. Michell-type structure.

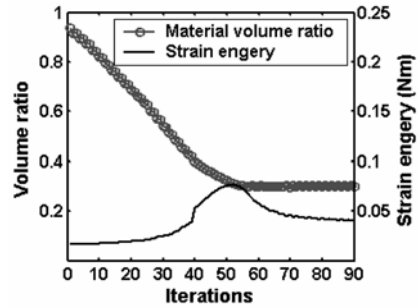


Figure 2. Objective and constraint.

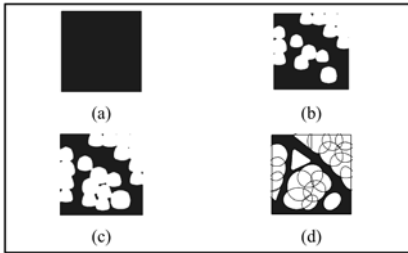


Figure 3. Iterative processes.

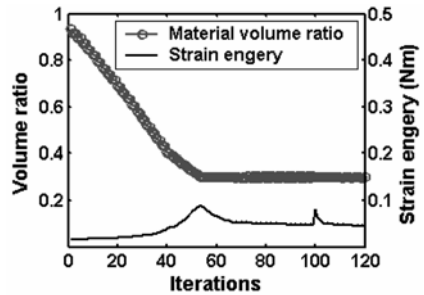


Figure 4. Objective and constraint.

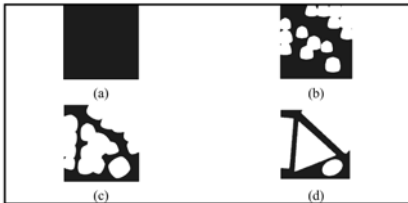


Figure 5. Iterative processes.

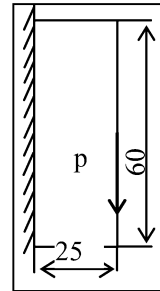


Figure 6. Cantilever beam.

Example 2: Consider a cantilever beam as shown in Figure 6. The beam is loaded with a concentrated vertical force $P = 800 \text{ N}$ at the middle point of the free hand. Assume that the modulus of elasticity and the Poisson ratio of the material are 200 Gpa and 0.3 , respectively. During the optimization process, the design domain is discretized by 27×62 quadrilateral elements, and the volume ratio is constrained to be 0.3 . Meanwhile, two basis geometric primitives are given, one is a circle, the other is a triangle. The objective function, the constraint and iterative processes are illustrated in Figures 7 and 8.

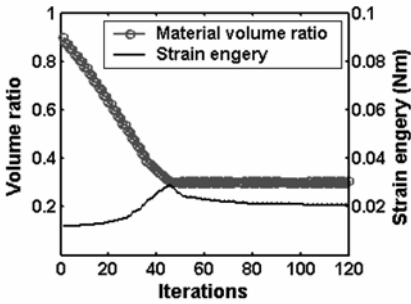


Figure 7. Objective and constraint.

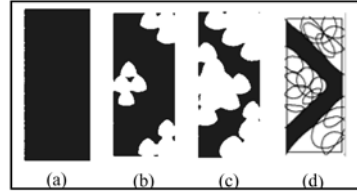


Figure 8. Iterative processes.

Figure 8(a) is the initial structure, and 18 in-between geometric primitives are inserted during the optimization process, and Figure 8(d) is the final result that is constructed by the given quadrangle, 1 triangle and 17 circles.

4. CONCLUSION

In order to reduce manufacture cost, we present a feature-based structural topology optimization method. Its main characteristic is that the final design is only constructed by the several given basis geometric primitives. Obviously, these simple geometric primitives can be easily and directly transferred to manufacturing instructions in machine tools, which ensures that the obtained topology can be conveniently manufactured.

In essence, the method uses a real valued function to implicitly represent complex material interfaces of a structure in order to guarantee that all the analysis can be implemented in the fixed Euler meshes, meanwhile Constructive Solid Geometry (CSG) method is employed to construct the structure by gradually inserting in-between geometric primitives during the optimization process. Furthermore, the topological derivative analysis is adopted to determine the insertion position of an in-between geometric primitive, while the morphing technology and the sensitivity analysis are together used to determine which basis geometric primitive is chosen to insert. In addition, Boolean operations on the geometric primitives are implemented by R-function method, which guarantees the regularity of the structure representation function, and which meets the need of the structure boundary smoothness for finite element analysis. Finally, in order to further simplify the final design so that each connected perforation in the final result is only represented by one basis geometric primitive, the shape matching techniques is used to merge these connected geometric primitives before the topology optimization process is finished.

It is well known in topology optimization that the emerging structure often progresses towards a pin-jointed frame that would have been iso-stressed in the

manner of Michell structures if the structure is subject to single loading case. However, the feature-based method simultaneously considers design objectives and manufacture constraints, and its final design is obtained by gradually subtracting basis features from the current structure, therefore the final result could not be the pin-jointed frame structures. Obviously, the structure obtained by the proposed method is associated with a low performance as compared with the corresponding result by usages of a Micro-approach, because a price must be paid for an extra machinable constraint.

ACKNOWLEDGEMENTS

This project is supported by the National Natural Science Foundation of China (No. 10332010) and China Postdoctoral Science Foundation (No. 2004036110).

REFERENCES

- [1] Allaire G. et al., Structural optimization using sensitivity analysis and a level-set method, *Journal of Computational Physics*, 194(1), 363–393 (2004).
- [2] Bendsoe, M.P. and Sigmund O., *Topology Optimization Theory. Methods and Applications*, Springer (2003).
- [3] De Ruiter, M.J. and Keulen, F.V., Topology optimization: Approaching the material distribution problem using a topological function description, in *Computational Techniques for Materials, Composites and Composite Structures*, B.H.V. Topping (ed.), Civil-Comp Press, Edinburgh, UK, pp. 111–119 (2000).
- [4] Eschenauer, H.A. and Olhoff, N., Topology optimization of continuum structures: A review, *Appl. Mech. Rev.*, 54(4), 331–389 (2001).
- [5] Garreau, S. et al., The topological asymptotic for PDE systems: The elasticity case, *SIAM Journal of Control Optimization*, 39(6), 1756–1778 (2001).
- [6] Novotny, A.A. et al., Topological sensitivity analysis, *Computer Methods in Applied Mechanics and Engineering*, 192, 803–829 (2003).
- [7] Pasko, A. et al., Function representation in geometric modeling: Concepts, implementation and applications, *The Visual Computer*, 11(8), 429–446 (1995).
- [8] Seungyong, L. et al., Polymorph: Morphing among multiple images, *IEEE Computer Graphics and Applications*, 18(1), 58–71 (1998).
- [9] Sokolowski, J. and Zochowski, A., On the topological derivative in shape optimization, *SIAM Journal of Control Optimization*, 37, 1251–1272 (1999).
- [10] Veltkamp, R.C., Shape matching: Similarity measures and algorithms, in *SMI 2001 International Conference on Shape Modeling and Applications*, SMI, Genova, Italy (2001).
- [11] Yulin, M. and Xiaoming, W., A level set method for structural topology optimization and its applications, *Advances in Engineering Software*, 35(7), 415–441 (2004).

Composites and Graded Materials

DESIGN OF FIBER REINFORCED SHAFTS SUBJECT TO LOCAL STRESS CONSTRAINTS THROUGH INVERSE HOMOGENIZATION

A Preliminary Study on Fiber Size Effect

Robert Lipton and Michael Stuebner

Mathematics Department, Louisiana State University, Baton Rouge, LA 70803, U.S.A.

lipton@math.lsu.edu, stuebner@math.lsu.edu

Abstract: A new inverse homogenization procedure is applied to design graded fiber reinforced shafts subject to local stress criteria. The method is based on new multiscale stress criteria given by macrostress modulation functions. The modulation functions quantify the intensity of local stress fluctuations at the scale of the microstructure due to the imposed macroscopic stress. The method is carried out for long cylindrical shafts reinforced with stiff cylindrical elastic fibers with generators parallel to the shaft. Benchmark examples are presented for shaft cross sections that possess reentrant corners typically seen in lap joints and junctions of struts.

Keywords: Pointwise stress constraints, optimal structural design.

1. INTRODUCTION

We present a computational design method for grading the microstructure inside composite media. The goal is to design a graded microstructure in order to control local stress in the vicinity of stress concentrations. The method has been developed by the authors in [10] and [14] and is based upon new rigorous multiscale stress criteria that captures the effect of local stress fluctuations at the scale of the microstructure [12, 13]. The multiscale criteria are given in terms of quantities dubbed macrostress modulation functions. The design methodology presented here is expressed in terms of a homogenized design problem that satisfies two requirements: The first is that the homogenized design problem is computationally tractable. The second is that the solution of the homogenized design problem provides the means to identify graded microstructures that deliver the required structural response while at the same

time provide local stress control. The approach used in this paper is in essence an inverse method that uses homogenization theory to identify optimal graded microgeometries. Because of this we refer to it as an inverse homogenization design method. To the best of our knowledge these techniques represent the first rigorously based approach to composite design in the presence of point wise stress constraints.

It is now well established that homogenization theory is an effective tool for the design of composites for optimal structural compliance and natural frequency, see [1, 3, 4, 5, 8, 15, 16, 17]. On the other hand relatively little work has been directed towards the solution of stress constrained composite design problems. Recently new efforts have initiated the development of numerical methods for structural optimization in the presence of stress constraints. The investigation given in [6] provides a numerical method for the stress constrained minimum volume design problem. The method is carried out using an empirical model known as the Solid Isotropic Microstructure with Penalization (SIMP) model [3]. The problem of mean square stress constrained structural optimization for fiber reinforced shafts is taken up in [9]. In that work a numerical algorithm is developed based on a suitable homogenized quantity (the covariance tensor) that rigorously encodes the mean square stress constraints. The work of [2] introduces a partial relaxation for topology optimization for minimum mean square stress using finite rank laminates. The rigorous theoretical context behind the homogenization approach to mean square stress (or gradient) constrained structural optimization has been worked out in [11].

To fix ideas we address the problem of reinforcement for a long shaft with constant cross section subjected to torsion loading. The microstructure within the shaft consists of long reinforcement fibers of constant cross section with isotropic shear modulus G_f embedded in a more compliant material with shear modulus G_m . The shaft together with the fibers are right cylinders with generators along the x_3 axis. The cross section of the reinforced shaft is specified by the region Ω in the $x_1 - x_2$ plane. The shaft cross section is divided up into small square subdomains of equal size. Each subdomain contains a single fiber cross section. The fiber cross section is circular and is centered inside the square subdomain. The radii of the fiber inside each square is chosen independently of the others. The side length of the square subdomain is denoted by ε . In this paper the diameter of the shaft cross section is 2 cm and ε is chosen to be 0.066 cm. Two design problems are carried out when the total fiber cross-sectional area is constrained to be 40% and 50%. The goal is to design a graded distribution of fibers across the cross section such that the following requirements are met:

- I. *The reinforced shaft has a torsional rigidity that is acceptable.*
- II. *The magnitude of the local point wise stress inside the composite is controlled over a designated subset of the cross section.*

The advantage of the inverse homogenization method introduced here is that it allows the designer to efficiently search the structural universe for good designs. It is based upon asymptotics that rigorously predict the actual local fields inside the composite when the length scale of the microstructure is sufficiently small. In this paper we compute two illustrative examples that record the stress distribution inside the designs generated by the inverse homogenization method. The designs presented in this paper were computed on a standard laptop computer in about fifteen minutes using inverse homogenization. It is found in Section 3 that the stress distribution inside the composite is well predicted by the asymptotic theory.

2. HOMOGENIZED DESIGN FORMULATION AND IDENTIFICATION OF OPTIMAL GRADED FIBER MICROGEOMETRIES

The inverse homogenization design method is a top down design approach. First a well posed homogenized design problem is developed. This design problem is given in terms of design variables that reflect the local microgeometry inside the composite. For the problem treated here the design variable for the homogenized design problem is given by the density function $\theta_f(\mathbf{x})$. The homogenized design problem is then solved to obtain an optimal density function. With the optimal density in hand we use it to recover an explicit graded fiber design that has structural properties close to that of the optimal homogenized design and satisfies prescribed point wise stress constraints. The homogenized design problem is described in the first subsection. The explicit link between homogenized designs and graded fiber reinforced designs that satisfy point wise stress constraints is provided in the second subsection.

2.1 Homogenized Design Problem

The design variable for the homogenized design problem is given by the density function $\theta_f(\mathbf{x})$. This function is interpreted as providing the local area fraction of the fiber phase in a homogenized design. The resource constraint on the fiber phase is given by

$$\int_{\Omega} \theta_f(\mathbf{x}) dx_1 dx_2 \leq \Theta \times (\text{Area of } \Omega), \quad (1)$$

where $0 < \Theta < 1$. At each point the local area fraction satisfies the box constraint given by

$$0 < \theta_f^{\min} \leq \theta_f \leq \theta_f^{\max} < 1. \quad (2)$$

Here the upper and lower bounds given in (2) correspond to the entire design domain being filled with composite material. In this treatment the local fiber

area fraction θ_f changes continuously with position according to the condition

$$|\theta_f(\mathbf{x}) - \theta_f(\mathbf{x} + \mathbf{h})| \leq K|\mathbf{h}|. \quad (3)$$

Here the constant K is prescribed by the designer. The universe of admissible designs given by all local area fractions θ_f satisfying the resource constraint, box constraints, and (3) is denoted by D_Θ .

The compliance in shear for the matrix and fiber are given by $S_m = (2G_m)^{-1}$ and $S_f = (2G_f)^{-1}$ respectively. Here the matrix is more compliant and $S_m > S_f$. For a given $\theta_f(\mathbf{x})$ we introduce the effective shear compliance $S^E(\theta_f(\mathbf{x}))$ associated with a locally periodic microgeometry made from fibers with circular cross sections centered inside square unit cells. The unit period cell for this configuration is denoted by Q . The area fraction of Q occupied by the fiber cross section is set to $\theta_f(\mathbf{x})$. The shear compliance inside Q is written $S(\theta_f(\mathbf{x}), \mathbf{y})$ and takes the value S_f for points \mathbf{y} in the fiber and S_m for \mathbf{y} in the matrix. The unit vectors $\mathbf{e}^1 = (1, 0)$ and $\mathbf{e}^2 = (0, 1)$ are introduced and for each \mathbf{x} in Ω we introduce the periodic fluctuating stress potentials $w^i(\mathbf{x}, \mathbf{y})$, $i = 1, 2$ that solve the microscopic equilibrium equation

$$-\text{div}_{\mathbf{y}} (S(\theta_f(\mathbf{x}), \mathbf{y})(\nabla_{\mathbf{y}}(w^i(\mathbf{x}, \mathbf{y})) + \mathbf{e}^i)) = 0, \mathbf{y} \text{ in } Q. \quad (4)$$

Here the \mathbf{x} coordinate appears a parameter and all differentiations are carried out with respect to the \mathbf{y} variable. The effective compliance tensor is a function of the local area fraction of fibers θ_f and from symmetry the effective compliance tensor is isotropic and given by

$$[S^E(\theta_f(\mathbf{x}))]_{ij} = s^E(\theta_f(\mathbf{x}))\delta_{ij}, \quad (5)$$

where the effective compliance is given by

$$s^E(\theta_f(\mathbf{x})) = \left(\int_Q S(\theta_f(\mathbf{x}), \mathbf{y})(\partial_{y_1} w^1(\mathbf{x}, \mathbf{y}) + \mathbf{e}_1^1) d\mathbf{y} \right). \quad (6)$$

The macroscopic stress potential ϕ^H vanishes on the boundary of the shaft cross section and satisfies

$$-\text{div} (S^E(\theta_f)\nabla\phi^H) = 1 \quad (7)$$

inside the cross section. The torsional rigidity for the homogenized shaft cross section made from a homogenized material with compliance $S^E(\theta_f)$ is given by

$$\mathcal{R}(\theta_f) = 2 \int_{\Omega} \phi^H dx_1 dx_2. \quad (8)$$

The macroscopic stress in the homogenized shaft is given by $\sigma^H = R\nabla\phi^H$ where R is the rotation matrix associated with a counter clock wise rotation of $\pi/2$ radians.

The multiscale stress criterion is given in terms of the macrostress modulation function introduced in [12]. The macrostress modulation function captures the interaction between the macroscopic stress $\sigma^H(\mathbf{x})$ and the microstructure. The microscopic response to the imposed macroscopic stress is given by $\sigma(\mathbf{x}, \mathbf{y}) = R[\sum_{i=1}^2 (\nabla_{\mathbf{y}}(w^i(\mathbf{x}, \mathbf{y})) + \mathbf{e}^i) \partial_{x_i} \phi^H(\mathbf{x})]$. The relevant interaction is described by the macrostress modulation function $f(\theta_f, \sigma^H)$ given by

$$f(\theta_f(\mathbf{x}), \sigma^H(\mathbf{x})) = \sup_{\mathbf{y} \text{ in } Q} \{|\sigma(\mathbf{x}, \mathbf{y})|\}. \tag{9}$$

Physically the macrostress modulation provides an upper envelope on the oscillating point wise local stress in the composite [12].

From the symmetry of the microstructure it easily follows that macrostress modulation for a locally periodic microgeometry made from fibers with circular cross sections centered inside square unit cells is of the form

$$f(\theta_f(\mathbf{x}), \sigma^H(\mathbf{x})) = f(\theta_f(\mathbf{x}), \nabla \phi^H(\mathbf{x})) = A(\theta_f(\mathbf{x})) |\nabla \phi^H(\mathbf{x})|, \tag{10}$$

where for $0 < \theta_f^{\min} \leq \theta_f \leq \theta_f^{\max} < 1$,

$$A(\theta_f) = \sup_{\mathbf{y} \text{ in } Q} \{|\nabla_{\mathbf{y}} w^1(\mathbf{x}, \mathbf{y})|\}. \tag{11}$$

We enforce the stress constraint by adding a penalty term to the torsional rigidity and the homogenized design problem is to minimize

$$L(\theta_f) = -\mathcal{R}(\theta_f) + l \int_{\Omega} (f(\theta_f, \nabla \phi^H))^p dx_1 dx_2, \tag{12}$$

over all θ_f in D_{Θ} where $l > 0$ and ϕ^H satisfies

$$-\text{div} (S^E(\theta_f) \nabla \phi^H) = 1 \tag{13}$$

and vanishes at the boundary. The computational examples are carried out for a domain with reentrant corners of interior angle $3\pi/2$. In view of the strength of the associated singularity at the reentrant corners the power “ p ” appearing in the penalty term is chosen to be less than 3. We mention in closing that the constraint (3) provides an upper bound on the spatial variation of the homogenized designs. This constraint provides the compactness necessary for a well posed design problem [10].

2.2 Identification of Graded Fiber Design from the Homogenized Design

In this subsection it is shown how the optimal design $\hat{\theta}_f$ for the homogenized problem is used to identify a graded fiber design satisfying the requirements (I)

and (II). The examples considered in this treatment are given for a structural domain specified by an “X” shaped cross section. All interior angles for the reentrant corners are fixed at $3\pi/2$ radians. The tip to tip length of each leg of the “X” shaped domain is 2cm. The width of each leg is $2/3$ cm. In order to describe the graded fiber composite, the shaft cross section Ω is partitioned into the N square subdomains \mathcal{S}^k , $k = 1, \dots, N$ and $\Omega = \cup_k^N \mathcal{S}^k$. The side length of these subdomains is given by $\varepsilon = 0.066$ cm.

Table 1. Torsional rigidities.

Design #	Fiber-Area	Torsional Rigidity
H1	40%	0.452
1	40%	0.441
H2	50%	0.486
2	50%	0.475

The building block for the microstructure is the square unit cell filled with a centered circular fiber cross section. The area fraction of the fiber phase inside the unit cell is given by θ_f . A microstructure is obtained by rescaling the unit cell by the factor $\varepsilon \times \nu$, $0 < \nu \leq 1$, so that it becomes the period cell for a $\varepsilon \times \nu$ periodic composite. A graded fiber composite is constructed by placing an $\varepsilon \times \nu$ periodic composite inside each square subdomain \mathcal{S}^k . The area fraction of fibers in each subdomain is given by the constant θ_f^k and these constants can change between subdomains. We note that choosing $\nu = 1$ corresponds to placing one fiber cross section inside \mathcal{S}^k . Smaller values of ν correspond to progressively finer periodic distributions of fiber cross sections inside \mathcal{S}^k . For future reference this type of locally periodic microstructure will be called a (ε, ν) -graded periodic fiber microstructure. Let $\sigma^{\varepsilon, \nu} = (\sigma_{13}^{\varepsilon, \nu}, \sigma_{23}^{\varepsilon, \nu})$ denote the in plane stress inside the shaft and denote the torsional rigidity of the cross section by $\mathcal{R}^{\varepsilon, \nu}$.

The relation between the optimal design for the homogenized problem and the pointwise in stress and torsional rigidity for the (ε, ν) -graded periodic fiber microstructure is given by the following theorem, see [10, 14].

Theorem 1 (Identification of graded microstructure). *Given the minimizing density $\hat{\theta}_f$ and associated stress potential $\hat{\sigma}^H$ for the homogenized problem we consider sets of the form*

$$A_T = \{\mathbf{x} \in \Omega : f(\hat{\theta}_f(\mathbf{x}), \hat{\sigma}^H(\mathbf{x})) \leq T\}. \tag{14}$$

For fixed choices of $\delta > 0$ and $t > T$ one can choose ε and ν small enough such that the (ε, ν) -graded periodic microstructure for which the the part of A_T over which the stress constraint

$$|\sigma^{\varepsilon, \nu}(\mathbf{x})| \leq t \tag{15}$$

is violated has measure (area) less than δ ,

$$|\mathcal{R}^{\varepsilon, \nu} - \mathcal{R}(\hat{\theta}_f)| < \delta, \tag{16}$$

and

$$\sum_{k=1}^{\hat{N}} |\mathcal{S}^k| \hat{\theta}_f^k \leq \Theta \times (\text{Area of } \Omega) + \delta. \tag{17}$$

For these designs the area fractions of the fibers inside each \mathcal{S}^k are denoted by $\hat{\theta}_f^k$ and are chosen according to

$$\hat{\theta}_f^k = \frac{1}{|\mathcal{S}^k|} \times \int_{\mathcal{S}^k} \hat{\theta}_f(\mathbf{x}) dx_1 dx_2. \tag{18}$$

The homogenized design formulation together with Theorem 1 comprise the inverse homogenization method for identifying microstructures that satisfy point wise stress constraints while delivering a torsional rigidity close to that given by the optimal design $\hat{\theta}_f$ for the homogenized design problem.

3. INVERSE HOMOGENIZATION AND GRADED FIBER DESIGNS FOR THE X-SHAPED CROSS SECTION

In this section we display the results of the numerical calculations. The calculations were carried out using the gradient minimization algorithm introduced in [14]. All calculations are done for the choice $p = 1$ in the Lagrangian (12). The shear stiffness of the matrix is assigned the value $G_m = 1$ GPa and the shear stiffness of the fiber phase is assigned the value $G_f = 2$ GPa. For all examples θ_f is constrained to lie between $0.2 \leq \theta_f \leq 0.7$.

The optimal homogenized designs corresponding to the area of fiber cross sections given by 40% and 50% are denoted as designs H1 and H2 respectively. Plots of the fiber density field $\hat{\theta}_f$ for these designs are given in Figures 1(a) and 3(a) for these designs. The contour plots of the macrostress modulation function $f(\hat{\theta}_f(\mathbf{x}), \hat{\sigma}^H(\mathbf{x}))$ for these designs are given in Figures 1(b) and 3(b).

The (ε, ν) -graded periodic microstructure is constructed from the optimal homogenized design according to the prescription of Theorem 1. All designs are carried out for the choice $\varepsilon = 0.066$ and $\nu = 1$. We compute the average of $\hat{\theta}_f(\mathbf{x})$ over each square \mathcal{S}^k according to (18) and denote it by $\hat{\theta}_f^k$. The area fraction of the fiber inside \mathcal{S}^k is set to $\hat{\theta}_f^k$. The first fiber design is carried out subject to the constraint that the total area of fiber cross sections is fixed at 40%. This design is referred to as design 1. Design 2 is carried out with the total area of fiber cross sections fixed at 50%. The fiber designs are displayed in Figures 2(a) and 4(a).

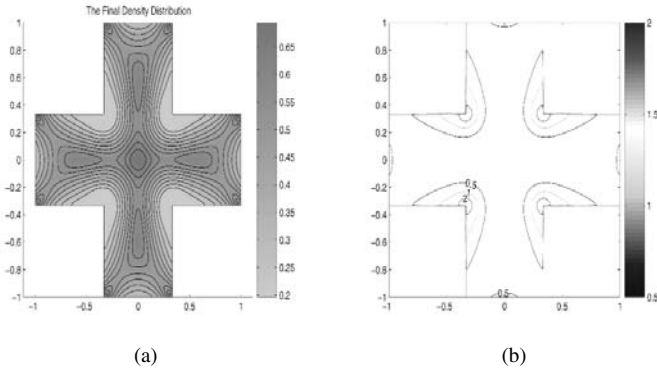


Figure 1. (a) $\hat{\theta}_f(\mathbf{x})$ for design H1. (b) Contour plot of $f(\hat{\theta}_f(\mathbf{x}), \sigma^H(\mathbf{x}))$.

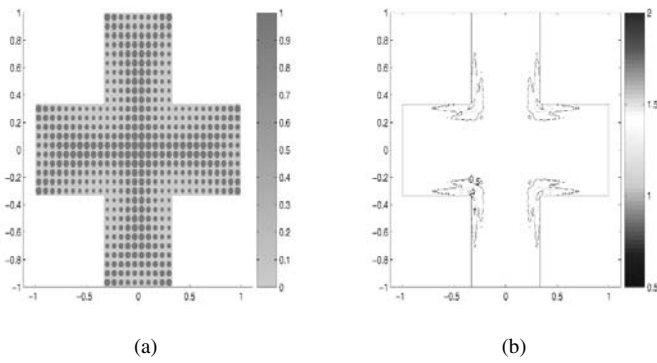


Figure 2. (a) Graded fiber design 1. (b) Contour plot of magnitude of in plane stress.

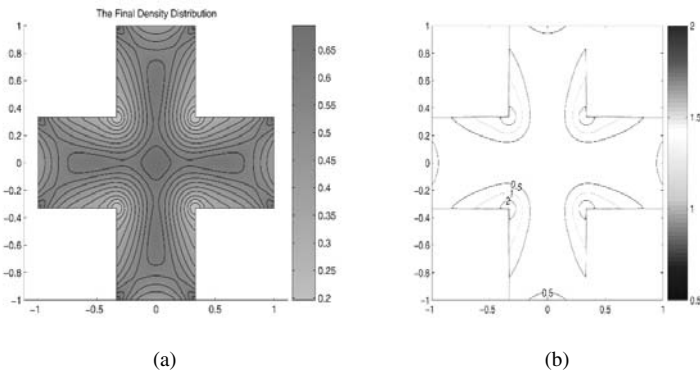


Figure 3. (a) $\hat{\theta}_f(\mathbf{x})$ for design H2. (b) Contour plot of $f(\hat{\theta}_f(\mathbf{x}), \sigma^H(\mathbf{x}))$.

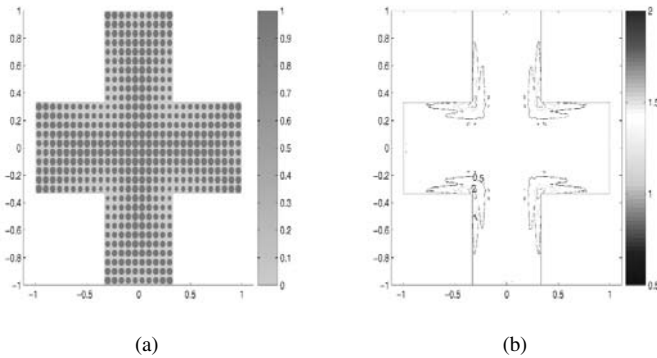


Figure 4. (a) Graded fiber design 2. (b) Contour plot of magnitude of in plane stress.

The level lines of the magnitude of the stress field for designs 1 and 2 are plotted in Figures 2(b) and 4(b). It follows from Figures 2(b) and 4(b) that the point wise stress behavior in designs 1 and 2 are well represented by the level curves of the macrostress modulation functions for the optimal homogenized designs H1 and H2 respectively. The values of the torsional rigidities for each design are listed in Table 1. The torsional rigidity of the homogenized designs and the actual designs compare well.

ACKNOWLEDGMENT

Research supported by NSF grant DMS-0406374 and by AFOSR grant FA9550-05-1-0008.

REFERENCES

- [1] Allaire, G., *Shape Optimization by the Homogenization Method*, Springer, New York (2002).
- [2] Allaire, G., Jouve, F. and Mallot, H., Topology optimization for minimum stress design with the homogenization method, *Struct. Multidisc. Optim.*, 28, 87–98 (2004).
- [3] Bendsoe, M.P. and Sigmund, O., *Topology Optimization, Theory, Methods and Applications*, Springer, Berlin (2003).
- [4] Cherkaev, A. and Kohn, R.V., *Topics in the Mathematical Modelling of Composite Materials, Progress in Nonlinear Differential Equations and their Applications*, Birkhauser, Boston, MA (1997).
- [5] Cherkaev, A., *Variational Methods for Structural Optimization*, Springer, New York (2000).
- [6] Duysinx, P. and Bendsoe, M.P., Topology optimization of continuum structures with local stress constraints, *Int. J. Num. Meths. Eng.*, 43, 1453–1478 (1998).

- [7] Kohn, R.V. and Strang, G., Optimal Design and Relaxation of Variational Problems, *Communications on Pure and Applied Mathematics*, 34, Part I: 113–137, Part II: 139–182, Part III: 357–377 (1986).
- [8] Lewinski, T. and Telega, J.J., *Plates, Laminates and Shells. Asymptotic Analysis and Homogenization*, World Scientific, Singapore (2000).
- [9] Lipton, R., Design of functionally graded composite structures in the presence of stress constraints, *International Journal of Solids and Structures*, 39, 2575–2586 (2002).
- [10] Lipton, R., Homogenization and design of functionally graded composites for stiffness and strength, in *Nonlinear Homogenization and its Application to Composites, Polycrystals, and Smart Materials*, P. Ponte Castaneda and J.J. Telega (eds), NATO Science series II Mathematics, Physics, and Chemistry, Vol. 170, Springer Verlag, Berlin, pp. 169–192 (2004).
- [11] Lipton, R., Stress constrained G closure and relaxation of structural design problems, *Quarterly of Applied Mathematics*, 62, 295–321 (2004).
- [12] Lipton, R., Assessment of the local stress state through macroscopic variables, *Phil. Trans. R. Soc. Lond. A.*, 361, 921–946 (2003).
- [13] Lipton, R., Homogenization theory and the assessment of extreme field values in composites with random microstructure, *SIAM J. on Appl. Math.*, 65, 475–493 (2004).
- [14] Lipton, R. and Stuebner, M., Optimal design of graded microstructure through inverse homogenization for control of pointwise stress, *Quarterly Journal of Mechanics and Applied Mathematics*, published electronically, November (2005).
- [15] Lurie, K., *Applied Optimal Control Theory of Distributed Systems*, Plenum Press, New York (1993).
- [16] Olhoff, N., On optimum design of structures and materials, *Meccanica*, 31, 143–161 (1996).
- [17] Tartar, L., *An Introduction to the Homogenization Method in Optimal Design*, Springer Lecture Notes in Mathematics, Vol. 1740, Springer, Berlin, pp. 45–156 (2000).

HIERARCHICAL OPTIMIZATION OF MATERIAL AND STRUCTURE FOR THERMAL TRANSIENT PROBLEMS

J.M. Guedes¹, E. Lubrano¹, H.C. Rodrigues¹ and S. Turteltaub²

¹*IDMEC, Instituto Superior Tecnico, Av. Rovisco Pais, 1049-001 Lisboa, Portugal*

²*Faculty of Aerospace Engineering, Delft University of Technology, Kluyverweg 1, 2629 HS Delft, The Netherlands*

{jmguedes, edmilsonl, hcr}@ist.utl.pt, s.r.turteltaub@lr.tudelft.nl

Abstract: This paper describes a multiscale computational algorithm to simultaneously optimize the macroscopic material distribution and the microscopic material layout of two-phase, non-homogeneous composite structures. The optimization of the composite material is performed within the context of transient thermal conduction problems. The objective is to identify the non-homogeneous composite that minimizes the difference, at a prescribed time T , between the actual values of the temperature field and a target temperature distribution. The methodology is illustrated with a relatively simple test problem that indicates that the procedure can successfully identify an optimal material layout at the micro- and macro-scales.

Keywords: Multiscale optimization, hierarchical method, transient optimization, adjoint method.

1. INTRODUCTION

Multiscale optimization techniques have been developed and applied for problems involving mechanical structures within the framework of time-independent (elastostatic) problems (see, e.g. Rodrigues *et al.*, 1999, 2002; Bendsoe and Sigmund, 2003). This formulation, frequently referred to as a hierarchical model, can be used in conjunction with a homogenization approach for a locally periodic composite whose characteristic cell is made of two base materials (materials 1 and 2). Accordingly, it is assumed that the problem has two length scales: A global (or macro-) scale, related to the material distribution of the composite within a structure Ω and a local (or micro-) scale, connected to the topology of the material unit cell Y_x in the neighborhood of a macroscopic point x . The macroscale distribution of the composite is characterized by the volume fraction ω of material 1 and the microscale topo-

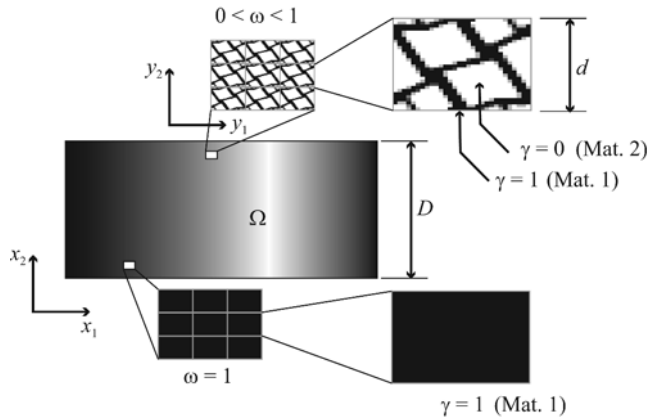


Figure 1. Macroscale region Ω and locally-periodic cell-level microstructures.

logy is described by a regularized characteristic function γ of material 1 that, alternatively, can be interpreted as a microscale volume fraction. The two-scale approach for a locally-periodic composite is shown schematically in Figure 1.

The homogenized (or “equivalent”) macroscopic properties of the periodic material are derived through modeling at the material characteristic cell level. Assuming that the values of ω and γ can be locally modified (and thus used as design variables), the hierarchical optimization method consists of identifying the spacial distribution of material that minimizes or maximizes a given objective functional.

Time-dependent objective functionals have been studied in the context of heat conduction, quasi-static thermomechanics and elasto-dynamics (see, e.g., Turteltaub, 2001, 2002a,b, 2005). In these references, however, only a simple rule of mixtures based on the Hashin–Shtrikman bounds was used to characterize the composite material. The present formulation is a combination of the hierarchical optimization approach and the optimization method for time-dependent objective functionals. For simplicity, only a transient heat conduction problem is treated, although the present formulation can be naturally extended to thermomechanical problems. The design objective considered here is to identify locally a non-homogeneous material and its distribution that minimizes the difference between the actual temperature distribution at a prescribed time T and a desired target distribution. We consider that the periodic composite is made out of two materials; one high-conducting (material 1) and the other low-conducting (material 2). The equivalent thermal properties are obtained through homogenization, thus connecting the two scales in the problem.

2. FORMULATION OF THE PROBLEM

2.1 Transient Heat Conduction Problem

The physical framework under consideration corresponds to a transient heat conduction problem. The heat flux \mathbf{q} is assumed to depend linearly on the temperature gradient (Fourier’s law), i.e., at a (macroscopic) point \mathbf{x} and at time t one has

$$\mathbf{q}(\mathbf{x}, t) = \mathbf{K}^H(\mathbf{x})\nabla_{\mathbf{x}}\theta(\mathbf{x}, t), \tag{1}$$

where \mathbf{K}^H is the homogenized conductivity tensor and $\nabla_{\mathbf{x}}$ is the gradient with respect to the macroscopic material point \mathbf{x} . Furthermore, assuming that the internal energy depends linearly on the temperature, then the balance of energy of a rigid material, in a region Ω and for a time interval $[0, T]$, can be expressed as

$$\operatorname{div}_{\mathbf{x}} \mathbf{q}(\mathbf{x}, t) = (\rho c)^H(\mathbf{x})\dot{\theta}(\mathbf{x}, t) \quad \text{in } \Omega \times (0, T], \tag{2}$$

where $(\rho c)^H$ is the homogenized heat capacity and ρ and c are the mass density and the specific heat per unit mass, respectively. A superimposed dot indicates a derivative with respect to time. We consider a transient heat conduction problem in $\Omega \times (0, T]$ where the fields satisfy (1) and (2) together with the following initial and boundary conditions:

$$\begin{cases} \theta(\mathbf{x}, t) = \hat{\theta}(\mathbf{x}, t) & \text{on } \partial\Omega_t \times (0, T], \\ \mathbf{q}(\mathbf{x}, t) \cdot \mathbf{n} = \hat{q}(\mathbf{x}, t) & \text{on } \partial\Omega_q \times (0, T], \\ \mathbf{q}(\mathbf{x}, t) \cdot \mathbf{n} = h(\theta^a(\mathbf{x}, t) - \theta(\mathbf{x}, t)) & \text{on } \partial\Omega_h \times (0, T], \\ \theta(\mathbf{x}, 0) = \hat{\theta}_0(\mathbf{x}) & \text{in } \Omega, \end{cases} \tag{3}$$

where $\hat{\theta}$ is a prescribed temperature on $\partial\Omega_t$, \hat{q} is a prescribed heat flux through $\partial\Omega_q$, natural or forced convection is prescribed on $\partial\Omega_h$ (where h is the film coefficient – assumed constant – and θ^a is the sink temperature) and $\hat{\theta}_0$ is the initial temperature field. The vector \mathbf{n} is the outward unit normal vector to the boundary $\partial\Omega = \Omega_t \cup \Omega_q \cup \Omega_h$.

2.2 Homogenized Properties

The material occupying the structural domain Ω is assumed to be a locally periodic composite, i.e. at each (macroscopic) point \mathbf{x} , the small-scale layout of the material is obtained by a periodic repetition of a characteristic cell $Y_{\mathbf{x}}$. This characteristic cell is assumed to be made of two isotropic linear conducting materials, one with a high conductivity and the other with a low conductivity. The high-conducting material has mass density ρ_1 , specific heat per unit mass c_1 and isotropic conductivity coefficient κ_1 . The respective properties for the low-conducting material are ρ_2 , c_2 and κ_2 .

It is further assumed that the relative dimensions of the structure and material cell introduces two scales: A macro scale, associated to a characteristic length D (e.g., of the order of a side length of a rectangular structure Ω), and a micro scale associated to a characteristic length d (e.g., of the order of the side length of a characteristic cell Y_x). As shown schematically in Figure 1, the characteristic ratio $\epsilon = d/D$ of each cell is assumed sufficiently small so that there is a clear separation of scales. Fluctuations in space at the macroscopic scale are measured as functions of \mathbf{x} whereas variations within a cell are measured as functions of a microscale variable $\mathbf{y} := \mathbf{x}/\epsilon$. In particular, inside each cell Y_x , the microstructure is described by a pseudo-characteristic function $\gamma(\mathbf{x}, \mathbf{y})$. The function γ can take values between 0 and 1, where 1 corresponds to material 1 (high conducting material) and 0 corresponds to material 2 (low conductivity). In Figure 1, regions occupied by the high- and low-conducting materials are graphically associated to black and white zones, respectively.

In accordance with the previous interpretation of the function γ , the conductivity \mathbf{K}^ϵ at a point \mathbf{y} inside a cell Y_x can be described as

$$\mathbf{K}^\epsilon(\mathbf{x}, \mathbf{y}) := (\gamma^p(\mathbf{x}, \mathbf{y})(\kappa_1 - \kappa_2) + \kappa_2) \mathbf{I}, \quad (4)$$

where \mathbf{I} is the identity tensor and the power p is interpreted in the sense of the SIMP method (see e.g. Rozvany, 1997; Bendsoe and Sigmund, 2003).

For a given microstructure characterized by $\gamma(\mathbf{x}, \mathbf{y})$ and following the regular perturbation method, the Cartesian components of the homogenized conductivity \mathbf{K}^H in a basis $\{\mathbf{e}_i\}_{i=1,2}$ are obtained as

$$K_{ij}^H(\mathbf{x}) = \frac{1}{|Y_x|} \int_{Y_x} \mathbf{K}^\epsilon(\mathbf{x}, \mathbf{y}) [\hat{\mathbf{e}}_i - \nabla_{\mathbf{y}}\phi^{(i)}(\mathbf{y})] \cdot [\hat{\mathbf{e}}_j - \nabla_{\mathbf{y}}\phi^{(j)}(\mathbf{y})] dv_{\mathbf{y}}, \quad (5)$$

where $|Y_x|$ is the volume of the unit microstructural cell in a neighborhood of the point \mathbf{x} . In (5), the vectors $\hat{\mathbf{e}}_i$ and $\hat{\mathbf{e}}_j$ can be interpreted as representing unit temperature gradients in the direction of the Cartesian vectors \mathbf{e}_i and \mathbf{e}_j , respectively (with units of temperature per length). Furthermore, the Y_x -periodic fields $\phi^{(i)}$ (with $i = 1, 2$ for two-dimensional problems) are solutions of the following ‘‘cell problems’’:

$$\operatorname{div}_{\mathbf{y}} \{(\gamma^p(\mathbf{x}, \mathbf{y})(\kappa_1 - \kappa_2) + \kappa_2) [\hat{\mathbf{e}}_i - \nabla_{\mathbf{y}}\phi^{(i)}(\mathbf{y})]\} = 0, \quad i = 1, 2. \quad (6)$$

The homogenized heat capacity $(\rho c)^H$ is computed as

$$(\rho c)^H(\mathbf{x}) = \frac{1}{|Y_x|} \int_{Y_x} [\gamma(\mathbf{x}, \mathbf{y})(\rho_1 c_1 - \rho_2 c_2) + \rho_2 c_2] dv_{\mathbf{y}}. \quad (7)$$

For the subsequent analysis, it is convenient to interpret the homogenized properties as functionals of γ (for a fixed point \mathbf{x}).

2.3 Optimal Design Problem

The objective functional in the present problem is a measure of the difference between the actual temperature field $\theta(\mathbf{x}, T)$ at a given time T and a target temperature field $\theta^{tg}(\mathbf{x})$, i.e.,

$$J[\theta, \gamma] := \frac{1}{2} \int_{\Omega} (\theta(\mathbf{x}, T) - \theta^{tg}(\mathbf{x}))^2 dv_x . \tag{8}$$

Define the design space \mathcal{A} as

$$\mathcal{A} = \left\{ \gamma \mid 0 \leq \gamma(\mathbf{x}, \mathbf{y}) \leq 1, \int_{\Omega} \left(\frac{1}{|Y_x|} \int_{Y_x} \gamma(\mathbf{x}, \mathbf{y}) dv_y \right) dv_x \leq \bar{V} \right\} , \tag{9}$$

where \bar{V} is a given upper bound on the global amount of material 1 used. The objective functional J given by (9) can be seen as a functional of γ since the temperature field θ satisfies problem (1)–(7) and is therefore an implicit function of the material properties. The optimization problem can be expressed as follows:

$$\begin{cases} \text{Given } \Omega, \hat{q}, \hat{\theta}_0, \hat{\theta}, h, \theta^a, \kappa_{1,2}, \rho_{1,2}, c_{1,2}, \theta^{tg}, T, \bar{V} \\ \text{Find } \gamma^* \in \mathcal{A} \text{ such that} \\ J[\theta^*, \gamma^*] \leq J[\theta, \gamma] \quad \forall \gamma \in \mathcal{A} , \end{cases} \tag{10}$$

where θ and θ^* are, respectively, the solutions to problem (1)–(7) for γ^* and γ .

2.4 Problem Separation: Multiscale Design

In the heat conduction problem, under the foregoing assumptions of separation of length scales, the macroscopic heat conduction problem is linked to the microstructure via the homogenized properties. Similarly, for the design problem, we will consider a separation between a macroscale design (structure) and a microscale design (material) following the approach presented by Rodrigues *et al.* (2002). Specifically, the macroscale design variable is taken as the volume fraction $\omega(\mathbf{x})$ of the high-conducting material in each periodic cell Y_x (in a neighborhood of a point \mathbf{x}), whereas the microscale design variable is taken as the regularized characteristic function $\gamma(\mathbf{x}, \mathbf{y})$ that describes the details of the microstructure in each cell. The link between these two design variables is

$$\omega(\mathbf{x}) = \frac{1}{|Y_x|} \int_{Y_x} \gamma(\mathbf{x}, \mathbf{y}) dv_y . \tag{11}$$

We now reformulate problem (10) as a multiscale design problem. We consider $\omega(\mathbf{x})$ and $\gamma(\mathbf{x}, \mathbf{y})$ as independent design variables and treat (11) as a constraint. To this end, define the design spaces \mathcal{A}_ω and \mathcal{A}_γ as

$$\mathcal{A}_\omega = \left\{ \omega \mid \int_{\Omega} \omega(\mathbf{x}) dv_x \leq \bar{V} \right\} \tag{12}$$

and

$$\mathcal{A}_\gamma = \{\gamma \mid 0 \leq \gamma(\mathbf{x}, \mathbf{y}) \leq 1\} . \tag{13}$$

Observe that, in view of the pointwise constraints on γ imposed in the definition of the set \mathcal{A}_γ in (13), then, fulfillment of the constraint (11) leads to $0 \leq \omega(\mathbf{x}) \leq 1$. The use of independent design variables ω and γ is analogous to the multiscale approach where \mathbf{x} and \mathbf{y} are treated as independent space variables that are connected through the relation $\mathbf{y} = \mathbf{x}/\epsilon$. From this point of view, macroscopic changes in material design are measured in terms of ω while microscopic changes are measured locally in terms of γ .

The objective functional J is now interpreted as an explicit and implicit function of the variables θ , ω and γ and we use a superimposed hat to emphasize this dependence. Consequently, the design problem (10) can be expressed alternatively as follows:

$$\left\{ \begin{array}{l} \text{Given } \Omega, \hat{q}, \hat{\theta}_0, \hat{\theta}, h, \theta^a, \kappa_{1,2}, \rho_{1,2}, c_{1,2}, \theta^{lg}, T, \bar{V} \\ \text{Find } \{\omega^*, \gamma^*\} \in \mathcal{A}_\omega \times \mathcal{A}_\gamma \text{ such that} \\ \hat{J}[\theta^*, \omega^*, \gamma^*] \leq \hat{J}[\theta, \omega, \gamma] \quad \forall \{\omega^*, \gamma^*\} \in \mathcal{A}_\omega \times \mathcal{A}_\gamma , \\ \omega(\mathbf{x}) = \frac{1}{|Y_{\mathbf{x}}|} \int_{Y_{\mathbf{x}}} \gamma(\mathbf{x}, \mathbf{y}) dv_{\mathbf{y}} , \end{array} \right. \tag{14}$$

where θ^* and θ are the solutions to problem (1)–(7) for $\{\omega^*, \gamma^*\}$ and $\{\omega, \gamma\}$, respectively.

2.5 Necessary Conditions

In order to obtain the necessary conditions satisfied by the constrained optimization problem (14), one can introduce an augmented Lagrangian functional L that includes the objective functional \hat{J} as well as the constraints imposed by the heat conduction problem (1)–(7) and the design constraints (11)–(13). The constraints can be included in the Lagrangian L via a lagrange multiplier field $\lambda(\mathbf{x})$ associated to the constraint (11), a scalar multiplier Λ connected to the global constraint in the definition of the set \mathcal{A}_ω in (12) and an adjoint temperature field $\bar{\theta}(\mathbf{x}, t)$ related to problem (1)–(7). The pointwise constraints in the definition of the set \mathcal{A}_γ in (13) can be treated separately and will not be included in the Lagrangian L . For brevity, the explicit form of L is not shown.

The optimal solution is denoted as $\{\theta^*, \omega^*, \gamma^*\}$. A variation of L with respect to γ implies that $\delta_\gamma L \geq 0$ for all $\delta\gamma = \gamma - \gamma^*$, hence

$$\int_\Omega \frac{1}{|Y_{\mathbf{x}}|} \int_{Y_{\mathbf{x}}} \left[\lambda - p\gamma^{p-1}(\kappa_1 - \kappa_2) \left(\delta_{im} - \frac{\partial \phi^{(i)}}{\partial y_m} \right) \left(\delta_{jm} - \frac{\partial \phi^{(j)}}{\partial y_m} \right) \right. \\ \left. \times \int_0^T \left(\frac{\partial \theta^*}{\partial x_i} \frac{\partial \bar{\theta}}{\partial x_j} \right) dt - (\rho_1 c_1 - \rho_2 c_2) \int_0^T \dot{\theta}^* \bar{\theta} dt \right] \delta\gamma dv_{\mathbf{y}} dv_{\mathbf{x}} \geq 0 , \tag{15}$$

where the inequality is valid $\forall \delta \gamma(\mathbf{x}, \mathbf{y})$ and $\forall (\mathbf{x}, \mathbf{y}) \in \Omega \times Y_{\mathbf{x}}$. Stationarity with respect to the macroscale design variable ω (i.e., $\delta_{\omega} L = 0$) implies that

$$\lambda(\mathbf{x}) = \Lambda, \quad \forall \mathbf{x} \in \Omega. \tag{16}$$

Stationarity with respect to the temperature field θ is equivalent to the (strong) formulation of the following adjoint problem (see, e.g., Turteltaub, 2002a):

$$\left\{ \begin{array}{ll} \operatorname{div}_{\mathbf{x}} (\mathbf{K}^H \nabla_{\mathbf{x}} \bar{\theta}(\mathbf{x}, t)) + (\rho c)^H(\mathbf{x}) \dot{\bar{\theta}}(\mathbf{x}, t) = 0 & \text{in } \Omega \times (T, 0] \\ \bar{\theta}(\mathbf{x}, t) = 0 & \text{on } \partial\Omega_t \times (T, 0], \\ \mathbf{K}^H \nabla_{\mathbf{x}} \bar{\theta}(\mathbf{x}, t) \cdot \mathbf{n} = 0 & \text{on } \partial\Omega_q \times (T, 0], \\ \mathbf{K}^H \nabla_{\mathbf{x}} \bar{\theta}(\mathbf{x}, t) \cdot \mathbf{n} = -h \bar{\theta}(\mathbf{x}, t) & \text{on } \partial\Omega_h \times (T, 0], \\ (\rho c)^H(\mathbf{x}) \bar{\theta}(\mathbf{x}, T) = \theta^*(\mathbf{x}, T) - \theta^{tg}(\mathbf{x}) & \text{in } \Omega. \end{array} \right. \tag{17}$$

Observe that the adjoint problem is solved from $t = T$ to $t = 0$, hence the last condition in (17) – related to the “error” between actual and target values at time T – is treated as an initial condition.

3. NUMERICAL IMPLEMENTATION

The numerical procedure implemented to solve the necessary conditions and obtain the optimal solution, closely follows the algorithm presented in Rodrigues *et al.* (2002). It requires two finite element models: A macroscale (global) and a microscale (local) model. The macroscale model approximates the global domain Ω and interpolates the functions depending on $\mathbf{x} \in \Omega$. The microscale model approximates the local domain $Y_{\mathbf{x}}$ and interpolates the functional dependencies on $\mathbf{y} \in Y_{\mathbf{x}}$. Macro- and microscale finite elements are denoted as Ω^E and Y^e , respectively, with $E = 1, \dots, N$ and $e = 1, \dots, n$. The local and global temperature fields are approximated using 4-noded isoparametric elements and the design variables ω and γ are interpolated as constants in the respective macro- and micro-elements. Although the size of the computational problem is relatively large, the uncoupling between the micro- and macroscopic problems achieved through the multiscale-hierarchical design formulation greatly facilitates the computational work. The numerical implementation assumes that all points \mathbf{x} within the same global finite element have equal microstructure, hence the number of local problems is equal to the number of finite elements in the global mesh. Furthermore, all these local problems are independent of each other and can be solved simultaneously, e.g., using parallel processing methodologies.

For the design problem, it is assumed that we are given the geometry of the domain Ω and the boundaries $\partial\Omega_t$, $\partial\Omega_q$ and $\partial\Omega_h$, initial and boundary conditions $\hat{\theta}_0$, $\hat{\theta}$, \hat{q} and θ^a , film coefficient h , material data $\kappa_{1,2}$, $\rho_{1,2}$, $c_{1,2}$ and design input data T , θ^{tg} and \bar{V} . Further, it is assumed that suitable macro- and

micro-mesh have been constructed with elements Ω^E and Y^e . The basic steps of the procedure are as follows:

- 1) Assume initial values for ω and γ ; solve the cell problems (6) within each element Ω^E and use (5) and (7) to compute \mathbf{K}^H and $(\rho c)^H$.
- 2) Solve sequentially the heat conduction problem (1)–(3) and the adjoint problem (17) to compute θ and $\hat{\theta}$.
- 3) For each element Ω^E in the global mesh, update the micro design variable γ that satisfies the necessary condition (15).
- 4) Calculate a new ω for each element using (11) and determine the new values for the homogenized properties \mathbf{K}^H and $(\rho c)^H$ by solving the cell problems (6) within each element Ω^E .
- 5) Check whether the variables ω and \mathbf{K}^H have converged. If convergence has been achieved, accept the solution. Otherwise, compute a new multiplier Λ and repeat the procedure from step 2).

4. NUMERICAL EXAMPLE

To illustrate the use of the hierarchical optimization method applied within the context of a transient problem, we consider an example similar to the one presented by Turteltaub (2001). The structural domain Ω is defined as a 3×2 rectangular domain. The boundary and initial conditions are given as follows: the initial temperature field is uniform $\hat{\theta}_0(\mathbf{x}) = 100$, the flux is constant along the boundary $\partial\Omega_q = \partial\Omega$ and set to $\hat{q} = -10$ and the design time is $T = 10$, where the definition of non-dimensional quantities can be found in Turteltaub (2001). Concerning the materials, the properties used are the following: For material 1, $\kappa_1 = 1$ and $(\rho_1 c_1) = 10$, and for material 2, $\kappa_2 = 10^{-3}$ and $(\rho_2 c_2) = 1$. The volume upper bound is set equal to 60% and the initial design is uniform with ω set to 0.6. The macroscale finite element model has a mesh with 30×20 four-noded isoparametric elements and the microscale one has a 35×30 mesh. The target temperature is chosen such that it is preferable to concentrate the high-conducting material towards the periphery of the domain (see Turteltaub, 2001).

Figure 2 shows the distribution of material as well as the material cell geometry at selected locations (macro elements). Note that the unit cell Y_x is always kept aligned with the global Cartesian basis, hence a rotation of material axes should be achieved through the lay-out of the microstructure.

The target temperature and the actual temperature field for the optimal material layout $\{\omega^*, \gamma^*\}$ are presented in Figure 3. The corresponding error (i.e., the pointwise difference between the actual and target temperatures) is shown in Figure 4. In this particular example, comparing the temperature scale in

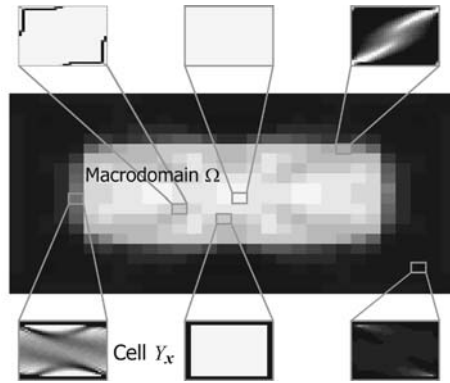


Figure 2. Optimal material layout in the structure Ω . The insets correspond to the detailed microstructure in a characteristic cell Y_x at selected points.

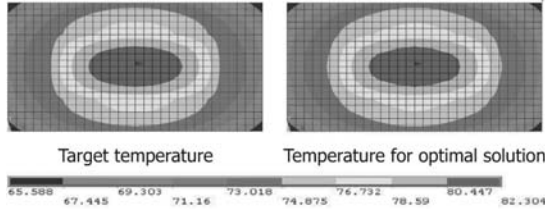


Figure 3. Target temperature (left) and actual temperature (right) at time T for the optimal material layout.

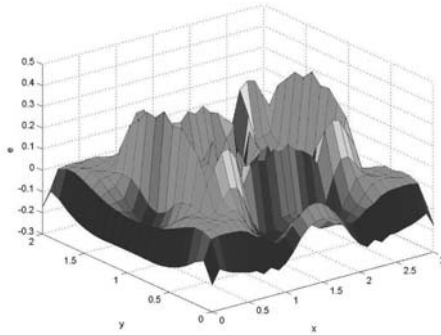


Figure 4. Pointwise difference between the target temperature and the actual temperature for the optimal material layout.

Figure 3 with the scale in Figure 4, it is clear that the difference between the target temperature and the actual temperature is quite small, which indicates that the procedure can indeed find an optimal solution.

5. CLOSING REMARKS

A computational model was presented for the optimization of materials and structure within the context of transient heat transfer problems. The proposed approach is based on the hierarchical model presented in Rodrigues *et al.* (2002) for elasto-static applications and extends previous models for transient problems using simpler material models (see, e.g., Turteltaub, 2001, 2002a).

The hierarchical model, which uncouples the problem into local and global sub-problems, has several advantages: (i) uncoupling the problem permits the hierarchical solution model where the sensitivities (gradient information) required by the global optimization problem are obtained during the solution of the local problem and at no extra cost; (ii) formulating and solving separately the material optimization problem will allow for the introduction of material specific design constraints, namely the ones due to technological limitations and (iii) the structure of the local problem (material optimization) is ideally suited to take advantage of parallel processing techniques.

ACKNOWLEDGMENTS

The support of projects FCT/POCTI/1999/EME/35983 (JMG, HCR, EL) and NATO-RTA P129 (JMG, HCR, ST) is gratefully acknowledged.

REFERENCES

- Bendsoe, M.P. and Sigmund, O. (2003) *Topology Optimization: Theory, Methods and Applications*, Springer, Berlin.
- Rodrigues, H., Jacobs, C., Guedes, J.M. and Bendsoe, M.P. (1999) Global and local optimization models applied to anisotropic bone adaptation, in *Synthesis in Bio Solid Mechanics*, M.P. Bendsoe and P. Pedersen (eds.), Kluwer Academic Publishers, Dordrecht, pp. 213–224.
- Rodrigues, H., Guedes, J.M. and Bendsoe, M.P. (2002) Hierarchical optimization of material and structure, *Struc. Mult. Opt.*, **24**(1), 1–10.
- Rozvany, G. I. N. (1997) *Topology Optimization in Structural Mechanics*, CISM Courses and Lectures, 374, Springer-Verlag, Vienna.
- Turteltaub, S. (2001) Optimal material properties for transient problems, *Struc. Mult. Opt.*, **22**(2), 157–166.
- Turteltaub, S. (2002a) Functionally graded materials for prescribed field evolution, *Comp. Meth. App. Mech. Eng.*, **191**(21–22), 2283–2296.
- Turteltaub, S. (2002b) Optimal control and optimization of functionally graded materials for thermomechanical processes, *Int. J. Sol. Struct.*, **39**(12), 3175–3197.
- Turteltaub, S. (2005) Optimal non-homogeneous composites for dynamic loading, *Struc. Mult. Opt.*, **30**(2), 101–112.

OPTIMIZATION OF FOAM FILLED STRUCTURES USING GRADIENT ALGORITHMS

A. Lipka and E. Ramm

Institute of Structural Mechanics, University of Stuttgart, Germany

lipka@statik.uni-stuttgart.de, eramm@statik.uni-stuttgart.de

Abstract: This paper proposes a method to improve the application of cellular materials in structural elements. The distribution of the density of different foams is being controlled by material topology optimization method. Due to the very special properties of cellular materials and resulting applications this concept is applied in order to determine the density distribution of polymeric and metal foam as core material in sandwich structures and in thin-walled hollow sections. The first objective that is being investigated is the optimization of the overall buckling behavior. In contrast to the well-known maximization of stiffness leading to lightweight structures under static loading, the second objective is the maximization of the structural energy absorption with respect to quasi-static loading. Due to the large number of design variables in material based topology optimization, mathematical programming (MP) methods combined with variational adjoint methods to determine the sensitivities turn out to be efficient and robust.

Keywords: cellular materials, density distribution, gradient based topology optimization.

1. INTRODUCTION

Cellular solids are commonly used in a variety of practical applications. The mechanical, thermal and acoustic properties provide opportunities for diverse structural implementations: For example, the high specific stiffness of sandwich structures is utilized in light weight structures, the high property of absorbing energy suggests the implementation of cellular solids in impact absorbers. The improvement of the production methods allows reproduceable pore geometry as well as the adaption of pore size distribution to the boundary conditions for example layers of polymeric foams with different density (stiffness) in a sandwich panel. Since the mechanical behavior of metallic porous materials is decisively influenced by the density and the shape and size of pores (Ashby and Gibson, 1988; Jemiole and Turteltaub, 2000), diverse

micro- and macroscopic material models have been developed to display the correlation of the density and the mechanical properties. Up to now only in a few investigations optimization algorithms are used to improve the mechanical behavior of metal foam structures, for example using genetic algorithms or algorithms that have originally been developed for the simulation of remodelling of living bone to adapt the density distribution for the achievement of highest possible stiffness. Topology optimization of two-dimensional structures was very much influenced by the fundamental paper of Bendsoe and Kikuchi in 1988 and has been an active area of research since then. In order to generate realistic designs by structural optimization the nonlinear structural response, e.g. buckling or plasticity, has to be considered (Buhl et al., 2000; Kemmler et al., 2005; Schwarz and Ramm, 2001; Schwarz et al., 2001). Porous materials are usually utilized in topology optimization in order to relax the integer “1-0” (black and white) problem, allowing to identify zones with and without design material. For this process materials with a micro-structure are introduced like the micro-cell approach, with a rectangular hole and homogenized to a macroscopic material law. In the present contribution the concept is not used as a mathematical vehicle; rather we assume the existence of a “real” physically existing material with a varying intermediate density (grey zones); in other words the porosity is being introduced as a design variable which is then being adjusted by the controlling optimization process. In this respect we like to refer to “natural” material like the spongiosa in bones and tissues with a varying density. Phenomenological material models are used in order to determine the density distribution of polymeric and metal foams as well as light weight concrete as core material in sandwich structures and in thin-walled hollow sections.

2. MATERIAL BASED TOPOLOGY OPTIMIZATION

Material Models in Topology Optimization. For material based topology optimization different porous material models were developed. They can be divided into two different groups. One group relaxes the 1-0 (“black and white”) optimization problem in an exact way. The rank-n laminates are well known representatives of those optimal materials. The other group, the suboptimal materials, e.g. used in the SIMP (Solid Isotropic Microstructure with Penalty for intermediate density) approach do not relax the optimization problem exactly, but have the advantage that the solution renders a nearly “black and white” design pattern. The SIMP approach is based on a relation between density and the Young’s modulus and is very similar to the mechanical behavior of metal foams characterized by the Young’s modulus E_{eff}

$$E_{\text{eff}} = \left(\frac{\rho}{\rho_0} \right)^\beta E_0 \quad \text{with} \quad \beta \geq 2, \quad (1)$$

with the density ρ_0 and the Young's modulus E_0 of the bulk material. β is a penalization parameter driving the solution more into the "black and white" situation. A SIMP-like method was considered in a pioneering paper by Bendsøe (1989) for the first time. For large-scale topology optimization SIMP was developed by Rozvany and Zhou (1991), the term "SIMP" has been introduced since 1992 (e.g. Rozvany et al., 1992) and is applied today in several industrial and research codes. A detailed discussion of various porous materials used in topology optimization is given e.g. in Maute (1998) or Eschenauer and Olhoff (2001). They basically differ in the dependency of the material stiffness on the relative density.

2.1 Modelling of Cellular Solids

Gibson/Ashby Model – Small Strain. Ashby et al. (2000) analyze the behavior of cellular solids with single cell models on a micro level. The macroscopic force-deformation relation is associated with the deformation of the cell ribs and their elastic and elastoplastic buckling. Ashby and Gibson (1988) developed relations between the density and the parameters of various cellular solids based on the geometrical parameters (cell ribs and faces). For Young's modulus E of a closed cell metal foam, Ashby et al. (2000) derive the following relation to the density ρ :

$$E = \alpha E_s \left[0.5 \left(\frac{\rho}{\rho_s} \right)^2 + 0.3 \left(\frac{\rho}{\rho_s} \right) \right] \quad (2)$$

with the density ρ_s and Young's modulus E_s of the bulk material. The parameter α is chosen in the following range:

$$0.5 \leq \alpha \leq 1. \quad (3)$$

Without loss of generality, the parameter was chosen 0.8 in the investigated examples. For open cell porous foams the following relation is given:

$$E = (0.1 \div 4.0) E_s \left(\frac{\rho}{\rho_s} \right)^2. \quad (4)$$

For the elastic material behavior, Poisson's ratio ν is chosen in the limits as given in Equation (5).

$$\nu = 0.32 \div 0.34. \quad (5)$$

Young's modulus of metal foams scales with the factor $(\rho/\rho_s)^2$. For closed cell porous foams a further linear term is added (Equation (2)). This connection between density and stiffness is very similar to the equations describing the porous material of the SIMP-approach used in topology optimization. For the determination of an optimized density distribution under elastic material

behavior, the correlations for the porous material of the SIMP-approach have been replaced in this study by Equations (2) and (4) and the explicit derivatives of the material tensor have been identified.

Hyperelastic Ogden Like Model – Finite Strain. The correlation between density and material parameters, which is described by Gibson and Ashby, was verified in the related literature and the corresponding parameters for the particular material were identified. It has to be annotated though that the developed material models are mainly based on one-dimensional investigations. The objective of the work of Jemiolo and Turteltaub (2000) is the extension to the general three-dimensional case with emphasis on compressible behavior with large deformations. They introduce a free energy function based on the established hyperelastic material models of Ogden:

$$W(\lambda_1, \lambda_2, \lambda_3, \rho) = \sum_{i=1}^N (2m_i (\lambda_1^{\alpha_i} + \lambda_2^{\alpha_i} + \lambda_3^{\alpha_i} - 3)) + \sum_{i=1}^N (n_i ((\lambda_1\lambda_2)^{\beta_i} + (\lambda_2\lambda_3)^{\beta_i} + (\lambda_3\lambda_1)^{\beta_i} - 3) + p_i (J^{-\gamma_i} - 1)). \quad (6)$$

The postulated strain energy is a function of the principal stretches λ and describes their changes from the reference to the current configuration. $N \leq 1$ is an integer which determines the number of terms in the strain energy function and is chosen depending on the required accuracy of the model. $J = \lambda_1\lambda_2\lambda_3$ denotes the volume ratio. The parameter p_i is controlling the compression behavior

$$p_i = \frac{2(m_i\alpha_i + n_i\beta_i)}{\gamma_i}. \quad (7)$$

For the special case $N=1$ the functions m_i and n_i are determined as follows:

$$m = \frac{1}{6\alpha} \left(\frac{2(2\beta + 3\gamma)K_2 - \beta K_1}{\alpha\beta - \gamma(\beta - 2\alpha)} \right), \quad (8)$$

$$n = \frac{1}{3\beta} \left(\frac{\alpha K_1 - (\alpha + 3\gamma)K_2}{\alpha\beta - \gamma(\beta - 2\alpha)} \right). \quad (9)$$

For the correlation between the parameters $m, n, \alpha, \beta, \gamma$, the so-called Kelvin-Modules K_1, K_2 and the relative density $\bar{\rho}$, related functions have to be assumed.

$$K_1(\bar{\rho}) = 3E_s\bar{\rho}^2, K_2(\bar{\rho}) = \frac{3}{4}E_s\bar{\rho}^2, \alpha(\bar{\rho}), \beta(\bar{\rho}), \gamma(\bar{\rho}). \quad (10)$$

E_s describes the Young’s Modulus of the corresponding bulk-material. The non-linear material behavior is described by the parameters $\alpha_i, \beta_i, \gamma_i$. For PE-foam the authors in Jemiolo and Turteltaub (2000) choose a parabolic function,

for PU-foam linear correlations are assumed. The procedure to determine the linear relation for the PE-foam and the quadratic for the PU-foam is specified in detail in Jemiolo and Turteltabu (2000). The relations were not modified for the implementation of topology optimization problems. The stresses and material parameters that are necessary for the implementation are computed by the common gradients of the indicated potential with respect to the stretches:

$$\boldsymbol{\tau}_A = \lambda_A \frac{\delta W}{\delta \lambda_A}, \quad \mathbf{C}_{AB}^\tau = \lambda_A \frac{\delta}{\delta \lambda_A} \left(\lambda_B \frac{\delta W}{\delta \lambda_B} \right), \quad (11)$$

where $\boldsymbol{\tau}_A$ describes the Kirchhoff-stresses and \mathbf{C}_{AB}^τ denotes the corresponding material matrix in principal directions. For further derivations and implementations in the form of a Total-Lagrangian formulation it is referred to the literature on FE-analysis.

3. DESIGN CRITERIA

Material topology optimization problems are characterized by a large number of optimization variables and a few constraints; in this study only one constraint exists. Therefore, the sensitivities are efficiently determined by adjoint methods. The following objectives have been investigated:

Stiffness-Nonlinear Kinematics. The classical objective to get stiff structures is to minimize the strain energy with respect to a certain load level

$$f = \sum_{i=1}^{n_{ele}} \frac{1}{2} \int_{\Omega} \mathbf{E}^T \mathbf{C} \mathbf{E} |J| d\Omega. \quad (12)$$

Here the Green–Lagrange-strains \mathbf{E} are used to take the nonlinear kinematics into account.

Displacement Level for a Prescribed Load – “End-Compliance”. Minimizing the displacements for a certain load level leads to minimization of the “end-compliance” defined by:

$$f_{EC} = \bar{\lambda} \mathbf{P}^T \bar{\mathbf{u}}, \quad (13)$$

where $\bar{\mathbf{u}}$ denotes the displacements related to the prescribed load-level.

Load Level for Prescribed Displacements. The following objective can be used to adjust a load-displacement curve when a displacement controlled algorithm is utilized:

$$f_{\bar{\lambda}} = \bar{\lambda}. \quad (14)$$

Maximization of Critical Load. Assuming linear pre-buckling behavior and deformations in the pre-buckling area are not taken into account, the critical load is approximated by a linear eigenvalue analysis:

$$(\mathbf{K}_e + \lambda_i \mathbf{K}_g) \Phi_i = 0. \tag{15}$$

\mathbf{K}_e describes the linear elastic stiffness matrix and Φ_i denotes the eigenmodes corresponding to the eigenvalues λ_i . The geometric stiffness matrix $\mathbf{K}_g(\bar{\mathbf{u}})$ is determined after the displacement field $\bar{\mathbf{u}}$ is determined through a linear analysis

$$\mathbf{K}_e \bar{\mathbf{u}} = \mathbf{P}. \tag{16}$$

3.1 Examples

In the present study where metal- and polymeric foams have been investigated, the Gibson and Ashby model was implemented for small strains. Large strain analyses are based on the hyperelastic material model of Jemiolo and Turteltaub. In the first example the influence of the density distribution on the global stability behavior of a beam with a hollow rectangular cross section is investigated. The hollow section was made of aluminum with an aluminum foam core. As displayed in Figure 1, the left edge of the section is clamped. Horizontal supports are assumed in the middle of the beam. On the right side the structure is vertically supported. The load with is applied on the face sheets on the right hand side. The face sheets and the foam core are discretized with 2560 quadratic hexahedral elements. The first two critical loads and their cor-

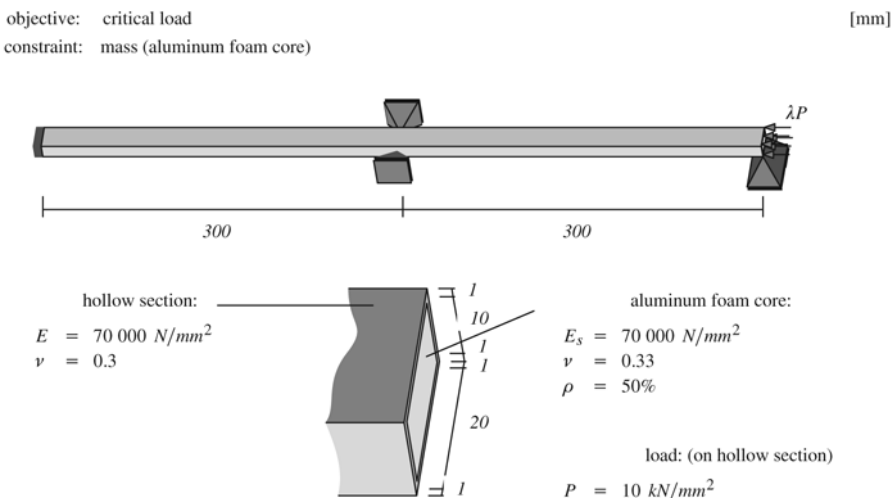


Figure 1. Eigenmode and eigenvalues, initial configuration.

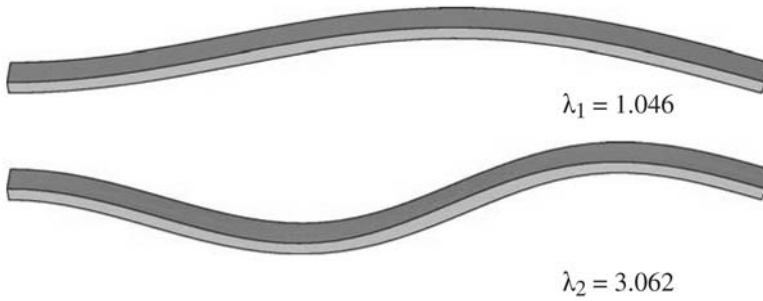


Figure 2. Eigenmode and eigenvalues, initial configuration.



Figure 3. Eigenmode and eigenvalues, initial configuration.

responding eigenmodes (Figure 2) are determined by an eigenvalue analysis for a homogeneous metal foam filling and a relative density of 50% of the bulk material. At the beginning of the optimization process the space within the hollow section consists of equally distributed mass of a closed cell porous aluminum foam. The material parameters are given in Figure 1.

As expected, a concentration of the metal foam with higher density and stiffness occurs within the design space around the clamped support and in the range of the maximum deflection of the eigenmode (Figure 3). The optimized density distribution is basically used for the reinforcement of the hollow section with respect to buckling rather than for the load carrying procedure. A comparison of the lowest critical load of the initial system with a homogeneous density distribution shows an increase of about 40% of the critical load. An interchange of the eigenvalues could not be observed. Furthermore only single eigenvalues do exist due to the horizontal support in the middle, the structure is not symmetric. The objective in the following example is to fit the nonlinear structural response of a polymeric foam cube to a prescribed characteristic.

Figure 4 shows the cube with a load applied on the top. The steel plate and the design space of the foam cube, were discretized with 890 quadratic hexahedral elements. Because of symmetry, the computation was carried out for one quarter of the symmetric system. The optimization of the density distribution of the polymeric foam core leads to quite different results depending on the objective. On the one hand the minimization of the strain energy was investigated, on the other hand the objective was the so called “end-compliance”.

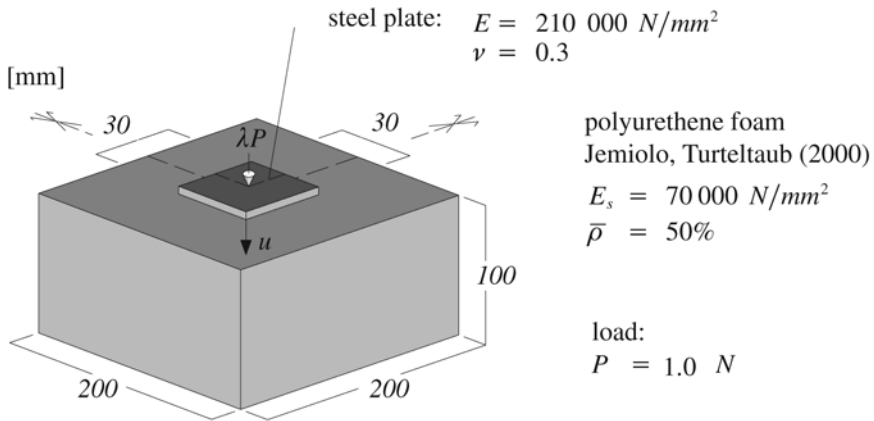


Figure 4. PE-foam specimen: geometry, material data and load.

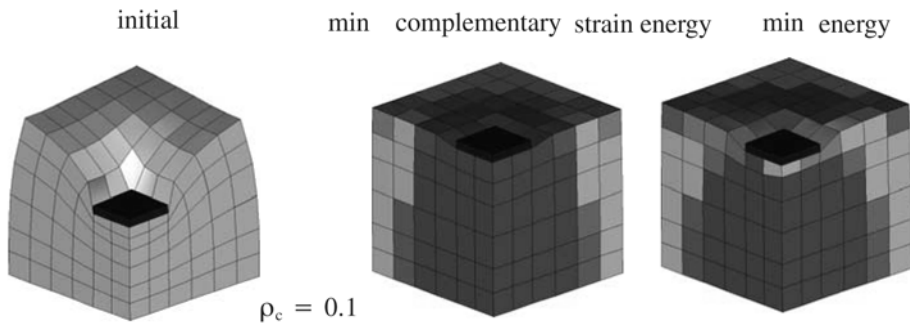


Figure 5. Deformation with homogeneous density distribution and optimization results.

The optimization leads to density distributions displayed in Figure 5 and the corresponding load-displacement-curve in Figure 6.

As expected, the displacement for the prescribed load level decreases remarkably. Apart from that a softer increase of the gradient of the load-displacement-curve for the objective “minimization of the strain energy” can be observed, which is caused by the area of higher porosity directly below the load plate.

The displacement controlled structural analyses show distinctly different load-displacement characteristics. The objectives “strain energy” and “end-compliance” can only be interpreted when the whole load-displacement-path is known. Under very small load and therefore in the range of linear behavior the same density distributions are achieved, as expected. With an increase of the load level and correspondingly growing nonlinearity, completely different load-displacement curves for the optimized density distributions were achieved. The design criterion “end-compliance” leads to structures of very

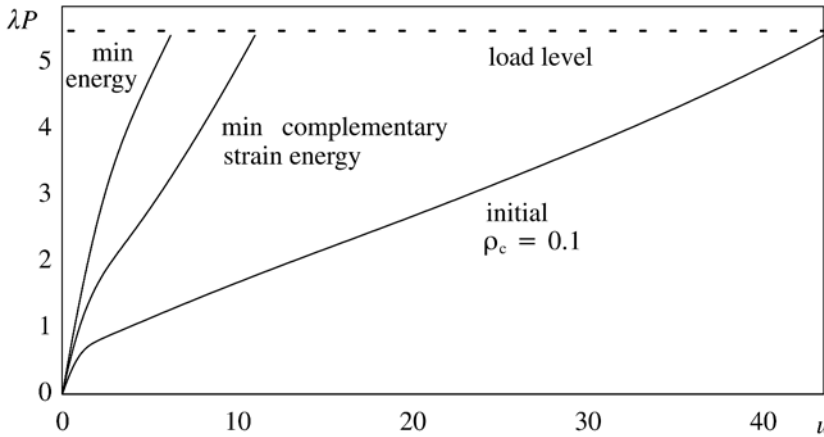


Figure 6. Load-displacement diagrams with homogenous and optimized foam core.

high stiffness in the beginning which soften under an increasing deformation. The objective “minimal strain energy” is an integral statement, where no direct correlation between the stiffness and a certain load level exists. To get better control on the overall structural response another objective was investigated. The objective is to fit the load-displacement curve to prescribed points. The required density distribution is determined by the optimization process. The starting system is again the cube with a homogeneous porosity as displayed in Figure 4. The optimization problem is formulated as a “least-square” problem for n points on the desired load-displacement curve:

$$\min f = \min \sum_{i=1}^n w_i ((\lambda_i P_i)^* - \lambda_i P_i). \tag{17}$$

$\lambda_i P_i$ defines the computed load levels for a certain density distribution. The points on the desired curve are described by $(\lambda_i P_i)^*$. w_i is a weighting factor to control the optimization process. In Figure 6 the load-displacement curve of the structural response of the initial configuration with a homogeneous density distribution is shown in black. In addition two points A and B on the desired load-displacement curve are defined. The gray curve shows the result of the optimization process.

The achieved load-displacement curve does not exactly coincide with the two points but is relatively close. The results can be improved by increasing the solution space with a finer discretization on the one hand and an increase of the number of prescribed points on the desired load-displacement curve on the other hand. To get a softer structural response another two points C/D were selected as objectives (see Figure 8). They are located below the initial curve; the resulting load-displacement-curve of the optimized density for this

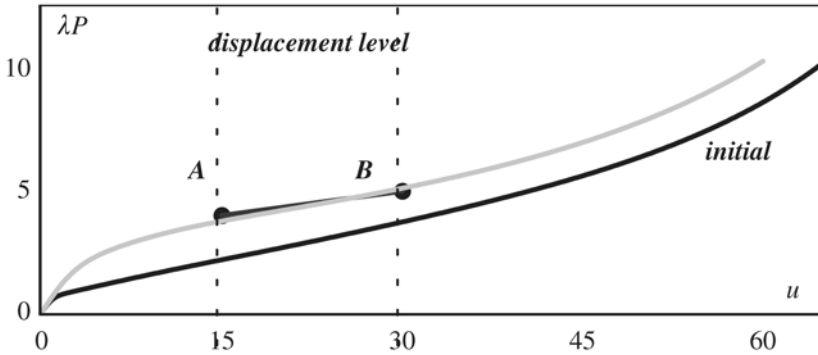


Figure 7. Load-displacement diagrams with homogenous and optimized foam core.

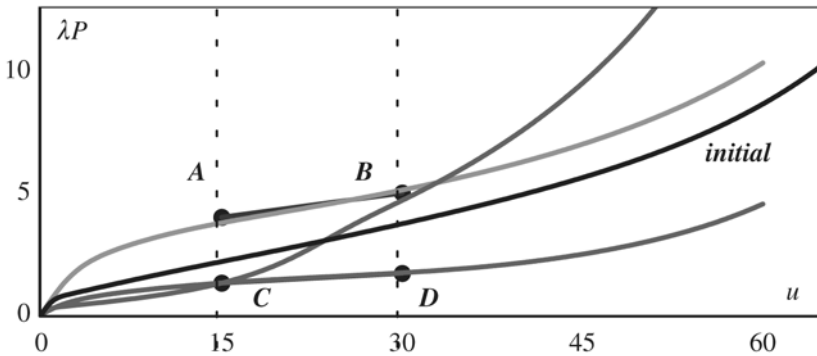


Figure 8. Load-displacement diagrams with homogenous and optimized foam core.

alternative design fits the prescribed values again very well. To get an idea of the potential of this method the third curve displayed in Figure 8 with target points C/B shows a soft impact in the beginning and high energy absorption at the end of the loading process.

The results point out how the density distribution and therefore the structural response can be controlled in a way that allows the realization of structures with completely different structural behavior. For example an optimal crash mat for sports activities such as high jumping is as light as possible and its behavior under deformation is characterized by a soft impact at the beginning and a maximum absorption of energy at the end of its loading to provide maximum landing protection.

4. CONCLUSION

It is shown in the present contribution that the methods originally developed and applied for topology optimization problems are suitable to determine the density distribution of foam structures according to the loading requirements. The relation describing the dependence of the material parameters on the density is used to determine the derivatives with respect to the optimization variables, i.e. the sensitivities. The optimization variables can be the densities of each finite element as well as the density of layers within sandwich panels as a whole. The large optimization problems including nonlinear structural behavior were solved with variational adjoint methods to determine the sensitivities and an optimality criteria method has been proven to be efficient and robust. With this concept it is possible to optimize very different structures such as sandwich panels and arbitrary three-dimensional structures. To show the potential of the method, further interesting optimization problems are discussed during the presentation.

ACKNOWLEDGEMENT

This work is part of the research projects of the German Research Foundation (DFG) under contract No. Ra 218/19. The support is gratefully acknowledged.

REFERENCES

- Ahmer Wadee, M. (1999) Experimental evaluation of interactive buckle localization in compression sandwich panels, *J. Sandwich Structures & Materials*, 1(3), 230–254.
- Ashby, M., Evans, T., Fleck, N.A., Gibson, L.J., Hutchinson, J.W. and Wadley, H.N.G. (2000) *Metal Foams: A Design Guide*, Butterworth Heinemann, Boston, MA.
- Ashby, M.F. and Gibson, L.J. (1988) *Cellular Solids – Structure and Properties*, Pergamon Press, Oxford.
- Bendsøe, M.P. (1989), Optimal shape design as a material distribution problem, *Struct. Optim.*, 1, 193–202.
- Bendsøe, M.P. and Kikuchi, N. (1988) Generating optimal topologies in structural design using a homogenization method, *Comp. Meth. Appl. Mech. Eng.*, 71, 197–224.
- Buhl T., Pedersen, C.B.W. and Sigmund, O. (2000) Stiffness design of geometrically non-linear structures using topology optimization, *Struct. Optim.*, 19, 93–104.
- Eschenauer, H.A. and Olhoff, N. (2001) Topology optimization of continuum structures: A review, *Appl. Mech. Rev.*, 54(4), 331–390.
- Jemiolo, S. and Turteltaub, S. (2000) A parametric model for a class of foam-like isotropic hyperelastic materials, *J. Appl. Mech.*, 67, 248–254.
- Kemmler, R., Lipka, A. and Ramm, E. (2005) Large deformations and stability in structural optimization, *Struct. Multidisc. Optim.*, accepted for publication.
- Maute, K. (1998) Topologie- und Formoptimierung von duennwandigen Tragwerken, PhD Thesis Bericht Nr. 25, Institut für Baustatik, Universität Stuttgart, Germany.
- Rozvany, G.I.N. and Zhou, M. (1991) Applications of the COC algorithm in layout optimization, in *Engineering Optimization in Design Processes*, Proc. Int. Conf., Karlsruhe, Ger-

- many, September 1990, H. Eschenauer, C. Mattheck and N. Olhoff (eds), Springer-Verlag, Berlin, pp. 59–70.
- Rozvany, G.I.N., Zhou, M. and Birker, T. (1992) Generalized shape optimization without homogenization, *Struct. Optim.*, 4, 250–254.
- Schwarz, S. and Ramm, E. (2001) Sensitivity analysis and optimization for nonlinear structural response, *Eng. Comp.*, 18, 610–641.
- Schwarz, S., Maute, K. and Ramm, E. (2001) Topology and shape optimization for elastoplastic structural response, *Comp. Meth. Appl. Mech. Eng.*, 190, 2135–2155.

Fluids and Materials

THE DARCY–STOKES TOPOLOGY OPTIMIZATION PROBLEM

Niclas Wiker, Anders Klarbring and Thomas Borrvall

Division of Mechanics, Department of Mechanical Engineering, Linköping University, SE-581 83 Linköping, Sweden

nicwi@ikp.liu.se, andkl@ikp.liu.se, thomas.borrvall@erab.se

Abstract: This paper treats the optimal layout of mixtures of regions of Stokes viscosity dominated flow and regions of Darcy porous flow. The problem of minimizing the potential of the state problem, representing essentially dissipation, is formulated, and can be shown to have a solution under appropriate filtering of the design. It can also be shown that the unfiltered design has a zero–one property. An area-to-point flow problem is solved for various filter radii.

Keywords: Topology optimization, Stokes flow, Darcy flow, area-to-point flow.

1. INTRODUCTION

Topology optimization (TO) in fluids was initiated by Borrvall and Petersson a few years ago. Their first work in this area concerned optimal regions of Stokes flow (Borrvall and Petersson, 2003) and they also soon realized that their earlier work on TO of linear elastic solids could be mimicked when dealing with porous media (Borrvall and Petersson, 2002). Such media can be modelled by the Darcy flow equation and the TO problem posed was to find the topology of a mix of two materials with different permeability. This problem was inspired by the speculative monograph of Bejan (2000) who claims that geometric form in flow systems, both natural and engineering, can be seen as consequences of optimization principles and he points at lungs, arterial systems, river drainage basins, cooling of electronics and even traffic flow as examples of such systems.

In this work we take the standpoint that several of the systems indicated by Bejan are better modelled as consisting of one region of free flow, or channels, and one region of porous flow, instead as consisting of regions of different porous flows. We let the free flow region be described by Stokes equation, and the porous flow by the Darcy equation. That is, we would like to use TO to find

the optimal layout of Stokes and Darcy regions. This problem can be treated by a generalization of Stokes equations, that is similar to the Brinkman system used in Borrvall and Petersson (2003). However, in this paper both the inverse permeability α and the viscosity μ will depend on the design.

Evgrafov (2005a) extended the work of Borrvall and Petersson to the “pure” black and white TO problem. Extensions to the Navier–Stokes’ equation is reported in Gersborg-Hansen et al. (2005) and Evgrafov (2005b).

2. STATE PROBLEM

The flow takes place on a two- or three-dimensional domain Ω . The boundary of this domain, $\partial\Omega$, is divided into two parts, Γ_u and Γ_t . On Γ_u the flow velocity \mathbf{u}_Γ is prescribed, and on Γ_t the surface traction \mathbf{t}_Γ is prescribed. The state problem consist in finding the velocity \mathbf{u} and the pressure p such that the following equations are satisfied:

$$\begin{aligned} \alpha \mathbf{u} - 2 \operatorname{div} (\mu \mathbf{D}(\mathbf{u})) + \nabla p &= \mathbf{g} & \text{in } \Omega \\ \operatorname{div} \mathbf{u} &= s & \text{in } \Omega \\ \mathbf{u} &= \mathbf{u}_\Gamma & \text{on } \Gamma_u \\ -p \mathbf{n} + 2\mu \mathbf{D}(\mathbf{u}) \mathbf{n} &= \mathbf{t}_\Gamma & \text{on } \Gamma_t. \end{aligned} \tag{1}$$

Here, \mathbf{g} is a given force, s is a given volume source term and $\mathbf{D}(\mathbf{u}) = \frac{1}{2}(\nabla \mathbf{u} + \nabla \mathbf{u}^T)$ is the rate-of-deformation tensor. The parameters α and μ are an inverse permeability and a viscosity, respectively. When μ equals zero and α is strictly positive, \mathbf{u} can be eliminated from the first two equations of (1), resulting in a Poisson equation modelling porous flow. On the other hand, if α equals zero, μ is strictly positive and constant, and s is constant, then the system essentially becomes Stokes equations of viscosity dominated flow. Thus, the possibility of formulating a topology optimization problem which, on the basis of (1), at each point of Ω , chooses between Darcy and Stokes flow, is obvious. Note that when μ is constant and s is zero, (1) is known as Brinkman’s problem.

A velocity field \mathbf{u} that is a solution of (1) in the standard weak sense is also a solution of the minimization problem

$$\min_{\mathbf{u} \in \mathcal{U}_{\operatorname{div}}} \mathcal{J}_\eta(\mathbf{u}), \tag{2}$$

where the total potential power functional is

$$\mathcal{J}_\eta(\mathbf{u}) = \frac{1}{2} a_\eta^D(\mathbf{u}, \mathbf{u}) + \frac{1}{2} a_\eta^S(\mathbf{u}, \mathbf{u}) - \langle \mathbf{f}, \mathbf{u} \rangle,$$

and the set of admissible velocities is

$$\mathcal{U}_{\operatorname{div}} = \{ \mathbf{u} \in \mathbf{H}^1(\Omega) : \mathbf{u} = \mathbf{u}_\Gamma \text{ on } \Gamma_u \text{ and } \operatorname{div} \mathbf{u} = s \text{ in } \Omega \}.$$

The total potential power functional is made up from the following functionals:

$$a_\eta^D(\mathbf{u}, \mathbf{v}) = \int_\Omega \alpha \mathbf{u} \cdot \mathbf{v} \, d\Omega, \quad a_\eta^S(\mathbf{u}, \mathbf{v}) = 2 \int_\Omega \mu \mathbf{D}(\mathbf{u}) : \mathbf{D}(\mathbf{v}) \, d\Omega,$$

$$\langle \mathbf{f}, \mathbf{v} \rangle = \int_\Omega \mathbf{g} \cdot \mathbf{v} \, d\Omega + \int_{\Gamma_t} \mathbf{t}_\Gamma \cdot \mathbf{v} \, d\Gamma,$$

The reason for using the subscript η in the two bilinear forms a_η^D and a_η^S is that these will in the next section depend on the design.

3. OPTIMIZATION PROBLEM

In the optimization process, we control the shift between the two types of flows, Stokes and Darcy, by introducing a design variable field η . This field belongs to $L^\infty(\Omega)$, takes values in the interval $[0, 1]$, and $\alpha = \alpha(\eta)$ and $\mu = \mu(\eta)$ are continuous functions. To obtain a cost function we substitute these functions into $\mathcal{J}_\eta(\mathbf{u})$ and define

$$\phi(\eta) = \min_{\mathbf{u} \in \mathcal{U}_{\text{div}}} \mathcal{J}_\eta(\mathbf{u}) = \mathcal{J}_\eta(\mathbf{u}^*),$$

where \mathbf{u}^* is the solution of (2). As indicated in Borrvall and Petersson (2003), with this definition of cost function, we get an optimization problem which will minimize the dissipated power in the system and maximize the flow velocities at the applied volume forces inside the domain, and at the tractions on the boundary. When $s \neq 0$ an alternative interpretation is also that we want to minimize the pressure at the location of the volume source. This choice of cost function will also make the sensitivity analysis particularly easy.

As is well known, topology optimization problems are usually not well-posed unless a regularization of the design variable is introduced. Yet, the problem of Borrvall and Petersson (2003) is an exception: since it can be proven that the objective function is lower semi-continuous in the correct topology, existence of solutions holds and no regularization is needed. However, when extending the problem formulation of Borrvall and Petersson by letting the viscosity term μ depend on the design variable, this property seems to be lost and a regularization needs to be introduced. To that end we let the design variable be filtered: the design η is calculated from an unfiltered design ξ by the convolution

$$\eta(\mathbf{y}) = \int_{\Omega_\xi} \xi(\mathbf{x}) \psi(\mathbf{y}, \mathbf{x}) \, d\mathbf{x} = S(\xi)(\mathbf{y}), \quad \mathbf{y} \in \Omega,$$

where we have used $S(\xi) : L^\infty(\Omega_\xi) \rightarrow L^\infty(\Omega)$ to denote the convolution functional. The integral kernel ψ is zero for $|\mathbf{x} - \mathbf{y}| > R$, where R is the filter radius, and Ω_ξ is an extension of Ω by a set of width R .

Including the regularization, our optimization problem is stated in the the variable ξ and becomes

$$\min_{\xi \in \mathcal{H}_\xi} \phi(S(\xi)), \quad (3)$$

where

$$\mathcal{H}_\xi = \{\xi \in L^\infty(\Omega_\xi) : 0 \leq \xi \leq 1 \text{ in } \Omega_\xi, \int_{\Omega} S(\xi) d\Omega \leq \gamma|\Omega|\}.$$

It can be proved that if $\mu(\eta) > 0$ for $\eta \in [0, 1]$, then there exists a solution of (3). In this respect we may note the difference from the corresponding result in Borrvall and Petersson (2003): in that paper μ was constant, $\alpha = \alpha(\eta)$ was required to be convex and no regularization was needed; in this paper both μ and α depend on the design and these dependencies are continuous but not necessarily convex.

To be more specific about how α and μ depend on η , we point at a result showing that linear functions produce zero–one designs. To that end, note that problem (3) is equivalent to an optimization problem where both the design variable ξ and the state variable \mathbf{u} are treated as optimization variables, i.e., to the problem

$$\min_{(\xi, \mathbf{u}) \in \mathcal{H}_\xi \times \mathcal{U}_{\text{div}}} \mathcal{J}(\mathbf{u}, S(\xi)). \quad (4)$$

If a pair (ξ, \mathbf{u}) solves (4), then ξ solves (3) and, conversely, if ξ solves (3), then there is a \mathbf{u} such that the pair solves (4). Let \mathbf{u}^* be a partial solution of (4). Then a solution ξ^* of (3) or, equivalently, the other part of a solution of (4), can be characterized as the solution of

$$\min_{\xi \in \mathcal{H}_\xi} \mathcal{J}(\mathbf{u}^*, S(\xi)). \quad (5)$$

This fact follows since a solution $\hat{\xi}$ of (5) satisfies $\mathcal{J}(\mathbf{u}^*, S(\hat{\xi})) \leq \mathcal{J}(\mathbf{u}^*, S(\xi))$ for all $\xi \in \mathcal{H}_\xi$, and a solution (ξ^*, \mathbf{u}^*) of (4) satisfies $\mathcal{J}(\mathbf{u}^*, S(\xi^*)) \leq \mathcal{J}(\mathbf{u}, S(\xi))$ for all $(\xi, \mathbf{u}) \in \mathcal{H}_\xi \times \mathcal{U}_{\text{div}}$. Thus,

$$\mathcal{J}(\mathbf{u}^*, S(\hat{\xi})) \leq \mathcal{J}(\mathbf{u}^*, S(\xi^*)) \leq \mathcal{J}(\mathbf{u}, S(\xi))$$

for all $(\xi, \mathbf{u}) \in \mathcal{H}_\xi \times \mathcal{U}_{\text{div}}$. Note that this reasoning is strictly related to the min-min character of (4). In, for instance, stiffness optimization of elastic structures, where there is a min-max saddle point structure, a similar property is not true.

It is straightforward to prove that if $\alpha = \alpha(\eta)$ and $\mu = \mu(\eta)$ are *linear functions*, then (5) has (essentially) a zero–one solution, i.e., ξ takes only the values zero and one. Thus, our problem has a discrete strictly topological character even though it is stated as a continuous problem.

For the numerical solution it was argued in Borrvall and Petersson (2003) that a linear function $\alpha(\eta)$ may impose a severe penalization of the design, resulting in a high risk of ending up in local minima. Therefore, a strictly convex function, where the degree of penalization is controlled by a parameter q , was used. We follow this strategy also in the following, but for $\mu(\eta)$ we take a linear function. Thus, the following explicit forms of functions are used:

$$\alpha(\eta) = \bar{\alpha} + (\underline{\alpha} - \bar{\alpha})\eta \frac{1 + q}{\eta + q}, \quad \mu(\eta) = \underline{\mu} + (\bar{\mu} - \underline{\mu})\eta,$$

where $\bar{\alpha}$ and $\bar{\mu}$ are the physical parameters for Darcy and Stokes flow, respectively, and $\underline{\alpha} = 0$ while $\underline{\mu} = \varepsilon > 0$ for a small ε . A strictly positive lower bound on μ is required for the proof of existence of a solution as well as for finite element convergence.

4. NUMERICAL SOLUTIONS

As a demonstration of the proposed design method, we have studied a type of area-to-point flow problem discussed in Bejan (2000). A similar problem was also treated in Borrvall et al. (2002) and Borrvall and Petersson (2002), but in those works the goal was to find optimal regions of Darcy flow with different permeability.

Consider the square shaped domain with side length L , shown in Figure 1. Most of the boundary has a non-slip condition, i.e. $\mathbf{u}_\Gamma = \mathbf{0}$, and on the remaining part a traction condition has been prescribed. For simplicity this has been set to zero as well, i.e. $\mathbf{t}_\Gamma = \mathbf{0}$. In every point inside the domain, fluid is added (like rain falling down on a bed of sand, $s \neq 0$), and the goal is to transport this fluid out from the domain through the point-like boundary part Γ_t , with length $|\Gamma_t| = 0.1L$.

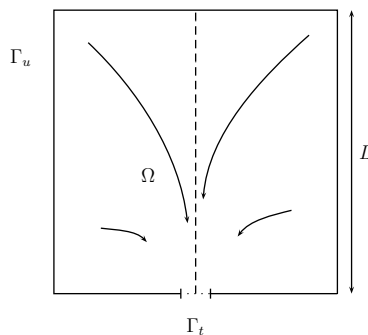


Figure 1. The design domain for the area-to-point flow problem. The dashed line in the middle indicates the line of symmetry used in most of the computations.

With one exception (right picture in Figure 2, below) symmetry was utilized when solving the problems, in order to reduce the computational load. The discretization was made with a finite element grid of 54×108 velocity elements and 27×54 pressure elements, see Borrvall and Petersson (2003) for details. For the implementation, the in-house C++ class library *TO++* written by Borrvall was used. This library contains, among other things, a direct solution method for solving the state problem, and MMA (see Svanberg, 1987) for the optimization problem.

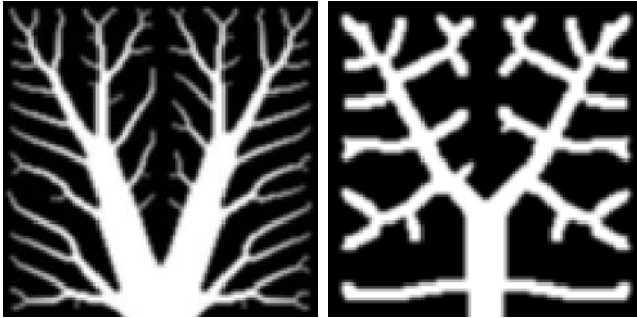


Figure 2. Optimal regions with different permeability of Darcy flow (left) and regions of Stokes (white) and Darcy (black) types of flow (right). Prescribed volume fraction was $\gamma = 0.3$ in both cases. Note the non-symmetric solution due to not using symmetry conditions during the computations.

In order to avoid local optimal solutions as much as possible, it is suggested in Bendsoe and Sigmund (2003) and Borrvall and Petersson (2003) that the computations should be carried out using an iterative procedure, where the penalty parameter q is altered successively. This involves solving the problem in several steps, where one uses a low value on q in the first step in order to make the problem more convex. As an initial guess on the design variable, η is in this step set to a constant value γ , where γ is the prescribed volume fraction of Stokes flow. In the next step, the obtained design solution is used as an initial guess when re-solving the problem with a new, increased value on q . Here, we have adopted this strategy and used three steps with q set to 0.00001, 0.01 and 10.0, respectively.

We have studied the influence of the filter radius R . The remaining parameters, the inverse permeability $\bar{\alpha}$, the viscosity $\bar{\mu}$, and the volume source term s , have been held constant. Regarding specific values, $\bar{\alpha}$ and $\bar{\mu}$ have been chosen such that we may interpret the solution as representing water that slowly trickles through a domain of clean sand, creating channels of Stokes flow. In numbers this means $\bar{\alpha} = 10.4 \cdot 10^6$ and $\bar{\mu} = 10.40 \cdot 10^{-6}$. For s we simply take $s = 1$. The value of the filter radius has been set relative to the

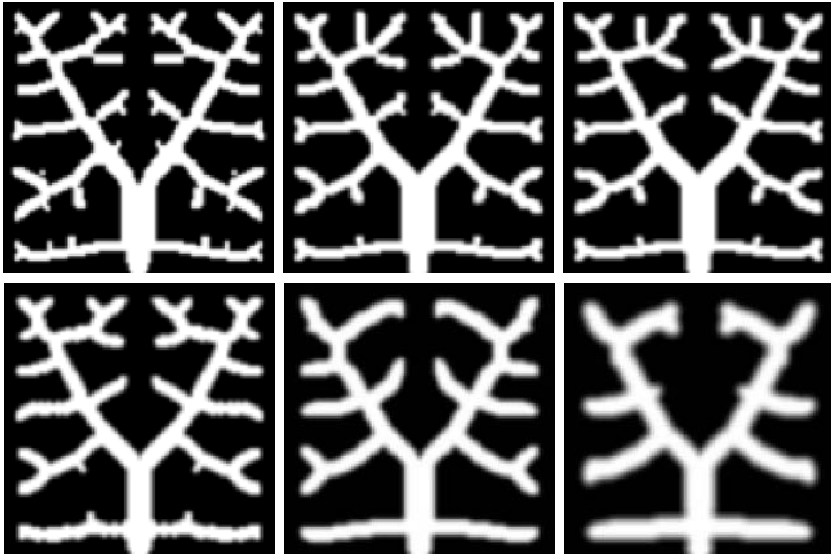


Figure 3. The result of increasing the filter radius. Starting from the top left corner, $R = 1.5, 1.7, 1.9, 2.1, 2.5, 3.5 \times [\text{e.s.l.}]$.

size of the velocity elements, e.g., $R = 2 \times [\text{e.s.l.}]$, where e.s.l. means elements side length.

As a first result, we have made a comparison between a pure Darcy problem with two materials with different permeability (see Borrvall et al., 2002, for a description of that problem) and the Stokes vs. Darcy problem treated in this paper. The results are seen in Figure 2, where we note the significant difference in the character of the two solutions. Also, bearing in mind that the computations have been carried out without using symmetry conditions on neither of the problems, a solution does not necessarily have to be symmetric. However, looking at the value of the objective function for the Stokes vs. Darcy problem, it indicates a local optimum since a better value is obtained using symmetry for the same set of parameters.

For the next example, the effect of changing the filter radius R was studied for fixed $\gamma = 0.3$. Looking at the sequence of pictures in Figure 3 the effect of R on the size of the smallest channels is quite clear: when R increases the smallest channels increases in size, and due to constraint on allowed amount of Stokes flow in the system, the channels decrease in number. Also, the boundary between Stokes and Darcy flow becomes more blurry with increasing filter radius. This is due to the smoothing effect of the filter operator.

In all figures shown so far, the filtered design has been plotted. In Figure 4, however, the unfiltered design variable is shown together with the filtered one,

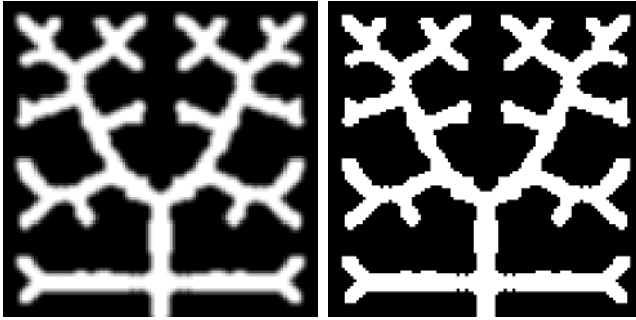


Figure 4. The filtered (left) and unfiltered (right) design variable for filter radius $R = 2.1 \times$ [e.s.l.].

and as is to be expected, the unfiltered design is practically purely black-and-white.

REFERENCES

- Bejan, A. (2000) *Shape and Structure, from Engineering to Nature*, Cambridge University Press, Cambridge, UK.
- Bendsøe, M.P. and Sigmund, O. (2003) *Topology Optimization: Theory, Methods and Applications*, Springer-Verlag, Berlin, Germany.
- Borrvall, T. and Petersson, J. (2002) Topology optimization in fluid mechanics, in *The Frithiof Niordson Volume, Proceedings from DCAMM International Symposium on Challenges in Applied Mechanics*, P. Pedersen and N. Olhoff (eds), The Danish Center for Applied Mathematics and Mechanics, Lyngby, Denmark, pp. 207–216.
- Borrvall, T., Klarbring, A., Petersson, J., Torstenfelt, B. and Karlsson, M. (2002) Topology optimization in fluid mechanics, in *Proceedings of the Fifth World Congress on Computational Mechanics (WCCM V)*, H.A. Mang, F.G. Rammerstorfer and J. Eberhardsteiner (eds), Vienna University of Technology, Vienna, Austria, <http://wccm.tuivien.asd.at>
- Borrvall, T. and Petersson, J. (2003) Topology optimization of fluids in Stokes flow, *International Journal for Numerical Methods in Fluids*, 41, 77–107.
- Evgrafov, A. (2005a) The limits of porous materials in the topology optimization of Stokes flow, *Applied Mathematics and Optimization*, in press.
- Evgrafov, A. (2005b) Topology optimization of slightly compressible fluids, *ZAMM*, in press.
- Gersborg-Hansen, A., Sigmund, O. and Haber, R.B. (2005) Topology optimization of channel flow problems, *Structural and Multidisciplinary Optimization*, 30, 181–192.
- Svanberg, K.A. (1987) The method of moving asymptotes – A new method for structural optimization, *International Journal for Numerical Methods in Engineering*, 24, 359–373.

TOPOLOGY OPTIMIZATION OF FLUID PROBLEMS BY THE LATTICE BOLTZMANN METHOD

Anton Eygrafov, Georg Pingen and Kurt Maute
*Center for Aerospace Structures, Department of Aerospace Engineering Sciences,
University of Colorado, Boulder, CO 80309-0429, U.S.A.*
{antone,pingen,maute}@colorado.edu

Abstract: We consider the optimal design of flow domains for Navier–Stokes. The problem is solved by a topology optimization approach varying the effective porosity of a fictitious material. The boundaries of the flow domain are represented by potentially discontinuous material distributions. Navier–Stokes flows are traditionally approximated by finite element and finite volume methods. These schemes, however, are particularly sensitive to the discretization of the flow along the boundaries, leading to significant robustness issues in the case of non-smooth boundary representations. Therefore, we study the potential of the lattice Boltzmann method for approximating low Mach-number incompressible viscous flows for topology optimization. In the lattice Boltzmann method the geometry of flow domains is defined in a discontinuous manner, similar to the approach used in material based topology optimization. In addition, this non-traditional discretization method features parallel scalability and allows for high-resolution fluid meshes. In this paper, we show how the variation of the porosity can be used in conjunction with the lattice Boltzmann method for the optimal design of fluid domains. An adjoint formulation of the sensitivity equations will be presented and the potential of this topology optimization approach will be illustrated by a numerical examples.

Keywords: Navier–Stokes flow, lattice Boltzmann method, topology optimization.

1. INTRODUCTION

The optimal control of fluid flows has received considerable attention by engineers and mathematicians, owing to its importance for many technical and bio-medical applications. The reader is referred to the recent monographs of Gunzburger (2003) and Mohammadi and Pironneau (2001). Traditionally, the geometry of flow domains is optimized by varying the shape of obstacles and/or channel walls. We refer, for example, to the body of work by Jameson

(1988) and co-workers on shape optimization for external and internal flows. Shape optimization methods, however, allow varying only the shape of boundaries present in the initial design. This limitation can be overcome by extending and applying the concepts of topology optimization developed for design problems in solid mechanics to flow problems. These concepts allow generating complex, often non-intuitive optimal geometries and do not require an initial, close to optimum design to start with. We refer to the monograph of Bendsoe and Sigmund (2003), for an overview of topology optimization methods.

While the field of topology optimization is well established for the optimal design of solids and structures, little work has been done for the optimal design of fluid domains. In their pioneering work, Borrvall and Petersson (2003) considered the optimal design of Stokes flow problems by distributing inhomogeneous porous materials with a spatially varying Darcy permeability tensor. This approach was generalized by Evgrafov (2005a), to include both limiting cases of porous materials, i.e., pure solid and pure flow regions are allowed to appear in the design domain as a result of the optimization procedure. The Stokes theory is only valid for flows with a small Reynolds number $Re < 1$. To overcome this limitation, Gersborg-Hansen et al. (2005) extended the approach of Borrvall and Petersson (2003) to laminar incompressible Navier–Stokes flows at low Reynolds numbers. Evgrafov (2005b) studied the well-posedness of topology optimization problems for incompressible Navier–Stokes flows in the original infinite-dimensional setting, and proposed to relax the incompressibility constraint, amongst other modifications, to achieve such a well-posedness.

Internal and external Navier–Stokes flows are typically approximated by finite element and finite volume methods. While these discretization methods are well established as high-fidelity simulation tools, their accuracy and numerical robustness strongly depends on the quality of the fluid mesh, in particular as Reynolds and Mach numbers increase. This mesh sensitivity significantly affects the suitability of traditional discretization methods for material based topology optimization methods seeking to represent the geometry of the flow domains by “0-1” discontinuous material distributions. Therefore we propose to simulate the underlying flow problem by the lattice Boltzmann method (LBM), a cellular automata approach for simulating low Mach-number incompressible viscous flows. In contrast to finite element and finite volume schemes, the lattice Boltzmann method does not discretize the Navier–Stokes but operates on a discrete form of the Boltzmann equations. The geometry of obstacles and channel walls is defined by turning off nodes in typically structured fluid meshes. This approach allows describing complex geometries without the need for generating fluid meshes aligned with the contours of the flow domain. In addition, LBM solvers can be efficiently parallelized allowing for high-resolution fluid meshes. The potential of the lattice Boltzmann method has been recently recognized for a broad range of technical applica-

tions and for complex biological flow problems. Here, we present a design approach that exploits the unique features of the lattice Boltzmann method for topology optimization purposes.

2. THE LATTICE BOLTZMANN METHOD

In recent years, the lattice Boltzmann method described by McNamara and Zanetti (1988) and Succi (2001) has become a popular alternative to conventional, Navier–Stokes equations based computational methods for a variety of problems in fluid dynamics. It has been successfully compared to a number of finite element and finite volume methods (see, for example, Breuer et al., 2000), as well as to analytical solutions of the Navier–Stokes equations (see, for example, Mei et al., 2002).

The lattice Boltzmann method was originally derived as an extension of the lattice gas automaton. It can also be directly derived from the Boltzmann equation with the Bhatnagar–Gross–Krook (BGK) collision operator (see Bhatnagar et al., 1954; He and Lou, 1997). The numerical scheme of the LBM can be derived starting with the Boltzmann equation as shown by Yu et al. (2005):

$$\frac{\partial f}{\partial t} + \xi \cdot \nabla f = -\frac{1}{\lambda}(f - f^{eq}), \tag{1}$$

where f is the distribution function, ξ is the velocity vector, λ is the relaxation time, f^{eq} is the equilibrium distribution function, and $-\frac{1}{\lambda}(f - f^{eq})$ is the BGK collision operator of Bhatnagar et al. (1954). Equation (1) is discretized in the velocity space, the displacement space, and time. Separating the discretized equation into a local collision and a global propagation step yields the following numerical scheme:

$$\begin{aligned} \text{Collision:} \quad & \tilde{f}_\alpha(\vec{x}_i, t) = f_\alpha(\vec{x}_i, t) - \frac{1}{\tau}[f_\alpha(\vec{x}_i, t) - f_\alpha^{eq}(\vec{x}_i, t)], \\ \text{Propagation:} \quad & f_\alpha(\vec{x}_i + \delta t \vec{e}_\alpha, t + \delta t) = \tilde{f}_\alpha(\vec{x}_i, t), \end{aligned} \tag{2}$$

where \vec{e}_α is the velocity vector belonging to some discrete set depending on the lattice chosen, f_α is the distribution function associated with the corresponding lattice site velocity, \vec{x}_i represents the location in physical space, $\vec{e}_\alpha \delta t$ is the displacement step, δt is the time step, and $\tau = \frac{\lambda}{\delta t}$ is the dimensionless relaxation time.

The exact form of the velocity vector \vec{e}_α in Equation (2) depends on the lattice configuration. In this study, we use the two dimensional, nine velocity D2Q9 lattice model, in which the velocity space is discretized by nine velocity vectors at each lattice site. For low Mach number flow conditions, the equilibrium distribution function f^{eq} in Equation (2) can be derived by a Taylor series expansion of the Maxwell–Boltzmann equilibrium distribution, as shown by

He and Lou (1997):

$$f_{\alpha}^{\text{eq}} = w_{\alpha} \rho \left[1 + 3(\vec{e}_{\alpha} \cdot \vec{u}) + \frac{9}{2}(\vec{e}_{\alpha} \cdot \vec{u})^2 - \frac{3}{2}\vec{u}^2 \right], \quad (3)$$

where the vector \vec{u} represents the macroscopic velocities and w_{α} are lattice weights that depend on the lattice geometry. The macroscopic parameters, such as density, velocity, pressure, and viscosity can be evaluated as follows:

$$\begin{aligned} \rho(\vec{x}, t) &= \sum_{\alpha=0}^8 f_{\alpha}(\vec{x}, t), \\ \rho \vec{u}(\vec{x}, t) &= \sum_{\alpha=0}^8 \vec{e}_{\alpha} f_{\alpha}(\vec{x}, t), \\ p(\vec{x}, t) &= c_s^2 \rho(\vec{x}, t), \\ \nu &= (\tau - 1/2)c_s^2 \delta t, \end{aligned} \quad (4)$$

where c_s is the lattice speed of sound defined by $c_s = c/\sqrt{3}$. Under the low Mach number assumption, the Chapman–Enskog expansion allows verifying that the macroscopic quantities obtained in this manner approximate solutions to the Navier–Stokes equations within $O((\text{Ma})^2)$.

For topology optimization purposes, the above scheme is augmented by a continuous optimization model smoothly “transforming” fluid sites into solid and vice versa. We adopt the LBM porosity model introduced by Spaid and Phelan (1997) for solving the Brinkman equations for porous flows in place of the Navier–Stokes equations. The porosity model requires only a minor modification of the collision step (2) in the LBM algorithm. Instead of using the macroscopic velocity defined in Equation (4) when evaluating the equilibrium distribution (3), we scale it by a factor $0 \leq (1 - \beta(\vec{x}))\tau \leq 1$, where the parameter β is related to the porosity, defined in detail by Spaid and Phelan (1997). The parameters $d(\vec{x}) = \beta(\vec{x})\tau$ at every lattice point are the design variables. The macroscopic velocity \vec{u} in a porous region can be computed as follows:

$$\vec{u}^{\sim}(t, \vec{x}) = (1 - d(\vec{x}))\vec{u}(t, \vec{x}), \quad (5)$$

where $\vec{u}^{\sim}(t, \vec{x})$ is substituted into (3). When $d(\vec{x}) = 0$, \vec{x} is a pure fluid point, when $d(\vec{x}) = 1$, \vec{x} is a pure solid point, and when $0 < d(\vec{x}) < 1$ \vec{x} is occupied by a porous medium.

This simple idea allows us to control the fluid in a simple and continuous fashion. By using the lattice Boltzmann method we can solve the same physical system as done by Borrvall and Petersson (2003), applying a conventional Navier–Stokes based fluid solver to the solution of the Brinkman equation. However, whereas Borrvall and Petersson must drive the porosity to infinity in

order to recover a pure fluid, thus leading to numerical problems, we can continuously vary between solid and fluid by letting $0 < d(\vec{x}) < 1$, creating no numerical problems. Note that employing LBM as the fluid solver, we avoid the numerical difficulties related to the need to drive the inverse permeability coefficient to infinity in the traditionally used Navier–Stokes based Brinkman system.

In this study we consider only optimization problems for steady-state flow conditions. To write the governing equations in a compact form, all design variables $\{d(\vec{x}_1), \dots, d(\vec{x}_L)\}$ are collected into a vector $\vec{d} \in [0, 1]^L$, where $L \in \mathbb{N}$ is the number of lattice points. Similarly, all distribution functions $f_\alpha(\cdot)$ are collected into a vector $\vec{f} \in \mathbb{R}^{rL}$. The steady-state variant of the time-dependent LBM equations (2) is formulated as follows:

$$\Pi(\vec{f}) = \vec{f} + \vec{\Delta}(\vec{\beta}(\vec{d}), \vec{f}). \tag{6}$$

The mapping $\Pi : \mathbb{R}^{rL} \rightarrow \mathbb{R}^{rL}$ is responsible for the “propagation” part of the discrete Boltzmann equation. The collision operator $\vec{\Delta}$ is the only design-dependent part of the system and is highly nonlinear in \vec{f} .

A generic topology optimization problem for steady-state flow conditions can be written as follows:

$$\begin{aligned} & \min_{(\vec{d}, \vec{f}) \in [0, 1]^L \times \mathbb{R}^{rL}} \mathcal{F}(\vec{d}, \vec{f}), \\ \text{s.t. } & \begin{cases} \vec{1}^T \vec{d} \geq \gamma L, \\ \vec{f} \text{ solves (6),} \end{cases} \end{aligned} \tag{7}$$

where \mathcal{F} is a particular performance functional. Note that the above optimization problem has a control in coefficients structure. Assuming the performance functional and the governing steady-state equations are smooth functions of the optimization variables, the problem (7) can be solved by any large-scale gradient-based optimization algorithm. In this study, we use SNOPT by Gill et al. (2002), a commercial implementation of a penalty-based SQP algorithm.

3. NUMERICAL IMPLEMENTATION

In this section we briefly summarize the key components of the numerical implementation of the proposed optimization method. This includes finding the steady-state solution, determining the sensitivities, and parallelizing the code.

The standard LBM algorithm is an explicit time-marching scheme for computing time-dependent flows. In order to compute steady-state flow solutions, the flow needs to be advanced in time until convergence, that is the difference between two or more successive flow states vanishes. The steady-state condition can be written as follows:

$$|\vec{f}_t - \vec{f}_{t-1}|_\infty \leq \varepsilon \tag{8}$$

for $\varepsilon > 0$. Satisfying the above condition is equivalent to finding an approximate solution to the following fixed-point problem:

$$\vec{M}(\vec{f}) - \vec{f} = \vec{0}. \quad (9)$$

Here, the operator \vec{M} performs one collision and one propagation step, which is exactly what is needed to advance the flow to the next time step.

The sensitivities of the performance functional \mathcal{F} in Equation (7) are computed analytically by the adjoint method. The gradient of the objective function \mathcal{F} with respect to the design variables d_i can be written as follows:

$$\frac{d\mathcal{F}}{dd_i} = \frac{\partial\mathcal{F}}{\partial d_i} + \sum_j \frac{\partial\mathcal{F}}{\partial f_j} \frac{\partial f_j}{\partial d_i}, \quad (10)$$

where f_j the distribution function governed by the fixed-point formulation (9). To evaluate the above equation by the adjoint method the transpose of the Jacobian J of the fixed-point problem (9) needs to be computed. For a $n_x \times n_y$ D2Q9 lattice, J is a sparse unsymmetric square matrix of size $(n_x \cdot n_y \cdot 9)^2$. In the presence of no-slip boundary conditions the Jacobian J is singular, which in general precludes the use of the Implicit Function Theorem to perform the sensitivity analysis. This problem can be easily dealt with by excluding some of the “superfluous” particle distributions associated with the no-slip boundary conditions from the fixed-point system (9).

Due to the local nature of the lattice Boltzmann method, it is well suited for parallelization. Since the collision step occurs locally at each lattice site and the propagation step only impacts neighboring lattice sites, only information along the boundary of the subdomain treated by each processor must be transferred to the corresponding neighboring processor. Thus the convergence time scales almost linearly for parallel computations, making the lattice Boltzmann method ideal for parallelization.

4. NUMERICAL EXAMPLES

In order to illustrate the viability of the LBM-based approach for topology optimization, we consider the numerical example of a pipe bend (see Figure 1), which is analogous to one of the examples presented by Borrvall and Petersson (2003). We minimize the pressure drop between inlet and outlet, which has a comparable effect to the power loss objective used by Borrvall and Petersson. The volume fraction of fluid is restricted to at most 25%, which is again equivalent to the value used by Borrvall and Petersson.

As shown in Figure 1, a parabolic velocity profile at the inlet and the density at the outlet are prescribed. In addition, the outlet velocities are forced to be normal with respect to the boundary.

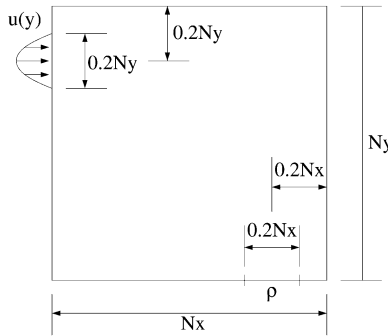


Figure 1. Pipe bend design domain with inlet and outlet conditions.

In our computations we use $(nx - 1) \times (ny - 1)$ design variables for a lattice of size $nx \times ny$, i.e., one design variable between four lattice sites. We obtain the porosity at each node, required by Equation(5), by interpolating from the four surrounding design variables, which results in a small filtering/averaging effect that leads to a smoothing of the results. This smoothing yields density gradients at the fluid-structure interface. Therefore, the resulting plots of nodal densities presented below seem a bit “blurred” at the interfaces. In addition, in our computational experience we obtained better convergence results when instead of the linear scaling in Equation (5) we used a polynomial scaling $(1 - d)^\alpha$ for some $\alpha > 1$. We obtained best results with $\alpha \in [2.5, 3]$.

Using the described setup of the pipe bend design problem and performing the optimization at various Reynolds numbers ($RE = 1, 10, 20, 100$), where RE is defined with respect to the inlet width ($L = 0.2Ny$), we obtain the results shown in Figure 2. From these results, it can be seen that the topology of the pipe is slightly curved and remains similar for the given range of Reynolds numbers. From close observation, one can notice a stronger curvature in the pipe for $RE = 100$, as would be expected from the physics of the problem. This is due to the following competing physical effects, which lead to the optimal solution. First, in order to reduce the shear stress along the walls (τ_w), the pipe must be as short and as wide as possible. This explains the resulting straight pipe shown by Borrvall and Petersson (2003), who use a Stokes model where the power dissipation depends solely on the shear. Second, in order to reduce the momentum loss in the pipe due to the turning of the flow, it is advantageous to turn the flow slowly and continuously, rather than abruptly. Thus, the optimal solution will result from the combined effect of minimizing the shear stresses at the walls and minimizing the momentum loss due to the turning of the flow. Therefore we expect a nearly straight pipe for low Reynolds numbers (Stokes limit) and increasing curvature of the pipe for larger Reynolds numbers, as shown by the numerical results in Figure 2.

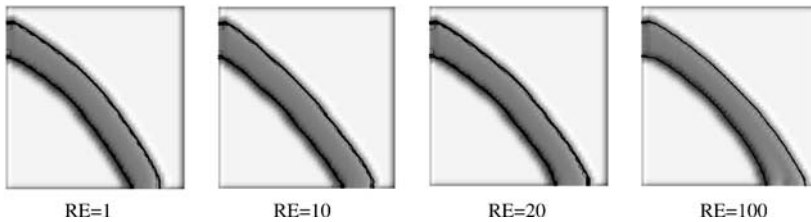


Figure 2. Pipe bend optimization results at various Reynolds numbers.

Table 1. Comparison of pipe bend optimizations at different Reynolds numbers.

<i>RE</i>	<i>Initial Objective</i>	<i>Final Objective</i>	<i>Opt. Iterations</i>	<i>Avg. LBM Iterations</i>
1	0.0609	0.00166838	340	5907
10	0.6117	0.01648804	1310	11254
20	1.2217	0.03501250	765	18842
100	3.8590	0.19987795	1897	44702

Note: Optimization for $RE = 100$ was not completely converged within the allotted optimizer iterations.

Table 1 compares the initial objective value (pressure drop plus penalty factor), final objective value, number of optimizer iterations, and average number of LBM iterations to steady state per optimization for the four different Reynolds numbers, where the objective values are given in lattice units. It was found that it is advantageous to start the optimization with an infeasible solution ($d = 0.1$ everywhere), since the convergence to steady state in the LBM program slows down significantly for larger porosities due to the large pressure drop that must be established. The reader can see from the number of optimizer iterations and average number of LBM iterations that the optimization process is fairly costly. This is a concern since both iteration numbers, in particular the one for the LBM steady-state iterations, increase with increasing lattice sizes.

The objective value versus optimizer iteration is plotted in Figure 3. Figure 4 shows the topology of the pipe bend at different optimizer iterations. The reader can observe that the general topology is obtained after only a few iterations. Thus the optimizer convergence could be increased, for example, by switching to a shape optimization approach once the general topology has been found. The convergence of the LBM time-marching scheme towards steady-state flow solutions can be significantly improved by switching to implicit schemes, as suggested by Bernaschi and Succi (2003). Both options of improvement are included in our future research plans.

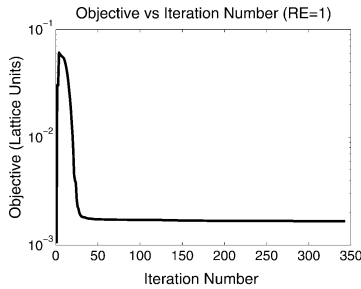


Figure 3. Objective vs. optimizer iteration (RE = 1).



Figure 4. Bend design vs. optimizer iteration (RE = 1).

5. CONCLUSIONS

We have presented a novel approach to flow topology optimization based on the lattice Boltzmann method. A numerical study has illustrated how the lattice Boltzmann method can be employed to solve topology optimization problems arising in fluid mechanics. The results obtained so far indicate that LBM suites ideally for topology optimization owing to its ability to compute flows in complex geometries represented by discontinuous material distributions, ease of parallel implementation, and scalability. While the present study renders the proposed LBM-based topology optimization method a promising alternative to Navier–Stokes based flow optimization, there are many questions left open before the methodology can be efficiently used to solve problems of practical engineering interest.

ACKNOWLEDGMENT

The author acknowledges the support of the National Science Foundation under grant DMI-0348759. The opinions and conclusions presented in this chapter are those of the authors and do not necessarily reflect the views of the sponsoring organization.

REFERENCES

Bendsøe, M.P. and Sigmund, O. (2003) *Topology Optimization: Theory, Methods, and Applications*, Springer-Verlag, Berlin.

- Bernaschi, M. and Succi, S. (2003) Accelerated lattice Boltzmann scheme for steady-state flows, *Int. J. Mod. Phys. B*, 17(1–2), 1–7.
- Bhatnagar, P.L., Gross, E.P. and Krook, M. (1954) A model for collision processes in gases. I. Small amplitude processes in charged and neutral one-component systems, *Phys. Rev.*, 94(3), 511–525.
- Borrvall, T. and Petersson, J. (2003) Topology optimization of fluids in Stokes flow, *Internat. J. Numer. Methods Fluids*, 41(1), 77–107.
- Breuer, M., Bernsdorf, J., Zeiser, T. and Durst, F. (2000) Accurate computations of the laminar flow past a square cylinder based on two different methods: Lattice-Boltzmann and finite-volume, *Int. J. Heat and Fluid Flow*, 21, 186–196.
- Evgrafov, A. (2005a) On the limits of porous materials in the topology optimization of Stokes flows, *Appl. Math. Optim.*, online, DOI: 10.1007/s00245-005-0828-z.
- Evgrafov, A. (2005b) Topology optimization of slightly compressible fluids, *ZAMM Z. Angew. Math. Mech.*, online, DOI: 10.1002/zamm.200410223.
- Gersborg-Hansen, A., Sigmund, O. and Haber, R. (2005) Topology optimization of channel flow problems, *Struct. and Multidisc. Optim.*, online, DOI: 10.1007/s00158-004-0508-7.
- Gill, P.E., Murray, W. and Saunders, M.A. (2002) SNOPT: An SQP algorithm for large-scale constrained optimization. *SIAM J. Optim.*, 12(4), 979–1006.
- Gunzburger, M.D. (2003) *Perspectives in Flow Control and Optimization*, Advances in Design and Control, Society for Industrial and Applied Mathematics (SIAM), Philadelphia, PA.
- He, X. and Lou, L.-S. (1997) A priori derivation of the lattice Boltzmann equation, *Phys. Rev. E*, 55(6), 6333–6336.
- Jameson, A. (1988) Aerodynamic design via control theory, *Journal of Scientific Computing*, 3, 233–260.
- McNamara, G.R. and Zanetti, G. (1988) Use of the Boltzmann equation to simulate lattice-gas automata, *Phys. Rev. Lett.*, 61(20), 2332–2335.
- Mei, R., Yu, D., Shyy, W. and Luo, L.-S. (2002) Force evaluation in the lattice Boltzmann method involving curved geometry, *Phys. Rev. E*, 65(4), 041203:1–041203:14.
- Mohammadi, B. and Pironneau, O. (2001) *Applied Shape Optimization for Fluids*, Numerical Mathematics and Scientific Computation, Oxford University Press, New York.
- Spaid, M.A.A. and Phelan, F.R. (1997) Lattice Boltzmann methods for modelling microscale flow in fibrous porous media, *Physics of Fluids*, 9(9), 2468–2474.
- Succi, S. (2001) *The Lattice Boltzmann Equation: For Fluid Dynamics and Beyond*, Numerical Mathematics and Scientific Computation, Oxford University Press.
- Yu, D., Mei, R. and Shyy, W. (2005) Improved treatment of the open boundary in the method of lattice Boltzmann equation, *Prog. Comp. Fluid Dynamics*, 5(1/2), 3–12.

A CLASS OF OPTIMAL TWO-DIMENSIONAL MULTIMATERIAL CONDUCTING LAMINATES

Nathan Albin¹, Andrej Cherkaev¹ and Vincenzo Nesi²

¹*Department of Mathematics, University of Utah, Salt Lake City, UT 84112, U.S.A.*

²*Department of Mathematics, Università degli Studi di Roma "La Sapienza",
00185 Rome, Italy*

albin@math.utah.edu, cherk@math.utah.edu, nesi@mat.uniroma1.it

Abstract We introduce a family of optimal anisotropic two-dimensional multimaterial laminate composites which correspond to extreme overall conductivity. These laminates attain the translation bounds and generalize all previously known constructions for these bounds. The method of construction is based on the analysis of the fields in optimal structures.

Keywords: Structural optimization, multicomponent optimal composites, bounds, polyconvexity, rank-one convexity, multiwell variational problem.

1. INTRODUCTION

The problem of the optimal structure of a periodic composite has been the subject of substantial work in various communities. Since the pioneering work of Hashin and Shtrikman (1962), two techniques have been used to solve the problem. On one hand, *outer bounds* on the effective tensors are established, which depend only on the physical properties of the constituent materials and on their relative volume fractions. On the other hand, the effective tensors of periodic microstructures are used to establish an *inner bound* on the set of effective tensors. An outer bound is found to be optimal if it coincides with an inner bound.

Though the G-closure problem for two conducting materials in two dimensions was solved more than twenty years ago in Hashin and Shtrikman (1962), Tartar (1979, 1985) and Lurie and Cherkaev (1984), the solution for three-material mixtures is still not known. The translation bound, which is related to the polyconvex envelope of an auxiliary energy, is always attainable for two-material composites. However, for multimaterial composites the bound is attainable only in a special range of volume fractions of the components

(Hashin and Shtrikman, 1962; Milton, 1981; Lurie and Cherkaev, 1985; Milton and Kohn, 1988; Gibiansky and Sigmund, 2000). Additionally, there are results for improved bounds in the case of small volume fractions of the best or worst conductor (Talbot et al., 1995; Nesi, 1995).

In this paper, we construct a family of structures which realize the translation bound by analyzing the (pointwise) fields in optimal structures. In particular, our family of structures generalizes the structures of multimaterial composites found in Milton and Kohn (1988), and those found in Gibiansky and Sigmund (2000). Additionally, we discuss a new pointwise constraint on the fields in the materials inside any translation-optimal structure which supplements the translation bound. This constraint determines a new necessary condition for the attainability of the translation bound. Our method is based on the analysis of the fields in optimal structures. The results are presented for *two-dimensional linear conductivity*, although much of the method applies to various other types of physical phenomena both in two and three dimensions.

2. NOTATIONS AND BOUNDS

2.1 Multiphase Conducting Mixtures

Consider a two-dimensional periodic multiphase structure. The unit periodicity cell $\Omega = [0, 1]^2$ is divided into N parts $\Omega_1, \dots, \Omega_N$ occupied with materials with isotropic conductivity tensors

$$K_i = k_i I \quad \text{for } i = 1, \dots, N, \quad (1)$$

where I is the two-by-two identity matrix. We assume the conductivities are ordered so that $0 < k_1 < \dots < k_N$. The conductivity equations applied to the periodicity cell are written as

$$\operatorname{div} K(x) \nabla u(x) = 0 \text{ in } \Omega, \quad \int_{\Omega} \nabla u(x) \, dx = e, \quad (2)$$

where $K : \Omega \rightarrow \{K_1, \dots, K_N\}$ is the variable conductivity tensor defined by

$$K(x) = K_i \quad \text{if } x \in \Omega_i, \quad i = 1, \dots, N, \quad (3)$$

K_1, \dots, K_N are given by (1), and where e is the prescribed external field acting on Ω .

Assume that the periodicity cell with material layout defined by $K(x)$ is subject to the homogeneous external field e that is gradient of a linear potential $e^T x$. The energy stored in the material is given by

$$W(K, e) = \inf_{u \in H_{\#}^1(\Omega) + e \cdot x} \int_{\Omega} \nabla u(x) \cdot K(x) \nabla u(x) \, dx,$$

where $H_{\#}^1(\Omega)$ is the space of locally H^1 functions on \mathbb{R}^2 which are Ω -periodic with zero mean. The infimum is taken over functions with fixed affine part plus a variable periodic oscillating part:

$$u(x) = e \cdot x + \text{osc}(x), \quad \int_{\Omega} \nabla u(x) \, dx = e.$$

The affine part, $e \cdot x$, is prescribed by the loading. The minimization is taken over the zero-mean oscillating part, $\text{osc}(x)$.

The effective tensor K^* of the structure with the partition Ω_i is defined as a homogeneous material that stores the same energy as the mixture under the same homogeneous loading. That is,

$$e \cdot K^* e = \inf_{u \in H_{\#}^1(\Omega) + e \cdot x} \int_{\Omega} \nabla u(x) \cdot K(x) \nabla u(x) \, dx \quad \forall e \in \mathbb{R}^2.$$

In order to completely determine K^* , it suffices to consider the response of the same structure to the two orthogonal loadings (see Lurie and Cherkaev, 1984; Francfort and Milton, 1994).

$$e = e_1 = r_1(1, 0)^T \quad \text{and} \quad e = e_2 = r_2(0, 1)^T. \tag{4}$$

The response in this case means the sum of the energies of these loadings:

$$W(K, e_1) + W(K, e_2). \tag{5}$$

This functional can be conveniently rewritten in terms of two-by-two matrices. We write (4) as

$$E = \text{diag}(r_1, r_2). \tag{6}$$

Given any pair of potentials $U = (u_1, u_2)$, we define the two-by-two gradient matrix as the matrix whose rows consist of the gradients of u_1 and u_2 :

$$DU = \{DU_{ij}\}_{i,j \in \{1,2\}}, \quad DU_{ij} = \frac{\partial u_i}{\partial x_j}.$$

The sum of energies (5) becomes

$$\mathcal{W}(K, E) = \inf_{U \in H_{\#}^1(\Omega)^2 + Ex} \int_{\Omega} \langle DU(x) K(x), DU(x) \rangle \, dx$$

where $\langle \cdot, \cdot \rangle$ is the inner product defined on two-by-two matrices by

$$\langle A, B \rangle = \text{tr}(AB^T).$$

The effective tensor K^* is the unique (symmetric) tensor satisfying the relation

$$\langle E K^*, E \rangle = \inf_{U \in H_{\#}^1(\Omega)^2 + Ex} \int_{\Omega} \langle DU(x) K(x), DU(x) \rangle \, dx \quad \forall E \in \mathbb{R}^{2 \times 2}.$$

3. BOUNDS

3.1 Wiener and Translation Bounds

The effective conductivity satisfies the following inequality bounds (see, for example, Cherkaev, 2000; Milton, 2002).

1. The Wiener bounds:

$$\left(\sum_{i=1}^N \frac{m_i}{k_i} \right)^{-1} \leq \lambda_{\min}(K^*) \leq \lambda_{\max}(K^*) \leq \sum_{i=1}^N m_i k_i. \quad (7)$$

where $\lambda_{\min}(K^*)$ and $\lambda_{\max}(K^*)$ are the minimum and maximum eigenvalues of K^* respectively and where $m_i = |\Omega_i|$ are the *relative volume fractions* of the materials, $m_1 + m_2 + m_3 = 1$. The inequalities place the pair of eigenvalues of any effective tensor in a rectangular box in the eigenvalue plane. The bound is sharp: The effective tensor of the anisotropic laminate satisfies both inequalities as equalities. Moreover, for multicomponent ($N \geq 3$) structures, the bound is achieved at certain intervals of the sides of the box (Cherkaev and Gibiansky, 1996).

2. The translation bounds:

$$\frac{\text{tr } K^* - 2k_1}{\det K^* - k_1^2} \leq 2 \sum_{i=1}^N \frac{m_i}{k_i + k_1}, \quad (8)$$

$$\frac{\text{tr } K^* - 2k_N}{\det K^* - k_N^2} \geq 2 \sum_{i=1}^N \frac{m_i}{k_N + k_i}. \quad (9)$$

These bounds are sharp for certain values of the m_i , k_i , and the degree of anisotropy of K^* as is discussed later in this paper.

3.2 Conditions of Realizability of the Translation Bounds

The translation bounds (8) and (9) are not sharp for all values of the parameters m_i and k_i . Intuitively, we see this from the fact that the formulas for the bounds still depend on k_1 (respectively k_N) when $m_1 = 0$ (respectively $m_N = 0$) as was discussed in Milton and Kohn (1988). Besides, for m_1 or m_N near 0, there are better bounds (Talbot et al., 1995; Nesi, 1995), so the translation bounds cannot be sharp. In the rest of the paper we focus primarily on the lower bound (8). Similar constructions exist for the upper bound (9) by duality arguments.

THEOREM 1 (REALIZABILITY THEOREM) *A structure realizes the bound (8), if the following conditions hold on the pointwise field DU when the structure is placed in to a properly scaled diagonal external field E in (6) (compare to Grabovsky, 1996; Milton, 2002).*

(P1) $\text{tr } DU = 1$ a.e. in Ω_1 .

(P2) $DU = \frac{k_1}{k_i+k_1}I$ a.e. in Ω_i for $i = 2, \dots, N$.

(P3) DU is diagonal in Ω_1 .

In fact, the theorem is true if (P1)–(P3) hold in an approximate sense. In particular, if the piecewise constant “fields” in a sequential laminate satisfy (P1)–(P3) then the laminate is optimal. It is in this sense that we refer to the fields in laminate structures from now on.

In addition, we show that in order for a laminate structure to satisfy the bound, the field in the first material cannot be “too anisotropic”.

THEOREM 2 *If a laminate structure satisfies the bound (8) then (under the assumptions of the previous theorem) the field in the first material must satisfy the relation*

$$\det DU \geq \frac{k_1 k_N}{(k_N + k_1)^2} \quad \text{in } \Omega_1. \tag{10}$$

Indeed, this inequality easily follows from the fact that the fields in a layer of lamination must be in a rank-one connected.

The inequality (10) limits the applicability of (8); the bound cannot be satisfied by laminates that are either extremely anisotropic or that contain too small an amount of the first material. The T^2 -structures described below satisfy the condition (10) as equality and therefore represent the boundary of applicability of the translation bound for laminates.

4. THE OPTIMAL STRUCTURES

4.1 Known Structures

The first type of isotropic structures to attain the translation bound was described in Milton (1981) (see Figure 1a). The construction for the lower bound (8) (K^* is isotropic) is possible if m_1 is large enough. All such constructions satisfy $K_1 \leq K^* \leq K_2$. Milton’s construction was extended to anisotropic composites later in Milton and Kohn (1988) (see Figure 1c). The topology of the optimal structures is not unique as follows from Lurie and Cherkvaev (1985) where an alternative construction was given for structures with exactly the same volume fractions and effective properties as those presented by Milton (see Figure 1b). In Cherkvaev and Gibiansky (1996) three-material anisotropic structures that have effective tensors with eigenvalues on an interval of the sides of the Wiener box not only in its corner were introduced (see Figure 1e). There are no similar structures in the two-material case.

In Gibiansky and Sigmund (2000) a new construction was described that significantly increased the set of optimal points of the translation bounds (8)

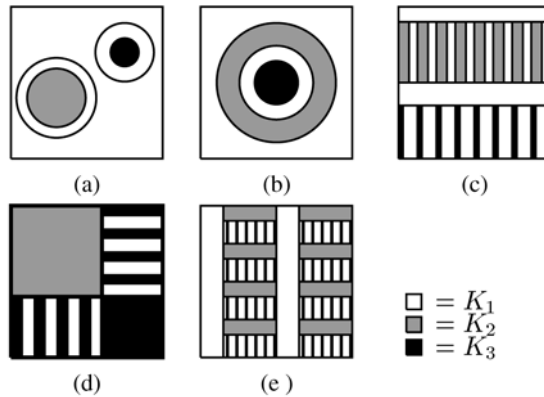


Figure 1. Previously known three-phase structures optimal for the translation bound (8).

and (9) for the case $N = 3$. The paper focuses on the problem of bulk moduli, but the authors extend the results to the conductivity problem as well. Their structures were the surprising result of a numerical simulation. Using a “topology optimization” algorithm developed earlier by Sigmund, the authors searched for optimal structures by computer. They found a structure which lies outside the Kohn and Milton range of parameters (m_1 is too small for any of the previous constructions to apply) but which numerically appears to satisfy the translation bound. The surprise occurred when the authors attempted to replace the computer output with a similar, but simpler structure for which the effective properties could be analytically computed. The simplified structure was optimal for the translation bounds. Instead of iterated laminates or coated spheres, they used the Marino and Spagnolo (1969) type structures (re-invented by Sigmund, 2000) that consist of rectangular domains with special conductivities that make separation of variables possible in the homogenization equations. Reinterpreting their results slightly, we divide the cell of periodicity into four rectangular subdomains. The opposite squares are occupied by K_2 and K_3 , and the remaining rectangles are filled with laminates from K_1 and K_3 (see Figure 1d). The effective conductivity of the laminate depends on the volume fraction of materials in it. This conductivity (or, equivalently, the fraction of the materials in the laminate) is chosen in such a way that the conductivity equation (2) permits a separation of the variables if the external fields are homogeneous. Because of this feature, the solution is analytic and so are the effective properties. Using Maple, the authors then found that the structures are optimal for the translation bound (8). The authors also described more complicated structures that were optimal for larger values of m_1 and which coincided with the previously known structures at the point $K^* = K_2$.

4.2 Optimal Laminates

Here we describe a new family of optimal microstructures for the case $N = 3$. They are the laminates with the special property that the fields inside the layers of pure material satisfy the sufficient conditions (P1)–(P3). We observe that they also necessarily satisfy the applicability condition (10). To find an optimal structure, we assign the fields in layers to be optimal and choose the volume fractions to allow compatibility for lamination. We begin with some degenerate cases and work toward the general structure.

A Parameterization. The phase K_1 and its volume fraction m_1 play a special role in the bound (8) and in the associated optimal structures. For this reason, it is convenient to introduce the fraction p of K_2 relative to K_3 ,

$$p = \frac{m_2}{1 - m_1}, \quad 1 - p = \frac{m_3}{1 - m_1}.$$

Using p -notation, the translation bound (8) for three material mixtures is rewritten as

$$\frac{1}{2} \cdot \frac{\text{tr } K^* - 2k_1}{\det K^* - k_1^2} \leq \frac{m_1}{2k_1} + (1 - m_1) \left(\frac{p}{k_2 + k_1} + \frac{1 - p}{k_3 + k_1} \right). \tag{11}$$

If we think of $p \in [0, 1]$ as a parameter of the problem, we can write the requirement that a structure attains bound (8) as

$$m_1 = \frac{\frac{1}{2} \cdot \frac{\text{tr } K^* - 2k_1}{\det K^* - k_1^2} - \left(\frac{p}{k_2 + k_1} + \frac{1 - p}{k_3 + k_1} \right)}{\frac{1}{2k_1} - \left(\frac{p}{k_2 + k_1} + \frac{1 - p}{k_3 + k_1} \right)}. \tag{12}$$

Furthermore, the ‘‘coating principle’’ discussed in this section is an operation on structures which increases m_1 , preserves p , and preserves the equality in (12). For this reason, it is convenient to fix p and plot the values of K^* where the bound (8) is sharp in the eigenvalue plane. From these values, we can recover via (12) the value of m_1 (and thus all other volume fractions) for each plotted point.

The Lamination Formula. The effective properties tensor K^* of a laminate from two anisotropic materials with conductivity tensors A and B , in volume fractions m and $1 - m$ respectively, and with normal n to the layers, is given by the representation (see, for example Cherkaev, 2000; Milton, 2002)

$$K^* = L(K_A, K_B, n, m) = mK_A + (1 - m)K_B - \mathcal{N}, \tag{13}$$

where

$$\mathcal{N} = m(1 - m)(K_B - K_A)n[n^T(mK_B + (1 - m)K_A)n]^{-1}n^T(K_B - K_A).$$

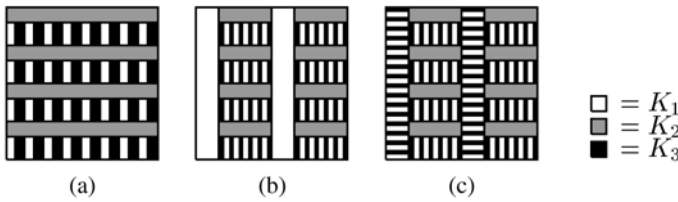


Figure 2. A selection structures optimal for (8): (a) a T -structure, (b) a T -structure with one layer of “coating”, (c) a T^2 -structure.

Coating with K_1 Preserves Optimality. In order to describe the variety of the optimal structures, we make the following observation.

THEOREM 3 (THE COATING PRINCIPLE) *If a structure K^* is optimal for the translation bound (8), then all structures obtained by laminating it with material K_1 are also optimal for (8). The laminating can be iterated so that the original structure is “coated” by K_1 .*

This observation allows us to describe only the *extremal* structures that attain the bound (8) in the sense that they contain the minimal amount of K_1 .

In particular, the coating principle immediately proves the optimality of all optimal two-phase structures – the laminates of second rank. These structures are the result of the coating of the pure phase K_2 (which is trivially optimal for (8)). The two-phase structures correspond to $p = 1$ (see (11) and (12)).

The coating principle also plays an important role in the analysis of multiphase mixtures. Notice that the coating changes the volume fractions, m_i , but it preserves the value of p . Since coating increases the value of m_1 , the principle allows to look for the optimal structures with the lowest value of m_1 . Every optimal structure generates a set of optimal coated structures.

T-Structures. The simplest optimal structure is the T -structure. It is assembled as a sequence of laminates. First, K_1 and K_3 are laminated with normal in the x_1 -direction. Then, the resulting composite is laminated with K_2 with the normal in the x_2 -direction. Figure 2a illustrates the construction of the T -structure. The effective properties of the T -structure are found by iterating the lamination formula for two materials K_A and K_B with normal n and in relative amounts m and $1 - m$ respectively,

$$K_T = L \left(K_2, L \left(K_1, K_3, n_1, \frac{m_1}{m_1 + m_3} \right), n_2, m_2 \right),$$

where $n_1 = (1, 0)^T$ and $n_2 = (0, 1)^T$.

THEOREM 4 *For all values of $p \in [0, 1]$, there exists a T -structure with the given value of p that is optimal for the translation bound (8).*

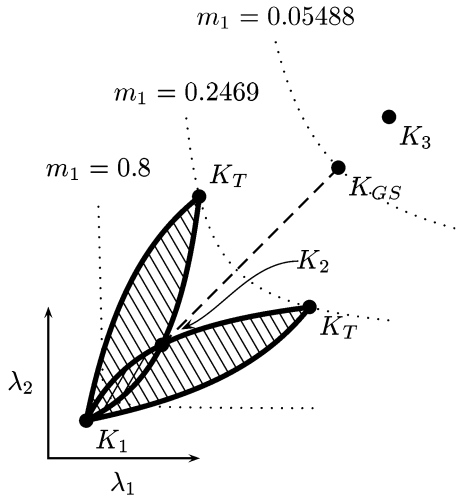


Figure 3. The set of optimal structures formed by coating the optimal T -structure.

It may seem surprising that we have found that there is always an optimal T -structure for any p . Keep in mind that we consider structures with fixed relative volume fractions of K_2 and K_3 but with arbitrary fraction of K_1 .

Coated T-Structures. From the optimal T -structure, we obtain a set of optimal structures by coating with K_1 according to Theorem 3. The obtained region is shaded in the eigenvalue plane in Figure 3. The calculation corresponds to the parameters

$$k_1 = 1, \quad k_2 = 2, \quad k_3 = 5, \quad p = \frac{1}{60}. \tag{14}$$

It is convenient to represent an anisotropic material by two symmetric points (λ_1, λ_2) and (λ_2, λ_1) in the plane of eigenvalues to avoid ordering the eigenvalues. Particularly, the optimal T -structure is represented by two points, both labeled K_T . The domain optimal structures given by coating the T -structure is the union of two lens-shaped regions in the plane. The boundaries of this set are the laminate curves. Recall that rather than fixing volume fractions, we fix the value p which in turn fixes the ratio of m_2 to m_3 . The figure also includes some dotted curves of constant volume fraction. Those closer to K_1 indicate larger values of m_1 than those farther away. Any point where one of these curves intersects the region of optimal coated T-structures is an optimal point for the translation bound (8) with the volume fractions given through m_1 and p .

An extremely anisotropic T -structure with an additional layer of K_1 instead of coating in the x -direction is shown in Figure 2b. We notice that these op-

timal structures that attain the translation bound are topologically equivalent to the extremal structures that attain the Wiener bound, Figure 1e (see Cherkaev and Gibiansky, 1996). The structures differ by a single parameter: the relative fraction of K_1 in the inner layer. Although these two structures are both optimal, they are optimal for different bounds. Therefore, it is not yet known if the structures with intermediate values of the parameter are optimal for some generalized bound. They are not optimal for any of the bounds (7)–(9). However, these structure would give a fair approximation to the boundary of all optimal structures.

T²-Structures. Next, we enlarge the class of optimal structures by considering a generalization of the T -structure. We laminate the T -structure with a laminate of K_1 and K_3 in the orthogonal direction as seen in Figure 1c. The effective tensor of such T^2 -structures is found from the iterative procedure

$$K_{T2} = L(K_T, K'_{13}, n_1, \omega_2), \quad K_T = L(K_2, K_{13}, n_2, \omega_1),$$

$$K'_{13} = L(K_1, K_3, n_2, v'), \quad K_{13} = L(K_1, K_3, n_1, v).$$

The properties depend on four structural parameters: $v, v', \omega_1, \omega_2$ that all vary in $[0, 1]$ and subject to the constraint that fixes p . The T^2 -structures form a class of optimal anisotropic structures between the T -structures and the isotropic structures of Gibiansky and Sigmund, as is stated the following theorem.

THEOREM 5 *For all values of $p \in [0, 1]$ there exists a family of T^2 -structures optimal for the bound (8) and with variable anisotropy. The optimal parameters of optimal structures satisfy the relations*

$$v = \Theta, \quad v' = \omega_1 \Theta,$$

where

$$\Theta = \frac{k_1(k_3 - k_2)}{(k_2 + k_1)(k_3 - k_1)} \leq \frac{1}{2} \tag{15}$$

and

$$(1 - 2p\Theta)\omega_1\omega_2 + p\Theta(\omega_1 + \omega_2) - p = 0, \quad \frac{p(1 - \Theta)}{1 - p\Theta} \leq \omega_1, \omega_2 \leq 1. \tag{16}$$

This construction generates a curve of eigenvalue pairs of effective tensors that passes through T -structure and the isotropic point of Gibiansky and Sigmund.

The volume fractions in the optimal laminates are

$$m_1 = \Theta(\omega_1(1 - \omega_2) + \omega_2(1 - \omega_1)), \quad m_2 = \omega_1\omega_2, \quad m_3 = 1 - m_1 - m_2. \tag{17}$$

The effective tensors have eigenvalues λ_1, λ_2 parameterized by

$$\lambda_1 = \frac{\omega_1 k_2(k_1 + k_3) + (1 - \omega_1)k_3(k_1 + k_2)}{\omega_2(k_1 + k_3) + (1 - \omega_2)(k_1 + k_2)}, \tag{18}$$

$$\lambda_2 = \frac{\omega_2 k_2(k_1 + k_3) + (1 - \omega_2)k_3(k_1 + k_2)}{\omega_1(k_1 + k_3) + (1 - \omega_1)(k_1 + k_2)}. \tag{19}$$

The T^2 structures are extreme in the sense that (10) is satisfied as equality everywhere in Ω_1 .

The extreme values of ω_1 or ω_2 correspond to the T -structure. On the other hand, when $\omega_1 = \omega_2$, we obtain an isotropic structure whose volume fractions satisfy the equality $m_1 = 2\Theta(\sqrt{m_2} - m_2)$ (compare to Gibiansky and Sigmund, 2000, formula (49)!). The T^2 -structures are a generalization of both the T -structures and the Gibiansky-Sigmund structure with minimal amount of m_1 . The parameters ω_1, ω_2, ν and ν' are determined based on the requirements (P1)–(P3) on the fields inside the phases of an optimal structure.

Recall that we do not fix m_2 . Instead we fix $p = m_2/1 - m_1$ and allow the volume fractions to vary subject to this constraint. Using this, the natural limits $0 \leq \omega_1, \omega_2 \leq 1$ and the values of the volume fractions given in (17), we find (16).

The relation between the effective properties of optimal mixtures is symmetric to the interchanging $\omega_1 \leftrightarrow \omega_2$ in spite of the nonsymmetric iterative procedure.

The Set of Optimal Structures. Combining the extremal T^2 -structures with the coating principle, we obtain a variety of optimal structures because each T^2 -structure can be coated, increasing the amount m_1 but keeping relative fraction p . The set of all coated T^2 -structures with the given value of p forms a subset of structures optimal for the translation bound (8). This set is illustrated in the eigenvalue plane in Figure 4a for parameters as in (14). The set of optimal structures is bounded by the solid boundary, which is the union of coated T -structures (the curves between K_1 and K_T) and the T^2 -structures (the curve passing through K_{GS}). The closed region bounded by the dotted lines represent the previously known optimal structures of Kohn and Milton, and Gibiansky and Sigmund.

5. DISCUSSION

Curves of constant volume fraction are indicated in Figure 4a by the dotted lines. In particular the curve passing through K_T represents the case $m_1 = \Theta(1 - m_2)$ while the curve passing through K_{GS} represents the case $m_1 = 2\Theta(\sqrt{m_2} - m_2)$.

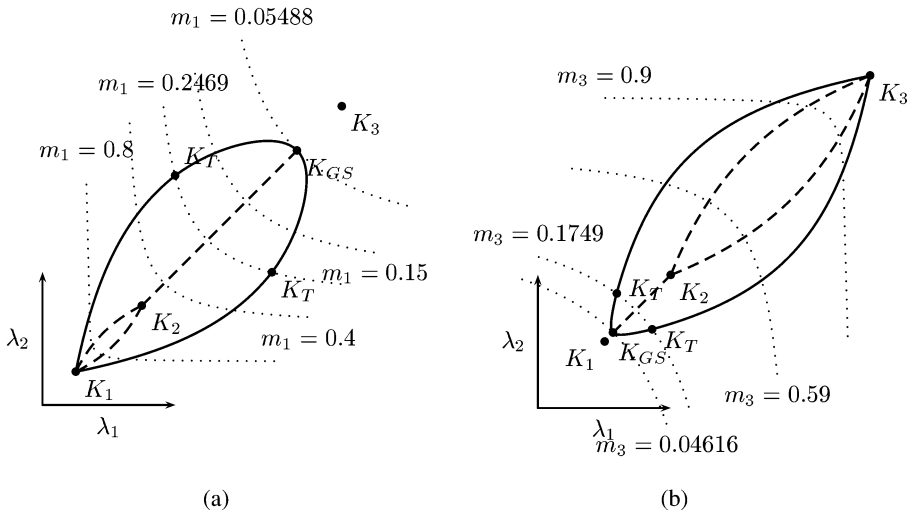


Figure 4. (a) Optimal points for the lower translation bound for $m_2/1 - m_1 = 1/60$. (b) Optimal points for the upper translation bound for $m_2/1 - m_3 = 1/41$.

Our results can be rewritten for the fixed volume fractions instead of fixed parameter $p = m_2/(1 - m_1)$. For example, consider the question of the G-closure when

$$m_1 = 0.4, \quad m_2 = 0.01, \quad m_3 = 0.59.$$

We need only examine Figure 4a and the corresponding figure for the upper bound, Figure 4b. The optimal points of the lower bound marked by the thick dashed curve in Figure 5 are the intersection of the curve of constant $m_1 = 0.4$ with the optimal region shown in Figure 4a. The dot in Figure 5 marks the point where this curve intersects the dashed Gibiansky–Sigmund line. Similarly, the optimal points marked by the thick curve on the upper bound in Figure 5 are points where the line of constant volume fraction $m_3 = 0.59$ intersects the set of optimal points in Figure 4b. The solid portion of the curve marks the intersection with the Kohn–Milton region.

Look again at Figure 4a. As long as $m_1 \geq 2\Theta(\sqrt{m_2} - m_2)$, the intersection of the constant m_1 curve and the region of optimal points is a connected section of the curve which includes the isotropic point. Thus, the intersection can be described by the most anisotropic point only. For $m_1 > \Theta(1 - m_2)$ this most anisotropic point is a coated T -structure. For $m_1 \leq \Theta(1 - m_2)$, it is a T^2 -structure. We summarize this in the following theorem.

THEOREM 6 *Let the volume fractions m_1, m_2 and m_3 be given.*

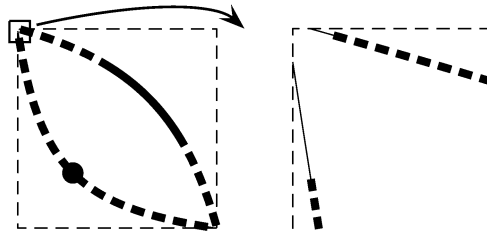


Figure 5. (Left) The bounds (7)–(9) with known optimal points indicated by thick lines. (Right) A magnification of the upper-left corner.

- (i) If $m_1 > \Theta(1 - m_2)$, then (8) is sharp. Moreover, there exists a set of optimal tensors whose most anisotropic member is that given by the optimal coated T -structure with the given volume fractions.
- (ii) If $2\Theta(\sqrt{m_2} - m_2) \leq m_1 \leq \Theta(1 - m_2)$, then (8) is sharp. Moreover, there exists a set of optimal tensors whose most anisotropic member is that given by the optimal T^2 -structure satisfying the volume fraction constraints. In particular, the parameters ω_1 and ω_2 for this most anisotropic structure can be found by solving simultaneously the equations

$$m_1 = \Theta\omega_1(1 - \omega_2) + \Theta\omega_2(1 - \omega_1), \quad m_2 = \omega_1\omega_2.$$

References

Cherkaev, A. and Gibiansky, L. (1996) Extremal structures of multiphase heat conducting composites, *Int. J. Solids Structures*, 33(18), 2609–2623.

Cherkaev, A. (2000) *Variational Methods for Structural Optimization*, Applied Mathematical Sciences, Vol. 140, Springer-Verlag, New York.

Francfort, G.A. and Milton, G.W. (1994) Sets of conductivity and elasticity tensors stable under lamination, *Comm. Pure Appl. Math.*, 47(3), 257–279.

Gibiansky, L.V. and Sigmund, O. (2000) Multiphase composites with extremal bulk modulus, *J. Mech. Phys. Solids*, 48(3), 461–498.

Grabovsky, Y. (1996) Bounds and extremal microstructures for two-component composites: A unified treatment based on the translation method, *Proc. Roy. Soc. London Ser. A*, 452(1947), 919–944.

Hashin, Z. and Shtrikman, S. (1962) A variational approach to the theory of the effective magnetic permeability of multiphase materials, *J. Appl. Phys.*, 35.

Lurie, K.A. and Cherkaev, A.V. (1984) Exact estimates of conductivity of composites formed by two isotropically conducting media taken in prescribed proportion, *Proc. Roy. Soc. Edinburgh Sect. A*, 99(1–2), 71–87.

Lurie, K.A. and Cherkaev, A.V. (1985) Optimization of properties of multicomponent isotropic composites, *J. Optim. Theory Appl.*, 46(4), 571–580.

Marino, A. and Spagnolo, S. (1969) Un tipo di approssimazione dell'operatore $\sum_1^n ijD_i(a_{ij}(x)D_j)$ con operatori $\sum_1^n jD_j(\beta(x)D_j)$, *Ann. Scuola Norm. Sup. Pisa* (3), 23, 657–673.

- Milton, G.W. (1981) Concerning bounds on the transport and mechanical properties of multicomponent composite materials, *Appl. Phys.*, A26, 125–130.
- Milton, G.W. (2002) *The Theory of Composites*, Cambridge Monographs on Applied and Computational Mathematics, Vol. 6, Cambridge University Press, Cambridge.
- Milton, G.W. and Kohn, R.V. (1988) Variational bounds on the effective moduli of anisotropic composites, *J. Mech. Phys. Solids*, 36(6), 597–629.
- Nesi, V. (1995) Bounds on the effective conductivity of two-dimensional composites made of $n \geq 3$ isotropic phases in prescribed volume fraction: The weighted translation method, *Proc. Roy. Soc. Edinburgh Sect. A*, 125(6), 1219–1239.
- Sigmund, O. (2000) A new class of extremal composites, *J. Mech. Phys. Solids*, 48(2), 397–428.
- Talbot, D.R.S., Willis, J.R. and Nesi, V. (1995) On improving the Hashin–Shtrikman bounds for the effective properties of three-phase composite media, *IMA J. Appl. Math.*, 54(1), 97–107.
- Tartar, L. (1979) Estimation de coefficients homogénéisés, in *Computing Methods in Applied Sciences and Engineering*, Proc. Third Internat. Sympos., Versailles, 1977, I, Lecture Notes in Math., Vol. 704, Springer, Berlin, pp. 364–373.
- Tartar, L. (1985) Estimations fines des coefficients homogénéisés, in *Ennio De Giorgi colloquium*, Paris, 1983, Res. Notes in Math., Vol. 125, Pitman, Boston, MA, pp. 168–187.

New Approaches

MULTIDISCIPLINARY TOPOLOGY DESIGN AND PARTIAL DIFFERENTIAL GAMES

Introduction to Topology Games

Abderrahmane Habbal
University of Nice, France
habbal@unice.fr

Abstract: We use the Nash game theory to deal with multidisciplinary topology optimization. First, we introduce a basic Nash game framework. Then we apply it to the modeling of a multidisciplinary topology design problem arising from biomathematics.

Keywords: Static games, topology optimization, Nash equilibrium.

1. INTRODUCTION

When *multiobjective* optimization is involved, the habit is to select a scalar ersatz, usually a weighted version, and then to apply single objective optimization techniques. This approach has two major drawbacks. First, the choice of the ersatz (e.g. the weights) is arbitrary. Second, values of the objectives which could be of very disparate scales are compared. The optimum could then be dramatically dependent on a set of arbitrary choices. Moreover, the notion of optimum is meaningless, since it depends on which objective function is under consideration. For these reasons, the need for a natural and systematic approach to deal with multiobjective optimization has led us to restate multidisciplinary topology design problems within the *game theory* framework.

A game formulation could be easily settled for problems starting from simple multicriteria to fully complex multidisciplinary problems. In a game vocabulary, one could assign a subfamily of the design parameters to one player, and another subfamily to the second one. In the present paper, we illustrate this approach with an application to a multidisciplinary topology optimization problem arising from biomathematics.

2. PARTIAL DIFFERENTIAL GAMES

We outline a basic framework for the game-theoretic formulation of multidisciplinary topology design problems.

We shall consider a two-players game. The extension of the abstract framework to N-players games is straightforward.

Consider then two subsets S_1 and S_2 of two respective Banach spaces, W_1 and W_2 . A generic element of S_1 (or S_2) is called a strategy of the player one (or two). The set S_1 is called the set of admissible strategies for the player one, and the same for the set S_2 .

We shall frequently consider pairs $s = (s_1, s_2) \in S_1 \times S_2$ of strategies chosen by each player. The variables s_1 and s_2 may be in some simple cases the classical density functions which parameterize (by completion) the topology of given disjoint parts of the structure. In some other cases, the actual topology ρ of the whole structure may be obtained as a result from the interaction between s_1 and s_2 : $\rho = \rho(s_1, s_2)$.

For simplicity, let consider the case where the pairs of strategies intervene in the *same state equation*, which reads (using classical weak formulation):

$$\forall v \in V \quad a(\rho; u_\rho, v) = L(\rho; v). \quad (1)$$

Here, the response u_ρ of the system depends on the joint choice, maybe concurrent, of the parameters s_1 and s_2 .

The objectives of the two players are then respectively defined by:

$$j_1(s_1, s_2) = J_1(\rho; u_\rho) \quad \text{for the first player} \quad (2)$$

$$j_2(s_1, s_2) = J_2(\rho; u_\rho) \quad \text{for the second one.} \quad (3)$$

The new situation introduced here is that each player's objective strongly depends on the other's choice. Instead of optimality, one should consider the notion of equilibrium, a joint choice of strategies on which the two players agree (in some sense).

In the framework of static games, which is our case, the most used ones are the so-called *Pareto* and *Nash* equilibria.

Pareto Fronts. Let us define the set

$$P = \{(j_1(s), j_2(s)); \quad \text{for all } s \in S_1 \times S_2\}.$$

Then, the Pareto Front P_F is the subset of all $(\bar{x}, \bar{y}) \in P$ such that

$$\{x < \bar{x}; y < \bar{y}\} \cap P = \emptyset.$$

Any strategy pair $\bar{s} = (\bar{s}_1, \bar{s}_2) \in S_1 \times S_2$ such that $(\bar{x}, \bar{y}) = (j_1(\bar{s}), j_2(\bar{s})) \in P_F$ is called a *Pareto optimum* (or equilibrium). The Pareto front is also known as

the set of non-dominated strategies (the meaning is obvious from the definition of the front).

For the multiobjective designer, the Pareto Front is the best information support that could help to select a particular strategy. However, it has two drawbacks: it is in general very expensive to compute (in theory, one should explore more or less the whole design space), and it is not associated to an equilibrium notion, which makes it useless in dynamic games. The notion of Nash – or non-cooperative – equilibrium overcomes these two drawbacks.

Nash Equilibrium. By definition, a strategy pair $s^* = (s_1^*, s_2^*) \in S_1 \times S_2$ is said to be a Nash equilibrium (NE) if it solves the two coupled problems:

$$j_1(s^*) = \min_{s_1 \in S_1} j_1(s_1, s_2^*) \quad (4)$$

$$j_2(s^*) = \min_{s_2 \in S_2} j_2(s_1^*, s_2). \quad (5)$$

From the definition above, we emphasize that Nash equilibria strongly depend on the splitting of $s \in S_1 \times S_2$ into two independent variables $s_1 \in S_1$ and $s_2 \in S_2$. This *distribution of territories* is often not unique, thus giving rise to the problem of optimal partition of the strategies (which e.g. ensures that a Nash equilibrium is located *on* the Pareto front).

Differently from the Nash case, Pareto equilibria give no particular role to the splitting of $s \in S_1 \times S_2$ into two independent variables since the Pareto front only depends on the values $(j_1(s), j_2(s))$.

The main interest of using a Nash equilibrium is that it can be numerically computed using descent algorithms, with a cost comparable to classical single objective minimization. However, there are also two major difficult questions to address : the proof of existence and the interpretation of NE. In particular, a Nash equilibrium could be located out of the Pareto Front (being then a dominated strategy), which sometimes means that an iterative -dynamic- game should be defined in order to converge to an acceptable equilibrium.

2.1 Modeling Tumoral Angiogenesis as a Topology Game

Angiogenesis is the biological process by which networks of blood vessels are initiated and proliferate towards a mature vasculature – local circulatory system. At early development and growth, angiogenesis is necessary to go from the embryonic vasculogenesis into a complete and mature blood circulatory system. Moreover, angiogenesis plays an important role in wound healing and tissue repairing. But from other part, angiogenesis plays also a pathological role, being a fundamental step in the growth of cancer tumors and in tumoral metastasis, the ability of tumor cells to develop in other places using the blood and lymphatic networks. Recently, oncologists have suggested that the use of inhibitors of angiogenesis, an approach that is often referred to as

anti-angiogenesis, could prove effective in cancer treatment. Combined with directly curative drugs, anti-angiogenic drugs are intended to efficiently stop the expansion of tumoral mass, forcing the tumor to dormancy or even regression.

We shall model angiogenesis and anti-angiogenesis processes as resulting from a mathematical game between two players : activators of angiogenesis, willing to provide the tumor with an efficient feeding network of blood vessels, and inhibitors, with a specific action on the tumor vasculature.

From the activators viewpoint, the biological tissue surrounding the tumor, and located between close existing vessels and the tumor is seen as a porous medium, defined by its porosity distribution. The latter is defined as a result of an interaction between activators and inhibitors. Activators would like to design the porosity in order to yield the minimal pressure drop. From the inhibitors viewpoint, the same biological medium is seen as a linear elastic continuum, defined by its material elasticity tensor. As for the porosity, the material properties are defined as a result of an interaction between activators and inhibitors. Inhibitors would like to design the material distribution in order to provide the matrix with the minimal mechanical compliance.

Mathematical Modeling. We make two assumptions on the respective objectives of the activators and of the inhibitors. *The first one is that activators monitor angiogenesis in order to provide the tumor with an optimal drainage mechanism.* Natural circulatory networks, including human vascular network are known to have arterial branchings optimal structure with respect to the maximal-drainage objective; evidence is provided by Schreiner [1] “Arterial branchings closely fulfill several ‘bifurcation rules’ which are deemed to optimize blood flow. The question is whether these local criteria in conjunction with a general optimization principle can explain the overall structure of an arterial tree.” Schreiner concludes in the cited study that “The comparison between the model and real coronary arterial trees shows good agreement regarding structural appearance, morphometric parameters, and pressure profiles.” *The second assumption we make is that inhibitors are used by the host tissue which is willing to keep its structural integrity as a way to fight against the tumor growth.* Indeed, this assumption seems to gain audience among biologists. Based on in vitro studies, Helmlinger et al. [2] demonstrated that solid stress inhibits tumor growth in vitro, regardless of host species, tissue of origin, or differentiation state, which made Roose et al. [3] suggest that “the host tissue provides resistance to tumor growth.”

A Porous Media Model for the Tumor. The extracellular matrix as well as the tumoral vasculature are seen as a porous medium, which occupies a volume $\Omega \subset \mathbb{R}^N$ ($N = 2$ or 3), with a variable permeability denoted by ρ , which lies

between the matrix permeability ρ_M and blood vessel permeability ρ_V . The simplest *effective* model for porous media is the following, also known as the D’Arcy Law, where the physical variable is pressure p :

$$\begin{cases} -div(\rho \nabla p) &= Q & \text{in } \Omega \\ \rho \frac{\partial p}{\partial n} &= \rho g & \text{over } \Gamma_V \\ \frac{\partial p}{\partial n} &= 0 & \text{over } \Gamma_N \\ p &= 0 & \text{over } \Gamma_T \end{cases} \tag{6}$$

The right-hand side Q represents a residual source of nutrients by diffusion through the host tissue, it is assumed to be negligible compared to the inward blood flow g . It should be noticed that we do not take into account what happens inside the tumor itself, considering only its boundary Γ_T as an outlet.

Obviously, the pressure field depends on the permeability distribution.

As mentioned before, *we postulate that angiogenesis provides the tumor with an optimal drainage mechanism, i.e.* with a permeability such that the tumor optimal blood network minimizes the averaged pressure drop.

The pressure drop denoted by $L_1(\rho; p)$ is given by the formula:

$$L_1(\rho; p) = \int_{\Omega} Qp \, dx + \int_{\Gamma_V} \rho g p \, ds$$

A Structural Model for the Extracellular Matrix. Now, one may also consider the host surrounding tissue as a continuum medium, let say a linear isotropic, nonhomogeneous, elastic material. This model is of course a coarse approximation of the actual mechanical behavior of the living tissues, which is rather of visco-elastic nature [4]. This medium is composed of healthy and degraded tissues. The degradation could be due to established vascularization or to an early enzyme’s action, like as the MMPs family. The elasticity tensor \mathbf{E} lies then (in a certain sense) between the degraded material tensor \mathbf{E}_D , and the original – sane – extracellular matrix tensor \mathbf{E}_M .

Conforming to the linear elasticity classical equilibrium equations, the displacement vector $\mathbf{u} = (u_j)$ solves

$$\begin{cases} -div(\mathbf{E}\epsilon(\mathbf{u})) &= \mathbf{b} & \text{in } \Omega \\ \mathbf{u} &= \mathbf{0} & \text{over } \Gamma_V \\ \mathbf{E}\epsilon(\mathbf{u}) \cdot \mathbf{n} &= \mathbf{0} & \text{over } \Gamma_N \\ \mathbf{E}\epsilon(\mathbf{u}) \cdot \mathbf{n} &= \mathbf{t} & \text{over } \Gamma_T \end{cases} \tag{7}$$

The strain tensor denoted by $\epsilon(u)$ is defined with obvious notations as

$$\epsilon(\mathbf{u})_{ij} = \frac{1}{2} \left(\frac{\partial u_i}{\partial x_j} + \frac{\partial u_j}{\partial x_i} \right).$$

The mechanical stress tensor is given by $\sigma(\mathbf{u}) = \mathbf{E}\epsilon(\mathbf{u})$.

The body forces – such as selfweight – are denoted by \mathbf{b} , and the normal tension which models the stress induced by the tumor growth is denoted by \mathbf{t} . The tissue is assumed to be clamped to the mother vessel Γ_V . A related model can be found in [5] where the authors study the stress induced during avascular tumor growth.

The displacement vector \mathbf{u} depends on the elasticity tensor \mathbf{E} . The latter itself depends on the interaction between activators and inhibitors of tissue degradation.

As said in the introductory section, we assume that the host tissue is willing to keep its integrity, by using all available factors it could control (one example is inhibitors of MMPs). In continuum mechanics, it is usual to consider that such goal is achieved by maximizing the stiffness, or equivalently, minimizing the compliance:

$$L_2(\mathbf{E}; \mathbf{u}) = \int_{\Omega} \mathbf{b} \cdot \mathbf{u} \, dx + \int_{\Gamma_T} \mathbf{t} \cdot \mathbf{u} \, ds.$$

The Nash Game. We consider a two-players static game of complete information. The two players are the Tumoral Angiogenic Factors (TAF) which control activators distribution, denoted by μ , and anti-Angiogenic Factors (aAF) which control inhibitors distribution, denoted by k .

Strategy spaces are defined as follows:

- (TAF) is equipped with a strategy space

$$S_1 = \{ \mu \in L^\infty(\Omega), \quad 0 \leq \mu \leq 1, \quad \int_{\Omega} \mu \, dx \leq \gamma_1 |\Omega| \}.$$

- (aAF) is equipped with a strategy space

$$S_2 = \{ k \in L^\infty(\Omega), \quad 0 \leq k \leq 1, \quad \int_{\Omega} k \, dx \leq \gamma_2 |\Omega| \}.$$

The constraints on the relative volume fractions express the fact that there is only a limited available amount of activators and inhibitors.

A simultaneous (or blind) choice of $(\mu; k)$ prompts an interaction between TAF and aAF, which is modeled as follows:

- Interaction Law: $\theta = \mu(1 - k)$,
- Permeability: $\rho = \rho(\mu; k) = \rho_M + (\rho_V - \rho_M)P(\theta)$,
- Elasticity tensor: $\mathbf{E} = \mathbf{E}(\mu; k) = \mathbf{E}_M + (\mathbf{E}_D - \mathbf{E}_M)P(\theta)$,

where $P(\theta)$ is the identity, an exact homogenization operator, or an interpolated SIMP-like (Solid Isotropic Material Penalization) operator, see Rozvany et al. [6].

To end with the definition of the game, objective or loss functions are defined respectively as:

$$\text{Pressure Drop} \quad j_1(\mu; k) = L_1(\rho; p) \text{ for player (TAF),} \quad (8)$$

$$\text{Mechanical Compliance} \quad j_2(\mu; k) = L_2(\mathbf{E}; \mathbf{u}) \text{ for player (aAF),} \quad (9)$$

where p is the pressure solution to the Darcy equation (6), and \mathbf{u} is the displacement vector solution to the elasticity equation (7).

Existence of a Nash Equilibrium. We consider the cases where either $P(\theta) = \theta$ or $P(\theta)$ is a restriction operator, i.e. $P(\theta) = g \circ S_R(\theta)$, with g being a convex function and S_R a linear compact filter, see [7] for details. We have the

THEOREM 1 *There exists a Nash equilibrium, i.e. a pair of strategies $(\mu^*, k^*) \in S_1 \times S_2$ such that*

$$\mu^* \text{ solves} \quad \min_{\mu \in S_1} j_1(\mu, k^*) \quad (10)$$

$$k^* \text{ solves} \quad \min_{k \in S_2} j_2(\mu^*, k). \quad (11)$$

Proof. Let us first notice that the strategy spaces S_1 and S_2 are convex and compact for the weak-star L^∞ topology. □

From one part, in case of $P(\theta) = \theta$ and since the functions j_1 and j_2 are the respective compliances of Darcy and Elasticity equations, it is well known that these functions can be expressed as supremum envelops of continuous *affine* functions with respect to respectively μ and to k , so these functions are convex and weak-star lower semicontinuous.

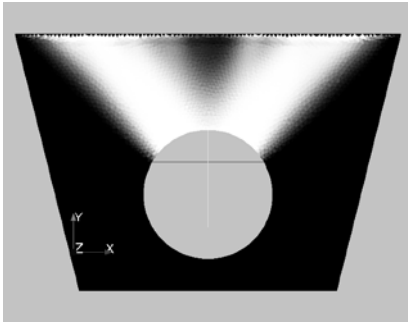
From another part, if $P(\theta)$ is a restriction operator, j_1 and j_2 can still be expressed as supremum envelops of continuous convex (but not necessarily affine) functions with respect to respectively μ and k . Convexity is preserved thanks to linearity of the filter, and to convexity of g . Compactness of the filter implies the weak-star lower semicontinuity of the objectives.

The assumptions are fulfilled in order to apply the Nash existence theorem, which yields the existence of a Nash equilibrium, see Aubin [8].

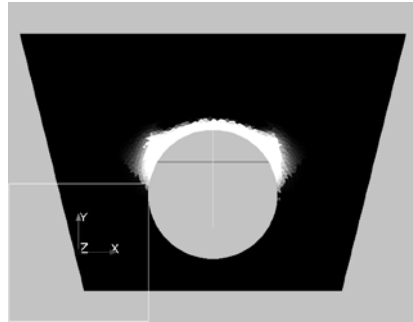
A Numerical Experiment. We consider the minimax (or duel) problem $j_2(\mu; k) = -j_1(\mu; k) = -L_1(\rho; p)$ which models a game where the first player aims to minimize the pressure drop, while on the contrary the second

one aims to maximize it (or, equivalently, wants to minimize the drainage of the network).

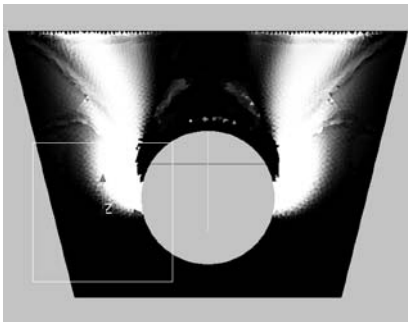
The case-study consists in a trapezium with an inlet in the upperside which models the source vessel, and a circular hole located at the center of the trapezium which models the tumour. The figures presented below show the evolution of the game, until a Nash equilibrium is reached.



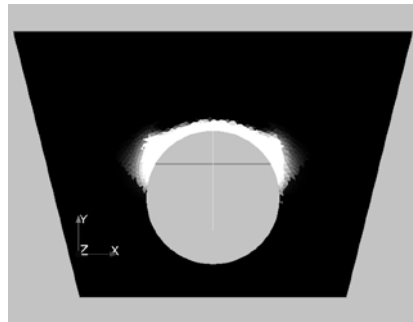
Density of activators, Nash iter = 1.



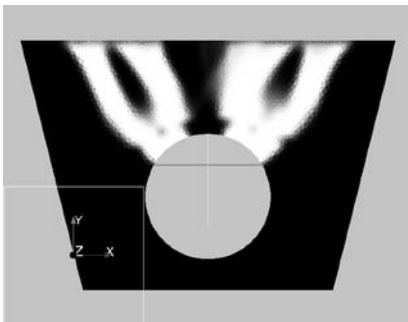
Density of inhibitors, Nash iter = 1.



Density of activators, Nash iter = 2.



Density of inhibitors, Nash iter = 2.



Nash Equilibrium Network $\rho(\mu^*, k^*)$.

Multiple channels arise as an equilibrium resulting from the game between activators and inhibitors.

REFERENCES

- [1] Schreiner, W. and Buxbaum, P.F., Computer-optimization of vascular trees, *IEEE Transactions on Biomedical Engineering*, 40(5), 482–491 (1993).
- [2] Helmlinger, G., Netti, P.A., Lichtenbeld, H.C., Melder, R.J. and Jain, R.K., Solid stress inhibits the growth of multicellular tumor spheroids, *Nature Biotechnology*, 15(8), 778–783 (1997).
- [3] Roose, T., Netti, P.A., Munn, L.L., Boucher, Y. and Jain, R.K., Solid stress generated by spheroid growth estimated using a linear poroelasticity model, *Microvascular Research*, 66, 204–212 (2003).
- [4] Fung, Y.C., *Biomechanics. Mechanical Properties of Living Tissues*, 2nd edn., Springer-Verlag, New York (1993).
- [5] Gibson, J.S., Jones, A.F., Byrne, H.M. and Dold, J.W., A mathematical model of the stress induced during avascular tumour growth, *J. Math. Biol.*, 40(6), 473–499 (2000).
- [6] Rozvany, T., Zhou, G.I.N. and Birker, M., Generalized shape optimization without homogenization, *Struct. Optim.*, 4, 250–254 (1992).
- [7] Borrvall, T. and Petersson, J., Topology optimization using regularized intermediate density control, *Comput. Methods Appl. Mech. Eng.*, 190(37–38), 4911–4928 (2001).
- [8] Aubin, J.P., *Mathematical Methods of Game and Economic Theory*, North-Holland, Amsterdam (1979).

COUPLING TOPOLOGICAL GRADIENT AND GAUSS–NEWTON METHOD

Jérôme Fehrenbach and Mohamed Masmoudi

Laboratoire MIP, CNRS-Université Paul Sabatier, Toulouse, France

Abstract: Topological asymptotic analysis is an emerging method that has been applied with success to shape optimization and shape inverse problems. However, it is not suitable for solving severely ill-posed inverse problems. It is a short term approach and it fails when applied to small inclusions detection in elastographic imaging.

We show in this paper that it is possible to solve this problem by coupling Gauss–Newton and topological gradient methods in a natural way. The data is the displacement under a small compression, only one component of the displacement is given. The inversion problem is solved in two steps. In a first step, we obtain a weight vector for the observations; this is performed by a dual Gauss–Newton method. The second step consists of computing the topological sensitivity relative to the insertion of an inclusion in the medium (a stiff disk), the cost function being weighted with the result of the first step. This method is applied to numerical experiments.

Keywords: Gauss–Newton method, topological gradient, inverse problem, elastography, medical imaging.

1. INTRODUCTION

Finding an optimal domain is equivalent to finding its characteristic function. At first sight this $0 - 1$ optimization problem is not differentiable, but it is possible to obtain the variation of a cost function when the characteristic function is switched from 0 to 1 or from 1 to 0 in a small region. It is called the topological gradient. It has been applied to shape optimization [7, 13, 18, 19] and to shape inverse problems [2, 9, 14, 17] giving very promising results. In comparison with relaxation methods (the characteristic function is replaced by a density function) the topological gradient can be seen as a regularization technique: it reduces the set of admissible solutions from $[0, 1]$ to $\{0, 1\}$.

Despite this nice property, the topological gradient fails when it is applied to small inclusions detection in elastographic imaging.

We show in this paper that it is possible to solve this difficult problem by coupling topological gradient and Gauss–Newton method.

The second basic idea of this paper is to start with uniform material property. A wrong initial guess does not help to find the solution. For this reason, short term approaches like the steepest descent method are not suitable for this kind of applications. It is also the case of conjugate gradient methods (Fletcher–Reeves and Polak–Ribiere) and BFGS [3], since they behave like the steepest descent method at the first iteration. We show in this paper that the first iteration of the gradient method creates inclusions on the boundary of the domain. This is equivalent to give a wrong initial guess for the remaining iterations. For this reason, our goal is to propose an algorithm having the capability to give a good localization of the inclusions at the first iteration.

We consider a plane stress model for a linear elastic medium. It has a uniform Poisson coefficient ν and its Young’s modulus takes two values, E in the background and KE in the inclusion, where $K \neq 1$ is called the contrast.

The data is the displacement under a small compression, only one component of the displacement is given (along the direction of compression), and the objective is to determine the location of the inclusions from these data.

Such an identification is of crucial importance in the medical imaging field. As a matter of fact, prostate or breast cancerous tumors are stiffer than the surroundings and Young’s modulus can be 4 to 10 or more times higher. Elastography is an ultrasonic imaging modality that provides an image (called elastogram) of the displacement of tissues after a small external compression [16]. A reliable detection of small inclusion of Young’s modulus using the analysis of elastograms would help early detection of cancers.

The paper is organized as follows: in Section 2 we present the direct and inverse problems of elasticity, in Section 3 we introduce the dual Gauss–Newton method and we show how to build weights for the residual vector. In Section 4 we estimate the topological gradient of the weighted cost function with respect to the insertion of a stiff inclusion, and in Section 5 we present numerical simulation results.

2. THE DIRECT AND INVERSE PROBLEMS

Let Ω be a 2D domain, its boundary $\partial\Omega$ is divided in two parts of positive measure: $\partial\Omega = \Gamma_N \cup \Gamma_D$. We consider $g \in H^{1/2}(\Gamma_N)$, $u_D \in H^{1/2}(\Gamma_D)$, $E \in L^\infty(\Omega)$ and $\nu \in \mathbf{R}$. The direct problem is (isotropic linear elasticity):

$$\begin{cases} \nabla \cdot \sigma(u) = 0 & \Omega \\ \sigma(u) \cdot n = g & \Gamma_N \\ u = u_D & \Gamma_D, \end{cases} \quad (1)$$

where

$$\sigma(u) = \frac{\nu E}{(1 + \nu)(1 - 2\nu)} \text{tr} \epsilon(u) I + \frac{E}{2(1 + \nu)} \epsilon(u)$$

is the stress tensor and $\epsilon(u) = \frac{1}{2}(\nabla u + \nabla u^T)$ is the linearized strain tensor. The solution u of (1) is the elastic displacement of the body Ω .

The variational formulation of this problem reads

$$\begin{cases} \text{find } u \in \mathcal{V} \text{ s.t.} \\ \forall v \in \mathcal{V} \quad a(u, v - u) = \ell(v - u), \end{cases} \tag{2}$$

where $\mathcal{V} = \{u \in H^1(\Omega)^2 \mid u|_{\Gamma_D} = u_D\}$,

$$a(u, v) = \int_{\Omega} \sigma(u) : \epsilon(v) \, dx \quad \text{and} \quad \ell(v) = \int_{\Gamma_N} g \cdot v \, dl.$$

The functions g and u_D , and the Poisson coefficient ν are assumed to be fixed. The solution u of (1) depends on the spatial distribution of Young’s modulus E , and the parameter-to-state map is defined by

$$\begin{aligned} U : L^\infty(\Omega) &\longrightarrow \mathcal{V}(\Omega) \\ E &\longmapsto u_E, \end{aligned}$$

where u_E is the solution of (1). It is proved in [6] that the parameter-to-state map U is differentiable, and has a compact differential, at every point where E is bounded below by a positive constant.

We consider also a continuous linear observation map $L : \mathcal{V} \rightarrow X$ where X is a Hilbert space. In the case of radial elastography (when the probe gives a radial image), the observation map consists of taking the radial component of a vector field.

The inverse problem is: given an observation, determine Young’s modulus distribution E . The data is denoted u_{obs} and it is the measurement estimation of Lu_E .

The inverse problem is

$$\min_E j_0(E) := \frac{1}{2} (\|LU(E) - u_{\text{obs}}\|^2).$$

It is highly ill-posed, the classical way to improve its stability is to add a Tikhonov regularization term [11], and look for the minimum of

$$j_\alpha(E) := \frac{1}{2} (\|LU(E) - u_{\text{obs}}\|^2 + \alpha \|E\|^2).$$

Among known techniques for minimizing the cost-function j_α in the context of elastography, let us mention the steepest descent method [15] and Gauss–Newton method [4–6, 10]. The topological sensitivity [1, 2, 7] of j_α with

respect to the insertion of an inclusion has also been considered in the frame of this work, but it does not give satisfying results.

These methods do not allow to find very small inclusions, we propose in the following to couple the Gauss–Newton and topological gradient methods.

3. GAUSS–NEWTON METHODS

In this section, we introduce the dual Gauss–Newton method, that will provide us with a weight vector for the observations.

3.1 Primal Gauss–Newton Method

After discretization, we keep the same notations of j, u_E, E, \dots . Then the cost function $j : \mathbf{R}^p \rightarrow \mathbf{R}$ is of the form

$$j_0(E) = \frac{1}{2} \|F(E)\|^2,$$

where $F : \mathbf{R}^p \rightarrow \mathbf{R}^n$ is the residual $F := LU(E) - u_{\text{obs}}$, it is a differentiable vector-valued function. For the sake of simplicity we do not consider the regularization term $\alpha \|E\|^2$.

The well-known Gauss–Newton algorithm for the minimization of j_0 is defined as follows:

$$\begin{cases} E_0 \text{ is given} \\ E_{k+1} = E_k + d_k, \text{ where} \\ DF^T(E_k)DF(E_k)d_k = -DF^T(E_k)F(E_k), \quad k \geq 0. \end{cases} \quad (3)$$

3.2 Dual Gauss–Newton Method

In our context, we have $p > n$, hence the matrix DF^TDF is singular, and the resolution of (3) requires the use of techniques [3, 11] like Levenberg–Marquardt, discrepancy principle, etc. There exists an alternative that we call the dual Gauss–Newton method [12]. When $p > n$ and DF is surjective, the matrix $DFDF^T$ is invertible, and the following problem:

$$\begin{cases} \min \|d\| & \text{s.t.} \\ DFd = -F \end{cases} \quad (4)$$

is equivalent to its Euler–Lagrange optimality condition

$$\begin{cases} DFDF^T\lambda = F \\ d = -DF^T\lambda. \end{cases} \quad (5)$$

A heuristic justification for the introduction of (4) is the following: the asymptotic expansion of F around E_k is

$$F(E_k + d) = F(E_k) + DF(E_k)d + R(E_k, d),$$

where the rest $R(E_k, d)$ is small: $\|R(E_k, d)\| = o(\|d\|)$. In order to cancel the two first terms, the descent direction has to satisfy $DF(E_k)d = -F(E_k)$. Among the affine vector space of solutions, taking d with minimal norm should make the rest $R(E_k, d)$ small.

In this paper we do not iterate the dual Gauss–Newton method, but we solve (5) once and use the vector $\lambda \in \mathbf{R}^n$ as a weight for the residual $LU(E) - u_{\text{obs}}$. More precisely, we are interested in the topological sensitivity of the following “weighted” cost function

$$j_W(E) = F(E)^T \lambda,$$

where

$$F(E) = LU(E) - u_{\text{obs}}. \quad (6)$$

This makes sense for the following reason: the descent direction given by the dual Gauss–Newton algorithm is $d = -DF^T \lambda = -D(F^T \lambda)$. Then $-d$ is the gradient of the cost function $F^T \lambda$, and it is natural to consider the topological variation of $F^T \lambda$. Notice that, thanks to the positivity of $DF DF^T$, the cost function $F^T \lambda$ is positive.

3.3 A Zero Memory Gauss–Newton Implementation

The linear system in (5) is solved using the conjugate gradient (CG) method. It gives a good approximation of λ after a few iterations because $DF DF^T$ is the discrete version of a compact operator: its eigenvalues tend rapidly towards zero. Each iteration of CG requires performing the product of $DF DF^T$ by a vector, this can be performed without computing and storing the whole Jacobian [6, 8]. More precisely, when a vector x is given, $y = DF DF^T x$ is computed in two steps: $t = DF^T x$ is evaluated by solving an adjoint equation, and $y = DF t$ is evaluated by solving a direct problem.

4. THE TOPOLOGICAL GRADIENT

In this section, we study the topological sensitivity of the cost function $J_W(u) := (Lu - u_{\text{obs}})^T \lambda$ with respect to the insertion at point x_0 of a very stiff disk. The Young’s modulus takes two values, 1 in the background and $K \gg 1$ in the inclusions.

The cost function J_W depends linearly on u , hence the adjoint is the solution $p \in \mathcal{V}_0$ of

$$\forall w \in \mathcal{V}_0, \quad a(w, p) = -(Lw)^T \lambda, \quad (7)$$

where $\mathcal{V}_0 = \{u \in H^1(\Omega) \mid u|_{\Gamma_D} = 0\}$.

The inclusion is εB where B is the unit disk. The first term in the asymptotic expansion of the cost function j_W is

$$\varepsilon^2 |B| \varepsilon(u) M \varepsilon(p),$$

where M is the elastic moment tensor of the disk inclusion. It is proved in [1] that the coefficients of the tensor M satisfy $m_{pq}^{ij} = m_{qp}^{ij}$, $m_{pq}^{ij} = m_{ij}^{pq}$ and have the following expression depending on the Lamé coefficients of the material $\lambda_0 = \frac{E\nu}{(1+\nu)(1-2\nu)}$ and $\mu_0 = \frac{E}{2(1+\nu)}$, and on $\kappa = \frac{\lambda_0 + 3\mu_0}{\lambda_0 + \mu_0}$:

$$m_{11}^{11} = m_{22}^{22} = (\lambda_0 + 2\mu_0)(K - 1) \frac{(\lambda_0 + \mu_0)(1 + 2\kappa K - K) + \mu_0(\kappa - 1)}{1 + K(\lambda_0 + \mu_0)(1 + \kappa K)},$$

$$m_{11}^{22} = (\lambda_0 + 2\mu_0) \frac{\lambda_0(K - 1)(1 + \kappa K) + \mu_0(K - 1)^2}{(\mu_0 + K(\lambda_0 + \mu_0))(1 + \kappa K)},$$

$$m_{12}^{12} = \frac{\mu_0(K - 1)(1 + \kappa)}{1 + \kappa K}.$$

The topological gradient of j at the point x_0 is:

$$T(x_0) = \varepsilon(u) M \varepsilon(p) + (K - 1) \sigma(u) : \varepsilon(p). \quad (8)$$

The procedure for calculating the topological sensitivity of J_W goes as follows:

1. The initial guess is $E \equiv 1$. Compute the direct state u ,
2. The weight λ is determined by solving

$$(DF DF^T + \alpha I) \lambda = F, \quad (9)$$

where α is a Tikhonov regularization parameter and $F = Lu - u_{\text{obs}}$,

3. compute the adjoint state p solution of (7),
4. compute $\varepsilon(u)$ and $\varepsilon(p)$,
5. at each point x_0 , determine the value of $T(x_0)$, using (8).

The higher isovalues of T give the location of the inclusion.

5. APPLICATION TO A NUMERICAL EXPERIMENT

A numerical simulation was conducted in order to simulate an in vitro experiment [20]. The method described in Section 4 is applied as follows. The domain Ω is an annulus, on the inner boundary Γ_D a uniform radial displacement is applied, and the outer boundary Γ_N is free, see Figure 1.

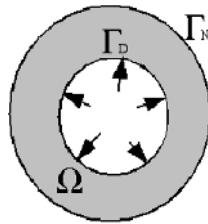


Figure 1. The domain Ω and the Dirichlet boundary.

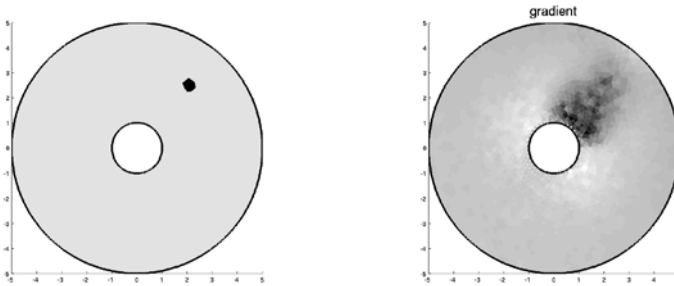


Figure 2. The inclusion (left); the gradient of j_0 (right).

The elasticity problem is discretized using P1 finite elements. It is implemented using Matlab and GetFem++, the mesh has 3077 elements and 1606 nodes. The total computation time for the procedure described above is about 1 minute on a desktop computer (Intel Pentium M processor, 1.6 GHz, 512Mo RAM).

The Poisson coefficient is $\nu = 0.45$. We insert 1 or 2 inclusions in the domain, where Young’s modulus is 4 times higher than in the background. The data are perturbed with 0.1% noise, and with 1% noise (white Gaussian noise). The weight λ is computed by solving (9).

Once the weight λ is known, the adjoint state p is computed. The topological gradient is computed with $K = 50$ (value of the contrast).

The results on different geometries are displayed in Figures 2–7.

The following observations can be made:

- (1) The gradient of the classical cost function $j_0 = \frac{1}{2} \|F\|^2$ gives no interesting information: its maximum is on the boundary, see Figure 2 right.
- (2) The topological gradient of j_0 gives no interesting results, see Figure 3 left.
- (3) The topological gradient of the weighted cost function $j_w = F^T \lambda$ detects the location of the inclusion with a reasonable accuracy, even for noisy measures (Figure 3 right, Figures 5 and 7).

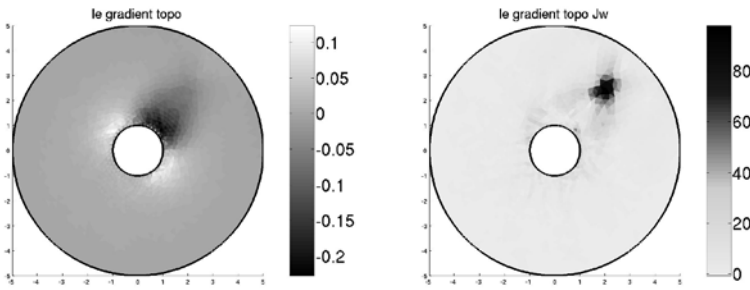


Figure 3. The topological gradient of j_0 with 0.1% noise (left); the topological gradient of j_W (right).

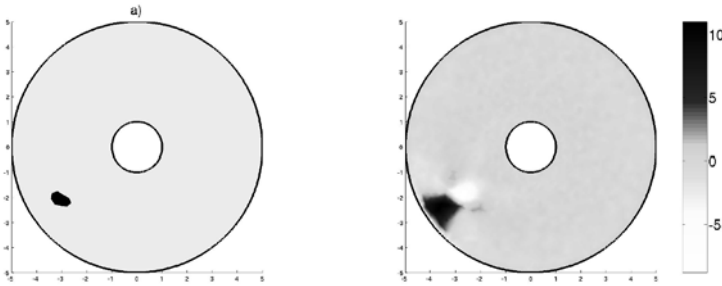


Figure 4. The inclusion (left); the weight λ for 0.1% noise (right).

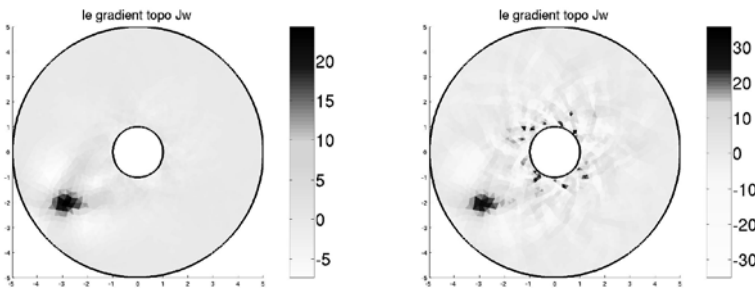


Figure 5. The topological gradient of j_W with 0.1% noise (left) and 1% noise (right).

- (4) Our method to determine the weight is justified *a-posteriori*: this weight gives more importance to the measures that are located “in front” and “behind” the inclusion (relatively to the compression direction), see Figures 4 right and 6 right. These are precisely the points where the displacements are the more affected by the inclusion, and the data are the more relevant to detect it. In the points “in front” of the inclusion, the

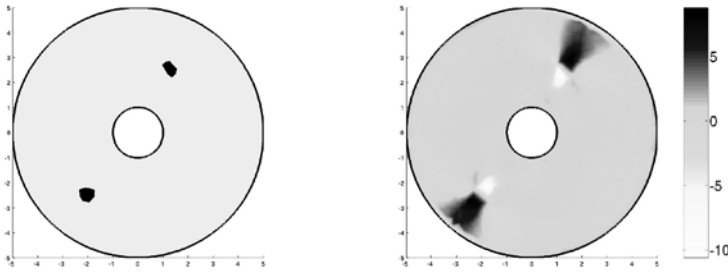


Figure 6. The inclusion (left); the weight λ for 0.1% noise (right).

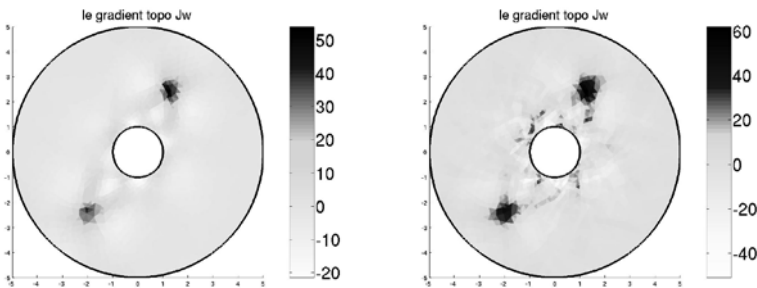


Figure 7. The topological gradient of j_W with 0.1% noise (left) and 1% noise (right).

weight takes negative values and this makes sense: at these points F also takes negative values, hence $F^T \lambda$ decreases when F gets closer to zero.

- (5) When more noise is added, the detection of inclusions becomes much less accurate.

6. CONCLUSIONS

We presented in this paper a method for the detection of small inclusions in an elastic medium, when the data is the radial displacement at each point. The first step consists of finding a weight for the measurements that gives importance to the data in the relevant zones, this weight is determined using a dual Gauss–Newton method and an efficient implementation. The second step consists of computing the topological sensitivity of the so weighted cost function.

Unlike classical methods, this method gives satisfying results for small inclusions.

ACKNOWLEDGEMENT

This work was supported in part by ACINIM-IMEG CNRS project (France).

REFERENCES

- [1] H. Ammari and H. Kang, *Reconstruction of Small Inclusion from Boundary Measurements*, Lecture Notes in Mathematics, Vol. 1846, Springer (2004).
- [2] S. Amstutz, I. Horchani and M. Masmoudi, Crack detection by the topological gradient method, *Control and Cybernetics*, 34(1), 81–101 (2005).
- [3] J. Dennis and R. Schnabel, *Numerical Methods for Unconstrained Optimization and Non-linear Equations*, Classics in Appl. Math. Sci., SIAM (1996).
- [4] M. Dooley, P. Meaney and J. Bamber, Evaluation of an iterative reconstruction method for quantitative elastography, *Phys. Med. Biol.*, 45, 1521–1540 (2000).
- [5] M. Dooley, S. Srinivasan, S. Pendergrass, Z. Wu and J. Ophir, Comparative evaluation of strain-based and model-based modulus elastography, *Ultrasound Med. Biol.*, 31(6), 787–802 (2005).
- [6] J. Fehrenbach, M. Masmoudi, R. Souchon and P. Trompette, Detection of inclusion of Young's modulus, preprint.
- [7] S. Garreau, Ph. Guillaume and M. Masmoudi, The topological asymptotic for PDE systems: The elasticity case, *SIAM J. Control. Optim.*, 39(6), 1756–1778 (2001).
- [8] A. Griewank, *Evaluating Derivatives, Principles and Techniques of Algorithmic Differentiation*, Frontiers in Applied Mathematics, SIAM (2000).
- [9] M. Hassine and M. Masmoudi, The topological asymptotic expansion for the Quasi-Stokes problem, *ESAIM Control Optim. Calc. Var.*, 10(4), 478–504 (2004).
- [10] F. Kallel and M. Bertrand, Tissue elasticity reconstruction using linear perturbation method, *IEEE Transactions on Medical Imaging*, 15(3), 299–313 (1996).
- [11] A. Kirsch, *An Introduction to the Mathematical Theory of Inverse Problems*, Springer (1996).
- [12] M. Masmoudi, Conception de circuits passifs de tres haute fidelite, *Matapli*, 31 (1990).
- [13] M. Masmoudi, *The Topological Asymptotic*, Computational Methods for Control Applications, International Series GAKUTO (2002).
- [14] M. Masmoudi, J. Pommier and B. Samet, The topological asymptotic expansion for the Maxwell equation and some applications, *Inverse Problems*, 21, 547–564 (2005).
- [15] A. Oberai, N. Gokhale and G. Feijoo, Solution of inverse problems in elasticity imaging using the adjoint method, *Inverse Problems*, 19, 297–313 (2003).
- [16] J. Ophir, I. Cespedes, H. Ponnekanti, Y. Yazdi and X. Li, Elastography: A quantitative method for imaging the elasticity of biological tissues, *Ultrasonic Imaging*, 13, 111–134 (1991).
- [17] B. Samet, S. Amstutz and M. Masmoudi, The topological asymptotic for the Helmholtz equation, *SIAM J. Control. Optim.*, 42(5), 1523–1544 (2003).
- [18] A. Schumacher, *Topologieoptimisierung von Bauteilstrukturen unter Verwendung von Lophpositionierungskriterien*, Thesis, Universität-Gesamthochschule-Siegen (1995).
- [19] J. Sokolowski and A. Zochowski, On the topological derivative in shape optimization, *SIAM J. Control Optim.*, 37, 1241–1272 (1999).
- [20] R. Souchon, O. Soualmi, M. Bertrand, J.Y. Chapelon, F. Kallel and J. Ophir, Ultrasonic elastography using sector scan imaging and a radial compression, *Ultrasonics*, 40(1–8), 867–871 (2002).

AUTHOR INDEX

- Abdalla, M.M., 169
Achtziger, W., 185, 413
Albin, N., 569
Allaire, G., 3, 137
Allinger, P., 229
Ananthasuresh, G.K., 455
Berggren, M., 301, 365
Borrvall, T., 551
Bourdin, B., 207
Bruns, T.E., 323
Burger, M., 181
Capdeboscq, Y., 197
Cardoso, E.L., 391
Chambolle, A., 207
Cheng, G., 107, 505
Cherkaev, A., 569
Cho, S., 217
Choi, K.K., 493
Clausen, P.M., 261
Dammann, B., 365
Diaz, A.R., 117
Dobson, D.C., 311
Du, J., 43
Dühring, M.B., 375
Duysinx, P., 23
Evgrafov, A., 559
Fehrenbach, J., 595
Feijóo, R.A., 469
Fleury, C., 23
Fonseca, J.S.O., 391
Gao, H., 439
Gaspar, Z., 77
Gei, M., 157
Gersborg-Hansen, A., 365
Gomes, A.A., 343
Graczykowski, C., 55
Guedes, J.M., 527
Guo, X., 439
Gürdal, Z., 169
Gutiérrez, S., 137
Ha, S.-H., 217
Habbal, A., 585
Hougaard, K., 127
Hyun, J.S., 251
Izui, K., 291
Jacobs, T., 23
Jang, G.W., 251
Jensen, J.S., 355, 387
Jog, C.S., 33
Jouve, F., 3
Kang, J., 493
Kawamoto, A., 185
Kim, C., 493
Kim, M.-G., 217
Kim, Y.Y., 251
Klarbring, A., 551
Kočvara, M., 403
Lewiński, T., 55
Lipka, A., 537
Lipton, R., 517
Logo, J., 77
Lubrano, E., 527
Lund, E., 89, 147
Masmoudi, M., 595
Matsui, K., 291, 333
Maute, K., 559
Mei, Y., 505
Moon, H., 493
Nam, S.J., 251
Nesi, V., 569
Neves, M.M., 99
Nishiwaki, S., 291, 333
Novotny, A.A., 469
Olhoff, N., 43
Padra, C., 469
Park, J.H., 251
Pedersen, C.B.W., 229
Pedersen, N.L., 67
Pedersen, P., 67
Pingen, G., 559
Pomezanski, V., 77
Prasad, J., 117
Querín, O.M., 77
Ramm, E., 537
Raulli, M., 277
Riishede, J., 127
Rodrigues, H.C., 527
Rovati, M., 157

- Rozvany, G.I.N., 77
Schramm, U., 239
Setoodeh, S., 169
Sigmund, O., 261, 355, 387
Silva, E.C.N., 291
Sokolowski, J., 479
Stainko, R., 181
Stegmann, J., 89, 147
Stingl, M., 403
Stolpe, M., 185
Stuebner, M., 517
Suleman, A., 343
Svanberg, K., 425
Taroco, E., 469
Terada, K., 291, 333
Turteltaub, S., 527
Van Miegroet, L., 23
Veber, D., 157
Wadbro, E., 301
Wang, B., 107
Wang, M.Y., 13
Wang, Semyung, 493
Wang, Shengyin, 13
Wang, X., 505
Werme, M., 425
Wiker, N., 551
Yoo, Y., 269
Yoon, G.H., 355
Yoshimura, M., 291
Zhou, M., 239
Zochowski, A., 479

SUBJECT INDEX

- 2D and 3D problems, 375
- 2D continuum, 67
- acoustic horn, 301
- acoustic-structure interaction, 355
- actuators, 291
- adjoint method, 527
- adjoint sensitivity analysis, 217
- aileron control reversal, 343
- analytical solutions, 77
- area-to-point flow, 551
- asymptotic expansion, 469, 479
- automatic design, 251
- bilevel programming, 413
- bi-material structures, 43
- bio-inspired mimetic, 439
- biomimetics, 169
- bistable mechanisms, 117
- bistable structures, 117
- bounds, 569
- branch and bound, 185
- CAD, 229
- CAE, 229
- cellular automata, 169
- cellular materials, 107, 537
- checkerboard control, 77
- compliant mechanisms, 117
- composite structures, 147
- COMSOL, 365
- concurrent design of materials and structures, 107
- contact problem, 479
- continuous modeling of amino acid types, 455
- Cosserat theory, 157
- coupled problems, 355
- Darcy flow, 551
- density distribution, 537
- density method, 261
- design, 239
- discrete material optimization, 147
- dispersion properties, 127
- dual algorithm, 33
- dynamics, 355
- efficiency, 301
- eigenvalue problems, 147
- elastography, 595
- electro-mechanical, 277
- energy functional, 479
- explicit boundary, 217
- feature-based, 505
- FEM, 365
- FEMLAB, 365
- finite deformation, 333
- finite element method, 291
- first order sensitivities, 425
- flaw tolerance, 439
- Floquet–Boch wave theory, 99
- fluid dynamics, 365
- fluids and mechanisms, 323
- Fourier series, 343
- free material, 67
- free material optimization, 403
- Gauss–Newton method, 595
- geometric nonlinearities, 217, 391
- geometry optimization, 413
- global optimization, 185
- gradient based topology optimization, 537
- H -measures, 137
- harmonic loading, 355
- heat dissipation, 107
- Helmholtz equation, 301, 375
- hierarchical method, 527
- homogenization, 137
- homogenization design method, 269, 333
- hybrid elements, 33
- hyper-optimality, 77
- impedance imaging, 197
- implicit representation, 505
- incompressibility, 261
- industrial applications, 229
- industrial integration, 229
- internal length scale, 157
- inverse folding, 455
- inverse problem, 595
- KKT-system, 181
- laminate, 89
- laminate design optimization, 147
- large scale optimization, 229
- lattice Boltzmann method, 559
- level set, 23

- level set method, 3, 13, 217, 343
- linearized elastic stability, 99
- local stress constraints, 181
- magnetic fields, 269
- material design, 439
- material distribution, 301
- mechanism design, 185
- medical imaging, 595
- MEMS, 277
- Michell-like cantilevers, 55
- micropolar continua, 157
- minimum weight problem, 55
- mixed formulation, 261, 355
- mode matching, 311
- modified density approach, 269
- morphing airfoil, 343
- multicomponent optimal composites, 569
- multi-physics, 493
- multi-physics optimal design, 207
- multiscale optimization, 527
- multi-tubular heat exchanger, 107
- multiwell variational problem, 569
- Nash equilibrium, 585
- Navier–Stokes flow, 559
- non-gradient methods, 77
- non-matching meshes, 277
- one-shot methods, 181
- optical fibres, 127
- optimal design, 67, 137, 311, 479
- optimal structural design, 517
- optimization, 89, 439
- Padé expansions, 375
- parameter design, 13
- penalization, 67, 89
- penalty methods, 323
- perimeter penalization, 207
- periodic structures, 117
- phase-field, 207
- phase-field methods, 181
- piezoelectric actuators, 391
- pointwise stress constraints, 517
- polarization tensors, 197
- polyconvexity, 569
- pressure loads, 261
- protein sequence design, 455
- R-function, 505
- radial basis functions, 13
- radiation properties, 301
- rank-one convexity, 569
- reliability, 493
- rigid link mechanism, 251
- room acoustics, 375
- semidefinite programming, 403
- sensitivity analysis, 365
- sensors, 291
- sequential integer linear programming, 425
- shape matching, 505
- shape optimization, 3, 13, 23, 217, 479
- shape sensitivity analysis, 469
- shell, 89
- SIMP, 77, 261
- smart structures, 291
- software, 239
- solid isotropic material with penalization, 269
- sound power radiation, 43
- spring-connected blocks, 251
- static games, 585
- stiffness optimization, 185
- Stokes flow, 551
- stress, 89
- stress constraints, 425
- structural-acoustical analysis, 43
- structural optimization, 569
- structures, 323
- synthesis, 251
- three-dimensional structures, 33
- tileable structures, 117
- time-harmonic loading, 43
- topological derivative, 217, 469, 479, 505
- topological gradient, 3, 595
- topology benchmarks, 77
- topology design, 43
- topology optimization, 3, 13, 23, 55, 77, 99, 107, 127, 147, 157, 169, 181, 239, 269, 277, 291, 301, 323, 333, 343, 365, 375, 387, 391, 425, 455, 493, 505, 551, 559, 585
- transient optimization, 527
- trusses, 67
- truss optimization, 413
- two-scale periodic materials, 99
- uncertainty, 493
- velocity extension method, 217
- vibration, 291
- waveguide coupler, 311
- wave-propagation, 387
- X-FEM, 23

Mechanics

SOLID MECHANICS AND ITS APPLICATIONS

Series Editor: G.M.L. Gladwell

Aims and Scope of the Series

The fundamental questions arising in mechanics are: *Why?*, *How?*, and *How much?* The aim of this series is to provide lucid accounts written by authoritative researchers giving vision and insight in answering these questions on the subject of mechanics as it relates to solids. The scope of the series covers the entire spectrum of solid mechanics. Thus it includes the foundation of mechanics; variational formulations; computational mechanics; statics, kinematics and dynamics of rigid and elastic bodies; vibrations of solids and structures; dynamical systems and chaos; the theories of elasticity, plasticity and viscoelasticity; composite materials; rods, beams, shells and membranes; structural control and stability; soils, rocks and geomechanics; fracture; tribology; experimental mechanics; biomechanics and machine design.

1. R.T. Haftka, Z. Gürdal and M.P. Kamat: *Elements of Structural Optimization*. 2nd rev.ed., 1990
ISBN 0-7923-0608-2
2. J.J. Kalker: *Three-Dimensional Elastic Bodies in Rolling Contact*. 1990 ISBN 0-7923-0712-7
3. P. Karasudhi: *Foundations of Solid Mechanics*. 1991 ISBN 0-7923-0772-0
4. *Not published*
5. *Not published*.
6. J.F. Doyle: *Static and Dynamic Analysis of Structures. With an Emphasis on Mechanics and Computer Matrix Methods*. 1991 ISBN 0-7923-1124-8; Pb 0-7923-1208-2
7. O.O. Ochoa and J.N. Reddy: *Finite Element Analysis of Composite Laminates*.
ISBN 0-7923-1125-6
8. M.H. Aliabadi and D.P. Rooke: *Numerical Fracture Mechanics*. ISBN 0-7923-1175-2
9. J. Angeles and C.S. López-Cajún: *Optimization of Cam Mechanisms*. 1991
ISBN 0-7923-1355-0
10. D.E. Grierson, A. Franchi and P. Riva (eds.): *Progress in Structural Engineering*. 1991
ISBN 0-7923-1396-8
11. R.T. Haftka and Z. Gürdal: *Elements of Structural Optimization*. 3rd rev. and exp. ed. 1992
ISBN 0-7923-1504-9; Pb 0-7923-1505-7
12. J.R. Barber: *Elasticity*. 1992 ISBN 0-7923-1609-6; Pb 0-7923-1610-X
13. H.S. Tzou and G.L. Anderson (eds.): *Intelligent Structural Systems*. 1992
ISBN 0-7923-1920-6
14. E.E. Gdoutos: *Fracture Mechanics. An Introduction*. 1993 ISBN 0-7923-1932-X
15. J.P. Ward: *Solid Mechanics. An Introduction*. 1992 ISBN 0-7923-1949-4
16. M. Farshad: *Design and Analysis of Shell Structures*. 1992 ISBN 0-7923-1950-8
17. H.S. Tzou and T. Fukuda (eds.): *Precision Sensors, Actuators and Systems*. 1992
ISBN 0-7923-2015-8
18. J.R. Vinson: *The Behavior of Shells Composed of Isotropic and Composite Materials*. 1993
ISBN 0-7923-2113-8
19. H.S. Tzou: *Piezoelectric Shells. Distributed Sensing and Control of Continua*. 1993
ISBN 0-7923-2186-3
20. W. Schiehlen (ed.): *Advanced Multibody System Dynamics. Simulation and Software Tools*.
1993 ISBN 0-7923-2192-8
21. C.-W. Lee: *Vibration Analysis of Rotors*. 1993 ISBN 0-7923-2300-9
22. D.R. Smith: *An Introduction to Continuum Mechanics*. 1993 ISBN 0-7923-2454-4
23. G.M.L. Gladwell: *Inverse Problems in Scattering. An Introduction*. 1993 ISBN 0-7923-2478-1

Mechanics

SOLID MECHANICS AND ITS APPLICATIONS

Series Editor: G.M.L. Gladwell

24. G. Prathap: *The Finite Element Method in Structural Mechanics*. 1993 ISBN 0-7923-2492-7
25. J. Herskovits (ed.): *Advances in Structural Optimization*. 1995 ISBN 0-7923-2510-9
26. M.A. González-Palacios and J. Angeles: *Cam Synthesis*. 1993 ISBN 0-7923-2536-2
27. W.S. Hall: *The Boundary Element Method*. 1993 ISBN 0-7923-2580-X
28. J. Angeles, G. Hommel and P. Kovács (eds.): *Computational Kinematics*. 1993
ISBN 0-7923-2585-0
29. A. Curnier: *Computational Methods in Solid Mechanics*. 1994 ISBN 0-7923-2761-6
30. D.A. Hills and D. Nowell: *Mechanics of Fretting Fatigue*. 1994 ISBN 0-7923-2866-3
31. B. Tabarrok and F.P.J. Rimrott: *Variational Methods and Complementary Formulations in Dynamics*. 1994 ISBN 0-7923-2923-6
32. E.H. Dowell (ed.), E.F. Crawley, H.C. Curtiss Jr., D.A. Peters, R. H. Scanlan and F. Sisto: *A Modern Course in Aeroelasticity*. Third Revised and Enlarged Edition. 1995
ISBN 0-7923-2788-8; Pb: 0-7923-2789-6
33. A. Preumont: *Random Vibration and Spectral Analysis*. 1994 ISBN 0-7923-3036-6
34. J.N. Reddy (ed.): *Mechanics of Composite Materials*. Selected works of Nicholas J. Pagano.
1994 ISBN 0-7923-3041-2
35. A.P.S. Selvadurai (ed.): *Mechanics of Poroelastic Media*. 1996 ISBN 0-7923-3329-2
36. Z. Mróz, D. Weichert, S. Dorosz (eds.): *Inelastic Behaviour of Structures under Variable Loads*. 1995 ISBN 0-7923-3397-7
37. R. Pyrz (ed.): *IUTAM Symposium on Microstructure-Property Interactions in Composite Materials*. Proceedings of the IUTAM Symposium held in Aalborg, Denmark. 1995
ISBN 0-7923-3427-2
38. M.I. Friswell and J.E. Mottershead: *Finite Element Model Updating in Structural Dynamics*.
1995 ISBN 0-7923-3431-0
39. D.F. Parker and A.H. England (eds.): *IUTAM Symposium on Anisotropy, Inhomogeneity and Nonlinearity in Solid Mechanics*. Proceedings of the IUTAM Symposium held in Nottingham,
U.K. 1995 ISBN 0-7923-3594-5
40. J.-P. Merlet and B. Ravani (eds.): *Computational Kinematics '95*. 1995 ISBN 0-7923-3673-9
41. L.P. Lebedev, I.I. Vorovich and G.M.L. Gladwell: *Functional Analysis*. Applications in Mechan-
ics and Inverse Problems. 1996 ISBN 0-7923-3849-9
42. J. Menčík: *Mechanics of Components with Treated or Coated Surfaces*. 1996
ISBN 0-7923-3700-X
43. D. Bestle and W. Schiehlen (eds.): *IUTAM Symposium on Optimization of Mechanical Systems*.
Proceedings of the IUTAM Symposium held in Stuttgart, Germany. 1996
ISBN 0-7923-3830-8
44. D.A. Hills, P.A. Kelly, D.N. Dai and A.M. Korsunsky: *Solution of Crack Problems*. The
Distributed Dislocation Technique. 1996 ISBN 0-7923-3848-0
45. V.A. Squire, R.J. Hosking, A.D. Kerr and P.J. Langhorne: *Moving Loads on Ice Plates*. 1996
ISBN 0-7923-3953-3
46. A. Pineau and A. Zaoui (eds.): *IUTAM Symposium on Micromechanics of Plasticity and
Damage of Multiphase Materials*. Proceedings of the IUTAM Symposium held in Sèvres,
Paris, France. 1996 ISBN 0-7923-4188-0
47. A. Naess and S. Krenk (eds.): *IUTAM Symposium on Advances in Nonlinear Stochastic
Mechanics*. Proceedings of the IUTAM Symposium held in Trondheim, Norway. 1996
ISBN 0-7923-4193-7
48. D. İeşan and A. Scalia: *Thermoelastic Deformations*. 1996 ISBN 0-7923-4230-5

Mechanics

SOLID MECHANICS AND ITS APPLICATIONS

Series Editor: G.M.L. Gladwell

49. J.R. Willis (ed.): *IUTAM Symposium on Nonlinear Analysis of Fracture*. Proceedings of the IUTAM Symposium held in Cambridge, U.K. 1997 ISBN 0-7923-4378-6
50. A. Preumont: *Vibration Control of Active Structures*. An Introduction. 1997 ISBN 0-7923-4392-1
51. G.P. Cherepanov: *Methods of Fracture Mechanics: Solid Matter Physics*. 1997 ISBN 0-7923-4408-1
52. D.H. van Campen (ed.): *IUTAM Symposium on Interaction between Dynamics and Control in Advanced Mechanical Systems*. Proceedings of the IUTAM Symposium held in Eindhoven, The Netherlands. 1997 ISBN 0-7923-4429-4
53. N.A. Fleck and A.C.F. Cocks (eds.): *IUTAM Symposium on Mechanics of Granular and Porous Materials*. Proceedings of the IUTAM Symposium held in Cambridge, U.K. 1997 ISBN 0-7923-4553-3
54. J. Roorda and N.K. Srivastava (eds.): *Trends in Structural Mechanics*. Theory, Practice, Education. 1997 ISBN 0-7923-4603-3
55. Yu.A. Mitropolskii and N. Van Dao: *Applied Asymptotic Methods in Nonlinear Oscillations*. 1997 ISBN 0-7923-4605-X
56. C. Guedes Soares (ed.): *Probabilistic Methods for Structural Design*. 1997 ISBN 0-7923-4670-X
57. D. François, A. Pineau and A. Zaoui: *Mechanical Behaviour of Materials*. Volume I: Elasticity and Plasticity. 1998 ISBN 0-7923-4894-X
58. D. François, A. Pineau and A. Zaoui: *Mechanical Behaviour of Materials*. Volume II: Viscoplasticity, Damage, Fracture and Contact Mechanics. 1998 ISBN 0-7923-4895-8
59. L.T. Tenek and J. Argyris: *Finite Element Analysis for Composite Structures*. 1998 ISBN 0-7923-4899-0
60. Y.A. Bahei-El-Din and G.J. Dvorak (eds.): *IUTAM Symposium on Transformation Problems in Composite and Active Materials*. Proceedings of the IUTAM Symposium held in Cairo, Egypt. 1998 ISBN 0-7923-5122-3
61. I.G. Goryacheva: *Contact Mechanics in Tribology*. 1998 ISBN 0-7923-5257-2
62. O.T. Bruhns and E. Stein (eds.): *IUTAM Symposium on Micro- and Macrostructural Aspects of Thermoplasticity*. Proceedings of the IUTAM Symposium held in Bochum, Germany. 1999 ISBN 0-7923-5265-3
63. F.C. Moon: *IUTAM Symposium on New Applications of Nonlinear and Chaotic Dynamics in Mechanics*. Proceedings of the IUTAM Symposium held in Ithaca, NY, USA. 1998 ISBN 0-7923-5276-9
64. R. Wang: *IUTAM Symposium on Rheology of Bodies with Defects*. Proceedings of the IUTAM Symposium held in Beijing, China. 1999 ISBN 0-7923-5297-1
65. Yu.I. Dimitrienko: *Thermomechanics of Composites under High Temperatures*. 1999 ISBN 0-7923-4899-0
66. P. Argoul, M. Frémond and Q.S. Nguyen (eds.): *IUTAM Symposium on Variations of Domains and Free-Boundary Problems in Solid Mechanics*. Proceedings of the IUTAM Symposium held in Paris, France. 1999 ISBN 0-7923-5450-8
67. F.J. Fahy and W.G. Price (eds.): *IUTAM Symposium on Statistical Energy Analysis*. Proceedings of the IUTAM Symposium held in Southampton, U.K. 1999 ISBN 0-7923-5457-5
68. H.A. Mang and F.G. Rammerstorfer (eds.): *IUTAM Symposium on Discretization Methods in Structural Mechanics*. Proceedings of the IUTAM Symposium held in Vienna, Austria. 1999 ISBN 0-7923-5591-1

Mechanics

SOLID MECHANICS AND ITS APPLICATIONS

Series Editor: G.M.L. Gladwell

69. P. Pedersen and M.P. Bendsøe (eds.): *IUTAM Symposium on Synthesis in Bio Solid Mechanics*. Proceedings of the IUTAM Symposium held in Copenhagen, Denmark. 1999
ISBN 0-7923-5615-2
70. S.K. Agrawal and B.C. Fabien: *Optimization of Dynamic Systems*. 1999
ISBN 0-7923-5681-0
71. A. Carpinteri: *Nonlinear Crack Models for Nonmetallic Materials*. 1999
ISBN 0-7923-5750-7
72. F. Pfeifer (ed.): *IUTAM Symposium on Unilateral Multibody Contacts*. Proceedings of the IUTAM Symposium held in Munich, Germany. 1999
ISBN 0-7923-6030-3
73. E. Lavendelis and M. Zagrzhvsky (eds.): *IUTAM/IFToMM Symposium on Synthesis of Non-linear Dynamical Systems*. Proceedings of the IUTAM/IFToMM Symposium held in Riga, Latvia. 2000
ISBN 0-7923-6106-7
74. J.-P. Merlet: *Parallel Robots*. 2000
ISBN 0-7923-6308-6
75. J.T. Pindera: *Techniques of Tomographic Isodyne Stress Analysis*. 2000
ISBN 0-7923-6388-4
76. G.A. Maugin, R. Drouot and F. Sidoroff (eds.): *Continuum Thermomechanics*. The Art and Science of Modelling Material Behaviour. 2000
ISBN 0-7923-6407-4
77. N. Van Dao and E.J. Kreuzer (eds.): *IUTAM Symposium on Recent Developments in Non-linear Oscillations of Mechanical Systems*. 2000
ISBN 0-7923-6470-8
78. S.D. Akbarov and A.N. Guz: *Mechanics of Curved Composites*. 2000
ISBN 0-7923-6477-5
79. M.B. Rubin: *Cosserat Theories: Shells, Rods and Points*. 2000
ISBN 0-7923-6489-9
80. S. Pellegrino and S.D. Guest (eds.): *IUTAM-IASS Symposium on Deployable Structures: Theory and Applications*. Proceedings of the IUTAM-IASS Symposium held in Cambridge, U.K., 6–9 September 1998. 2000
ISBN 0-7923-6516-X
81. A.D. Rosato and D.L. Blackmore (eds.): *IUTAM Symposium on Segregation in Granular Flows*. Proceedings of the IUTAM Symposium held in Cape May, NJ, U.S.A., June 5–10, 1999. 2000
ISBN 0-7923-6547-X
82. A. Lagarde (ed.): *IUTAM Symposium on Advanced Optical Methods and Applications in Solid Mechanics*. Proceedings of the IUTAM Symposium held in Futuroscope, Poitiers, France, August 31–September 4, 1998. 2000
ISBN 0-7923-6604-2
83. D. Weichert and G. Maier (eds.): *Inelastic Analysis of Structures under Variable Loads*. Theory and Engineering Applications. 2000
ISBN 0-7923-6645-X
84. T.-J. Chuang and J.W. Rudnicki (eds.): *Multiscale Deformation and Fracture in Materials and Structures*. The James R. Rice 60th Anniversary Volume. 2001
ISBN 0-7923-6718-9
85. S. Narayanan and R.N. Iyengar (eds.): *IUTAM Symposium on Nonlinearity and Stochastic Structural Dynamics*. Proceedings of the IUTAM Symposium held in Madras, Chennai, India, 4–8 January 1999
ISBN 0-7923-6733-2
86. S. Murakami and N. Ohno (eds.): *IUTAM Symposium on Creep in Structures*. Proceedings of the IUTAM Symposium held in Nagoya, Japan, 3-7 April 2000. 2001
ISBN 0-7923-6737-5
87. W. Ehlers (ed.): *IUTAM Symposium on Theoretical and Numerical Methods in Continuum Mechanics of Porous Materials*. Proceedings of the IUTAM Symposium held at the University of Stuttgart, Germany, September 5-10, 1999. 2001
ISBN 0-7923-6766-9
88. D. Durban, D. Givoli and J.G. Simmonds (eds.): *Advances in the Mechanis of Plates and Shells The Avinoam Libai Anniversary Volume*. 2001
ISBN 0-7923-6785-5
89. U. Gabbert and H.-S. Tzou (eds.): *IUTAM Symposium on Smart Structures and Structonic Systems*. Proceedings of the IUTAM Symposium held in Magdeburg, Germany, 26–29 September 2000. 2001
ISBN 0-7923-6968-8

Mechanics

SOLID MECHANICS AND ITS APPLICATIONS

Series Editor: G.M.L. Gladwell

90. Y. Ivanov, V. Cheshkov and M. Natova: *Polymer Composite Materials – Interface Phenomena & Processes*. 2001 ISBN 0-7923-7008-2
91. R.C. McPhedran, L.C. Botten and N.A. Nicorovici (eds.): *IUTAM Symposium on Mechanical and Electromagnetic Waves in Structured Media*. Proceedings of the IUTAM Symposium held in Sydney, NSW, Australia, 18-22 Januari 1999. 2001 ISBN 0-7923-7038-4
92. D.A. Sotiropoulos (ed.): *IUTAM Symposium on Mechanical Waves for Composite Structures Characterization*. Proceedings of the IUTAM Symposium held in Chania, Crete, Greece, June 14-17, 2000. 2001 ISBN 0-7923-7164-X
93. V.M. Alexandrov and D.A. Pozharskii: *Three-Dimensional Contact Problems*. 2001 ISBN 0-7923-7165-8
94. J.P. Dempsey and H.H. Shen (eds.): *IUTAM Symposium on Scaling Laws in Ice Mechanics and Ice Dynamics*. Proceedings of the IUTAM Symposium held in Fairbanks, Alaska, U.S.A., 13-16 June 2000. 2001 ISBN 1-4020-0171-1
95. U. Kirsch: *Design-Oriented Analysis of Structures. A Unified Approach*. 2002 ISBN 1-4020-0443-5
96. A. Preumont: *Vibration Control of Active Structures. An Introduction (2nd Edition)*. 2002 ISBN 1-4020-0496-6
97. B.L. Karihaloo (ed.): *IUTAM Symposium on Analytical and Computational Fracture Mechanics of Non-Homogeneous Materials*. Proceedings of the IUTAM Symposium held in Cardiff, U.K., 18-22 June 2001. 2002 ISBN 1-4020-0510-5
98. S.M. Han and H. Benaroya: *Nonlinear and Stochastic Dynamics of Compliant Offshore Structures*. 2002 ISBN 1-4020-0573-3
99. A.M. Linkov: *Boundary Integral Equations in Elasticity Theory*. 2002 ISBN 1-4020-0574-1
100. L.P. Lebedev, I.I. Vorovich and G.M.L. Gladwell: *Functional Analysis. Applications in Mechanics and Inverse Problems (2nd Edition)*. 2002 ISBN 1-4020-0667-5; Pb: 1-4020-0756-6
101. Q.P. Sun (ed.): *IUTAM Symposium on Mechanics of Martensitic Phase Transformation in Solids*. Proceedings of the IUTAM Symposium held in Hong Kong, China, 11-15 June 2001. 2002 ISBN 1-4020-0741-8
102. M.L. Munjal (ed.): *IUTAM Symposium on Designing for Quietness*. Proceedings of the IUTAM Symposium held in Bangkok, India, 12-14 December 2000. 2002 ISBN 1-4020-0765-5
103. J.A.C. Martins and M.D.P. Monteiro Marques (eds.): *Contact Mechanics*. Proceedings of the 3rd Contact Mechanics International Symposium, Praia da Consolação, Peniche, Portugal, 17-21 June 2001. 2002 ISBN 1-4020-0811-2
104. H.R. Drew and S. Pellegrino (eds.): *New Approaches to Structural Mechanics, Shells and Biological Structures*. 2002 ISBN 1-4020-0862-7
105. J.R. Vinson and R.L. Sierakowski: *The Behavior of Structures Composed of Composite Materials*. Second Edition. 2002 ISBN 1-4020-0904-6
106. Not yet published.
107. J.R. Barber: *Elasticity*. Second Edition. 2002 ISBN Hb 1-4020-0964-X; Pb 1-4020-0966-6
108. C. Miehe (ed.): *IUTAM Symposium on Computational Mechanics of Solid Materials at Large Strains*. Proceedings of the IUTAM Symposium held in Stuttgart, Germany, 20-24 August 2001. 2003 ISBN 1-4020-1170-9

Mechanics

SOLID MECHANICS AND ITS APPLICATIONS

Series Editor: G.M.L. Gladwell

109. P. Ståhle and K.G. Sundin (eds.): *IUTAM Symposium on Field Analyses for Determination of Material Parameters – Experimental and Numerical Aspects*. Proceedings of the IUTAM Symposium held in Abisko National Park, Kiruna, Sweden, July 31 – August 4, 2000. 2003
ISBN 1-4020-1283-7
110. N. Sri Namachchivaya and Y.K. Lin (eds.): *IUTAM Symposium on Nonlinear Stochastic Dynamics*. Proceedings of the IUTAM Symposium held in Monticello, IL, USA, 26 – 30 August, 2000. 2003
ISBN 1-4020-1471-6
111. H. Sobieckzky (ed.): *IUTAM Symposium Transsonicum IV*. Proceedings of the IUTAM Symposium held in Göttingen, Germany, 2–6 September 2002, 2003
ISBN 1-4020-1608-5
112. J.-C. Samin and P. Fiset: *Symbolic Modeling of Multibody Systems*. 2003
ISBN 1-4020-1629-8
113. A.B. Movchan (ed.): *IUTAM Symposium on Asymptotics, Singularities and Homogenisation in Problems of Mechanics*. Proceedings of the IUTAM Symposium held in Liverpool, United Kingdom, 8-11 July 2002. 2003
ISBN 1-4020-1780-4
114. S. Ahzi, M. Cherkaoui, M.A. Khaleel, H.M. Zbib, M.A. Zikry and B. LaMatina (eds.): *IUTAM Symposium on Multiscale Modeling and Characterization of Elastic-Inelastic Behavior of Engineering Materials*. Proceedings of the IUTAM Symposium held in Marrakech, Morocco, 20-25 October 2002. 2004
ISBN 1-4020-1861-4
115. H. Kitagawa and Y. Shibutani (eds.): *IUTAM Symposium on Mesoscopic Dynamics of Fracture Process and Materials Strength*. Proceedings of the IUTAM Symposium held in Osaka, Japan, 6-11 July 2003. Volume in celebration of Professor Kitagawa's retirement. 2004
ISBN 1-4020-2037-6
116. E.H. Dowell, R.L. Clark, D. Cox, H.C. Curtiss, Jr., K.C. Hall, D.A. Peters, R.H. Scanlan, E. Simiu, F. Sisto and D. Tang: *A Modern Course in Aeroelasticity*. 4th Edition, 2004
ISBN 1-4020-2039-2
117. T. Burczyński and A. Osyczka (eds.): *IUTAM Symposium on Evolutionary Methods in Mechanics*. Proceedings of the IUTAM Symposium held in Cracow, Poland, 24-27 September 2002. 2004
ISBN 1-4020-2266-2
118. D. Ieşan: *Thermoelastic Models of Continua*. 2004
ISBN 1-4020-2309-X
119. G.M.L. Gladwell: *Inverse Problems in Vibration*. Second Edition. 2004
ISBN 1-4020-2670-6
120. J.R. Vinson: *Plate and Panel Structures of Isotropic, Composite and Piezoelectric Materials, Including Sandwich Construction*. 2005
ISBN 1-4020-3110-6
121. *Forthcoming*
122. G. Rega and F. Vestroni (eds.): *IUTAM Symposium on Chaotic Dynamics and Control of Systems and Processes in Mechanics*. Proceedings of the IUTAM Symposium held in Rome, Italy, 8–13 June 2003. 2005
ISBN 1-4020-3267-6
123. E.E. Gdoutos: *Fracture Mechanics. An Introduction. 2nd edition*. 2005
ISBN 1-4020-3267-6
124. M.D. Gilchrist (ed.): *IUTAM Symposium on Impact Biomechanics from Fundamental Insights to Applications*. 2005
ISBN 1-4020-3795-3
125. J.M. Huyghe, P.A.C. Raats and S. C. Cowin (eds.): *IUTAM Symposium on Physicochemical and Electromechanical Interactions in Porous Media*. 2005
ISBN 1-4020-3864-X
126. H. Ding and W. Chen: *Elasticity of Transversely Isotropic Materials*. 2005
ISBN 1-4020-4033-4
127. W. Yang (ed): *IUTAM Symposium on Mechanics and Reliability of Actuating Materials*. Proceedings of the IUTAM Symposium held in Beijing, China, 1–3 September 2004. 2005
ISBN 1-4020-4131-6

Mechanics

SOLID MECHANICS AND ITS APPLICATIONS

Series Editor: G.M.L. Gladwell

128. J.-P. Merlet: *Parallel Robots*. 2006 ISBN 1-4020-4132-2
129. G.E.A. Meier and K.R. Sreenivasan (eds.): *IUTAM Symposium on One Hundred Years of Boundary Layer Research*. Proceedings of the IUTAM Symposium held at DLR-Göttingen, Germany, August 12–14, 2004. 2006 ISBN 1-4020-4149-7
130. H. Ulbrich and W. Günthner (eds.): *IUTAM Symposium on Vibration Control of Nonlinear Mechanisms and Structures*. 2006 ISBN 1-4020-4160-8
131. L. Librescu and O. Song: *Thin-Walled Composite Beams*. Theory and Application. 2006 ISBN 1-4020-3457-1
132. G. Ben-Dor, A. Dubinsky and T. Elperin: *Applied High-Speed Plate Penetration Dynamics*. 2006 ISBN 1-4020-3452-0
133. X. Markenscoff and A. Gupta (eds.): *Collected Works of J. D. Eshelby*. Mechanics and Defects and Heterogeneities. 2006 ISBN 1-4020-4416-X
134. R.W. Snidle and H.P. Evans (eds.): *IUTAM Symposium on Elastohydrodynamics and Microelastohydrodynamics*. Proceedings of the IUTAM Symposium held in Cardiff, UK, 1–3 September, 2004. 2006 ISBN 1-4020-4532-8
135. T. Sadowski (ed.): *IUTAM Symposium on Multiscale Modelling of Damage and Fracture Processes in Composite Materials*. Proceedings of the IUTAM Symposium held in Kazimierz Dolny, Poland, 23–27 May 2005. 2006 ISBN 1-4020-4565-4
136. A. Preumont: *Mechatronics*. Dynamics of Electromechanical and Piezoelectric Systems. 2006 ISBN 1-4020-4695-2
137. M.P. Bendsøe, N. Olhoff and O. Sigmund (eds.): *IUTAM Symposium on Topological Design Optimization of Structures, Machines and Materials*. Status and Perspectives. 2006 ISBN 1-4020-4729-0